Calculating Nature Naturally: Toward Quantum Simulation of Quantum Fields

Natalie Klco

A dissertation
submitted in partial fulfillment of the
requirements for the degree of

Doctor of Philosophy

University of Washington

2020

Reading Committee:

Martin J. Savage, Chair

David B. Kaplan

Stephen R. Sharpe

Program Authorized to Offer Degree:
Physics

University of Washington

Abstract

Calculating Nature Naturally:
Toward Quantum Simulation of Quantum Fields

Natalie Klco

Chair of the Supervisory Committee:
Professor and Senior INT Fellow Martin J. Savage
Department of Physics

Physics experiments are carefully designed to have precisely controlled inputs and to interact with an isolated aspect of nature in such a way that the results can be inverted to systematically inform our knowledge of the Hamiltonian of the universe. From the other direction, computation imprints the precisely-known isolated Hamiltonian of a distributed computational framework with a conjecture of the universe's Hamiltonian to calculate the physical implications of a proposed theoretical design. In this way, physics is able to connect theory and experiment, even in non-perturbative physical regimes eluding analytic solution. The recent emergence of experimentally controllable quantum systems inspires the possibility of dramatically altering the paradigm with which properties of quantum many body systems are calculated—employing quantum systems at the center of the precisely-known computational framework. Beyond intellectual entertainment, this proposal of leveraging quantum properties of entanglement, interference and superposition as advantageous computational resources illuminates the only currently envisioned avenue for calculating dynamical properties of large quantum systems.

The research presented in this dissertation contributes to the practical and conceptual formulation of quantum simulation for lattice field theories. Beginning in the scalar field, an explicit exploration is presented of the quantum resources required for digital time evo-

lution on a position-space lattice with varying digitization protocols. Using the ground state of the interacting scalar field as a ubiquitous example, techniques are developed allowing quantum operations for the preparation of entangled wavefunctions to exhibit the localization present in the exponentially localized correlations of the simulated field. Applying these techniques to lattices of large spatial volume provides a non-dynamical approach for initializing beyond-classical ground state wavefunctions informed by tractable classical calculations. Demonstrated on superconducting quantum circuits, simulations of dynamical quantum fluctuations in one-dimensional U(1) and SU(2) gauge theory are presented. Utilizing the recently developed quantum frequency processor, vacuum polarization due to external charges in U(1) gauge theory and the binding energy of light nuclei in pionless effective field theory are calculated. Error mitigation techniques for current hardware are further developed and applied to the state preparation of a wavefunction localized in Hilbert space with a symmetry-dominated entanglement structure. With the presented combination of field-inspired circuit design, quantum implementation of small gauge theories, and initial quantification of entanglement fluctuations in the scattering of low-energy nuclei, the research associated with this dissertation has developed practical techniques and long-term perspectives on the design of field theories for quantum simulation and vice versa.

TABLE OF CONTENTS

ACKNOWLEDGMENTS

Martin Savage: Through our interactions, we have discovered of a previously unknown fundamental symmetry of nature. This symmetry is not broken by quantum fluctuations. It is realized non-locally and is preserved independent of the presence of classical communication intended to break it. It has both plagued and enriched every exploration we have taken of the physical world. It has taught me more about myself than I had intended to learn. May we never grow to break this symmetry, but continue to develop techniques for thriving within and celebrating our symmetric world. Thank you for going on this research adventure with me, for setting high bars and supporting me to reach them, for demonstrating how to pursue big ideas with rigorous physics as a guide, and for sharing with me your perspectives and knowledge that will shape the rest of my life.

The odds are quite dismal, considering the billions of families on this earth, that my family would be the perfect one for me. And yet somehow this has happened [1]. It has been a blast and an honor to grow with this family. My father, Steve, who continues to demonstrate the power of research and a focused pursuit for knowledge, educating (and probably saving) us all with the explorations of his nights and weekends. My mother, JoEllen, who continues to be an inspiring role model in the hard sciences, cleverly brainwashed me at an early age to appreciate the beauty of mathematics, and continues to support my deep and sometimes-damaging passions from physics to music. I am grateful to my sister, Abigail, for trusting me to officiate her beautiful wedding and for tackling every big life milestone in bombastic, though infinitely controlled, succession allowing me to fly under the radar of conventional parental aspirations. More seriously, I am grateful to Abby, Brian, and baby Charlotte for

[1] Intentionally ignoring the role of extensive interactions at impressionable ages to keep the magic alive.

demonstrating how life can be lived so masterfully, even in a space that is so foreign to me. My team of uncles for painfully silly humor and powerful support. In particular, for Randy and Laura who exercise my explanatory skills from the curvature of spacetime to the double slit experiment and more globally encourage my humanity. Finally, Francisco who brought freedom and clarity before the pain.

My academic acknowledgements begin long ago, first distinguished by the existence and design of Pleasant View School for the Arts and the dedicated and innovative teachers who epitomized the program: including Samantha Burchfield, Jean Kefalidis, and Julie Werren (Filliez). From high school, I am grateful to Matt Brown and Ric Thompson for the zest of rigor they introduced to my scientific interests, to Jennifer Austin and Melinda Muzi for fostering a deep respect for words and language, and to Jack Elliott and Chris Irwin for....everything; for pushing me to master myself in every way with a friend as my guide. At Ohio University, the Honors Tutorial College was to me a haven for creative connections and consumingly focused intellectual experiences. I am grateful to Roger Braun, Leah Crosby, Andre Gribou, and the OU percussion studio for challenging my passions in dramatic, life-altering ways and continuing to be an endless source of artistic inspiration. I am forever indebted to the OU physics faculty among them David Drabold, Charlotte Elster, Ken Hicks, Peter Jung, Martin Kordesch, Madappa Prakash, Nancy Sandler, Eric Stinaff, Sergio Ulloa, and in particular Daniel Phillips for instilling in me a vision of what it means to be a physicist. I was fortunate to experience the intensity of this program with the classmates of Helen Cothrel, Taylor Grueser and Andrew Dewald and with the mentorship of Sean Krupa. In the latest chapter of my education at the University of Washington, I have been honored to become a part of the research community of physicists who call this institution home. I am grateful for David Kaplan; his unapologetic honesty frequently leaves me reflective and only occasionally disturbed—challenging me not only to become a deeper physicist, but a better overall representative of humanity. I am grateful for Silas Beane for his sharp perspectives

and his remarkable penchant for critically-timed guidance. Steve Sharpe for the artwork of his teaching, his mentorship, and for introducing me to the lattice. Kenny Roche for sharing his intensity and passion for the computation of nature. Further, my life has become indelibly marked by interactions with the UW physics community, including Boris Blinov, Steve Ellis, Dave Hertzog, Andreas Karch, Jerry Miller, Ann Nelson, Sanjay Reddy, and Devin Walker. I am grateful to have been a part of the thrilling intellectual environment of the Institute for Nuclear Theory and have greatly benefitted over the years from the support of thoughtful staff including Katie Hennessey, Catherine Provost, and Linda Vilett.

I am grateful for the friends I have met throughout this PhD journey. For the solidarity of my cohort and the support of my office mate, Jason Hempstead. For Mike Wagman and Dorota Grabowska for manipulating me into experiencing quantum field theory (QFT) in my first year and for demonstrating the simultaneous intensity and beauty of graduate school. Brandon Robinson, who became a good friend while guiding my introduction to QFT with clarity, perspective, and musical creativity. Mike Campbell and Derek Horkel for the late night QFT discussions around the refrigerator. Jesse Stryker for a multitude of interesting and supportive discussions in The Office. Jenny Lilieholm for enjoying 6 am quantum discussions, sharing with me the highs and lows of hunting ions, climbing mountains packing textbooks for the top, and for discussing quantum mechanics while practicing karate on the beach. Mike Smith for leading the DRiP program with me and for emanating a perpetual ascent towards greatness. Ting Lin for talking physics while working out, physicsing in parallel, and for being so completely himself. Lynn Bahrych for scrutinizing my explanations of quantum mechanics and for sharing with me the beauty of Osprey Pond and its community of visitors. I am grateful for Rebecca Woodgate, Ander Holroyd, and the UW bell tower for enlightening me to the world of change ringing and for educating my body and mind to perform and understand the governing aural mathematics.

I am grateful for recent collaborators represented by the publications associated with

this dissertation for a plethora of interesting discussions. In particular, Pavel Lougovski for perpetually fake-apologetically ambushing me with physics conversations. The research presented in this dissertation has further benefitted from conversations with Ramya Bhaskar, Stephen Jordan, Aidan Murran, John Preskill, Alex Shaw, Roxanne Springer, Nathan Wiebe, and the Microsoft Quantum Group. I am grateful to previous collaborators of the BUQEYE collaboration, Dick Furnstahl, Daniel Phillips, and Sarah Wesolowski for sharing with me their victories and precision of thought. Finally, I am grateful for and excited to join the global community of physicists who have created a welcoming and supportive environment throughout my travels, full of clever individuals excited to share their knowledge with young researchers. Looking back, it is clear that the giants having raised me by their height are numerous. I do not regard lightly the fortune of my interactions, and will forever cherish the opportunities I have had to share intellectual endeavours, from fascinations to obsessions, with breathtaking people.

Financially, work associated with this dissertation has been supported by the Institute for Nuclear Theory with DOE grant No. DE-FG02-00ER41132, Fermi National Accelerator Laboratory PO No. 652197, the U.S. Department of Energy, Office of Science, Office of Advanced Scientific Computing Research (ASCR) quantum algorithm teams program under field work proposal number ERKJ333 and quantum Testbed Pathfinder program under field work proposal number ERKJ335, the Aspen Center for Physics supported by National Science Foundation grant PHY-1607611, the ARCS (Achievement Rewards for College Scientists) foundation, and by a Microsoft PhD fellowship. This work has benefitted from the support of Travis Humble with the ORNL Quantum Hub and Donny Greenberg with IBM Q for facilitating access to IBM's superconducting quantum technology. Classical computations throughout this thesis have been implemented through Wolfram Mathematica and quantum circuits were typeset using the latex package Qcircuit, originally developed by Bryan Eastin and Steven Flammia.

DEDICATION

..to the world as it could be..

Chapter 1

INTRODUCTION

1.1 Informal Introduction

We are living on a complexity frontier. Broad aspects of scientific discovery are currently being limited by an inability to calculate and understand properties of strongly-correlated quantum many-body systems. Inspired by recent experimental progress, scientists from many disciplines—all areas of physics (high energy, condensed matter, nuclear, experimental, theoretical), computer scientists, chemists, engineers, mathematicians—are coming together to see whether a shared vision of the future can be made into a reality. This vision is the processing of information quantum mechanically.

What draws scientists like me to this vision is the realization that many of our open, grand challenge problems are hard. And not just hard in the sense that can be handled by brute force and a couple of PhD cycles, but non-perturbative and exponentially demanding in the classical computing resources necessary to address them. This is not to say that we are not learning things—e.g., many-body methods and lattice QCD have taught us much about the structure of the hadrons, light nuclei and particle interactions—there is real value and knowledge to be gained by pushing these barriers classically. But the fight is always against an exponential barrier: exponential barriers in the number of particles present and exponential barriers when introducing a chemical potential or a matter/anti-matter asymmetry that produces a sign problem fooling clever tricks of Monte Carlo sampling.

The audacity of computing the universe from first principles is forcing us to reflect and acknowledge something fundamental. That these exponential barriers largely exist because, at a basic physical level, we're doing it wrong. By "it", I mean nature. Doing nature wrong. We are contorting nature to be represented in a way that we know to be unnatural. And we

know this simply by the basic realization that every complete description of quantum mechanics thus far devised requires exponential memory to represent in a classical computer. If I limit it in some significant ways, I can get it down to a nice polynomially scaling theory, but we have learned over the years that those features that make the spaces grow exponentially are essential to realize this theory's impressive agreement with experiment. Every particle in the universe really does seem to require its own Hilbert space, and entanglement among these vector spaces is non-negotiable.

So the question becomes, how do we calculate more naturally? By providing the computer with an example of the quantum world can I do better? And the answer, theoretically, is yes. Improvements do exist. In contrived problems but also in very natural problems like the scattering of wave packets in an interacting scalar field where a scheme has been devised that requires only polynomial quantum computational resources—polynomial in the number of particles, the precision and the energy of the scattering process at both strong and weak coupling. Now the question is whether we can make such advantages real. And the community is well on its way to doing that with recent experimental developments in this area—experimental evidence for supremacy in the arena of random circuits and evidence of reaching thresholds in qubit design necessary for error correction on trapped ion systems.

So, if I am providing my computational framework with a piece of the quantum world, how much of the quantum world need I provide? How must it be connected and manipulated? Quantum computers will need to be married to large classical computing resources to organize the control and manipulation; how large? Where is the line between the quantum and classical computers? This is application specific. When simulating fields for particle interactions, does the entire field need to be stored in or represented with the quantum system? How can the quantum properties of entanglement, interference, and superposition be used to redesign the way we think about and conduct our calculations? These are some of the questions currently driving this field forward.

So, inspired by experiment, scientists are coming together with a shared vision of the future. This vision is the processing of information quantum mechanically, with expected

non-perturbative impact on the capability of calculating and simulating quantum many-body systems from molecules to nuclei. The content of this dissertation contributes to early demonstrations and considerations for simulating quantum field theories with the use of quantum devices.

1.2 Introduction

Since the early days of computational development, curiosities have grown about the relation between computation and physics—both how the laws of physics limited computational capacity and how computational design could inspire the development of physical law [1, 2, 3, 4]. For the simulation of physical systems, this meant considering how discrete computational architectures could be made compatible with observations of continuous symmetries, how finite computational resources could be made compatible with expectations of infinite precision or exponentially growing information, and how reversibility in the laws of fundamental particles could impact the design of computational architectures.

In a unique perspective, information can be conceived as more fundamental than energy and matter—rather than perceiving the electrons and quarks as fundamental, these consist of binary units of information. And at the most basic level of complexity, an information process runs what we think of as physics. Fredkin developed this perspective in the mid-1950s, when he found himself at MIT Lincoln Labs down the hall from IBM's most powerful computer at the time, freshly installed, and himself with a great deal of intellectual and temporal freedom. With these circumstances, he became a unique person with a deep interest in first principal physics who also had an unbridled, intimate computing experience. It was in this time that he developed a world view incorporating the discretization of spacetime, demands on nature such as "a finite volume of space should contain a finite amount of information", and the idea that "the dynamics of physical reality will be ultimately better captured by a single recursive algorithm [such as a cellular automata] than by the mathematics of conventional physics" [5].

In the early 1980s came some further creative thoughts on computation and the simu-

lation of nature. Paul Benioff reformulated the standard Turing machine as a device that evolves under Schrödinger time evolution [6]. In this quantum Turing machine, the tape is represented by a finite lattice of quantum spin systems and the computation process is described by a pure state evolving under the action of a given Hamiltonian. At pre-determined points in time, the wavefunction of the system would snap into states that exactly coincide with the states of a Turing machine subject to various classical instructions. This creation was motivated by the realization that some simple quantum mechanical lattices were capable of modeling complex systems, so why not design a quantum mechanical lattice to model the complex system of computation? As such, Benioff devised a way that classically understood computing could progress reversibly through unitary dynamics subject to the laws of quantum mechanics.

About a year later, Feynman transforms these simmering ideas into what is now considered to be the first vision of a true quantum computer [7]. Rather than quantum dynamics designed to snap periodically into basis states to agree with a classical Turing machine, this vision of Feynman's is that the system can evolve, superposition states galore, with interference and entanglement as features of the simulation that are much more natural to describe with the quantum world than the classical one. At this time, Feynman had recently spent a year interacting with a researcher on sabbatical at Caltech as a Fairchild Distinguished Scholar, Dr. Ed Fredkin, sharing his view that the universe may be more naturally described as a computation, evolving step-by-step creating complex dynamics out of simple local rules. Inspired by his interactions, Feynman bolstered the perspective with quantum mechanics and constructed an inspiring prospect of fundamentally changing the way we think about calculating properties of nature. In this way, he envisions a path forward for the quantitative analysis of quantum many body systems with resources that scale with only the volume of the system. And this possibility hinges on the *mutual intersimulatability* of quantum systems—that "with a suitable class of quantum machines [perhaps with a single class incorporating a single universal quantum machine] you could imitate any quantum system, including the physical world" [7].

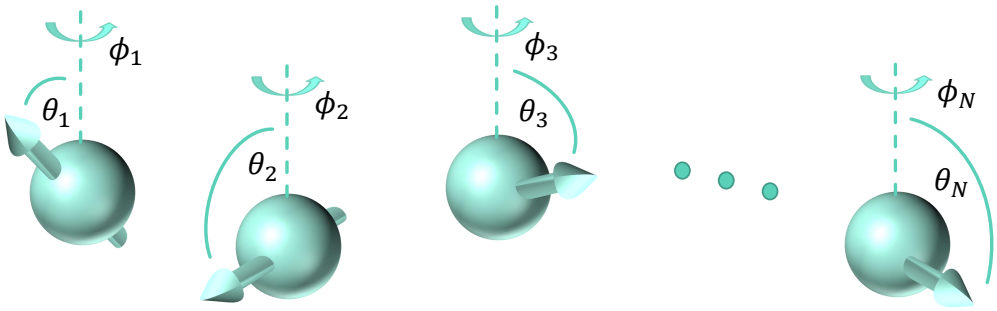

Figure 1.1: A collection of *independent* qubits with quantum state parameterized by polar and azimuthal angles for each qubit.

In order to leverage quantum systems for the digital simulation or calculation of properties of other quantum systems, it is convenient to first mechanise the quantum world. This is conventionally done through the ubiquitous two-state quantum system. When such a two-state system is physically controllable and manipulatable, it is bestowed with the computationally-inspired name of *qubit*. All possible pure-state superpositions of the two states of a qubit can be accurately visualized as living on the surface of a sphere with state (or coordinate) described by a polar angle and an azimuthal angle as shown in Fig. 1.1. At the poles are the basis states designated zero and one such that the state of each qubit can be parameterized as

$$|\psi\rangle = \cos\frac{\theta}{2}|0\rangle + e^{i\phi}\sin\frac{\theta}{2}|1\rangle \quad . \tag{1.1}$$

Measurements are projective and probabilistic such that a state at the equator corresponds to a 50% probability of measuring the qubit in either of these basis states when measured in the z-basis. Adding more qubits, each described by two angles, produces a collection of *independent* qubits as shown in Fig. 1.1. In defining this collection of independent qubits, $2N$ real numbers are necessary, two for every qubit and thus a linearly growing cost for defining the state of the system. However, in nature, there exists correlations. And in particular, such a strong correlation can be created that the state of one quantum object is completely determined by the state of another. This is not a rare scenario, it occurs anytime a particle

decays in the presence of a conserved quantity. For example, if two decay products are known to have originated from a spin 0 particle, measurement of the spin state of one final state particle determines the necessary spin state of the other. The physical definition of this use of "determines" needs to be made more concrete, how should such correlations be described? A tempting answer is with the simple states

$$|01\rangle \qquad \text{or} \qquad |10\rangle \quad . \tag{1.2}$$

These states are easily seen to produce the observed perfect anticorrelations when measured in the z-basis described above. However, there is an alternative to consider: one can break the tensor product structure and write states that are true inhabitants of the higher dimensional Hilbert space of the quantum system as a whole. In this case, the consideration is for a state of the form

$$|\psi\rangle = \frac{|01\rangle + |10\rangle}{\sqrt{2}} \quad , \tag{1.3}$$

which cannot be written as a tensor product state of two *independent* qubits

$$|\psi\rangle \neq |\psi_1(\theta_1, \phi_1)\rangle \otimes |\psi_2(\theta_2, \phi_2)\rangle \quad . \tag{1.4}$$

States that cannot be written in the form of a tensor product of their basic quantum constituents are called *entangled*. As such, Fig. 1.1 depicts a parameterization of all *unentangled* states. The entangled state of Eq.(1.3) clearly produces the observed anticorrelations when measured in the z-basis, but is it necessary? This question attempting to avoid the inclusion of states such as these in our quantum mechanics is asked reluctantly for two reasons. First, its inclusion raises the original intellectual concerns of quantum mechanics regarding the violation of locality [8], that the state of a quantum particle can be dependent on the state of a second quantum particle even when the two are separated at macroscopic distances. Second, inclusion of states such as these raise practical concerns of computability as they require working with an expoenentially growing Hilbert space with the number of qubits. This necessity of entangled states was the question posed to the universe in a cleverly designed, experimentally accessible inequality [9, 10]. The realization was made that, while these two

representations are indistinguishable when measured in the Z-basis, they are distinguishable when measured in a second, non-commuting basis. By combining measurements in a variety of bases, a clear distinction could be made between classically correlated unentangled states and quantum mechanically correlated entangled states. While there are valid reasons not to include entangled states for human comfort, nature demands them. By now, the experimental observation of Bell's inequality violation has been observed numerous times, recently between two photons distributed via satellite [11, 12, 13, 14, 15, 16, 17, 18]. And the answer every time (and maybe the universe is getting annoyed at our repetition) is yes. Entangled states with built-in quantum correlations are necessary. And once they are included, the full exponentially growing Hilbert space of quantum mechanics is necessary. So to represent a state of N qubits, rather than the $2N$ real numbers for *independent* qubits in Fig. 1.1, an arbitrary quantum state is a vector in 2^N dimensional Hilbert space and defined by 2^N complex numbers (up to normalization and a global phase).

Beyond the dramatic scaling of information necessary to define entangled wavefunctions, it is worth appreciating the novel distribution of that information. In evaluating the information (quantified as the deviation of the entanglement entropy from its maximal value) contained within a subsystem of an average quantum state, it is found that the information decreases exponentially in the size (e.g., number of qubits) of the quantum system [19] for a fixed subsystem-to-system ratio. Average classical information storage techniques do not present this property. Gaining access to a third of an average (roughly homogeneously structured) classical database is expected to provide roughly one third of the stored information. This fundamental observation of rapidly vanishing information in subsystems demonstrates how quantum information cannot be consistently considered a local property of a wavefunction, but rather is stored non-locally in the correlations between local subsystems. While this delocalization can be imagined useful for protecting quantum information from local noise sources (able to access only approximate mixed states carrying little of the stored information), reliably manipulating and translating this type of distributed information remains an area of active research.

It is sensible to pause for a moment to consider the implications of this conclusion on universal scales—that it requires an exponentially growing number of complex numbers to describe the state of a system in the quantum mechanical Hilbert space. Imagine first a computational scheme to store and manipulate each of those complex numbers, as is often the case in the classical simulation of dynamical quantum systems. For a moment, humour the bold (and also wrong, but wrong in a way that underestimates the necessary resources) claim that one of these complex numbers could be stored on each of the fundamental particles—every electron, every photon, every neutrino etc., stores a complex number. Designed in a computational framework of this type, the collection $\sim 10^{100}$ fundamental particles in the universe would be capable of representing the quantum wavefunction of only ~ 300 qubits. In smaller units, the complex numbers defining the wavefunction of 50 qubits quickly reaches petabyte scales of memory, demanding modern high-performance computing architectures just to store the quantum state. This is even before any time evolution or calculation is performed. In a classical approach to quantum systems, a large portion of the universe is required to calculate properties of an infinitesimal version of itself, an arguably unnatural representation of nature. While it is interesting at a basic level to think about redesigning calculations of subatomic systems to be implemented on quantum devices, the motivations are deeper—this complete reformulation seems fundamentally necessary if the level of control and understanding of large quantum many-body systems appearing in long-range plans across the sciences is to be achieved. Simply, the computational capacity of the universe is remarkably different when that universe is governed by quantum, rather than classical, laws.

Encouragingly, it is not always necessary to simultaneously represent the entirety of a wavefunction to calculate properties of a quantum system. In particular, Monte Carlo methods, creating the foundation of successes in lattice QCD [20], allow importance sampling of gauge configurations in the calculation of field correlation functions. With these methods and their increasingly sophisticated evolutions, precise calculation of many properties of nature's diverse quantum systems can be achieved using classical computers. The upper limit of this category includes properties for which a viable computational path is fathomed, though chal-

lenges the limits of our computational capabilities. For an example of a perceived-attainable challenge, decades on classical exaflop (10^{18} floating point operations per second) computing environments are predicted to be necessary to achieve many near-term precision goals for predicting—directly from the interactions of quarks and gluons—observables relevant to upcoming experiments exploring nuclear electromagnetic distributions and three-body forces [21]. Unfortunately, some properties reside in a further category for which no viable path of computation is currently known. While the introduction of a quantum processing unit (QPU) will not provide a global solution for all properties in this latter category, it is reasonable to expect the quantum device to aid in the calculation of dynamical properties where exponentially growing portions of the Hilbert space become entangled.

The periodization of prehistoric chronology did not occur until the early 19th century as a museum organizational system. The Renaissance, between the 14th and 17th centuries, was not labeled for its historical importance until the late 19th century. While it is rare to be sufficiently self-aware to declare the historical significance of modern times, knowledgable extrapolations of scientific progress have envisioned the development of a disruptive technology. Considering now to be "the before" from this perspective, modern times have been named the Noisy Intermediate-Scale Quantum, or NISQ, era [22]. The NISQ era is characterized by the capability of controlling tens to hundreds of qubits that function with no mechanism to make them robust to faults or errors in the calculation. In this sense, the NISQ era is a time to develop both theoretical understanding and experimental techniques propelled by the availability of small systems to test ideas; it is not expected that quantum supremacy will be achieved for computations relevant to large-scale scientific application before high-fidelity and/or error-corrected devices become available. However, evidence for quantum supremacy in the specific olympian event of sampling random quantum circuits has already been established [23]. But while the transition boundaries are intellectually inspiring and vital in bringing a vision to a tangible reality—the first time the computer is faster than the humans with slide rules or the first time the plane leaves the ground further than the human can jump—the bulk that changes the world is not expected here in the NISQ-era.

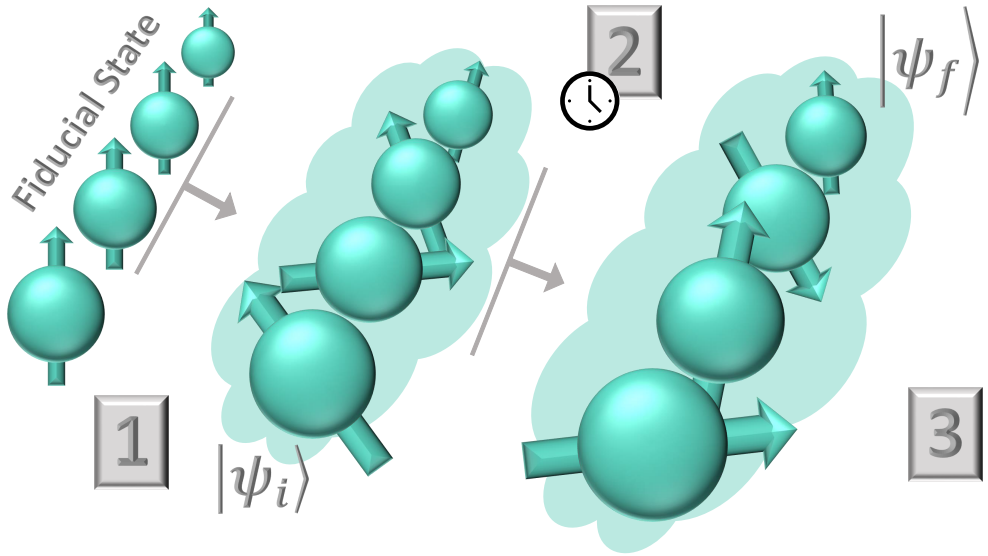

Figure 1.2: Abstraction of the three basic steps of quantum simulation: state preparation, time evolution, and measurement. These operations progress the computation from the basic fiducial state to the initial $|\psi_i\rangle$ and final $|\psi_f\rangle$ state of the simulated system.

As described in Fig. 1.2, there are three main steps in quantum simulation. The first, state preparation, takes a fiducial state of qubits naturally hardware accessible and creates an initial state relevant to the simulation. Usually, the fiducial state is chosen to be the state $|0\rangle^{\otimes n}$, an alternate basis vector, or a similarly simple state to initialize within the quantum hardware. The initial wavefunction may be the ground state of the theory onto which localized particle excitations are subsequently created, an excited state of the theory, or may be an excited state of the microscopic degrees of freedom expected to fragment and produce macroscopic excitations under time evolution. In the former two scenarios, the initial wavefunction to be prepared is likely to be highly entangled. The process of state preparation has been identified as the step with dominant resource costs for simulating scattering in scalar quantum field theory[24, 25]. This result is expected to be qualitatively representative of resource estimates for the quantum simulation of more complex field theories. As such, a

substantial portion of the research discussed in this dissertation (Chapters5, 6, and 7) focuses on the initialization of ground state wavefunctions, leveraging their locality and entanglement structure.

Abstractly, the preparation or initialization of a quantum state onto a quantum register can be expressed as the design of a quantum operator, U, with the desired wavefunction residing in the first column

$$U|0\rangle^{\otimes n} = |\psi\rangle \qquad U = \begin{pmatrix} \begin{pmatrix} \\ \psi \\ \\ \end{pmatrix} & \begin{pmatrix} \\ ? \\ \\ \end{pmatrix} & \cdots & \begin{pmatrix} \\ ? \\ \\ \end{pmatrix} \end{pmatrix} \quad . \tag{1.5}$$

The notation of U has been chosen to indicate the unitary property of this operation, not its uniqueness—the evolution from fiducial state wavefunction to initial simulation state wavefunction can be done in an infinite number of ways. With this flexibility comes an opportunity to design the state preparation protocol leveraging physical properties and energy scales of the simulated system.

Just as is the case in the classical exploration of quantum many-body systems, the ability to prepare cost-efficient approximations to wavefunctions of interest is valuable. Such approximations may be used to study the sensitivity of observables to wavefunction deviations while maintaining key features, to controllably begin a calculation for later refinement (e.g., by subsequent quantum phase estimation relying on a non-vanishing initial overlap), or to reduce computational overhead when higher accuracy is made irrelevant by other contributions to the uncertainty floor (e.g., the presence of mitigated hardware noise). There is no reason to hire a professional musician if the amplification system convolves their art with uncontrolled waveforms. In Chapter 7, as presented in Ref. [26] associated with this dissertation

> Natalie Klco and Martin J. Savage. "Minimally-Entangled State Preparation of Localized Wavefunctions on Quantum Computers". *Phys. Rev. A* 102.1 (2020), p. 012612. DOI: 10.1103/PhysRevA.102.012612. arXiv: 1904.10440 [quant-ph]

resides a demonstration preparing a small localized wavefunction on superconducting qubits. The localization present is in the binary-interpreted Hilbert space, similar to the localization seen in the ground state of the massive scalar field when digitized in the basis of position-space field eigenstates. Beyond the scalar field, such Hilbert space localization can be seen in gauge fields near strong coupling when digitized in the basis of electric eigenstates or at weak coupling when digitized in the basis of magnetic eigenstates. Though basis dependent, it is natural to find a hierarchy within Hilbert space.

A natural question to ask then in the framework of digital quantum computation is whether an inexpensive method exists to prepare a wavefunction with local support in the Hilbert space. Inexpensive is here referred to in terms of the digital quantum gate resource requirements. It is found that such localization cannot be achieved without entangling operators on the quantum register. However, using the minimum number of entangling operators necessary to entangle all qubits into the global wavefunction, it is found that a wavefunction can be created that is exponentially localized in the binary-interpreted Hilbert space. Not only useful for its potential application to the noisy simulation of lattice fields, the initialization of this localized wavefunction provides a means of practically quantifying hardware errors, isolated between single- and two-qubit rotations, in terms of wavefunction asymmetries. This use has been here demonstrated both to improve single-qubit rotations *in medium*, where the medium is considered to be an intermediate wavefunction of the quantum calculation, and as a monitor of the two-qubit entangling operations. When interspersed with a calculation of interest, these state preparations provide temporally correlated calibration information to track fluctuations of the quantum device with time, allowing for more informed data analysis of device measurements in the NISQ-era.

In Chapters 5 and 6, a new circuit structure is presented and utilized for initializing the ground state of a non-interacting and interacting scalar field as presented in Ref. [27] associated with this dissertation

> Natalie Klco and Martin J. Savage. "Systematically Localizable Operators for Quantum Simulations of Quantum Field Theories". *Phys. Rev. A* 102.1 (2020), p. 012619.

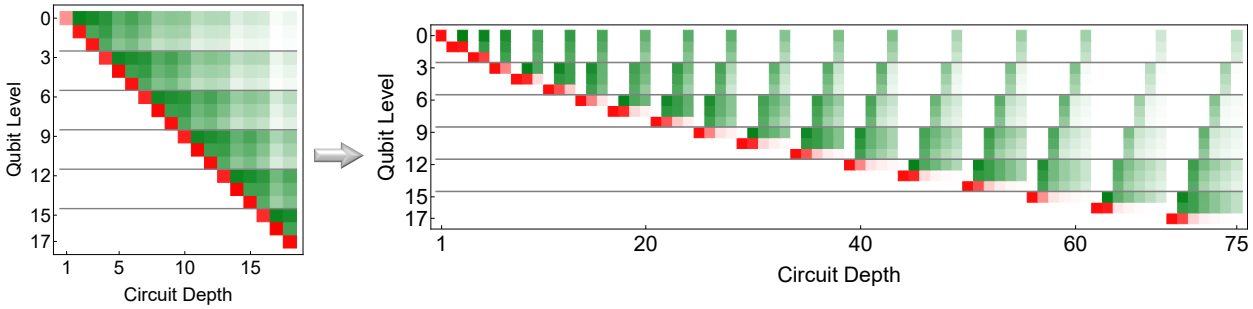

Figure 1.3: Diagram of a quantum circuit transformed to be spatially-localized. The red squares indicate the placement of a vector of y-axis rotation operators with shading dictated by the maximum value of the rotation angle. Green squares vertically above a rotation operator indicate the associated control on previous qubits with shading dictated by the average sensitivity of the rotation angles to that control. Angles for this demonstration are calculated from a free scalar field with open boundary conditions, with mass $\hat{m} = 0.3$, field truncation $\phi_{\max} = 3.5$, number of sites $N = 6$, and qubits digitizing each site $n_Q = 3$.

DOI: 10.1103/PhysRevA.102.012619. arXiv: 1912.03577 [quant-ph].

The notable property of this circuit structure is its ability to manifest the localization present in the simulated field as physically localized quantum operators. While this capacity for localization begins with initial decisions in the assignment of hardware Hilbert spaces to Hilbert spaces of the field creating spatially localized quantum correlations on the quantum hardware, many generic circuit approaches for initialization are unable to leverage this property of wavefunctions.

Shown pictorially in Fig. 1.3 is an example of the hardware manifestation of localized correlations of the simulated field. This figure describes the structure of two quantum circuits (left and right) for preparing the ground state of the free scalar field with open boundary conditions, mass of 0.3 in lattice units, and a field space truncation of 3.5. Three qubits are used to digitize the field at each of six spatial lattice sites. These qubits are labeled 0-17 with the three-qubit lattice site structure depicted with gray horizontal lines. Each column

in these diagrams contains information on a set of quantum gates to be implemented. Every quantum gate used in this example has the same form: a single qubit rotation (red blocks) about the y-axis acting in a particular Hilbert space of the previous qubits (green blocks) i.e., "controlled" on the previous qubits. Every specific Hilbert space of the control qubits may come with a different rotation angle on the target qubit. Thus, the last column of the left hand circuit depiction at circuit depth 18 represents information of 2^{17} different rotations acting on qubit 17 given different configurations of qubits 0-16. Note, importantly, that the circuit depth index on the x-axis is not linear with the number of quantum gates in the circuit as each column represents the presence of 2^h quantum gates, where h is the number of controls on the operator. The red squares located on the target qubit have a shading that is controlled by the average angle of the 2^h rotations represented in the column. The green squares indicate the presence of a control and are shaded by the average difference of angles in the collection associated with Hilbert spaces differing only in the value of this control. In this way, the shading of controls indicates their relative importance in modifying the angle acting on the target qubit. For example, if a rotation is associated with completely unshaded (white) controls, the angle is independent of the control qubits and thus the rotation is effectively an SU(2) operator acting solely in the Hilbert space of the target qubit.

On the left, it is seen that controls exhibit a hierarchy with controls close to the target qubit playing a role of increased importance compared to more distant control qubits. This feature is a direct result of the choice to digitize the field in the basis of field eigenstates on a spatial lattice (see Chapter 3 for further detail). Because this local information is present in every column of the circuit, it is not surprising that the average angle (depicted by red squares) in each collection of quantum gates is of approximately the same magnitude. This would indicate that e.g., all 2^{17} quantum gates associated with the last column are equally important, though it is clear that their controls are not. To address this imbalance, the circuit on the right has been designed using a simple transformation of each circuit element on the left. Each column is expanded, isolating relevant rotations to capture local correlations. The 2^{17} rotations at circuit depth 75 are still present in the circuit, but now are associated with

target rotation angles (depicted by red squares) that are exponentially suppressed in the lattice distance of the quantum gates, reflecting the similar exponential suppression of the site-wise correlations in the scalar field.

The main result of the research presented in Chapter 5 is a proof of principle that physical properties of the simulated field (demonstrated by, but not limited to, the property of localized correlations with the mass of the lightest particle) can be advantageously leveraged for the design of quantum simulations for hardware implementation. These results are inspiring for their clear application to interacting field theories and those with more complex group structure; excitations localized in Hilbert space is a common property of gauge theories when expressed in natural bases, even at strong couplings. In Chapter 6, presenting the work of Ref. [28] associated with this dissertation

> Natalie Klco and Martin J. Savage. "Fixed-Point Quantum Circuits for Quantum Field Theories" (Feb. 2020). arXiv: `2002.02018 [quant-ph]`

it will be shown how this localization leads to a convergence of circuit elements in the bulk of a translationally invariant field, forging a path by which classically tractable calculations may be leveraged to initialize classically intractable quantum simulations as an alternative to adiabatic methods requiring dynamic evolution.

The feasibility and efficiency of the second step of quantum simulation shown in Fig. 1.2, time evolution, is the main feature driving interest in quantum simulation across subatomic physics. The basic process of time evolution for a time-independent Hamiltonian evolves the initial quantum state to the final quantum state with a propagator of the form $U = e^{-i\hat{H}t}$. As this operator may not be readily available among the natural operations on quantum hardware, it is commonly broken apart into a series of simpler operations and performed sequentially

$$e^{-i\hat{H}t} = \lim_{N_{\rm Trot}\to\infty} \left(e^{-iH_1 \frac{t}{N_{\rm Trot}}} e^{-iH_2 \frac{t}{N_{\rm Trot}}} \cdots e^{-iH_M \frac{t}{N_{\rm Trot}}} \right)^{N_{\rm Trot}} \tag{1.6}$$

$$\approx \left(e^{-iH_1 \frac{t}{N_{\rm Trot}}} e^{-iH_2 \frac{t}{N_{\rm Trot}}} \cdots e^{-iH_M \frac{t}{N_{\rm Trot}}} \right)^{N_{\rm Trot}} + \sum_{i<j} [H_i, H_j] \frac{t^2}{2N_{\rm Trot}} + \mathcal{O}(t^3) \quad . \tag{1.7}$$

Due to the non-commuting nature of terms within a non-trivial Hamiltonian, this process produces errors scaling with the temporal extent of the time propagation. To combat this systematic error, the full time evolution is broken into small steps with the systematic error polynomially suppressed as the number of steps is taken to infinity. This process is known as Trotterization and each small time step of the propagation known as a Trotter step [29]. Time evolution using this method in one spatial dimension of U(1) and SU(2) gauge theory has been implemented on superconducting qubits in Refs. [30, 31] associated with this dissertation and presented in Chapters 8 and 9

> N. Klco et al. "Quantum-classical computation of Schwinger model dynamics using quantum computers". *Phys. Rev. A* 98.3 (2018), p. 032331. DOI: 10.1103/PhysRevA.98.032331. arXiv: 1803.03326 [quant-ph]
>
> Natalie Klco, Jesse R. Stryker, and Martin J. Savage. "SU(2) non-Abelian gauge field theory in one dimension on digital quantum computers". *Phys. Rev. D* 101.7 (2020), p. 074512. DOI: 10.1103/PhysRevD.101.074512. arXiv: 1908.06935 [quant-ph].

This method of time evolution is not unique to quantum simulation and is commonly used throughout the exploration of many-body quantum dynamics. Of the developing number of post-Trotter techniques for implementing Hamiltonian dynamics on quantum hardware [32, 33, 34, 35, 36], Trotterization is unique in requiring zero auxiliary qubits.

When interactions in the Hamiltonian are local, as is the case for most physically relevant lattice Hamiltonians, Trotterized quantum simulated time evolution exemplifies an alluring property: the computational time necessary to simulate time evolution scales linearly with the temporal extent of the simulation and explicitly does not scale with the size of the system [37]. These two features abide by Feynman's vision of simulating physical systems with computational resources scaling only with the spacetime volume captured in the simulation [7]. Considering a macroscopic perspective of time evolution, it is quite natural that the passage of time does not scale with the sample of space under observation. Naturally, the information content and thus the computational capacity of a portion of nature may

be expected to be in linear relation to its spacetime extent. However, this efficient relation cannot be achieved in representations of quantum dynamics on classical computing architectures as the Hilbert space and time evolution operators grow exponentially—requiring the coordination and communication of exponentially growing hardware frameworks pushing the limits of technology currently culminating in exascale computing.

To see that the spacetime claim of the previous paragraph is reasonable, consider the time evolution of a Hamiltonian with nearest neighbor interactions. Upon Trotterization, as described in Eq. 1.7, each Trotter step is comprised of sequential evolutions for each neighboring pair of sites. Commutativity at distances beyond the interaction allow parallelization of half of the operators. The second half can then be implemented in a second sub time step. As a result, the clock time of a single Trotter step is independent of the spatial volume and set by the non-locality of the interactions. This process is pictorially represented in Fig. 1.4. Each site may be a single qubit, as in the case of a spin system, or collection of qubits, as in the case of the scalar field. The colored bands represent localized laser pulses that may be used to produce the local unitary time evolutions. One pair of the left and right pulses shown in this figure constitutes a single Trotter step. For a physical implementation such as the laser system inspiring this picture, it is reasonable that the time required to implement this Trotter step scales as $\sim 2\frac{t}{N_{\text{Trot}}}$, with the factor of 2 associated with parallelizability and thus the distance of the interaction. For a system with distance-3 interactions, the time required to implement the Trotter step scales as $\sim 3\frac{t}{N_{\text{Trot}}}$, etc. To maintain a constant precision on the time evolution operator focusing on the leading Trotter error, the number of Trotter steps must scale as $N_{\text{Trot}} \sim \frac{Vt^2}{2\epsilon}$, where the sum of Hamiltonian commutators produce a volume factor by locality. While the number of Trotter steps scales with the volume, their duration for a fixed t scales inversely with the volume leaving the complete time evolution to be volume-independent. Similarly, the quadratically scaling Trotter errors and linearly suppressed Trotter time step leads to the above claim that the time-to-completion for a real time evolution of a local Hamiltonian scales only with the temporal extent of the simulation. Note that, if the locality constraint is lifted, the depth of the single trotter step naïvely begins

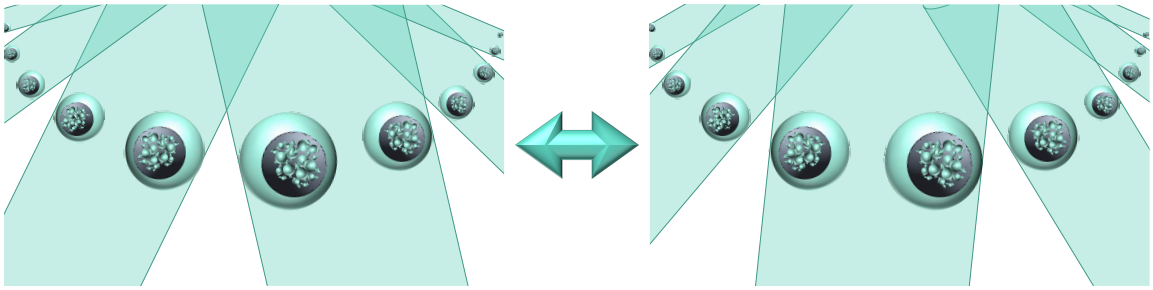

Figure 1.4: Abstract depiction of the implementation of parallel time evolution operators for the Trotterized time evolution of a nearest-neighbor, local lattice Hamiltonian. All interactions are implemented in a process of depth two.

scaling polynomially with the volume to a power controlled by the number of bodies present in Hamiltonian interaction terms with possible polynomial improvements [38]. While these scalings for quantum simulation are theoretically inspiring, it remains an active research goal to realize this scenario on physical quantum hardware.

The third step of quantum simulation shown in Fig. 1.2, measurement, is naturally sensitive to the quantity being measured. To emphasize the current flexibility of quantum simulation design, note that even this basic assumption is currently being challenged with ideas for learning a classical "shadow" or classical representation of a quantum state capable of contributing to the knowledge of a range of observables chosen after interaction with the hardware, rather than before [39, 40]. The design of quantum measurements focuses on extracting information. If that information is dispersed across a large Hilbert space or distributed between multiple bases, the number of measurements needed to obtain a precise answer may grow unfavorably. An example of this difference with respect to operator basis will be seen in Chapter 10 where the measurement of the SU(2) electric plaquette expectation value is better statistically conditioned than its magnetic counterpart living in the conjugate basis where the gauge invariant space becomes delocalized in the Hilbert space. To avoid the signal to noise problems associated with diffusion of the probability distribution over an exponentially large space, it is often advantageous to confine measurement to a single qubit.

Figure 1.5: Basic circuit techniques for measuring inner products, matrix elements and expectation values of unitary operators through entanglement of an auxiliary qubit.

Some standard techniques [41] for doing so are shown in Fig. 1.5. Using the left circuit in which two quantum states are conditionally swapped depending on the state of the auxiliary qubit, the probability of measuring the auxiliary qubit to be in the computational $|0\rangle$ state is made to reflect the inner product

$$P(0) = \frac{1 + |\langle\psi_1|\psi_2\rangle|^2}{2} \quad . \tag{1.8}$$

In this manner, matrix elements of operators can be calculated as long as the two states in the transition can be prepared and the operator can be implemented quantum mechanically. The latter requirement is commonly achieved for Hermitian operators by calculating their unitary decompositions (e.g., in the Pauli basis) and combining the results of ensemble measurements in multiple bases. For diagonal matrix elements, the circuit may be implemented with only a single copy of the wavefunction as shown at right. Ensemble measurement of the auxiliary qubit is equivalently calculated to produce

$$P(0) = \frac{1 + \Re\langle\psi|U|\psi\rangle}{2} \quad , \tag{1.9}$$

where the imaginary part can be calculated through the introduction of an S phase gate. With these basic techniques, for example, vacuum correlation functions of a field could be calculated with an ensemble of vacuum-initialized quantum states each paired with a single auxiliary qubit. Further success has been achieved measuring observables non-linear in the density matrix, such as the entanglement entropy, through interference of individually prepared copies of the quantum state [42, 43]. With the close connection between quantum

simulation and interferometers [44], the processes of initialization, evolution, and measurement demands a high-dimensional organization of interference effects.

The three steps for quantum simulation outlined above are not independent. In particular the three are intimately linked by the choice of basis, or representation of the simulated field. An explicit example of such connection has been explored for the scalar field in Chapter 3 following Ref. [45] associated with this dissertation

> Natalie Klco and Martin J. Savage. "Digitization of scalar fields for quantum computing". *Phys. Rev.* A99.5 (2019), p. 052335. DOI: 10.1103/PhysRevA.99.052335. arXiv: 1808.10378 [quant-ph].

In particular, the way that degrees of freedom of the simulated field are distributed within the qubit Hilbert space impacts the computation at all levels. For example, when representing a free scalar field through oscillators on a momentum-space lattice, as is common for perturbative theoretical calculations, preparing the ground state wavefunction becomes simple; the ground state is a tensor product of harmonic oscillator ground states requiring no entanglement between oscillators. The initialization can be further simplified when the field is digitized in the fock basis of oscillator excitations such that the ground state is not only a tensor product state, but a single state, $|0\rangle^{\otimes n}$ in the computational basis. However, state preparation is only the first step of quantum simulation—the effects of field representation should be considered also on time evolution operators. When latticized with momentum-space oscillators, interactions present in the Hamiltonian, while conserving momentum, tend to be non-local in the oscillators. This is the case for a simple quartic interaction. In particular, oscillators of equal and opposite momentum may interact, producing a conglomerate of contributions to the time evolution operator that are not easily made simultaneously local from the perspective of quantum hardware. This simultaneous locality is, however, clearly achieved through the use of a spatial lattice [25, 24]. While the ground state structure in this basis is more complex, the advantages of a localized time evolution operator are significant, especially in light of the role the time evolution operator can play in adiabatic state prepa-

rations in addition to the simulation of real time dynamic processes. Further scrutiny of the fock space field digitization on a spatial lattice is addressed in Chapter 3. Furthermore, the distribution of entanglement represented by the physical qubits is sensitive to the choice of basis and can naturally impact the quantum resources necessary for simulation as demonstrated in Chapter 5. Becoming adept at designing quantum simulations of field theories with this interplay of quantum resources in mind has been a tangible goal of the research presented in this thesis.

The content of this thesis focuses on digital, rather than analog, quantum simulation. For classical technologies, analog solutions tend to be robust, reliable, and available historically earlier than their digital counterparts. A similar relation is expected for quantum technologies. In designing an analog simulation, a quantum system must be tuned to emulate the dynamics of interest, leaving the process of time evolution to be achieved through the natural time evolution of the hardware quantum system. However, restricting calculations to analog hardware is akin to restricting communication to the use of similes—always required to express ideas through their relation to other things. Digital systems enable the ability to say new things, independent from what has existed before. Rather than searching for ways to contort a quantum system to naturally have the same dynamics as e.g., lattcized quarks and gluons, digital technology allows unique choreography of dynamics. It is this flexibility and freedom that inspires the digital language used in this thesis. With its capability of capturing the dynamics of both frameworks, this language, and the style of thinking it inspires, is expected to encourage development of hybrid quantum systems—those combining multiple quantum architectures (potentially mixing both digital and analog) to leverage their unique strengths. A physical example that can be easily imagined is the use of different quantum architectures for the gauge field than used for the fermionic content of a field theory simulation. As the techniques of quantum simulation progress and expand in capability, periodically assessing the natural language used, scaling between the general framework of digital circuitry to hardware-efficient languages [46, 47] is likely to be advantageous.

A map organizing the research presented in this thesis is shown in Fig. 1.6. The three

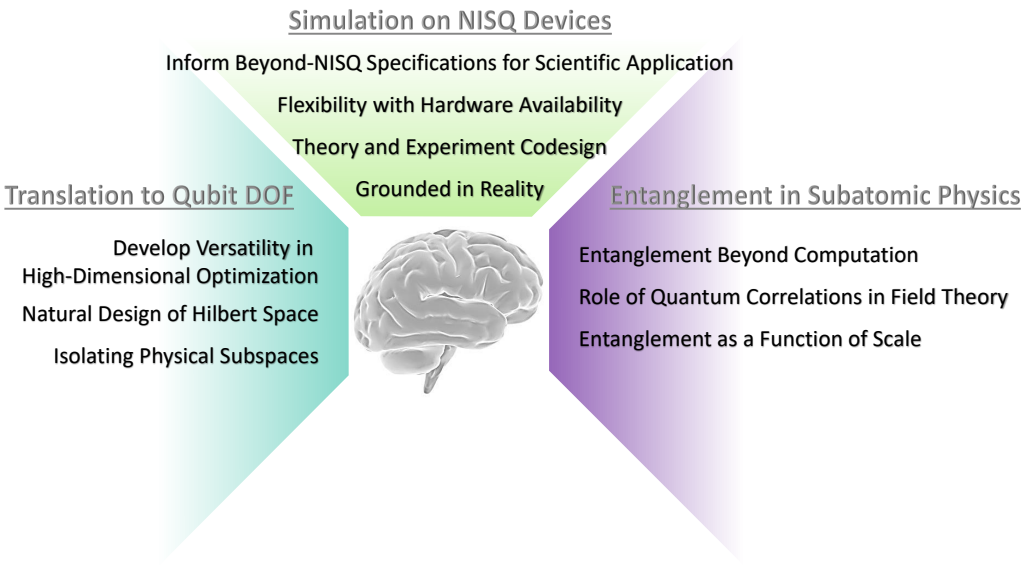

Figure 1.6: Mind map designating the three main pathways of the *quantum simulation for quantum field theory* research presented in this thesis. In clockwise order, the paths include the design of field theory qubit representations and their implications for required large-scale quantum simulation resources, near-term implementation of small field theories on quantum devices, and exploration of entanglement in the subatomic world regardless of the ability to leverage it for computational advantage. The publications presented for this thesis in these three categories are Refs. [48, 45, 27, 28], Refs. [30, 49, 26, 31], and Ref. [50].

paths are made distinct by their time scales of expected impact on the quantum simulation of field theories from the left clockwise as long-term, near-term and unknown term. The first category, the translation to qubit degrees of freedom, informs the long-term vision of this research. Building on the impact of Hilbert space structure on quantum simulation resource requirements discussed above, this avenue looks to design representations of quantum field theories for implementation on architectures not limited by presently available capabilities.

The second category, simulating small field theories on NISQ-era quantum devices, grounds this research in reality. While the idea of computing with quantum degrees of freedom is a fascinating construct that dramatically changes the theoretical computational capacity of the universe, the goal of this research is not only to marvel at the natural beauty, but to put it to work in calculating properties of nuclear many body systems. Towards this goal, interacting with experimentalists and testing algorithmic modifications to simulations on quantum hardware facilitates a process of codesign. Such interactions are of high importance for making strides within and beyond the NISQ-era as simulations must be both *flexible* and *guiding* with respect to hardware developments. The *flexibility* aspect involves the ability to translate simulations from one architecture to another between natural gate sets and potentially modifying the theory substantially to make simulated interactions compatible with natural features of the quantum device. A common example of this is the treatment of the gauge field in the Schwinger model which tends to be integrated out when working with trapped ions and retained when working on superconducting architectures. The *guiding* aspect associated with this codesign refers to the determination of necessary specifications or beneficial features of the hardware for simulating quantum fields of interest. Such considerations include qubit connectivity, native gate sets, dominant noise properties, ability to systematically control and mitigate sources of error, availability of robust Hilbert sub-spaces etc.

The third category, entanglement in subatomic systems, at its heart is a purely academic exploration of the role of entanglement in the structure of nuclei and in particle interactions. Along with growing experimental evidence for non-factorizability of parton distribution functions and maximally entangled features of proton structure, it is intriguing to consider the

transition of entangled microscopic degrees of freedom to hadronic interactions with suppressed entanglement fluctuations, as discussed in Chapter 11 and Ref. [50] associated with this dissertation

> Silas R. Beane et al. "Entanglement Suppression and Emergent Symmetries of Strong Interactions". *Phys. Rev. Lett.* 122.10 (2019), p. 102001. DOI: 10.1103/PhysRevLett.122.102001. arXiv: 1812.03138 [nucl-th].

In spite of its basic intentions, understanding the natural entanglement structure of such quantum systems is likely to aid in their future quantum simulation, as supported by Chapter 5 where localized correlations of the simulated field are leveraged to improve preparation of a ground state quantum wavefunction.

The organization of this dissertation begins with simulation of the scalar field in Part I dominantly addressing research interests of category 1. Part II dominantly addresses research interests of category 2, calculating time evolution and static properties in the Schwinger model and SU(2) gauge theory on superconducting and photonic quantum architectures. Part III dominantly addresses research interests of category 3 with an exploration of the role of entanglement in the symmetries of the low-energy scattering of nucleons.

The aspiration of simulating field theories on quantum devices is inherently multidisciplinary. As such, this dissertation presents a diversified trajectory toward developing tangible ways of efficiently quantumly calculating properties of highly-correlated quantum systems—a common feature of scientific grand challenges throughout subatomic physics. By developing theoretical flexibility to manipulate the structure of interactions and entanglement (both natural and synthetic) within a Hilbert space representing dynamical quantum fields, this research supports the expected necessity that successful applications of quantum simulation be codesigned in close coordination with the actively forming landscape of quantum technologies. The progress of this research is but a small contribution towards the larger goal of one day studying the emergent properties of quantum chromodynamics by emulating the interactions of quarks and gluons with controllable atomic-scale quantum architectures.

Chapter 2

THE LATTICE SCALAR FIELD

The content of this chapter is associated with Ref. [45]:

Natalie Klco and Martin J. Savage. "Digitization of scalar fields for quantum computing". *Phys. Rev.* A99.5 (2019), p. 052335. DOI: 10.1103/PhysRevA.99.052335. arXiv: 1808.10378 [quant-ph]

2.1 Lattice Scalar Field Theory with Qubits

The continuum Lagrange density describing the dynamics of a scalar field with self interactions, retaining only renormalizable terms in 3+1 dimensions, is

$$\mathcal{L} \;=\; \frac{1}{2}(\partial_\mu\phi)^2 - \frac{1}{2}m^2\phi^2 - \frac{\lambda}{4!}\phi^4 \quad , \tag{2.1}$$

with a Hamiltonian density of

$$\mathcal{H} \;=\; \frac{1}{2}\Pi^2 + \frac{1}{2}(\boldsymbol{\nabla}\phi)^2 + \frac{1}{2}m^2\phi^2 + \frac{\lambda}{4!}\phi^4 \quad . \tag{2.2}$$

The conjugate momentum operator, $\Pi(\mathbf{x})$ has the standard equal-time commutation relation with the field operator, $[\ \phi(\mathbf{x}), \Pi(\mathbf{y})\ ] = i\delta^3(\mathbf{x}-\mathbf{y})$. Numerical evaluation of observables resulting from this Hamiltonian density can be accomplished by discretizing space with a cubic grid with a distance between adjacent lattice sites on the Cartesian axes of a (the lattice spacing) and extent L in each direction, as previously defined. The number of sites in each spatial direction is L/a. The discretized Hamiltonian on a d-dimensional spatial lattice is

$$H \;=\; a^d \sum_{\mathbf{x}} \frac{1}{2}\Pi^2 - \frac{1}{2}\phi\boldsymbol{\nabla}_a^2\phi + \frac{1}{2}m_0^2\phi^2 + \frac{\lambda_0}{4!}\phi^4 \quad , \tag{2.3}$$

where the discretized Laplacian operator is defined as

$$\boldsymbol{\nabla}_a^2\phi(\mathbf{x}) = \sum_{j=1}^{d} \left(\phi(\mathbf{x}+a\hat{\mu}_j) + \phi(\mathbf{x}-a\hat{\mu}_j) - 2\phi(\mathbf{x})\right)/a^2 \quad ,$$

where $\hat{\mu}_j$ is the unit vector in the j^{th} direction. The quantities m_0 and λ_0 are bare parameters that are tuned to recover, for example, correct values of the ϕ mass, M_ϕ, and the 4ϕ scattering amplitude. The conjugate momentum is required to satisfy

$$[\ \phi(\mathbf{x}), \Pi(\mathbf{y})\ ] \ = \ \frac{i}{a^d}\delta^d_{\mathbf{x},\mathbf{y}}\ \hat{I} \quad , \tag{2.4}$$

where $\hat{I}$ is the identity operator in field space. Redefining the fields, Hamiltonian and mass as $\hat{\phi} = a^{(d-1)/2}\phi$, $\hat{\Pi} = a^{(d+1)/2}\Pi$, $\hat{H} = aH$, $\hat{m}_0 = am_0$, $\hat{\lambda}_0 = a^{3-d}\lambda_0$, Eq. (2.3) can be written in terms of dimensionless quantities,

$$\hat{H} \ = \ \sum_{\mathbf{x}} \ \frac{1}{2}\hat{\Pi}^2 - \frac{1}{2}\hat{\phi}\hat{\boldsymbol{\nabla}}_a^2\hat{\phi} + \frac{1}{2}\hat{m}_0^2\hat{\phi}^2 + \frac{\hat{\lambda}_0}{4!}\hat{\phi}^4 \quad , \tag{2.5}$$

with an equal-time commutator of

$$\left[\ \hat{\phi}(\mathbf{x}), \hat{\Pi}(\mathbf{y})\ \right] \ = \ i\delta^d_{\mathbf{x},\mathbf{y}}\ \hat{I} \quad . \tag{2.6}$$

The eigenstates of the momentum operator, $|\mathbf{k}\rangle$, satisfy $\hat{\mathcal{K}}|\mathbf{k}\rangle = \mathbf{k}|\mathbf{k}\rangle$ where $\mathbf{k}$ is quantized by the boundary conditions, and, for example, takes the values $\mathbf{k} = \mathbf{n}\frac{2\pi}{L}$ for PBCs, where the integer-triplets $\mathbf{n}$ are constrained to lie within the first Brillouin zone $|n_{x,y,z}| < \frac{L}{2a}$. The finite-difference operator that is used to define the latticized $\hat{\mathbf{K}} = \hat{\boldsymbol{\nabla}}_a^2\hat{\phi}$ has eigenvalues such that $\hat{\mathbf{K}}|\mathbf{k}\rangle = \hat{\mathbf{k}}|\mathbf{k}\rangle$ with $\hat{k}_j = \frac{2}{a}\sin\left(\frac{k_j a}{2}\right)$.

The construction of the latticized Hamiltonian in Eq. (2.5) is such that the long-distance, or low-energy, quantities (compared to π/a) will be faithfully reproduced in numerical evaluations up to corrections that are polynomial in the lattice spacing, $\sim (aE)^n$, or exponential in the volume, $\sim e^{nM_\phi L}$ (for spatially localized states). Therefore, such lattice frameworks should be considered as low-energy effective field theories (EFTs), with an ultra-violet (UV) cut-off set by the inverse lattice spacing. Considerable effort by the LQCD community

has been put in to construct improved actions in which additional terms are added to the Lagrange density that are parametrically suppressed by powers of the lattice spacing and consistent with the underlying (hyper-)cubic symmetry of the spacetime lattice. The additional terms in the QCD action are termed the Symanzik action [51, 52]. Coefficients of the operators in the Symanzik action depend upon the lattice spacing and the discretized action, and are determined both by tree-level matching and nonperturbatively through tuning for higher precision. As an example, the Wilson discretization of the light-quark field in LQCD calculations leads to spatial finite-difference discretization errors that scale linearly with the lattice spacing, $\mathcal{O}(a)$. By adding one dimension-5 operator to the lattice action, the Sheikholeslami-Wohlert term [53], and tuning its coefficient, this improved action produces low-energy and long-distance observables that have errors at $\mathcal{O}(a^2)$. In principle, an arbitrary number of operators in the Symanzik action can be included in numerical computations to improve the action to high orders. However, the requirements for such calculations that include, for instance, four-quark operators, make this impractical. We will apply similar considerations when proposing improvements for the digitization of the scalar field onto quantum degrees of freedom.

2.2 The Continuum Position Space Free Ground State

The renormalizable Hamiltonian density describing the dynamics of an interacting real scalar field of mass m is,

$$\mathcal{H} \;=\; \frac{1}{2}\Pi^2 + \frac{1}{2}(\boldsymbol{\nabla}\phi)^2 + \frac{1}{2}m^2\phi^2 + \frac{\lambda}{4!}\phi^4 \quad . \tag{2.7}$$

where the conjugate momentum operator, $\Pi(\mathbf{x})$ has the standard equal-time commutation relation with the field operator, $[\ \phi(\mathbf{x}), \Pi(\mathbf{y})\ ] = i\delta^3(\mathbf{x}-\mathbf{y})$. In order to numerically evaluate observables in this field theory, space is discretized onto a cubic grid with a distance between adjacent lattice sites on the Cartesian axes of a (the lattice spacing) and extent L in each direction. The number of sites in each spatial direction is $N = L/a$. In terms of dimensionless quantities and replacing the $\boldsymbol{\nabla}\phi$ operator with a nearest-site finite-difference approximation,

the Hamiltonian density for a d-dimensional non-interacting lattice scalar field theory can be written as,

$$\mathcal{H} \;\rightarrow\; \frac{1}{2}\sum_{\mathbf{j}}\left[\,\hat{\Pi}^2(\mathbf{j})+\hat{m}^2\hat{\phi}^2(\mathbf{j})+\sum_{\boldsymbol{\mu}}\left(\hat{\phi}(\mathbf{j})-\hat{\phi}(\mathbf{j}+\hat{\boldsymbol{\mu}})\right)^2\,\right] \quad , \tag{2.8}$$

where $\hat{\boldsymbol{\mu}}$ are unit vectors in the d-spatial dimensions, and the sum over $\mathbf{j}$ corresponds to the sum over all of the lattice sites. The notation $\hat{m}=am$ and $\hat{\phi}$ are introduced to denote the dimensionless mass and field operator (using powers of the lattice spacing). Throughout, ϕ will be used to denote $\hat{\phi}$ for simplicity in notation. In one spatial dimension, the lattice Hamiltonian for continuous-field wavefunctions can be written as,

$$\mathcal{H} \;\rightarrow\; \sum_{j}^{N} -\frac{1}{2}\frac{\partial^2}{\partial\phi(j)^2}+\frac{1}{2}\hat{m}^2\phi^2(j)+\frac{1}{2}\left(\phi(j)-\phi(j+1)\right)^2 \quad , \tag{2.9}$$

where the nearest-site finite-difference operator is used to represent $\boldsymbol{\nabla}\phi$. In one dimension, the ground state of the latticized scalar field is

$$\langle\phi_0,\phi_1,\cdots,\phi_{N-1}|\psi_0\rangle=\frac{\det\mathbf{K}^{1/4}}{\pi^{N/4}}e^{-\frac{1}{2}\boldsymbol{\phi}^T\mathbf{K}\boldsymbol{\phi}} \tag{2.10}$$

where N is the number of sites in the spatial lattice and $\boldsymbol{\phi}$ is a vector of field operators. The correlation matrix among the oscillators located at each site is determined by the energy momentum relation defining the propagator with periodic boundary conditions.

$$G^{(0)}(\hat{r})=\langle\psi_0|\phi_0\phi_{\hat{r}}|\psi_0\rangle=\frac{1}{N}\sum_{p=-\lceil\frac{N}{2}\rceil+1}^{\lfloor\frac{N}{2}\rfloor}\frac{1}{2\sqrt{\hat{m}^2+4\sin^2\left(\frac{\pi}{N}p\right)}}e^{i\frac{2\pi p\hat{r}}{N}}=\frac{1}{2}\mathbf{K}^{-1}_{0\hat{r}} \quad . \tag{2.11}$$

in the infinite volume limit at non-zero lattice spacing, the momentum modes become continuous between $\pm\pi$

$$G^{(0)}(\hat{r}) \quad \xrightarrow{N\rightarrow\infty,\,a\neq 0} \quad \int_{-\pi}^{\pi}\frac{\mathrm{d}p}{2\pi}\frac{1}{2\sqrt{\hat{m}^2+4\sin^2\left(\frac{p}{2}\right)}}e^{ip\hat{r}} \quad . \tag{2.12}$$

In the continuum limit, $a\rightarrow 0$, the lattice momentum tends to the continuum momentum and the two point correlation function becomes

$$G^{(0)}(r) \quad \xrightarrow{N\rightarrow\infty,\,a\rightarrow 0} \quad \frac{1}{2\pi}K_0(mr) \quad , \tag{2.13}$$

where K_0 is the 0^{th} modified bessel function of the first kind with the fourier representation

$$K_0(mr) = \frac{1}{2}\int_{-\infty}^{\infty} \mathrm{d}t \ \frac{e^{imrt}}{\sqrt{1+t^2}} = \frac{1}{2}\int_{-\infty}^{\infty} \mathrm{d}p \ \frac{e^{ipr}}{\sqrt{m^2+p^2}} \quad . \tag{2.14}$$

At small mass,

$$G^{(0)}(r) \quad \xrightarrow{N\to\infty, a\to 0, m\to 0} \quad -\frac{1}{2\pi}\left(\log(mr) + \gamma - \log 2\right) \quad , \tag{2.15}$$

with γ the Euler-Mascheroni constant and the presence of a formally infinite constant $\log m$ that regulates the vanishing mass scale. At large argument, the bessel function is exponentially decaying,

$$\lim_{z\to\infty} K_\nu(z) = \sqrt{\frac{\pi}{2}}\frac{e^{-z}}{\sqrt{z}}\left(1+\mathcal{O}\left(z^{-1}\right)\right) \quad , \tag{2.16}$$

and thus the two point correlation function at large distances in the continuous infinite volume becomes

$$G^{(0)}(r) \quad \xrightarrow{N\to\infty, a\to 0, r\to\infty} \quad \frac{1}{\sqrt{8\pi}}\frac{e^{-mr}}{\sqrt{mr}} \quad . \tag{2.17}$$

The exponentially decreasing correlation functions in the ground state of this massive theory are key components to the localizability of quantum circuits designed to prepare this state on a quantum register, as will be discussed in Chapter 5.

The matrix $\mathbf{K}$ can be calculated exactly by decoupling the N oscillators. Guided by the solution for a single site with mass term $\frac{m^2}{2}\phi^2$ having ground state $\psi_0(\phi) = \left(\frac{m}{\pi}\right)^{\frac{1}{4}} \exp\left[-\frac{m\phi^2}{2}\right]$, the groundstate of a larger lattice is structured as

$$\psi_0\left(\phi_0, \phi_1, \cdots, \phi_{N-1}\right) = \prod_{i=0}^{N-1}\left(\frac{\sqrt{2\lambda_i}}{\pi}\right)^{\frac{1}{4}} \exp\left[-\frac{\sqrt{2\lambda_i}\left(v_i.\{\phi_0, \phi_1, \cdots, \phi_{N-1}\}\right)^2}{2}\right] \quad , \tag{2.18}$$

where λ_i and v_i are the eigenvalues and orthonormal eigenvectors of the interaction matrix, $\mathbf{M}$, consisting of the mass term and the gradient term. Using a finite difference representation of the gradient operator,

$$\phi(x)\nabla^2\phi(x) \to \phi(x)\frac{\phi(x-1)+\phi(x+1)-2\phi(x)}{2a^2} \quad , \tag{2.19}$$

the interaction to be summed over all space (with the lattice spacing set to unity) becomes

$$\frac{\hat{m}^2}{2}\phi(x)^2 - \frac{1}{2}\phi(x)\nabla^2\phi(x) \to \frac{\hat{m}^2+2}{2}\phi(x)^2 - \phi(x)\phi(x+1) \quad . \tag{2.20}$$

For a two site lattice, $N = 2$, with periodic and open boundary conditions, this interaction can be represented in matrix form with each site in its own linear vector space,

$$\mathbf{M}_{\text{PBC}} = \begin{pmatrix} \frac{\hat{m}+2}{2} & -1 \\ -1 & \frac{\hat{m}+2}{2} \end{pmatrix} \qquad \mathbf{M}_{\text{OBC}} = \begin{pmatrix} \frac{\hat{m}+2}{2} & -\frac{1}{2} \\ -\frac{1}{2} & \frac{\hat{m}+2}{2} \end{pmatrix} \quad . \tag{2.21}$$

For lattices with more than two sites,

$$\mathbf{M}_{PBC} = \begin{pmatrix} \frac{\hat{m}+2}{2} & -\frac{1}{2} & 0 & \cdots & 0 & -\frac{1}{2} \\ -\frac{1}{2} & \frac{\hat{m}+2}{2} & \ddots & \ddots & & 0 \\ 0 & \ddots & \ddots & & \ddots & \vdots \\ \vdots & \ddots & & & \ddots & 0 \\ 0 & & \ddots & \ddots & \ddots & -\frac{1}{2} \\ -\frac{1}{2} & 0 & \cdots & 0 & -\frac{1}{2} & \frac{\hat{m}+2}{2} \end{pmatrix} \tag{2.22}$$

$$\mathbf{M}_{\text{OBC}} = \begin{pmatrix} \frac{\hat{m}+2}{2} & -\frac{1}{2} & 0 & \cdots & 0 & 0 \\ -\frac{1}{2} & \frac{\hat{m}+2}{2} & \ddots & \ddots & & 0 \\ 0 & \ddots & \ddots & & \ddots & \vdots \\ \vdots & \ddots & & & \ddots & 0 \\ 0 & & \ddots & \ddots & \ddots & -\frac{1}{2} \\ 0 & 0 & \cdots & 0 & -\frac{1}{2} & \frac{\hat{m}+2}{2} \end{pmatrix} \quad . \tag{2.23}$$

By diagonalizing these interactions and inserting the eigenvalues and orthonormal eigenvectors into Eq.(2.18), the correlation matrix $\mathbf{K}$ can be analytically expressed as a function of the mass. The following are a few explicit examples with periodic boundary conditions

$$\mathbf{K}^{N=2}_{\text{PBC}} = \begin{pmatrix} \frac{1}{2}\left(\hat{m} + \sqrt{\hat{m}^2+4}\right) & \frac{1}{2}\left(\hat{m} - \sqrt{\hat{m}^2+4}\right) \\ \frac{1}{2}\left(\hat{m} - \sqrt{\hat{m}^2+4}\right) & \frac{1}{2}\left(\hat{m} + \sqrt{\hat{m}^2+4}\right) \end{pmatrix} \tag{2.24}$$

$$\mathbf{K}^{N=3}_{\text{PBC}} = \begin{pmatrix} \frac{1}{3}\left(\hat{m} + 2\sqrt{\hat{m}^2+3}\right) & \frac{1}{3}\left(\hat{m} - \sqrt{\hat{m}^2+3}\right) & \frac{1}{3}\left(\hat{m} - \sqrt{\hat{m}^2+3}\right) \\ \frac{1}{3}\left(\hat{m} - \sqrt{\hat{m}^2+3}\right) & \frac{1}{3}\left(\hat{m} + 2\sqrt{\hat{m}^2+3}\right) & \frac{1}{3}\left(\hat{m} - \sqrt{\hat{m}^2+3}\right) \\ \frac{1}{3}\left(\hat{m} - \sqrt{\hat{m}^2+3}\right) & \frac{1}{3}\left(\hat{m} - \sqrt{\hat{m}^2+3}\right) & \frac{1}{3}\left(\hat{m} + 2\sqrt{\hat{m}^2+3}\right) \end{pmatrix} \tag{2.25}$$

$$\mathbf{K}^{N=4}_{\text{PBC}} = \begin{pmatrix} \frac{1}{4}\left(\hat{m} + 2\sqrt{\hat{m}^2+2} + \sqrt{\hat{m}^2+4}\right) & \frac{1}{4}\left(\hat{m} - \sqrt{\hat{m}^2+4}\right) & \frac{1}{4}\left(\hat{m} - 2\sqrt{\hat{m}^2+2} + \sqrt{\hat{m}^2+4}\right) & \frac{1}{4}\left(\hat{m} - \sqrt{\hat{m}^2+4}\right) \\ \frac{1}{4}\left(\hat{m} - \sqrt{\hat{m}^2+4}\right) & \frac{1}{4}\left(\hat{m} + 2\sqrt{\hat{m}^2+2} + \sqrt{\hat{m}^2+4}\right) & \frac{1}{4}\left(\hat{m} - \sqrt{\hat{m}^2+4}\right) & \frac{1}{4}\left(\hat{m} - 2\sqrt{\hat{m}^2+2} + \sqrt{\hat{m}^2+4}\right) \\ \frac{1}{4}\left(\hat{m} - 2\sqrt{\hat{m}^2+2} + \sqrt{\hat{m}^2+4}\right) & \frac{1}{4}\left(\hat{m} - \sqrt{\hat{m}^2+4}\right) & \frac{1}{4}\left(\hat{m} + 2\sqrt{\hat{m}^2+2} + \sqrt{\hat{m}^2+4}\right) & \frac{1}{4}\left(\hat{m} - \sqrt{\hat{m}^2+4}\right) \\ \frac{1}{4}\left(\hat{m} - \sqrt{\hat{m}^2+4}\right) & \frac{1}{4}\left(\hat{m} - 2\sqrt{\hat{m}^2+2} + \sqrt{\hat{m}^2+4}\right) & \frac{1}{4}\left(\hat{m} - \sqrt{\hat{m}^2+4}\right) & \frac{1}{4}\left(\hat{m} + 2\sqrt{\hat{m}^2+2} + \sqrt{\hat{m}^2+4}\right) \end{pmatrix} \tag{2.26}$$

and open boundary conditions

$$\mathbf{K}_{\text{OBC}}^{N=2} = \begin{pmatrix} \frac{1}{2}\left(\sqrt{\hat{m}^2+1}+\sqrt{\hat{m}^2+3}\right) & \frac{1}{2}\left(\sqrt{\hat{m}^2+1}-\sqrt{\hat{m}^2+3}\right) \\ \frac{1}{2}\left(\sqrt{\hat{m}^2+1}-\sqrt{\hat{m}^2+3}\right) & \frac{1}{2}\left(\sqrt{\hat{m}^2+1}+\sqrt{\hat{m}^2+3}\right) \end{pmatrix} \tag{2.27}$$

$$\mathbf{K}_{\text{OBC}}^{N=3} = \begin{cases} \hat{r}=0 & \begin{cases} \mathbf{K}_{00}=\mathbf{K}_{22} & \frac{\left(2\sqrt{\hat{m}^2+2}+\sqrt{\hat{m}^2-\sqrt{2}+2}+\sqrt{\hat{m}^2+\sqrt{2}+2}\right)}{4} \\ \mathbf{K}_{11} & \frac{1}{2}\left(\sqrt{\hat{m}^2-\sqrt{2}+2}+\sqrt{\hat{m}^2+\sqrt{2}+2}\right) \end{cases} \\ \hat{r}=1 & \frac{\sqrt{\hat{m}^2-\sqrt{2}+2}-\sqrt{\hat{m}^2+\sqrt{2}+2}}{2\sqrt{2}} \\ \hat{r}=2 & \frac{1}{4}\left(-2\sqrt{\hat{m}^2+2}+\sqrt{\hat{m}^2-\sqrt{2}+2}+\sqrt{\hat{m}^2+\sqrt{2}+2}\right) \end{cases} \tag{2.28}$$

where the unique matrix elements of the symmetric matrix $\mathbf{K}_{\text{OBC}}^{N=3}$ have been listed organised by dimensionless site distance $\hat{r}$ such that e.g., the $\hat{r}=1$ matrix element applies to $\mathbf{K}_{01}, \mathbf{K}_{12}$, and their symmetric transpose counterparts.

When periodic boundary conditions are chosen, the $\mathbf{K}$ matrix can be solved exactly. The above mass interaction matrix is circulant with parameters

$$\mathbf{M}_{\text{PBC}} \;:\quad c_0 = \frac{\hat{m}^2+2}{2} \quad c_1 = -\frac{1}{2} \quad c_{N-1} = -\frac{1}{2} \quad . \tag{2.29}$$

The eigenvectors of this matrix are calculated from fourier space as

$$v_k = \frac{1}{\sqrt{N}}\left(1, \omega_k, \omega_k^2, \cdots, \omega_k^{N-1}\right) \qquad \omega_k = \exp\left[i\frac{2\pi k}{N}\right] \tag{2.30}$$

where the index spans the dimensionality of the space, $k = \{0, 1, \cdots, N-1\}$. The associated eigenvalues satisfy the lattice dispersion relation

$$\lambda_k = c_0 - \frac{1}{2}\left(\omega_k + \omega_k^{N-1}\right) \tag{2.31}$$

$$= \frac{\hat{m}^2+2}{2} - \frac{1}{2}\left(e^{i\frac{2\pi k}{N}} + e^{i\frac{2\pi k}{N}(N-1)}\right) \tag{2.32}$$

$$= \frac{\hat{m}^2+2}{2} - \frac{1}{2}\left(e^{i\frac{2\pi k}{N}} + e^{-i\frac{2\pi k}{N}}\right) \tag{2.33}$$

$$= \frac{\hat{m}^2+2}{2} - \cos\left(\frac{2\pi k}{N}\right) \tag{2.34}$$

$$= \frac{1}{2}\left(\hat{m}^2 + 4\sin^2\left(\frac{\frac{2\pi k}{N}}{2}\right)\right) \tag{2.35}$$

$$= \frac{1}{2}\left(\hat{m}^2 + \hat{k}^2\right) \quad . \tag{2.36}$$

This expression defines the lattice momentum as the finite volume quantized modes periodically convolved. Using these circulant eigenvalues and eigenvectors to inform the decoupled ground state of Eq. (2.18), matrix elements of $\mathbf{K}$ are identified to be

$$K_{i,j} = \frac{1}{2N}\sum_{k=0}^{N-1}\left(\omega_k^i(\omega_k^*)^j + \omega_k^j(\omega_k^*)^i\right)\sqrt{2\lambda_k} \tag{2.37}$$

$$= \frac{1}{N}\sum_{k=0}^{N-1}\cos\left(\frac{2\pi k}{N}(i-j)\right)\sqrt{m^2+\hat{k}^2} \quad , \tag{2.38}$$

As the finite volume truncation is lifted, the momentum quantization approaches continuity within the UV truncation set by the remaining lattice spacing,

$$K_{\hat{r}} = \frac{1}{2\pi}\int_{-\pi}^{\pi} \mathrm{d}p \;\cos\left(p\hat{r}\right)\sqrt{\hat{m}^2 + 4\sin^2\left(\frac{p}{2}\right)} \quad . \tag{2.39}$$

In the continuum limit, taking the integration bounds to infinity and the lattice momentum to continuum momentum, this expression contains an oscillatory integrand with growing magnitude at large argument—demonstrating a damaging sign problem and lack of convergence. Using the double exponential transformations for oscillatory integrals of Refs. [54, 55, 56], this the continuum limit of the $\mathbf{K}$ matrix elements are found to be numerically equivalent (away from $\hat{r} = 0$) with the following, substantially better-behaved expression

$$K_{\hat{r}} = -\frac{m^2}{\pi\hat{r}^2}\int_0^{\infty}\frac{\cos(rt)}{(t^2+m^2)^{\frac{3}{2}}} \tag{2.40}$$

Consulting Eq. (10.32.11) of Ref.[57],

$$K_\nu(xz) = \frac{\Gamma\left(\nu+\frac{1}{2}\right)(2z)^\nu}{\pi^{\frac{1}{2}}x^\nu}\int_0^{\infty}\frac{\cos(xt)\,\mathrm{d}t}{(t^2+z^2)^{\nu+\frac{1}{2}}} \quad , \tag{2.41}$$

the infinite volume continuum limit of the $\mathbf{K}$ matrix is captured by the first modified bessel function,

$$\mathbf{K}(r) = -\frac{m}{\pi r}K_1(mr) \quad \xrightarrow{r\to\infty} \quad -\sqrt{\frac{m}{2\pi}}\frac{e^{-mr}}{r^{\frac{3}{2}}} \quad . \tag{2.42}$$

This function decays exponentially at large distances, differing from the two point correlation function only in polynomial factors of the separation. In the massless limit, Eq. (2.38) becomes

$$K_{\hat{r}}^{m=0} = \frac{1}{N}\csc\left(\frac{\pi + 2\pi\hat{r}}{2N}\right)\csc\left(\frac{\pi - 2\pi\hat{r}}{2N}\right)\sin\left(\frac{\pi}{N}\right) \quad \xrightarrow{N\to\infty} \quad \frac{4}{\pi - 4\pi\hat{r}^2} \tag{2.43}$$

where $\hat{r}$ is an integer and thus $\cos^2(\pi\hat{r})$ evaluates to unity.

Chapter 3

QUBIT DIGITIZATION AND TIME EVOLUTION OF THE SCALAR FIELD

The content of this chapter is associated with Ref. [45]:
Natalie Klco and Martin J. Savage. "Digitization of scalar fields for quantum computing". *Phys. Rev.* A99.5 (2019), p. 052335. DOI: 10.1103/PhysRevA.99.052335. arXiv: 1808.10378 [quant-ph]

Qubit, operator and gate resources required for the digitization of lattice $\lambda\phi^4$ scalar field theories onto quantum computers are considered, building upon the foundational work by Jordan, Lee and Preskill, with a focus towards noisy intermediate-scale quantum (NISQ) devices. The Nyquist-Shannon sampling theorem, introduced in this context by Macridin, Spentzouris, Amundson and Harnik building on the work of Somma, provides a guide with which to evaluate the efficacy of two field-space bases, the eigenstates of the field operator, as used by Jordan, Lee and Preskill, and eigenstates of a harmonic oscillator, to describe $0+1$- and $d+1$-dimensional scalar field theory. We show how techniques associated with improved actions, which are heavily utilized in Lattice QCD calculations to systematically reduce lattice-spacing artifacts, can be used to reduce the impact of the field digitization in $\lambda\phi^4$, but are found to be inferior to a complete digitization-improvement of the Hamiltonian using a Quantum Fourier Transform. When the Nyquist-Shannon sampling theorem is satisfied, digitization errors scale as $|\log|\log|\epsilon_{\rm dig}|||\sim n_Q$ (number of qubits describing the field at a given spatial site) for the low-lying states, leaving the familiar power-law lattice-spacing and finite-volume effects that scale as $|\log|\epsilon_{\rm latt}||\sim N_Q$ (total number of qubits in the simulation). For localized(delocalized) field-space wavefunctions, it is found that $n_Q\sim 4(7)$ qubits per spatial lattice site are sufficient to reduce theoretical digitization errors below error contributions associated with approximation of the time-evolution operator and noisy

implementation on near-term quantum devices. [1]

3.1 Introduction

While offering the potential to greatly refine calculations that can be performed through classical computation, Quantum Computing (QC) also holds the potential to enable calculations of quantities in quantum field theories and other quantum many-body systems that are not possible with classical techniques [37, 58, 59, 60, 61, 24, 25, 62, 63, 64, 65, 66, 67, 68, 69, 70, 71, 72, 73, 74]. In particular, real-time dynamics, such as the fragmentation of quarks into hadrons at particle accelerators, the dynamics of non-equilibrium systems, and the nature of finite-density systems for which sampling with classical computation is limited by sign problems, are key areas for which a *quantum advantage* is anticipated to be achieved. Quantum devices with a range of underlying qubit architectures without error correction are now becoming available for domain scientists to seek inroads into these problems and other important scientific applications, and to envisage attributes of quantum devices necessary to outperform classical computations of scientific significance. The performance of present day quantum devices is limited by a number of basic attributes, including coherence times and the number of gates (specifically entangling gates) that can be applied prior to decoherence, the accuracy and precision of applied gates, the number and interconnectivity of qubits, and the lack of error correction. While significant efforts are in progress to reduce or eliminate these deficiencies, and remarkable progress is being made, these limitations are expected to persist in near-term quantum devices. This has led John Preskill to name the present and upcoming time period the "NISQ era" (Noisy Intermediate-Scale Quantum era) [22]. While formidable in its destruction of pure quantum states, quantum noise has been recently suppressed sufficiently for a number of small quantum simulations of physical systems [75, 76, 77, 78, 30, 79], encouraging the expectation of meaningful scientific applications of NISQ-era devices.

---

[1] Only classical computing resources have been used to obtain the results presented in this work.

Scalar field theories are ubiquitous in physics, from describing densities in condensed matter systems, to fundamental fields in the electroweak sector from which the Higgs Boson emerges after spontaneous symmetry breaking. The quantum theory describing the dynamics of a self-interacting, real scalar field represents, perhaps, the simplest quantum field theory (QFT) that can be explored through direct digitization of the field with a quantum computer. Such studies are anticipated to provide important insights into how quantum devices can be used to simulate gauge field theories, such as quantum electrodynamics (QED) and quantum chromodynamics (QCD) that describe the interactions in electronic systems and between quarks and gluons responsible for the nuclear forces and the structure and dynamics of strongly interacting matter. It is exciting to observe the advances that are being made in developing [24, 25, 62, 63, 68, 70, 80, 81, 82, 83, 72, 73, 84, 85, 86, 30, 87, 88, 74, 89, 90, 91, 92, 93, 94, 95, 96] and implementing [64, 65, 67, 66, 69, 95, 71, 75, 97, 30] algorithms for both Abelian and non-Abelian gauge theories and scalar field theories that may be useful for QFT calculations with quantum computers.

It is not expected that NISQ-era devices will surpass the computational capabilities of classical devices for the evolution of scalar fields discussed in this paper. While an advantage may be found in a contrived endeavour for increased precision in the ground state energy of a non-local spatial wavefunction (see section 3.3.3), the more-likely regimes of *quantum advantage* in simulation are those highlighted at the beginning of this introduction. Creating a computational framework making these systems accessible, taking advantage of superpositions and interference while remaining robust to quantum noise, is arduous and has become the focus of many current avenues of research; porting the knowledge and understanding of high-performance classical computation will be vital but insufficient to achieve this goal. As is the case in classical computing, performance and scaling of quantum devices for scientific application cannot be completely understood before computations are implemented at scale on hardware. While quantum calculations at scale are unreasonable today and the currently-available hardware is likely far from future fault-tolerant devices, this document examines scalar quantum field theory calculations on near-term quantum devices in preparation for a

future in which substantial quantum resources allow exploration of classically-unattainable states of matter.

In a series of foundational papers, Jordan, Lee and Preskill (JLP) formulated and analyzed scalar field theories for quantum computers [24, 25, 62, 63] and estimated the resource-requirement scaling of calculations of static properties and of elastic and inelastic particle scattering processes determined through direct time evolution. A real scalar field, $\phi(\mathbf{x})$, is discretized on a spatial lattice using techniques that are standard in lattice QCD (LQCD) calculations using classical computers. The spacing between lattice sites along a cartesian axis is denoted by a and the extent of each spatial direction is denoted by L, and $\phi(\mathbf{x})$ is subject to, for example, periodic boundary conditions (PBCs) or twisted boundary conditions (e.g. Refs. [98, 99, 100, 101]) in each direction. However, in NISQ-era quantum computations, $\phi(\mathbf{x})$ can only assume values from a modest-sized set of possibilities, with extreme values of $|\phi(\mathbf{x})| \leq \phi_{\max}$ and a digitization $\delta_{\phi(\mathbf{x})}$. Therefore, the computational layout of these JLP simulations is that a number of qubits, n_Q, describe the value of $\phi(\mathbf{x})$ at each position $\mathbf{x}$, with a total number of qubits of $N_Q = n_Q \left(L/a\right)^d$ for spatial dimension, d. This system is evolved under the action of the time-evolution operator, $\hat{U}(t) = e^{-i\hat{H}t}$ where $\hat{H}$ is the Hamiltonian operator, to evolve isolated wave packets forward in time to determine scattering amplitudes.

In work by Macridin, Spentzouris, Amundson and Harnik (MSAH) [86, 88], focused on phonon-electron interactions and building upon work by Somma [102], it was emphasized that the Nyquist-Shannon (NS) sampling theorem should be considered in the architecture of a quantum computer, the mapping of $\phi(\mathbf{x})$ and the implementation of the Hamiltonian to achieve the desired accuracies in quantum simulations. The localization of the $\phi(\mathbf{x})$ wavefunction in ϕ-space and its curvature determine the extent and interval of sampling in ϕ-space, i.e. $\phi_{\max}$ and $\delta_{\phi(\mathbf{x})}$ (which dictate n_Q), required to reproduce the ϕ-space wavefunction with exponential precision, scaling as $|\log|\log|\epsilon_{\text{dig}}|||\sim n_Q$, where ϵ_{dig} is the error introduced through digitization, thereby removing inaccuracies due to field digitization. These studies of the NS sampling theorem determined the minimum number of qubits per phonon field

required to accurately describe harmonic oscillator (HO) wavefunctions up to a given excitation level of the phonon field [102, 86, 88]. The digitization errors make contributions that are parametrically smaller than spatial lattice-spacing artifacts and spatial finite-volume effects, which typically scale as $|\log|\epsilon_{\text{latt}}|| \sim N_Q$, where ϵ_{latt} is the error introduced by the non-zero spatial lattice spacing.

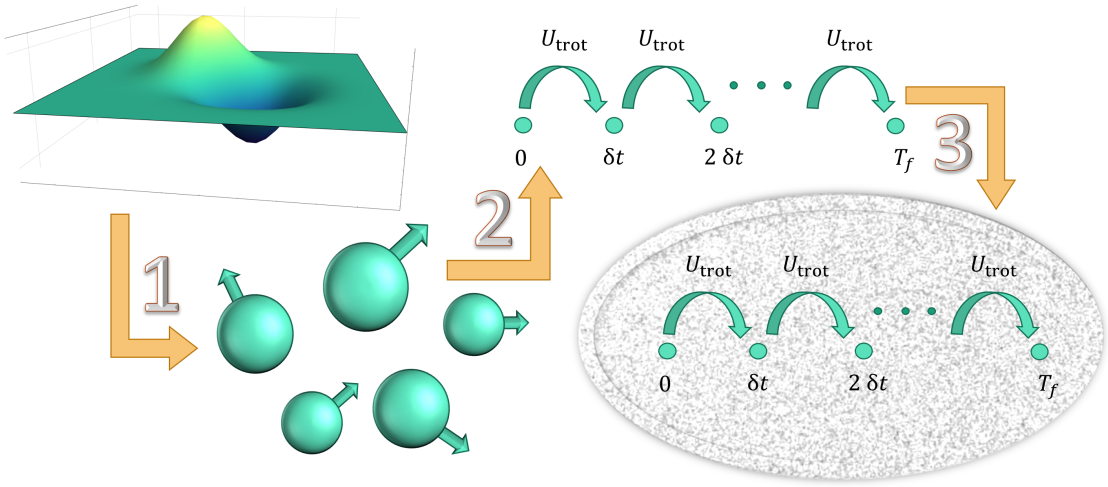

Figure 3.1: Identifying three distinct sources of error in quantum simulations of scalar field theory: (1) the error of digitizing and latticizing the continuous field onto qubit degrees of freedom; (2) the error of simulation due to the use of approximations to the exact digitized propagator; (3) the error due to noise in the quantum device's implementation of the approximate digitized propagator. The first two sources of error are independent of the quantum hardware. The first is the main focus of this paper.

The use of ϵ in this paper indicates the precision to which the ground state energy of the continuous scalar field can be reproduced by a Hamiltonian digitized with qubit degrees of freedom (step (1) of Fig. 3.1). This is a theoretical source of systematic error accompanying the formulation of the Hamiltonian before it is implemented on hardware or employed in a simulation algorithm. Most importantly, this is *not* the ϵ commonly used in the quantum simulation literature to express the precision with which properties of a

given Hamiltonian can be extracted on quantum hardware (steps (2,3) of Fig. 3.1). Thus, ϵ here characterizes the physics of field-digitization necessary to map the system onto a qubit Hamiltonian, and does not include precision reductions entering from the Hamiltonian simulation (e.g., Trotterization) or phase estimation that may be implemented to extract features of this system on quantum hardware. Examples of progress in bounding these latter sources of error can be found in Refs. [103, 104, 105, 106, 107]. The distinction between these three sources of error are depicted in Fig. 3.1. The scalar field begins in a continuous representation in a formally-infinite-dimensional Hilbert space. With the reduction in step (1), this infinite dimensional Hilbert space is truncated, digitized, and formulated on qubit degrees of freedom. Step (2) designs a quantum simulation algorithm to approximate the time evolution of the quantum state e.g., Trotterization, which introduces errors scaling polynomially in the temporal digitization step size δt. Step (3) implements this approximate time evolution on quantum hardware susceptible to noise and (likely) without quantum error correction in the NISQ-era.

The digitization errors represented in step (1) of Fig. 3.1 are the only errors considered in the main text of this paper. The results presented in this work establish the precision of low-energy calculations that could be obtained on an ideal quantum device with exact implementation of the time evolution operator based upon formal considerations of digitizations and discretizations that must be performed when formulating the field theories onto quantum devices with a modest number of qubits. These are presented in order to determine the best-case scenarios for modest-sized devices of the near term, and intentionally neglect the errors of steps (2,3) necessary to accurately reflect the precision attainable with realistic NISQ-era devices. Simulations of the effects of first-order Trotterization (2) and simple unitary gate noise (3) can be found in Appendix H of Ref. [45]. Together, Appendix H and the main text indicate that digitization errors (1) may be controlled to high precision with a number of qubits reasonable for the NISQ era, leaving the steps (2,3) to dominate the current scalar simulation error budget.

In this work, we consider implications of the digitization of scalar fields when mapped to

qubit degrees of freedom, with a focus on the associated limits in accuracy of calculations on NISQ-era scale devices. In particular, we examine digitizing 0+1 and 1+1 dimensional $\lambda\phi^4$ scalar field theory describing a single real scalar field, including estimating qubit requirements, estimating the number of operators and number of gates required for such simulations, and extrapolating these estimates to d+1-dimensional simulations [2]. As the sign of the mass-squared term in the Hamiltonian determines whether the ground state of these theories are localized around $\phi = 0$ or are delocalized around two minima of the potential, estimates are provided for both situations. Making a connection with classical calculations of lattice QFTs, we discuss Hamiltonian improvement that can be included to parametrically reduce the impact of the field digitization by powers of $\delta^2_{\phi(\mathbf{x})}$. However, as used in Refs. [24, 25, 62, 63] and emphasized in Refs. [102, 86, 88], the use of the Quantum Fourier Transform (QuFoTr) on the n_Q qubits at each spatial site to evaluate the action of the conjugate-momentum term in the Hamiltonian, and the freedom it provides in applying phases in field conjugate-momentum space, provides the opportunity to arbitrarily improve the digitized Hamiltonian, removing all polynomials in $\delta_{\phi(\mathbf{x})}$ and rendering digitization effects to be exponentially small (once the conditions imposed by the NS sampling theorem are satisfied). Analogous implementations have been utilized previously in Monte-Carlo calculations of non-relativistic systems [108, 109]. We present the complete operator structure required to implement simulations with $n_Q = 3, 4, 5$ qubits per spatial site, along with associated quantum circuits for $n_Q = 3$. As different bases in ϕ-space can be used to span the Hilbert space at each point in space, we examine the JLP implementation using the eigenstates of the ϕ-operator and a basis defined by the eigenstates of a harmonic oscillator (HO), that is distinct from the frameworks developed in Refs. [102, 88, 86]. From our analysis, we conclude that the properties and dynamics of interacting scalar field theories may be simulated with only a modest number of qubits per site required to render digitization artifacts negligible compared to other expected

[2] The necessary ingredients for this extrapolation are detailed resource requirements for implementation of 1.) the 0+1 dimensional self-interacting scalar field and 2.) the nearest-neighbor finite-difference gradient operator. We analyze these two pieces in depth and subsequently discuss the compilation procedure for applying the analysis to scalar lattices of arbitrary size and dimensionality.

systematic errors [3] in the NISQ-era.

3.2 Implications of the Nyquist-Shannon Sampling Theorem

The work of MSAH [86, 88] stressed the importance of the NS Sampling Theorem, implicit in the work of Somma [102], which is central to signal processing, communications and data compression, to quantum computations. It is worth reminding the reader of its main elements and implications. While the results of this theorem are used implicitly in the formulation and analysis of LQCD calculations, connections between the two are typically not dwelt upon.

Consider the reconstruction of a real function, $C(x)$, that has support only between $x = 0$ and $x = x_{\rm max}$ in position space and between $k = -k_{\rm max}$ and $k = +k_{\rm max}$ in momentum space, from discrete sampling. If $C(x)$ is sampled over the interval $x \in [0, L]$ with $L > x_{\rm max}$ and at intervals of $\delta x < \frac{\pi}{k_{\rm max}}$ then the NS Sampling Theorem ensures that $C(x)$ can be reconstructed up to corrections that are exponentially small. The Poisson resummation formula is at the heart of this result, which is also used extensively in deriving, for example, finite-volume effects in LQCD calculations. The implications of this theorem are clear. As long as the function is sampled in both position-space and momentum-space over the entire region where the function has support, then it can be reconstructed with only exponentially small errors introduced by the discretization. In quantum simulations of field theories, and in particular the computation of the low-lying eigenstates and eigenvalues, this imposes constraints for both the spatial discretization and the digitization of the field at any given spatial site. From the viewpoint of lattice calculations, this dictates that the lattice spacing must be small enough to include all spatial-momentum states that contribute (to the level of precision to which the calculation is being performed), and the volume large enough to contain the eigenstates of interest, in order for deviations between the calculated eigenstates and eigenvalues and the true eigenstates and eigenvalues to be exponentially small. For LQCD calculations, this underpins Lüscher's finite-volume analysis of QCD observables [110,

[3] see processes (2,3) of Fig. 3.1 and Appendix H of Ref. [45]

111, 112], which is used extensively to both quantify uncertainties and to extract S-matrix elements.

The NS theorem does not specify how to "cover" the region of support in position-space and momentum-space, i.e. what basis should be used to span the spaces, and some bases will be better than others for any given function. For smooth functions that fall exponentially (or as a Gaussian) at large distances, the plane-wave basis is efficient, defined over the spatial interval where the function has support and with a discretization that encompasses its highest frequency component. For a more localized function, such as those that fall as a Gaussian at large distance, eigenstates of the HO that are approximately tuned to the function can also be efficient.

For quantum computations of a field theory using a given set of basis functions to define the spatial discretization and the field digitization, including plane waves or eigenstates of the HO, this theorem dictates the number of qubits required to achieve a desired accuracy. The number of qubits and the number and complexity of operators required to execute the computation are basis dependent. Identifying the optimal basis with which to perform the quantum computation requires examining both the number of qubits and the number of gates required to perform the computation with the desired precision.

It is worth commenting that the NS sampling bounds are likely satisfied in LQCD calculations of localized quantities, such as hadron masses and nuclear bound states. Therefore, the eigenvalues and eigenstates obtained in such calculations would be exponentially close to the values associated with the lattice Hamiltonian if infinite statistics were accumulated in the stochastic sampling of the quantum fields. The power-law deviations that scale as $\sim (aE)^n$ result from deviations in the lattice Hamiltonian from the continuum Hamiltonian and are not due to under-sampling in the NS sense. We are unaware of the NS theorem being implemented in classical quantum Monte-Carlo calculations, and consider the possibility worthwhile to explore.

3.3 0+1 Dimensional Scalar Field Theory

In order to demonstrate some important features of the construction presented in the previous section, we examine a 0+1 dimensional non-interacting scalar field theory, which is simply a HO. After a further field and Hamiltonian redefinition, $\hat{\phi} = \frac{1}{\sqrt{\hat{m}_0}}\bar{\phi}$, $\hat{\Pi} = \sqrt{\hat{m}_0}\bar{\Pi}$, $\hat{H} = \hat{m}_0\bar{H}$, the HO is described by the Hamiltonian,

$$\bar{H} \;=\; \frac{1}{2}\bar{\Pi}^2 + \frac{1}{2}\bar{\phi}^2 \quad , \tag{3.1}$$

with a commutation relation $\left[\ \bar{\phi}, \bar{\Pi}\ \right] = i\hat{I}$. It is the digitization of this system that was studied by Somma [102] and by MSAH [86, 88] with the identification $\bar{\phi} \to X$, $\bar{\Pi} \to P$ and $\bar{H} \to H_h$. Without field digitization, $\delta_{\bar{\phi}} = 0$, this is simply the Hamiltonian describing a HO without self-interactions, with energy eigenstates $|\psi_n\rangle$ and energy eigenvalues $E_n = n + \frac{1}{2}$. The conjugate momentum operator can be identified with a derivative in field space, $\bar{\Pi} = -i\frac{d}{d\bar{\phi}}$, to satisfy the equal-time commutation relation.

3.3.1 Jordan-Lee-Preskill Basis

When the field is digitized, $\bar{\phi} \to \tilde{\phi}$ (using the notation of MSAH), and sampled at regular intervals $\delta_{\tilde{\phi}} \neq 0$, the conjugate momentum operator can be replaced by a finite difference operator in field space, in analogy with lattice field theory spatial discretization. It has a matrix representation in $\tilde{\phi}$-space of

$$\langle\tilde{\phi}'|\ \tilde{\Pi}^2\ |\tilde{\phi}\rangle \;=\; \frac{1}{\delta_{\tilde{\phi}}^2}\begin{pmatrix} 2 & -1 & 0 & 0 & \cdots & -1 \\ -1 & 2 & -1 & 0 & 0 & \cdots \\ \vdots & \vdots & \vdots & \vdots & \vdots & \vdots \\ 0 & 0 & \cdots & -1 & 2 & -1 \\ -1 & 0 & 0 & \cdots & -1 & 2 \end{pmatrix} \quad , \tag{3.2}$$

and acts in the space defined by field values $-\bar{\phi}_{\max}, -\bar{\phi}_{\max} + \delta_{\tilde{\phi}}, \cdots, -\frac{\delta_{\tilde{\phi}}}{2}, \frac{\delta_{\tilde{\phi}}}{2}, \cdots, \bar{\phi}_{\max} - \delta_{\tilde{\phi}}, \bar{\phi}_{\max}$. For a space spanned by $n_s = 2^{n_Q}$ basis states in field space, the field takes values

$$\bar{\phi} \;=\; -\bar{\phi}_{\max} \;+\; \delta_{\tilde{\phi}}\,\beta_\phi \quad , \quad \delta_{\tilde{\phi}} \;=\; \frac{2\bar{\phi}_{\max}}{n_s - 1} \quad , \tag{3.3}$$

where $\beta_\phi = 0, 1, ..., n_s - 1$. Note that this formulation allows the field operator to be decomposed as $\phi = \frac{\bar{\phi}_{\max}}{n_s - 1} \sum_{j=0}^{n_Q - 1} 2^j \sigma_j^z$ (with qubits labeled right to left in tensor product spaces) and thus requires only single-qubit Pauli-Z operators for its implementation. As is familiar from classical lattice simulations, the momentum modes of this system satisfying PBCs are,

$$k_{\tilde{\phi}} = -k_{\tilde{\phi}}^{\max} + \beta_k \, \delta k_{\tilde{\phi}} \quad , \quad k_{\tilde{\phi}}^{\max} = \frac{\pi}{\delta_{\tilde{\phi}}} \quad , \quad \delta k_{\tilde{\phi}} = \frac{2\pi}{\delta_{\tilde{\phi}} n_s} \quad , \tag{3.4}$$

with $\beta_k = 1, 2, ..., n_s$. It is interesting to note that this conjugate momentum-space basis may not be optimal in terms of the number of gates in a quantum circuit required to apply the Hamiltonian to any given state. Satisfying the NS theorem does not require any particular momentum components to be present in the conjugate momentum-space basis set and, as such, there is freedom to shift each momentum state by the same constant momentum. It is convenient to shift each basis state in conjugate momentum space by $\Delta k_{\tilde{\phi}} = -\delta k_{\tilde{\phi}}/2$, so that

$$k_{\tilde{\phi}}^{\Delta} = -k_{\tilde{\phi}}^{\max} + \left(\beta_k - \frac{1}{2} \right) \, \delta k_{\tilde{\phi}} \quad , \tag{3.5}$$

which is equivalent to imposing twisted boundary conditions in field space [98, 99, 100, 101], resulting in +1's in the off-diagonal corners of Eq. (3.2) and momentum states that are symmetrically distributed within the edges of the first Brillouin zone between values of $\pm \frac{\pi}{\delta_{\tilde{\phi}}} \frac{n_s - 1}{n_s}$. For any choice of basis states spanning conjugate momentum space, the finite-difference operator has matrix elements

$$\langle k'_{\tilde{\phi}} | \, \tilde{\Pi}^2 \, | k_{\tilde{\phi}} \rangle = \hat{k}_{\tilde{\phi}}^2 \, \delta_{k_{\tilde{\phi}}, k'_{\tilde{\phi}}} \quad , \quad \hat{k}_{\tilde{\phi}}^2 = \frac{4}{\delta_{\tilde{\phi}}^2} \, \sin^2 \left(\frac{k_{\tilde{\phi}} \, \delta_{\tilde{\phi}}}{2} \right) \quad . \tag{3.6}$$

The Hamiltonian resulting from this field digitization is denoted by $\bar{H} \to \tilde{H}$. The precision expected from computations on an ideal quantum computer for a range of values of $\bar{\phi}_{\max}$ is shown in Fig. 3.2. Encouragingly, this calculation indicates that a $\bar{\phi}_{\max}$ of 4.7 for a 4-qubit representation of the scalar field can achieve a precision of better than $10^{-3}\%$ on the energies of the lowest 5 eigenstates of the HO with an ideal quantum simulation. For explicit

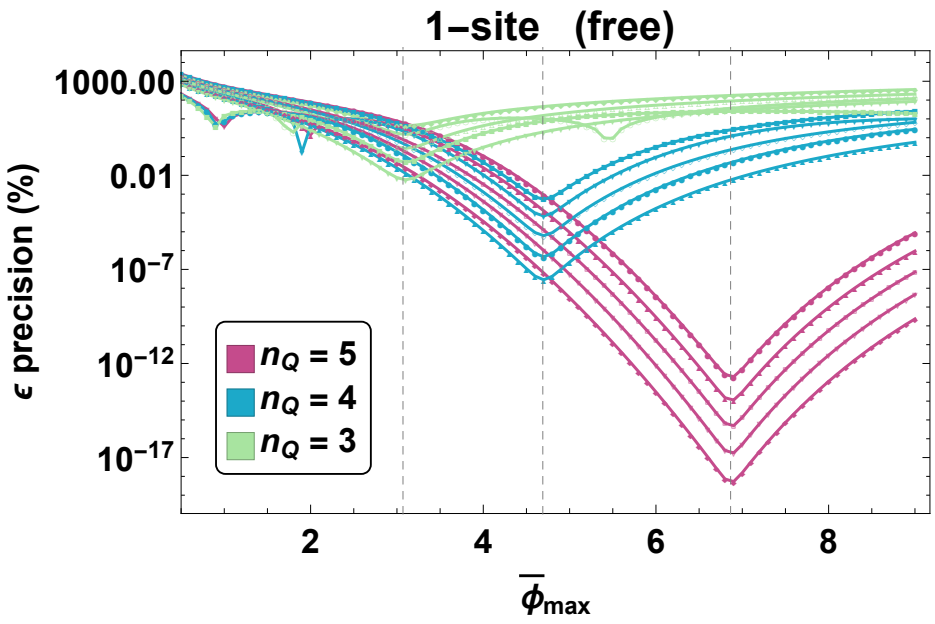

Figure 3.2: The precision of the energies of the lowest five states of the HO in Eq. (3.1) expected from calculations on an ideal quantum computer with JLP digitizations over a range of values of $\bar{\phi}_{\max}$ for a system digitized on $n_Q = 3$, $n_Q = 4$ and $n_Q = 5$ qubits (minimized at $\bar{\phi}_{\max}$ =3.1, 4.7, and 6.9, respectively) . The vertical gray-dashed lines correspond to saturation of the NS sampling bound.

examples of this field digitization implementation with three, four, and five qubits per site, see Appendix A of Ref. [45].

With any finite computing device, classical or quantum, only a finite representation of a continuous quantity is possible. In the JLP formulation, $|\phi|$ is bounded by $\phi_{\max}$ and sampled at intervals dictated by the number of qubits per site. Focusing on the $\phi_{\max}$ truncation of the scalar field and allowing an infinite momentum-space coverage, formal quantum field theory studies [113, 114] have shown that the asymptotic perturbative series becomes convergent. For a sufficiently large $\phi_{\max}$, results for low-lying quantities are exponentially close to those obtained with unbounded values of the field.

In a quantum simulation of this HO, the JLP framework using the eigenstates of $\tilde{\phi}$ and its

conjugate momentum can be used, as discussed above. By tuning $\bar{\phi}_{\max}$ to be larger than the spatial support of the n^{th} state of the HO at some level of precision, the NS sampling bound will be satisfied for these levels as long as the largest value of $|k_{\tilde{\phi}}|$ in Eq. (3.4) is greater than the region of support in conjugate momentum-space of the n^{th} state. The action of the Hamiltonian on this set of qubits is most easily accomplished in two parts, as prescribed by JLP. First, the $\tilde{\phi}^2$ operator, represented by a diagonal matrix in this basis, is directly evaluated. Second, a QuFoTr is performed to render the matrix representation of $\tilde{\Pi}^2$ diagonal and thus easily evaluated. The ability to move back and forth between representations in which $\tilde{\phi}$ or $\tilde{\Pi}$ is diagonal is typically not practical in classical field theory computations and permits more freedom in choosing the operators that can be applied in either representation. Using the $\tilde{\Pi}$ operator in momentum space that is conjugate to the finite-difference operator, Eq. (3.6), yields exponentially-converged eigenvalues and eigenvectors for the lowest n states (by the NS sampling theorem). However, these quantities differ from the corresponding HO quantities by even powers of $\delta_{\tilde{\phi}}$ because of the difference between $\hat{k}^2_{\tilde{\phi}}$ and $k^2_{\tilde{\phi}}$ in Eq. (3.6), as shown in Fig. 3.3. However, if instead, the $k^2_{\tilde{\phi}}$ eigenvalues in $\tilde{\Pi}^2$ are used in the quantum computation, corresponding to using $\bar{\Pi}^2$ and not $\tilde{\Pi}^2$, the eigenvalues and eigenvectors of the lowest n states are exponentially close to the $\delta_{\tilde{\phi}} = 0$ undigitized HO quantities [102, 86, 88], as can be observed in Fig. 3.3. In performing the quantum simulations discussed in this paragraph, as the number of qubits is increased from being insufficient to satisfy the NS sampling bound to exceeding the bound for a given state, the deviation between the true and calculated energies will reduce as a polynomial in $\delta^2_{\tilde{\phi}}$ until the NS sampling bound is satisfied, from which point on the gains will become exponentially small. It would appear that working at this saturation point is an effective way to perform such computations.

Perturbatively Improved Hamiltonian

It is interesting to note that terms can be added to the finite-difference conjugate-momentum operator $\tilde{\Pi}$ in Eq. (3.2) to systematically improve it by powers of $\delta^2_{\tilde{\phi}}$. Finding the improvement term is straightforward in conjugate-momentum space, which can then be transformed into

$\tilde{\phi}$ space. By including appropriate terms to systematically cancel deviations from the true conjugate-momentum operator,

$$\begin{aligned} \hat{k}^2_{\tilde{\phi}} &= \frac{4}{\delta^2_{\tilde{\phi}}} \sin^2\left(\frac{k_{\tilde{\phi}}\ \delta_{\tilde{\phi}}}{2}\right) \rightarrow k^2_{\tilde{\phi}} - \frac{k^4_{\tilde{\phi}}\ \delta^2_{\tilde{\phi}}}{12} + \ldots \\ \hat{k}'^2_{\tilde{\phi}} &= \frac{4}{\delta^2_{\tilde{\phi}}} \sin^2\left(\frac{k_{\tilde{\phi}}\ \delta_{\tilde{\phi}}}{2}\right) + \frac{4}{3\delta^2_{\tilde{\phi}}} \sin^4\left(\frac{k_{\tilde{\phi}}\ \delta_{\tilde{\phi}}}{2}\right) \rightarrow k^2_{\tilde{\phi}} - \frac{k^6_{\tilde{\phi}}\ \delta^4_{\tilde{\phi}}}{90} + \ldots \quad . \end{aligned} \tag{3.7}$$

and the corresponding effective action can be derived that is parametrically improved. In $\tilde{\phi}$-space, the first term in this improvement is reproduced by an additional term in the Hamiltonian of the form,

$$\delta\tilde{H} = \frac{1}{24}\ \delta^2_{\tilde{\phi}}\ \tilde{\Pi}^4 \quad . \tag{3.8}$$

The quadratic improvement in the energy of the ground state of the HO due to the inclusion of this improvement term in the Hamiltonian is shown in Fig. 3.3. Numerical improvements on the order of one to two orders of magnitude in the accuracy of the improved calculations versus the unimproved calculations are found, and that the residual dependence on $\delta_{\tilde{\phi}}$ becomes $\mathcal{O}\left(\delta^4_{\tilde{\phi}}\right)$.

For systematic errors arising from approximation of the conjugate-momentum operator with a finite difference operator, the exact form of errors introduced into the Hamiltonian are well known. If the situation was not so fortunate, the polynomial digitization errors could still be systematically removed. Through a series of modest-sized calculations (in which $\bar{\phi}_{\max}$ is chosen large enough) at a range of digitization scales, the leading polynomial dependence on the small parameter, $\delta_{\tilde{\phi}}$, may be calculated and removed through the introduction of additional Hamiltonian terms. While the form of such terms may be systematically informed perturbatively or by the simple availability of independent higher-dimension operators [115], their choice is not unique as the necessity is only to provide polynomial dependence at the correct order for cancellation. This follows the procedure of Symanzik improvement [51, 53, 116]. Such improvement procedures are broadly applicable and have been crucial for calculating observables in lattice gauge theories—modestly increasing the complexity of the action rather than calculating closer to the continuum.

The Impact of Noise

In the previous sections, we have considered a full non-perturbative improvement of the field conjugate-momentum operator implemented in field space through a QuFoTr, and a perturbative improvement that systematically eliminates increasing orders in the digitization introduced by finite-difference approximations of derivatives in field space. These correspond to different matrices for $\bar{\Pi}^2$ acting on the basis states in field conjugate-momentum space. The exact $\bar{\Pi}^2$ provides exponential precision in the low-lying eigenstates of the system, but deviations from this matrix may lead to only polynomial precision—as evidenced from the behavior of the perturbatively improved Hamiltonians and Fig. 3.3. Imperfect gates and decoherence will result in an imperfect application of $\bar{\Pi}^2$—introducing errors into calculations of observables and potentially making superfluous, at a practical level, the exponentially small improvements in digitization errors below the threshold of quantum noise.

In the presence of noisy gates and decoherence, it remains preferable to work with the exact $\bar{\Pi}^2$ operator, but the precision of its application is limited. For a given level of desired precision, the digitization and extent of the field basis required to ensure that the precision matches that of the noise can be determined. This would require an iterative tuning procedure in which multiple measurements are performed, systematically increasing $\bar{\phi}_{\max}$ and decreasing $\delta_{\tilde{\phi}}$ until the results of calculations become stable. These may or may not correspond to a situation that satisfies the NS sampling bound, depending upon the magnitude of the noise. In Fig. 3.3, the results of calculations are shown with the use of the unimproved, improved and exact conjugate-momentum operator through QuFoTr with the inclusion of different levels of gate-noise. The noise is included as an offset to each diagonal element of $\bar{\Pi}^2$ after QuFoTr from a Gaussian distribution of width σ in conjugate-momentum space. The value of $\bar{\phi}_{\max} = 5.5$ is chosen to allow for a precision of $\sim 10^{-12}$ for an ideal quantum computer for digitizations below a critical value of $\delta_{\tilde{\phi}}$. For a given gate-noise level, there is a value of $\delta_{\tilde{\phi}}$ below which smaller digitizations do not improve the precision of the calculation. The conclusion is that the error associated with digitization can be reduced below errors

from other sources for an arbitrary number of low-lying energy eigenstates with only a small number of qubits.

The impact of different sampling ranges in $\bar{\phi}$ space upon the precision of calculations with an ideal quantum computer (perfect gates), is shown in the left panel of Fig. 3.4. The employed value of $\bar{\phi}_{\max}$ limits the overall precision of calculations as $\delta_{\tilde{\phi}} \to 0$ (states per site $n_s \to \infty$) due to under sampling of the field at large $\bar{\phi}$, which is suppressed by $\sim e^{-\phi^2/2}$ for a HO wavefunction. The field truncation also limits the precision of calculations for large values of $\delta_{\tilde{\phi}}$ due to under sampling of the field in momentum space. In between these regimes, the NS saturation point is found—perceived as a simple discontinuity in the first derivative—where the position-space sample rate becomes sufficient to capture the structure of momentum-space. Tracking this saturation point with the gray band of Fig. 3.4 shows a precision that increases exponentially in the number of states and thus double-exponentially in the number of qubits ($n_s = 2^{n_Q}$). The coefficients of this precision scaling are calculated to be $\epsilon \sim (1.8(2) \times 10^3)\ 2^{-2.234(4)n_s}$, which serves as a general estimate for qubit requirements to capture the low-energy Hilbert space of localized scalar fields.

An interesting observation that can be drawn from Fig. 3.3 is that, for the parameters of the calculations explored, reducing the amount of noise in the application of the field conjugate-momentum operator below $\sim 10^{-13}$ will have little impact on the precision of the extracted final result. The demonstration is made more concrete in the right panel of Fig. 3.4, where the noise level is fixed and the precision of calculations are determined over a range of $\bar{\phi}_{\max}$. For this noise level, there is no improvement in precision as $\bar{\phi}_{\max}$ is increased beyond ~ 3.5. These are simple special cases of a general conclusion, that for a given calculation designed with a set of digitization parameters, there is a level of noise in the quantum device(s) below which the precision of the results will be only minimally impacted. This general conclusion works in both directions and emphasizes the importance of matching precision in the qubit representation to that available from the NISQ hardware. Exceeding precision in either direction would result in a wasteful use of quantum resources—using extra qubits and gates to represent the physical system with a precision beyond the

quantum hardware's capability to resolve or using a noise-resilient quantum device to probe physics beyond that represented in the qubit representation of the system.

One plausible scenario in which it may be beneficial to exceed the precision of the quantum hardware with the qubit mapping is in the presence of post-measurement noise-mitigation techniques as shown for implementations of variational quantum eigensolvers in [117, 77, 30]. By extrapolating in a parameter scaling with the noise of the system (in the NISQ-era, this is conventionally a number increasing with the number of two-qubit interactions), the precision of a calculation can be improved beyond the precision capable for any ensemble measurement with the device at a fixed noise parameter. In this case, it is the extrapolated precision of the quantum hardware that needs to be balanced with the theoretical precision of the qubit mapping in order to optimize the use of quantum resources.

It can be seen from Figs. 3.3 and 3.4 that the simple [4], yet physically-motivated, noise model implemented here does not significantly modify the results of calculations above the effective noise level. As has been shown for the use of momentum-space phases associated with finite difference field-space $\tilde{\Pi}^2$ operators in section 3.3.1, there exist simple modifications to the conjugate-momentum space phases that modify the precision convergence by introducing polynomial sources of error. Having now determined that gaussian random noise on conjugate-momentum space phase gates does not result in such a dramatic degradation of the calculation's precision above the noise tolerance, we proceed with noiseless calculations—remembering that this property must be monitored as noise models become more accurate and relevant to specific hardware implementations.

[4]While this structure of quantum noise is acknowledged to be quite primitive, it is a simple model of issues expected in real quantum devices—in this case, a gaussian-distributed over- or under-rotation in the application of phases in conjugate-momentum space—leading to substantial theoretical considerations. It is expected that current research in error correction on small quantum devices [118, 119, 120, 121, 122, 123] will allow quantum noise and decoherence to be modeled in a more accurate, architecture-specific way when designing calculations for quantum hardware.

3.3.2 Harmonic Oscillator Basis

As we have discussed previously, any set of basis states can be used to digitize the field, $\bar{\phi}$, in $\bar{H}$ in Eq. (3.1). If the basis spans the $\bar{\phi}$-space and $\bar{\Pi}$-space of the lowest-lying eigenstates, the NS sampling theorem ensures exponential convergence to those eigenstates and associated eigenvalues. A basis that is commonly used, beyond the eigenstates of the $\bar{\phi}$ operator, is formed by a finite set of eigenstates of a HO with angular frequency ω_ϕ that is tuned to optimize convergence in the number of states. If ω_ϕ is tuned to $\omega_\phi = 1$, the basis states are the eigenstates of $\bar{H}$ in Eq. (3.1) and the evolution matrix is diagonal in the basis, and the number of basis states required to converge to the lowest N eigenstates is obviously equal to N. For $\omega_\phi \neq 1$, the basis states are not eigenstates, and the evolution matrix is not diagonal.

It should be emphasized that bases formed from HO eigenstates, that are explored in this section, are different in nature to those formed from digitized HO eigenstates, that have been considered previously [102, 86, 88]. In those works, the eigenstates of the HO were digitized onto the eigenstates of the field operator, e.g. $\langle\bar{\phi}|\psi_n\rangle \rightarrow \langle\bar{\phi}_i|\psi_n^d\rangle$, reducing each field-space eigenstate from a continuous function to a discrete set. It was the properties and time-evolution of the $|\psi_n^d\rangle \sim \sum_i \psi_n(\phi_i)|\phi_i\rangle$ using the JLP framework that were examined in Refs. [102, 86, 88]. A HO basis was also used in the pioneering calculations of the deuteron ground state energy using the IBM and Rigetti quantum hardware by an ORNL team [78]. The mapping of the system onto qubits was accomplished using a 2nd quantization framework, where occupancy of quantum states is encoded in the orientation of the qubit. In contrast, we consider a first quantized mapping with HO basis states mapped directly onto states of the quantum register.

Unlike the situation found with the JLP digitization of $\bar{\phi}$ in terms of eigenstates of the $\bar{\phi}$ operator, where it is valuable to QuFoTr into conjugate-momentum space to evaluate the exact action of $\bar{\Pi}^2$, digitization of the field space is accomplished explicitly by the HO basis with the coverage in field and conjugate-momentum spaces determined by the maximum number of basis states and the value of ω_ϕ. As such, quantum circuits implementing the ac-

tion of the Hamiltonian in the HO basis can be constructed in $\bar{\phi}$ space only. The Hamiltonian and ladder operators defining the basis states are,

$$\begin{aligned} H_{\text{basis}} &= \frac{1}{2}\bar{\Pi}^2 + \frac{1}{2}\omega_\phi^2\ \bar{\phi}^2 \ = \ \omega_\phi \left(a^\dagger_{\omega_\phi} a_{\omega_\phi} + \frac{1}{2} \right) \\ a_{\omega_\phi} &= \sqrt{\frac{\omega_\phi}{2}}\ \bar{\phi} + i\sqrt{\frac{1}{2\omega_\phi}}\bar{\Pi} \ , \ a^\dagger_{\omega_\phi} \ = \ \sqrt{\frac{\omega_\phi}{2}}\ \bar{\phi} - i\sqrt{\frac{1}{2\omega_\phi}}\bar{\Pi} \quad , \end{aligned} \tag{3.9}$$

and the Hamiltonian in Eq. (3.1) can be conveniently written in terms of the basis operators,

$$\bar{H} \ = \ \frac{1}{2}\bar{\Pi}^2 \ + \ \frac{1}{2}\omega_\phi^2 \bar{\phi}^2 + \frac{1}{2}\left(1-\omega_\phi^2\right)\bar{\phi}^2 \ = \ H_{\text{basis}} \ + \ \delta H_{\omega_\phi} \quad . \tag{3.10}$$

The eigenvalues and eigenstates of $\bar{H}$, in Eq. (3.1), are determined by diagonalizing the Hamiltonian matrix formed from matrix elements of $\bar{H}$ in a truncated basis of eigenstates of H_{basis}, in Eq. (3.9). An explicit example of the HO basis for three qubits-per-site may be found in the Appendix Sec. C of Ref. [45]. Figure 3.5 shows the precision of calculations of the ground state energy of the HO Hamiltonian in Eq. (3.1) expected on an ideal quantum computer as a function of the size of the HO basis for different values of ω_ϕ. Obviously, when $\omega_\phi = 1$ the error vanishes. For ω_ϕ tuned to be in the vicinity of $\omega_\phi = 1$ the precision obtained with the HO basis is better than that obtained with field-space digitization discussed in the previous sections. However, poor choices of ω_ϕ lead to inferior precision compared with field-space digitization.

The time-evolution induced by H_{basis} is simple, involving only single-phases, and the quantum circuit to implement it corresponds to only phases applied to each qubit. Since there are no interactions in this basis, all operators commute and there is no need for a Trotter decomposition, as the total phase can be determined and applied in one application. When detuned away from $\omega_\phi = 1$, the size of the Trotter step required to time-evolve the system will be determined by the detuning. In such a detuned scenario, the operator structure from δH_{ω_ϕ} involves interactions between all qubits, as evidenced in Appendix C of Ref. [45].

In Table 3.1, comparisons in the types and numbers of operations and gates required to time-evolve the HO described by $\bar{H}$ in Eq. (3.1) between the field-digitization basis and a

tuned/detuned HO basis are presented. The 2-qubit, CNOT gate requirements are distinguished separately as their presence often represents the largest source of noise on NISQ-era quantum hardware. The numbers in Table 3.1 are accumulated for a standard implementation of multi-Pauli gates [41] and do not represent expected reductions of the HO basis operations through parity calculation or cancellations that may occur for particular choices of the operator ordering [38]. From Table 3.1, it is clear that a tuned HO basis requires significantly fewer operations to evolve a free HO than does the field-digitization basis. This is because the eigenstates of the system correspond exactly to the basis states. However, a detuned HO basis involves an exponentially-growing number of multi-qubit operations, leading to significantly more operations than the field-digitization basis. Even when the eigenbasis is unknown, JLP has resource requirements limited to 2-body operators. As a detuned HO basis shares features of a self-interacting system (detailed subsequently), we conclude that, for this very simple system, the field-digitization basis examined in detail in the works of JLP is more robust than a generic HO basis. By this, we mean that for the evolution of an arbitrary, apriori unknown system, the field-digitization basis will typically require fewer quantum computational resources while possibly requiring fewer qubits, as seen from Fig. 3.5.

It is interesting to consider whether the tuned HO could be used as a "standard candle" for the calibration of quantum hardware. Its eigenstates and eigenenergies are known to infinite precision and thus could be considered not only as a calibration source but also as a calculation to distinguish the computational precision capable on classical and quantum hardware. Using the details above and specifically the information of Table 3.1, it can be seen that the tuned HO requires 0 two-qubit gates to implement. As such, it contains no entanglement and thus no unique signal that could not be generated with other predetermined rotation gates to quantify and explore noise in NISQ-era hardware.

3.3.3 $\lambda\phi^4$ Scalar Field Theory: Comparing Bases

After the field and Hamiltonian redefinition of Eq. (3.1), the interacting 0+1 scalar field is described by,

$$\bar{H} \;=\; \frac{1}{2}\bar{\Pi}^2 + \frac{1}{2}\bar{\phi}^2 + \frac{\bar{\lambda}_0}{4!}\bar{\phi}^4 \quad , \tag{3.11}$$

where $\hat{\phi} = \frac{1}{\sqrt{\hat{m}_0}}\bar{\phi}$, $\hat{\Pi} = \sqrt{\hat{m}_0}\bar{\Pi}$, $\hat{H} = \hat{m}_0\bar{H}$, and $\hat{\lambda}_0 = \hat{m}_0\bar{\lambda}_0$. This system has been numerically studied previously by Somma [102]. A value of $\bar{\lambda}_0 = 32$ will be chosen as a representative case of strong coupling, where the system is no longer a HO (nor perturbatively close) and the basis selection for the description of the wavefunction between JLP digitization and HO basis functions is relevant within the multi-dimensional space of precision, qubits, gate decompositions, and tuning requirements.

When using the digitization techniques of JLP, introducing additional interactions does not introduce new challenges. The only necessary modifications to the method are rescalings of the sampling distributions (applying considerations for both field and conjugate-momentum space coverage). In the case of $\lambda\phi^4$ with $\lambda = 32$, introduction of the self-interaction shrinks the domain over which the wavefunction has support as shown in the lower left panel of Fig. 3.6. As a result, smaller values of $\bar{\phi}_{\max}$ may be used for precise calculations. This can be seen in a comparison between Fig. 3.4 and the upper panel of Fig. 3.6. For a $\bar{\phi}_{\max}$ of 2.5, the highest precision attainable with $\lambda = 0$ and $\lambda = 32$ differs by ~ 5 orders of magnitude. The precision with $\bar{\phi}_{\max}$ of 2.5 saturates with 18 states for $\lambda = 32$, but saturates with only 6 states for $\lambda = 0$, indicating that the value of $\bar{\Pi}_{\max}$ has also increased with the introduction of the self-interaction, requiring a smaller value of $\delta_{\tilde{\phi}}$ in order to accurately represent the enlarged Fourier space. This trade-off can be seen in the lower-right panel of Fig. 3.6. To capture the Gaussian structure of the free HO requires only the inclusion of a small region of $\bar{\Pi}$ around zero. For 6 states, the maximum value of the momentum can be determined by Eq. (3.4) to be ± 2.62. This value is indicated by the vertical, gray dashed lines in Fig. 3.6. Outside of this region, the exponential behavior turns power-law and inclusion of this portion of the wavefunction no-longer informs the sampling

about the physical momentum space, only about artifacts of the truncation. By fitting a continuous Gaussian of infinite spatial extent to the wavefunction at left and plotting its Fourier transform on the right (small-dashed curves), 6 states are found to lead to a $\delta_{\tilde{\phi}}$, and thus a maximum $k_{\tilde{\phi}}$, that captures the Gaussian central region of the wave function. For $\lambda = 32$, this maximum value in momentum space is no longer sufficient to saturate the NS sampling limit. There is a significantly larger domain in momentum space before the wavefunction transitions to power-law behavior, not appearing until $\bar{\Pi}$ values of $\sim \pm 10$. Again, with Eq. (3.4), 18 states per site are seen to be required for this truncation in momentum space, a value in agreement with the location of the NS saturation point seen in the upper panel of Fig. 3.6.

By comparing the gray band in Fig. 3.4, the scaling of the NS saturation for the free 1-site HO, with the highest precisions attained in the upper panel of Fig. 3.6, it can be seen that the number of states (or qubits) required to achieve a particular precision is relatively stable for this self-interaction. The values of $\bar{\phi}_{\max}$ along this band are skewed from those in the free theory, but the maximum precision attained through distribution of a fixed number of wavefunction sample points is not. As this self-interaction causes a smooth deformation of the wavefunction, trading extent in field space for that in conjugate-momentum space, it is not surprising that the interacting ground state wavefunction achieves similar precision given similar quantum resources.

When using a basis of HO wavefunctions, the main consideration is, again, assuring that the chosen representation of the wavefunction sufficiently spans both field and conjugate-momentum space. With JLP, $\bar{\phi}_{\max}$ is used to control the domain of support in field space while $\delta_{\tilde{\phi}}$ (or equivalently the number of states per site) is used to control the domain of support in momentum space. With the HO basis functions, the parameters to be tuned are ω_ϕ and the number of states. Unlike the lattice-parameters of JLP, these parameters give correlated modifications to field and conjugate-momentum space. Increasing ω_ϕ creates basis functions that are more localized in field space while exploring higher momentum-space truncations. Increasing the number of states also increases the momentum-space truncation,

but expands the field-space region of support. Because of these correlations, it is meaningful to compare JLP's dependence of $\bar{\phi}_{\max}$ with a combination of n_Q and ω_ϕ dictating the extent of the HO wavefunction basis, $\sqrt{\frac{2^{n_Q}}{\omega_\phi}}$, reflecting the fact that $\sqrt{\langle\phi^2\rangle} \sim \sqrt{2^{n_Q}}$ and $\sim 1/\sqrt{\omega_\phi}$.

In Fig. 3.7, the expected precision of the ground-state energy is shown as a function of $\bar{\phi}_{\max}$ and $\sqrt{\frac{2^{n_Q}}{\omega_\phi}}$ for JLP (dashed) and HO (solid) bases, respectively. Values on the left of the minimum of each curve have reduced precision due to insufficient sampling in field space, while to the right of the minimum, the precision is reduced due to insufficient sampling in momentum space. Only at the minimum is the sampling in both spaces optimal. It can be concluded that for these parameters, values of $\bar{\phi}_{\max}$ or ω_ϕ can be selected (for $n_Q \geq 3$) such that the errors introduced by digitization are significantly smaller than those expected from computations on NISQ-era hardware. As such, the digitization of the scalar field is not expected to limit the accuracy of NISQ-era computations. For $n_Q < 3$, the field digitization is expected to provide a limit to the accuracy of NISQ-era computations. Comparing the basis choices given a fixed number of qubits, there is a value of the HO basis parameters that produce a higher-precision result in this system than a $\bar{\phi}_{\max}$-tuned JLP wavefunction digitization. For a desired precision, the HO basis offers a larger acceptable window in the basis tuning parameters than does the JLP field digitization basis. This translates, through the circuit descriptions of figures in Appendices A and C of Ref. [45], to reduced sensitivity on the exact angles applied in the Z-axis rotation gates. This sensitivity will be relevant in the NISQ era with imperfect gate fidelities, and will continue to be relevant once fault-tolerant quantum computing is available (where the precision determines the number of T gates [5] needed to decompose any Z-axis rotation with expected scaling of $\left|\log_2|\epsilon_\theta|\right|$ [124, 125, 126].)

While Fig. 3.7 shows desirable qualities when using HO basis functions to digitally describe the wavefunction, quantum simulations of quantum systems have many resource re-

[5]The T gate, $\begin{pmatrix} 1 & 0 \\ 0 & e^{i\pi/8} \end{pmatrix}$, is the gate commonly added to the Clifford group to create universal quantum computation. Its proliferation is considered a meaningful cost model for many plausible implementations considered for future fault-tolerant quantum computing.

quirements to consider beyond qubit number and necessary precision of rotation angles. Specifically, a large consideration in the feasibility of successfully implementing a quantum calculation in the NISQ era is the number and type of gates required to implement a single Trotter step of the time-evolution operator. These gate counts are detailed in Table 3.2. For JLP, the 1-body operators from the QFT and $\binom{n}{2}$ 2-body operators from the terms quadratic in the field and its conjugate momentum are still present. The $\lambda\phi^4$ interaction term introduces only $\binom{n}{4}$ 4-body operators and additional contributions to the identity and 2-body operators. The latter can be consolidated with the operators previously identified and thus does not contribute to the gate cost (it does, however necessitate separate operator coefficient structures in field and conjugate-momentum space). The fact that operators are limited to interacting between a number of qubits equal to the highest power of field interaction included in the Hamiltonian is a feature of JLP not shared by the HO basis. Here, the additional 2-qubit CNOT gates required to implement the QuFoTr for JLP field digitization are quickly outnumbered by the CNOT gates required to implement the k-body operators for k limited by the number of qubits in the site-register.

The fact that the scaling of CNOTs in the JLP basis is limited to n_Q^4 is advantageous when considering the noise landscape of NISQ-era hardware dominated by 2-qubit interactions. In Table 3.1 and Table 3.2, the CNOT gate counts generally do not include cancellations that may occur for particular operator orderings in the Trotterization [38]. In the JLP basis, we have performed a manual circuit compilation of the $\lambda\phi^4$ scalar field theory, eliminating pairs of adjacent CNOT gates, resulting in the CNOT gate counts shown in the right-most column of Table 3.2. While the $\bar{\phi}^2$ operator set by itself does not permit a reduction of the number of gates, in combination with the $\bar{\phi}^4$ operator set, and also among the $\bar{\phi}^4$ operators, redundant CNOT operations in the leading Trotter expansion can be removed. While a similar reduction can be applied to the circuits of the HO basis, many changes of Pauli bases between operations make systematic cancellation difficult. As was the case with the JLP basis, it is not expected that carrying out this elimination in the HO basis will change the scaling of the CNOT-operator accumulation. A discussion of this manual compilation is

given in Appendix B of Ref. [45].

Delocalized Wavefunctions: $m^2 < 0$

As mentioned in the introduction, $\lambda\boldsymbol{\phi}^4$ scalar field theory in 3+1 dimensions is a cornerstone of the standard model of electroweak interactions [127, 128, 129], where $\boldsymbol{\phi}$ is an electroweak doublet of complex real scalar fields. At low energies, its potential is such that the vev of $\langle\boldsymbol{\phi}\rangle \neq 0$, breaking the electroweak gauge group $\mathrm{SU}(2)_L \otimes \mathrm{U}(1)_Y \to \mathrm{U}(1)_Q$ down to that of quantum electrodynamics. This minimal symmetry-breaking mechanism, the Higgs mechanism, generates masses for the weak gauge bosons and the fermions, and gives rise to a single physical scalar particle, the Higgs boson [130, 131, 132, 133]. In a 0+1 dimensional theory, the parameter regime $-\mu^2 = m^2 < 0$ produces a potential that contains two minima located at $\phi = \pm\frac{\sqrt{3!}\mu}{\sqrt{\lambda}}$. For any physical value of μ, the ground state wavefunction of the Hamiltonian is symmetric under $\phi \to -\phi$ and non-degenerate and, as such, respects the discrete global Z_2 symmetry of the Hamiltonian, with a vev of $\langle\phi\rangle = 0$. However, it is delocalized with maxima near the two minima of the potential. The wavefunction of the 1^{st}-excited-state of the system is similar to that of the ground state, but it is antisymmetric under $\phi \to -\phi$. As μ becomes large, and the components of both wavefunctions become increasingly localized around the minima of the potential, the energy difference between the ground state and the 1^{st}-excited-state becomes exponentially small, determined by the barrier-penetration amplitude for transitioning from $+\phi$ to $-\phi$.

It is again relevant to consider alternate digitizations for representing the distributions in field and conjugate-momentum space. For large $\mu^2 > 0$, (where the quantity $\frac{\mu}{\sqrt{\lambda}}$ is large with respect to the wavefunction's natural spatial extent), the field space wavefunction expands toward two localized and distinct regions of support. This is the case for the parameter values of $\mu = 2, 5$ and $\lambda = 1$ chosen in Fig. 3.8 and in Fig. 3.9. This enlarged field-space coverage demands similarly-large values of $\bar{\phi}_{\max}$ when working in the JLP digitization, or smaller values of ω_ϕ in defining the HO basis. Achieving these requirements can be accomplished in either basis when they are tuned, as shown in Fig. 3.8. An additional consideration in

considering the configuration of quantum simulations is that the 1^{st}-excited-state is becoming very close in energy with the ground state, a feature that is not present in the previously considered situations. A low-precision calculation, resulting from the use of a small number of qubits, will be unable to resolve the ground state from the 1^{st}-excited-state, and the wavefunctions emerging from such calculations will likely be arbitrary combinations of the two. Higher-precision calculations, requiring a larger number of qubits, will be required to resolve the low-lying states in such systems. For such delocalized states, in contrast to the results obtained from a potential with $m^2 > 0$ in Fig. 3.7, the JLP basis can be tuned to produce higher precision in the ground-state energy than the HO basis with the same number of qubits. This outcome is not surprising—if the wavefunction is deformed into a distribution that is far from Gaussian, as seen in Fig. 3.9, a set of HO basis functions is no longer expected to offer superior coverage in the digital sampling. An interesting result of this demonstration is the degree to which the formulation of JLP, in which the basis is a periodic collection of delta functions agnostic to the structure of the wavefunction, is capable of exceeding the precision of a basis specialized for an alternate symmetry of the low-lying wavefunctions. The ability of JLP to perform with precision when applied to a range of systems, and thus require little knowledge of the structure of the low-lying states, will be a desirable feature of quantum simulations of more sophisticated, strongly-interacting field theories.

In these types of systems, and others, with near-degenerate low-lying states, the impact of noise in the quantum device upon correctly identifying the ground state wavefunction is expected to be significant. As discussed in Appendix H of Ref. [45], the noise levels (from either the propagator approximation of step (2) or the intrinsic gate implementation noise of step (3) in Fig. 3.1) present in calculations with multiple degenerate extrema in the potential producing delocalized low-lying states will limit the systems that can be reliably explored as energy splittings are buried below the software (2) and hardware (3) noise levels.

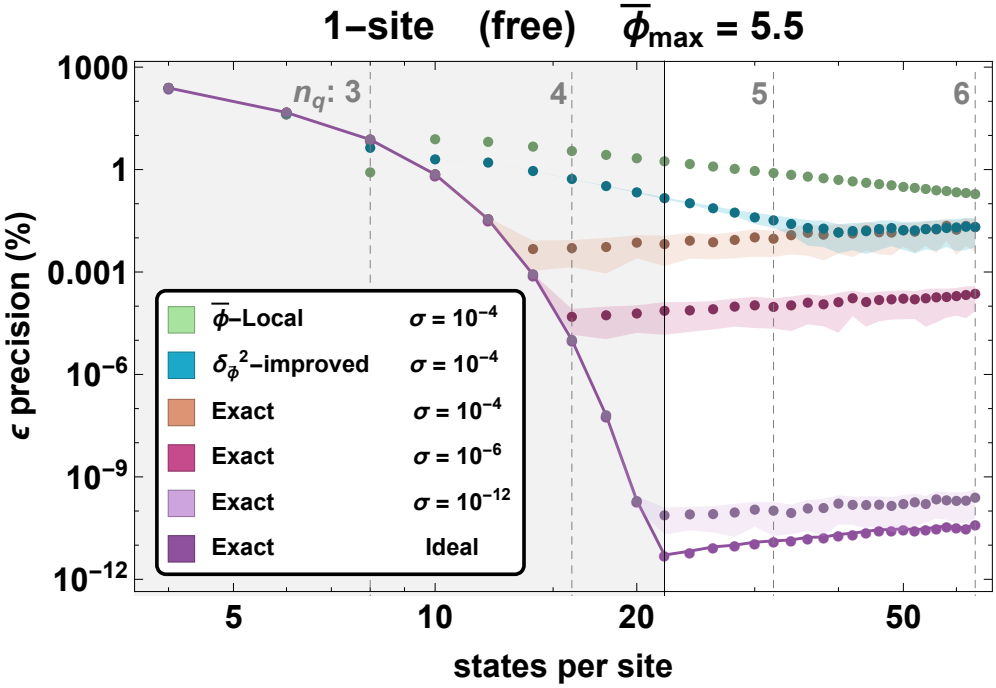

Figure 3.3: The precision of the ground state energy of the HO in Eq. (3.1) for unimproved, improved and exact conjugate-momentum operators, over a range of digitizations of $\bar{\phi}$ with different levels of gate noise. The light-green points correspond to implementing the finite-difference conjugate momentum operator, the light-blue corresponds to the $\mathcal{O}(\delta_{\bar{\phi}}^2)$-improved conjugate momentum operator, and the purple-points correspond to the exact conjugate momentum operator. Gaussian noise with a width σ is added to the diagonal elements of the eigenvalues of the conjugate momentum operators (resembling a simplified version of process (3) in Fig. 3.1). The maximum value of the field is fixed to be $\bar{\phi}_{\rm max} = 5.5$, enabling a precision of $\sim 10^{-12}$ for an ideal quantum computer. The vertical light-gray dashed lines correspond to the number of qubits associated with the number of states, while the solid darker-gray line corresponds to the naïve estimate of saturation of the NS sampling bound based upon the properties of the HO ground state wavefunction (the six calculations cross the latter of these lines top-to-bottom in the order of the legend). For the computational errors anticipated in the NISQ-era, 4 qubits are seen to be sufficient to eliminate the digitization of the scalar field as a source of important error.

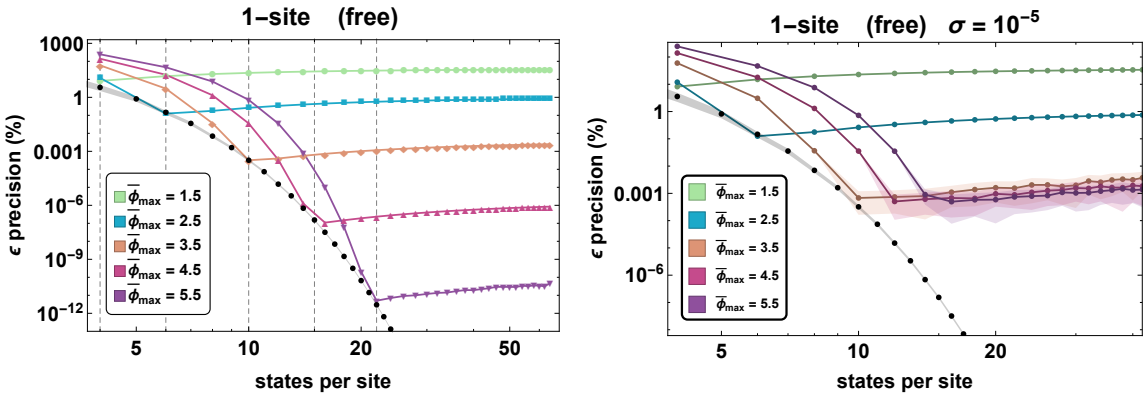

Figure 3.4: The precision of calculations of the ground state energy of the HO in Eq. (3.1). The left panel shows expectations for an ideal quantum computer for different values of $\bar{\phi}_{\max}$ as a function of the number of states. The vertical gray-dashed lines correspond to the location of inflection points predicted by the NS sampling theorem for the indicated values of $\bar{\phi}_{\max}$. A fit to the grey points calculated at the NS saturation point indicates $\epsilon \sim (1.8(2) \times 10^3)\ 2^{-2.234(4) n_s}$, quantifying the double-exponential scaling between ϵ and n_Q. The right panel shows the expected precision from a device with noise at the level of $\sigma = 10^{-5}$ in the application of the field conjugate-momentum operator (as described in the text). In both panels, the NS saturation points arise left-to-right in the top-to-bottom order of the legend.

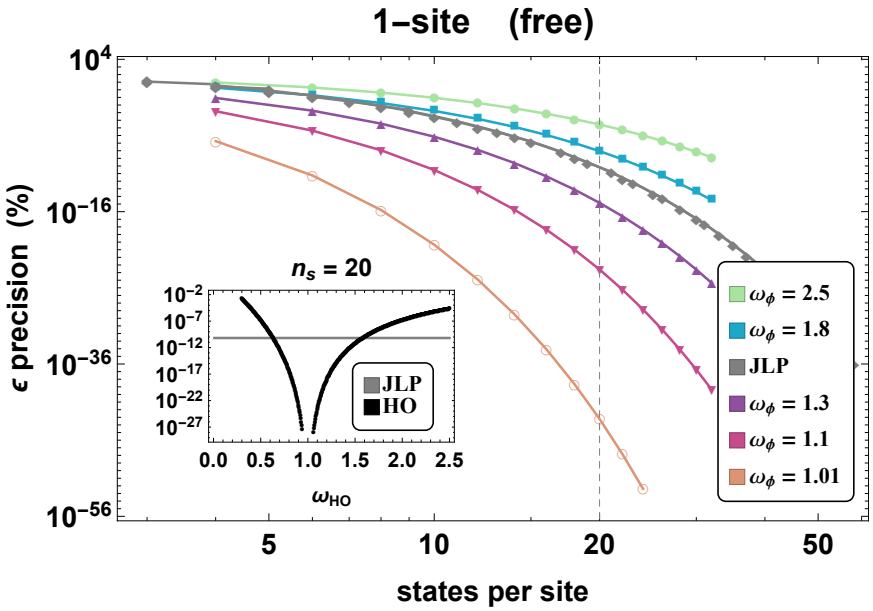

Figure 3.5: The expected precision of the ground state energy of the HO Hamiltonian in Eq. (3.1) on an ideal quantum computer using a HO basis defined by ω_ϕ in Eq. (3.9) as a function of the number of basis states. The inset figure shows the scaling for a HO basis of 20 states, which is a slice of the main figure indicated by a vertical gray dashed line (the calculations cross this line top-to-bottom in the order of the legend). In the limit of $\omega_\phi = 1$ the lowest-lying basis state is an eigenstate, and $\epsilon = 0$. Tuning ω_ϕ to be in the vicinity of the optimal value $\omega_\phi = 1$ outperforms field-space digitization, shown by the gray JLP curve.

Basis	n_Q	0-body	1-body	2-body	3-body	4-body	5-body	6-body	QFT	CNOTs
	2	1	8	2					✓	8
	3	1	14	6					✓	24
JLP	4	1	20	12					✓	48
	5	1	26	20					✓	80
	6	1	32	30					✓	120
JLP	n_Q	1	$6n_Q - 4$	$2 * \binom{n_Q}{2}$					✓	$8\binom{n_Q}{2}$
	2	1	2							0
	3	1	3							0
$\text{HO}_{\omega\equiv 1}$	4	1	4							0
	5	1	5							0
	6	1	6							0
$\text{HO}_{\omega\equiv 1}$	n_Q	1	n_Q							0
	2	1	3	1						2
	3	1	4	4	3					20
$\text{HO}_{\omega\neq 1}$	4	1	5	5	11	7				96
	5	1	6	6	16	26	15			352
	6	1	7	7	22	42	57	31		1120

Table 3.1: Resource requirements for one step in the Trotterized time evolution of a HO in the field-digitization JLP basis, a tuned HO basis, and a detuned HO basis. CNOT counts are based upon a standard multi-Pauli implementation requiring $2(k-1)$ CNOTs for each k-body operator. When a QuFoTr is required (JLP), the standard CNOT counts of $2\binom{n_Q}{2}$ for this operation (and its inverse) are included. With the expected limitations in the number of gate operations applied in NISQ-era devices, only systems with $n_Q \leq 4$ may be practical.

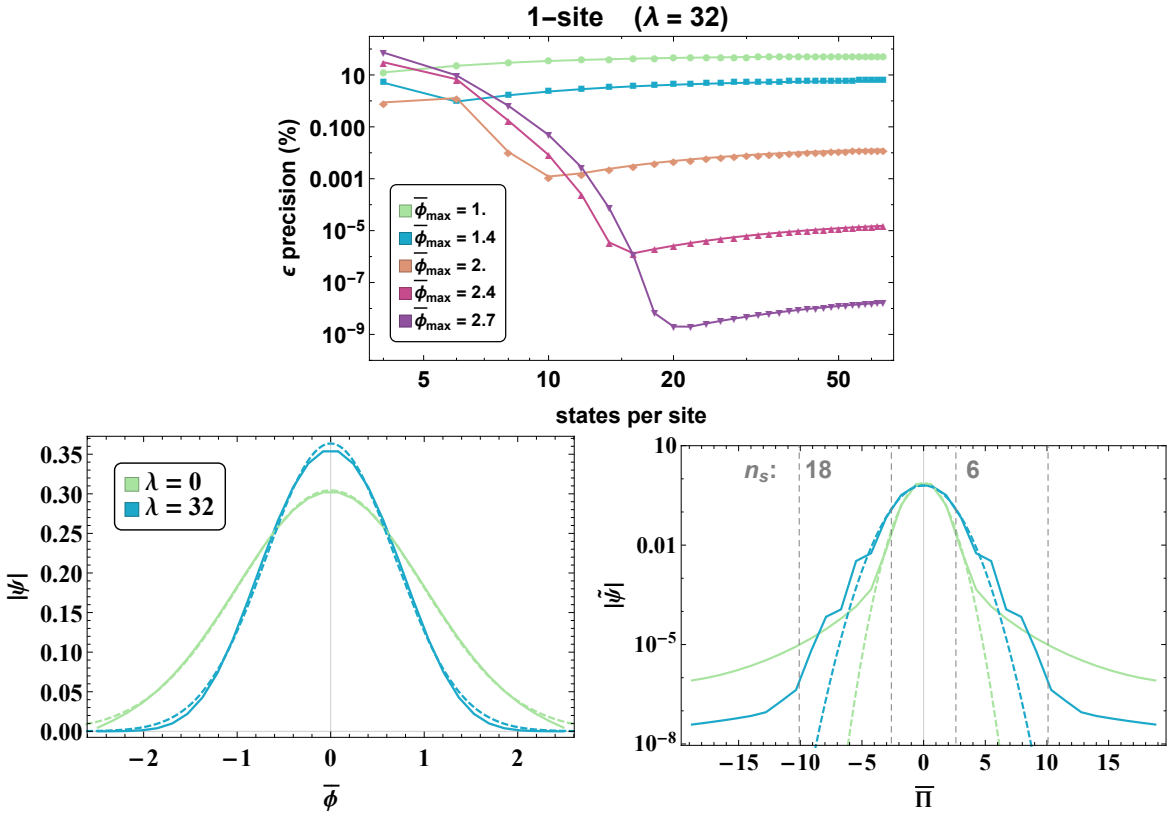

Figure 3.6: The panel in the upper row shows the expected precision of calculations of the ground-state energy of a 1-site $\lambda\phi^4$ scalar field theory performed with an ideal quantum computer for different values of $\bar{\phi}_{\max}$ as a function of the number of states (the NS saturation points arise left-to-right in the top-to-bottom order of the legend). The lower row shows the field and conjugate-momentum space wavefunctions (left and right, respectively) for the free(green or lightly-shaded) and interacting(blue or darkly-shaded), 1-site $\lambda\phi^4$ shown at constant $\bar{\phi}_{\max} = 2.5$. The introduction of non-zero λ reduces the spatial support of the wavefunction while increasing its support in momentum space. The small-dashed green(lightly-shaded) and blue(darkly-shaded) lines in the right panel are Fourier transforms of Gaussian fits to the wavefunctions in the left panel. The vertical, gray dashed lines in the right panel show the truncations in $\bar{\Pi}$ for 6 and 18 states—the location of NS saturation for $\bar{\phi}_{\max} = 2.5$ as seen in Figs. 3.4 and the first row here.

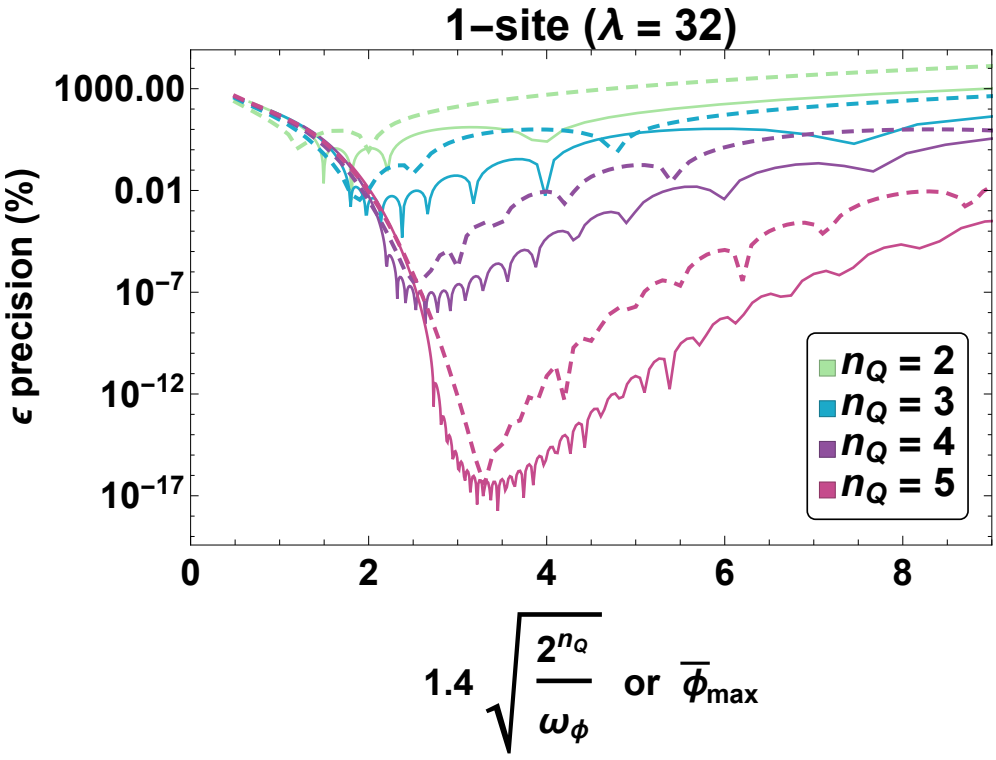

Figure 3.7: Exploration of sensitivity in JLP field digitization (dashed lines) and the HO basis (solid lines) to tuning of digitization parameters determining the low-energy states in momentum space. For JLP, the relevant parameter is $\bar{\phi}_{\rm max}$, while for the HO basis it is a combination of the frequency defining the basis, ω_ϕ and the number of states, $\sim \sqrt{2^{n_Q}/\omega_\phi}$. The horizontal axes of the HO curves have been rescaled to $1.4\sqrt{2^{n_Q}/\omega_\phi}$ to align them with the JLP curves. These tuning curve pairs are minimized with smaller values of ϵ in the top-to-bottom order of the legend.

Basis	n_Q	0-body	1-body	2-body	3-body	4-body	5-body	6-body	QFT	CNOT$_{\text{uncompiled}}$	CNOT$_{\text{compiled}}$
	2	1	8	2					✓	8	8
	3	1	14	6					✓	24	24
JLP	4	1	20	12		1			✓	54	52
	5	1	26	20		5			✓	110	96
	6	1	32	30		15			✓	210	164
JLP	n_Q	1	$4n_Q - 6$	$2*\binom{n_Q}{2}$		$\binom{n_Q}{4}$			✓	$8\binom{n_Q}{2} + 6\binom{n_Q}{4}$	
	2	1	3	2						4	
	3	1	5	9	4					34	
HO	4	1	6	16	18	10				164	
	5	1	7	22	32	44	22			612	
	6	1	8	29	44	84	98	46		1982	

Table 3.2: Resource requirements for one first-order-Trotterized step of time evolution for 1-site $\lambda\phi^4$ scalar field theory in the field-digitization JLP basis and HO basis. CNOT counts are based upon a standard multi-Pauli implementation requiring $2(k-1)$ CNOTs for each k-body operator. When the QFT is required (JLP), the standard CNOT counts of $2\binom{n_Q}{2}$ for this operation (and its inverse) are included in the second-to-last column. The last column contains the required CNOT gates after manual compilation (see Appendix B of Ref. [45]). With the expected limitations in the number of gate operations applied in NISQ-era devices, only systems with $n_Q \leq 4$ may be practical.

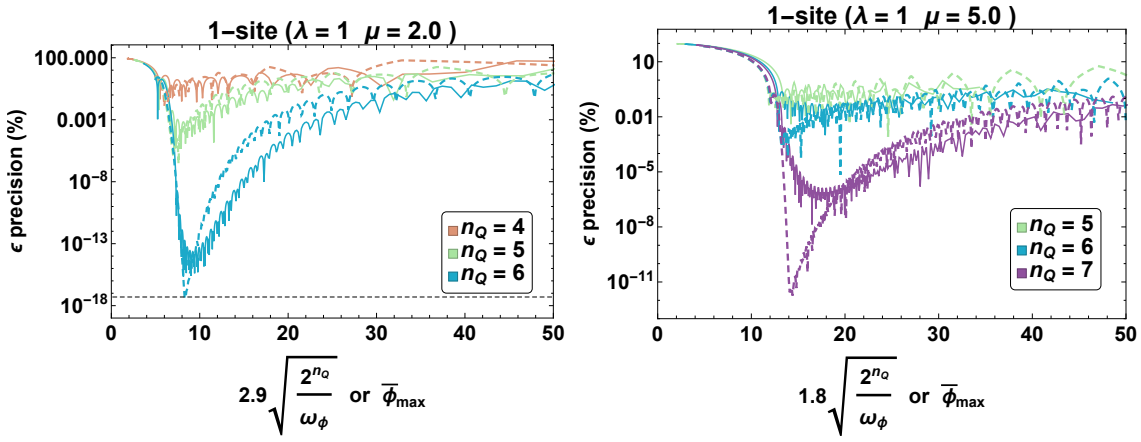

Figure 3.8: Exploration of the sensitivity in JLP field digitization (dashed lines) and the HO basis (solid lines) to tuning of digitization parameters determining the low-energy states for a 0+1-dimensional scalar field theory with $m^2 < 0$, with $\mu = 2$ (left panel) and $\mu = 5$ (right panel), resulting in delocalized wavefunctions. For JLP, a relevant parameter is $\bar{\phi}_{\max}$, while for the HO basis it is a combination of the frequency defining the HO basis, ω_ϕ, and the number of states per site. The horizontal axes of the HO curves have been rescaled to $2.9\sqrt{2^{n_Q}/\omega_\phi}$ in the left panel and $1.8\sqrt{2^{n_Q}/\omega_\phi}$ in the right panel to align them with the JLP curves. The black-dashed horizontal line in the left panel corresponds to the precision required to distinguish between the ground state and 1^{st} excited state for $\mu = 2$. The corresponding line for $\mu = 5$ in the right panel lies many orders of magnitude beyond the range of the figure. In both panels, the tuning curve pairs are minimized with smaller values of ϵ in the top-to-bottom order of the legend.

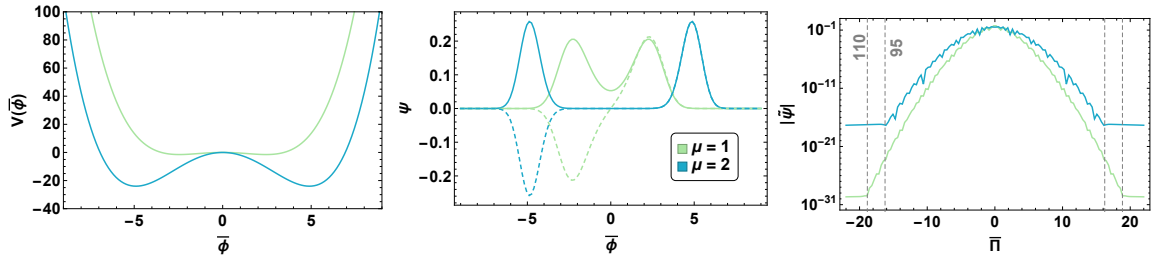

Figure 3.9: The potentials (left panel) and wavefunctions (center and right panels) of the ground states (solid curves) and 1^{st} excited states (dashed curves) for systems with $m^2 < 0$. The center panel shows the spatial wavefunctions for $\lambda = 1$ and $\mu = 1, 2$, while the right panel shows the corresponding momentum-space wavefunctions. These wavefunctions result from using the JLP basis with $\overline{\phi}_{\rm max} = 9$ and $n_Q = 7$ qubits. (The vertical dashed-grey lines in the right panel indicate the number of states at which the NS bound is saturated and thus an increase in $\bar{\phi}_{\rm max}$ would be profitable over an increase in quantum states).

3.4 1+1 Dimensional $\lambda\phi^4$ Scalar Field Theory

The detailed analysis of $0+1$ scalar field theory presented in the previous sections provides a solid foundation with which to consider scalar field theory in higher spatial dimensions with NISQ-era quantum computers. In section 2.1, the Hamiltonian for scalar field theory in $d+1$ dimensions was presented, along with its naïve layout on a spatial lattice. The operator structure for multiple spatial sites is the same as for one spatial site except for the presence of the $\phi\nabla^2\phi$ operator, which includes contributions from particle motion into the Hamiltonian. The naïve representation of this operator as $\phi\nabla_a^2\phi$ introduces terms that couples the fields at two adjacent spatial sites. In general, smearing the fields to tame high-energy quantum fluctuations, while preserving low-energy observables, will introduce couplings beyond adjacent spatial sites, but these can be implemented with operations on two sites also.

In the situation with $d > 0$, the text-book way to construct field theory calculations is to work with HO's for each spatial-momentum mode, i.e. define fields in terms of quanta with well-defined spatial momentum. In perturbative calculations that can be performed by hand, this method is extremely efficient. In numerical computations of non-perturbative field theories, such as LQCD, the system is typically defined with regard to fields in position space, while components of calculations involve determining eigenvectors of the Dirac operator in the presence of a particular configuration of gauge fields. In the study of systems with few sites in each spatial direction, it is likely the case that calculating with the momentum-space modes is efficient [94]. First implementation of this quantization procedure on quantum devices has been completed by an ORNL team [134]. However, as argued by JLP [24, 25, 62, 63], as the interactions that are local in position space, such as $\lambda\phi^4$, become non-local[6] in momentum space (distant momentum oscillators are capable of producing momentum-conserving contributions to the Hamiltonian), time evolving the system to a given state

[6]For discussions of the implementation of non-local quantum interactions dominating the cost of quantum chemistry systems, see Refs. [135, 136, 137, 138, 139, 140] where alternate choices of qubit mappings or quantum simulation methods are explored to increase the locality of quantum operations.

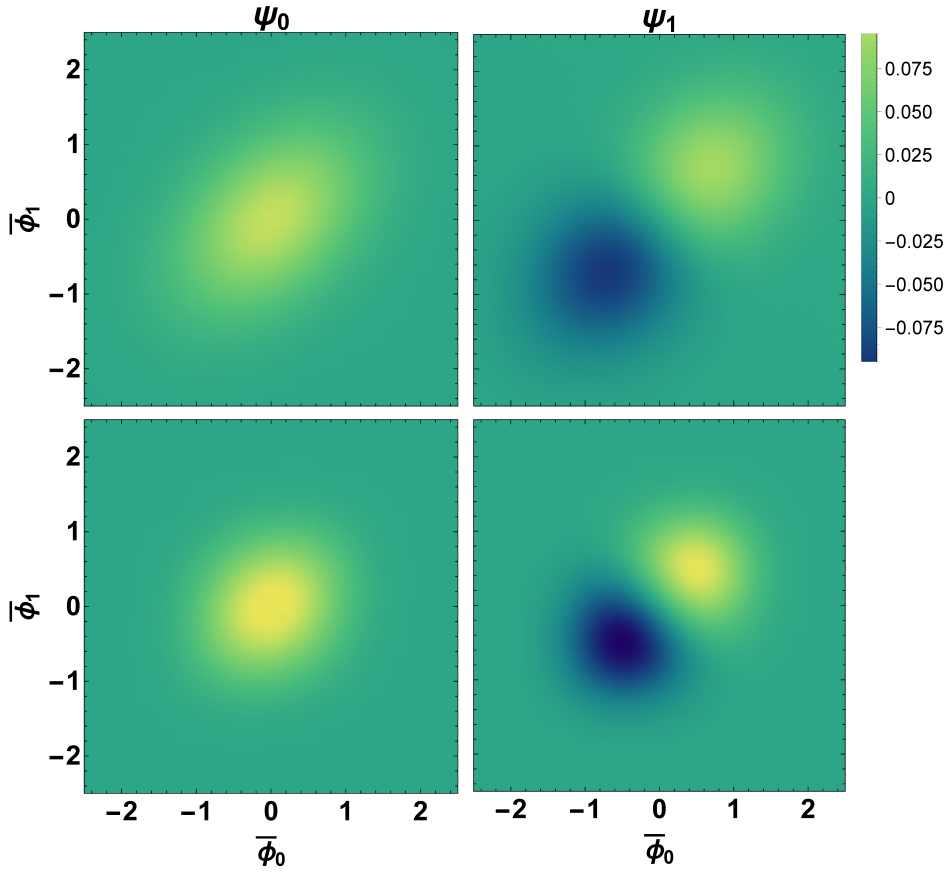

Figure 3.10: The ground and first-excited state wavefunctions for 2-site $\lambda\phi^4$ scalar field theory with $\lambda = 0$ and $\lambda = 32$ (top and bottom, respectively). The first excited state shows positive correlation between the oscillations at the two spatial sites $\left(\bar{\phi}_0, \bar{\phi}_1\right)$.

defined in momentum-space will become increasingly inefficient with increasing system size relative to a state defined in position space [24, 25, 62, 63, 138]. For the remaining discussion, we will limit ourselves to states and operations defined in position space.

Application of the $d+1$-dimensional $\lambda\phi^4$-Hamiltonian time evolution operator to a position-space state can be accomplished site-by-site, and involve at most d neighboring two-site interactions at each site. Therefore, for a system with $(L/a)^d$ spatial lattice sites, this will require $(L/a)^d$ such applications. This being the case, study of the 2-site 1+1 dimen-

sional $\lambda\phi^4$ theory provides a complete inventory of the operations and gate counts required to perform a $d+1$-dimensional $\lambda\phi^4$ calculation, and we have performed such estimates and numerical calculations in this 2-site theory. Given this 2-site locality and quantum hardware capable of parallelizing the implementation of gates acting in separate tensor product spaces, application of the Hamiltonian to a position-space state can be accomplished with a circuit of constant depth with increasing lattice size [37]. The field-space wavefunctions associated with the ground state and first-excited state of the 2-site $1+1$ dimensional theory are shown in Fig. 3.10, with the wavefunction at site-0 denoted by $\bar{\phi}_0$ and at site-1 by $\bar{\phi}_1$. A large value of the self-interaction coupling, λ, focuses this correlation in $\left(\bar{\phi}_0, \bar{\phi}_1\right)$.

As seen in Fig. 3.11, the 2-site $\lambda\phi^4$ theory experiences double-exponential convergence in n_Q to the un-digitized value. However, just as the use of a finite-difference operator in the field-space implementation of $\bar{\Pi}^2$ introduced polynomial deviations in $\delta_{\bar{\phi}}$ (see results from local and improved operators in Fig. 3.3), the finite-difference implementation of $\phi\nabla_a^2\phi$ in position space introduces analogous polynomial deviations in a from the continuum limit. These lattice-spacing errors are not shown in Fig. 3.11. Thus, this method converges to the continuum value with lattice-spacing errors that scale as $\epsilon \sim 2^{N_Q}$. Of course, with a large quantum computer, it could become possible to remove these polynomial lattice-spacing artifacts through use of the QuFoTr and subsequent implementation of the exact lattice phases in Fourier space to create a smeared, non-local gradient operator (exactly as was done in field space). Rather than requiring a QuFoTr to be applied on each of the modest-sized qubit registers associated with individual lattice sites, this proposal would require a QuFoTr across the entire lattice—an entangling operation amongst all N_Q qubits. At least in the NISQ era, it is expected that such global operations will be prohibitive both in gate fidelity as well as coherence time. For this reason, the finite-difference form of the gradient operator, demanding only local interactions between the qubit registers at neighboring sites, appears to be optimal [24, 25, 62, 63].

When implementing the gradient operator as a finite difference, there is only one set of operators $\bar{\phi}(x)\bar{\phi}(x+1)$ acting between the spatial sites that need be additionally considered.

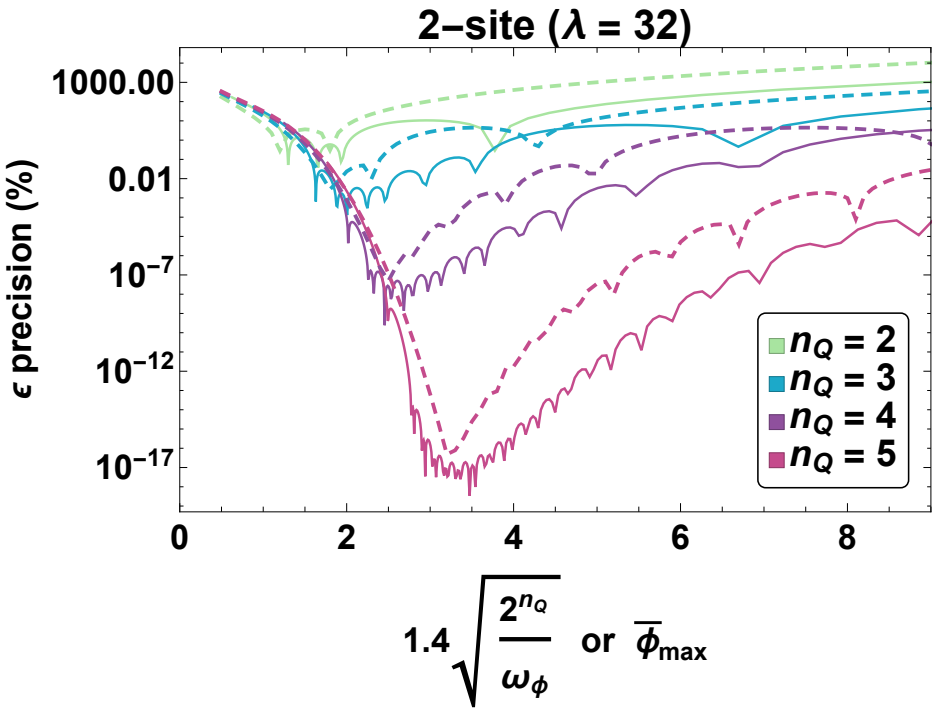

Figure 3.11: The precision of the calculated ground-state energy for the 2-site lattice $\lambda\phi^4$ scalar field theory with $\lambda = 32$ performed with an ideal quantum computer for different numbers of qubits as a function of support in field space. For JLP, the relevant parameter is $\bar{\phi}_{\max}$, while for the HO basis it is a combination of the frequency defining the HO basis, ω_ϕ, and the number of states per site. The shown precision does not include deviations of this 2-site $1+1$ dimensional theory from the continuum limit of the $1+1$ dimensional theory for which the number of spatial sites approaches infinity for a fixed spatial extent. The horizontal axes of the HO curves have been rescaled to $1.4\sqrt{2^{n_Q}/\omega_\phi}$ to align them with the JLP curves. These tuning curve pairs are minimized with smaller values of ϵ in the top-to-bottom order of the legend.

Basis	n_Q	2-body	3-body	4-body	5-body	6-body	7-body	8-body	9-body	10-body	11-body	12-body	CNOT
	2	4											8
	3	9											18
JLP	4	16											32
	5	25											50
	6	36											72
	n_Q	n_Q^2											$2n_Q^2$
	2	1	6	9									80
	3	1	8	30	56	49							1,152
HO	4	1	10	47	140	271	330	225					11,264
	5	1	12	68	244	630	1204	1668	1612	961			89,600
	6	1	14	93	392	1186	2772	5154	7560	8541	7182	3969	626,688

Table 3.3: Operators associated with the additional $\bar{\phi}(x)\bar{\phi}(x+1)$ operator resulting from the finite-difference spatial gradient operator $\phi\nabla_a^2\phi$ for time evolution of 2-site lattice $\lambda\phi^4$ scalar field theory in the JLP and HO field-digitization bases. CNOT counts are based upon a standard multi-Pauli implementation requiring $2(k-1)$ CNOTs for each k-body operator.

Table 3.3 shows the nature and number of pauli terms associated with this additional operator in the $1+1$-dimensional Hamiltonian[7]. In this 1+1-dimensional system, the coefficient of the mass term in field space is modified by two of the terms in the $\phi\nabla_a^2\phi$ operator, but the operator structure is unaltered. As mentioned above, the quantum resources calculated in this paper may be easily combined to determine the requirements for larger lattices in d-dimensions, for example

$$\text{CNOT}_{lattice}(n_Q, d, L/a) = L^d a^{-d}\ \text{CNOT}_{\text{1-site}}(n_Q) + dL^d a^{-d}\ \text{CNOT}_{\bar{\phi}(x)\bar{\phi}(x+1)}(n_Q) \qquad (3.12)$$

expresses the total number of CNOT gates required to evolve the field across a lattice with $\text{CNOT}_{\text{1-site}}(n_Q)$ extracted from Tables 3.1 or 3.2 for the free or self-interacting fields, respec-

[7]These gate counts are in addition to those resulting from action on the individual sites that have been determined in previous sections of this paper.

tively, $\text{CNOT}_{\bar{\phi}(x)\bar{\phi}(x+1)}(n_Q)$ extracted from Table 3.3, n_Q the number of qubits used to digitize the field at each site, d the dimensionality of space, L the spatial extent in each dimension, and a the lattice spacing in each dimension. The nearest-neighbor interactions between sites in the JLP digitization requires all n_Q^2 2-body operators that can be created between the two site registers. This is contrasted by the HO basis where operators between the two site registers are not limited to 2-body qubit interactions, but require tensor product Pauli operators acting on up to all $2n_Q$ qubits. Because of this dramatic difference in the structure of necessary operators, even for the smallest number of qubits per spatial site, the JLP basis requires fewer resources to implement the $\phi\nabla_a^2\phi$ operator—emphasizing the importance of an application's physical representation onto qubit degrees of freedom in quantification of its required quantum resources.

3.5 Summary and Outlook

Quantum computing and quantum information science is anticipated to provide disruptive changes to scientific computing and to the ways that we think about addressing scientific challenges. The prospect of being able to explore quantities in quantum many-body systems, including quantum gauge field theories such as quantum chromodynamics, that require exponentially-large classical computing resources, such as for dense matter or in the time-evolution of non-equilibrium systems, is truly exciting. In this work, we have built upon foundational works by Jordan, Lee and Preskill [24, 25, 62, 63] on how to formulate scalar field theory on quantum computers to determine properties of the scalar particle and interactions, both elastic and inelastic, between particles. In an attempt to understand the magnitude of resources required for even modest quantum computations in a simple field theory, our work has focused on the digitization of scalar field theories with only a small number of qubits per spatial lattice site. The recent work by Macridin, Spentzouris, Amundson and Harnik [86, 88], which, building upon the work of Somma [102], emphasized the utility of the Nyquist-Shannon (NS) sampling theorem, is a theme for our work as it provides an important guide for tuning digitization parameters in quantum field theories for the

accurate representation of field and conjugate-momentum spaces on quantum devices (and may also have implications for classical calculations).

In addition to an in-depth exploration of the requirements for a basis of eigenstates of the field operator, as introduced by JLP, we have introduced and explored the resources required for, and the utility of, a basis of harmonic oscillator eigenstates. We have performed operator decompositions of the Hamiltonians for a small number of qubits in $0+1$ and $1+1$ dimensional systems. As tunings are required in both bases for an optimal computation on an ideal quantum device, we find that both bases are effective, but that the JLP basis appears to be more robust for systems that are delocalized in field space or not smooth in either field or conjugate-momentum space. We considered the impact of noise on calculations in such systems and found that parameters defining the field theory should be tuned given the limits in precision imposed by the quantum device in order to optimize the scientific productivity of the calculation. In either basis, when tuned, a quantum device with $n_Q = 3$ or $n_Q = 4$ qubits used to define the field at each spatial lattice site is found to be able to provide a precision of better than $\sim 10^{-6}$ for a given lattice spacing for a potential with $m^2 > 0$. Separating the spatial lattice-spacing systematic error from the digitization systematic error in field space, the digitization error in the space of low-lying energy eigenstates, ϵ_{dig}, is found to scale as $|\log|\log|\epsilon_{\text{dig}}|||| \sim n_Q$ for n_Q qubits per site, while the lattice spacing error, ϵ_{latt}, scales as $|\log|\epsilon_{\text{latt}}|| \sim N_Q$ where N_Q is the total number of qubits in the simulation.

The lessons learned from studying the digitization of a scalar field onto qubit degrees of freedom have been numerous. The following is an itemized summarization of those lessons appearing in 0+1 dimensional field theory—before the additional complications of a lattice spacing and spatial momentum are introduced in section 3.4.

1. The scalar field digitization techniques of Jordan-Preskill-Lee [24, 25, 62, 63, 102, 86, 88], a momentum-space mode expansion [94] and a harmonic oscillator basis are relevant for NISQ-era hardware implementations. The number of qubits per site needed to reduce the digitization and discretization systematic errors below near-term hardware

noise levels are $n_Q \sim 4$ for potentials with $m^2 > 0$ and $n_Q \gtrsim 6$ for potentials with $m^2 < 0$. These qubit requirements are consistent with those of Refs. [102, 86, 88] and extend these modest requirements to delocalized field-space wavefunctions.

2. When the Nyquist-Shannon sampling bound, introduced in this context by Macridin, Spentzouris, Amundson and Harnik [86, 88], building on work by Somma [102], is saturated, field and conjugate-momentum space are described to comparable accuracy and the ground-state energy can be reproduced with a precision scaling with the number of qubits in the site register as $|\log|\log|\epsilon|||\sim n_Q$. For a free theory in 0+1 dimensions, the coefficients of this relationship are calculated to be $\epsilon_{(\%)} = (1.8(2)\times 10^3)\ 2^{-2.234(4)n_s}$. This rapid convergence is responsible for item 1.

3. In order to enjoy the double-exponential convergence of item 2, the conjugate-momentum operator must be constructed with exact phases in momentum space, leading to a highly-non-local operator in field space. This is possible through use of the quantum Fourier transform as an efficient entangling operation among all qubits in the register [102, 86, 88]. Note that for spatial dimensions greater than zero, the size of the qubit register that undergoes QuFoTr grows with precision of the scalar field digitization, and not the size of the spatial lattice. Given the qubit estimates of item 1, global entanglement within this register is a reasonable goal for NISQ-era hardware.

4. The implementation of *exact* phases required in item 3 does not supersede the effects of noise. Under a generic noise model on phases in conjugate-momentum space, the double-exponential convergence stated in item 2 is only seen up to a precision barrier set by the magnitude of the noise. In spite of this physical limitation, the use of exact phases is still recommended as it minimizes the number of states needed in the quantum system and is no more costly than implementation of conjugate-momentum operators local in field space. As an additional feature, using exact phases in momentum space yields symmetry between the gates required in field and conjugate-momentum space.

This analysis, shown in Figs. 3.3 and 3.4, informs a balancing between the noise level of the quantum system and the precision with which the quantum field theory is mapped onto qubits. It is naturally expected that there will be advantages in "matching" the precision of a calculation to the noise level in a given quantum device or vice-versa.

5. While the relative precision attainable with the JLP and HO bases depends on the structure of the low-energy wavefunctions, the comparatively-burdensome operator structure of the HO basis may be a deciding factor in the NISQ era. While JLP Pauli operators are limited to 1-, 2-, and m-body qubit interactions for $\lambda\phi^m$, the HO basis includes all k-body operators up to $k = n_Q$. These operators necessitate larger numbers of CNOT gates, the two-qubit entangling gates dominating the error contribution for many instances of near-term hardware.

6. Gate decompositions can be sensitive to symmetries that may be broken through classically-inconsequential truncation artifacts. When truncating spaces to contain states that have interactions beyond the truncated space (e.g., in the HO basis), it is preferable to truncate *after* construction of the Hamiltonian in an enlarged space to remove edge-effects in the interactions. When deciding upon boundary conditions (e.g., in the JLP basis), it is beneficial to consider alternatives (such as twisted boundary conditions) that symmetrize the distribution of wavefunction samples in Fourier space.

7. For the near-term, including and beyond the NISQ-era, digitization and discretization of the field onto qubits need not limit the accuracy obtained in simulations of scalar field theory. Rather, the software approximation of the propagator (e.g., through Trotterization) and hardware gate-error rates (currently above 10^{-4} in the simple model of Appendix H of Ref. [45]) are expected to be the dominant limitations to simulations of the scalar field.

The content of this paper has provided information to make a hardware-specific, informed decision on the parameters chosen to implement a scalar field on quantum devices. For exam-

ple, imagine a future in which the application of CNOT gates become relatively inexpensive [8], rotation gates contain small but non-negligible errors in their rotation angle, and a hypothetical goal is to simulate a 0+1-dimensional scalar field with quartic self-interaction to at least $10^{-11}\%$ precision. Both the JLP and HO bases are capable of achieving this goal, as seen in Fig. 3.7. However, given the wider range of tuning parameters allowable in the HO basis, making the precision more robust to noise in the rotation gates' angles, an informed choice might be to work with a HO basis. Imagine, as a modification to this scenario, that gates are expensive (either due to short coherence times or to their imperfect fidelity) but qubits are cheap. In this case, the contents of Table 3.2 raise concerns over the 612 entangling gates required to implement the Trotterized circuit in the HO basis. Instead, it may be logical to use JLP digitization, add one qubit to increase the range of the tuning parameter $\bar{\phi}_{\max}$ capable of satisfying the above precision requirement, and as a result require only one third of the previous number of CNOT gates for each Trotter step, a number also more amenable to the NISQ era. It is further found that small calculations of $\lambda\phi^4$ scalar field theories can be performed with a modest number of qubits. For example, an ideal $\sim$ 60-qubit device could be used to describe such a system with up to $\sim$ 20 spatial lattice sites (with three qubits per site defining the field digitization), arranged in a number of dimensions, at the 10^{-6} level. Observing that this error is below that expected for digital gate implementation on NISQ-era devices of this size indicates that properties of a scalar field independent of digitization artifacts will be accessible to quantum devices with fewer than 100 qubits. Beyond the digitization errors (step (1) of Fig. 3.1) that have here been demonstrated to be controllable with qubit requirements appropriate for the NISQ era, the quantum simulation errors arising from necessary approximation of the time evolution operator (step (2) of Fig. 3.1) and imperfect implementation on noisy hardware (step (3) of Fig. 3.1) now remain as the dominant sources of uncontrolled error in calculations of the scalar field implemented on quantum hardware.

---

[8] This is the case for many models of fault-tolerant quantum computing

Analyses such as we have presented in this work, are expected to play a role in optimizing the output of quantum devices in any scientific application domain. Their use in tuning digitization parameters to "match" the precision of calculations to specific hardware will become increasingly important to make the best use of available hardware at any given time, as is the case in classical high-performance computing. With rapid development of quantum hardware in the NISQ era, it is likely that the optimal layout of a quantum system onto qubit degrees of freedom will have significant variability, both with choice of quantum architecture and with time. Having a detailed map of the resource landscape is thus critical for creating informed decisions for implementing calculations across a range of quantum architectures.

Chapter 4

ENTANGLEMENT MEASURES OF THE POSITION-SPACE SCALAR FIELD

The content of this chapter is associated with Ref. [27]:
Natalie Klco and Martin J. Savage. "Systematically Localizable Operators for Quantum Simulations of Quantum Field Theories". *Phys. Rev. A* 102.1 (2020), p. 012619. DOI: 10.1103/PhysRevA.102.012619. arXiv: 1912.03577 [quant-ph]

In this chapter the (1×1)-site mutual information and (1×1)-site negativity representing the ultraviolet entanglement structure of the spatially latticized scalar field are calculated employing mainly the $(n \times m)$-generalizable oscillator decorrelation methods devised in Ref. [141]. The nearest-neighbor localization of (1×1)-site (UV) negativity is understood to be one piece of a larger picture in which $(n \times n)$-site negativity is localized at lattice distances increasing with n. Thus, the ultraviolet entanglement structure of the spatially latticized scalar field presents genuine multi-site entanglement present at distances scaling with the number of sites in the two subsystems [142, 143, 144, 145, 146, 147, 148, 149, 150, 151, 152, 153, 154]. When macroscopic collections of sites are considered in the lattice continuum limit, the long-range entanglement structure of the scalar field ground state is restored, as expected in light of the Reeh-Schlieder theorem [155, 156] and potential of entanglement harvesting [157, 158, 159, 160, 161, 162, 163]. Exploring in detail the UV and IR entanglement structures of latticized fields is expected to informed decisions in the creative design process necessary for physically implementing quantum simulations of quantum field theories.

4.1 Two-site Von Neumann Entanglement Entropy

The wavefunction for the ground state of the scalar field is

$$\psi(\vec{\phi}) = \frac{\det \mathbf{K}^{1/4}}{\pi^{N/4}} \int \mathrm{d}\vec{\phi}\; e^{-\frac{1}{2}\phi^T \mathbf{K}\phi}\; |\phi_1, \phi_2, \ldots, \phi_N\rangle \quad . \tag{4.1}$$

For two sites, the wavefunction explicitly becomes

$$\psi(\phi_1, \phi_2) = \frac{\det \mathbf{K}^{1/4}}{\pi} \int \mathrm{d}\phi_1 \mathrm{d}\phi_2 \;\; \exp\left[-\frac{1}{2} \begin{pmatrix} \phi_1 & \phi_2 \end{pmatrix} \begin{pmatrix} K_{00} & K_{01} \\ K_{01} & K_{00} \end{pmatrix} \begin{pmatrix} \phi_1 \\ \phi_2 \end{pmatrix} \right] \;\; |\phi_1, \phi_2\rangle \quad . \tag{4.2}$$

The associated two-site density matrix is

$$\rho = \left(\frac{\det \mathbf{K}^{1/4}}{\pi} \right)^2 \int \mathrm{d}\phi_1 \mathrm{d}\phi_2 \mathrm{d}\phi_1' \mathrm{d}\phi_2' \;\; \varphi(\phi_1, \phi_2) \varphi^*(\phi_1', \phi_2') \;\; |\phi_1, \phi_2\rangle\langle\phi_1', \phi_2'| \tag{4.3}$$

where

$$\varphi(\phi_1, \phi_2) = \exp\left[-\frac{1}{2} \begin{pmatrix} \phi_1 & \phi_2 \end{pmatrix} \begin{pmatrix} K_{00} & K_{01} \\ K_{01} & K_{00} \end{pmatrix} \begin{pmatrix} \phi_1 \\ \phi_2 \end{pmatrix} \right] \quad . \tag{4.4}$$

The reduced density matrix for the first site (or more generally a single site in the case of periodic boundary conditions) is

$$\rho_1 = \mathrm{Tr}_2 \rho \tag{4.5}$$

$$= \left(\frac{\det \mathbf{K}^{1/4}}{\pi} \right)^2 \int \mathrm{d}\bar{\phi}_2 \int \mathrm{d}\phi_1 \mathrm{d}\phi_2 \mathrm{d}\phi_1' \mathrm{d}\phi_2' \;\; \varphi(\phi_1, \phi_2) \varphi^*(\phi_1', \phi_2') \;\; \langle\bar{\phi}_2|\phi_1, \phi_2\rangle\langle\phi_1', \phi_2'|\bar{\phi}_2\rangle \tag{4.6}$$

$$= \left(\frac{\det \mathbf{K}^{1/4}}{\pi} \right)^2 \int \mathrm{d}\bar{\phi}_2 \int \mathrm{d}\phi_1 \mathrm{d}\phi_2 \mathrm{d}\phi_1' \mathrm{d}\phi_2' \;\; \varphi(\phi_1, \phi_2) \varphi^*(\phi_1', \phi_2') \;\; \delta(\bar{\phi}_2 - \phi_2) |\phi_1\rangle\langle\phi_1'| \delta(\phi_2' - \bar{\phi}_2) \tag{4.7}$$

$$= \left(\frac{\det \mathbf{K}^{1/4}}{\pi} \right)^2 \int \mathrm{d}\phi_1 \mathrm{d}\phi_2 \mathrm{d}\phi_1' \;\; \varphi(\phi_1, \phi_2) \varphi^*(\phi_1', \phi_2) \;\; |\phi_1\rangle\langle\phi_1'| \quad , \tag{4.8}$$

where $\varphi = \varphi*$ are kept distinguishable for organizational purposes only. The Von Neumann entanglement entropy is

$$S(\rho_1) = -\mathrm{Tr} \rho_1 \log \rho_1 \quad . \tag{4.9}$$

To take the matrix log of this infinite-dimensional matrix, one can consider expanding the log into its power series, expressing the power series as an internal binomial series. This

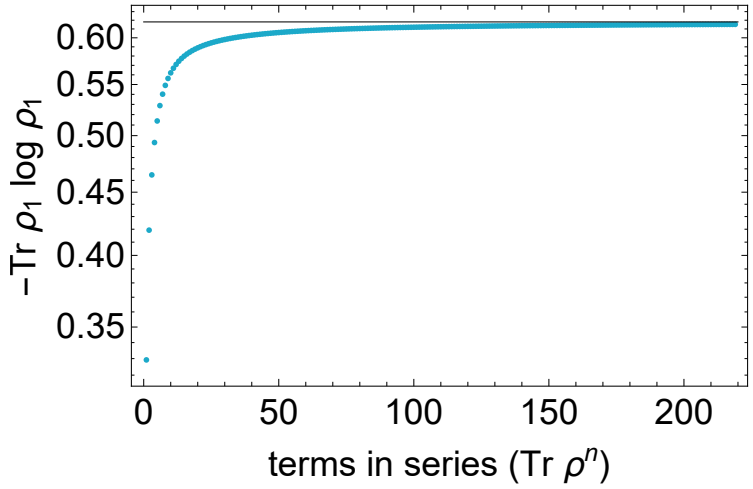

Figure 4.1: With high precision in the **K** matrix evaluation, the Von Neumann entanglement entropy converges when calculated as the nested series expansions of Eq. (4.13) with a field mass of $m = 0.3$.

takes the log and expresses it with terms that are traces over powers of the density matrix $\mathrm{Tr}\rho^m$, which can be calculated straightforwardly.

$$-\mathrm{Tr}\rho_1 \log \rho_1 = -\mathrm{Tr}\rho_1 \sum_{m=1}^{\infty} \frac{(-1)^{m+1}}{m} (\rho_1 - I)^m \tag{4.10}$$

$$= -\sum_{m=1}^{\infty} \frac{(-1)^{m+1}}{m} \mathrm{Tr}\rho_1 (\rho_1 - I)^m \tag{4.11}$$

$$= -\sum_{m=1}^{\infty} \frac{(-1)^{m+1}}{m} \mathrm{Tr}\rho_1 \sum_{j=0}^{m} \binom{m}{j} \rho_1^j (-1)^{m-j} \tag{4.12}$$

$$= -\sum_{m=1}^{\infty} \sum_{j=0}^{m} \frac{(-1)^{j+1}}{m} \binom{m}{j} \mathrm{Tr}\rho_1^{j+1} \tag{4.13}$$

Unfortunately, as shown in Fig. 4.1, this approach does not converge quickly.

Rather than expanding the entanglement entropy, the analytic properties of the function may be leveraged. Using the replica trick,

$$\ln Z = \lim_{n\to 0} \frac{Z^n - 1}{n} = \lim_{n\to 0} \frac{\partial Z^n}{\partial n} \quad , \tag{4.14}$$

and the entanglement entropy may be written as

$$S(\rho) = \lim_{n\to 0} \mathrm{Tr}\frac{\rho^{n+1}-\rho}{n} = \lim_{n\to 0}\frac{\mathrm{Tr}\rho^{n+1}-1}{n} \quad . \tag{4.15}$$

These relations comes from writing the exponentiated matrix as $e^{n\ln Z}$, expanding the exponential in a power series, cancelling the first term with the 1, dividing out the single factor of n and then sending n to zero to isolate the second term of the exponential. The Von Neumann entanglement entropy can also be calculated using the variant

$$S(\rho) = -\lim_{n\to 1}\frac{\partial}{\partial n}\mathrm{Tr}\rho^n \quad . \tag{4.16}$$

This is inspired by the derivative with respect to the exponent producing a log factor

$$-\lim_{n\to 1}\frac{\partial}{\partial n}\mathrm{Tr}\rho^n = -\lim_{n\to 1}\frac{\partial}{\partial n}\sum \lambda^n = -\lim_{n\to 1}\sum \lambda^n \log\lambda = -\sum \lambda\log\lambda \quad , \tag{4.17}$$

where λ are the eigenvalues of the reduced density matrix.

To employ the above techniques, key quantity to inform this entanglement calculation is $\mathrm{Tr}\rho^s$ extended to continuous s. Below will be written an expression for the trace of powers of the density matrix requiring only the determinant of a $2n\times 2n$ dimensional matrix. For example, the trace of the third power of the density matrix is

$$\mathrm{Tr}\rho_1^3 = \left(\frac{\det \mathbf{K}^{1/2}}{\pi}\right)^3 \int \mathrm{d}\phi_1\mathrm{d}\phi_1'\mathrm{d}\phi_1''\mathrm{d}\phi_2\mathrm{d}\phi_2'\mathrm{d}\phi_2'' \tag{4.18}$$

$$\varphi(\phi_1,\phi_2)\varphi^*(\phi_1',\phi_2)\varphi(\phi_1',\phi_2')\varphi^*(\phi_1'',\phi_2')\varphi(\phi_1'',\phi_2'')\varphi^*(\phi_1,\phi_2'') \tag{4.19}$$

$$= \left(\frac{\det \mathbf{K}^{1/2}}{\pi}\right)^3 \int \mathrm{d}\phi_1\mathrm{d}\phi_1'\mathrm{d}\phi_1''\mathrm{d}\phi_2\mathrm{d}\phi_2'\mathrm{d}\phi_2'' \exp\left(-\frac{1}{2}\bar{\phi}^T\bar{\mathbf{K}}\bar{\phi}\right) \tag{4.20}$$

$$= \left(\frac{\det \mathbf{K}^{1/2}}{\pi}\right)^3 \sqrt{\frac{2\pi^6}{\det\bar{\mathbf{K}}_3}} \quad , \tag{4.21}$$

where $\bar{\phi}$ and $\bar{K}$ are p-dimensional

$$\bar{\phi} = \begin{pmatrix}\phi_1 & \phi_1' & \phi_1'' & \phi_2 & \phi_2' & \phi_2''\end{pmatrix} \quad \bar{\mathbf{K}}_3 = \left(\begin{array}{c|c} 2K_{00}I & K_{01}C_3 \\ \hline K_{01}C^T & 2K_{00}I \end{array}\right) \tag{4.22}$$

with

$$\mathbf{K} = \begin{pmatrix} K_{00} & K_{01} \\ K_{01} & K_{00} \end{pmatrix} \qquad C_3 = I_3 + P_3 \qquad P_3 = \begin{pmatrix} 0 & 0 & 1 \\ 1 & 0 & 0 \\ 0 & 1 & 0 \end{pmatrix} \tag{4.23}$$

where C is a second-order circulant matrix. Generalizing this procedure,

$$\mathrm{Tr}\rho_1^n = \left(\frac{\det K^{1/2}}{\pi}\right)^n \sqrt{\frac{(2\pi)^{2n}}{\det \bar{\mathbf{K}}_n}} \tag{4.24}$$

where $\bar{\mathbf{K}}_n$ is a $2n \times 2n$ block-circulant matrix with the diagonal elements $2K_{00}\mathbb{I}_{n\times n}$ and the off-diagonal elements $K_{01}C_n$ and $K_{01}C_n^T$. While the necessary determinant of $\bar{\mathbf{K}}$ is inexpensive to calculate and can be expressed analytically through properties of the circulant matrices, a profitable direction for extension to continuous matrix dimensions is to express the determinant as

$$\det \bar{\mathbf{K}}_n = \left(4K_{00}^2 - 4K_{01}^2\right) \left(\sum_{i=0}^{\lceil \frac{n-2}{2} \rceil} (-1)^i \binom{n-1-i}{i} (2K_{00})^{n-1-2i} K_{01}^{2i} \right)^2 \tag{4.25}$$

$$= \left[\left(K_{00} + \sqrt{K_{00}^2 - K_{01}^2} \right)^n - \left(K_{00} - \sqrt{K_{00}^2 - K_{01}^2} \right)^n \right]^2 \quad . \tag{4.26}$$

The trace of single-site density matrix powers is thus

$$\mathrm{Tr}\rho_1^n = \frac{2^n \eta^n}{(K_{00}+\eta)^n - (K_{00}-\eta)^n} \quad , \tag{4.27}$$

where the replacement $\eta = \sqrt{\det \mathbf{K}} = \sqrt{K_{00}^2 - K_{01}^2}$ has been made. This leads to a Von Neumann entanglement entropy of

$$S(\rho_1) = -\lim_{n\to 1} \frac{\partial}{\partial n} \mathrm{Tr}\rho_1^n \tag{4.28}$$

$$= \frac{(K_{00}+\eta)\log(K_{00}+\eta) - (K_{00}-\eta)\log(K_{00}-\eta) - 2\eta\log(2\eta)}{2\eta} \tag{4.29}$$

When evaluated with the two-site $\mathbf{K}$ matrix as defined in Eq. (2.11), the one-site Von Neumann entanglement entropy is calculated to be $S(\rho_1) = 0.618$ for a two-site lattice. This value is shown with a gray horizontal line in Fig. 4.1.

4.2 N-site Lattice Continuum Entanglement Entropy and Mutual Information

The entanglement entropy of a bipartite quantum system quantifies the correlation, both classical and quantum, between two subsystems, 1 and 2, described by a density operator $\hat{\boldsymbol{\rho}}_{1,2}$, and can be written as,

$$S(\hat{\boldsymbol{\rho}}_1) = \mathrm{Tr}_1 \left[\, \hat{\boldsymbol{\rho}}_1 \log \hat{\boldsymbol{\rho}}_1 \, \right] \quad , \qquad \text{where} \qquad \hat{\boldsymbol{\rho}}_1 = \mathrm{Tr}_2 \left[\, \hat{\boldsymbol{\rho}}_{1,2} \, \right] \quad , \tag{4.30}$$

where $\mathrm{Tr}_j \left[\, ... \, \right]$ denotes a partial trace over the states in the Hilbert space of system j. The mutual information (MI) is useful in quantifying classical and quantum correlations between two subsystems within a larger system,

$$I(1:2) = S(\hat{\boldsymbol{\rho}}_1) + S(\hat{\boldsymbol{\rho}}_2) - S(\hat{\boldsymbol{\rho}}_{1,2}) \quad , \qquad \text{where} \qquad \hat{\boldsymbol{\rho}}_{1,2} = \mathrm{Tr}_{3,4,...} \left[\quad \hat{\boldsymbol{\rho}}_{1,2,3,4,....} \, \right] \quad . \tag{4.31}$$

Following closely the calculation of Ref. [141], the entanglement entropy (and thus the mutual information) can be calculated for the scalar field ground state of Eq. (2.10) with subsystems of arbitrary sites. Naturally, this is achieved by de-correlating the Gaussians to solve entanglement contributions in an uncorrelated frame. The density matrix of the lattice of oscillators is

$$\hat{\boldsymbol{\rho}} \propto \int \mathrm{d}\boldsymbol{\phi} \mathrm{d}\boldsymbol{\phi}' \int \mathrm{d}\bar{\boldsymbol{\phi}} \exp \left[-\frac{1}{2} \begin{pmatrix} \boldsymbol{\phi} & \bar{\boldsymbol{\phi}} \end{pmatrix} \mathbf{K} \begin{pmatrix} \boldsymbol{\phi} \\ \bar{\boldsymbol{\phi}} \end{pmatrix} - \frac{1}{2} \begin{pmatrix} \boldsymbol{\phi}' & \bar{\boldsymbol{\phi}} \end{pmatrix} \mathbf{K} \begin{pmatrix} \boldsymbol{\phi}' \\ \bar{\boldsymbol{\phi}} \end{pmatrix} \right] \, |\boldsymbol{\phi}\rangle\langle\boldsymbol{\phi}'| \quad . \tag{4.32}$$

where $\boldsymbol{\phi}$ and $\boldsymbol{\phi}'$ have dimensionality equal to the number of sites in the primary subsystem and $\bar{\boldsymbol{\phi}}$ has dimension equal to the number of remaining sites in the lattice that are removed via partial tracing. The dimensionality constant contains determinant factors and factors of π that set the trace to unity but will not be needed for calculating the entanglement properties of the state. The matrix quantifying correlations between oscillators is next partitioned to distinguish the $\boldsymbol{\phi}$ target subsystem with $\bar{\boldsymbol{\phi}}$ the traced degrees of freedom,

$$\hat{\boldsymbol{\rho}}_1(\boldsymbol{\phi}, \boldsymbol{\phi}') \propto \exp \left[-\frac{1}{2} \begin{pmatrix} \boldsymbol{\phi} & \boldsymbol{\phi}' \end{pmatrix} \left(\begin{pmatrix} A & 0 \\ 0 & A \end{pmatrix} - \begin{pmatrix} B \\ B \end{pmatrix} (2C)^{-1} \begin{pmatrix} B^T & B^T \end{pmatrix} \right) \begin{pmatrix} \boldsymbol{\phi} \\ \boldsymbol{\phi}' \end{pmatrix} \right] \quad \mathbf{K} = \left(\begin{array}{c|c} A & B \\ \hline B^T & C \end{array} \right) \tag{4.33}$$

where a partial gaussian integration has been performed over the sites in the barred space. Recall that the partial integration of a gaussian integral can be done analytically as

$$\int \cdots \int \exp\left[-\frac{1}{2}\phi^T K \phi\right] \, \mathrm{d}\phi_{m+1} \cdots \mathrm{d}\phi_n = \frac{(2\pi)^{\frac{n-m}{2}}}{\sqrt{\det W_0}} \exp\left[-\frac{1}{2} u^T U u\right] \tag{4.34}$$

where

$$\bar{\mathbf{K}}\phi = \begin{pmatrix} U_0 & V \\ V^T & W_0 \end{pmatrix} \begin{pmatrix} u \\ w \end{pmatrix} \qquad U = U_0 - V W_0^{-1} V^T \quad . \tag{4.35}$$

Note that no assumption has currently been made on the boundary conditions or structure of the correlations. With the compact notation of Ref. [141], the reduced density matrix may be written as

$$\hat{\boldsymbol{\rho}}_1 \propto \exp\left[-\frac{1}{2}\left(\boldsymbol{\phi}^T \gamma \boldsymbol{\phi} + \boldsymbol{\phi}'^T \gamma \boldsymbol{\phi}'\right) + \boldsymbol{\phi}^T \beta \boldsymbol{\phi}'\right] \tag{4.36}$$

where

$$\gamma = A - \frac{1}{2} B C^{-1} B^T \qquad \text{and} \qquad \beta = \frac{1}{2} B C^{-1} B^T \quad . \tag{4.37}$$

The quadratic terms of the oscillators within the primary space are decoupled by a change of variables diagonalizing γ,

$$\gamma = V^T \gamma_D V \qquad \tilde{\boldsymbol{\phi}} = \gamma_D^{\frac{1}{2}} V \boldsymbol{\phi} \qquad \tilde{\boldsymbol{\phi}}^T = \boldsymbol{\phi} V^T \gamma_D^{\frac{1}{2}} \tag{4.38}$$

for both the primed and unprimed coordinates resulting in

$$\hat{\boldsymbol{\rho}}_1 \propto \exp\left[-\frac{1}{2}\left(\tilde{\boldsymbol{\phi}}^T \tilde{\boldsymbol{\phi}} + \tilde{\boldsymbol{\phi}}'^T \tilde{\boldsymbol{\phi}}'\right) + \tilde{\boldsymbol{\phi}}^T \beta' \tilde{\boldsymbol{\phi}}'\right] \qquad \beta' = \gamma_D^{-\frac{1}{2}} V \beta V^T \gamma_D^{-\frac{1}{2}} \quad . \tag{4.39}$$

The eigenvalues of the reduced density matrix are completely characterized by β'_i, the eigenvalues of β', through identifying $\hat{\boldsymbol{\rho}}_1$ as a tensor product of n one-dimensional density matrices where n is the number sites in the primary space. The eigenvalues of $\hat{\boldsymbol{\rho}}_1$ are then multiplicative combinations of the towers of eigenvalues for the individual oscillators

$$\xi_i = \frac{\beta'_i}{1 + \sqrt{1 - \beta'^2_i}} \qquad \lambda_{i,n} = (1 - \xi_i)\xi_i^n \qquad \lambda_{\hat{\boldsymbol{\rho}}_1}(\vec{n}) = \prod_i \lambda_{i,n} \quad . \tag{4.40}$$

where λ_{i,n_i} is the energy eigenvalue of the n^{th} eigenstate of the i^{th} oscillator characterized by β_i'. From these eigenvalues of the reduced density matrix, the entanglement entropy is calculated simply as

$$S(\hat{\boldsymbol{\rho}}_1) = -\sum_{\vec{n}} \lambda_{\hat{\boldsymbol{\rho}}_1}(\vec{n}) \log \lambda_{\hat{\boldsymbol{\rho}}_1}(\vec{n}) \tag{4.41}$$

where $\vec{n}$ is a unit vector whose elements indicate the order of the Hermite polynomial in the ground state wavefunction of each independent oscillator. For the entanglement entropy where additivity persists in the tensor product,

$$S(\rho_1 \otimes \rho_2) = S(\rho_1) + S(\rho_2) \tag{4.42}$$

the entanglement entropy is written succinctly as

$$S(\hat{\boldsymbol{\rho}}_1) = -\sum_i \left[\log(1-\xi_i) + \frac{\xi_i}{1-\xi_i} \log \xi_i \right] \quad . \tag{4.43}$$

From this general expression, the mutual information between two sites may be calculated through a combination of two calculations with different partitions of the $\mathbf{K}$ matrix with the A subsector being one- and two-dimensional. Upon calculation, it is demonstrated in Fig that the mutual information falls exponentially as shown above for the matrix elements of the K matrix itself.

For a lattice of two sites calculated with the above techniques,

$$\gamma = K_{11} - \frac{K_{12}^2}{2K_{11}} \qquad \beta = \frac{K_{12}^2}{2K_{11}} \tag{4.44}$$

leading to

$$\xi = \frac{K_{01}^2}{(K_{00}+\eta)^2} \quad . \tag{4.45}$$

The resulting Von Neumann entanglement entropy,

$$S(\rho) = \frac{K_{01}^2}{2K_{01}^2 - 2K_{00}(K_{00}+\eta)} \log\left[\frac{K_{01}^2}{(K_{00}+\eta)^2}\right] - \log\left[1 - \frac{K_{01}^2}{(K_{00}+\eta)^2}\right] \tag{4.46}$$

is in agreement with the above calculation using replica methods resulting also in the gray horizontal line of Fig. 4.1.

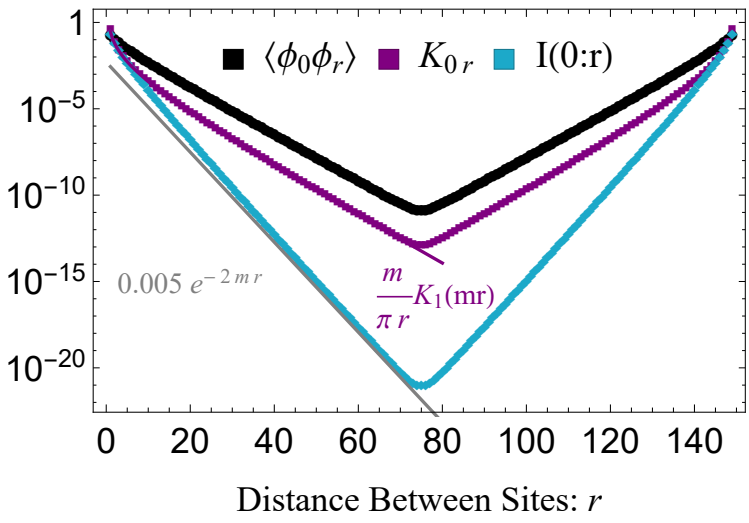

Figure 4.2: The two point correlation function, $\langle\phi_0\phi_r\rangle$, the correlation matrix, K_{0r}, and the mutual information, $I(0:r)$, in the ground state of a free one-dimensional lattice scalar field theory as a function of site separation with $\hat{m} = 0.3$ and $N = 150$ lattice sites.

4.3 N-site Lattice Continuum Negativity

The negativity [164] is a measure of entanglement quantifying purely-quantum correlations. As its name suggests, the negativity is the sum of all negative eigenvalues of the partially transposed density matrix and may be expressed in terms of the matrix square root

$$\mathcal{N}(\rho) = \frac{||\rho^\Gamma||_1 - 1}{2} = \frac{\mathrm{Tr}\sqrt{(\rho^\Gamma)^2} - 1}{2} = \frac{\sum|\lambda_i| - 1}{2} = -\sum_{\lambda_i<0}\lambda_i \tag{4.47}$$

where the λ_i are eigenvalues of (Hermitian) ρ^Γ and the unit trace of ρ^Γ has been employed. For calculating the negativity between two sites in a two-site lattice, $\mathcal{N}_{1|2}$, the Hilbert space of the first site is partially transposed and no Hilbert space is removed via tracing. The partial transpose of the two-site ground state density matrix over the degrees of freedom in the first site is

$$\rho_1^\Gamma = \int \mathrm{d}\phi_1\mathrm{d}\phi_1'\mathrm{d}\phi_2\mathrm{d}\phi_2'\ \langle\phi_0', \phi_1|\psi\rangle_0\langle\phi_0, \phi_1'|\psi\rangle_0\ |\phi_0, \phi_1\rangle\langle\phi_0', \phi_1'| \tag{4.48}$$

where the real wavefunction has been defined in Eq. (2.10). The eigenvectors of the partially transposed two-site ground state density matrix are symmetric and anti-symmetric combinations of tensor product Hermite polynomials with Gaussian envelopes

$$\psi^{\pm}_{n_1 n_2}(\phi_1,\phi_2) \propto \frac{H_{n_1}(\sqrt{\eta}\phi_1)H_{n_2}(\sqrt{\eta}\phi_2) \pm H_{n_2}(\sqrt{\eta}\phi_1)H_{n_1}(\sqrt{\eta}\phi_2)}{2} e^{-\frac{\eta}{2}(\phi_1^2+\phi_2^2)} \quad . \tag{4.49}$$

The associated eigenvalues appear in pairs of equal magnitude and opposite sign for the two symmetry states.

$$\rho^{\Gamma}\psi^{\pm}_{n_1,n_2}(\phi_1,\phi_2) = \pm\left(\frac{\det K^{1/2}}{\pi^{N/2}}\right)\frac{2\pi(-K_{12})^{n_1+n_2}}{(K_{11}+\eta)^{n_1+n_2+1}}\psi^{\pm}_{n_1,n_2}(\phi_1,\phi_2) \qquad \eta = \sqrt{\det K} \quad . \tag{4.50}$$

Calculating the magnitude of the sum of all negative eigenvalues is equivalent to calculating the sum of the magnitude all eigenvalues with $n_1 < n_2$. After performing such a sum, the negativity is found to be

$$\mathcal{N} = \sum_{\lambda_i<0}|\lambda_i| = -\frac{1}{2} + \sqrt{\det K}\sum_{n_1,n_2=0}^{\infty}\frac{|K_{12}^{n_1+n_2}|}{(K_{11}+\eta)^{n_1+n_2+1}} = \frac{|K_{12}|}{K_{11}-|K_{12}|+\eta} \quad . \tag{4.51}$$

As expected, this quantity vanishes when $K_{12} = 0$ and the two sites decouple to produce independent oscillators. The sign of K_{12} can be seen in Eq. (4.50) to be a contributing factor in the assignment of the positive or negative eigenvalues to the symmetric or anti-symmetric wavefunctions. The negativity is naturally independent of this assignment—sensitive to correlations on the off-diagonal of K regardless of their sign.

The negativity calculation can be generalized to larger systems through a similar framework to that of Ref. [141] and summarized above for calculation of the entanglement entropy. Example density matrices for $N = 4$ spatial sites are

$$\rho_{1|2} = \mathrm{Tr}_{3,4}\rho^{\Gamma_1} = \left(\frac{\det K^{1/2}}{\pi^{N/2}}\right)\int \mathrm{d}\phi_1\mathrm{d}\phi_2\mathrm{d}\phi_1'\mathrm{d}\phi_2'\mathrm{d}\phi_3\mathrm{d}\phi_4$$
$$\varphi(\phi_1',\phi_2,\phi_3,\phi_4)\varphi^*(\phi_1,\phi_2',\phi_3,\phi_4)\ |\phi_1,\phi_2\rangle\langle\phi_1',\phi_2'| \tag{4.52}$$

and

$$\rho_{1|3} = \mathrm{Tr}_{2,4}\rho^{\Gamma_1} = \left(\frac{\det K^{1/2}}{\pi^{N/2}}\right)\int \mathrm{d}\phi_1\mathrm{d}\phi_1'\mathrm{d}\phi_2\mathrm{d}\phi_3\mathrm{d}\phi_3'\mathrm{d}\phi_4$$
$$\varphi(\phi_1', \phi_2, \phi_3, \phi_4)\varphi^*(\phi_1, \phi_2, \phi_3', \phi_4)\ |\phi_1, \phi_3\rangle\langle\phi_1', \phi_3'| \quad . \quad (4.53)$$

A matrix structure for a multi-dimensional gaussian can be built to express these density matrices. This time, the $\mathbf{K}$ matrix is partitioned into three spaces: $\boldsymbol{\phi}_1$ and $\bar{\boldsymbol{\phi}}$ representing the partially transposed subspace and the traced space, respectively, leaving $\boldsymbol{\phi}_2$ as the comparative space for $\mathcal{N}_{1|2}$.

$$\mathrm{Tr}_{\bar{\phi}}\rho_{1|2}^{\Gamma_1} = \int \mathrm{d}\bar{\boldsymbol{\phi}}\ \exp\left[-\frac{1}{2}\begin{pmatrix}\boldsymbol{\phi}_1' & \boldsymbol{\phi}_2 & \bar{\boldsymbol{\phi}}\end{pmatrix}\mathbf{K}\begin{pmatrix}\boldsymbol{\phi}_1' \\ \boldsymbol{\phi}_2 \\ \bar{\boldsymbol{\phi}}\end{pmatrix} - \frac{1}{2}\begin{pmatrix}\boldsymbol{\phi}_1 & \boldsymbol{\phi}_2' & \bar{\boldsymbol{\phi}}\end{pmatrix}\mathbf{K}\begin{pmatrix}\boldsymbol{\phi}_1 \\ \boldsymbol{\phi}_2' \\ \bar{\boldsymbol{\phi}}\end{pmatrix}\right] \quad (4.54)$$

with

$$\mathbf{K} = \left(\begin{array}{c|c|c} A & B & D \\ \hline B^T & C & F \\ \hline D^T & F^T & E \end{array}\right) \quad . \quad (4.55)$$

For a bipartition negativity calculation quantifying the quantum correlations between two halves of a quantum system, A and C are $\left(\frac{N}{2}\right)$-dimensional while E is zero dimensional. For a two-site negativity calculation, A and C are one-dimensional while E is $(N-2)$-dimensional for an N-site lattice. Thus, to calculate $\mathcal{N}_{1|j}$ for increasing values of j quantifying the separation dependence of two-site quantum correlations, the $\mathbf{K}$ matrix need only be rearranged placing site j at the second position. Combining the terms in the gaussian defines

$$\bar{\mathbf{K}} = \begin{pmatrix} A & 0 & 0 & B & D \\ 0 & A & B & 0 & D \\ 0 & B^T & C & 0 & F \\ B^T & 0 & 0 & C & F \\ D^T & D^T & F^T & F^T & 2E \end{pmatrix} \qquad \text{basis:} \quad \begin{pmatrix} \boldsymbol{\phi}_1 \\ \boldsymbol{\phi}_1' \\ \boldsymbol{\phi}_2 \\ \boldsymbol{\phi}_2' \\ \bar{\boldsymbol{\phi}} \end{pmatrix} \quad (4.56)$$

The partial transpose can be seen to make the subblocks of B and B^T off-diagonal rather

than diagonal as they otherwise would be. Conducting the integrals over $\bar{\boldsymbol{\phi}}$,

$$\mathrm{Tr}_{\bar{\phi}}\rho_{1|2}^{\Gamma} \propto \exp\left[-\frac{1}{2}\begin{pmatrix}\boldsymbol{\phi}_1 & \boldsymbol{\phi}_1' & \boldsymbol{\phi}_2 & \boldsymbol{\phi}_2'\end{pmatrix}\left(\begin{pmatrix}A & 0 & 0 & B\\ 0 & A & B & 0\\ 0 & B^T & C & 0\\ B^T & 0 & 0 & C\end{pmatrix} - \begin{pmatrix}D\\ D\\ F\\ F\end{pmatrix}(2E)^{-1}\begin{pmatrix}D^T & D^T & F^T & F^T\end{pmatrix}\right)\begin{pmatrix}\boldsymbol{\phi}_1\\ \boldsymbol{\phi}_1'\\ \boldsymbol{\phi}_2\\ \boldsymbol{\phi}_2'\end{pmatrix}\right] \tag{4.57}$$

where the proportionality contains factors of 2π scaling with the dimensionality of the $\bar{\boldsymbol{\phi}}$ space and a determinant of E to the half power.

$$\begin{aligned}\mathrm{Tr}_{\bar{\phi}}\rho_{1|2}^{\Gamma_1} \propto \exp\Bigg[-\frac{1}{2}\Bigg(&\begin{pmatrix}\phi_1 & \phi_2\end{pmatrix}\begin{pmatrix}A-\frac{1}{2}DE^{-1}D^T & -\frac{1}{2}DE^{-1}F^T\\ -\frac{1}{2}FE^{-1}D^T & C-\frac{1}{2}FE^{-1}F^T\end{pmatrix}\begin{pmatrix}\phi_1\\ \phi_2\end{pmatrix}\\ &+\begin{pmatrix}\phi_1' & \phi_2'\end{pmatrix}\begin{pmatrix}A-\frac{1}{2}DE^{-1}D^T & -\frac{1}{2}DE^{-1}F^T\\ -\frac{1}{2}FE^{-1}D^T & C-\frac{1}{2}FE^{-1}F^T\end{pmatrix}\begin{pmatrix}\phi_1'\\ \phi_2'\end{pmatrix}\Bigg)\\ &+\begin{pmatrix}\phi_1 & \phi_2\end{pmatrix}\frac{1}{2}\begin{pmatrix}DE^{-1}D^T & DE^{-1}F^T-2B\\ FE^{-1}D^T-2B^T & FE^{-1}F^T\end{pmatrix}\begin{pmatrix}\phi_1'\\ \phi_2'\end{pmatrix}\Bigg]\end{aligned} \tag{4.58}$$

From this structure, the matrices analogous to those of Eq. (4.37) are identified to be

$$\gamma = \begin{pmatrix}A-\frac{1}{2}DE^{-1}D^T & -\frac{1}{2}DE^{-1}F^T\\ -\frac{1}{2}FE^{-1}D^T & C-\frac{1}{2}FE^{-1}F^T\end{pmatrix} \quad \beta = \frac{1}{2}\begin{pmatrix}DE^{-1}D^T & DE^{-1}F^T-2B\\ FE^{-1}D^T-2B^T & FE^{-1}F^T\end{pmatrix} \tag{4.59}$$

again structured as in Eq. (4.36). Implementing analogous diagonalizations to those in Eqs. (4.38) and (4.39) and determining eigenvalues of the full density matrix as stated in Eq. (4.40), the negativity can be calculated by summing all non-negative eigenvalues. Because additivity is not a property of the negativity, a calculation of the negativity of the decoupled oscillators does not generically produce the negativity of the tensor producted density matrices. In the case of two-site negativities, there are two decoupled oscillators with towers of eigenvalues defined by $\xi_{1,2}$. For the latticized continuous scalar field, if the negativity is non-zero, one of these oscillators contains no negativity ($\xi_1 > 0$) while the other has eigenvalues of alternating sign ($\xi_2 < 0$). In such a case, the negativity calculation may be simplified to

$$\mathcal{N}_{1|2}(\rho_1 \otimes \rho_2) = -\sum_{n=0}^{\infty}\sum_{m=0}^{\infty}\lambda_{1,n}\lambda_{2,2m+1} = -\frac{\xi_2}{1+\xi_2} \quad , \tag{4.60}$$

equal to the negativity of the second decoupled oscillator.

Of great interest is the pattern of negativity in comparison to that of the mutual information above. Rather than falling exponentially, the negativity for large lattices is localized to extent of the fundamental interaction, here the finite difference gradient operator. Using a forward-difference gradient operator as shown in Eq. (2.9) produces rapidly decaying negativity for small lattices reaching zero negativity for all but nearest neighbor negativities e.g., for a lattice of thirteen sites for $m = 0.3$. In this light, the negativity is sensitive and characteristic of the ultraviolet properties of the interaction while the mutual information is sensitive and characteristic of the infrared theory's correlations.

To further support this observation, the finite difference operator in Eq. (2.9) can be modified or smeared to produce different ultraviolet interactions approximating the gradient. For a somewhat pathological example, using a symmetrized finite difference operator,

$$\nabla\hat{\phi}(x) = \frac{\hat{\phi}(x+1) - \hat{\phi}(x-1)}{2} \tag{4.61}$$

$$\nabla^2\hat{\phi} = \frac{\hat{\phi}(x+1)^2 + \hat{\phi}(x-1)^2 - \hat{\phi}(x+1)\hat{\phi}(x-1)}{4} \quad . \tag{4.62}$$

The portion of the Hamiltonian in position space $\frac{\hat{m}}{2}\hat{\phi}^2 + \frac{1}{2}\left(\nabla\hat{\phi}\right)^2$ becomes (with PBCs) the circulant matrix with first row

$$\left(\tfrac{1}{2}\left(\hat{m}^2 + \tfrac{1}{2}\right) \quad 0 \quad -\tfrac{1}{8} \quad 0 \quad \cdots \quad 0 \quad -\tfrac{1}{8} \quad 0\right) \quad . \tag{4.63}$$

The resulting correlation matrix differs only in the eigenvalues of the diagonalization

$$K_{\hat{r}} = \frac{1}{N}\sum_{k=0}^{N-1} \cos\left(\frac{2\pi k}{N}\hat{r}\right)\sqrt{m^2 + \sin^2\left(\frac{2\pi k}{N}\right)} \quad . \tag{4.64}$$

Calculating the negativity with this smearing exhibits rapidly suppressed (with lattice volume) non-zero values at only even site separations $\hat{r} = 2, 4, 6, \cdots$ when lattices are small. For large lattices, the only non-zero negativity is found at distance $\hat{r} = 2$, set by the UV smearing structure of the gradient operator. This structure of non-zero negativity beyond the scale of UV smearing for small volumes, rapidly suppressed as the infinite volume is approached, has been previously observed for a series of interacting oscillators [146]. With such

localized quantum correlations manipulatable through varying UV completions as well as exponentially decaying mutual information, it is natural to suspect that a logically-designed quantum circuit for initializing the ground state of the scalar field will demonstrate corresponding localization of entangling operators. Explicit digital quantum circuit constructions for the state preparation of the scalar field, both free and interacting, motivated by this suspicion are found in Chapter 5.

Before moving forward to leverage the entanglement structure of the continuum in the initialization of digital wavefunctions, it is interesting to observe the two-qubit mutual information and negativity for a small qubit-digitized scalar field. The result shown here is qualitatively representative of a wide range of parameters, with $m = 1.0$, $\phi_{\max} = 3.0$, $\lambda = 0$, $n_Q = 3$, and $N = 3$ chosen for concreteness and computability. The two qubit mutual information and negativity for all pairs of two qubits in the digitized field are shown in Fig. 4.3. As can be seen, the two-qubit negativity is abruptly zero outside of a site whereas the mutual information decays smoothly throughout the quantum register. Furthermore, there is a hierarchy seen in both entanglement measures within the site indicating that the first qubits are more highly entangled than later qubits. Being used to represent field values in a binary representation, later qubits within a site are responsible for resolving structure of the wavefunction at increasingly short length scales. As such, this hierarchy translates into greater entanglement within the low-frequency structure of the ground state wavefunction. Noting the obvious, unlike the mutual information the two-qubit negativity is structurally unchanged beyond translational invariance with periodic versus open boundary conditions as neither choice results in entanglement beyond the single site.

$$MI = \begin{pmatrix}
 & 0.8380 & 0.5256 & 0.01179 & 0.01165 & 0.004136 & 0.0008516 & 0.0008435 & 0.0003267 \\
0.8380 & & 0.5236 & 0.01169 & 0.01155 & 0.004123 & 0.0008435 & 0.0008354 & 0.0003236 \\
0.5256 & 0.5236 & & 0.004658 & 0.004631 & 0.002339 & 0.0003267 & 0.0003236 & 0.0001267 \\
0.01179 & 0.01169 & 0.004658 & & 0.8395 & 0.5034 & 0.01179 & 0.01169 & 0.004658 \\
0.01165 & 0.01155 & 0.004631 & 0.8395 & & 0.5009 & 0.01165 & 0.01155 & 0.004631 \\
0.004136 & 0.004123 & 0.002339 & 0.5034 & 0.5009 & & 0.004136 & 0.004123 & 0.002339 \\
0.0008516 & 0.0008435 & 0.0003267 & 0.01179 & 0.01165 & 0.004136 & & 0.8380 & 0.5256 \\
0.0008435 & 0.0008354 & 0.0003236 & 0.01169 & 0.01155 & 0.004123 & 0.8380 & & 0.5236 \\
0.0003267 & 0.0003236 & 0.0001267 & 0.004658 & 0.004631 & 0.002339 & 0.5256 & 0.5236 &
\end{pmatrix} =$$

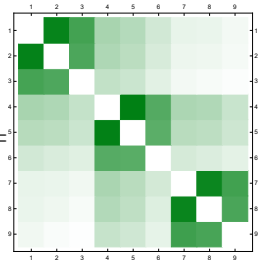

$$\mathcal{N} = \begin{pmatrix}
 & 0.2636 & 0.01735 & 0 & 0 & 0 & 0 & 0 & 0 \\
0.2636 & & 0.004114 & 0 & 0 & 0 & 0 & 0 & 0 \\
0.01735 & 0.004114 & & 0 & 0 & 0 & 0 & 0 & 0 \\
0 & 0 & 0 & & 0.2655 & 0.01784 & 0 & 0 & 0 \\
0 & 0 & 0 & 0.2655 & & 0.004039 & 0 & 0 & 0 \\
0 & 0 & 0 & 0.01784 & 0.004039 & & 0 & 0 & 0 \\
0 & 0 & 0 & 0 & 0 & 0 & & 0.2636 & 0.01735 \\
0 & 0 & 0 & 0 & 0 & 0 & 0.2636 & & 0.004114 \\
0 & 0 & 0 & 0 & 0 & 0 & 0.01735 & 0.004114 &
\end{pmatrix} =$$

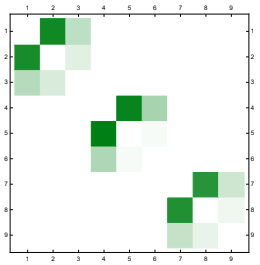

Figure 4.3: Two-qubit mutual information and negativity calculated in a three-site lattice digitized with three qubits per site and open boundary conditions.

Chapter 5

SYSTEMATICALLY LOCALIZABLE STATE PREPARATION

The content of this chapter is associated with Ref. [27]:
Natalie Klco and Martin J. Savage. "Systematically Localizable Operators for Quantum Simulations of Quantum Field Theories". *Phys. Rev. A* 102.1 (2020), p. 012619. DOI: 10.1103/PhysRevA.102.012619. arXiv: 1912.03577 [quant-ph]

Correlations and measures of entanglement in ground state wavefunctions of relativistic quantum field theories are spatially localized over length scales set by the mass of the lightest particle. We utilize this localization to design digital quantum circuits for preparing the ground states of lattice scalar quantum field theories. Controlled rotations that are exponentially localized in their position-space extent are found to provide exponentially convergent wavefunction fidelity. These angles scale with the correlation between sites and the classical two-point correlation function, as opposed to the more localized mutual information or the hyper-localized negativity. We anticipate that further investigations will uncover quantum circuit designs with controlled rotations dictated by the measures of entanglement. This work is expected to impact quantum simulations of systems of importance to nuclear physics, high-energy physics, and basic energy sciences research.

5.1 Introduction

Ubiquitous in modern physics, quantum field theories (QFTs) are used to quantitatively describe physical systems from the dynamics of quarks and gluons in the early universe, to the structure of matter in dense astrophysical objects, to the structure and properties of common and exotic materials. The 20th century established the prominence of renormalizable QFTs with local gauge symmetries in describing the strong and electroweak interactions, three of

the four fundamental forces in nature. Also at this time effective field theories (EFTs) were established as powerful tools to broadly describe nuclear forces, the properties of hadrons, and lattice regulated field theories over wide kinematic regimes. While significant progress has been made in developing precise analytic frameworks and classical numerical calculations of low-lying observables in non-perturbative systems, other classes of observables—notably real-time dynamics and properties of high density systems—remain to be addressed.

Since the early 1980's, it has been imagined that the attributes of quantum systems making their at-scale classical computation so onerous will be more naturally represented on quantum computational devices [7]. In quantitative support of this perspective, the complexity class BQP (Bounded Error Quantum Polynomial) has recently been shown to extend beyond the regime of classical polynomial-time calculations [165]. This result indicates that there are problems efficiently accessible to quantum computers but not to classical computers. While the application of quantum computing to scientific applications is only now beginning and it is anticipated that more than a decade of research and development will be required to perform calculations comparable to results of nuclear physics (NP) [166] and high-energy physics (HEP) experiments, there is growing excitement at the prospect of addressing real-time dynamics of highly inelastic processes and the structure of high density systems using quantum computers. Throughout the development toward full-scale quantum simulation, significant physical insight and advances in classical algorithms are expected to emerge that will impact the NP, HEP, and Basic Energy Science (BES) research programs.

Scalar and pseudoscalar fields play key roles in NP, HEP, and BES at both phenomenological and fundamental levels. Perhaps the most famous scalar particle is the $J^\pi = 0^+$ isosinglet σ-field (with vacuum quantum numbers), which has been the subject of decades of debate about its nature but is now firmly established [167]. The Higgs boson [130, 168] has the same quantum numbers as the σ, and is the remnant of electroweak symmetry breaking driven by a doublet of complex scalar fields that gives rise to the short-range weak interactions and the long-range electromagnetic interactions [128, 127, 129]. Scalar fields also play a central role in phenomenological self-consistent relativistic mean-field theories, pro-

viding attractive interactions in the dynamics of large numbers of nucleons (for example, see Ref. [169]). Finally, the pion (and kaon) fields are identified as pseudo-Goldstone bosons associated with the spontaneous breaking of the chiral symmetries of quantum chromodynamics (QCD) (for example, see Ref. [170]). They have been known to be central to NP since the very earliest days and dominate the long-distance behavior of the nucleon-nucleon interaction. In momentum-space, while not required to describe the very low-energy dynamics of nucleon-nucleon (NN) scattering [171, 172, 173, 174] or low-lying inelastic electroweak processes [174], pions are required to correctly describe processes even at modest energies. Since NN effective field theory (NNEFT) was formulated starting in the early 1990's [175, 176, 177, 178, 171, 172], including both pionless and pionful frameworks, efforts have been ongoing to develop numerical techniques to predict low-energy properties of larger nuclear systems based upon NNEFT systematic power-counting arguments. Explicitly sampling over dynamical pion fields, e.g., with a lattice discretization of spacetime (for example, Refs. [179, 180, 181, 182, 183]), constitutes a persisting line of such developments. It is anticipated that quantum simulation of low-energy multi-nuclear systems with dynamical pion fields will provide a quantum advantage in computing real-time dynamics of systems of interest to NP research, e.g., Ref. [47]. Therefore, it is timely to develop efficient quantum algorithms and quantum circuits for state preparation and subsequent Hamiltonian time evolution of scalar and (pseudo-)scalar quantum fields on a spatial lattice.

In using quantum computers to predict observables of importance to NP, HEP, and BES research, preparing the initial wave function on the quantum register presents one of the major challenges [184, 25, 24, 62, 63, 22]. For example, to determine S-matrix elements of an interacting lattice field theory using the prescription of Jordan, Lee and Preskill (JLP) [25, 24, 62, 63], localized wave packets of the non-interacting theory are initially prepared. The system is then adiabatically flowed to arrive at localized wave packets in the fully interacting theory, evolved in time through a Trotterized evolution operator, and measured. The final distribution of particles determines the of S-matrix elements of interest. While a perfect initialization would ensure that vacuum fluctuations are accurately captured, an imperfect

initialization may allow a background of particles to emerge and evaporate during this process. For example, in calculating the inelastic scattering of two nucleons directly from QCD, a high fidelity preparation of the quantum vacuum is crucial for isolating the process of interest from a complex array of strong interaction backgrounds such as glueballs, pions, and baryon-anti-baryon systems.

Even in the absence of wave packets, preparation of the ground state of the non-interacting lattice field theory remains nontrivial. Focusing on free lattice scalar field theory, the ground state of this coupled system can be defined by N harmonic oscillators, where N is the number of spatial sites of the underlying lattice that discretizes space. Such systems of coupled harmonic oscillators have been considered previously from the view point of quantum information science, including the behavior of mutual information and negativity, e.g. Ref. [146]. It is most easily represented as the tensor product of the ground state wavefunctions of each of the momentum eigenstates, which can be Fourier transformed into position space. Correspondingly, this wavefunction is the sum over products of oscillator states, one at each spatial site, coupled through the gradient operator in the Hamiltonian. This leads to a high-dimensional Gaussian wave function in the continuum limit, with a non-diagonal covariance matrix in field space. As the classical and quantum correlations—for instance the two-point function, its inverse and measures of entanglement—fall exponentially with spatial separation, the off-diagonal elements in this covariance matrix fall correspondingly. It is this scaling with separation that allows for a quantum computer to be initialized into the ground state of a lattice field theory with the number of operations scaling as a polynomial in the spatial volume.

In this work, we design localizable quantum circuits to prepare the ground states of lattice scalar field theories, both free and interacting, on digital quantum computers. Building upon the foundational papers of JLP [25, 24, 62, 63], Somma [102], and more recent works [30, 45, 86, 26, 134], the required controlled operations in these circuits are organized to correspond to spatial separations between field operators—providing a useful relation between the angles of the controlled rotations and the classical and quantum correlations of the QFT.

Before presenting numerical results in interacting $\lambda\phi^4$ scalar field theory, much of our paper explores free field theory because a number of helpful analytic results are found. Our results are connected to the growing literature exploring the entanglement in fundamental particle interactions and QFTs [185, 159, 186, 187, 188, 189, 190, 191, 192, 193, 156, 50, 194, 195] as well as the literature on area-law entanglement scalings and tensor network simulatability [196, 197, 198, 199, 200]. It is also allows for truncations based upon spatial localization to be systematically implemented at the circuit level, and for the subsequent loss of fidelity in the prepared wave function to be systematically quantified.

5.2 Quantum Circuits for Real Wavefunctions

The preparation of an arbitrary real wavefunction $|\psi\rangle$ on n_Q qubits decomposed as $|\psi\rangle = \sum_{x=0}^{2^{n_Q}-1} \psi(x)|x\rangle$ can be implemented by allowing a rotational degree of freedom for each introduced subspace of Hilbert space, similar to the procedure described in Ref. [201, 202], as demonstrated in the circuit of Fig. 5.1. In this design, new qubits are introduced at the

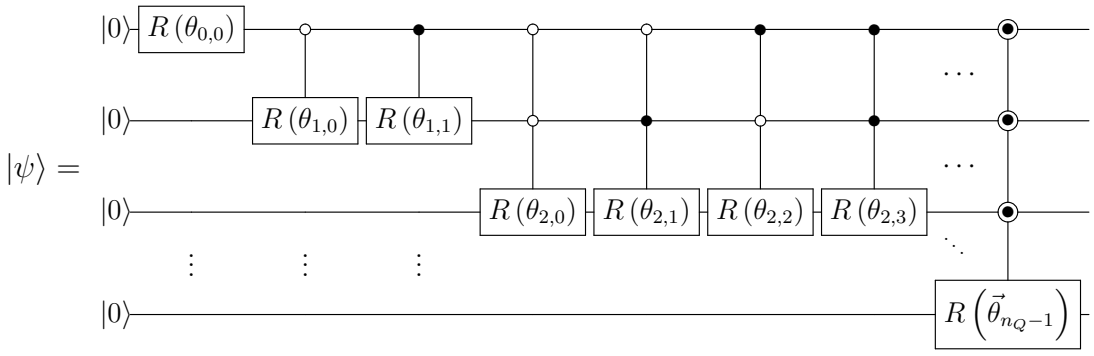

Figure 5.1: A circuit that can prepare an arbitrary real wavefunction by acting individually in increasing bipartitions of the Hilbert space.

bottom of the circuit and become the least significant bit in the binary interpretation of

the linearized Hilbert space [1]. Rotation operators are y-axis rotations, as above, and the extension of the circuit is shown pictorially with the last circuit element representing 2^{n_Q-1} y-axis rotations, each with (n_Q-1) controls. The angles are notated as $\theta_{\ell,k}$ where ℓ indicates the level that runs from 0 to n_Q-1 and k indexes the angles within the level running from 0 to $2^\ell-1$. For example, the angle $\theta_{2,1}$ is the second angle in level 2 and is thus located in the doubly controlled rotation gate with controls active on the state $|k\rangle = |01\rangle$. Thus, the associated gate may be read directly from the angle label where the number of controls is ℓ and the binary for which those controls are active is the binary representation of k. The collection of gates at each level are compacted graphically into a single gate with partially filled controls and a vector of angles as shown at the right side of Fig. 5.1. This circuit element is equivalent to the uniformly controlled gates defined in Ref. [203]. Note that the gates in a particular level commute (explicitly acting on different sectors of the Hilbert space) so may be implemented in any order while levels must be implemented in increasing sequential order. Solving for the angles $\theta_{\ell,k}$ may be done through ratios of various bipartitions of the wavefunction samples,

$$\begin{aligned} \theta_{\ell,k} &= \arctan\sqrt{\frac{\sum_{x=x_{\min}}^{x=x_{\max}}\psi(x)^2}{\sum_{y=y_{\min}}^{y=y_{\max}}\psi(y)^2}} \\ x_{\min} = 2^{n_Q-\ell-1}(2k+1) \quad &, \quad x_{\max} = 2^{n_Q-\ell}(1+k)-1 \\ y_{\min} = k2^{n_Q-\ell} \quad &, \quad y_{\max} = 2^{n_Q-\ell-1}(2k+1)-1 \end{aligned} \quad . \tag{5.1}$$

On occasion, it may be convenient to solve for the angles corresponding to the wavefunction interpreted in reverse binary order. On three qubits, for example, this distorts the

[1] Note that this is the opposite scheme to that implemented in Sec. 7.2 above for the exponential, where qubits were introduced at the top of the qubit staff becoming the most significant qubit. This choice results from the decision to build the exponential from left to right in the binary-interpreted Hilbert space while here additional qubits are used to increase the digitization rather than expand the space.

wavefunction through the following interchanges of the quantum states

$$\psi(0) \leftrightarrow \psi(0) \quad \psi(1) \leftrightarrow \psi(4) \quad \psi(2) \leftrightarrow \psi(2) \quad \psi(3) \leftrightarrow \psi(6) \quad \psi(5) \leftrightarrow \psi(5) \quad \psi(7) \leftrightarrow \psi(7) \quad . \tag{5.2}$$

If this choice is made for the angle calculation, a swap network is needed at the end of the circuit to reorient the qubits. If the state is simply being measured after preparation (rather than, for example, time evolved), this reversal may be handled by simply reading the computational basis states backwards when classically recording measurements.

There are many ways one might consider implementing the above circuit, specifically the ℓ-controlled rotations. One way is to build the gates level-by-level utilizing the decompositions of Refs. [204, 205]. With basic decompositions, the number of required CNOT gates for each n-controlled unitary scales as $\mathcal{O}(3^{n-1})$ and thus the circuit of n_Q qubits requires a number of CNOT gates scaling as $\mathcal{O}(2^{n_Q+1}3^{n_Q})$. Rather than the circuit structure of Fig. 5.1, we propose the circuit of Fig. 5.2 as an alternative capable of creating the same arbitrary real wavefunctions but with a number of CNOTs scaling only as $\mathcal{O}(2^{n_Q})$ with the number of qubits. The gate at the right in Fig. 5.2, suggesting extrapolation to n_Q qubits with

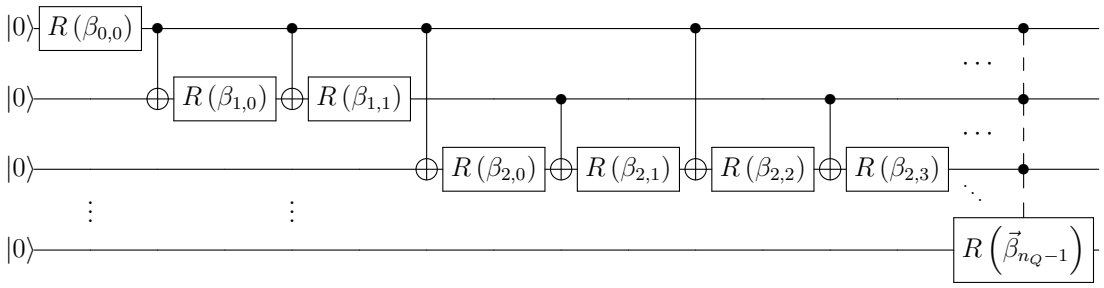

Figure 5.2: A circuit with $\mathcal{O}(2^{n_Q})$ CNOTs capable of preparing an arbitrary real wavefunction by implementing single-qubit gates defined by linear combinations of the rotation angles used in Fig. 5.1 interleaved with CNOTs of varying control and target placements.

dashed vertical connectivity, represents a collection of 2^{n_Q-1} CNOTs with staggered controls alternating with the same number of single-qubit rotations. The structure of these controls

must allow all linearly independent combinations of the θs to be created through the βs at every level. This symmetry can be assured through repeated bisection e.g., level $\ell = 4$ for the 5-qubit system is structured as shown in Fig. 5.3, where the empty boxes represent the y-

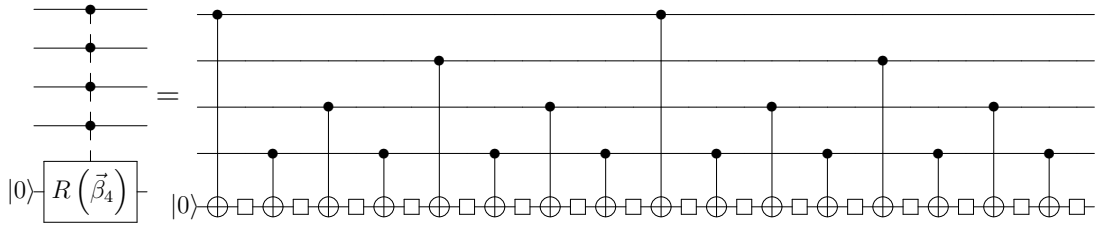

Figure 5.3: An example of the controlled rotation shown in Fig. 5.2 for level 4 ($\ell = 4$), where an ℓ-controlled unitary defined by a vector of rotation angles connected by a dashed vertical stem represents a series of 2^ℓ CNOT operators interleaved with 2^ℓ single-qubit rotations. The targets of the CNOTs act on the $(\ell + 1)^{\text{th}}$ qubit while the controls are placed from top to bottom of the qubit staff as increasing bipartitions. The angles defining the 2^ℓ single-qubit rotations are defined from left-to-right by the sequential elements of the angle vector, β_ℓ, that are defined in Eq. (5.5).

axis rotations with angles defined by the 16-dimensional vector of angles, $\vec{\beta}_4$. Systematically, CNOTs of increasing length appear with frequency decreasing in powers of two. Each level in this procedure contains 2^ℓ rotations and the same number of CNOTs with the exception of $\ell = 0$ where there are 0 CNOTs. Thus, the total number of these circuit elements required to initialize an arbitrary positive, real wavefunction is

$$\text{rotations}(n_Q) = \sum_{\ell=0}^{n_Q-1} 2^\ell = 2^{n_Q} - 1 \qquad \text{CNOT}(n_Q) = \sum_{\ell=1}^{n_Q-1} 2^\ell = 2^{n_Q} - 2 \quad . \tag{5.3}$$

Instead of applying high-dimensional controls to apply rotations to various sub spaces of the Hilbert space, this circuit always implements single-qubit rotations whose angles are linear combinations of the previous angles specifically chosen to balance for an equivalent unitary

operator. Using the fact that

$$XR(\theta)X = R(-\theta) \tag{5.4}$$

the linear combinations of β angles associated with the original θ angles can be read directly from the circuit structure. For the 3-qubit example,

$$\begin{aligned}
\theta_{0,0} &= \beta_{0,0} & \theta_{2,0} &= \sum_{k=0}^{2^2-1} \beta_{2,k} \\
\theta_{1,0} &= \sum_{k=0}^{2^1-1} \beta_{1,k} & \theta_{2,1} &= \beta_{2,0} - \beta_{2,1} - \beta_{2,2} + \beta_{2,3} \\
\theta_{1,1} &= -\beta_{1,0} + \beta_{1,1} & \theta_{2,2} &= -\beta_{2,0} - \beta_{2,1} + \beta_{2,2} + \beta_{2,3} \\
& & \theta_{2,3} &= -\beta_{2,0} + \beta_{2,1} - \beta_{2,2} + \beta_{2,3}
\end{aligned} \tag{5.5}$$

A block diagonal translation matrix with blocks of size 2^ℓ each containing all linearly independent vectors of $\{1, -1\}$ can be constructed and inverted to translate the calculations of $\theta_{\ell,k}$ into values for $\beta_{\ell,k}$ to be implemented more efficiently. An example of this matrix is given in Eq. 5.9 of the next subsection. It should be noted that this inversion need be calculated only once for any n_Q as it is angle-independent. The following subsection provides an explicit example of this process for the preparation of a Gaussian wavefunction.

5.2.1 Preparation of a Gaussian

The Gaussian wavefunction is of particular importance for bosonic degrees of freedom and the ground states of scalar field theories. Its preparation on a register of qubits has been previously considered in Refs. [184, 206, 102, 207] both recursively and dynamically. Here we largely recover the recursive findings with the circuitry described previously, though we provide explicit circuits for the method without calculating the angles on qubits, and take advantage of the symmetry of the Gaussian to reduce the necessary quantum resources with respect to more general implementation strategies [202, 203, 208]. This section, and the discussions of the symmetrized exponential above, could be considered to provide an inexpensive initialization for Somma Inflation [102], where eigenstates of the harmonic oscillator

are prepared efficiently through tuned time evolution from a narrow state with Gaussian-distributed amplitudes. [2]

Beginning with the well-localized [3] Gaussian wavefunction, the state vector is a digital sampling of the continuous Gaussian

$$|\psi\rangle = \mathcal{N} \sum_{x=0}^{2^{n_Q}-1} \exp\left[-\frac{\left(x-\mu_{n_Q}\right)^2}{2\sigma_{n_Q}^2}\right]|x\rangle \qquad \mathcal{N}^{-1} = \sqrt{\sum_{x=0}^{2^{n_Q}-1} \exp\left[-\frac{\left(x-\mu_{n_Q}\right)^2}{\sigma_{n_Q}^2}\right]} \quad . \tag{5.6}$$

The n_Q-dependent factors associated with the mean and standard deviation account for the scaling of the sampling grid as the number of qubits is increased,

$$\mu_{n_Q} = 2^{n_Q-1}\mu \quad , \quad \sigma_{n_Q} = 2^{n_Q-1}\sigma \quad , \tag{5.7}$$

such that adding a qubit increases the sampling resolution rather than distorting the wavefunction. A value of $\mu = 1$ places the peak of the Gaussian at the site 2^{n_Q-1}. To place the peak in the center of the binary Hilbert space, symmetrizing the sample points as would be done in Ref. [45] for a field-space wavefunction about $\phi = 0$, the value of μ is also n_Q-dependent $\mu_{\text{center}} = 1 - \frac{1}{2^{n_Q}}$. As an example, the vector of angles calculated from Eq. (5.17) that would be used to implement a 3-qubit Gaussian of $\sigma = 0.2$ centered symmetrically in the Hilbert space using the circuit of Fig. 5.1 would be

$$\vec{\theta} = (\theta_{0,0}, \theta_{1,0}, \theta_{1,1}, \theta_{2,0}, \theta_{2,1}, \theta_{2,2}, \theta_{2,3})^T = (0.785, 1.562, 0.009, 1.562, 1.364, 0.207, 0.009)^T \quad . \tag{5.8}$$

The first angle, due to the symmetry between the Hilbert space half spaces is simply $\arctan 1 = \frac{\pi}{4}$. To translate these angles to the angles implemented in the improved tree

[2] The evolution process is completed with two separate operators: the free propagator and the field operator. The free propagator allows the Gaussian wavepacket to expand to encompass a larger number of states. Propagating next with the field operator allows cancellation of the imaginary components of the wavefunction from the free propagation. This proposal is similar to an adiabatic evolution between harmonic oscillator Hamiltonians with differing values of ω. However, Somma Inflation requires the quantum resources of only a single Trotter step.

[3] Gaussian wavefunctions that are not well localized may, as usual, be implemented with periodic boundary conditions by including image Gaussians at distances defined by the Hilbert space dimension. Once such a target wavefunction is established, Eq. (5.17) and subsequent procedures are unchanged.

circuit of Fig. 5.2, one analyses the action of each of the 2^ℓ states of the control inputs at level ℓ to produce the block diagonal translation matrix described by Eq. (5.5). Under inversion, all linearly independent combinations of the $\theta_{\ell,k}$'s at each level ℓ are captured in the β angles of the tree circuit,

$$\vec{\beta} = \begin{pmatrix} 1 & 0 & 0 & 0 & 0 & 0 & 0 \\ 0 & 1 & 1 & 0 & 0 & 0 & 0 \\ 0 & -1 & 1 & 0 & 0 & 0 & 0 \\ 0 & 0 & 0 & 1 & 1 & 1 & 1 \\ 0 & 0 & 0 & 1 & -1 & -1 & 1 \\ 0 & 0 & 0 & -1 & -1 & 1 & 1 \\ 0 & 0 & 0 & -1 & 1 & -1 & 1 \end{pmatrix}^{-1} \vec{\theta}$$

$$= (0.785, 0.776, 0.785, 0.677, 0.0, 0.099,\ 0.785)^T \quad . \tag{5.9}$$

Given that the Gaussian is a symmetric function, it is apparent that the $2^{n_Q} - 1$ angles of Eq. (5.17) are not providing independent information to the state preparation. Guided by the symmetrization (or anti-symmetrization) shown in the circuit of Fig. 7.1—introducing a qubit at the top of the stave (most-significant in the binary-interpreted Hilbert space) in the $|\pm\rangle$ state to copy the distribution and a string of CNOTs to reflect the second half space—an arbitrary real, symmetric wavefunction can be implemented with fewer quantum resources. By effectively replacing the final level ($\ell = n_Q - 1$) with a symmetrization, this trades 2^{n_Q-1} CNOTs for only $n_Q - 1$ CNOTs. As can be intuited, only the first half of the $\vec{\theta}_\ell$ is retained at each level with the control on the level-0 qubit removed. The first angle thus becomes $R\left(\frac{\pi}{4}\right) = H$ as noted above for any symmetric wavefunction. In terms of the angles calculated in Eq. (5.17), the circuit with multi-controlled quantum gates becomes that of Fig. 5.4. As shown in this figure, the gate associated with $\theta_{\ell,k}$ is an $(\ell - 1)$-controlled rotation still with controls dictated by the binary interpretation of k but now omitting the top qubit. The remaining relevant angles for the 3-qubit example above are,

$$\vec{\theta} = (\theta_{1,0}, \theta_{2,0}, \theta_{2,1}) = (1.5618, 1.5616, 1.364)^T \quad . \tag{5.10}$$

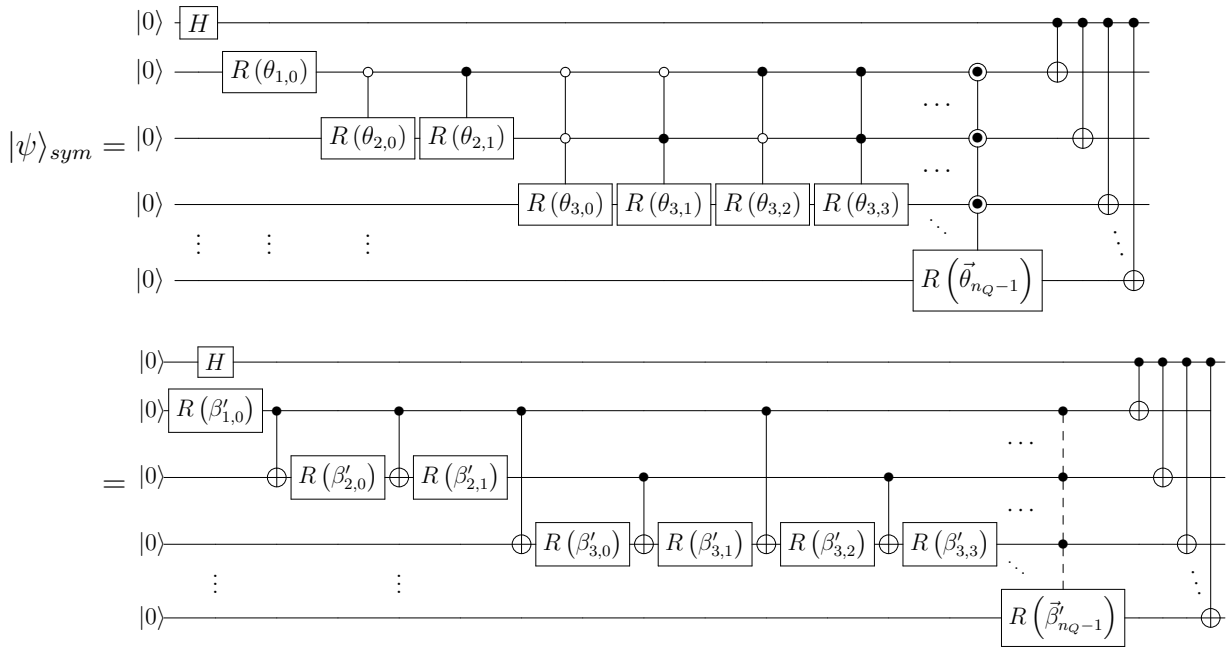

Figure 5.4: The upper circuit shows that in Fig. 5.1 specialized to the implementation of a real wavefunction that is symmetric in the binary-interpreted Hilbert space. By leveraging linear combinations of rotation angles, the highly controlled rotation gates can be replaced by the lower (tree) circuit described by Fig. 5.2 and Fig. 5.3. An explicit example of transforming $\theta \to \beta'$ angles is given in Eqs. (5.10) and (5.11) for an $n_Q = 3$ Gaussian wavefunction.

The associated β' angles are constructed as linear combinations at each level as above,

$$\vec{\beta}' = \left(\beta'_{1,0}, \beta'_{2,0}, \beta'_{2,1}\right) = \begin{pmatrix} 1 & 0 & 0 \\ 0 & 1 & 1 \\ 0 & -1 & 1 \end{pmatrix}^{-1} \quad \theta = (1.562, 0.099, 1.463)^T \quad , \tag{5.11}$$

and can, similarly to the relationship between the circuits of Fig. 5.1 and Fig. 5.4, be implemented by removing the final layer of the tree circuit of Fig. 5.2, relabeling the angles, and adding a qubit at the top of the stave for symmetrization. This final circuit is shown in the

second line of Fig. 5.4. Thus, the resource costs become,

$$\text{Rotations}(n_Q) = \sum_{\ell=0}^{n_Q-2} 2^\ell = 2^{n_Q-1} \qquad \text{CNOT}(n_Q) = 2^{n_Q-1} + n_Q - 3 + \delta_{n_Q,1} \quad , \tag{5.12}$$

specifically relevant for the preparation of any eigenstate of the harmonic oscillator and generally relevant for preparing an arbitrary real, symmetric (or antisymmetric) wavefunction centered in the Hilbert space.

5.3 Digitized Wavefunctions

Determining properties and dynamics of scalar fields on a quantum computer will require digitizing the scalar field at each lattice site [25, 24, 62, 63]. There have been a number of recent studies to quantify such digitization artifacts as understood from the Nyquist-Shannon (NS) Sampling Theorem [102, 30, 45, 86, 26, 134]. It has been shown that, if the field truncation and digitization are informed by NS saturation and correlated in the computational design as qubits are added, the precision of low energy observables can be made to scale double exponentially with the number of qubits used to represent the field at each lattice site. We choose to symmetrically digitize the field at each site, using the basis $\{\ |\phi_i\rangle\ \}$, defined by eigenvectors of the field operator, $\hat{\phi}_i$ [45, 26]. For a mapping of each spatial site onto a qubit register of n_Q qubits, and hence a Hilbert space of dimensionality $n_s = 2^{n_Q}$, the Hilbert space of each site in this representation is spanned by $\left\{ |-\phi_{\max}\rangle\ ,\ |-\phi_{\max}+\delta_\phi\rangle\ ,\ \cdots\ ,\ |-\frac{\delta_\phi}{2}\rangle\ ,\ |\frac{\delta_\phi}{2}\rangle\ ,\ \cdots\ ,\ |\phi_{\max}-\delta_\phi\rangle\ ,\ |\phi_{\max}\rangle \right\}$ with field-space lattice spacing $\delta_\phi = \frac{2\phi_{\max}}{n_s-1}$.

To recover the digitized version of the analytic entangled wave function, it is convenient to start with a wave function with all elements of the lattice-digitized wave functions appearing with equal weight (e.g. a Hadamard operation has been applied to each qubit on each site),

$$|\psi_i\rangle \ = \ \frac{1}{\sqrt{n_s^N}} \sum_{i_0,i_1,\cdots,i_{N-1}=0}^{n_s-1} |\phi_0^{(i_0)}\rangle \otimes |\phi_1^{(i_1)}\rangle \otimes \cdots \otimes |\phi_{N-1}^{(i_{N-1})}\rangle \ . \tag{5.13}$$

We then define a non-unitary operator from Eq. (2.10),

$$\hat{\Gamma} \ = \ e^{-\frac{1}{2}\hat{\boldsymbol{\phi}}^T \mathbf{K} \hat{\boldsymbol{\phi}}} \quad , \tag{5.14}$$

that reproduces the wave function, once appropriately normalized, in the continuum. The digitized wave function is defined as

$$|\psi_d\rangle \;=\; A\hat{\Gamma}|\psi_i\rangle \quad , \tag{5.15}$$

where A is the normalization constant, that produces a real wave function across the Hilbert space. The operator is invariant under the symmetry $\boldsymbol{\phi} \to -\boldsymbol{\phi}$, and hence the $n_s^N - 1$ independent real numbers is reduced to $\frac{1}{2}n_s^N - 1$ independent real numbers due to the reflection symmetry in field space.

This method of wavefunction digitization is appropriate when the continuum wavefunction is known or can be approximated with a suitable basis of continuum functions. Being a solvable theory, the ground state of the free scalar field can be expressed analytically. For an interacting theory, it is possible to construct approximate forms of the continuum ground state by diagonalizing in a truncated basis of Hermite polynomials, the free eigenbasis. When far from the perturbative regime, it is also possible to begin directly with the digitized Hamiltonian implemented in Ref. [45]. Both of these techniques become tenuous at large spatial volumes. It is expected that the non-perturbative techniques for characterizing and capturing the vacuum structure of QCD will be vital for informing and designing the quantum circuits necessary to initialize the ground states of non-trivial field theories onto qubit degrees of freedom.

5.4 Quantum Circuits for Ground State Wavefunctions

The following reminds the reader of a generic quantum circuit for preparing wavefunctions with real amplitudes, and introduces a systematic restructuring of the operators to naturally embed localized correlations. The restructuring begins by (at most) doubling the number of quantum operations, in the process making manifest the physically-intuitive removal of long-distance circuit elements. For the lattice scalar field ground state, where two-point correlation functions decay exponentially with separation, this localization allows for truncations of the quantum circuit to approximate the ground state with exponentially

improvable fidelity. More generally, this restructuring is expected to be advantageous for position-space qubit representations of field theories exhibiting cluster decomposition or for generic quantum states where classical and/or quantum correlations are suppressed with distance e.g., separation on physical hardware.

5.4.1 Controlled Rotations: the θ-Angles

In a previous works [184, 206, 26], circuits have been established to prepare an arbitrary real, positive wavefunction with a focus on gaussian-distributed amplitudes. The following circuit is reproduced from Ref. [26],

$|\psi\rangle =$ 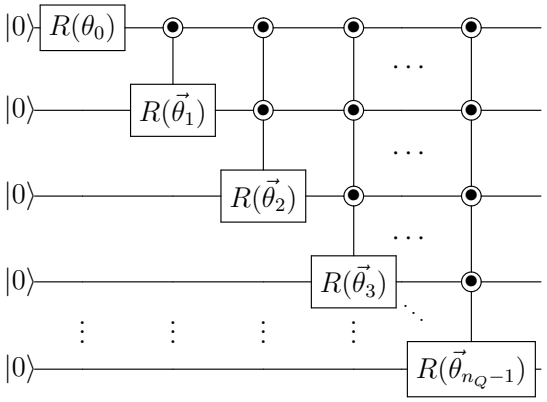

$$, \quad R(\theta) = \begin{pmatrix} \cos\theta & -\sin\theta \\ \sin\theta & \cos\theta \end{pmatrix} \quad , \quad (5.16)$$

where the circle-dot controlled operator represents a set of operators each controlled on a different binary state of the control qubits. This circuit is defined by $2^{n_Q} - 1$ rotations and can be implemented with $2^{n_Q} - 2$ CNOT gates. The θ_ℓ vectors at level ℓ have length 2^ℓ with element $\theta_{\ell,k}$ associated with the binary control value of k on the above qubits as read from top to bottom in the qubit register. The values of the rotation angles are easily defined through ratios of bipartitions of the wavefunction, $|\psi\rangle$,

$$|\psi\rangle = \sum_{x=0}^{2^{n_Q}-1} \psi(x)|x\rangle \qquad \theta_{\ell,k} = \arctan \sqrt{\frac{\sum_{x=x_{\min}}^{x=x_{\max}} \psi(x)^2}{\sum_{y=y_{\min}}^{y=y_{\max}} \psi(y)^2}}$$

$$\begin{aligned} x_{\min} &= 2^{n_Q-\ell-1}(2k+1) \quad , \quad x_{\max} = 2^{n_Q-\ell}(1+k) - 1 \\ y_{\min} &= k2^{n_Q-\ell} \quad , \quad y_{\max} = 2^{n_Q-\ell-1}(2k+1) - 1 \end{aligned} \quad . \quad (5.17)$$

As constructed, the qubit at level-0 is the "most-significant" qubit in the binary register. Its binary value controls whether the amplitude resides in the first or second half of the wavefunction when represented in a one dimensional binary-interpreted Hilbert space. If the wavefunction is symmetric in this computational basis, Eq. (5.17) indicates that $\theta_0 = \frac{\pi}{4}$. Analyzing the structure of these rotation angles further, a symmetric wavefunction will be defined by angles satisfying

$$\theta_0 = \frac{\pi}{4} \quad , \quad \theta_{\ell,j} + \theta_{\ell,2^{n_Q}-1-j} = \frac{\pi}{2} \; \forall \;\; \ell > 0, j \in \{0, 1, ..., 2^{\ell-1} - 1\} \quad , \tag{5.18}$$

reducing the rotational degrees of freedom by two. Returning to the wavefunction from the θ angles can be accomplished by

$$\psi(x) = \prod_{\ell=0}^{2^{n_Q}-1} \begin{cases} \cos\left(\theta_{\ell,\lfloor x 2^{\ell-n_Q} \rfloor}\right) & \text{if } b_\ell = 0 \\ \\ \sin\left(\theta_{\ell,\lfloor x 2^{\ell-n_Q} \rfloor}\right) & \text{if } b_\ell = 1 \end{cases} \tag{5.19}$$

where b is the binary representation of x read from left to right e.g., in a two-qubit system, $x = 2$ is associated with $b_0 = 1$ and $b_1 = 0$. This translation from $\theta_{l,j}$ angles to the wavefunction is a simple result of the y-axis rotation gates in Eq. (5.16) chosen to parameterize the circuit.

5.4.2 Systematically Localizable Operators: the α-Angles

If correlations in the target wavefunction are localized, the structure of the θ-circuit is not optimal in localizing corresponding controlled circuit elements. To make operator localization explicit, the α rotation angles are introduced to systematically isolate sensitivity to long-distance controls by decomposing each level, beginning with interactions local with respect to the target qubit. The basis of this decomposition lies in the circuit identity shown in

Eq. (5.20).

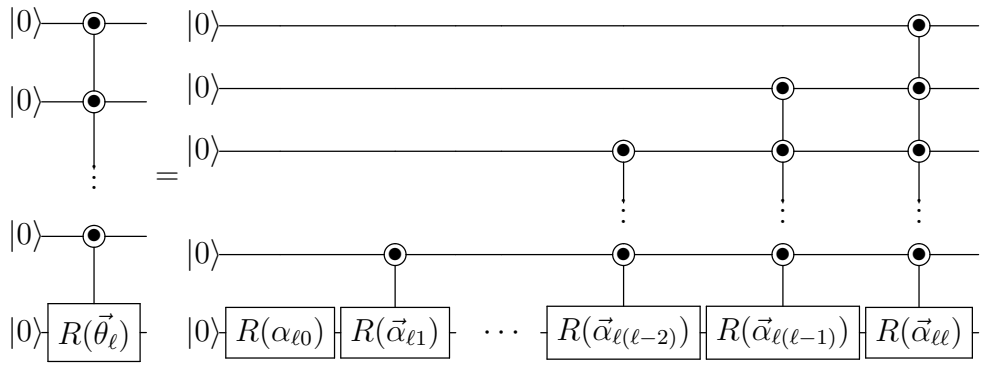

. (5.20)

While translating from the θ- to α-circuits increases the number of circuit elements by at most a factor of two, the modified structure allows the localized correlations and entanglement of the ground state of the free scalar field to become manifest in the form of exponentially-suppressed rotation angles (as the associated controls increase in spatial extent). Thus, systematically truncating operators by locality in the α-basis allows such wavefunctions to be approximated with high fidelity. The α-angles satisfying the above decomposition are:

$$\alpha_{\ell 0} = \sum_{m=0}^{2^\ell} \frac{\theta_{\ell,m}}{2^\ell} \qquad \alpha_{\ell h,k} = \sum_{m=0}^{2^{\ell-h}-1} \frac{\theta_{\ell,(k+m2^h) \bmod 2^\ell}}{2^{\ell-h}} - \sum_{m=0}^{2^{\ell-h+1}-1} \frac{\theta_{\ell,(k+m2^{h-1}) \bmod 2^\ell}}{2^{\ell-h+1}} \quad . \tag{5.21}$$

The first index ℓ indicates the level from which the operator originates and thus the qubit location of the target rotation, the second index h indicates the number of controls on the operator, and the final index k indicates the binary-interpreted value of the associated controls (read from top to bottom). To determine the α's in terms of θ's, one considers the average wavefunction across the range of Hilbert subspaces satisfying the relevant subset of controls. For the single qubit operator, this is the average rotation of all angles in the level. For $\vec{\alpha}_{\ell 1}$, this is the average rotation amongst even(odd) binary-interpreted Hilbert subspaces of the previous ℓ qubits. From this mean value, subtractions are made to remove mean value rotations applied previously by operators of higher locality. The role of the added circuit elements is thus to sequentially isolate the spatially local correlations. It follows that the relation,

$$\theta_{\ell k} = \alpha_{\ell 0} + \sum_{h=1}^{\ell} \alpha_{\ell h, k \bmod 2^h} \quad , \tag{5.22}$$

can be used to translate back to the θ- angles from the α-angles.

Note that a decomposition exists also for incomplete collections of localized circuit elements isolated from the fully-controlled operator of Eq. (5.20). Such a decomposition is implemented by setting $\vec{\alpha}_{\ell h} = 0$ for any set of h's (not including $h = \ell$) and calculating subsequent α-angles recursively as

$$\alpha_{\ell h,k} = \sum_{m=0}^{2^{\ell-h}-1} \frac{\theta_{\ell,(k+m2^h)}}{2^{\ell-h}} - \sum_{m=1}^{h-1} \alpha_{\ell m,k \bmod 2^m} - \alpha_{\ell 0} \qquad , \qquad \alpha_{\ell 0} = \sum_{k=0}^{2^\ell-1} \frac{\theta_{\ell k}}{2^\ell} \quad . \tag{5.23}$$

One such partial decomposition useful for the scalar field ground state creates on *site-wise controls*, where the operators controlling on a partial spatial site are set to zero. For example, in an eight-site lattice with two qubits per site, the θ operator at level $\ell = 7$ can be, for instance, decomposed into operators with h values of 0, 1, 3, 5, and 7 only. An explicit example of the quantum circuit and numerical values of site-wise α-angles is provided in Appendix F of Ref. [27].

Without any particular symmetry assumed of the wavefunction, the α-representation naturally exhibits symmetries. If the full decomposition of all $\vec{\alpha}$'s is implemented (as opposed to site-wise controls), the following symmetries are present

$$\alpha_{\ell h,k} = -\alpha_{\ell h,k+2^{h-1}} \quad . \tag{5.24}$$

These angular symmetries maintain the number of independent rotational degrees of freedom at 2^ℓ for each level

$$2^0 + \sum_{m=0}^{\ell-1} 2^{\ell-m-1} = 2^\ell \quad . \tag{5.25}$$

Of course, if the level is not fully decomposed with all $\ell + 1$ operators, this symmetry will manifest only for the angles up to the first absent operator. The α-angles present additional symmetries in the case of symmetric wavefunctions in the binary-interpreted Hilbert space. From Eqs. (5.18) and (5.21), $\alpha_{\ell 0} = \frac{\pi}{4}\ \forall \ell$. Additionally,

$$\alpha_{\ell h,k} = -\alpha_{\ell h,2^h-1-k} \tag{5.26}$$

leaving only 2^{h-2} independent rotational degrees of freedom per localizing operator and $2^{\ell-1}$ rotations per level

$$1+\sum_{h=2}^{\ell} 2^{h-2} = 2^{\ell-1} \quad . \tag{5.27}$$

As expected for a wavefunction with well-defined parity, and demonstrated intuitively in the replacement of a level by a single-qubit Hadamard on the most significant qubit (of the binary representation), the number of angles needed to define the symmetric wavefunction is $2^{n_Q-1}-1$.

It is illuminating to see how the circuit requirements for preparing the GHZ and W states

$$|\mathrm{GHZ}\rangle_n = \frac{|0\rangle^{\otimes n}+|1\rangle^{\otimes n}}{\sqrt{2}} \quad , \quad |\mathrm{W}\rangle_n = \frac{|10\ldots0\rangle+|01\ldots0\rangle+\cdots+|00\ldots1\rangle}{\sqrt{n}} \quad , \tag{5.28}$$

changes from the θ-representation to the α-representation. In both states, the MI and negativity are translationally invariant. Recall, however, that the two states are characterized by distinct entanglement patterns and cannot be mixed through local (non-entangling) operations and classical communication (LOCC) [209, 210, 211]. For the n-qubit GHZ state, genuine n-partite entanglement is present that is fragile to the removal or measurement of any one qubit. This fragility is quantified by the vanishing of bipartite negativity $\mathcal{N}(\hat{\boldsymbol{\rho}}_1)=0$ indicating that, after one qubit is removed, all remaining correlations in the GHZ state are classical and quantified by non-vanishing MI. In contrast, the W-state contains no genuine n-partite entanglement though is robust to qubit removal in retaining high degrees of entanglement within reduced density matrices. As the entanglement structure should dictate the necessary circuit connectivity for state preparation, it is natural to expect these two states to be created by circuits of distinct structure. Angles capable of initializing the GHZ state are:

$$|\mathrm{GHZ}\rangle_n: \quad \theta_0 = -\frac{3\pi}{4} \quad , \quad \theta_{\ell k} = \begin{cases} 0 & k \bmod 2 = 0 \\ \pi/2 & k \bmod 2 = 1 \end{cases} \rightarrow \quad \alpha_0 = -\frac{3\pi}{4} \quad , \quad \alpha_{\ell 1,1} = \frac{\pi}{2} \quad , \tag{5.29}$$

where each level, $\ell \geq 1$, contains $2^{\ell-1}$ non-zero θ-rotations of equal importance or a single localized α-rotation with $h=1$. While it is well known that the GHZ state can be created

with such a string of nearest-neighbor controlled operations, deriving this structure with the α-angles is encouraging that the proposed transformation allows fragile entanglement to be captured through a series of localized quantum gates. The angles capable of initializing the W-state are

$$|W\rangle_n : \qquad \theta_{\ell 0} = \arccos\sqrt{\frac{n-\ell-1}{n-\ell}} \quad , \tag{5.30}$$

where each level contains a single non-zero θ-angle with increasing value as ℓ increases and thus as the rotations become highly controlled and non-local. With a single θ-angle at each level, there is no advantage to using α-angles. As the two-qubit negativity in the W-state, $\mathcal{N}_{W_n}$, is non-zero and constant for increasing qubit separations,

$$\mathcal{N}_{W_n} = \frac{\sqrt{4+(n-2)^2}-(n-2)}{2n} \quad , \tag{5.31}$$

it is not surprising that fully-controlled rotations are necessary without distance truncation.

5.5 Preparing the Non-Interacting Digitized Lattice Scalar Field Ground State

The previous sections have highlighted the potential of preparing the ground state of a lattice scalar field theory with quantum circuits constructed in terms of the α-rotation angles, that are designed to correlate with physical spatial separation. In this section, we elaborate on the attributes and features of these quantum circuits, focusing on the scaling of the $\alpha_{\ell h,k}$ angles with h the number of controls, and on the scaling of the fidelity of the wavefunction as truncations in the number of controls and/or the magnitude of $\alpha_{\ell h,k}$ are imposed. We numerically examine the forms of the angles, in particular the hierarchies that are present, and compare with the $\mathbf{K}$ matrix or two-point correlations, the MI and the negativity.

Before embarking on numerical explorations, it is worth gaining insight from a perturbative expansion of the $\mathbf{K}$ matrix, defined in Eq. (5.14). While it might have been helpful to establish analytic results without perturbatively expanding in separation, the appearance of arctan() functions in the relation between angles and values of the wavefunction render such results unwieldy. By assigning a parametric scaling of $\mathbf{K}_{ij} \to Q^{|i-j|}\mathbf{K}_{ij}$,

where Q is introduced as an expansion parameter ($Q = 1$ is set at the end), and expanding Eq. (5.14), the angles $\alpha_{\ell h,k}$ can be written as a perturbative expansion in powers of Q. Using Eq. (2.42), it is straightforward to show that the controlled rotation angles scale as $\alpha_{\ell h,k} \sim Q^{\hat{r}} \sim \mathbf{K}_{1\hat{r}+1}, \mathbf{K}_{12}\mathbf{K}_{1\hat{r}}, ..., \mathbf{K}_{12}^{\hat{r}} \to \hat{m}K_1(\hat{m}\hat{r})/\hat{r} \to \sqrt{\hat{m}}e^{-\hat{m}\hat{r}}/\hat{r}^{3/2}$, where $\hat{r} = \lceil (h - \ell \bmod n_Q)/n_Q \rceil$ is the spatial distance (in lattice units) between the lattice sites of the maximally separated qubits in the controlled operation. This analysis reveals that the α-angles scale in essentially the same way as the K matrix and two-point correlation function, not with the MI or negativity.

Take, for example, the controlled rotations acting on the highest qubit of the 3rd spatial site ($l = 11$, as counting starts from $l = 0$) for a lattice scalar field theory with $n_Q = 4$ qubits per site. The spatial separation vanishes, $\hat{r} = 0$, for $h = 0, 1, 2, 3$ and hence all of the rotation angles correspond to interactions within a spatial site, scaling as $\alpha_{\ell h,k} \sim \mathcal{O}(1)$ (determined by K_{11}). The $h = 4, 5, 6, 7$ rotation angles are controlled by the adjacent site, with $\hat{r} = 1$, and scale as $\alpha_{\ell h,k} \sim \mathcal{O}(\mathrm{K}_{12})$. The $h = 8, 9, 10, 11$ rotation angles are controlled by the site that is two lattice spacings separated, $\hat{r} = 2$, and scale as $\alpha_{\ell h,k} \sim \mathcal{O}(\mathrm{K}_{13})$. Expanding to higher orders in the Q-expansion shows that the angles receive additional contributions that are further suppressed by powers of K_{ij} compared to the leading order contributions. For a generic lattice system with sufficiently large spatial volume, $\hat{m}N \gg 1$ and with control operations between the first and midpoint lattice site scaling as $\sim \sqrt{\hat{m}}e^{-\hat{m}N/2}/(N/2)^{3/2}$, this perturbative expansion demonstrates the potential of mappings and quantum circuits that are arranged to reflect the underlying physical system when working to a pre-determined level of precision in a computation.

To numerically verify the scaling results obtained with this perturbative expansion, we analyze a digitized free lattice scalar field theory with open boundary conditions, with the field at each site encoded onto two qubits, $n_Q = 2$, ten spatial sites, $N = 10$, a field truncation of $\phi_{\max} = 3.5$, and a mass of $\hat{m} = 0.3$ ($\hat{m}N = 3$). The relation between the α-angles and the spatial extent of the associated controls is shown in the right panel of Fig. 5.5. For the sake of comparison, the corresponding relation between the θ-angles and control distance are shown

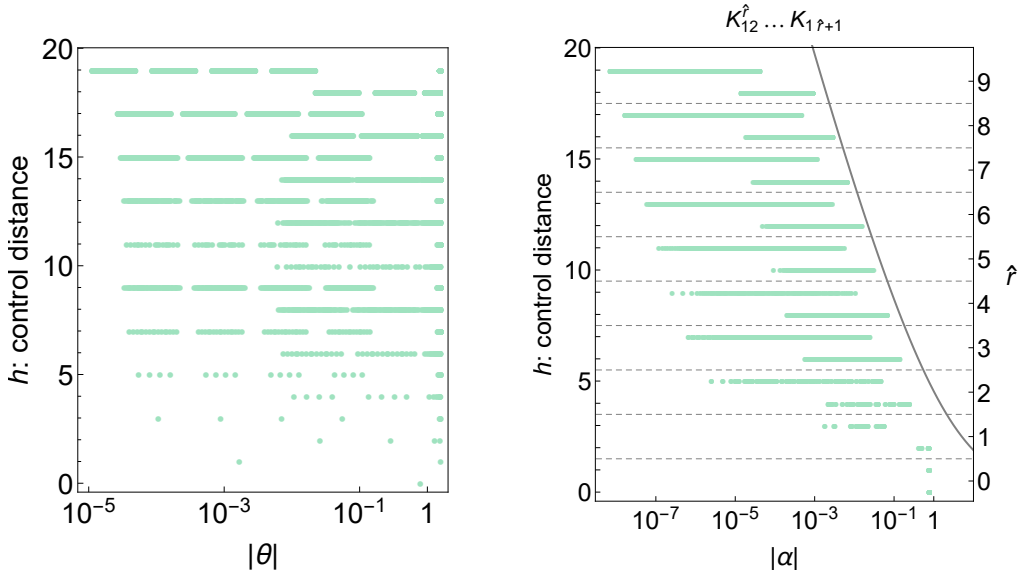

Figure 5.5: The magnitude of the controlled rotation angles $\theta_{\ell,k}$ (left panel) and $\alpha_{\ell h,k}$ (right panel) as related to the control distance, h, (directly related to spatial separation) for a ten-site ($N = 10$) spatial lattice with two qubits per site, $n_Q = 2$. The light green points show the results of numerical computations while the light-grey curve (right panel) shows the (normalized) theoretical asymptotic form of the inverse two-point function, $|\alpha|_{\max}(\hat{r}) \sim M_\alpha K_1(M_\alpha \hat{r})/\hat{r} \to \mathbf{K}_{1\,\hat{r}+1}$ with M_α tending to the scalar mass $\hat{m}$ at large volumes.

in the left panel of Fig. 5.5, which makes clear the absence of the correlations exhibited by the α-angles. The magnitude of the α-angles at a given control distance typically span orders of magnitude, but are bounded above by $|\alpha|_{\max}(\hat{r}) \sim M_\alpha K_1(M_\alpha \hat{r})/\hat{r} \to \mathbf{K}_{1\hat{r}}$ with M_α tending to $\hat{m}$ at large volumes, as expected from the perturbative analysis. For this lattice volume and scalar mass, shown in Fig. 5.5, the extracted value is $M_\alpha \sim 2\hat{m}$. The numerical exploration of this circuit structure at this and larger masses, consistent with the perturbative analysis, indicates that the angles scale with $\mathbf{K}$ and the inverse two-point correlation function once lattice artifacts become negligible. Interestingly, this suggests that there may be an even more efficient quantum circuit design with angles scaling with the measures of entanglement

as opposed to the correlation functions.

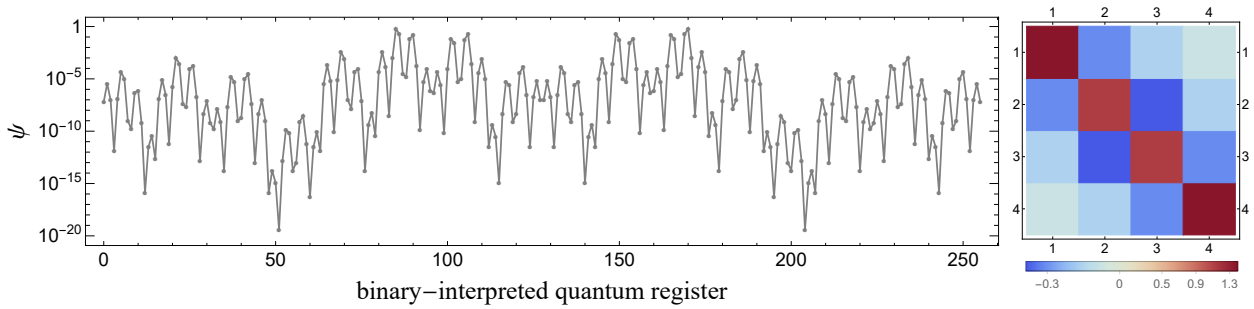

Figure 5.6: The wave function (left) and associated correlation matrix **K** (right) of the one-dimensional digitized lattice scalar field theory with two qubits per site ($n_Q = 2$), four spatial sites ($N = 4$), $\hat{m} = 0.3$, $\phi_{\max} = 3.5$, and with open boundary conditions imposed on the field.

While we have shown that the α-angle scaling with control distance is consistent with **K** and the inverse two-point function, this relation is only helpful if it provides a wavefunction from the truncated circuit application that is perturbatively close to the true wavefunction, and with a quantifiable associated systematic error. It is straightforward to numerically determine the fidelity of a wavefunction created with a quantum circuit that is truncated in the number of control elements applied to any given qubit, or in the tolerance of the magnitude of any given rotation angle. Truncations in each, or both, can be determined in order to perform a computation to a pre-determined level of precision, that is exponentially convergent.

To explore the impact of these truncations, we have studied a system of four spatial sites ($N = 4$) with fields digitized with two qubits per site ($n_Q = 2$) and open boundary conditions. The ground state wave function of this system with $\hat{m} = 0.3$ ($\hat{m}N = 1.2$) and $\phi_{\max} = 3.5$ is shown in Fig. 5.6. This theory has similarities with the two-site ($N = 2$) lattice systems with $n_Q = 2$ that is detailed in Appendix D of Ref. [27]. Figure 5.7 shows the monotonically decreasing wavefunction fidelity resulting from the α-angles and θ-angles

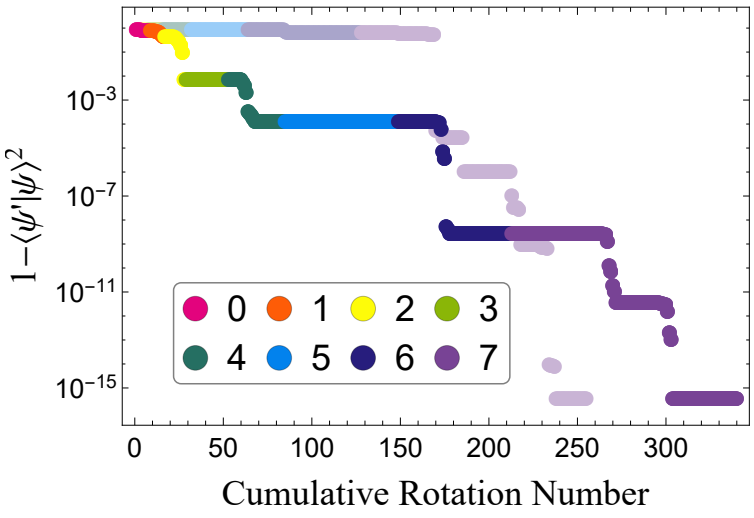

Figure 5.7: Fidelity of the prepared ground state wavefunction as a function of the h-organized α-angle (dark) and θ-angle (light) truncation value for a lattice scalar theory with $\hat{m} = 0.3$, $N = 4$, $n_Q = 2$, and $\phi_{\max} = 3.5$. Controlled rotation angles $\alpha_{\ell h,k}$ are set equal to zero when their magnitude is below the truncation value. Points are colored according to, h, the number of controls on the associated operator for the rotation angle at the truncation boundary.

ordered first by control distance and then by magnitude. That is to say that the $\alpha_{\ell h,k}$ and $\theta_{h,k}$ with h-values above and magnitudes below a given truncation value are set equal to zero. We observe that, modulo the notable step-like structure, the α-circuit allows the wavefunction to be systematically improved by incorporating circuit elements in an order dictated by the locality and magnitude of their associated rotations. Therefore, we can limit the number of α-angles by defining a hardware connectivity and a threshold below which the angle is set equal to zero, and there is a direct, but structured, relation between the truncation value in spatial separation and the fidelity of the prepared wavefunction. Shown in lighter shades of color in Fig. 5.7, this feature is not present in the θ-angles, where substantial improvement in the fidelity is not achieved until the maximally delocalized rotation operators are included.

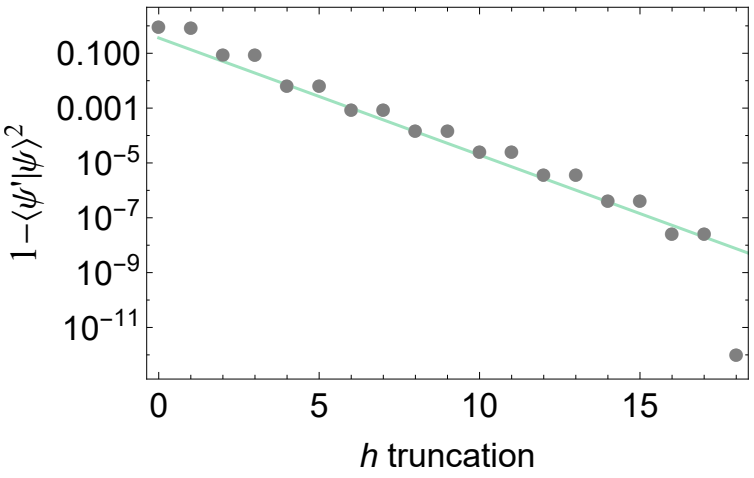

Figure 5.8: Fidelity of the prepared ground state wavefunction as a function of the control distance truncation for a lattice scalar theory with $\hat{m} = 0.3$, $N = 10$, $n_Q = 2$, and $\phi_{\max} = 3.5$. The green line corresponds to a fit with the form $Ze^{-\eta(h_{\text{trunc}}+1)}$ with $Z = 0.97(10)$ and $\eta = 0.98(2)$ of the even h_{trunc} calculations between $h_{\text{trunc}} = 4, 14$.

For limited connectivity and number of operators, the α-circuit is capable of initializing wavefunctions with fidelity improved by multiple orders of magnitude.

Figure 5.8 shows the fidelity of the prepared wavefunction as a function of control distance truncation, h_{trunc}. A step-like behavior is observed, which is related to the number of qubits defining the field at a single lattice site, n_Q. For these parameters ($N = 10, n_Q = 2, \hat{m} = 0.3, \phi_{\max} = 3.5$), the results show exponential convergence of the wavefunction such that a high fidelity wavefunction can be prepared even with limited spatial connectivity of quantum hardware.

The reorganization of the quantum circuit used to prepare a general ground state of a lattice scalar field theory, from the θ- to the α-parameterization, allows for truncations in the number of controls or the number of rotation operations, or both, with a pattern that follows $\mathbf{K}$ and the inverse two-point correlation function. These truncations can be removed to systematically improve the fidelity of the wavefunction prepared in the quantum

register. These attributes make α-angle quantum circuits preferable for initializing quantum simulations of scalar field theories.

Our free-field calculations have been performed on relatively small systems, with only a modest number of (classically-simulated) qubits. As a result, field-digitization, lattice artifacts and finite-volume effects are expected to be significant. Figure 4.2 shows the size of finite-volume effects and the separations required for the inverse two-point function to approach its asymptotic behavior, which occurs at distances larger than the volumes we have considered in the extraction of the α-angles. A fit to the mass associated with the exponential fall off of the control sensitivity in the angles furnishes a mass that differs from than the lightest mass in the spectrum. As the discrepancy decreases with increasing input scalar mass, it is expected to be attributed to finite-volume effects. However, more thorough investigations utilizing significantly larger classical computational resources are required to firmly establish this to be the case.

5.6 Interacting $\lambda\phi^4$ Scalar Field Theory

The localization method explored in previous sections using non-interacting lattice scalar field theories can be implemented for interacting field theories, such as $\lambda\phi^4$. While closed form analytic derivations are generally unavailable for interacting field theories, the applicability of the circuit localization can be demonstrated numerically.

There are a number of available paths forward. The Hamiltonian for the continuum-field lattice theory can be diagonalized with the necessary imposition of momentum mode truncations, Λ_k, building upon the lowest energy basis state written as a tensor product of harmonic oscillator ground states. The non-diagonal Hamiltonian matrix elements are then computed from the interaction term, $\lambda\phi^4$. The ground state wave function, after transforming back into position space, would then be sampled on the qubit digitized lattice sites following the method employed above to analyze the non-interacting scalar field theory. However, for this demonstration it was found to be sufficient to work directly in the digitized space. The lattice Hamiltonian operator in Eq.(2.8) is supplemented with an interaction term of the

form,

$$\hat{\mathcal{H}}_{\rm int} \;=\; \frac{\lambda}{4!}\sum_{\mathbf{j}}\hat{\phi}^4(\mathbf{j}) \quad , \tag{5.32}$$

and matrix elements of the full Hamiltonian are computed in the eigen basis of the $\hat{\phi}$ operator, given in Eq. (5.13). As discussed previously [24, 102, 86, 45], the $\hat{\Pi}$ operator can be replaced with a discrete operator in the digitized space of each lattice site without introducing polynomial-scaling digitization errors, as presented in Appendix E of Ref. [45], with either periodic or twisted boundary conditions in field space. The Hamiltonian matrix for systems up to nine spatial sites was diagonalized using Mathematica's intrinsic functions and also a Lanczos algorithm on a classical computer in the sector containing the ground state and the sector containing a single-particle excitation (at rest). The initial vectors (interpolating operators) used to start the Lanczos iteration corresponded to one with equal amplitudes (the ground-state sector), and to one with an application of $\sum_{\mathbf{j}}\hat{\phi}(\mathbf{j})$ to the ground-state initial vector.

For demonstration, the α-angles are shown in Fig. 5.9 as a function of control distance for both free field theory and interacting field theory, and with a heavier mass than considered earlier. We choose $N = 8$, $m = 1.6$, $\phi_{\rm max} = 1.7$ and $n_Q = 2$, with $\phi_{\rm max} = 1.3$ and $\lambda = 32$ in the interacting theory, after tuning (as discussed in Ref. [45]) using an $n_Q = 3$ system on a smaller lattice. The single-site projected wavefunctions are well localized within the chosen $\phi_{\rm max}$ field truncations. The results are shown in Fig. 5.9. In the free field theory, a fit to the asymptotic form $\alpha_{\rm max}(\hat{r}) \sim c_1 e^{-M_\alpha \hat{r}}/\hat{r}^{3/2}$ gives $M_\alpha = 1.53(3)$ to be compared with the mass extracted from the truncated $\mathbf{K}$ matrix of $M_{\mathbf{K}} = 1.55(1)$, two-point function of $M_{\rm 2pt} = 1.3(1)$ and inverse 2-pt function of $M_G = 1.51(1)$. The parenthetical errors express only statistical uncertainties associated with the fit. We attribute the statistically significant differences between these masses and the input mass to finite lattice spacing and finite volume effects. In the interacting theory, we find $M_\alpha = 1.86(2)$ compared with $M_{\rm 2pt} = 1.82(1)$ and inverse 2-pt function of $M_G = 1.86(1)$. It is interesting to note that the mass of the scalar from the Hamiltonian is $M_\phi = 2.22$. This both indicates the presence of

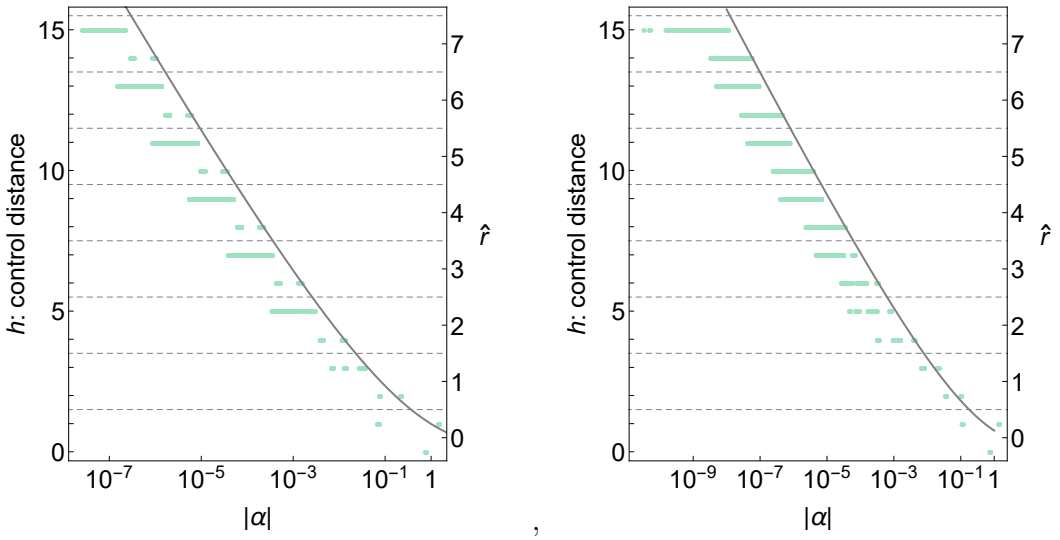

Figure 5.9: α-angles as a function of control distance, h. The left panel shows the results (green points) from free field theory with $N = 8$, $m = 1.6$, $\phi_{\max} = 1.7$ and $n_Q = 2$, while the right panel shows those from interacting $\lambda\phi^4$ field theory with the same parameters as the free results except for $\phi_{\max} = 1.3$ and with $\lambda = 32$. The grey curve corresponds to fits of the form $c_1 e^{-M_\alpha \hat{r}}/\hat{r}^{3/2}$ to the maximum α angle for each h.

finite volume and digitization effects as well as supports the relation between the suppression of alpha angles and the correlation functions as discussed for the free field above. Due to significant digitization errors for $n_Q = 2$, the results of the calculations are sensitive to the value chosen for $\phi_{\max}$. This sensitivity is expected (as seen in the tuning procedures of Ref. [45]) and will exponentially decrease with increasing n_Q once $\phi_{\max}$ is larger than the range of fields over which the ground state wave function has support. In both sectors, the classical computations (Mathematica) converge rapidly to the lowest-lying states, and the limitation in the size of the classical computation is imposed by the dimensionality of the underlying Hilbert space. By performing calculations of systems with $N = 4 - 8$ lattice sites, the ground state energy density and single particle mass are seen to have converged to better than one percent of their infinite-volume values (which are determined by exponential

extrapolation forms). Finite-volume systematic errors in these quantities are expected to be dictated by M_ϕ, and to scale with $\sim e^{-M_\phi N}$, along with multiplicative polynomial terms, for large lattice extents. The θ-angles and α-angles are extracted from the resulting ground-state wave function using the methods described previously. After exploring the scaling with lighter masses, it is found that the results becomes less stable and more sensitive to the choice of $\phi_{\max}$, though exponential suppression is retained with m_α values deviating from the scaling of correlation functions. As the α-angles are suppressed by spatial distance and finite volume effects are reduced at the expense of lattice spacing artifacts with heavy masses, it is not surprising that the heavy mass regime captures more closely the asymptotic structure of α-angle suppression. The α-angles make explicit an exponential hierarchy in control operators resulting from the structure of the ground-state wave function. Numerically determining the angles at large control distances requires precision in the classical determination of the wave function at the corresponding control level. For near term quantum computations that are relatively low precision, only a modest number of control distances will be required, along with comparable precision in the classical computation of the α-angles and their truncation.

The results presented in this section demonstrate a hierarchically localized quantum circuit preparing the ground state of an interacting field theory on a quantum register of qubits. As with the circuit preparing a non-interacting theory, the α-angles decrease exponentially as a function of increasing control distance, enabling an exponentially-precise preparation for a given control distance. The calculations we have performed are demonstrative only. Preparing for simulations of scalar field theory at-scale using a quantum computer would require more substantial classical calculations using a quantum simulator capable of assigning up to $\gtrsim 30$ qubits (depending on the mass) to accomplish the required parameter tuning, and the determinations of the α-angles necessary to prepare the ground state within pre-specified tolerances.

5.7 Summary and Conclusions

Preparing the initial state of a quantum many-body system or a quantum field theory on a quantum computer is an essential and challenging part of quantum simulations. To allow the subsequent processes of time evolution and measurement to be implemented straightforwardly, it is important that the initial state is prepared at high fidelity with respect to the target wavefunction. For scalar field theory, correlations fall exponentially with the mass of the particle as a function of space-like separation. The mutual information, expressing the quantum and classical correlations between subsystems (bound and distillable entanglement), falls exponentially with twice the mass of the particle as a function of space-like separation. Strikingly, the entanglement measure of negativity (distillable entanglement) is found to be completely localized to the region over which the operators in the Hamiltonian are distributed. These three features suggest that quantum circuits describing latticized scalar field theory can be constructed with entangling operations of limited spatial extent set by the mass of the particle. We have found one such quantum circuit design employing controlled rotation angles whose magnitudes falls exponentially with spatial separation—consistent with the behavior of correlation functions. This design permits truncations in the control distance and/or the α-angles at the cost of introducing a quantifiable degradation in the wavefunction fidelity. While the design of the α-circuit marks important progress in connecting quantum circuit design to correlations in the underlying physical system, it is natural to suspect that an even more efficient quantum circuit may be possible with rotation angles that scale with twice the particle mass (or even faster) reflecting measures of the underlying entanglement.

Our results have qualitatively shown that circuit operations can be localized over a length scale that is consistent with the lightest mass excitation in the spectrum (mass of the scalar particle), consistent with the behavior of ground-state correlation functions. However, the demonstrated systems in both the free theory and interacting theory have substantial finite-volume effects (systematic errors), depending upon the mass of the scalar, and significant

digitization errors for two qubits per lattice site. The latter errors, and the dependence on simulation parameters, such as the maximum value of the scalar field at each site, are found to be substantially reduced when using three or more qubits per site. It is encouraging that the exponential suppression of α-angles, and thus localization of the quantum circuit, is found to be robust in the presence of these systematic errors. While our method holds significant promise in preparing the ground state of massive, interacting field theories, the results presented in this paper are not sufficient to inform a quantum simulation of the continuum theory with fully-quantified uncertainties [212]. Much larger scale classical simulations, are required with more qubits per site and more lattice sites, in order to calculate localized α-angles for a latticized scalar field with controlled systematic errors to be used in a simulation on a quantum computer. We anticipate that accomplishing these classical simulations will require (co-)developing software that can utilize heterogeneous capability pre-exascale or exascale supercomputers.

Pseudo-scalar fields play central roles in nuclear physics, with pions providing the long-range component of the nuclear forces. In classical numerical simulations of effective field theories describing low-energy systems of nucleons and hyperons, dynamical pion fields remain a challenge to include at scale. The new algorithm that we have presented here is relevant for efficiently preparing pion fields on a digital quantum computer. Our results are anticipated to have applicability beyond one-dimensional lattice scalar field theory—aiding in circuit design for any system exhibiting a mass gap or many-body systems with significantly localized spatial correlations, including QCD and the standard model.

Chapter 6

FIXED-POINT CIRCUITRY IN THE BULK

The content of this chapter is associated with Ref. [28]:
Natalie Klco and Martin J. Savage. "Fixed-Point Quantum Circuits for Quantum Field Theories" (Feb. 2020). arXiv: 2002.02018 [quant-ph]

Renormalization group ideas and effective operators are used to efficiently determine localized unitaries for preparing the ground states of non-interacting scalar field theories on digital quantum devices. With these methods, classically computed ground states in a small spatial volume can be used to determine operators for preparing the ground state in a beyond-classical quantum register, even for interacting scalar field theories. Due to the exponential decay of correlation functions and the double exponential suppression of digitization artifacts, the derived quantum circuits are expected to be relevant already for near-term quantum devices.

6.1 Introduction

Quantum field theories (QFTs) describing the properties and dynamics of fundamental particles and quantum many-body systems are anticipated to be addressed with analog quantum simulation and digital quantum computation [7, 25, 24, 62, 63, 213]. In addition to being essential to scientific applications in nuclear physics, high-energy physics and basic energy sciences, the distributed quantum degrees of freedom of QFTs provide a framework underlying the design of large-scale quantum simulators and fault tolerant quantum computers. Numerical evaluations of QFTs typically involve discretizing spacetime into a lattice of points on which matter fields are defined, with gauge fields defined on the links between grid points. Physical predictions can be derived from such calculations by extrapolating to the limit of

infinite spatial or spacetime volume and the continuum limit where the distance between grid points vanishes. This can be accomplished by computing in sufficiently large volumes with sufficiently fine discretizations, then extrapolating using known forms.

Preparing the ground state of a QFT Hamiltonian on digital quantum computers is challenging and has been identified as a leading contribution in estimates of the quantum resources required to simulate scattering in scalar field theory [184, 24, 25, 63]. When spatially digitizing the scalar field, the efficiency of the quantum Fourier transform performed on each site can lead to a protection, through the Nyquist-Shannon sampling theorem, from induced systematic errors depending polynomially on the field digitization spacing [24, 25, 102, 86, 88, 45].

Preparing an arbitrary real function with support across the Hilbert space of a quantum register requires an exponentially large number of entangling gates. In the special case of a Gaussian profile, where the wave packet expands retaining its shape under time evolution, *Somma Inflation* can be used to transform a Gaussian with support localized in the Hilbert space to a Gaussian with support distributed throughout the Hilbert space without an exponential increase in the number of entangling gates [102]. While individual Gaussians are a start, the scalar field ground state correlates Gaussians on each spatial site determined by the gradient operator. Thus, introducing the spatial gradient operator creates entanglement among spatial sites, significantly increasing the number of entangling gates that are required to prepare the ground state [45, 134, 26, 27]. As previously shown, the number of required unitary operators for ground state preparation scales linearly with the spatial volume in massive QFTs due to the exponential localization of classical correlations and entanglement [27]. It was found that the rotation angles defining the unitary transformations become exponentially suppressed as the operators they define becomes increasingly non-local.

In this work, the properties of the ground states of non-interacting scalar field theories and the symmetries of the corresponding quantum circuits are exploited to derive spatially localized effective operators for initializing large instances of ground-state wavefunctions, defining

analytic "fixed points" of the localizable quantum circuits. The systematic errors associated with these effective operators are shown to be exponentially suppressed. In analogy with effective operators used in effective field theories induced or renormalized by removing degrees of freedom, these effective operators are determined by integrating (tracing) over contributions from fields on lattice sites that are not involved in the controlled operations used to entangle the state on a given lattice site. The unitary transformations associated with these effective operators rapidly evolve toward fixed points as the number of sites integrated out becomes large. The implication is that relatively small systems with dimensions determined by the correlation length, and solved with classical computing resources, can be used to determine the controlled unitary rotation operations required to prepare ground states on a quantum computer capable of simulating a larger quantum field than classically possible. This is also true for interacting scalar field theories.

6.2 Initial Observations at $n_Q = 1$

For a basic proof of concept of the presence of fixed points to the angles defining the quantum circuits for state preparation, we begin by considering the scalar field digitized onto only a single qubit per site. Providing only sign information about the field value at each site, this digitization is far too coarse to capture properties of the simulated field with meaningful accuracy. However, with a single qubit per site, the manifestation of localization can already be seen in the structure of the quantum circuit as the lattice is extended. While the two point correlation with this coarse digitization flattens, the $\mathbf{K}$ matrix (with which the localizable α-angles scale) remains exponentially suppressed at long distances.

Due to the asymmetric structure of the θ-circuit (entangling new qubits always at the end of a one-dimensional qubit register), the correlations of the field are also embedded asymmetrically. This allows a decomposition of the $\hat{\Gamma}$ sampling operator of Eq. (5.14) with "left" nearest neighbor correlations contributing to the θ-angles at each level. For example, with $N = 4$ and $n_Q = 1$ and simplifying to the first band truncation of the correlation

matrix,

$$\mathbb{K} = \begin{pmatrix} K_{00} & K_{01} & 0 & 0 \\ K_{01} & K_{11} & K_{12} & 0 \\ 0 & K_{12} & K_{22} & K_{23} \\ 0 & 0 & K_{23} & K_{33} \end{pmatrix} \quad , \tag{6.1}$$

the $\hat{\Gamma}$ operator can be decomposed into site-local contributions as,

$$\hat{\Gamma} = \hat{\Gamma}_0\hat{\Gamma}_1\hat{\Gamma}_2\hat{\Gamma}_3 \tag{6.2}$$

$$= e^{-\frac{1}{2}K_{00}\hat{\phi}_0^2}e^{-\frac{1}{2}(K_{11}\hat{\phi}_1^2+2K_{01}\hat{\phi}_0\hat{\phi}_1)}e^{-\frac{1}{2}(K_{22}\hat{\phi}_2^2+2K_{12}\hat{\phi}_1\hat{\phi}_2)}e^{-\frac{1}{2}(K_{33}\hat{\phi}_3+2K_{23}\hat{\phi}_2\hat{\phi}_3)} \quad . \tag{6.3}$$

Taking the evaluations of each of these operators in the computational basis leads to the digitized ground state wavefunction

$$\begin{aligned} |\psi\rangle &= \hat{\Gamma}H^{\otimes 4}|0\rangle^{\otimes 4} \\ &= \gamma_0^0\gamma_{00}^1\gamma_{00}^2\gamma_{00}^3|0000\rangle + \gamma_0^0\gamma_{00}^1\gamma_{00}^2\gamma_{01}^3|0001\rangle + \gamma_0^0\gamma_{00}^1\gamma_{01}^2\gamma_{10}^3|0010\rangle + \gamma_0^0\gamma_{00}^1\gamma_{01}^2\gamma_{11}^3|0011\rangle \\ &+ \gamma_0^0\gamma_{01}^1\gamma_{10}^2\gamma_{00}^3|0100\rangle + \gamma_0^0\gamma_{01}^1\gamma_{10}^2\gamma_{01}^3|0101\rangle + \gamma_0^0\gamma_{01}^1\gamma_{11}^2\gamma_{10}^3|0110\rangle + \gamma_0^0\gamma_{01}^1\gamma_{11}^2\gamma_{11}^3|0011\rangle \\ &\cdots \end{aligned} \tag{6.4}$$

where

$$\gamma_{i,j}^k = \langle ij|\hat{\Gamma}_k|ij\rangle \quad . \tag{6.5}$$

Note that the distribution of these gamma evaluations exactly mimic the distribution of sine and cosine functions of theta angles. Conveniently, these gammas isolate the individual θ-angles at each level so that no recursive or level-ordered calculation of the thetas is needed. This is due to the high degree of constraint coming from the fact that $\gamma_x^j = \gamma_{\bar{x}}^j$, where x is some binary string and $\bar{x}$ is that binary string with each bit flipped. As will always be the case for a symmetric wavefunction, the first angle is calculated to be $\pi/4$,

$$\tan\theta_0 = \frac{\gamma_1^0}{\gamma_0^0} = \frac{e^{-\frac{1}{2}K_{00}\phi_1^2}}{e^{-\frac{1}{2}K_{00}\phi_0^2}} = \tan\frac{\pi}{4} \quad . \tag{6.6}$$

Given that the field values in the computational basis are independent of the site, the notation used for the eigenvalues will drop the site label ($\hat{\phi}_n|k\rangle = \phi_k$. For $n_Q = 1$, there are only two

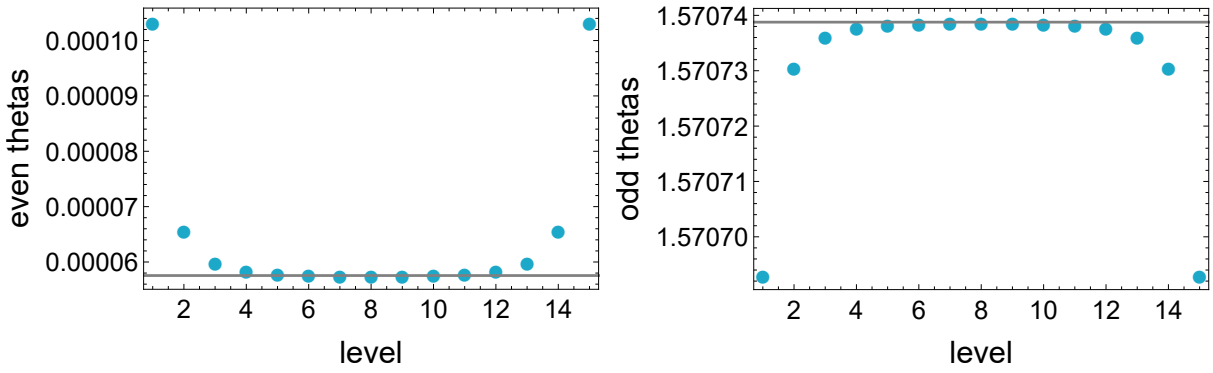

Figure 6.1: Rotation angles (θ-angles) converging by level to the value calculated from the bulk $\mathbf{K}$ matrix. Note that the odd θ-angles are significantly larger than the even θ-angles. By wavefunction symmetry, the sum of these two angles is expected to be $\pi/2$.

field values $\{\phi_0, \phi_1\} = \{-\phi_{\max}, \phi_{\max}\}$). It can be seen from the state above that the n_Q state truncation makes only two non-trivial θ-angles per level beyond the 0^{th}-level (alternating for a length of 2^ℓ),

$$\tan\theta_{\ell\ \text{even}} = \frac{\gamma^\ell_{01}}{\gamma^\ell_{00}} = \frac{e^{-\frac{1}{2}(K_{\ell\ell}\phi_1^2 + 2K_{\ell-1,\ell}\phi_0\phi_1)}}{e^{-\frac{1}{2}(K_{\ell\ell}\phi_0^2 + 2K_{\ell-1,\ell}\phi_0\phi_0)}} \qquad \tan\theta_{\ell\ \text{odd}} = \frac{\gamma^\ell_{11}}{\gamma^\ell_{10}} = \frac{e^{-\frac{1}{2}(K_{\ell\ell}\phi_1^2 + 2K_{\ell-1,\ell}\phi_1\phi_1)}}{e^{-\frac{1}{2}(K_{\ell\ell}\phi_0^2 + 2K_{\ell-1,\ell}\phi_0\phi_1)}} \quad . \tag{6.7}$$

Just as the diagonal and off-diagonal matrix elements of $\mathbf{K}$ each converge to a single value in the bulk, the θ-angles also converge. As the $\mathbf{K}$ matrix can be calculated much larger than the associated wavefunction can be calculated, stored, and decomposed into angles, these asymptotic angles offer a robust initialization mechanism in spite of missing the volume artefacts at the boundaries.

For example, with $m = 0.3$ and $\phi_{\max} = 3.5$, the 50-site correlation matrix is calculated to have bulk $\mathbf{K}$ values of $K_{00} = 1.327331669$ and $K_{01} = -0.398482253$. Figure 6.1 shows the even and odd θ-angles in each level converging to the angles calculated with these bulk $\mathbf{K}$ values. For this simplified system, constructing an approximate ground state using only the bulk $\mathbf{K}$ values produces a ground state approximation with 10^{-9} fidelity even for small lattices.

Taking this simplified system further, consider now a circuit redesigned for systematic localization (the α-circuit). At the level of $h = 0$, the α-angle, $\alpha_{\ell 0}$ is simply the average of the theta angles in the level. As all levels contain an even number of θ-angles alternating between two values, all angles $\alpha_{\ell 0}$ are the same, independent of $\ell > 0$

$$\alpha_{\ell 0} = \frac{\theta_{\ell \text{ even}} + \theta_{\ell \text{ odd}}}{2} \qquad \ell > 0 \quad . \tag{6.8}$$

In the bulk, this becomes

$$\alpha_{\ell 0}^{\text{bulk}} = \frac{1}{2}\left(\arctan \frac{e^{-\frac{1}{2}(K_{00}^{\text{bulk}}\phi_1^2 + 2K_{01}^{\text{bulk}}\phi_0\phi_1)}}{e^{-\frac{1}{2}(K_{00}^{\text{bulk}}\phi_0^2 + 2K_{01}^{\text{bulk}}\phi_0\phi_0)}} + \arctan \frac{e^{-\frac{1}{2}(K_{00}^{\text{bulk}}\phi_1^2 + 2K_{01}^{\text{bulk}}\phi_1\phi_1)}}{e^{-\frac{1}{2}(K_{00}^{\text{bulk}}\phi_0^2 + 2K_{01}^{\text{bulk}}\phi_0\phi_1)}}\right) \tag{6.9}$$

For a symmetric wavefunction, the θ angles $\theta_{\ell k}$ and $\theta_{ell\ 2^\ell - k - 1}$ sum to $\pi/2$, leading to the conclusion

$$\alpha_{\ell 0}^{\text{bulk}} = \frac{1}{2}\frac{\pi}{2} = \frac{\pi}{4} \quad . \tag{6.10}$$

Now, for distance $h = 1$ operators in the systematic localization, the transformations are

$$\alpha_{\ell 1,0}^{\text{bulk}} = \frac{1}{2^{\ell-1}} \sum_{n=0}^{2^{\ell-1}-1} \theta_{\ell,2n} - \alpha_{\ell 0} = \theta_{\ell,\text{even}} - \frac{\pi}{4} \tag{6.11}$$

$$\alpha_{\ell 1,1}^{\text{bulk}} = \frac{1}{2^{\ell-1}} \sum_{n=0}^{2^{\ell-1}-1} \theta_{\ell,2n+1} - \alpha_{\ell 0} = \theta_{\ell,\text{odd}} - \frac{\pi}{4} \quad . \tag{6.12}$$

At the next distance, $h = 2$, the theta summations now sum every fourth θ-angle. Still divided by the total number of angles in the summation, the new sum remains $\theta_{\ell \text{ even}}$ or $\theta_{\ell \text{ odd}}$. Subtracting off now the $\alpha_{\ell 0}$ rotation and the relevant $\alpha_{\ell 1,k}$ contribution, one finds that

$$\alpha_{\ell 2,k}^{\text{bulk}} = 0 \quad . \tag{6.13}$$

As levels increase, the initial theta sum is always the even or odd theta value. Subtracting from this the previous relevant α-angles (those acting in the same controlled sub-Hilbert space), it can easily be seen that the bulk values of all higher alpha angles are zero

$$\alpha_{\ell h,k}^{\text{bulk}} = 0 \qquad \text{for h} \geq 2 \tag{6.14}$$

With the θ-angles, all levels contain half of each $\theta_{\ell \text{ even}}$ and $\theta_{\ell \text{ odd}}$. While it may be appropriate to truncate one of these angles (them being inverse arctangent arguments of each other), there are at least $2^{\ell-1}$ angles at each level whose bulk values are non-zero. However, translating to the alpha circuit, the bulk angles with h values greater than or equal to 2 are exactly zero. This vanishing of α-angles comes from the distance-2 truncation in matrix elements of the **K** matrix, naturally decaying exponentially. Thus, from the numerical observation on the θ-angles above, fidelities of 10^{-9} can be achieved on these $n_Q = 1$ ground state wavefunctions with only $h = 1$ operators. All contributions from more extended operators $h \geq 2$ are boundary effects that vanish in the bulk or infinite volume.

Focusing further to increase the digitized representation of the field, n_Q, similar convergence in the bulk rotation angles is found. In general, the θ-angles on the last qubit in the site at the center of an odd-site lattice are calculated with the following equation structure

$$\theta = \arctan \sqrt{\frac{\sum_{\phi_{i>\lfloor \frac{N}{2} \rfloor}} \psi^2 \left(\phi_{\lfloor \frac{N}{2} \rfloor} = x \right)}{\sum_{\phi_{i>\lfloor \frac{N}{2} \rfloor}} \psi^2 \left(\phi_{\lfloor \frac{N}{2} \rfloor} = x + \delta_\phi \right)}} \quad . \tag{6.15}$$

To generalize this expression to other θ-angles in the site, the evaluation ratio on the site is expanded beyond δ_ϕ and to generalize to other sites, the summations are taken to be all sites "below" the site of interest. Define three variables: the active site x, the number of qubits back within the site b, and the partitioned field values φ_k^a, φ_k^u of the active site and its upper nearest neighbor ϕ_a, ϕ_u.

$$x = \left\lfloor \frac{\ell}{n_Q} \right\rfloor \qquad b = (n_Q - 1) - \ell \bmod n_Q \tag{6.16}$$

$$\varphi_k^a = \phi_{\max} - 2^{b+1} \delta_\phi (k \bmod 2^{n_Q - b - 1}) \qquad \varphi_k^u = \phi_{\max} - \delta_\phi \left(\left\lfloor \frac{kk}{2^{n_Q - b - 1}} \right\rfloor \bmod 2^{n_Q} \right) \tag{6.17}$$

$$\theta_{\ell k}^x = \arctan \sqrt{\frac{\sum\limits_{\phi_{i>x}} \sum\limits_{j=0}^{2^b - 1} \psi^2 \left(\phi_u = \varphi_k^u, \phi_a = \varphi_k^a - \delta_\phi 2^b - j\delta_\phi \right)}{\sum\limits_{\phi_{i>x}} \sum\limits_{j=0}^{2^b - 1} \psi^2 \left(\phi_u = \varphi_k^u, \phi_a = \varphi_k^a - j\delta_\phi \right)}} \tag{6.18}$$

First focus on the determination of θ_{5i} in a translationally invariant system with open boundary conditions truncated at K_{01} to be concrete

$$\theta_{5(x)} = \arctan \sqrt{\frac{\sum\limits_{\phi_3,\phi_4} \psi^2\left(\phi_2 = x\right)}{\sum\limits_{\phi_3,\phi_4} \psi^2\left(\phi_2 = x + \delta_\phi\right)}} \quad . \tag{6.19}$$

The terms in the wavefunction evaluations associated with the sites above may be moved outside of the sums and canceled in the ratio. The terms associated with the sites below the site of interest can be broken into the neighboring site and all others

$$\theta_{5(x)} = \arctan \sqrt{\frac{1}{e^{-\left(K_{00}(2x\delta_\phi+\delta_\phi^2)+2K_{01}\phi_1\delta_\phi\right)}} \frac{\sum\limits_{\phi_3} e^{-\left(K_{00}\phi_3^2+2K_{01}x\phi_3\right)} \left(\sum\limits_{\phi_4} e^{-\left(K_{00}\phi_4^2+2K_{01}\phi_3\phi_4\right)}\right)}{\sum\limits_{\phi_3} e^{-\left(K_{00}\phi_3^2+2K_{01}(x+\delta_\phi)\phi_3\right)} \left(\sum\limits_{\phi_4} e^{-\left(K_{00}\phi_4^2+2K_{01}\phi_3\phi_4\right)}\right)}} \quad . \tag{6.20}$$

No information of the sites above are present beyond the nearest neighbor (site 1) in the multiplicative factor. At $n_Q = 2$, there are 4 choices of ϕ_1 values and 2 choices of x for the site-2 ratios (ϕ_0 and ϕ_2 so $x = 0, 2$). Using this expression to calculate $\theta_{5,0}$ by setting $x = \frac{3\delta_\phi}{2}$ and $\phi_1 = \frac{3\delta_\phi}{2}$, one finds the exact same result as the calculated θ-angles to machine precision (as must be the case)

$$\theta_{50} = 1.504405583287704 \quad .$$

To shift back one site and calculate θ_{30}, all that changes in this expression is the number of sites integrated in the nested sum. Now there are two sites below the site of interest and its lower nearest neighbor

$$\theta_{3x} = \arctan \sqrt{\frac{1}{e^{-\left(K_{00}(2x\delta_\phi+\delta_\phi^2)+2K_{01}\phi_0\delta_\phi\right)}} \frac{\sum\limits_{\phi_2} e^{-\left(K_{00}\phi_2^2+2K_{01}x\phi_2\right)} \left(\sum\limits_{\phi_3,\phi_4} e^{-\left(K_{00}\phi_3^2+2K_{01}\phi_2\phi_3+K_{00}\phi_4^2+2K_{01}\phi_3\phi_4\right)}\right)}{\sum\limits_{\phi_2} e^{-\left(K_{00}\phi_2^2+2K_{01}(x+\delta_\phi)\phi_2\right)} \left(\sum\limits_{\phi_3,\phi_4} e^{-\left(K_{00}\phi_3^2+2K_{01}\phi_2\phi_3+K_{00}\phi_4^2+2K_{01}\phi_3\phi_4\right)}\right)}} \quad . \tag{6.21}$$

Using this expression, the theta value $\theta_{3,0}$ is calculated in agreement to machine precision as

$$\theta_{30} = 1.5044050315494097 \quad .$$

This differs from θ_{50} (the associated theta on the next site) at the 10^{-7} level. The only difference in the calculation is the number of sites integrated over to form the "bulk weight distribution" separated with parenthesis appearing in both the numerator and denominator of the wavefunction ratio. These are interesting quantities to look at. For a single site contributing to the distribution, as a function of the free site value (the lower-neighbor to the site of interest), the bulk weight distributions have values

$$\mathcal{B}_{\phi_4}(\phi_3) = \left(\sum_{\phi_4} e^{-\left(K_{00}\phi_4^2 + 2K_{01}\phi_3\phi_4\right)} \right) \tag{6.22}$$

$$= \{4.88114, 0.568028, 0.568028, 4.88114\} \tag{6.23}$$

$$\mathcal{B}_{\phi_3\phi_4}(\phi_2) = \left(\sum_{\phi_3,\phi_4} e^{-\left(K_{00}\phi_3^2 + 2K_{01}\phi_2\phi_3 + K_{00}\phi_4^2 + 2K_{01}\phi_3\phi_4\right)} \right) \tag{6.24}$$

$$= \{2.7834, 0.322669, 0.322669, 2.7834\} \tag{6.25}$$

It is their nearly stable ratio that is responsible for the bulk stability of the theta angles

$$\frac{\mathcal{B}_{\phi_4}(\phi_3)}{\mathcal{B}_{\phi_3\phi_4}(\phi_2)} = \{1.75366, 1.76041, 1.76041, 1.75366\} \tag{6.26}$$

Understanding these distributions is necessary to truly localize the θ-angle calculations. If they go to constant ratios for all values of the lower-neighbor in the infinite volume limit, they can be canceled in the ratio and the theta expressions above become local.

If this is correct, the θ-angles at sites above center are equivalent (up to modifications of the $\mathbf{K}$ matrix) to θ-angles that would be calculated in the center of larger lattices (until the calculation becomes affected by the boundary, which occurs only at levels 0 and 1 for a K_{01} truncation). This also explains the convergence at higher levels, ℓ, as seen for example in the α-angles shown in Table 6.1

If the fields are taken to be continuous with no maximum truncation and an infinite spatial volume ($n_Q \to \infty$, $\phi_{\max} \to \infty$, and $N \to \infty$), then the bulk weight distribution is the

ℓ	h	k	α	index
3	3	0	-0.039440135431	11
5	3	0	-0.039440135431	4
7	3	0	-0.039440135430	169
9	3	0	-0.039440134978	680
11	3	0	-0.039439983175	2727
13	3	0	-0.039388895903	10918
15	3	0	-0.013951554730	43685

Table 6.1:

partial gaussian integral

$$\mathcal{B}^{\infty}(\phi_x) = \int_{-\infty}^{\infty} \exp\left[\begin{pmatrix} \phi_x & \phi_{x+1} & \cdots \end{pmatrix} \begin{pmatrix} 0 & K_{01} & 0 & \cdots \\ K_{01} & K_{00} & K_{01} & \ddots \\ 0 & K_{01} & K_{00} & \ddots \\ \vdots & \ddots & \ddots & \ddots \end{pmatrix} \begin{pmatrix} \phi_x \\ \phi_{x+1} \\ \vdots \end{pmatrix} \right] \quad . \tag{6.27}$$

While there are many incarnations of the Poisson resummation formula, the fundamental understanding is that summing a smooth function of a real variable at integer points is the same as summing its Fourier transform at integer points. The delta-function relation behind the poisson resummation formula making this statement more concrete is

$$\sum_{n=-\infty}^{\infty} \delta(x-n) = \sum_{n=-\infty}^{\infty} e^{2\pi i n x} \quad . \tag{6.28}$$

The field digitization described in Chapter 3 is $\phi_n = \frac{2n+1}{2}\delta_\phi$ for $n = \{-2^{n_Q-1}, \cdots, 0, \cdots, 2^{n_Q-1}-1\}$. Generalizing the bulk distribution with one integrated site as the lower neighbor to the active site ϕ_ℓ and the site below ϕ_b,

$$\mathcal{B}_1(\phi_\ell) = \sum_{\phi_b} e^{-\left(K_{00}\phi_b^2 + 2K_{01}\phi_\ell\phi_b\right)} = \sum_{n=-2^{n_Q-1}}^{2^{n_Q-1}-1} e^{-\left(K_{00}\left(\frac{2n+1}{2}\delta_\phi\right)^2 + 2K_{01}\phi_\ell\frac{2n+1}{2}\delta_\phi\right)} \tag{6.29}$$

$$\mathcal{B}_1^{\infty}(\phi_\ell) = \int \mathrm{d}\phi_b \; e^{-\left(K_{00}\left(\frac{2\phi_b+1}{2}\delta_\phi\right)^2 + 2K_{01}\phi_\ell\frac{2\phi_b+1}{2}\delta_\phi\right)} \left(\sum_{n=-\infty}^{\infty} \delta(\phi_b - n)\right) \tag{6.30}$$

$$= \int \mathrm{d}\phi_b \; e^{-\left(K_{00}\left(\frac{2\phi_b+1}{2}\delta_\phi\right)^2 + 2K_{01}\phi_\ell\frac{2\phi_b+1}{2}\delta_\phi\right)} \left(\sum_{n=-\infty}^{\infty} e^{2\pi i n\phi_b}\right) \tag{6.31}$$

$$= \int \mathrm{d}\phi_b \; e^{-\left(K_{00}\left(\frac{2\phi_b+1}{2}\delta_\phi\right)^2 + 2K_{01}\phi_\ell\frac{2\phi_b+1}{2}\delta_\phi\right)} + \int \mathrm{d}\phi_b \; e^{-\left(K_{00}\left(\frac{2\phi_b+1}{2}\delta_\phi\right)^2 + 2K_{01}\phi_\ell\frac{2\phi_b+1}{2}\delta_\phi\right)} \left(\sum_{n>0} 2\cos\left(2\pi n\phi_b\right)\right) \tag{6.32}$$

where in the second line the $\phi_{\max} \to \infty$ limit has been taken at fixed δ_ϕ. Each of these contributing terms:

$$\int \mathrm{d}\phi_b \; e^{-\left(K_{00}\left(\frac{2\phi_b+1}{2}\delta_\phi\right)^2 + 2K_{01}\phi_\ell\frac{2\phi_b+1}{2}\delta_\phi\right)} = \sqrt{\frac{\pi}{K_{00}\delta_\phi^2}} e^{\frac{K_{01}^2\phi_a^2}{K_{00}}} \tag{6.33}$$

This expression is independent of the details you choose to digitize the field ($n\delta_\phi$ or $\frac{2n+1}{2}\delta_\phi$). For the second,

$$\int \mathrm{d}x \; e^{-ax^2+bx+c}\cos dx = \frac{1}{2}\sqrt{\frac{\pi}{a}} e^{\frac{(b-id)^2}{4a}+c}\left(1 + e^{i\frac{bd}{a}}\right) = \sqrt{\frac{\pi}{a}} e^{\frac{b^2-d^2}{4a}+c}\cos\left(\frac{bd}{2a}\right) \tag{6.34}$$

Mapping the integral to this form

$$a = K_{00}\delta_\phi^2 \qquad b = -K_{00}\delta_\phi^2 - 2K_{01}\phi_\ell\delta_\phi \qquad c = -\frac{K_{00}\delta_\phi^2}{4} - K_{01}\phi_\ell\delta_\phi \qquad d = 2\pi n \tag{6.35}$$

$$\int \mathrm{d}\phi_b \; e^{-\left(K_{00}\left(\frac{2\phi_b+1}{2}\delta_\phi\right)^2 + 2K_{01}\phi_\ell\frac{2\phi_b+1}{2}\delta_\phi\right)} \left(\sum_{n>0} 2\cos\left(2\pi n\phi_b\right)\right) = 2\sqrt{\frac{\pi}{K_{00}\delta_\phi^2}} \sum_{n>0} e^{-\frac{n^2\pi^2 - K_{01}^2\phi_\ell^2\delta_\phi^2}{K_{00}\delta_\phi^2}} \cos\left(n\pi\left(1 + \frac{2K_{01}\phi_\ell}{K_{00}\delta_\phi}\right)\right) \tag{6.36}$$

To summarize:

$$\mathcal{B}_1^{\infty}(\phi_\ell) = \sqrt{\frac{\pi}{K_{00}\delta_\phi^2}} e^{\frac{K_{01}^2\phi_\ell^2}{K_{00}}} \left[1 + 2\sum_{n>0} e^{-\frac{n^2\pi^2}{K_{00}\delta_\phi^2}} \cos\left(n\pi\left(1 + \frac{2K_{01}\phi_\ell}{K_{00}\delta_\phi}\right)\right)\right] \tag{6.37}$$

$$= \sqrt{\frac{\pi}{K_{00}\delta_\phi^2}} \; e^{\frac{K_{01}^2\phi_\ell^2}{K_{00}}} \; \vartheta\left(3, \frac{\pi}{2}\left(1 + \frac{2K_{01}\phi_\ell}{K_{00}\delta_\phi}\right), e^{-\frac{\pi^2}{K_{00}\delta_\phi^2}}\right) \tag{6.38}$$

Alternatively, with the non-symmetric digitization $\phi_b = n\delta_\phi$,

$$\mathcal{B}_1^\infty(\phi_\ell) = \sqrt{\frac{\pi}{K_{00}\delta_\phi^2}} e^{\frac{K_{01}^2\phi_\ell^2}{K_{00}}} \left[1 + 2\sum_{n>0} e^{-\frac{n^2\pi^2}{K_{00}\delta_\phi^2}} \cos\left(\frac{2\pi n K_{01}\phi_\ell}{K_{00}\delta_\phi}\right)\right] \tag{6.39}$$

$$= \sqrt{\frac{\pi}{K_{00}\delta_\phi^2}}\, e^{\frac{K_{01}^2\phi_\ell^2}{K_{00}}}\, \vartheta\left(3, \frac{\pi K_{01}\phi_\ell}{K_{00}\delta_\phi}, e^{-\frac{\pi^2}{K_{00}\delta_\phi^2}}\right) \quad . \tag{6.40}$$

as

$$2\sum_{n>0} e^{-an^2}\cos bn = -1 + \vartheta\left(3, \frac{b}{2}, e^{-a}\right) \tag{6.41}$$

where ϑ is the elliptic theta function. If $\phi_{\max}$ is truly (or effectively) infinite, this expression should exactly reproduce the thetas.

6.3 Scalar Field Ground State

Working in the basis of eigenstates of the field operator $\hat{\phi}$ [24, 25], the position-space, digitized wavefunction of a scalar field ground state mapped onto a quantum register, $|\Omega\rangle$ is,

$$|\Omega\rangle = \sum_{\boldsymbol{\phi}} \psi(\boldsymbol{\phi})|\boldsymbol{\phi}\rangle \ , \ \psi(\boldsymbol{\phi}) \propto e^{-\frac{1}{2}\boldsymbol{\phi}^T\boldsymbol{K}\boldsymbol{\phi}} \ , \tag{6.42}$$

where the sum over $\boldsymbol{\phi}$ extends over the values of the field at each site for every spatial site. This state can be prepared from the fiducial state operationally with a non-unitary operator $\hat{\Gamma}$

$$\hat{\Gamma} = e^{-\frac{1}{2}\hat{\boldsymbol{\phi}}^T\mathbf{K}\hat{\boldsymbol{\phi}}} \quad , \quad |\Omega\rangle \propto \hat{\Gamma} H^{\otimes N}|0\rangle^{\otimes N} \quad . \tag{6.43}$$

The wavefunction is sampled at regular intervals, δ_ϕ, between field truncations $\pm\phi_{\max}$ on each site of an N-site lattice with n_Q qubits per site [25, 24, 45]. Being constructed from the field operators $\hat{\phi}_x|\phi_x\rangle = \phi_x|\phi_x\rangle$ at the site x, $\hat{\Gamma}$ can be considered to be an operator with wavefunction amplitudes along the diagonal in an infinite dimensional Hilbert space. An alternate identification of $\hat{\Gamma}$ satisfying the preparation requirement of Eq. (6.43) is the density matrix of the digitized ground state. Both perspectives will be useful in the identification of effective operators for the fixed-point circuit elements.

The symmetric matrix of site-wise correlations $\mathbf{K}$ is exponentially localized to the diagonal with the form e^{-mr}/r, the two-site mutual information falls, up to power law components, as e^{-2mr} with separation, and the negativity is localized at the ultraviolet length scale of the finite-difference momentum operator used to calculate $\mathbf{K}$ [141, 142, 27]. In explicit connection between the quantum circuitry necessary to prepare wavefunctions and their intrinsic correlations, it has been shown that the circuit operations to prepare the ground state of a massive scalar field can be localized [27]. This localization is controlled by the structure of $\mathbf{K}$. If the $\mathbf{K}$ matrix of correlations for a periodic lattice is truncated to be a band-diagonal matrix with vanishing K_{0i} for $i > d$, then quantum circuit elements can be made to depend only on the state of neighboring sites to a maximum distance d. This feature of the circuit prevails in spite of the non-zero mutual information extending beyond this radius. For clarity, in what follows the $\mathbf{K}$ truncation will be taken to be $d = 1$ unless otherwise noted and thus represent the largest contributions in the correlation hierarchy.

6.4 Quantum Circuitry

By defining the structure of a quantum circuit, an implicit definition is made of the symmetries and wavefunction features that are naturally created upon implementation. Ideally, designed quantum circuits have structures that parallel those of the theory being simulated. This allows, for example, decaying correlation functions to manifest as a hierarchy of operators with distance in the qubit register. In the following, the circuit presented in Ref. [27] is first reviewed. Having established physical properties of the field embedded in this structure, the discussion will then extend to determining fixed-point circuit parameters for ground state preparations larger than could be explicitly represented on classical devices.

Operators used in the localizable circuits can be defined by three numbers: two indices and an angle, as shown at the right of Fig. 6.2. The angle defines the rotation operator about the y-axis that acts on the target qubit. The two indices ℓ and k, define the target qubit index and the binary-interpreted integer value of the controls. Thus, declaring an angle of the form $\theta_{\ell,k}$ is equivalent to declaring a rotation operator along with its location

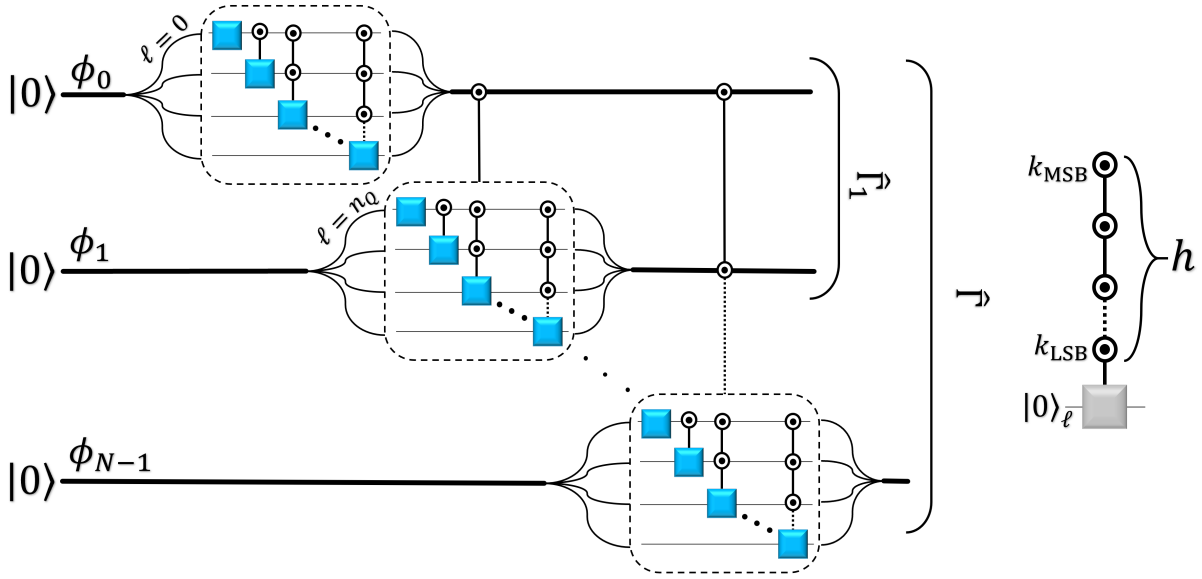

Figure 6.2: (color online) Quantum circuit for preparing an arbitrary real wavefunction. The open-closed controls indicate a set of operators controlled on each of the possible 2^h binary strings, k, with the most significant bit at the top. The blue squares indicate a corresponding set of R_y rotations with unique angles $\theta_{\ell,k}$.

and control values on previous qubits. The θ-circuit shown in Fig. 6.2 contains each of the 2^ℓ controlled operators with differing values of k acting on each qubit, ordered by ℓ from smallest to largest. Operators with equal ℓ and differing k commute.

Linear combinations of these θ-angles produce α-angles that are localized according to the two-point correlation function, and thus the exponentially decaying $\mathbf{K}$ [27]. These are denoted as $\alpha^{x,r}_{\ell h,k}$. The lower(upper) indices describe the associated controlled rotation at the level of qubits(sites). There is a many-to-one relationship between the qubit- and site-indices, respectively. For the qubit indices, ℓ and k remain as defined for the θ-angles. The additional index h is the "height" or number of controls. For the θ circuit, all operators are defined to have $h = \ell$. This equivalence between the operator height and its distance from the top of the qubit register is lifted for the α circuit in order to allow systematic localization of the operators and the relation becomes $k_{\max} = 2^h - 1$. For the site

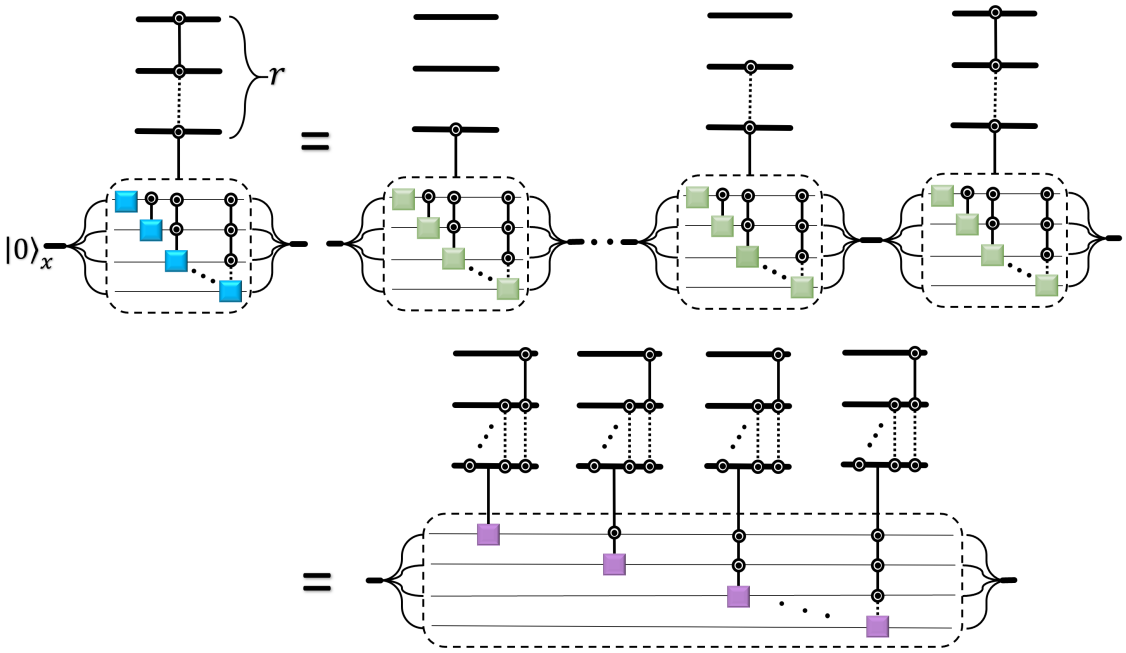

Figure 6.3: (color online) Site-wise expansion of angles $\theta_{\ell,k}$, appearing in rotation operators represented as blue squares, into angles $\alpha_{\ell h,k}$ appearing in rotation operators represented by purple squares. Diagonal continuation dots represent the inclusion of controlled operators with every intermediate number of controls.

indices, x is the site number at which the rotation acts and r is the site distance spanned by the operator. These indices are connected by $x = \lfloor \ell/n_Q \rfloor$ and $r = \lfloor h/n_Q \rfloor$, where $\lfloor y \rfloor$ denotes the floor of y.

The site-wise α-transformations are defined by expanding a θ-operator extending over multiple sites defined by angles $\vec{\theta}_\ell^x$ into rotations over a truncated number of sites with $h = \{\ell - (x-1)\, n_Q, \cdots, \ell - n_Q, \ell\}$ respectively being at physical distances $r = \{1, \cdots, x\}$. This process is shown diagrammatically in Fig. 6.3. At the left is a site-rotation controlled on the field at the r previous sites. It is desirable to isolate the sensitivity to controls at small spatial distance if the target wavefunction has localized correlations. This is shown diagrammatically with the green circuit at the right of Fig. 6.3 where site rotations controlled

at short distances are extracted from those controlled at long distances. A locality truncation removes circuit elements beginning at the right end of this circuit. In the second line of this diagram, the purple circuit has grouped operators acting on a particular qubit. Due to non-commutativity of rotations and controls, these angles are distinct from those of the previous expansion. It is the angles of the latter, purple circuit $\alpha^{x,r}_{\ell h,k}$ that are naturally related to the $\theta_{\ell,k}$ on the left through simple linear combinations and averaging [27]. The α angles for such decompositions with $\mathbf{K}$ truncated at $d = 1$ are equivalent to the θ-angles at distances 1, and vanishing for operators of greater spatial extent

$$\alpha^{x,r}_{\ell h,k} = \begin{cases} \theta^{x}_{\ell,k} & r = 1 \\ 0 & r > 1 \end{cases} . \tag{6.44}$$

This supports the statement that the α-angles are controlled by the $\mathbf{K}$ matrix, exponentially suppressed in spatial locality controlled by the mass of the lightest particle.

The nature of these quantum circuits used to prepare the digitized ground state is such that adding qubits to increase the density of states between the upper and lower values of the field at each site changes the number and values of the angles associated with the unitary operations. The additional field samples with each added qubit are interleaved with those at the previous field digitization, leading to a direct connection between the last qubit in each site and the high conjugate momentum modes. With increasing n_Q, angles associated with the last qubit in each site tend towards a constant value of $\pi/4$, the angle for which additional samples are simply copies of their lower-digitization-scale predecessors. This is a natural phenomena associated with the wavefunction being smooth or defined by an upper-bounded Fourier space. In the circuit language, if n_Q is taken to be large, the $\theta_{jn_Q-1,k}$-angles tend to $\pi/4$ for all integer $j \in \{1, ..., N\}$ and $k \in \{0, ..., 2^{jn_Q-1} - 1\}$. In the translation to localizable α-angles shown in Fig. 6.3, these long-distance controlled operators tend towards a single-qubit operator $R_y(\pi/4)$ on the last qubit. The α-angles thus demonstrate a localization not only in spatial distance from exponentially-decaying spatial correlation functions, but also within the sites due to the hierarchy of conjugate momentum

modes. In contrast, operators acting on early qubits in the digitization (associated with the low conjugate momentum modes) yield rotation angles that tend to a fixed, non-constant distribution as a function of the field values on controlled sites above. Given the expectation that small values of $n_Q \leq 5$ will be sufficient for foreseeable calculations of the scalar field on quantum hardware, the following will be focused on fixed n_Q, where angles defining local operators evolve to fixed points as the number of spatial sites in the lattice becomes large. Thus, for preparing lattices containing many correlation lengths, the number of unique local operators becomes independent of the lattice volume.

6.5 Fixed Point Circuit

For the particular case of the θ-circuit (see Fig. 6.2) where the state is prepared with asymmetric operations, the rotations on each site are dependent on the site register above the site on which the rotation acts. The associated θ-angles can be calculated from the ratio of sums of squared amplitudes in the wavefunction, marginalizing over the field on lower sites. Continuing with the $\mathbf{K}$ truncation at $d = 1$, the θ-angles are

$$\theta^x_{\ell,k} = \arctan \sqrt{\frac{\sum_{j=0}^{2^b-1} \langle \psi_{\rm n} | \hat{\Gamma}^{2,\rm eff}_x | \psi_{\rm n} \rangle}{\sum_{j=0}^{2^b-1} \langle \psi_{\rm d} | \hat{\Gamma}^{2,\rm eff}_x | \psi_{\rm d} \rangle}} \quad . \tag{6.45}$$

The states in the numerator and denominator are

$$\begin{aligned} |\psi_n\rangle &= \left|\phi\left(\kappa^{\phi_{x-1}}\right), \phi\left(2^{b+1}\kappa^{\phi_x} + 2^b + j\right)\right\rangle \\ |\psi_d\rangle &= \left|\phi\left(\kappa^{\phi_{x-1}}\right), \phi\left(2^{b+1}\kappa^{\phi_x} + j\right)\right\rangle \quad , \end{aligned} \tag{6.46}$$

where $\phi(\kappa^{\phi_x}) \equiv \phi(x; \kappa^{\phi_x})$ denotes the field value at digitization address κ^{ϕ_x} at site x

$$\phi\left(\kappa^{\phi_x}\right) = \phi_{\max} - \delta_\phi \kappa^{\phi_x} \quad . \tag{6.47}$$

The site index and inner-site qubit index are

$$x = \left\lfloor \frac{\ell}{n_Q} \right\rfloor \ , \ b = (n_Q - 1) - \ell \bmod n_Q \quad , \tag{6.48}$$

where the latter describes the location of the rotation within the site x by the number of qubits back it acts from the last qubit in the site. This is equal to the number of qubits within the site, but below the rotation, that need be additionally marginalized from the calculation. The index k has been interpreted in binary and grouped for its localization at each site of the scalar field

$$k = \{\kappa^{\phi_0}, \kappa^{\phi_1}, \cdots, \kappa^{\phi_{x-1}}\}_2 \quad . \tag{6.49}$$

The site-wise κ^{ϕ_n} index takes values in the range $\{0, ..., 2^{n_Q} - 1\}$ [1]. The effective operator, $\hat{\Gamma}^{2,\text{eff}}_x$, relevant for calculating θ at site x is a marginalization of $\hat{\Gamma}^2$ over the field values of all sites beneath the rotation location x,

$$\hat{\Gamma}^{2,\text{eff}}_x = \text{Tr}_{\boldsymbol{\phi}_>}\left[\hat{\Gamma}^2\right] \qquad \boldsymbol{\phi}_> = \{\phi_{x+1}, \phi_{x+2}, \cdots, \phi_{N-1}\} \quad . \tag{6.51}$$

Note that the reduced $\hat{\Gamma}^{2,\text{eff}}_x$ operator marginalizes in the probabilities, not the amplitudes. This is a manifestation of the use of y-axis rotations in the circuit construction, producing trigonometric functions of the rotation angles in the wavefunction amplitudes. Sums over squares of these amplitudes then sequentially remove qubits from the end of the register. In terms of the qubit reduced density matrix, the angles are defined by ratios of the diagonal matrix elements

$$\theta_{\ell,k} = \arctan\sqrt{\frac{\langle 2k+1|\hat{\rho}_\ell|2k+1\rangle}{\langle 2k|\hat{\rho}_\ell|2k\rangle}} \quad , \tag{6.52}$$

with $\hat{\rho}_\ell$ the ground state reduced density matrix of the first $\ell + 1$ qubits

$$\hat{\rho}_\ell = \text{Tr}_{q>\ell}\left[\hat{\rho}\right] \quad . \tag{6.53}$$

By marginalizing at the qubit level (rather than at the site level as done in Eq. (6.45)), the sums in the numerator and denominator over the 2^b values of the field at higher digitization

---

[1] As an example, for $n_Q = 2$, $x = 2$, and $k = 6$,

$$k = 6 = 0110 = \{1, 2\}_2 \quad , \tag{6.50}$$

such that $\kappa^{\phi_0} = 1$ and $\kappa^{\phi_1} = 2$. Thus, the control of $k = 6$ is associated with the scalar field on sites 0 and 1 of $\phi_0 = \phi_{\max} - \delta_\phi$ and $\phi_1 = \phi_{\max} - 2\delta_\phi$.

frequency in the site x are handled in the trace reduction of the density matrix. For the current application of initializing the ground state, the operator definition in Eq. (6.43) is more efficient for the construction of local effective operators.

If the qubit registers in the lower region of the circuit are taken to be continuous fields without field truncation,

$$\begin{aligned}\hat{\Gamma}_x^{2,\text{eff}} &\to \int_{\boldsymbol{\phi}_>} \hat{\Gamma}^2 \\ &\propto e^{-\hat{\boldsymbol{\phi}}_{\leq}^T \mathbf{K}_{x+1} \hat{\boldsymbol{\phi}}_{\leq} + K_{01}^2 \frac{\det \mathbf{K}_{\bar{x}-1}}{\det \mathbf{K}_{\bar{x}}} \hat{\phi}_x^2}\end{aligned} \quad , \tag{6.54}$$

where $\mathbf{K}_n$ is the first $n \times n$ sub-block in $\mathbf{K}$ and $\bar{x} = N - (x+1)$ is the number of sites below site x (the number of sites in $\phi_>$). Note that for the calculation of θ-angles with $\mathbf{K}$ truncation at $d = 1$, the field values above $\hat{\phi}_{x-1}$ may be ignored as they cancel in the ratio in Eq. (6.45). In this scenario, the effective operator reduces to a local operator

$$\hat{\Gamma}_x^{2,\text{eff}} \propto e^{-K_{00}\hat{\phi}_{x-1}^2 - 2K_{01}\hat{\phi}_{x-1}\hat{\phi}_x} e^{-\left(K_{00} - K_{01}^2 \frac{\det \mathbf{K}_{\bar{x}-1}}{\det \mathbf{K}_{\bar{x}}}\right)\hat{\phi}_x^2} \ . \tag{6.55}$$

This operator captures the effective $\mathbf{K}$ matrix of correlations relevant for the unitaries acting at site x, integrating out degrees of freedom in a manner resembling the renormalization group. With $d > 1$, the effective operator remains exponentially localized with the structure of $\mathbf{K}$. The ratio of determinants tends to a constant at large lattice sizes ($N \to \infty$), and can be expressed for continuous $\bar{x}$ fields as,

$$\frac{\det \mathbf{K}_{\bar{x}-1}}{\det \mathbf{K}_{\bar{x}}} = \frac{2}{K_{00} + \eta\left(1 + \frac{2}{-1 + (K_{00}-\eta)^{-\bar{x}}(K_{00}+\eta)^{\bar{x}}}\right)}, \tag{6.56}$$

$$\xrightarrow[\bar{x}\to\infty]{} \frac{2}{K_{00}\left(1 + \sqrt{1 - \frac{4K_{01}^2}{K_{00}^2}}\right)} \ , \tag{6.57}$$

with $\eta = \sqrt{K_{00}^2 - 4K_{01}^2}$. At large volumes, these two elements of the correlation matrix are

$$K_{00}^{\infty} = \frac{2\sqrt{4+m^2}}{\pi} \, E\left(\frac{4}{4+m^2}\right) \quad , \tag{6.58}$$

$$K_{01}^{\infty} = \frac{\sqrt{4+m^2}}{3\pi} \left[m^2 K\left(\frac{4}{4+m^2}\right) - (2+m^2) E\left(\frac{4}{4+m^2}\right)\right] \quad , \tag{6.59}$$

where K and E are the complete elliptic integrals of the first and second kind, respectively. Having analytic forms of the asymptotic $\mathbf{K}$ matrix elements and determinant ratio is a convenient but unnecessary feature of the non-interacting scalar field. They are computationally inexpensive and can be easily calculated for large volumes.

The determination of fixed-point circuit elements has occurred in the limit of infinite volume, infinite field truncation $\phi_{\max}$, and continuous quantum registers on marginalized lattice sites of the field. Leading corrections to the above expressions due to the finite extent of the lattice scale as $\mathcal{O}\left(e^{-mN}\right)$ up to polynomial factors scaling approximately as $1/\sqrt{N}$. To quantify the systematic uncertainties associated with assumed continuous quantum registers, consider the distribution upon marginalization of the field at a single lattice site,

$$\mathcal{B}_1(\phi_\ell) = \sum_{\phi_c} e^{-\left(K_{00}\phi_c^2 + 2K_{01}\phi_\ell\phi_c\right)} \quad . \tag{6.60}$$

Utilizing Poisson resummation to relate the ϕ-symmetrized Dirac comb, producing digitized field samples, to a sum over its Fourier modes, deviations are found to be exponentially suppressed,

$$\mathcal{B}_1^\infty(\phi_\ell) = \sqrt{\frac{\pi}{K_{00}\delta_\phi^2}} e^{\frac{K_{01}^2\phi_\ell^2}{K_{00}}} \left[1 + 2\sum_{n>0} e^{-\frac{n^2\pi^2}{K_{00}\delta_\phi^2}} \cos\left(n\pi\left(1 + \frac{2K_{01}\phi_\ell}{K_{00}\delta_\phi}\right)\right)\right] \quad , \tag{6.61}$$

where the term in brackets can written as an elliptic theta function. For fields digitized onto qubits with $\delta_\phi = \frac{2\phi_{\max}}{2^{n_Q}-1}$, the deviations from the continuum scale as $\mathcal{O}\left(e^{-2^{2n_Q}}\right)$, double exponentially in the number of qubits.

This rapid convergence is another manifestation of the Nyquist-Shannon sampling theorem, the effects of which can be seen in Fig. 6.4, where the convergence of a rotation angle in the center of the lattice is shown. The green points have been calculated through representation of the 2^{Nn_Q} dimensional digitized wavefunction for systems of up to 20 qubits. The blue points have had the effective operator replaced by the continuum and untruncated (in $\phi_{\max}$) effective operator of Eq. (6.55). As such, the N dependence of the blue closed points comes from the determinant ratio in Eq. (6.56) and the N dependence of the $\mathbf{K}$ matrix itself. If the infinite volume values of $\mathbf{K}$, as shown in Eqs. (6.58) and (6.59), are used, the open

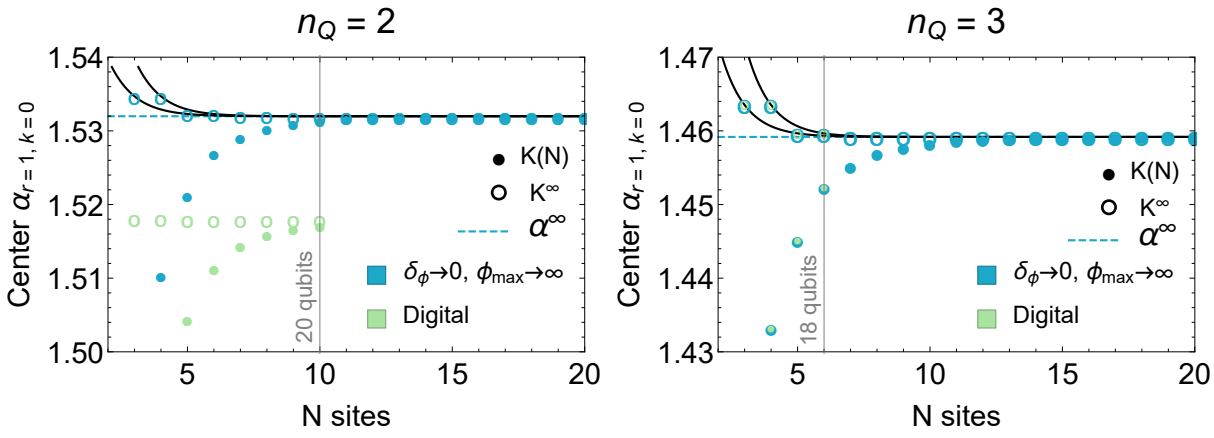

Figure 6.4: Evolution of an angle associated with a localized operator at the center of the lattice, $\alpha\left(x=\left\lfloor\frac{N}{2}\right\rfloor, r=1, \ell=n_Q\left(\left\lfloor\frac{N}{2}\right\rfloor+1\right)-1, h=2n_Q-1, k=0\right)$, with lattice size N. The scalar field is defined by $m=0.3$, truncated in correlations at K_{01}, and truncated for digitization with maximum field value $\phi_{\max}=3.5$. Blue points are the results of calculations approximating sites in the second half of the lattice to be continuous fields without field truncation. Green points are the results of calculations within a digitized and truncated qubit representation. Closed circles indicate the **K** matrix scales with system size, while open circles indicate that the infinite-volume **K** matrix elements are used. The solid black lines show the N dependence of the continuum calculations with infinite-volume **K** matrix elements, while the blue dashed line is the fixed-point α^∞ calculated for continuum sites in the lower half lattice in the limit of infinite volume.

points and black lines are recovered, demonstrating a rapid convergence to the continuum angles. The continuum values, α^{∞}, are shown as blue dashed lines which are calculated by defining the effective operator with Eqs. (6.57), (6.58), and (6.59).

On the left panel of Fig. 6.4, a coarse qubit digitization of $n_Q = 2$ is used on each site. The angle calculated in the continuum without field truncation agrees with that calculated in the digitized space to $\sim 1\%$. Thus, substituting the fixed-point α-angles for the digitized circuit provides sufficiently precise determinations of rotation angles necessary for initializing the ground state on even small instances of near-term quantum devices (where this precision matches that expected on hardware). Due to the double exponential convergence in the number of qubits used to digitize the field, increasing n_Q to 3 qubits (right panel of Fig. 6.4) shows good agreement between the angles defining the continuum and digitized circuits. Differences of angles in small volumes, where wavefunctions can be represented classically, are found to be $\sim 0.001\%$. While increasing n_Q requires additional circuit operations to prepare the ground state (see Fig. 6.3), the number of gates, $\mathcal{O}\left(N 2^{2n_Q}\right)$, grows more slowly than the ability to improve them. The double exponential convergence in digitization artifacts implies that increasing n_Q, and thus the fidelity of the wavefunction, parametrically improves the fidelity-to-gate ratio when using fixed-point circuits to initialize the scalar field ground state.

As the distance truncation, d, of $\mathbf{K}$ is raised, the effective operator relevant for calculating the θ-angles at a particular site becomes less local. The modification to the reduced $\mathbf{K}$ matrix in the effective operator is generally

$$\hat{\Gamma}^{2,\text{eff}} \propto e^{-\phi_{\leq}^{T}\left(A - BC^{-1}B^{T}\right)\phi_{\leq}} \quad , \tag{6.62}$$

with

$$\mathbf{K} = \left(\begin{array}{c|c} A & B \\ \hline B^{T} & C \end{array}\right) \ , \ [A] = (x+1) \times (x+1) \ . \tag{6.63}$$

It can be seen that the correction to the site-site correlations in the effective operator, $BC^{-1}B^{T}$, is non-zero only in the lower subblock of dimension d controlled by the largest non-zero K_{0d} retained in $\mathbf{K}$. This is consistent with the physical intuition that the off-diagonal elements of $\mathbf{K}$ control the site distance of communication throughout the lattice.

This localization to the lower sub-block is also connected to the localization of the effective operator(s) necessary to calculate θ-angles defining the fixed-point circuit.

6.6 Reflections

In this work, fixed-point quantum circuits have been introduced for the preparation of the non-interacting scalar field ground state on digital quantum hardware. Determining the circuit elements necessary to initialize large instances of the quantum field requires classical computational resources scaling only with the spatial distance of correlations. For the massive scalar field, these correlations decay exponentially with distance, leading to the ability to determine fixed point circuits for preparing the ground state on quantum devices for larger lattices than could be stored classically. This technique is also applicable to interacting scalar field theory.

In this work, the continuum limit (decreasing lattice spacing) has not been considered. Taking this limit is required to make predictions for physical observables with a complete quantification of uncertainties. As the lattice spacing is reduced, the number of lattice sites within a correlation volume increases. This scaling is power law with the lattice spacing. The fixed-point analysis that we have presented remains valid, but with an increased number of required α-angles.

While it is conceived that the ground state of an interacting theory can be initialized beginning from the non-interacting ground state adiabatically, there is no barrier to applying these fixed point methods to interacting ground states as well. This provides an alternative state preparation mechanism that avoids additional circuit depth scaling with unpredictable spectral gaps throughout the dynamical adiabatic process. While such applications evade analytic solution, both perturbative corrections to the circuit elements and non-perturbative analyses can be performed. The perturbative approach leverages the analytic control demonstrated here in defining the non-interacting state preparation circuit, though further exploration is necessary to understand the corrections when interactions are strong. Alternatively, it is viable to inform fixed point circuits for interacting ground states

non-perturbatively. Infinite volume limits of circuit elements can be reliably extrapolated from finite volume calculations capturing only the exponentially localized correlation length scale.

Fixed-point quantum circuits are expected to be relevant for initializing the ground states of fields defined by locally-interacting massive particles with exponentially decaying correlation functions or area-law entanglement. It is further anticipated that confining gauge theories will admit fixed-point quantum circuits, suggesting how classical calculations of the QCD vacuum could inform state preparation on beyond-classical quantum devices.

Chapter 7

INITIALIZATION OF A LOCALIZED WAVEFUNCTION ON SUPERCONDUCTING QUBITS

The content of this chapter is associated with Ref. [26]:

Natalie Klco and Martin J. Savage. "Minimally-Entangled State Preparation of Localized Wavefunctions on Quantum Computers". *Phys. Rev. A* 102.1 (2020), p. 012612. DOI: 10.1103/PhysRevA.102.012612. arXiv: 1904.10440 [quant-ph]

Initializing a single site of a lattice scalar field theory into an arbitrary state with support throughout the quantum register requires $\mathcal{O}(2^{n_Q})$ entangling gates on a quantum computer with n_Q qubits per site. It is conceivable that, instead, initializing to functions that are good approximations to states may have utility in reducing the number of required entangling gates. In the case of a single site of a non-interacting scalar field theory, initializing to a symmetric exponential wavefunction requires $n_Q - 1$ entangling gates, the minimal number necessary to create an entangled state of all n_Q qubits. This is compared with the $2^{n_Q-1} + n_Q - 3 + \delta_{n_Q,1}$ required for a symmetric Gaussian wavefunction. In this chapter, demonstrations are explored initializing 1-site ($n_Q = 4$), 2-site ($n_Q = 3$) and 3-site ($n_Q = 3$) non-interacting scalar field theories with symmetric exponential wavefunctions using IBM's quantum simulators and quantum devices (`Poughkeepsie` and `Tokyo`). With the digitizations attainable with $n_Q = 3, 4$, these tensor-product wavefunctions are found to have large overlap with a Gaussian wavefunction, and provide a suitable low-noise initialization for improvement and *Somma Inflation*. In performing these simulations, we have employed a workflow that interleaves calibrations to mitigate systematic errors in production. The calibrations allow tolerance cuts on gate performance including the fidelity of the symmetrizing Hadamard gate, both in vacuum ($|\mathbf{0}\rangle^{\otimes n_Q}$) and in medium ($n_Q - 1$ qubits initialized to an exponential function). The results obtained in this work are relevant to systems beyond scalar

field theories, such as the deuteron radial wavefunction, 2- and 3-dimensional cartesian-space wavefunctions, and non-relativistic multi-nucleon systems built on a localized eigenbasis.

7.1 Introduction

Quantum simulations of quantum field theories in condensed matter, high-energy and nuclear physics hold the potential to address Grand Challenge problems in each of these science domains that cannot be addressed using classical computation. Typical situations where a quantum advantage is expected to be achieved include the real-time dynamics of non-equilibrium multi-particle systems and high-density systems of fermions. Classical calculations of quantities in such systems typically encounter a sign problem in sampling over trajectories in a path integral. Quantum computing offers the potential to work with Hilbert space dimensionalities that are exponentially larger than those accessible with classical computers, and the real-time evolution of quantum wavefunctions in both non-relativistic systems and in quantum field theories. During the last two decades, impressive work has been accomplished in designing algorithms to simulate quantum field theories in the Hamiltonian framework, including scalar field theories, Abelian gauge theories and non-Abelian gauge theories [37, 59, 60, 24, 25, 64, 65, 66, 67, 68, 69, 70, 62, 81, 71, 102, 63, 72, 73, 86, 45, 74, 214, 215, 216, 87, 217, 218, 219, 220], as well as quantum many-body systems [221, 58, 61, 222, 223, 224, 225]. These efforts represent the first critical steps toward quantum simulation of such theories, but significant further efforts are required to realize a quantum simulation of quantum field theories that can be compared with experiment. The rapidly improving control of entanglement over macroscopic volumes of spacetime has enabled first calculations of simple spin-systems, field theories and non-relativistic effective field theories (EFT) to be performed on small trapped-ion systems, cold-atom systems, annealing devices and superconducting quantum devices [75, 76, 77, 78, 30, 79, 134].

This work explores the utility of minimally entangling quantum circuits [1] for preparing

[1] Minimal here refers to the number of entangling gates necessary to at least entangle all qubits in the register. This number is one less than the number of qubits in the register.

localized quantum states that are viable as approximations or starting points for further refinement. The ability to efficiently prepare physically relevant wavefunctions on quantum devices is imperative for the success of quantum simulation. Good progress is being made in understanding how to accomplish effective state preparation in a number of systems [202, 203, 184, 221, 208, 102, 226, 207]. An intriguing proposal is to evolve a narrow Gaussian wavefunction to a broad Gaussian wavefunction through application of polynomially efficient, tuned time evolution operators [102]. This exploits the fact that the two-qubit gate requirements for arbitrary wavefunction preparation scales inefficiently only with the dimension of the Hilbert space where the wavefunction has support. We will refer to this as *Somma Inflation* [102]. For the Gaussian wavefunction, it has been shown that implementation of Somma Inflation on a quantum device requires complexity scaling polynomially with n_Q and $\log \epsilon$ in the large-n_Q limit, consistent with the n_Q^2 cost of the Trotterized time evolution operator [45]. A Gaussian wavefunction prepared on a small subset of the intended qubits may be expanded to the full digitized space of large qubit number with polynomial cost. It is the preparation on this small subset in the NISQ era that is the focus of this work.

In the case of scalar quantum field theory, as for many problems of interest, the wavefunctions of the low-lying states of the non-interacting theory can be constructed from the eigenstates of the harmonic oscillator, the ground state of which is a Gaussian distribution. In working with a scalar field theory discretized on a lattice, described by a spatial grid of points with a real scalar field residing at each grid point, the field at each grid point is represented by a wavefunction distributed across a number of qubits, n_Q. One basis choice is defined by the eigenstates of the field operator at each spatial site and is efficient for Hamiltonian evolution [24]. In this basis, the ground state of the field theory is an entangled state of position-space field wavefunctions. In the study of the ground state or low-lying states of the scalar field theory, the system would ideally be initialized into one of, or a superposition of, these states. The tensor-product state with each spatial site in its ground state, is a (simple) superposition of states that has a significant overlap with the ground state of the field theory and low-lying excitations.

Previously, we built upon the seminal work of Jordan, Lee and Preskill, and subsequent works related to digitizing scalar field theories [102, 86], to understand what might be achievable with NISQ-era quantum devices in the context of the number of qubits required to suppress digitization artifacts below expected quantum noise levels and in the impact of gate fidelity [45]. The digitizations of scalar fields with a small number of qubits per spatial site indicate that the theoretical systematic errors introduced through digitization will not constrain the precision and accuracy of such computations, which instead are expected to be limited by the capabilities of the quantum hardware. We also detailed the qubit interactions and gate operations required to accomplish time-evolution of 1-site and 2-site $\lambda\phi^4$ theory in symmetric localized and delocalized states [45]. The gate operations for time evolving larger lattices can be easily built from these basic elements. In this work, we turn to the issue of state preparation for scalar field theory. At each site of a non-interacting massive scalar field, the field space (ϕ-space) is spanned by the eigenstates of a harmonic oscillator, and the ground state of the d-dimensional quantum field theory is an entangled state of these ϕ-space eigenstates induced by the $(\boldsymbol{\nabla}\phi)^2$ operator. Considering a 1-site system defined with n_Q qubits, initializing an arbitrary state requires $2^{n_Q} - 2$ entangling gates, while a wavefunction with definite reflection symmetry, such as the ground state, requires $2^{n_Q-1} + n_Q - 3 + \delta_{n_Q,1}$ entangling gates. As a symmetric exponential wavefunction requires only $n_Q - 1$ entangling gates to initialize, and can be tuned to have substantial overlap with the desired digitized ground state wavefunction, we suggest that such wavefunctions may provide an efficient means of state preparation for scalar field theory. It is this thesis that we examine more closely within the IBM Q Experience quantum ecosystem [227, 228].

7.2 Quantum Circuits

Due to the translational invariance of the ratio of function evaluations between binary-interpreted neighbors that are spaced equally on a one-dimensional grid, a wavefunction

with positive and real amplitudes distributed as an exponential of the form

$$|\psi\rangle = \frac{1}{\sqrt{\sum_{y=0}^{2^{n_Q}-1} \psi^2(y)}} \sum_{x=0}^{2^{n_Q}-1} \psi(x)|x\rangle \qquad \psi(x) = e^{\alpha x} \tag{7.1}$$

can be prepared on n_Q qubits without entanglement. This can be implemented through a particular choice of angle for each of n_Q qubit rotations about the y-axis,

$$R_y(\theta) = e^{-i\theta\sigma_y} = \begin{pmatrix} \cos\theta & -\sin\theta \\ \sin\theta & \cos\theta \end{pmatrix} \quad . \tag{7.2}$$

The first qubit, representing the nearest-neighbor connectivity on the grid and thus the least significant bit in the binary representation, is rotated by an angle $\theta_0 = \arctan(e^{\alpha})$. Subsequent qubits can be added to copy this ratio structure into the volume-doubled Hilbert space with a rotation on the newest qubit that determines the ratio at the boundary between the two half spaces. Fixing this ratio across the binary-interpreted boundary (between states $|2^{n_Q-1}-1\rangle$ and $|2^{n_Q-1}\rangle$), determines the angles necessary to prepare an exponential function across the amplitudes of a digitally controllable quantum state,

$$\theta_\ell = \arctan\exp\left(2^\ell\alpha\right) \quad . \tag{7.3}$$

If an exact copy (rescaled for normalization) of this exponential is desired, this can be achieved through the addition of a qubit in the $|+\rangle = H|0\rangle$ state (H is a Hadamard gate) as the most significant bit. Once this copy is created, the second half of the Hilbert space can be reversed in its binary interpretation through the implementation of 2-qubit CNOT gates. This procedure creates a wavefunction localized in the center of the binary Hilbert space with exponentially decaying tails, and is summarized in the circuit diagram of Fig. 7.1. Implementing this spatial parity is a simple case of the general reflection operators discussed in Ref. [207]. To antisymmetrize the wavefunction rather than symmetrize, the last introduced qubit should be in the state $|-\rangle$, rather than $|+\rangle$, which can be achieved through the implementation of an $\hat{X}$ Pauli operator before the Hadamard, or a $\hat{Z}$ Pauli operator following the Hadamard, as shown in Fig. 7.1.

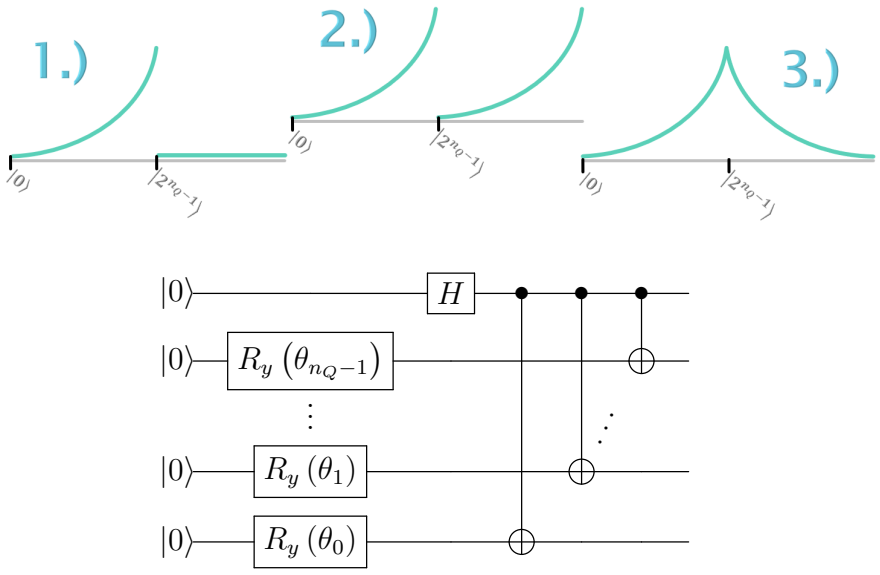

Figure 7.1: Quantum circuit for implementation of the symmetrized exponential wavefunction. The single qubit rotations, with angles defined by Eq. (7.3), prepare an exponential wavefunction on $n_Q - 1$ qubits while the Hadamard and CNOTs are responsible for duplication and subsequent symmetrization. The diagrams above depict the three-step process 1.) Establish an exponentially growing wavefunction in Half the Hilbert space through a single layer of $R_y(\theta)$ rotations 2.) Copy the exponential through a Hadamard on a the qubit most significant in the binary interpretation of the Hilbert Space 3.) Symmetrize through a series of two qubit entangling gates reversing the basis in the second half of the Hilbert space.

As will be emphasized in the following section on Gaussian initialization, the number of CNOT gates required to prepare the localized exponential wavefunction is significantly reduced (growing as $n_Q - 1$, the minimal number necessary to fully entangle the qubit register) with respect to that required to prepare arbitrarily structured localized wavefunctions, which scales as $\mathcal{O}(2^{n_Q})$. This feature makes the preparation of the symmetrized exponential wavefunction amenable to NISQ-era digital quantum devices. In addition to its low CNOT cost, the connectivity required for this implementation is significantly reduced. The qubit associated with the most significant qubit (the last qubit introduced for symmetrization) appears at the control bit for all CNOT gates. This requires one qubit to have connectivity with all other qubits but does not require connectivity amongst the $n_Q - 1$ previous qubits. Then by connectivity, the digitization achievable on the preparation of a localized symmetric exponential on a quantum device is set by the connectivity of the most-connected qubit. For example, on IBM's `Poughkeepsie`(`Tokyo`) device, the most-connected qubits have 6(3) nearest neighbors allowing a localized exponential to be prepared with $n_Q = 7(4)$. In the case that nearest-neighbor connectivity is preferred, a circuit with CNOTs only between neighboring qubits can be designed by doubling the number of CNOT gates in the symmetrization (see Appendix A of Ref. [26] for the explicit circuit translation). With this choice, the connectivity of `Poughkeepsie`(`Tokyo`) allows symmetric exponentials digitized with up to $n_Q = 20(17)$.

Because the scheme of Fig. 7.1 introduces additional samples of the wavefunction at the end of the binary-interpreted register rather than increasing the density between existing samples, the value of α_ℓ is n_Q dependent if increased digitization is desired (i.e., the scale of α is measured against the digitization of the Hilbert space). To increase the digitization of an exponential distribution constant in n_Q, α is scaled by a factor of $1/2$ with each added qubit. This is shown in Fig. 7.2 for a progression from 3 to 5 qubits. In this figure, an ideal quantum device ( see Appendix C of Ref. [26] for details of the resource icons used throughout this work.) is simulated with 1000 samples in the top row. Notice that this choice of rescaling α to increase the digitization of the localized exponential results in an increased number of

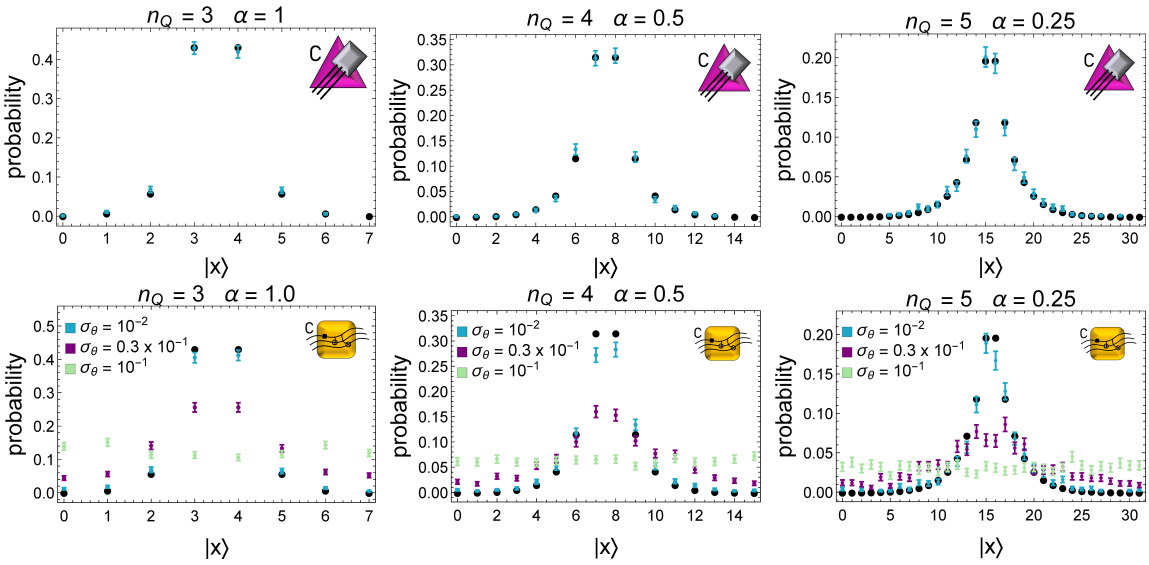

Figure 7.2: Simulations preparing a localized exponential on an ideal quantum device with 1000 samples. The top row demonstrates the functionality of the method on an ideal quantum simulator. The bottom row explores the effects of noisy quantum gates with Gaussian-distributed random errors with standard deviations of σ_θ for single-qubit rotations and $\sigma_{CNOT} = 10\sigma_\theta$ for 2-qubit entangling gates. Details of the resource icons used in figures throughout this work can be found in Appendix C of Ref. [26].

basis states within the wavefunction's region of support and thus a reduction in the signal-to-noise (StN) ratio. The bottom row of Fig. 7.2 shows the same progression with three levels of Gaussian noise on each gate (). As the CNOT errors tend to dominate current error rates, we set $\sigma_{CNOT} = 10\sigma_\theta$. Each single-qubit rotation is surrounded by SU(2) operators with angles sampled from a normal distribution of mean zero and standard deviation σ_θ. For CNOT gates, the control and target are surrounded by SU(2) $\otimes$ SU(2) operators with angles sampled from a normal distribution of mean zero and standard deviation σ_{CNOT}. While formulating a fairly primitive quantum noise model, this shows the sensitivity of the state preparation to the precision of angles achievable in quantum gate implementation.

7.3 Quantum Methods

Our state preparation calculations were performed on IBM's `Tokyo` and `Poughkeepsie` 20-qubit superconducting quantum devices [227] (), on IBM's default `qiskit` noisy quantum simulator [229] () with the noise models from `Tokyo` and `Poughkeepsie`, on `Qiskit`'s default ideal quantum simulator (), and on classical computers (laptops)(). Results obtained using `Poughkeepsie` are presented in this paper only. After developing the quantum logic and circuits using `Mathematica` [230], quantum circuits were compiled within `Qiskit` [229] using python notebooks, and executed through cloud-based access to IBM simulators and quantum devices through the IBM Q Hub at Oak Ridge National Laboratory. For each computation on a quantum device or simulator, 20 qubits were allocated to the process, while only 4, 6, or 9 "active" qubits and classical registers were acted on with gates or measured, depending on the particulars of the computation. For a given problem size, the selection of active qubits was determined by qubit connectivity and the results of the most recent IBM device calibration [227].

Two distinct workflows, *Calibration Production* (W1) and *State Preparation Production* (W2), were used to establish a symmetric exponential wavefunction centered on the midpoint of the Hilbert space. The calibration workflow of W1 involved:

	spatial sites	n_Q qubits per site	active qubit partition	date
	1	4	[5,11,15,**10**]	March 31, 2019
	2	3	[11,15,**10**] [8,14,**9**]	April 2, 2019
	2	3	[15, 17, **16**] [14, 18, **19**]	April 9, 2019
	3	3	[15, 17, **16**] [14, 18, **19**] [1, 3, **2**]	April 9, 2019

Table 7.1: (Color online) The map of active qubits of the `Poughkeepsie` chip employed for the 1-site, 2-site, and 3-site calculations. The bold face qubits denote those with appropriate connectivity to the other qubits in the bracket for the application of symmetrizing entangling gates.

1. **Multi-qubit measurement-error correction**: This was accomplished through an ensemble of measurements of the 2^{N_Q} state probabilities resulting from the quantum register being initialized into each of the possible computational basis states.

2. **Vacuum Hadamard calibration**: A sweep over a limited range of SU(2) y-angles in the neighborhood of $\pi/2$ corresponding to a Hadamard gate on the last qubit with the first $n_Q - 1$ qubits remaining in the $|\mathbf{0}\rangle^{\otimes n_Q - 1}$ state.

3. **In-medium Hadamard calibration**: A sweep over a limited range of SU(2) y-angles in the neighborhood of $\pi/2$ corresponding to a Hadamard gate on the last qubit with the first $n_Q - 1$ qubits transformed to establish an exponential profile on the first $2^{n_Q - 1}$ states in the space.

Analysis of the results obtained with W1, including the shape of the two exponentials created by the Hadamard gate on the last qubit, revealed an optimal, shape-preserving, SU(2) y-angle used in the subsequent W2 workflow. The state preparation workflow of W2 involved:

1. **Duplicate exponentials**: An exponential in the first half of the register was duplicated in the second half using the tuned SU(2) y-rotation (to recover a Hadamard gate)

on the last qubit (as in the Vacuum and In-medium calibration steps in the previous workflow).

2. **State Preparation**: A "reflection symmetric" exponential distribution, centered on the mid-point of the state-space, is produced by acting with $n_Q - 1$ CNOT gates controlled by the last qubit.

3. **CNOT error mitigation circuits**: the state preparation circuits are executed again, except with each CNOT gate replaced by an odd number, r, of such gates. Extrapolations in distributions obtained from these calculations allow for mitigation of the CNOT gate noise.

4. **Reproducibility runs**: The state preparation circuits are repeated multiple times to explore variability in the production, providing an estimate of the systematic error associated with device drift.

Each of the circuits in W1 and W2 are measured with 8000 shots for the single-site implementations.

For each observable in each production run, the number of counts accumulated in each state in the Hilbert space were recorded within the `Qiskit` suite. Standard statistical tools were used to convert the accumulated counts into probability distributions. The multi-qubit measurement-error correction results obtained in W1 are combined to form a $2^{n_Q} \times 2^{n_Q}$ matrix used to mitigate systematic errors inherent to the quantum device, and approximately simulated in the noisy simulator, that modify all other calibration and production measurements in W1 and W2, as described in Appendix B of Ref. [26].

7.4 Hadamard Tuning

The symmetrizing circuit of Fig. 7.1 relies upon the quality of the Hadamard operation and the stability of the control in CNOT operations. This section explores the former of these

sensitivities by scanning the first angle, θ, of the IBM $U_3(\theta, \phi, \lambda)$ operator with $\phi = 0$ and $\lambda = \pi$ (their values for Hadamard implementation). The angle, θ is responsible for modifications to the amplitude beyond phases and theoretically produces the Hadamard operation when $\theta = \pi/2$. For $n_Q = 4$, the action of the Hadamard in vacuum (i.e., implemented directly from the initial state $|0\rangle$) gives the probabilities of measuring states $|0\rangle$ and $|8\rangle$ that are shown as the purple points of Fig. 7.3. The lightly colored, joined (purple) points are the raw data from the device before correcting for measurement errors. It can be seen that the intersection of probabilities for these two states occurs at a probability $\sim 3\%$ lower than expected for the Hadamard operation. This is due to excitations of the other 14 states in the active Hilbert space (or even the other $2^{20} - 2$ states accessible by the `Poughkeepsie` chip) and is found to be well corrected by the measurement-error correction procedure proposed by IBM for their device (see Appendix B of Ref. [26]). The measured data with statistical uncertainties from 8000 shots at each angle and 8000 shots for each of the 16 calibration circuits used in the measurement-error correction are shown in the dark (purple) points of Fig. 7.3. The measurement-error corrected rotation of the $|0\rangle$ state has been fit to its theoretical sinusoidal form, with the a determination of $\cos^2(0.503(7)\theta - 0.03(1))$, in good agreement with the expected θ-dependence though conclusively shifted by fractions of a radian. A compensating shift to the definition of the digital Hadamard gate can be implemented to restore the expected symmetric z-basis superposition property of the gate.

The in-medium Hadamard tuning shown in Fig. 7.3 has the same interpretation as the vacuum measurements. The lightly colored, joined points are the data before measurement-error correction, while the dark points are the measurement-error corrected values with statistical uncertainties resulting from the 8000 samples of each Hadamard as well as each measurement-error correction calibration circuit. The description "in-medium" indicates that the corresponding asymmetry of the Hadamard gate (now observed from states $|7\rangle$ and $|15\rangle$) is probed in a background of the exponential wavefunction preparation—the other three qubits (5, 11, and 15) having been acted upon by the single-qubit rotation gates necessary to prepare the exponential wavefunction (see the circuit in Fig. 7.1). If the device was

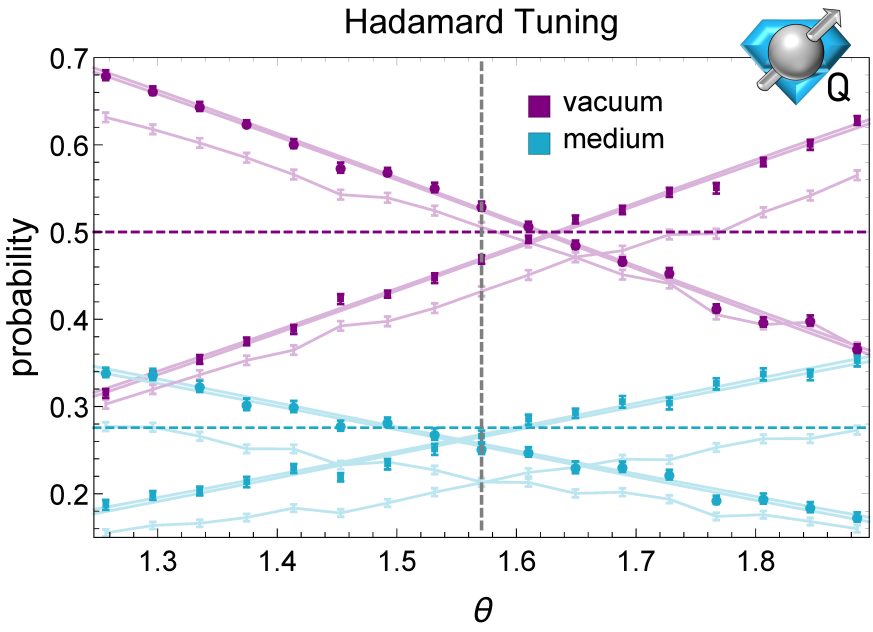

Figure 7.3: (Color online) For vacuum tuning of the Hadamard, probabilities in states $|0\rangle$ and $|8\rangle$ are measured after implementation of IBM's $U_3(\theta, \phi, \lambda) = U_3(\theta, 0, \pi)$ gate. The active qubits were: 5, 11, 15, and 10 of IBM chip `Poughkeepsie`. For in-medium tuning, probabilities in states $|7\rangle$ and $|15\rangle$ are shown after preparation of the half-space exponential and $U_3(\theta, 0, \pi)$ on qubit 10. Horizontal dashed lines indicate theoretical probabilities at which these states cross for the ideal Hadamard. When $\theta = \frac{\pi}{2}$, the gate theoretically implements the Hadamard gate, $U_3(\pi/2, 0, \pi) = H$. The light/dark points correspond to before/after measurement-error correction. Theoretically, this observable is insensitive to tuning ϕ and λ.

an ideal quantum simulator, the tuning procedure for the in-medium Hadamard would be equivalent to that in vacuum. However, due to residual many-body interactions between the qubits, the in-medium measurement requires a different angular shift to instantiate the copied exponential. Constrained by the theoretically calculated in-medium amplitude of 0.55, the input-angle-dependence for the evolution of the $|7\rangle$-state probability with the in-medium Hadamard was determined to be $0.55\ \cos^2(0.49(2)\theta + 0.05(2))$. Again, a shift in

the definition of the Hadamard angle is found, but of opposite sign to that found in vacuum.

The Z-basis probability measurements implemented here are theoretically only sensitive to modifications of the angle θ and insensitive to the phase angles ϕ and λ, while the quantum noise occurring in the device is capable of producing phases and rotations in any direction. Generically, the correction procedure we have used would be insufficient to correct the Hadamard gate; to do so would require more substantial calibrations e.g., gate set tomography [231, 232, 233, 234]. For our purposes in minimal-entanglement state preparation, however, where the current goal is preparation of localized probability distributions regardless of their phase content, it is possible to improve the implementation of the gate as observed in the Z-basis with significantly reduced quantum computational requirements.

With the observations above, it becomes relevant to define a smearing function intended to capture the distribution of quantum states produced when implementing an operator in hardware. We define the effective gate application (EGA) function, f, as the distribution of unitaries effectively implemented in a noisy quantum device

$$U_{\boldsymbol{\theta}}|\psi\rangle = \int \mathrm{d}\boldsymbol{\theta}' \; f\left(\boldsymbol{\theta}, \boldsymbol{\theta}'\right) U_{\boldsymbol{\theta}'}|\psi\rangle \quad . \tag{7.4}$$

For the Hadamard implementation, a 1-parameter family of gate operations is currently considered, but the EGA may be defined to be a higher-dimension distribution in which case $\boldsymbol{\theta}$ becomes a vector of parameters. The EGA may also be state- or medium-dependent as we have seen above. For an ideal quantum device, the EGA is the Dirac delta function. For the purposes of characterizing the U_3 gate in a way relevant to our goals, we calculate the EGA for both the vacuum and in-medium rotations. The data for this calculation can be seen in Appenndix B of Ref. [26]. This figure shows the deviation between the angle implied by the measured ratio of the two quantum states of dominant probability and the input angle to the U_3 gate as a function of the input angle. For the vacuum measurement, the two dominant quantum states are $|0\rangle$ and $|8\rangle$; for the in-medium measurement, the two dominant quantum states are $|7\rangle$ and $|15\rangle$. Before measurement-error correction, the device appears to under rotate by an amount scaling with the input angle. After measurement-error correction, this

angular dependence is removed in both in vacuum and in medium. From the 17 results in vacuum and 56 results in medium, the Gaussian approximations to the EGA functions are found to have the following parameters:

$$\begin{aligned} \mu_{\text{vac}} &= 0.0280(9) & \sigma_{\text{vac}} &= 0.0051(7) \\ \mu_{\text{med}} &= -0.012(1) & \sigma_{\text{med}} &= 0.045(1) \quad . \end{aligned} \tag{7.5}$$

Notice that the measurement in vacuum was found to be shifted from its expected value, but remained fairly stable, while the EGA in medium has only a small shift with a larger distribution over the implemented angles. In the next section, the in-medium Hadamard gate is corrected to prepare a symmetrized exponential. On-line confirmation of this tuning is performed by interspersing calibration measurements in the production workflow to allow for post-processing cuts to be applied.

7.5 Event Structure and Cuts

In this section, preparations of the symmetrized exponential are explored with two distinct agendas. The first agenda seeks to interpret the prepared quantum state to the highest possible accuracy. This will involve extrapolation over multiple preparation parameters to constrain our knowledge of the structure that the quantum state was intended to have. This is the type of procedure that would be desired if the tomography of the final wavefunction contained a desired computational result. However, it is often the case in state preparation that it is not the extrapolated wavefunction that is of interest, but rather the quality of the wavefunction existing in hardware in a single instantiation of the system. This is required for time evolving the created instance to explore the system dynamics. This second agenda does not allow for error extrapolation and instead, we propose to monitor and control its errors dynamically by collecting temporally correlated diagnostic information about a quantum device, parallel to the procedures utilized for the analysis of high-energy particle or nuclear scattering data.

When performing calculations on quantum devices, the 2-qubit gates are often found

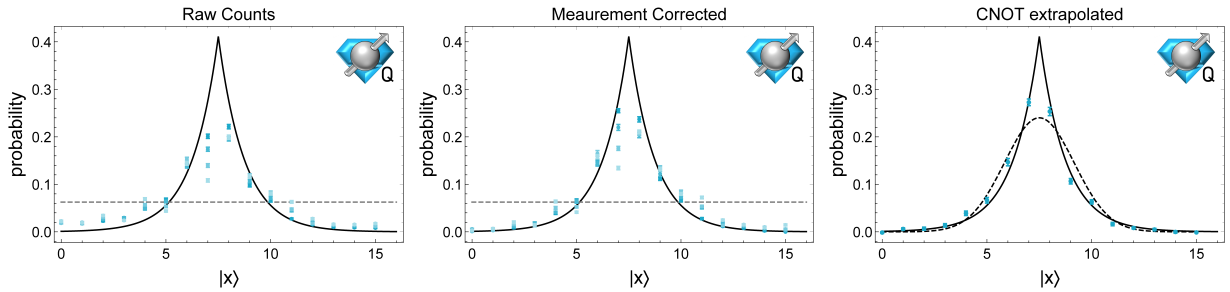

Figure 7.4: Progression of results for the symmetrized exponential wavefunction. The probabilities measured directly from the quantum device (left), the measurement-error corrected probabilities (middle) and the linearly extrapolated probabilities (right) implemented with a Hadamard angle of $\theta = 1.52$ in the $U_3(\theta, 0, \pi)$ gate. In the left two panels, the data points become lighter in color as $r = 1, 3, 5, 7$ with $r = 1$ the darkest of the four measurements. The horizontal dashed line shown at 2^{-4} is the classical saturation level. In addition to the theory curve for the implemented exponential at right, the dashed curve is the theoretically closest Gaussian state when digitized onto four qubits.

to be a dominant source of systematic error and mitigation has been explored through extrapolation of results with a range of exacerbated 2-qubit errors [77, 235, 78, 30, 236]. This approach is demonstrated in Fig. 7.4 where the $\alpha = 0.4$ exponential is prepared in hardware with a Hadamard angle of $\theta = 1.52$. The left panel shows, against the theoretical curve, the results as it is measured off the quantum device with error bars representing only statistical uncertainties. Increasing values of r, the number of CNOTs per CNOT within the circuit of Fig. 7.1, with $r = 1, 3, 5, 7$ become increasingly lighter in color. The introduction of additional CNOT pairs reduces the coherence of the quantum state and tends to move the probabilities towards their classical values depicted by the horizontal dashed line at a probability of 2^{-4}. Recall that the structure of this circuit places all CNOTs in the same direction with the control acting on the most significant qubit in the binary interpretation. If the control of the CNOT operation was truly left invariant with the operation and only

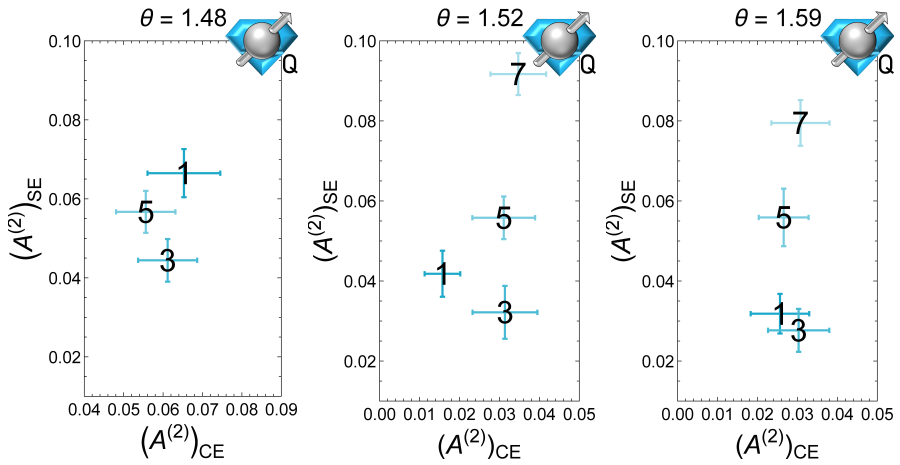

Figure 7.5: Two-norm asymmetry of the localized, symmetrized exponential wavefunction, $A^{(2)}_{SE}$, as a function of the time-correlated calibration asymmetry of the copied exponential, $A^{(2)}_{CE}$. These results are determined from CNOT-extrapolations of calculations at Hadamard θ values in the $U_3(\theta, 0, \pi)$ gate of $\theta = 1.48, 1.52$, and 1.59. The r-value (number of CNOTs per CNOT) is indicated on each point.

consulted for its value, the left half of this curve would be completely stable in the CNOT extrapolation. As seen in the r-dependence of the probabilities in state $|7\rangle$, it is not currently appropriate to assume this stability—the quantum state experiences non-negligible effects in the 0-controlled portion of the Hilbert space. The visual isolation of this feature in the symmetrized exponential state preparation makes this system a useful tool for future hardware diagnostics pertaining to the implementation of controlled operations.

In addition to the non-trivial interaction of the control, the range of CNOT results in Fig. 7.4 indicates that the 2-qubit gates, whose role in this state preparation is to simply reflect the binary interpretation of the second half of the Hilbert space, also twists the wavefunction. This twisting is seen naturally in the peak of Fig. 7.4 where the values in states $|7\rangle$ and $|8\rangle$ trade prominence with increasing r and is quantified in Fig. 7.5. The two-norm asymmetry of the copied exponential, $A^{(2)}_{CE}$ on the x-axis of Fig. 7.5, that is time-

correlated with each of the r-value data sets of Fig. 7.4 shows stability of the in-medium Hadamard. This is equivalent to stability in the implementation of the circuit of Fig. 7.1 with the CNOTs removed. As r is increased, the two-norm asymmetry of the symmetrized exponential, $A^{(2)}_{SE}$, is seen to systematically increase. Thus, the reduction in the symmetry at the peak between states $|7\rangle$ and $|8\rangle$ can be isolated as a result of the increased number of CNOTs and not temporal fluctuations of the in-medium Hadamard. Had any of the calibration implementations of the copied exponential (in-medium Hadamard) yielded $A^{(2)}_{CE}$ values outside the determined regime of acceptable asymmetry, the temporally correlated symmetrized exponential would be cut and only implemented once calibration stability is re-established. The pair of calibration and subsequent implementation of a symmetrized exponential is termed an *event*, and events are accepted or rejected based on the quality of their calibration. In this way, qualities of a quantum state can be monitored and maintained through temporal fluctuations of the device specifications without direct measurement of the calculation wavefunction. After the Hadamard tuning of section 7.4, no events were removed due to this threshold in the 1-site implementation.

In the second panel of Fig. 7.4, the measurement-error correction determined using the technique recommended by IBM has been implemented (see Appendix B of Ref. [26] for details). The uncertainties are larger as they now include the statistical uncertainties in the calibration matrix used in the measurement-error correction inversion, informed by the implementation of 2^4 low-depth circuits. The measurement-error correction can modify the symmetry determined for the localized wavefunction, implying the same for the imperfect measurement. Notice that an important role of the measurement-error correction is to reassign the background of "randomly recorded" measurements that would otherwise obscure the observation of the strongly suppressed tails of a localized wavefunction. In the third panel of Fig. 7.4, a linear extrapolation is performed with the first two r values (1,3) and uncertainties are extrapolated to the probability at $r = 0$. In addition to the intended continuous exponential wavefunction, a Gaussian wavefunction as written in Eqns. (5.6) and (5.7) with standard deviation $\sigma = 0.29$ and $n_Q = 4$ is shown. This is the Gaussian that, when digitized

onto four qubits, has the maximal overlap, $|\langle\psi^g|\psi^e\rangle|^2 = 0.98$, with the Gaussian at $\alpha = 0.4$. The motivation for assessing the state's relation to the Gaussian, as mentioned previously, is in the relevance of this form for the ground state of the scalar field. As can be seen visually,

	$A_{SE}^{(1)}$	$A_{SE}^{(2)}$	$\|\|\psi^2_{\text{hw}} - \psi^2_{\text{exp}}\|\|_1$	$\|\|\psi^2_{\text{hw}} - \psi^2_{\text{Gauss}}\|\|_1$
CNOT extrapolation $\theta = 1.48$	0.14(2)	0.08(1)	0.14(2)	0.21(2)
CNOT extrapolation $\theta = 1.52$	0.10(2)	0.053(9)	0.12(2)	0.21(2)
CNOT extrapolation $\theta = 1.59$	0.08(2)	0.040(7)	0.16(2)	0.18(2)
Calibration Window	0.10(3)	0.06(2)	0.14(3)	0.16(3)

Table 7.2: Properties of the symmetric exponential wavefunction with $\alpha = 0.4$ prepared on IBM's `Poughkeepsie`. The first and second columns quantify the asymmetry of the wavefunction while the third and fourth quantify the distance of the probability distribution measured on hardware, ψ^2_{hw}, from that of the intended exponential, ψ^2_{exp}, and the associated Gaussian distribution with largest wavefunction overlap, ψ^2_{Gauss}, on four qubits.

the state prepared in the quantum device is an approximation to the Gaussian wavefunction. The third and fourth columns of Table 7.2 calculate the one-norm deviation of the measured probability distributions with those associated with the exponential and Gaussian wavefunctons. If one makes the non-trivial assumption that the hardware wavefunction was composed of real, positive amplitudes as intended with the circuit of Fig. 7.1, the norm-squared overlap of the states prepared in hardware to the exponential and Gaussian wavefunctions would be calculated to be $\gtrsim 0.97$ for each system represented in Table 7.2. Of course, simply extending the observations of the EGA function defined in Sec. 7.4 to the second and third angles of the U_3 gate would indicate that this assumption is invalid at the level of fractions of radians per gate. These two quantifications of the Z-basis distribution of probability in the localized wavefunction are expected to correlate with the projection onto eigenstates of this form in an implementation of quantum phase estimation. For four qubits, it is seen that a noisy

implementation of a localized, symmetrized exponential is a viable option for approximating a Gaussian wavefunction with reduced quantum resources.

To explore the properties of the wavefunction that can be prepared in the device rather than the quality of the extrapolation that can be learned over a range of wavefunctions, we place a cut on the Hadamard angle used to copy the exponential into the second half of the Hilbert space as seen in the circuit of Fig. 7.1. This cut is directly related to a cut on the asymmetry allowed in the in-medium Hadamard as shown in the top left panel of Fig. 7.6 where the two-norm asymmetry, $A_{CE}^{(2)}$, is shown as a function of the input angle. The vertical lines indicate the region of θ allowed for accepted *events*. The two-norm is monitored between each set of 8000 samples and shown in the x-axis of the top right panel of Fig. 7.6 for the 11 events measured in this work. Depending on the desired level of stringency placed on the calibration's asymmetry measurement, a few events with $A_{CE}^{(2)}$ 1-σ higher than the rest could be removed for concern about fluctuations in the device properties. Due to the previous observation that asymmetries at the level 0.05 can be extrapolated to a good approximation of the exponential distribution, we choose a cut window on the calibration asymmetry of $A_{CE}^{(2)} = 0.1$, thus retaining all 11 *events* recorded. This retention is a testament to the stability of the four chosen qubits during the time period of this production ($\sim$ 3h) and is not expected to be maintained in the use of different qubits or as calculation times grow with circuit depth and qubit number.

Using *events* produced with Hadamard angles in the window shown in the top left panel of Fig. 7.6 with on-line monitoring of the in-medium Hadamard's asymmetry, the probability distribution in the lower panel of Fig. 7.6 is one representative distribution determined to have been prepared within the quantum device. The light-blue error bars indicate only statistical errors from the collection of 8000 samples in both the production and calibrations including propagation through the measurement-error correction procedure. The dark blue error bars include also systematic uncertainties on the probabilities in each state informed by variation in the calibration measurements of the copied exponential produced within the Hadamard angle window and surviving the asymmetry cut. The systematics include time fluctuations

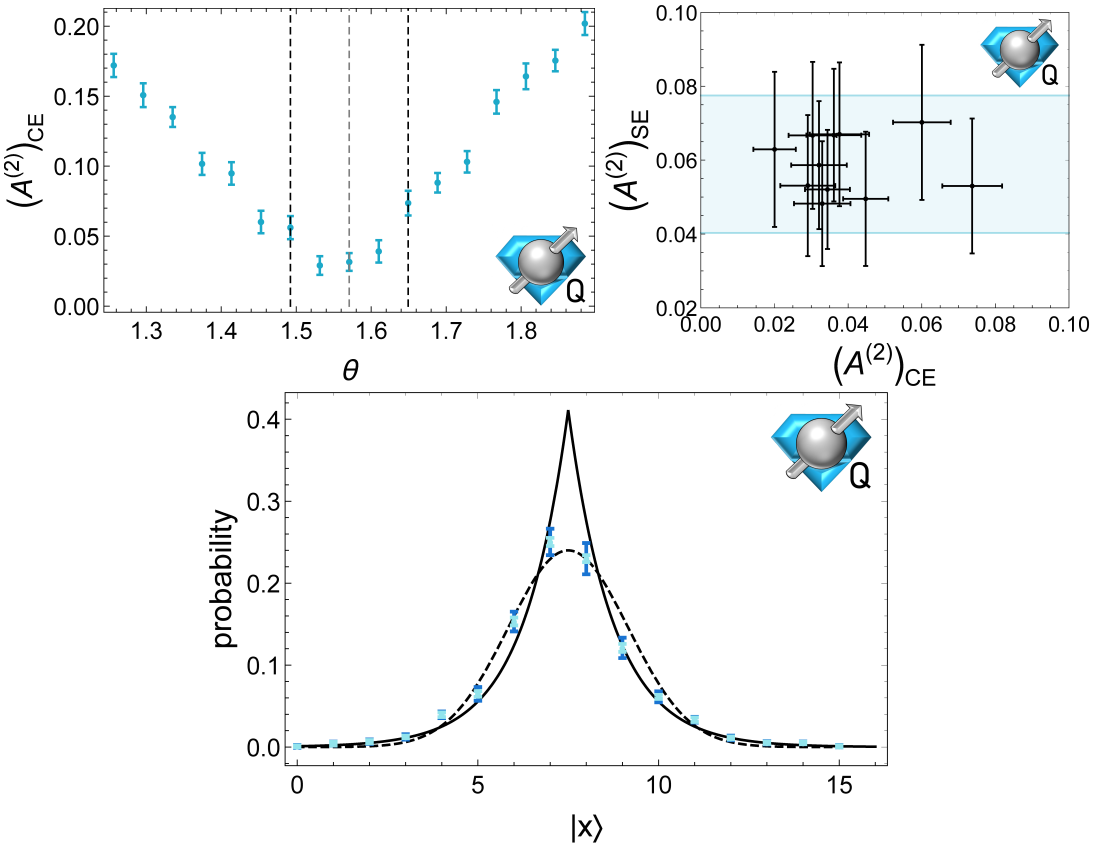

Figure 7.6: (Color online) Top left: Asymmetry calculated for the in-medium Hadamard copying the exponential distribution to the second half of the Hilbert space. Top right: Asymmetry of the localized, symmetrized exponential distribution, A_{SE}, as a function of the time-correlated calibration asymmetry for θ between the vertical dashed lines at left. Bottom: Representative probability distribution after preparation of an exponential wavefunction. Light blue error bars represent statistical uncertainties including that from the measurement-error correction. Dark blue error bars represent the full uncertainty including systematics of the in-medium Hadamard. Black curves are theoretical probability distributions for an exponential(solid) with $\alpha = 0.4$ and Gaussian(dashed) as written in Eqns. (5.6) and (5.7) with standard deviation $\sigma = 0.29$ and $n_Q = 4$.

in the device as well as the EGA distribution of the in-medium Hadamard as discussed in Section 7.4. Looking to Table 7.2, it can be seen that this single-circuit calibration window works quite well with comparable deviations of the probability distribution from the exponential and Gaussian state to those of the CNOT-extrapolated distributions. This success is largely due to the quality of 1- and 2-qubit gates on the set of qubits chosen for the collection of this data, which can be seen visually in the middle panel of Fig. 7.4 where the measurement-error corrected, $r = 1$ probability distribution is already quite representative of the intended exponential. It would appear that the preparation of high-quality states within calibration windows will be a vital capability before evolving wavefunctions to study quantum dynamics [2].

Before going further, it is interesting to realize why this procedure of preparing an exponential wavefunction rather than the desired Gaussian works so well in this application and where the advantage ceases. The momentum-space distribution of the exponential wavefunction is significantly larger than that of the Gaussian. Specifically, the cusp in the center of the space provides a large derivative contribution. The Nyquist-Shannon (NS) sampling theorem (applied in this context in Refs. [45, 86]) indicates that to capture the behaviour of the cusp more faithfully, the wavefunction needs to be sampled at a higher rate in field space—specifically at twice the rate of the highest frequency in Fourier space. If the wavefunction is sampled at a lower rate than dictated by the NS saturation point, the continuous reconstruction implied by the digitized samples is not unique. We leverage this lack of uniqueness by acknowledging the existence of a family of functions distinct in their ultraviolet (UV) completions, but equivalent in their IR digitizations up to the accuracy capable of the noisy quantum device. By shifting the samples away from the peak of the exponential (the $\phi = 0$ value is not included in the Hilbert space, see Ref. [45] for details), the UV

[2]While the fidelities of `Poughkeepsie` quantum gates allow for the initialization of an approximate wavefunction for the ground state of the scalar field, the connectivity of the device (see Appendix A of Ref. [26]) does not allow for subsequent time evolution. As shown in Ref. [45], all-to-all connectivity within the four qubits digitizing the field space of the single site would be required to implement the symmetric QuFoTr as well as the phases in position and momentum space.

cutoff on the exponential is lowered. When digitizing with more qubits, the UV cutoff will necessarily increase as the exponential is sampled more densely. While the overlap with the Gaussian remains high—e.g., digitization with $n_Q = 12$ yields $|\langle\psi^e|\psi^g\rangle|^2 \gtrsim 0.97$ with small n_Q-dependent tuning of the width parameter—the exponential wavefunction's precision on the ground state energy of the free scalar field is found to be saturated at $\sim 1\%$ achieved at the low digitization of $n_Q = 3$. If a higher precision is desired, the n_Q-stable, substantial overlap of the symmetrized exponential with the ground state of the free scalar field makes it a convenient starting point for more advanced preparation techniques [41, 237, 238, 239, 240, 48, 241] in which the necessary resources often scale with the initial state's overlap with the target wavefunction. To put the value of this achievable precision into perspective, the explorations of Ref. [45] determined that field-space wavefunctions digitized with $n_Q = 3$ were capable of achieving 0.01% precision on the ground state energy when utilizing the digitized Hamiltonian's exact ground state wavefunction. By acknowledging that the wavefunction does not need to be implemented to higher accuracy than the noisy quantum device is capable of preparing, it is possible to hide controlled theoretical systematics beneath the hardware noise floor—preparing a wavefunction with equivalent accuracy in hardware but requiring significantly fewer quantum resources, which scale only linearly with the number of qubits for the exponential wavefunction. The localized exponential-Gaussian pair is one example of a successful entanglement-minimized, digital approximation.

7.6 Multi-Site Preparation

As a first step toward initializing a lattice scalar field theory into its ground state, we extend the work in the previous sections to initialize a 2- and 3-site system ($n_s = 2, 3$) into a tensor product state of symmetric exponentials, $\langle x_1 x_2|\Psi\rangle = \psi_{\text{exp}}(x_1)\ \psi_{\text{exp}}(x_2)$ and $\langle x_1 x_2 x_3|\Psi\rangle = \psi_{\text{exp}}(x_1)\ \psi_{\text{exp}}(x_2)\ \psi_{\text{exp}}(x_3)$. This state is neither the true ground state for each site, nor the true ground state of the 2- or 3-site systems due to the lack of entanglement. We have explored the preparations of these systems in a number of different ways: with Gaussian gate noise, with the `Qiskit` noisy quantum simulator using the `Poughkeepsie`

noise model parameters, and directly with the `Poughkeepsie` quantum device. Both the 2- and 3-site systems were implemented with $n_Q = 3$ qubits per spatial site, corresponding to 64- and 512-dimensional Hilbert spaces. The reduced probability distributions for each site are expected to correspond to symmetric exponentials, while the distribution across the entire Hilbert space corresponds to the convolution of two or three symmetric exponentials. As the initialized wavefunctions are the tensor product of symmetric exponentials, without entanglement, the circuits for preparing these states correspond to parallel implementations of the gates necessary to prepare the state on a single site.

Figure 7.7 shows the results of preparations implemented on the quantum device `Poughkeepsie`, corrected for measurement errors. The top left panel of this figure shows the two-norm asymmetry in the 2-site symmetrized exponential, $A^{(2)}_{SE}$, correlated with the same quantity calculated for the copied exponential calibration, $A^{(2)}_{CE}$. The Hadamard θ-angles represented in this panel were scanned over a range of 1.41 to 1.73, spanning the theoretical value of $\pi/2$. For the blue points at $r = 1$, the two asymmetries are seen to be highly correlated with an asymmetry that generically increases in both the calibration and production as the Hadamard angle in the $U_3(\theta, 0, \pi)$ operator deviates from $\pi/2$. This angular distance from $\pi/2$ is represented in the saturation of the data points such that $\theta = 1.41$ is lightly shaded appearing in the top right corner while the $r = 1$ point for $\theta = 1.57$ is darkly shaded and appears in the lower left. This direct correlation does not persist for the purple points at $r = 5$. Instead, a vertical clustering is observed located at a large value of $A^{(2)}_{SE}$ indicating, as seen in the 1-site data, that the additional CNOTs produce an asymmetry that overshadows that from the Hadamard gate. In this case, all angles paired with $r = 5$ were unable to achieve symmetrized exponentials with two-norm asymmetries below $A^{(2)}_{SE} = 0.08$, in spite of the stability of their angle-correlated calibration asymmetries, $A(2)_{CE}$.

In the top right panel of Fig. 7.7, the probability distribution for the 2-site exponential preparation is shown after measurement-error correction and CNOT extrapolation with $r = 1, 3$ for a Hadamard implemented with $U_3\left(\pi/2, 0, \pi\right)$. The presentation of probabilities obtained from 2-site systems has been discussed previously, e.g. Ref. [45], where it is seen

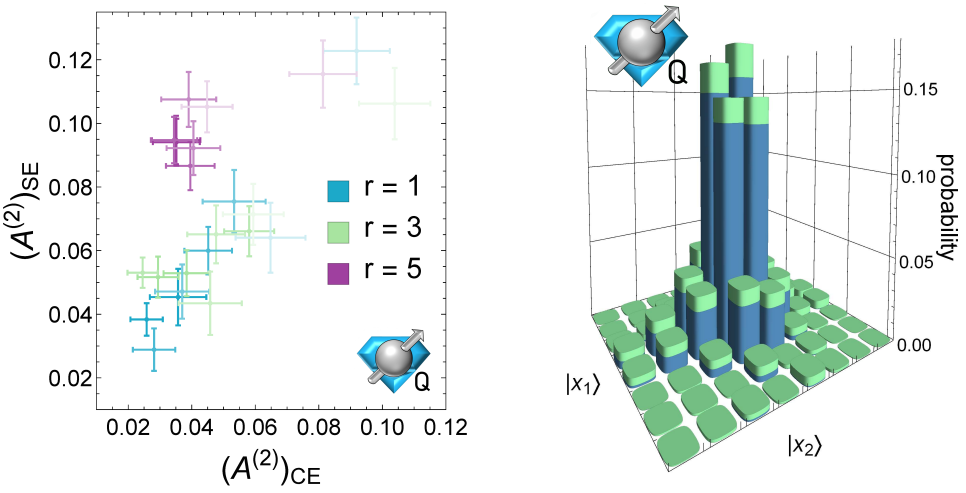

Figure 7.7: (Color Online) The 2-site and 3-site probability distributions of a symmetric exponential wavefunction initialized on each spatial site. The top left panel shows the two-norm asymmetry of the 2-site symmetrized exponential, $A^{(2)}_{SE}$, as a function of the angle-correlated calibration two-norm asymmetry of the copied exponential, $A^{(2)}_{CE}$. The colors indicate the CNOT extrapolation level while their saturation decreases with increasing distance of the $U_3(\theta, 0, \pi)$ input angle from $\pi/2$ for the symmetrizing Hadamard. The top right panel shows the CNOT-extrapolated probability distribution for $\theta = 1.57$ across the full 64-dimensional Hilbert space of the $n_Q = 3$ symmetrized exponential prepared over two sites and arranged into a grid. The light green regions span the 1-σ confidence intervals on the probability at each grid location.

to be useful to decompose the system into the probabilities at each site and represent the data in a 2D grid. When viewed in this way, the four-fold discrete rotational symmetry is apparent in the data, though imperfections are discernable outside the light-green bands representing the 1-σ confidence interval on the probability at each state in the Hilbert space.

Figure 7.8 shows the linearized Hilbert space representation of the 3-site symmetrized exponential. For three different Hadamard angles within a window defined about $\theta = \pi/2$, the

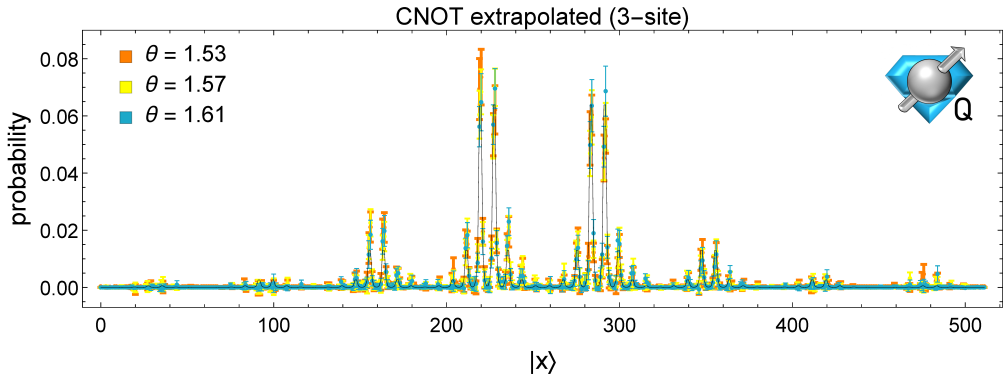

Figure 7.8: Three sites of non-interacting symmetrized exponential are prepared and extrapolated with data at $r = 1, 3, 5$ at three different values of the $U_3(\theta, 0, \pi)$ symmetrization angle within the tolerance cuts.

probability distributions are shown after constrained-inversion measurement-error correction and CNOT extrapolation using values of $r = 1, 3, 5$. The measurement calibration matrix created after implementation of the 512 circuits initializing computational basis states (with 400 shots each) can be seen in Appendix B of Ref. [26]. With 8000 shots per angle and a signal maximally rising to a probability of 0.08, it is encouraging that these preparations are capable of conclusively identifying the central and neighboring peak structures of the 3-site symmetrized exponential wavefunction.

By adding additional sites each with n_Q qubits, increasing the dimensionality of the system from 8 for 1 site to 64 for 2 sites to 512 for 3 sites, the statistical precision of the measurements is reduced for a fixed number of shots. For the chosen width of the exponential, where most of the measurements are localized within a few states, the precision is reduced by approximately a factor of two, as opposed to the ratio of Hilbert-space dimensionalities. More generally, the precision is determined by the number of states where the wavefunction has support, rather than the dimensionality of the full Hilbert space. Relying on the localization of the wavefunction to arrive at statistically significant results may be important when working with larger lattices of scalar fields.

two site	$A_{SE}^{(1)}$	$A_{SE}^{(2)}$	$\|\|\psi^2_{\rm hw} - \psi^2_{\rm exp}\|\|$	$\|\|\psi^2_{\rm hw} - \psi^2_{\rm G}\|\|$
Gaussian Noise $\sigma_\theta = 0.3 \times 10^{-1}$	0.059(8)	0.014(2)	0.78(1)	0.79(1)
Gaussian Noise $\sigma_\theta = 10^{-2}$	0.041(7)	0.013(3)	0.14(1)	0.18(1)
`Poughkeepsie` Noise Model	0.07(1)	0.019(3)	0.10(1)	0.16(1)
Calibration Window $A_{CE}^{(2)} \leq 0.4$	0.13(3)	0.04(1)	0.21(4)	0.18(4)
CNOT extrapolation $\theta = 1.57$	0.15(2)	0.05(1)	0.18(3)	0.21(3)
three site				
CNOT extrapolation $\theta = 1.53$	0.29(2)	0.053(6)	0.30(4)	0.32(4)
CNOT extrapolation $\theta = 1.57$	0.30(2)	0.053(7)	0.31(4)	0.34(4)
CNOT extrapolation $\theta = 1.61$	0.29(2)	0.049(7)	0.30(4)	0.31(4)

Table 7.3: (Color online) Properties of localized exponentials on two and three sites prepared with Gaussian noise, a quantum noise simulator with `Poughkeepsie`'s noise parameters, and with the quantum device `Poughkeepsie`. The first and second columns quantify the asymmetry of the wavefunction while the third and fourth quantify the distance of the probability distribution measured on hardware, $\psi^2_{\rm hw}$, from that of the intended exponential, $\psi^2_{\rm exp}$, and the associated Gaussian distribution with largest wavefunction overlap, $\psi^2_{\rm G}$.

As in the 1-site ($n_s = 1$) system, it is interesting to quantify the asymmetry of the measured probability distributions as well as their distance from both the intended symmetric exponential probability distribution and that of the nearest tensor product of Gaussian wavefunctions. These quantities calculated 1.) with Gaussian gate noise, 2.) on the quantum noise simulator with `Poughkeepsie`'s noise parameters extrapolated to the limit of vanishing CNOT noise, and 3.) on the `Poughkeepsie` hardware are shown in Table 7.3. Focusing on the 2-site implementation first, it is interesting to observe that none of the three classical noisy simulations ( ) effectively capture the level of asymmetry measured on the quantum device. Increasing the Gaussian gate noise, as implemented in Ref. [45], to $\sigma_\theta = 0.03$ dramat-

ically increases the deviation of the probability distribution from the localized exponential and Gaussian, as seen in the third and fourth columns, but produces a wavefunction that retains a level of symmetry greater than that of the hardware implementations. The same is true for the `Qiskit` noise simulator defined by `Poughkeepsie` noise parameters. Once again, the preparation of the exponential wavefunction allows an isolated environment for exploring the capabilities of the quantum device, this time suggesting that the classical simulations do not include all of the sources of asymmetry present in the quantum hardware. As noted previously noted, the $n_s(n_Q - 1)$ CNOT gates are identified as a source of additional asymmetry. Generic improvements to classical () and quantum () simulations will benefit from understanding, incorporating, and mitigating these identified effects, which are seen to be exacerbated with an increasing number of spatial sites prepared in parallel.

The second two columns of Table 7.3 indicate the distance of the measured probability distributions from the theoretical symmetrized exponential and Gaussian distributions. The chosen metric is the one norm of the state-by-state deviations. It can be seen from the 3-site CNOT extrapolations that the probability distribution's deviation from the intended exponential is fairly stable over a range of θ angles in the $U_3(\theta, 0, \pi)$ gate used to symmetrize the exponential. The presence of this stability is not surprising in that a noisy quantum environment will be somewhat insensitive to *small* modifications in the digital circuitry. This exploration has quantified *small* in this context for currently available superconducting devices giving effectively a resolution scale for implemented angles as in Eq. (7.5).

While this gate resolution scale limits the precision of prepared wavefunctions, it also provides the logic of a calibration window used in this work to monitor system performance in real time. Preparations passing the cuts are considered identical instances of a noisy preparation. This allows error mitigation to effectively be applied to the wavefunction prepared in the quantum device without post-process extrapolation. This, of course, will be necessary if time evolution of the prepared state is subsequently desired. As performed for the 2-site system, the window was set to allow asymmetries of the 2-site copied exponential $A_{CE}^{(2)} \leq 0.04$ for time-correlated calibrations. As seen for the $r = 1$ results in the top left

panel of Fig. 7.7, this cut retains four prepared distributions at angles (1.57, 1.57, 1.61, 1.64), a set located near, but not centered upon the theoretically exact angle of $\theta = 1.57$ (implementations with angles smaller than 1.57 are also present in Fig. 7.7 but do not pass the calibration asymmetry cut). The resulting wavefunctions may be combined to represent the average wavefunction the device is capable of preparing in hardware. The properties of the resulting probability distribution are comparable to those extrapolated from multiple preparations at increasing r values as shown in Table 7.3. This on-line method of calibration monitoring is expected specifically to aid in simulations of time evolution in which control of the state in hardware, rather than the extrapolated state, is vital.

The last column of Table 7.3 calculates the deviation of the various probabilty distributions from the theoretically nearest tensor-product Gaussian distributions ($\sigma = 0.31$). This state is also not the true ground state for the multi-site scalar lattice due to the absence of site-wise entanglement produced by interactions of the gradient operator, but better represent the ground state for each non-interacting site. For the 2-site and 3-site systems in Table 7.3, the one-norm probability distribution deviations are calculated to be only marginally larger than their intended-exponential counterparts. The precision of the device is insufficient to conclusively distinguish between these two wavefunction structures by deviations of their probability distributions and thus, the exponential is proposed as an appropriate low-noise, low-entanglement approximation for the Gaussian wavefunction.

In general, on a quantum device with all-to-all connectivity, once the state is prepared it can then be time evolved with e.g., the Trotterized time evolution operator. However, the connectivity of `Poughkeepsie` is not conducive to implementation of the time evolution operator as discussed in Ref. [45]. Not only is sufficient connectivity between sites absent, but the all-to-all connectivity needed for the evolution of a single site is not present for $n_Q \geq 3$. This work has shown how the available connectivity of `Poughkeepsie` could be used to approximate a wavefunction technically requiring much higher degree of 2-qubit entanglement. Unless a similar approximation can be made to the required gates present in the time evolution operator, additional qubit connectivity will be required to time evolve

instances of a scalar field.

7.7 Reflections

There are a number of items to discuss related to the work described in the previous sections. The first point is related to the impact of field digitization. We have found that a symmetric exponential wavefunction, which can be initialized with a minimal number of entangling gates, can be tuned to have a substantial overlap with a Gaussian wavefunction. While dense sampling of the function in the region of support would reveal a cusp at its symmetry point, with a limited number of qubits per site and the symmetry point placed mid-way between two states in the Hilbert space, as considered here, the cusp is not resolved and the sampled evaluations of the symmetric exponential can be interpolated smoothly. An additional consideration is that as the near-term devices are noisy, initializing the device with precision better than that of the noise will not improve the quality of the simulation. Therefore, until the noise in quantum devices drops below the percent level, a symmetric exponential wavefunction is likely to provide an adequate initialization state.

As is made clear in examining the 2- and 3-site systems compared with the 1-site system, for a multi-site lattice scalar field theory, the number of states in the Hilbert space rapidly becomes too large to completely sample, as is well known. The dimensionality of the measurement-error system(s) nominally scales with the square of the Hilbert-space dimensionality, becoming unmanageable even before the measurements of quantities of interest are considered. New algorithms will be required to isolate important quantities from the field theory computation to inform the quality of state preparation that do not scale with the Hilbert-space dimensionality, likely exploiting auxiliary qubits.

In establishing the symmetric exponential as a potentially useful state to prepare, we made use of the fact that duplication and reflection are straightforward at the circuit level, requiring only a Hadamard gate and $n_Q - 1$ CNOT gates, respectively. For wavefunctions that have vanishing derivative at the edges and have a constant logarithmic derivative within the half Hilbert space, such as an exponential function or a constant, such functions can be

initialized without entangling gates. Therefore, a step wavefunction, an exponential, and a uniform wavefunction can be initialized without CNOT gates.

More complicated periodic functions can also be initialized relatively simply. For instance, one period of a $\cos\phi$ or $\sin\phi$ function can be initialized using the general circuit described previously. Additional qubits can be included, and when acted on with a Hadamard gate lead to a wavefunction of multiple periods of the $\cos\phi$ or $\sin\phi$. This can also be accomplished by first initializing a quarter-period, then anti-symmetrizing and symmetrizing using Hadamard and Pauli $\hat{Z}$ gates.

In the Introduction, the small-n_Q approximate wavefunction preparation in this work was placed into the context of state preparation in the asymptotic regime of many qubits as a possible first step for Somma Inflation—the controlled evolution capable of expanding an initial Gaussian wavefunction to one with support over a larger portion of the Hilbert space. The quantum resources required to implement this inflation are equivalent to that of a single first-order Trotter step of time evolution, and will thus benefit from any future algorithmic improvements of the already-efficient time evolution operator. We find that the symmetrized exponential wavefunction is less costly than implementing the period of inflation (required two-qubit gates grow linearly rather than quadratically). Thus, in noisy hardware where an exponential approximation to the Gaussian wavefunction may introduce sub-leading theoretical systematics, the symmetrized exponential may be used without further post processing. For situations in which higher precision is desired in the wavefunction structure, either an adiabatic approach or the perturbative scheme of improvement proposed below may be implemented on small qubit registers. If inflating to larger qubit registers, the errors in the initial state will be propagated to the final Gaussian state. Further exploration is needed to optimize the properties of the initial narrow Gaussian wavefunction digitization and extent such that the inflated Gaussian is created to saturate the Nyquist Shannon sampling theorem (see e.g., Refs. [88, 45]) and thus efficiently utilize the available quantum resources.

Given the results that we have obtained, it is interesting to consider the possibility that a perturbative expansion in the application of entangling gates may be possible, that

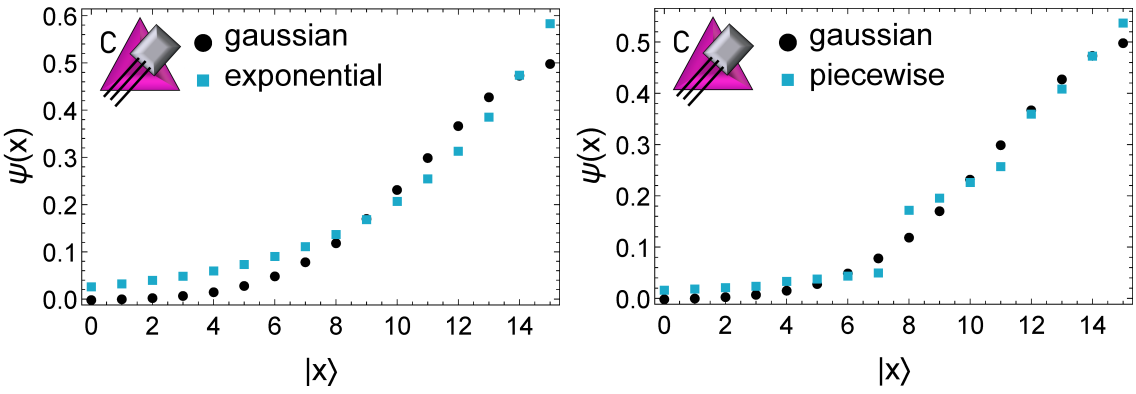

Figure 7.9: (Color online) The left panel shows an exponential wavefunction (blue, square points), initialized on a $n_Q = 4$ quantum register with three rotation angles calculated as in Eq. (7.3). This exponential wavefunction has an optimal overlap with the Gaussian wavefunction (black, circular points). The right panel shows a wavefunction (blue, square points) obtained by fitting the three rotation angles to maximize the overlap with the Gaussian wavefunction.

would, for example, order-by-order transform a symmetric exponential wavefunction, or some other variant thereof, into a Gaussian wavefunction. Such an expansion could be helpful in working with noisy quantum devices, as the noise would provide an upper limit to the required precision of the perturbative approximation. As a starting point, the single qubit rotations that define the exponential function can be modified to optimize the overlap with a Gaussian wavefunction, giving rise to a piece-wise wavefunction. While providing a better approximation to a Gaussian wavefunction than the exponential function, as shown in Fig. 7.9 for the case of $n_Q = 4$, this introduces higher-frequency components in field conjugate momentum space. We have not yet explored the utility of the piecewise wavefunction, nor the impact of the high-frequency conjugate momentum states, nor developed the quantum circuit perturbation theory, but intend to do so in subsequent work.

An important question to address is that of the utility of an initial state that is a tensor product of symmetric exponential wavefunctions at each point of a lattice scalar field theory.

Recalling the seminal work of Jordan, Lee and Preskill [24], who have detailed how to perform calculations in scalar field theory using a quantum computer, directly initializing a quantum computer into the ground state of an interacting scalar field theory is beyond the capabilities of a quantum computer due to its complexity. They proposed to compute, for instance, scattering S-matrix elements by initializing the lattice into the ground state of the free scalar field utilizing the preparation of multi-dimensional Gaussians with non-trivial covariance matrices discussed in Ref. [184]. Wavepackets of the non-interacting theory are prepared, and then the entire system is adiabatically evolved from the non-interacting theory to the interacting theory while retaining the asymptotic separation of the wavepackets. The system is then evolved forward in time. A similar adiabatic evolution process can be employed to arrive at the interacting ground state when the sites are prepared in a symmetric exponential wavefunction. As such states are the lowest-lying eigenstate of an attractive Dirac-delta function, $V^{(\delta)}(\phi) = -g\delta(\phi)$, where g is a coupling constant, the scalar field theory initialized into a tensor-product state of these wavefunctions can be adiabatically evolved from $V^{(\delta)}(\phi)$ to $V(\phi) = \frac{1}{2}m^2\phi^2 - \frac{1}{2}\phi\nabla_a^2\phi + \frac{1}{4!}\lambda\phi^4$. Therefore, the process outlined in Ref. [24] to accomplish scattering in scalar field theory remains unchanged when symmetric exponential wavefunctions are initialized, but the interactions that are adiabatically evolved are different. Of course, it is likely to be the case that the *devil is in the details* of actual quantum simulations, which remain to be performed.

7.8 Summary and Conclusions

State preparation on quantum devices is a key ingredient in the quantum simulation of systems of importance in biology, chemistry, physics and other areas. If the properties and dynamics of low-lying states of a quantum many-body system are the focus, a quantum device used to perform the simulation needs to be initialized to have significant overlap with these states. Without this, particularly in the near-term, isolating the physics of interest will be extremely challenging, and in most cases, not possible, through subsequent evolution and measurement of the system.

As the number of entangling gates involved in preparing a symmetric exponential wavefunction grows linearly with the number of qubits, they may provide good approximations to Gaussian wavefunctions with support over a small or modest number of states due to the inherent digitization of the field and resulting truncation in field-conjugate-momentum space. Improvement of this approximation can be made perturbatively or adiabatically, reaching the digitized Gaussian wavefunction using resources scaling exponentially with the region of support of the wavefunction. Inflating this Gaussian wavefunction may be implemented efficiently through simple unitary transformations [102]. Our studies of these wavefunctions, which include ideal quantum simulations, noisy quantum simulations and simulations on IBM Q Experience quantum devices, with measurement-error correction and CNOT-gate error mitigation, show that they may provide good starting points for subsequent time-evolution, with overlaps ~ 0.95 or greater for the small systems we have explored. Clearly, further studies and simulations are required to determine the extent of their utility. Our results show that even with the small systems that are presently available, the systematic errors and noise in initializing a Gaussian wavefunction are significantly more than in initializing a symmetric exponential wavefunction. In some of our initializations of a Gaussian wavefunction with 4 qubits per site, the CNOT errors were sufficiently large such that they could not be reduced through a standard extrapolation procedure. Following from the success in preparing the symmetrized exponential, there may be utility in seeking other approximate wavefunctions that also require fewer entangling gates than a Gaussian.

In order to accommodate fluctuations in gate operations and measurement errors during production running on the quantum devices, we employed a workflow comprised of a sequence of circuits that were run immediately prior to the symmetrized exponential wavefunction circuit. As detailed in the text, the results obtained from these other circuits, such as an Hadamard-gate in vacuum, were used to implement a set of data acceptance criteria (cuts), analogous to those used in the analysis of experimental data, that had to be satisfied to retain the results of the symmetrized exponential wavefunction circuit. Establishing these cuts was found to be a valuable component in analyzing the results of circuits executed on

the quantum devices. These types of integrated workflows are likely to be useful throughout the NISQ era.

We used IBM's `Poughkeepsie` to produce the results presented in this work from a quantum device, and used its noise parameters in noisy simulations. This was determined largely by availability, throughput and the gate- and qubit-fidelities that were available during this production. The interconnect fabric on `Poughkeepsie` prevents the preparation of symmetrized exponentials beyond $n_Q = 4$ qubits per spatial site with $(n_Q - 1)$ CNOTs [3], and also prevents Trotterized time-evolution for $n_Q = 3$ qubits per spatial site and larger. It would appear that improvement in qubit- and gate-fidelities for sufficiently connected qubit clusters are currently required to prepare and time evolve even a small lattice scalar field theory on such quantum devices.

The three stages of preparing the symmetric exponential wavefunction are informative about the qubit- and gate-fidelities of the quantum device, and may serve as a calibration benchmark for future simulations. The first stage involves the recursive generation of an exponential distribution distributed across half of the states in the Hilbert space. As this only involves y-axis rotations of all but one of the qubits, the fidelity of these rotations can be ascertained (after measurement-error correction), and these angles can be iteratively tuned to optimize the initialized state with regard to the target exponential function. The second stage of preparation is a single Hadamard gate applied to the last qubit, duplicating the exponential wavefunction in the first half of the Hilbert space into the second half. The fidelity of this operation can be determined and the gate operation tuned, both "in vacuum" and "in-medium" to optimize the symmetry of the wavefunction in the quantum register. The last stage of preparation corresponds to CNOT gates connecting each qubit to the last. As the CNOT fidelity is significantly worse than that of the single qubit gates, it is this stage where substantial noise and systematic twisting of the control qubit are observed. The

[3] If the number of CNOTs is allowed to double, then the symmetrization can be reconfigured for nearest-neighbor connectivity in a 1D string of qubits and thus the interconnect fabric on `Poughkeepsie` can support the preparation of a 20-qubit symmetrized exponential (see Appendix A of Ref. [26] for details).

CNOT errors are mitigated with the standard techniques of extrapolation, but this increases the uncertainty in the calculation, and is the limiting stage of the state preparation. The twisting of the control qubit introduces an additional asymmetry into the wavefunction that is visually apparent. We found that introducing cuts on the quality of the wavefunction at each stage of this process with time-correlated calibration circuits provided valuable improvement of the state preparation.

While our present work has been cast in the context of scalar field theory, it has broader application. One such example is in the state preparation of a weakly bound non-relativistic system such as the deuteron. At leading order in the pionless effective field theory (EFT) [173, 171, 172, 242], which recovers effective range theory for nucleon-nucleon scattering, the deuteron wavefunction is dominated by the s-wave exponential wavefunction, with contributions from the tensor force inducing s-d mixing suppressed in the power-counting. While recent quantum calculations employing the pionless EFT [78, 49, 243] have been performed in Fock-space, similar calculations could be performed in position space, in which the exponential function is the exact wavefunction at long-distances. The perturbative expansion that defines the pionless EFT could be implemented as a perturbative expansion in quantum circuits, which will be explored in subsequent work. Our 2-site and 3-site calculations demonstrate that we are now able to begin to simulate 2-dim. and 3-dim. systems in real space.

In this work, we find benefits in the use of tuned symmetric exponential wavefunctions—requiring only $(n_Q - 1)$ entangling gates—as approximations to Gaussian wavefunctions—requiring $\mathcal{O}\left(2^{n_Q}\right)$ entangling gates for small n_Q—for the initialization of scalar field theories in future quantum simulations. This is one example of the existence of wavefunctions closely resembling target wavefunctions on digitized Hilbert spaces, but requiring reduced entanglement. Identification of such wavefunction pairs allows the precision of state preparation to be advantageously matched to the precision of the quantum hardware. While our results have been implemented with IBM's Q Experience quantum devices, the conceptual developments are device independent. It would be interesting to explore these developments on

other quantum architectures, such as trapped ions or cold atoms.

Chapter 8

QUANTUM-CLASSICAL COMPUTATION OF SCHWINGER MODEL DYNAMICS

The content of this chapter is associated with Ref. [30]:
N. Klco et al. "Quantum-classical computation of Schwinger model dynamics using quantum computers". *Phys. Rev. A* 98.3 (2018), p. 032331. DOI: 10.1103/PhysRevA.98.032331. arXiv: 1803.03326 [quant-ph]

This chapter presents a quantum-classical algorithm to study the dynamics of the two-spatial-site Schwinger model on IBM's quantum computers. Using rotational symmetries, total charge, and parity, the number of qubits needed to perform computation is reduced by a factor of ~ 5, removing exponentially-large unphysical sectors from the Hilbert space. Our work opens an avenue for exploration of other lattice quantum field theories, such as quantum chromodynamics, where classical computation is used to find symmetry sectors in which the quantum computer evaluates the dynamics of quantum fluctuations.

8.1 Schwinger Model Preliminaries

The Schwinger model describes quantum electrodynamics in one space and one time dimension. It enjoyed popularity in the 1960's and 1970's as a "prototype" for the strong interactions as it shares with QCD a number of features, such as confinement and spontaneous breaking of chiral symmetry. After gauge-fixing, there is only one dynamical component of the photon field, which acquires a mass through quantum fluctuations. Charge is screened, the lightest excitation in the spectrum has the quantum numbers of the photon, and the vacuum of the theory enjoys a non-zero condensate, $\langle\psi\overline{\psi}\rangle$. The Lagrange density that defines

the continuum Schwinger model,

$$\mathcal{L} \;=\; \overline{\psi}\,(i\not{D} - m)\,\psi - \frac{1}{4}F_{\mu\nu}F^{\mu\nu} \quad , \tag{8.1}$$

can be spatially discretized with the Kogut-Susskind (staggered) action [244, 245, 246], mapped onto a (re-scaled) Hamiltonian density using the Jordan-Wigner transformation, and gauge-fixed by setting the temporal component of the gauge field to zero ($A_0 = 0$) on $N_{fs}/2$ spatial sites,

$$\begin{aligned} \hat{H} \;&=\; x \sum_{n=0}^{N_{fs}-1} \left(\sigma_n^+ L_n^- \sigma_{n+1}^- + \sigma_{n+1}^+ L_n^+ \sigma_n^-\right) \\ &+\; \sum_{n=0}^{N_{fs}-1} \left(l_n^2 + \frac{\mu}{2}(-)^n \sigma_n^z\right) \quad . \end{aligned} \tag{8.2}$$

This Kogut-Susskind action distributes the two components of the 1-dimensional fermion field across neighboring even-odd sites and results in two fermion sites per spatial site (see Figure 8.1 for a two-spatial-site example). The first term in $\hat{H}$ corresponds to the kinetic energy of the fermion field (a hopping term), the second term is the total energy in the electric field, and the third term is the mass term. The couplings in Eq. (8.2) are related to the value of the gauge coupling g, the lattice spacing a and the fermion mass m, $x = 1/(ag)^2$ and $\mu = 2m/(ag^2)$. The l_n's are integers, ranging between $-\infty$ and $+\infty$, describing the quantized electric flux in the link between the site n and $n+1$, while the $L_n^{\pm}$ are link lowering and raising operators acting as $L^{\pm}|l\rangle = |l \pm 1\rangle$. Two qubits are sufficient to describe the fermion occupation of a single spatial lattice site, one for the e^- and one the e^+. As low energy observables become insensitive to high-energy modes, the impact of the necessary ultraviolet cutoff on each l_n can be quantified and removed [247, 248, 249, 170, 51, 250]. While following naturally in Lagrangian dynamics as a Lagrange multiplier, the Gauss's Law constraint relating the electric flux entering and leaving a closed surface to the electric charge contained in that surface must be imposed "by hand" in the initial state of a Hamiltonian formulation. Approaching the strong coupling limit, in which $x, \mu \to 0$ with their ratio finite or simply $x \to 0$ for the massless case [245], the vacuum of the theory is perturbatively close

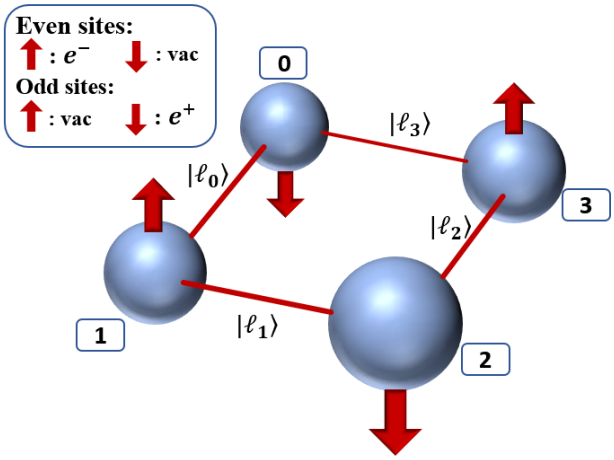

Figure 8.1: A schematic of the qubit and electric flux link structure of the two-spatial-site lattice Schwinger model. Even sites (marked 0 and 2) represent the electron content with spin up denoting the presence of an electron. Odd sites (marked 1 and 3) represent the positron content with spin down denoting the presence of a positron. The strong-coupling vacuum (unoccupied) state is antiferromagnetic.

to an anti-ferromagnetic phase with the e^- and e^+ qubits anti-aligned (see Fig. 8.1, without energy in the electric field).

The lattice representation of the Schwinger model as declared above conventionally utilizes staggered fermions [251, 245]. This choice is motivated by experiences of successful production of the Dirac equation in the continuum limit absent in more basic latticizations containing a two-component spinor on each lattice site. In the staggered approach, the two-component dirac spinors ($2^{\frac{d}{2}}$ are spread over two sites with left-handed fields and right handed fields distributed on even(odd) and odd(even) sites, respectively depending on convention.

Hermitian matrices for spinors in Euclidean signature (SO(D) rather than SO(D-1,1)) satisfy

$$\{\gamma^m, \gamma^n\} = 2\delta^{mn} \qquad \sigma^{mn} = \frac{1}{4}[\gamma^m, \gamma^n] \quad . \tag{8.3}$$

In two dimensions, appropriate gamma matrices, single generator, and chirality operators could be

$$\gamma^1 = \sigma^1 = \begin{pmatrix} 0 & 1 \\ 1 & 0 \end{pmatrix} \quad \gamma^2 = \sigma^3 = \begin{pmatrix} 1 & 0 \\ 0 & -1 \end{pmatrix} \quad \sigma^{12} = \frac{1}{2}\begin{pmatrix} 0 & -1 \\ 1 & 0 \end{pmatrix} \quad \gamma^5 = i\gamma^1\gamma^2 = \begin{pmatrix} 0 & -i \\ i & 0 \end{pmatrix} \tag{8.4}$$

or

$$\gamma^1 = \sigma^1 = \begin{pmatrix} 0 & 1 \\ 1 & 0 \end{pmatrix} \quad \gamma^2 = -\sigma^2 = \begin{pmatrix} 0 & i \\ -i & 0 \end{pmatrix} \quad \sigma^{12} = \frac{1}{2}\begin{pmatrix} -i & 0 \\ 0 & i \end{pmatrix} \quad \gamma^5 = i\gamma^1\gamma^2 = \begin{pmatrix} 1 & 0 \\ 0 & -1 \end{pmatrix} \quad . \tag{8.5}$$

Ref. [245] uses a basis in which the 0^{th} gamma matrix is diagonal and the chirality gamma matrix is σ^x

$$\gamma^0 = \sigma^z = \begin{pmatrix} 1 & 0 \\ 0 & -1 \end{pmatrix} \qquad \gamma^1 = \sigma^y = \begin{pmatrix} 0 & -i \\ i & 0 \end{pmatrix} \qquad \gamma^5 = i\gamma^0\gamma^1 = \sigma^x = \begin{pmatrix} 0 & 1 \\ 1 & 0 \end{pmatrix} \tag{8.6}$$

Any choice of pauli matrices as gamma matrices satisfies the anticommutation relations (as all square to 1 and anticommute with themselves). The main functional difference between these two bases is whether it is more convenient to have a diagonal γ^2 or a diagonal γ^5 (*Weyl representation*). In the former, it is shown that the gamma matrices may be taken real (implying the presence of real/majorana spinors). Due to the complex-valued eigenvectors (Weyl spinors) of the chirality operator (present in even dimensions), Majorana-Weyl spinors do not exist for SO(2). In the latter case, the two components of the spinor transform with equal and opposite phases, as seen by the diagonal generator.

In a scheme of staggered fermions, each lattice site contains a 1-component fermion field, $\phi(n)$. This field has anticommutation relations as expected for fermionic fields

$$\left\{\phi^\dagger(n), \phi(m)\right\} = -\delta_{nm} \qquad \{\phi(n), \phi(m)\} = 0 \quad . \tag{8.7}$$

Note that there is a factor of $\sqrt{a}$ in all fields to absorb the factor of a that normally appears in latticized commutation relations, $\phi(n) = \sqrt{a}\chi(x)$. Consider a Hamiltonian formed as

$$H = \frac{i}{2a}\sum_n \left[\phi^\dagger(n)\phi(n+1) - \phi^\dagger(n+1)\phi(n)\right] \quad . \tag{8.8}$$

First we can confirm Hamiltonian time dependence of the field

$$i\left[H,\phi(n)\right]=\dot{\phi}(n)=-\frac{1}{2a}\left[\sum_m \phi^\dagger(m)\phi(m+1)-\phi^\dagger(m+1)\phi(m),\phi(n)\right] \tag{8.9}$$

$$=-\frac{1}{2a}\left(\left[\sum_m \phi^\dagger(m)\phi(m+1),\phi(n)\right]-\left[\phi^\dagger(m+1)\phi(m),\phi(n)\right]\right) \tag{8.10}$$

$$=-\frac{1}{2a}\left(\left[\phi^\dagger(m),\phi(n)\right]\phi(m+1)-\left[\phi^\dagger(m+1),\phi(n)\right]\phi(m)\right) \tag{8.11}$$

$$=\frac{1}{2a}\left(\delta_{mn}\phi(m+1)-\delta_{m+1,n}\phi(m)\right) \tag{8.12}$$

$$=\frac{\phi(n+1)-\phi(n-1)}{2a} \tag{8.13}$$

In the staggered formalism, the time dependence at any site is determined by the spatial difference of the neighboring field values which live in the alternate even/odd classification. In this way, smoothness in field values at even(odd) sites translates to finite time dependence at odd(even) sites. Defining notation for the two-component field:

$$\psi=\begin{pmatrix}\psi_e\\ \psi_o\end{pmatrix}\qquad \psi_e(n)=\phi(n)\ n\text{ even}\qquad \psi_o(n)=\phi(n)\ n\text{ odd}\quad , \tag{8.14}$$

so that

$$\frac{\partial\psi_e(n)}{\partial t}=\frac{\Delta\psi_o}{\Delta x}=\frac{\psi_o^{n+1}-\psi_o^{n-1}}{2a}\qquad \frac{\partial\psi_o(n)}{\partial t}=\frac{\Delta\psi_e}{\Delta x}=\frac{\psi_e^{n+1}-\psi_e^{n-1}}{2a}\quad . \tag{8.15}$$

In the continuum, where the components live on the same lattice site, these time derivatives together lead to the massless Dirac equation ($i\gamma^\mu\partial_\mu\psi=0$)

$$\begin{pmatrix}1&0\\0&1\end{pmatrix}\frac{\partial\psi}{\partial t}=\begin{pmatrix}0&1\\1&0\end{pmatrix}\frac{\partial\psi}{\partial x}\quad . \tag{8.16}$$

Standard quantum computing conventions state that the $|0\rangle$ and $|1\rangle$ states are defined as vectors with an upper and lower component, respectively.

$$|0\rangle=\begin{pmatrix}1\\0\end{pmatrix}\qquad |1\rangle=\begin{pmatrix}0\\1\end{pmatrix}$$

Transforming the fermionic fields into spin degrees of freedom can be done through the Jordan Wigner transformation

$$\phi(n) = \prod_{\ell<n} \left(i\sigma^z(\ell)\right) \sigma^-(n) \qquad \sigma^{\pm} = \frac{\sigma^x \pm i\sigma^y}{2} \quad . \tag{8.17}$$

Transforming fields at adjacent locations (as is in the proposed Hamiltonian) the string of σ^zs squares to the identity and combines their $\pm$ imaginary factors

$$\phi^\dagger(n)\phi(n+1) = \sigma^+(n)\left(i\sigma^z(n)\right)\sigma^-(n+1) = -i\sigma^+(n)\sigma^-(n+1) \quad , \tag{8.18}$$

$$\phi^\dagger(n+1)\phi(n) = \sigma^+(n+1)\left(-i\sigma^z(n)\right)\sigma^-(n) = i\sigma^+(n+1)\sigma^-(n) \quad . \tag{8.19}$$

This localization of the z-strings makes the translation of the above Hamiltonian straightforward

$$H = \frac{1}{2a}\sum_n \left(\sigma^+(n)\sigma^-(n+1) + \sigma^+(n+1)\sigma^-(n)\right) \quad . \tag{8.20}$$

This free, massless Dirac field on a spatial lattice is equivalent to an antiferromagnetic spin chains.

All Dirac bilinears can be translated with the Jordan Wigner transformation into spin operators, including the vector charge density

$$j^\mu = \bar\psi\gamma^\mu\psi = \psi^\dagger\gamma^0\gamma^\mu\psi \qquad j^0 = \psi^\dagger\psi \text{ or } \frac{1}{2}\left[\psi^\dagger,\psi\right] \tag{8.21}$$

$$j^0 = \frac{1}{2}\left[\psi_e^\dagger,\psi_e\right] + \frac{1}{2}\left[\psi_o^\dagger,\psi_o\right] \overset{JW}{\to} \frac{1}{2}\left[\phi^\dagger(n),\phi(n)\right] = \frac{1}{2}\left[\sigma^+(n),\sigma^-(n)\right] = \frac{1}{2}\sigma^z(n) \quad , \tag{8.22}$$

the scalar density

$$\bar\psi\psi = \psi^\dagger\gamma^0\psi = \psi_e^\dagger\psi_e - \psi_o^\dagger\psi_o \tag{8.23}$$

$$\to (-1)^n\phi^\dagger(n)\phi(n) = (-1)^n\sigma^+(n)\sigma^-(n) \tag{8.24}$$

$$= (-1)^n\frac{1}{2}\left(1+\sigma^z(n)\right) \quad , \tag{8.25}$$

the axial-vector density

$$j_5^0 = \psi^\dagger\gamma_5\psi = \psi_e^\dagger\psi_o + \psi_o^\dagger\psi_e \tag{8.26}$$

$$\rightarrow \phi^\dagger(n)\phi(n+1) + \phi^\dagger(n+1)\phi(n) \tag{8.27}$$

$$= -i\left(\sigma^+(n)\sigma^-(n+1) - \sigma^+(n+1)\sigma^-(n)\right) \quad , \tag{8.28}$$

and the pseudoscalar density

$$j_5 = i\bar{\psi}\gamma^5\psi = i\psi^\dagger\gamma^0\gamma^5\psi = i\psi^\dagger \begin{pmatrix} 0 & 1 \\ -1 & 0 \end{pmatrix} \psi = i\left(\psi_e^\dagger\psi_o - \psi_o^\dagger\psi_e\right) \tag{8.29}$$

$$\rightarrow i(-1)^n\left(\phi^\dagger(n)\phi(n+1) - \phi^\dagger(n+1)\phi(n)\right) \tag{8.30}$$

$$= i(-1)^n\left(\sigma^+(n)i\sigma^z(n)\sigma^-(n+1) - \sigma^+(n+1)(-i\sigma^z(n))\sigma^-(n)\right) \tag{8.31}$$

$$= (-1)^n\left(\sigma^+(n)\sigma^-(n+1) + \sigma^+(n+1)\sigma^-(n)\right) \quad . \tag{8.32}$$

The axial charge $Q_5 = \int j_5^0(x)dx$ interchanges ψ_e with ψ_o and can thus be regarded as the spatial translation operator by a single unit of a . Attempts to use the continuum momentum operator containing a gradient ∂_1 connecting only odd or even sites results in a translation by $2a$.

The gauge field is defined on links as $U(n, n+1) = e^{iagA(n)} \equiv e^{i\theta(n)}$. Working in a fixed gauge with $A^0 = 0$, the electric field (the conjugate momenta of A) is has a single component $\mathbf{E}(x) = -\nabla V - \frac{\partial \mathbf{A}}{\partial t} = -\partial_0 A_1(x)$ (Ref. [245] uses the + sign version of this $E = \dot{A}$). This conjugate momentum should satisfy the canonical commutation relation $[A(n), E(m)] = \frac{i}{a}\delta_{n,m}$. The physically meaningful range of the vector potential is $0 \leq agA(n) < 2\pi$ for each link. At this point, alternate variables θ and L may be introduced with commutation $[\theta(n), L(m)] = i\delta_{nm}$ where $L(m) = \frac{1}{g}E(m)$ is the generator of cyclic translations in θ. By analogy to angular momentum, this leads to a conclusion that $L(m)$ is quantized to the integers.

The natural quantization of the electric field of the Schwinger model is a feature of the restricted space, rather than the lattice. The values at which the field is quantized can be imagined to function as a periodic background field. Interestingly, the physics of the Schwinger model is dependent on this background field [252]. For example, solving the equation of motion for the A_0 component in the axial gauge leads to a free parameter, the

background field, on the electric field. In 3 spatial dimensions, one can imagine a giant parallel-plate capacitor engulfing our universe creating a background electric field. However, the energetics of creating an electron-positron pair (2m) and that of separating the pair to the plates (background field times distance) is such that it is favorable for the vacuum to emit pairs until the background field is cancelled over all space. Thus, no background field parameter is present in four spacetime dimensions. In one spatial dimension, however, the compression of E into a line and the discretized shifts in the electric field cause a region of finite values of the background field, B, around $B = 0$ to also be stable with respect to pair production. Specifically, the difference in energies $\int \mathrm{d}^2x \frac{1}{2}E^2$ between the vacuum with and without a pair is

$$\Delta E = \frac{1}{2}L\left((B \pm e)^2 - B^2\right) \tag{8.33}$$

where L is the separation distance of the electron positron pair, e is the quantization described above, and the $\pm$ is associated with the left-right ordering of the positron and electron in the one-dimensional space. This difference in energy is zero when the background field is $\pm\frac{e}{2}$. Thus, if B is positive (such that $B - e$ lowers the energy), $\frac{e}{2}$ is the break-even point where it is no longer favorable to create pairs out of the vacuum. Pairs will be produced until $|B| \leq \frac{e}{2}$ in units of e. In this way, choosing a background field of $B = 12.37e$ will drive the theory to simply $0.37e$ and the physical properties of the schwinger model are characterized by a (usually rescaled) periodic parameter $\theta = \frac{2\pi B}{e}$. This dynamical perspective is consistent with the force on an electron-positron pair as a function of this background field

$$F = -\frac{\mathrm{d}E}{\mathrm{d}L} = -\frac{1}{2}\left(e^2 \pm 2eB\right) \quad \begin{cases} \text{repulsive} & |B| > \frac{e}{2} \\ 0 & |B| = \frac{e}{2} \\ \text{attractive} & |B| < \frac{e}{2} \end{cases} . \tag{8.34}$$

The force causing the charges to separate to spatial infinity becomes repulsive for $|B| > \frac{e}{2}$ and attractive for $|B| < \frac{e}{2}$. Thus, for theories that are defined at the boundary of this background field $\theta = \pi$, there is no background force on vacuum-produced pairs. For the calculations and

quantum simulations represented in this thesis, the background field will always be chosen to be zero $\theta = 0$, retaining an attractive force between vacuum electron-positron pairs.

Choosing a zero background field, the equation of motion for A_0 vanishes. Rather than having a propagating degree of freedom, the gauge field functions only as a lagrange multiplier enforcing Gauss' law to ensure that the fermionic content properly acts to source electric flux. The presence of an electron(positron) on a vertex increments(decrements) the quantized value the field on neighboring links. This process is predictable once a single link is defined (declaring the value of θ and/or the presence of closed loops of flux with periodic boundary conditions). As a result, there is only one dynamical link in the theory; this one link, along with the fermionic content, completely defines the physical lattice configuration of the field. With this observation, it is natural to consider "integrating out" or removing the Hilbert spaces (and thus the quantum registers) associated with all but one of the electric links.

To make the discussion of integrating the gauge field more concrete, consider the Schwinger model Hamiltonian in terms of spin operators

$$H = \frac{ag^2}{2}\left(\sum_{n=0}^{N-1} L_n^2 + \frac{\mu}{2}\sum_{n=0}^{N-1}(-1)^n\sigma_n^z + x\sum_{n=0}^{N-1}\sigma_n^+ L_n^+\sigma_{n+1}^- + \sigma_{n+1}^+ L_n^-\sigma_n^-\right) \quad , \tag{8.35}$$

where $\mu = \frac{2m}{g^2a}$ and $x = \frac{1}{g^2a^2}$. The relative negative signs on the mass terms of odd sites indicates that antimatter lives on sites with odd labels. For even sites (where all signs are positive), the larger contribution to the energy is the $|0\rangle = \begin{pmatrix}1\\0\end{pmatrix}$ state meaning that the spin up state is mapped to the electron-present state. By elimination, the spin-down state on even sites is the vacuum. On odd sites where the minus sign is present, it is the lower component that is the higher-energy contribution. Thus, the $|1\rangle = \begin{pmatrix}0\\1\end{pmatrix}$ state (or spin down) is identified with the presence of a positron and the spin up on these odd sites is the vacuum. Thus, the vacuum state (when beginning one's counting with 0) begins with an electron site in the down spin orientation and alternates from there: $\{1, 0, 1, 0, ..., 1, 0\}$. The direction of the change in the gauge field when an electron-positron vs positron-electron pair is created can thus be deduced. Beginning from the ground state and creating an electron-positron

pair at positions 0-1 causes an increase of the intermediate gauge field by 1. Alternately, creating a positron-electron pair from the ground state at positions 1-2 causes a decrease by 1 of the intermediate gauge link. To Summarize:

- Electrons live on even sites and are signaled by a spin-up/$|0\rangle$ state. From left-to-right, their presence increases the gauge field by 1 unit.

- Positrons live on odd sites and are signaled by a spin-down/$|1\rangle$ state. From left-to-right, their presence decreases the gauge field by 1 unit.

While these choices are largely conventional, consistency in convention is imperative for accurate calculation within the gauge invariant subsector so establishing a physical interpretation of the interactions of this lattice is valuable. The form of the Hamiltonian in Eq. 8.35 is written with quantum registers allocated for every one of N links in addition to the N qubits. To integrate out $N-1$ of the link Hilbert spaces, one needs only manually impose the Gauss' law constraint, that the following operator

$$\hat{L}_n - \hat{L}_{n-1} = \frac{\hat{\sigma}^z + (-1)^n}{2} \tag{8.36}$$

annihilates any physical state, where the right hand side counts the number of particles (electron or positron) on site n between links n and $n-1$. The encoded the link operators for zero background field and a single dynamical link chosen to reside at the end (or beginning) of the N-site lattice become

$$\hat{L}_n = \hat{L}_{N-1} + \frac{1}{2}\sum_{\ell=0}^{n}\left(\hat{\sigma}_\ell^z + (-1)^\ell\right) \quad . \tag{8.37}$$

Upon embedding the entire information of the gauge field into the value of the background electric field stored in a single register of qubits, the governing Hamiltonian becomes

$$H = \frac{ag^2}{2}\left(\sum_{n=0}^{N-1}\left[L_{N-1} + \frac{1}{2}\sum_{\ell=0}^{n}\left(\sigma_\ell^z + (-1)^\ell\right)\right]^2 + \frac{\mu}{2}\sum_{\ell=n=0}^{N-1}(-1)^n\sigma_n^z\right.$$

$$+x\sum_{n=0}^{N-2}\left(\sigma_n^+\sigma_{n+1}^- + \sigma_{n+1}^+\sigma_n^-\right) + x\left(\sigma_{N-1}^+ L_{N-1}^+\sigma_0^- + \sigma_0^+ L_{N-1}^-\sigma_{N-1}^-\right)\Bigg) \tag{8.38}$$

$$= \frac{ag^2}{2}\left(NL_{N-1}^2 + \sum_{n=0}^{N-1}\left[L_{N-1}\sum_{\ell=0}^{n}\left(\sigma_\ell^z + (-1)^\ell\right) + \frac{1}{4}\left(\sum_{\ell=0}^{n}\left(\sigma_\ell^z + (-1)^\ell\right)\right)^2\right]\right. \tag{8.39}$$

$$+\frac{\mu}{2}\sum_{n=0}^{N-1}(-1)^n\sigma_n^z + x\sum_{n=0}^{N-2}\left(\sigma_n^+\sigma_{n+1}^- + \sigma_{n+1}^+\sigma_n^-\right)$$

$$\left.+x\left(\sigma_{N-1}^+ L_{N-1}^+\sigma_0^- + \sigma_0^+ L_{N-1}^-\sigma_{N-1}^-\right)\right) \quad , \tag{8.40}$$

where the last term is present if spatial boundary conditions are chosen periodic. It is not a surprise that removing the gauge fields proliferates non-local interactions as the Hilbert spaces naturally imposing the local symmetry have been removed. The second term produces interactions demanding hub-spoke connectivity between each fermion site and the dynamical gauge link while the third term produces interactions (with magnitude scaling inversely with distance) between each pair of fermion sites. With this non-local Hamiltonian, the low-lying spectrum is unchanged in spite of dramatic qualitative changes to the wavefunction structure.

For implementation of the Schwinger model on quantum hardware, there is a third option that, like the original staggered formulation, retains locality of the Hamiltonian but, like the integrated gauge field formulation, reduces the gauge-variant Hilbert space. This is to project out the physical Hilbert space, mapping full physical configurations of the lattice to quantum states of a single lattice register. This choice is analogous to the mindset of removing unused notes from the keyboard to avoid accidentally striking them and thus generally requires non-trivial classical resources to prepare the Hilbert space for simulation (i.e., calculate Hamiltonian matrix elements in the symmetry projected space and process the resulting Hamiltonian for digital quantum implementation). This is the procedure implemented in following chapter where a $\sim$12 qubit calculation was projected and mapped onto the Hilbert space of two qubits. Beyond projecting into the physical subspace satisfying Gauss' law, projections were also made into the sector of positive CP symmetry. It is clear from the above discussion how the chosen representation of the gauge field may have

dramatic effects on demands of quantum hardware to simulate the Schwinger model. As quantum devices technologically evolve and advance, it will be increasingly important to command such theoretical flexibility to provide options for future codesign.

8.2 Introduction

Quantum field theories (QFTs), and in particular gauge field theories, provide the mathematical framework to describe three of the four fundamental forces of nature. In quantum chromodynamics (QCD), the gauge theory describing the strong interactions [253, 254, 255], the invariance of the laws of nature under $\mathrm{SU(3)_c}$ transformations necessitate the existence of eight gluon fields that transmit the forces between the quarks. When calculating QCD phenomena in the high energy (short distance) limit, perturbative techniques, such as Feynman diagram expansions, is efficacious. However, difficulties arise in applying such approaches to low-energy processes, in which color confinement and the spontaneous breaking of approximate chiral symmetries dominate structure and dynamics. This regime requires the use of low-energy effective field theories, such as chiral perturbation theory (χPT) [256], and numerical solutions using Lattice QCD (LQCD) [20]. Exascale classical computing will address Grand Challenge problems [257] in nuclear and high-energy physics by enabling high-precision LQCD calculations of many properties of hadrons and light nuclei as well as low-energy scattering processes. However, these resources are likely insufficient to address other questions and problems of importance, such as the structure, properties and dynamics of finite-density systems (due to the presence of sign problems in the algorithms used on conventional computers) or the fragmentation of high energy quarks and gluons into hadrons. Quantum computers may offer potential solutions in these systems that are inaccessible with conventional computing [37, 58, 59, 60, 25, 24, 64, 65, 66, 67, 68, 62, 69, 70, 71, 63, 72].

Existing and near-term quantum hardware is imperfect, with a small number of qubits, sparse qubit connectivity, and noisy quantum gates—all hallmarks of quantum computers in the NISQ (Noisy Intermediate-Scale Quantum) era [22]. These technical imperfections constrain the circuit depth and dimensionality of problems that can be solved on available

quantum computers. Nonetheless, recent advances in developing [25, 68, 70, 80, 82, 83, 72, 86] and implementing [64, 65, 67, 66, 69, 71, 75] quantum algorithms for QFT calculations have improved our understanding of the algorithmic complexity of the problem. On the other hand, rapid progress in quantum simulations of many-body systems, such as molecules and spin chains [258, 259, 260, 261], has mapped out potential ways to reduce complexity through combinations of classical and quantum computation methods, with variational approaches [262, 263] at the forefront of new developments.

In this work, we develop a hybrid quantum-classical computation strategy for a prototypical lattice gauge QFT—the Schwinger 1+1 dimensional model [264, 265] on the lattice. Using this strategy, we study the ground state properties as well as the real-time dynamics of particle and electric field energy density. In contrast to previous works [75, 97], we employ periodic boundary conditions (PBCs) endowing the lattice with discrete rotational symmetries and reflection symmetries. Projections into symmetry sectors lead to a refined classification of states in the Hilbert space by their momentum, charge and parity (projections used in LQCD calculations). This leads to a significant reduction of the Hilbert space of the system, confining calculations to physically allowed states. The task of determining the physical sectors of the Hilbert space is outsourced to classical computers. The dynamics of the model within each symmetry sector are evaluated using a digital quantum computer by applying unitary operators and implementing them as a sequence of one-qubit and two-qubit gates. As an exploration of what is currently practical on state-of-the-art quantum computers, we solve for the dynamics of the Schwinger model with one and two spatial lattice sites using IBM's quantum computer.

8.3 The Schwinger Model

Recent studies of the dynamic properties, such as charge fluctuations, entanglement entropy evolution, string breaking, and meson scattering in the Schwinger model have been performed in trapped ion systems [97, 75] or with classical tensor networks [83, 266, 267, 268]. In the former, open boundary conditions with vanishing background field are used to truncate

the gauge-field Hilbert space. Constraining the remaining non-dynamical links to satisfy Gauss's law results in long-range, two-body interactions that are feasible with trapped-ion-specific Mølmer-Sørensen gates, but are more severely burdensome in superconducting-circuit quantum computers. Our work enriches the current literature by retaining local interactions while removing from the calculation not only the exponentially-large, unphysical subspace but also the symmetry-sector-distinct regions of Hilbert space. As a result, inevitable errors occurring in today's noisy quantum systems are incapable of populating states outside of the correct, dynamical Hilbert space.

Considering first the theory with one spatial site, denoted as $0+1$, the dynamical degrees of freedom are two fermion sites ($N_{fs} = 2$), the electron and positron occupations, and two flux links. This system can be visualized as half of the $1+1$ system system with two spatial sites shown schematically in Fig. 8.1. Though there are many options in regulating the formally-infinite energy of the electric field, we choose to impose a cutoff on the energy in each electric flux link, $|l_n| \leq 1$ (this structure is reminiscent of U(1) quantum link models as discussed in [68]). Increasing this cutoff increases the physical Hilbert space dimension linearly and thus logarithmically increases qubit requirements. With two quantum states per fermion site and three per flux link, this system contains a total of 36 quantum states that naturally embed in the larger space of six qubits, one for each fermion and two for each link. These 36 states describe all sectors with charge $Q = 0, \pm 1$, with only a subset satisfying Gauss's law. Working in the $Q = 0$ sector, which can be connected to the strong-coupling ground state, reduces the number of states from 36 down to 5 (see Appendix A of Ref. [30]). Taking note of the utility of discrete space-time symmetries in nuclear and particle physics, we consider the transformation of these 5 states under the operation of $\hat{P}$, parity as defined by the symmetries of the staggered circle. The parity transformations reflect the system about axes that pass through two electron/positron sites. The 5 physical states are further classified into 3 $P = +1$ states and 2 $P = -1$ states. The quantum evolution of the $P = +1$ sector can be calculated using two qubits while that of the $P = -1$ sector using one qubit, thereby reducing the required number of qubits from 6 to 2. In these sectors, the

Hamiltonians take the form,

$$\mathrm{H}_{+} = \begin{pmatrix} -\mu & \sqrt{2}x & 0 \\ \sqrt{2}x & 1+\mu & x \\ 0 & x & 2-\mu \end{pmatrix}, \mathrm{H}_{-} = \begin{pmatrix} 1+\mu & x \\ x & 2-\mu \end{pmatrix}. \tag{8.41}$$

With two spatial sites, the state reduction procedure parallels that of the one-site theory. With an energy cutoff of $|l_n| \leq 1$ for each link, the 4 fermion sites and 4 flux links support a total number of 1296 quantum states contained in 12 qubits—a lattice-inspired implementation on a quantum computer with nearly 99.7% of the Hilbert space unphysical. Imposing the Gauss's Law constraint isolates the 13 physical states with $Q = 0$ (see Appendix A of Ref. [30]). These states can be projected against momentum. This corresponds to rotating the system by two (of the four) fermion sites and multiplying by a complex phase, $e^{-i\mathbf{k}\cdot\mathbf{x}}$ where $\mathbf{k}$ corresponds to an allowed momentum. The 13 states decompose into sectors defined by momentum, $\mathbf{k} = \mathbf{0}, \pm\mathbf{1}$ with 9 states residing in the $\mathbf{k} = \mathbf{0}$ sector, which contains the vacuum. The states in the $\mathbf{k} = \mathbf{0}$ sector can be further classified with respect to $\hat{P}$, providing a 5-state $P = +1$ sector and a 4-state $P = -1$ sector. For non-zero momentum, $\hat{P}$ transforms between states of opposite momentum, creating energy degeneracies between the momentum sectors. The Hamiltonians in these sectors are

$$\begin{aligned} \mathrm{H}_{\mathbf{k}=\mathbf{0},+} &= \begin{pmatrix} -2\mu & 2x & 0 & 0 & 0 \\ 2x & 1 & \sqrt{2}x & 0 & 0 \\ 0 & \sqrt{2}x & 2+2\mu & \sqrt{2}x & 0 \\ 0 & 0 & \sqrt{2}x & 3 & \sqrt{2}x \\ 0 & 0 & 0 & \sqrt{2}x & 4-2\mu \end{pmatrix}, \\ \mathrm{H}_{\mathbf{k}=\mathbf{0},-} &= \begin{pmatrix} 1 & \sqrt{2}x & 0 & 0 \\ \sqrt{2}x & 2+2\mu & -\sqrt{2}x & 0 \\ 0 & -\sqrt{2}x & 3 & \sqrt{2}x \\ 0 & 0 & \sqrt{2}x & 4-2\mu \end{pmatrix}, \end{aligned} \tag{8.42}$$

and $H_{\mathbf{k}=\pm\mathbf{1}} = \mathrm{diag}(1, 3)$, for which the nearest-neighbor interactions give rise to the band

diagonal structure. The naïve requirement of 12 qubits to describe this field theory has been reduced to 3. The matrices in Eq. (8.42) are organized in ascending total energy in the electric field. As the low-energy properties and dynamics of this system will become increasingly insensitive to contributions from high energy states, a further truncation can be made in which the total energy in the electric field is less than a second cutoff, $\tilde{\Lambda}$. To contain the $\mathbf{k} = \mathbf{0}$ $P = +1$ sector in two qubits, a cutoff of $\sum_n l_n^2 \leq 3 = \tilde{\Lambda}$ is imposed, which introduces a systematic error at the $\sim 1\%$-level in the low-lying energies for $x = 0.6$ and $\mu = 0.1$ (see Appendix B and F of Ref. [30]). It is important to note that these state reductions were accomplished with classical computing resources. The states comprising symmetry subspaces and Hamiltonian matrix elements over those subspaces were calculated using a classical computer. As can be seen in Appendix G of Ref. [30], these symmetry-projected Hamiltonian matrix elements require evaluations in an exponentially-growing Hilbert space. To explore systems larger than those that can be stored on a classical computer, it will be necessary to develop quantum algorithms to accomplish such reductions *in situ*.

8.4 Ground State Calculations

A reliable extraction of the ground state energy level in the $P = +1$ sector has been implemented using the variational quantum eigensolver (VQE) method [259] supplemented by classical Bayesian global optimization with Gaussian processes allowing for a minimal number of function calls to the quantum computer (for other implementations, see Refs. [117, 263]). The structure of the $P = +1$ Hamiltonian in Eq. (8.42) is that of a one-dimensional chain of $N = \tilde{\Lambda} + 1$ sites with local chemical potentials V_i and hopping amplitudes $t_{ij} = \sqrt{2}x$ for $|i - j| = 1$ and $t_{01} = t_{10} = 2x$. The chemical potential varies from one site to the next site by $1 \pm 2\mu$. From this perspective, it is known that a series of local and controlled rotations can construct the resulting N-site, real eigenfunction. VQE finds, with linear error extrapolation in the noise parameter r, the ground state energies of the $\mathbf{k} = \mathbf{0}$ and $\tilde{\Lambda} = 1, 2, 3$ spaces as $\langle H \rangle = -0.91(1)$ MeV, $-1.01(4)$ MeV, and $-1.01(2)$ MeV respectively (see Appendix E, H, and I of Ref. [30]). To manage inherent noise on the chip, we have performed computations

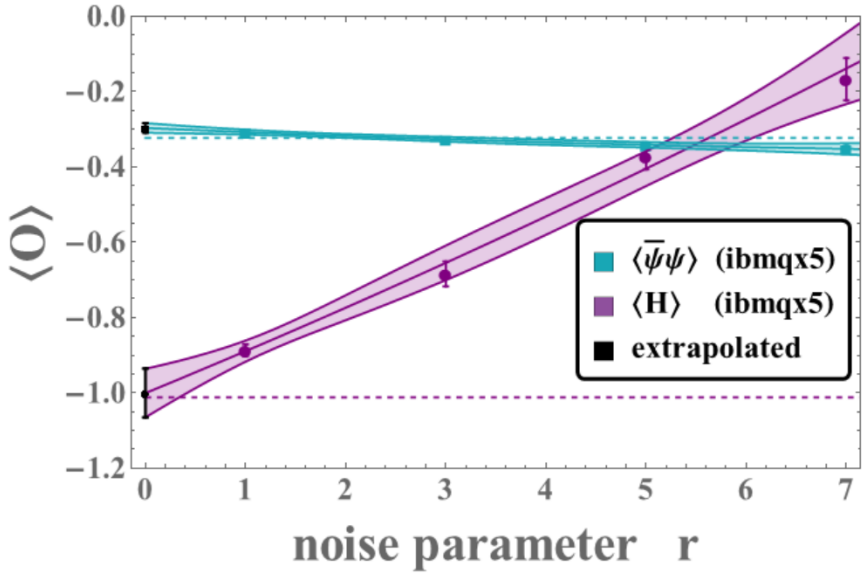

Figure 8.2: The $H^{\tilde{\Lambda}=3}_{\mathbf{k}=\mathbf{0},+}$ ground state energy and chiral condensate (purple, blue extrapolated to -1.000(65) and -0.296(13), respectively) expectation values as a function of r, the noise parameter. $r-1$ is the number of additional CNOT gates inserted at each location of a CNOT gate in the original VQE circuit. (1200 IBM allocation units and $\sim$ 6.4 QPU·s)

with a large number of measurement shots (8192 shots for ibmqx2 [269] and ibmqx5 [270]). For these variational calculations, the systematic measurement errors have been corrected via the readout-error mitigation strategy [261, 78]. Further, a zero-noise extrapolation error mitigation technique inspired by Refs. [271, 272] has been implemented. Examples of this zero-noise extrapolation technique are shown in Fig. 8.2, where the noise parameter r controls the accrual of systematic errors by inserting $r-1$ additional 2-qubit gates (CNOT^2) at every instance of a CNOT gate. In the limit of zero noise, this modifies CNOT simply by an identity.

For the results obtained on IBM quantum hardware, an estimate of the length of time the quantum processing unit (QPU) spent executing instructions based upon IBM benchmarking is provided [269, 270, 273]. This VQE calculation required 6.4 QPU-seconds and 2.4 CPU-

seconds with a total run time of 4 hours. Clearly, a majority of the time was spent in communications.

8.5 Dynamical Properties

Time evolving quantum systems is a key capability of quantum computers. Working with the $\mathbf{k} = \mathbf{0}$ $P = +1$ sector, we evolve the unoccupied state $|\chi_1\rangle_{\mathbf{k}=\mathbf{0},+}$ (see Fig. 8.1 and Appendix A of Ref. [30]) forward in time with two techniques. The first is through SU(4) parameterization of the evolution operator and the second is using a Trotter discretization of time. The former uses a classical computer to determine the 9 angles describing the time evolution over an arbitrary time interval, which is induced by the symmetric SU(4) matrix $U(\theta_i(t)) = e^{-i\mathrm{H}t}$, leading to the state $|\chi\rangle_{\mathbf{k}=\mathbf{0},+}(t) = U(\theta_i; t)|\chi_1\rangle_{\mathbf{k}=\mathbf{0},+}$ (see Appendix C of Ref. [30]). The most general form of the symmetric SU(4) matrix through its Cartan decomposition is $U = K^T C K$ where $C = e^{-i\sigma_x\otimes\sigma_x\theta_7/2} e^{-i\sigma_y\otimes\sigma_y\theta_8/2} e^{-i\sigma_z\otimes\sigma_z\theta_9/2}$ is generated by the Cartan subalgebra and K is a $\mathrm{SU}(2)\otimes\mathrm{SU}(2)$ transformation defined by the 6 angles, $\theta_{1,..6}$ [274, 275]. Fig. 8.3 shows the "zero-noise" extrapolated pair probability and expectation value of the energy in the electric field as a function of time calculated on ibmqx2 with the Cartan subalgebra circuit of Ref. [276].

The time evolution of this system has also been studied using a Trotterized operator (see Appendix D of Ref. [30]). It is discretized such that $e^{-i\mathrm{H}t} \rightarrow U_T(t, \delta t) = \lim_{N\rightarrow\infty} \left(\prod_j e^{-i\mathrm{H}_j \delta t} \right)^N$, where $\delta t = \frac{t}{N}$ and the Hamiltonian decomposition $\mathrm{H} = \sum_j \mathrm{H}_j$ (for the $\mathbf{k} = \mathbf{0}$ $P = +1$ $\tilde{\Lambda} = 3$ sector) is given by,

$$\begin{aligned} \mathrm{H} \;=\; & \frac{x}{\sqrt{2}}\, \sigma_x \otimes \sigma_x \;+\; \frac{x}{\sqrt{2}}\, \sigma_y \otimes \sigma_y \;-\; \mu\, \sigma_z \otimes \sigma_z \\ & + x \left(1 + \frac{1}{\sqrt{2}}\right)\, I \otimes \sigma_x \;-\; \frac{1}{2}\, I \otimes \sigma_z \\ & -\; (1+\mu)\; \sigma_z \otimes I \;+ x \left(1 - \frac{1}{\sqrt{2}}\right)\; \sigma_z \otimes \sigma_x \quad . \end{aligned} \tag{8.43}$$

We have optimized the sequence of operations in a first-order Trotterization. While Trotterization bypasses the classical resources needed in the previous time evolution implementation

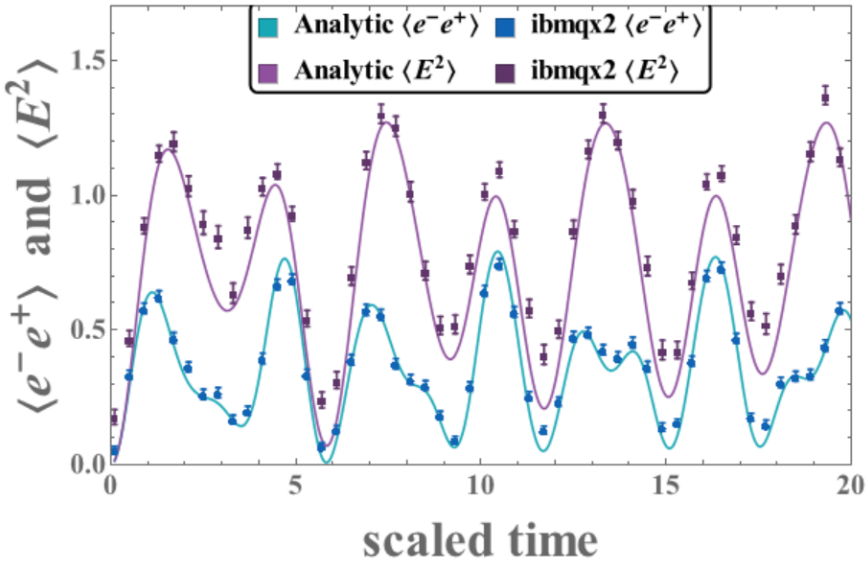

Figure 8.3: The probability of finding an e^+e^- pair (blue, lower line) and the expectation value of the energy of the electric field (purple, upper line) in the two-spatial-site Schwinger model following time evolution with $U(\theta_i(t))$ from the initial empty state. The solid curves are exact results while the the data points are quadratic extrapolations obtained with the ibmqx2 quantum computer using a circuit involving 3 CNOT gates [276]. (1000 IBM allocation units and $\sim$ 12.3 QPU·s)

to solve for the 9 angles of a symmetric SU(4) matrix, its demand for long coherence times is not satisfied with the T_2 times available on current quantum hardware. Using the reported gate specifications of ibmqx2 in terms of pulse sequences and their temporal extent, the T_2 coherence time of the device is reached after $\sim$ 10 time steps. This can be seen in Fig. 8.4 where the Trotterized evolution with $\delta t = 0.1$ saturates to the classical probability of 0.5 after a small number of steps—quantum coherence has been lost. This limitation in the number of coherent time steps encourages the use of larger values of δt (top data in shaded region), trading accuracy of the Trotterization for coherence maintained further into the time evolution. Even with this trade off, this method is currently unable to explore the low-energy

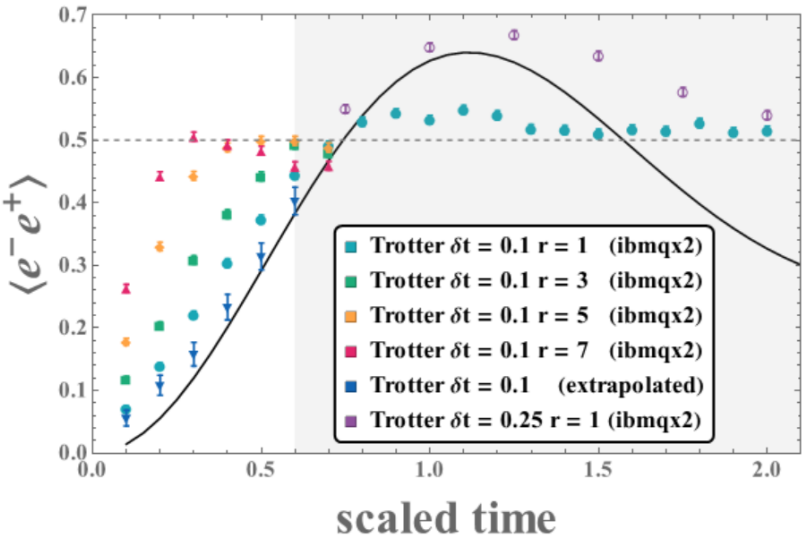

Figure 8.4: The probability of finding an e^+e^- pair in the two-spatial-site Schwinger model from the initial empty state following time evolution with $U_T(t, \delta t)$. In the unshaded region, the blue points (triangle markers with visible error bars) are quadratic extrapolations to zero noise using the data above each point at increasing values of the noise parameter, r. (260 IBM allocation units and ~ 3.6 QPU·s)

structure of the dynamic fluctuations.

8.6 Discussion and Outlook

Our work has identified key areas of future development needed to robustly explore quantum field theories with (imperfect) universal quantum computers. In order to explore more complex dynamics such as the scattering of hadrons or the time evolution of charge screening, a balance between the short-depth circuits of exact SU(2^n) propagator evolution and the manageable classical resources required to Trotterize must be developed. Regardless of the chosen method of time evolution, classical pre- and post-processing will continue to be invaluable for scientifically-relevant calculations on near-term quantum computers. By enforcing Gauss's law, momentum projecting states, and imposing the discrete symmetry of parity, the

exponential growth of the Schwinger model Hilbert space has been softened sufficiently to achieve calculations on IBM's superconducting quantum hardware. This reduction has made possible the exploration of static and dynamic observables within the current and foreseeable experimental quantum computing landscape lacking quantum error correction and limited by coherence times and gate fidelities. Requiring such a classical reduction in the process of building the physical, projected basis admittedly does not allow for advantage in the Hilbert space dimensionality accessible to the quantum vs classical computation. However, the space of advantage is multidimensional. By combining the strengths of the classical and quantum computers to respectively tame the Hilbert space and evolve it, the proposed heterogeneous framework profits in the exploration of time dependent, non-equilibrium, and finite density systems inaccessible to classical computations alone.

Our work represents one step toward solving QCD with NISQ era quantum computers to address Grand Challenge problems in nuclear and high-energy physics.

Chapter 9

SUBATOMIC MANY-BODY PHYSICS ON A QUANTUM FREQUENCY PROCESSOR

The content of this chapter is associated with Ref. [49]:
Hsuan-Hao Lu et al. "Simulations of Subatomic Many-Body Physics on a Quantum Frequency Processor". *Phys. Rev. A* 100.1 (2019), p. 012320. DOI: 10.1103/PhysRevA.100.012320. arXiv: 1810.03959 [quant-ph]

Along with the presence of vacuum fluctuations dynamically producing electron-positron pairs as simulated in Chapter 8, an additional property of interest from the perspective of nature is the localization of vacuum fluctuations to shield external charges. Through modification to the local Gauss' law constraint, placing the Hilbert space of a vertex into a higher super-selection sector, the vacuum can be analysed in the presence of a static charge. This combined heavy charge and localized shielding via vacuum fluctuations produce an effective heavy meson with a width and multi-particle interaction that can be characterized through variational preparation of the ground state on quantum hardware. Imagining the use of quantum devices not only to contribute to microscopic calculations of latticized fundamental fields but also to contribute to subsequent calculations in an effective field theory description, the quantum device could then be used to extend the microscopic calculations to larger systems of interacting heavy mesons. Rather than apply this thinking to an effective field theory of heavy mesons in the Schwinger model, the pionless effective field theory description of light nuclei was employed to quantumly calculate the binding energies of light nuclei. The stability and increased dimensionality of reliably controllable Hilbert space attainable with the quantum frequency processor allowed calculation of the three-body contributions to Schwinger model vacuum shielding effects and binding energies up to ^{4}He with controlled uncertainties.

Simulating complex many-body quantum phenomena is a major scientific impetus behind the development of quantum computing, and a range of technologies are being explored to address such systems. We present the results of the largest photonics-based simulation to date, applied in the context of subatomic physics. Using an all-optical quantum frequency processor, the ground-state energies of light nuclei including the triton (^{3}H), ^{3}He, and the alpha particle (^{4}He) are computed. Complementing these calculations and utilizing a 68-dimensional Hilbert space, our photonic simulator is used to perform sub-nucleon calculations of the two-body and three-body forces between heavy mesons in the Schwinger model. This work is a first step in simulating subatomic many-body physics on quantum frequency processors—augmenting classical computations that bridge scales from quarks to nuclei.

9.1 Introduction

Photonics is at the forefront of experimental quantum computing, as evidenced by pioneering demonstrations of the variational quantum eigensolver (VQE) algorithm [258, 259, 263], of molecular vibronic spectra and dynamics simulations [277, 278], and of experimental Hamiltonian learning [279]. It offers a versatile platform to process quantum information with low noise in a multitude of encodings, ranging from spatial or polarization degrees of freedom [280, 281], to temporal modes [282, 283]. Rapid progress in integrating optical components on-chip [284, 285, 286] is paving the way to large-scale spatial-encoding-based photonic quantum processors. Other encodings, however, also provide a path to scalable quantum architectures. For example, frequency encoding—routinely used in fiber optics to multiplex information transmission and processing—has been adapted for scalable quantum computing [287]. A single fiber can support thousands of frequency modes that can be manipulated in a massively-parallel fashion at the single-photon level. This particular framework for photonic quantum computing relies on qubits encoded in narrow frequency bins, where quantum gates are based on standard telecommunication equipment: electro-optic phase modulators (EOMs) and Fourier-transform pulse shapers [287]. A variety of basic quantum function-

alities have recently been demonstrated experimentally in this approach, in the form of a quantum frequency processor (QFP) [288, 289, 290].

Solving quantum many-body systems, whose resource requirements scale exponentially with the number of particles, is an area in which quantum devices are anticipated to provide a quantum advantage. Recently, quantum many-body problems in chemistry, condensed matter, and subatomic physics have been addressed with quantum computing using two-to-six superconducting qubits, for example Refs. [260, 261, 78, 30, 291], and up to tens of trapped ions, for example Refs. [75, 292, 293].

A major goal in nuclear physics research is to tie the effective field theory (EFT) descriptions of nuclear matter and heavy nuclei to their microscopic origin, quantum chromodynamics (QCD), through numerical calculations with lattice QCD. Important steps are being taken toward this objective [294, 295, 296, 297, 298, 299, 300, 301, 302, 303, 304, 305]. A hierarchy of EFT models [242, 306, 307] is used to describe heavier nuclei [308, 309, 310, 311], and lattice QCD calculations have been used to constrain EFT parameters over a range of unphysical quark masses [297, 296, 302, 303, 304]. However, such microscopic descriptions are computationally challenging for all but the lightest nuclei and hypernuclei [294, 295, 297, 298, 299, 300, 301] due to signal-to-noise problems [312, 313, 314, 315, 316]. Augmenting classical calculations with their quantum counterparts [317, 25, 24, 95] offers an analogous roadmap for quantum-enabled subatomic physics as depicted in Fig. 9.1. At the EFT level, a subatomic system can be simulated as a collection of nucleons with EFT parameters input from experimental data or from *ab initio*, Minkowski-space quantum simulations of lattice QCD. In this article, we take the first steps to meeting this Grand Challenge.

Here we report the first application of a QFP to many-body subatomic systems. With Hilbert spaces of up to 68 dimensions, this work represents the largest simulation of nuclei and lattice field theories on a photonic device to date. Using an EFT description, we experimentally implement the VQE algorithm to calculate the binding energies of ^{3}H, ^{3}He, and ^{4}He. Further, for the first time, we employ VQE to determine the effective interaction potential between composite particles directly from an underlying lattice quantum gauge field

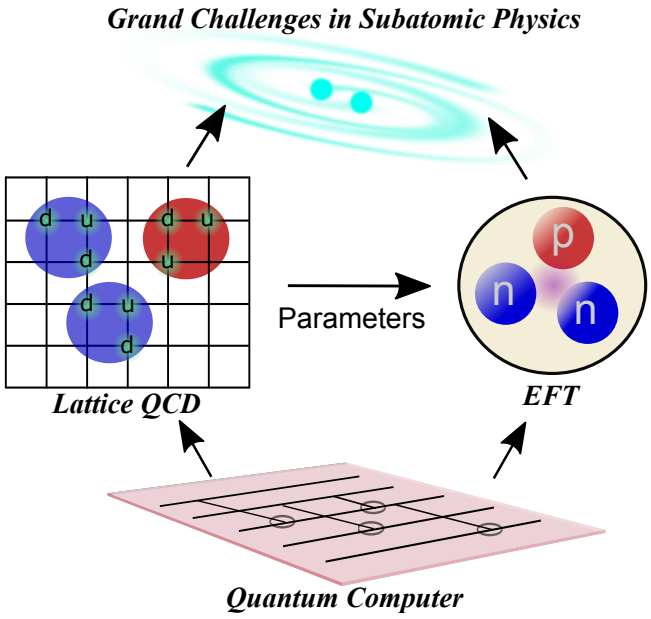

Figure 9.1: Quantum simulation for subatomic physics. Ideally, quantum simulation applied to both QCD (left-side) and EFT (right-side) will enable high-precision predictions of static and dynamic properties of nuclei and nuclear matter. EFT parameters may be determined from experiment, or by a complementary program of classical and quantum simulation.

theory, the Schwinger model. This serves as an important demonstration of how EFTs themselves can be both implemented and determined from first principles by means of quantum simulations.

9.2 Quantum Frequency Processor (QFP)

For implementing quantum simulations, we utilize our previously-developed QFP: a photonic device that processes quantum information encoded in equispaced narrow-band frequency bins, described by operators $c_n^\dagger$ (c_n) for $n \in \mathbb{Z}$ that create (annihilate) a photon in a mode centered at $\omega_n = \omega_0 + n\Delta\omega$, where $\Delta\omega$ is the frequency bin spacing and ω_0 is an offset [318, 287]. An arbitrary, unitary mode transformation matrix V can be implemented on QFP by interleaving pulse shapers and EOMs [287], and recent experiments have demonstrated

high-fidelity single-qubit [288, 289] and two-qubit [290] gates.

Figure 9.2 shows the experimental setup for our all-optical QFP. The input state preparation, frequency operations, and final energy measurements can all be realized with off-the-shelf fiber-optic components, including EOMs (EOSpace), pulse shapers (Finisar), and an optical spectrum analyzer (OSA; Yokogawa). The capability of transmitting optical information within a single-mode fiber from generation to detection facilitates parallel computations in a low-noise fashion.

As detailed in the Methods, for many-body Hamiltonians projected onto single-particle sub-spaces a variational wavefunction can be mapped onto a mode-entangled state of a single photon, so that the state preparation procedure in the VQE algorithm amounts to coherent frequency comb generation. However, more complicated (e.g., multi-photon) entangled photonic states could be employed as well, modifying only the "State Preparation" portion of the apparatus in Fig. 9.2. By working with multiple photons in the QFP, qubit degrees of freedom can be identified with photon occupations of frequency-bin pairs. For example, 10 frequency bins, discussed below, can be mapped onto 5 qubits with a 5-photon input state. Such a mapping and the ability to implement a universal gate set endows the QFP with similar quantum capabilities and scaling as other digital quantum devices. Note that the QFP utilized in this work can in principle support the Hilbert space of up to 33 qubits [288] [1]. Scaling this hardware to larger numbers of qubits will require further engineering in order to build multiple multi-photon sources and reduce loss in the system, which should ultimately enable a concrete quantum advantage over classical computing. This quantum advantage is not present in the single-photon methods employed in this work.

In this initial experiment, however, we focus on the simpler case of single-photon encoding for demonstrating the basic approach. The source we utilize for the state preparation is a wavelength-division multiplexing transmitter (Ortel) possessing four continuous-wave (CW) laser modules emitting single-tone optical signals at 192.0, 192.4, 192.8, and 193.2 THz. We

[1] Significant technical challenges remain in demonstrating entangling operations in a space of this size

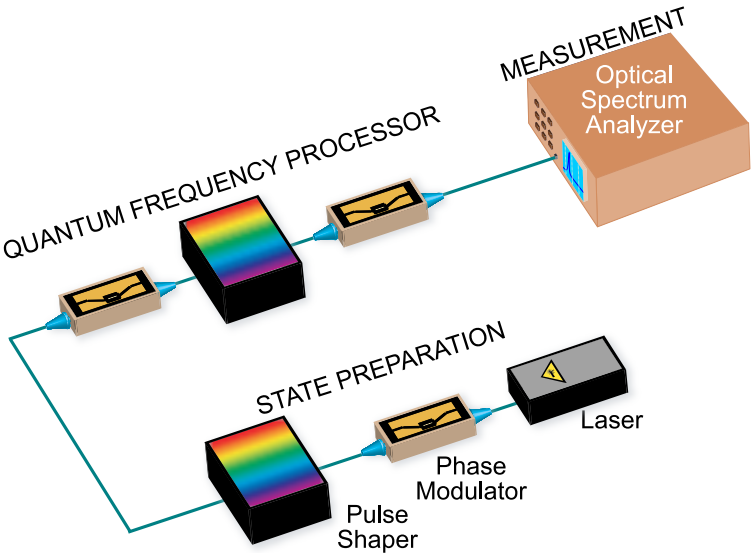

Figure 9.2: Experimental setup including our all-optical quantum frequency processor.

combine all four signals with a fiber coupler and send them through an EOM driven at 25 GHz, which creates four parallel frequency combs at the output (each of which contains ∼10 frequency bins) with a total of 40 available comb lines. This allows us to implement up to eight parallel Hadamard gates (50/50 beamsplitters): two comb lines per gate plus four comb lines for guardbands (i.e., two gates per each 10-line subcomb) to prevent cross-contamination during the subsequent frequency beamsplitting operations (photons from one gate jumping over to an adjacent gate during the calculation) [288]. We then choose the best five beamsplitters for the subsequent operation, excluding those with higher imbalance in reflectivity and transmissivity. Note that despite these calibration measures, we still observe the residual non-uniform performance across different gates stemming from the noise background of the input light source, and the optical path length change in the QFP due to temperature drifts in long-term measurements. Finally, filtering out extra input frequencies, as well as manipulating amplitude and phase for all five remaining frequency-bin pairs, is realized by a pulse shaper immediately following the comb generation.

9.3 Mapping Systems onto the QFP

In all quantum simulations here, our starting point is a second-quantized Hamiltonian $\mathcal{H}_{SQ}$ which, depending on the problem, contains one-, two-, and three-particle terms written as products of fermionic creation and annihilation operators. Our goal for these Hamiltonians is to compute the smallest eigenvalue using the QFP hardware. A scalable path to this goal has been outlined in the literature in the form of the VQE algorithm [117]. There, each fermionic operator in $\mathcal{H}_{SQ}$ is mapped onto a set of qubits such that fermionic commutation relationships are preserved. As a result $\mathcal{H}_{SQ}$ is mapped onto $\tilde{\mathcal{H}}_{SQ}$ which is a sum of strings of Pauli operators. Then quantum hardware is used to prepare a variational trial quantum state of qubits $|\Psi = \Psi(\theta_1, \cdots, \theta_M)\rangle$ in the form of a parameterized quantum circuit with M parameters. Subsequently, the expectation value of the Hamiltonian in the state $|\Psi\rangle$, $\langle\Psi|\tilde{\mathcal{H}}_{SQ}|\Psi\rangle$, is computed by repeating the state preparation and energy measurement multiple times. A classical computer calculates the direction in the parameter space and new parameter values $\{\theta'_1, \cdots, \theta'_M\}$ that yield a lower energy value. The energy calculation is then repeated on quantum hardware with the updated trial state $|\Psi(\theta'_1, \cdots, \theta'_M)\rangle$ until a (local) minimum of the energy is obtained.

For all pre-error-corrected quantum hardware—of which the QFP is an example—the depth of the circuit that prepares and measures the variational state $|\Psi\rangle$ is limited by noise. This effectively limits the size of fermionic systems that can be simulated on existing devices. To extend quantum simulations to subatomic systems beyond the deuteron [78] and Schwinger models beyond two spatial lattice sites [75, 30], we have recently proposed a preconditioning strategy [30] that transforms $\tilde{\mathcal{H}}_{SQ}$ into block-diagonal form by projecting it onto eigenstates of operators that represent good quantum numbers (e.g., parity, momentum, total spin) for the system of interest. As a result $\tilde{\mathcal{H}}_{SQ} = \bigoplus_i \mathcal{H}_i$, where $\mathcal{H}_i$ can now be interpreted as single-particle Hamiltonians acting on smaller subspaces than the original Hilbert space corresponding to $\tilde{\mathcal{H}}_{SQ}$. A Hamiltonian $\mathcal{H}_i$, specified by a $d \times d$ Hermitian matrix with elements h_{kl} in some basis, can be mapped onto a Hamiltonian $\mathcal{H}^i_{QFP}$ that describes

a frequency bin multiport device implementable with the QFP:

$$\mathcal{H}^i_{QFP} = \sum_{k=0}^{d-1} h_{kk} c_k^\dagger c_k + \sum_{\substack{k,l=0 \\ k<l}}^{d-1} [h_{kl} c_k^\dagger c_l + h_{kl}^* c_l^\dagger c_k], \tag{9.1}$$

where h_{kl} are the entries in $\mathcal{H}_i$. In this encoding, we have mapped the original Hamiltonian $\tilde{\mathcal{H}}_{SQ}$ onto a set of single-particle systems defined by Eq. (9.1). To find ground-state energies of each single-particle Hamiltonian $\mathcal{H}_i$ we implement a variant of the VQE algorithm adapted for the QFP hardware. For the trial variational wavefunction $|\Psi\rangle$ we utilize an ansatz based on unitary coupled-cluster (UCC) theory [117]. The UCC wavefunction can be written as

$$|\Psi\rangle = \exp\left(\sum_{k=1}^{d-1} \theta_k [c_0^\dagger c_k - c_k^\dagger c_0]\right) |10\cdots0\rangle, \tag{9.2}$$

where the state $|0\cdots1_k\cdots0\rangle$ denotes a single excitation (photon) in the frequency bin k, and none in the remaining $d-1$. The operator exponent can be evaluated explicitly in this case, leading to the following $(d-1)$-parameter state,

$$|\Psi\rangle = \cos\phi\,|10\cdots0\rangle - \frac{\sin\phi}{\phi} \sum_{k=1}^{d-1} \theta_k |0\cdots1_k\cdots0\rangle, \tag{9.3}$$

with $\phi = \sqrt{\sum_{k=1}^{d-1} \theta_k^2}$. In the context of the QFP, the UCC wavefunction $|\Psi\rangle$ represents a superposition of a single photon over d frequency bins.

With the Hamiltonian and UCC wavefunction defined, we use our QFP to estimate the expectation value $\langle \mathcal{H}^i_{QFP} \rangle = \mathrm{Tr}\left[|\Psi\rangle\langle\Psi| \mathcal{H}^i_{QFP}\right]$ for given parameter values $\{\theta_k\}$, by first preparing $|\Psi\rangle$ and experimentally reconstructing the elements of the single-particle density matrix $\rho_{kl} = (1/2)\langle\Psi|c_k^\dagger c_l + c_l^\dagger c_k|\Psi\rangle$. Measuring ρ_{kl} is equivalent to placing the state $|\Psi\rangle$ on a 50/50 beamsplitter implemented between frequency bins k and l, and recording the difference in the flux of detected particles in those modes immediately after the beamsplitter. Similarly, elements ρ_{kk} can be measured by preparing the state $|\Psi\rangle$ and measuring the photon flux in each mode k by using a photodetector. After repeating this process for all combinations of modes k and l, $\langle \mathcal{H}^i_{QFP} \rangle = \mathrm{Tr}[\rho \mathcal{H}^i_{QFP}] = \sum_{kl} \rho_{kl} h_{kl}$ can be estimated. Recent formulations of

VQE, which use the current estimate of the energy $\langle \mathcal{H}^i_{QFP} \rangle$ to generate parameter updates $\{\delta\theta_k\}$ via a gradient-based classical optimizer, generally require many evaluations of $\langle \mathcal{H}^i_{QFP} \rangle$ to arrive at converged parameters. We instead use a new method which merges the UCC ansatz with a many-body formalism called the anti-Hermitian contracted Schrödinger equation [319]. This allows us to approximate the gradient of parameters using the measured ρ_{kl} of each iteration [320] and arrive at convergence with significantly fewer evaluations of $\langle \mathcal{H}^i_{QFP} \rangle$. For example, in the problems we explore here our method required ∼20 iterations to converge compared to ∼500 iterations when using the BFGS algorithm [321].

In practice, the measurement of the elements ρ_{kl} using the single-photon state $|\Psi\rangle$ as an input is equivalent to a measurement with a coherent frequency comb where the relative amplitude of each comb line is set to $\theta_k \sin\phi/\phi$ (for lines $k = 1, \ldots, d-1$) and $\cos\phi$ (for the line $k = 0$) with respect to a reference coherent-state amplitude α. Indeed, one can verify by a direct calculation that $\langle \Psi_{\text{comb}} | \mathcal{H}^i_{QFP} | \Psi_{\text{comb}} \rangle = |\alpha|^2 \langle \Psi | \mathcal{H}^i_{QFP} | \Psi \rangle$ where,

$$|\Psi_{\text{comb}}\rangle = |\alpha \cos\phi\rangle \otimes |\alpha e^{i\pi} \frac{\theta_1 \sin\phi}{\phi}\rangle \otimes \cdots \otimes |\alpha e^{i\pi} \frac{\theta_{d-1} \sin\phi}{\phi}\rangle. \tag{9.4}$$

Moreover, the measurements of ρ_{kl} for non-overlapping sets of indices k, l can be implemented in parallel, thus reducing the simulation time, as the QFP has an intrinsic ability to perform the same operation on different sets of modes in parallel. Previously, we implemented near-unity fidelity frequency-bin beamsplitters in parallel, with a theoretical predicted fidelity $\mathcal{F} = 0.9999$. Such Hadamard gates can be achieved by driving two EOMs with π-phase-shifted sinewaves at frequency $\Delta\omega$ (with maximum temporal phase modulation $\Theta = 0.8169$ rad), and applying a step function with π-phase jump between the two computational modes on the central pulse shaper. The corresponding beamsplitter possesses 47.81% reflectivity $\mathcal{R}$ (mode-hopping probability) and 49.79% transmissivity $\mathcal{T}$ (probability of preserving frequency), with 2.4% of the photons scattered outside of the computational space.

Despite such high fidelity, the residual imbalance in $\mathcal{R}$ and $\mathcal{T}$ is undesirable, leading to higher error in calculation of the ρ_{kl} elements. Accordingly, in this work we further reduce the Hadamard gate's bias, achieving $\mathcal{R} = 48.7\%$ and $\mathcal{T} = 48.77\%$ (corresponding to a fidelity

$\mathcal{F} = 0.999999$) by increasing Θ to 0.8283 rad on both EOMs, while the QFP's central pulse shaper remains unchanged.

After setting up the Hadamard gates, we utilize the first pulse shaper to equalize the amplitude across all ten input frequency bins. The relative spectral phase within every frequency pair is also fine-tuned until we find the in-phase condition as the reference—defined such that the lower (higher) frequency bin obtains the maximum (minimum) optical power after the Hadamard operation. To compute ρ_{kl}, we manipulate the relative amplitude and phase of a frequency pair c_k and c_l, and record the optical power difference between two modes after the beam-splitting operation. To reconstruct the full density matrix, a total number of $d(d-1)/2$ beam-splitting operations is required in every iteration. Hence, the usage of five parallel beamsplitters (as well as the natural parallelization in pulse shapers and the OSA) reduces the required number of computations by a factor of five, before updating the trial state for the next iteration.

9.4 Nuclear Structure Calculations

Organizing principles rooted in the global symmetries of QCD have been successfully encoded in low-energy EFT frameworks describing nuclear forces, providing a systematically-improvable approach to calculations of nuclei. At low resolution, i.e. at long wavelengths, details about the strong but short-ranged nuclear forces, or about QCD, are not revealed, and the lightest nuclei can be understood in terms of contact interactions of pairs and triplets of nucleons [171, 173, 172, 322, 242]. In our model, we employ a Hamiltonian at next-to-leading order (NLO) in pionless EFT and adjust its parameters to the S-wave effective range expansions and the deuteron binding energy; the strength of the three-body contact is adjusted to the triton binding energy. The Coulomb force between protons is also included. We employ a finite basis consisting of eigenstates of the spherical harmonic oscillator with energy spacing $\hbar\omega = 22$ MeV in a discrete variable representation [323, 304], with the two-body and three-body potentials acting only between states with excitation energies up to and including $2\hbar\omega$. This discretization maps nucleon fields onto annihilation operators with

an interaction-momentum cutoff of 337 MeV. Next, we project this second-quantized Hamiltonian $\mathcal{H}_{SQ}$ onto Hilbert spaces with spin and parity of $J^\pi = 0^+$ for ^{4}He and $J^\pi = 1/2^+$ for ^{3}H and ^{3}He, and the resulting Hamiltonian matrices $\mathcal{H}_i$ are evaluated for the smallest eigenvalue on the QFP, as described in the Methods.

Figure 9.3 shows the ground-state energies of ^{3}H, ^{3}He, and ^{4}He computed with the VQE algorithm on the QFP, as a function of the effective spatial extent, L, of the model space. For the weakly-bound three-nucleon states of ^{3}H and ^{3}He, the energy is found to decrease noticeably with increasing L. For these systems as well as ^{4}He, extrapolations to large model spaces can be reliably performed (shown as shaded regions) using the leading-order expression given in the supplemental material. For each nucleus, the model-space-extrapolated binding energy (shown as the red point at right) is consistent within systematic-dominated uncertainties with the corresponding tuned NLO EFT prediction. We note that the underlying Hamiltonian of NLO pionless EFT is known to reproduce experimental data to much better than the naive $\sim 10\%$ accuracy based upon power counting due to the relative size of

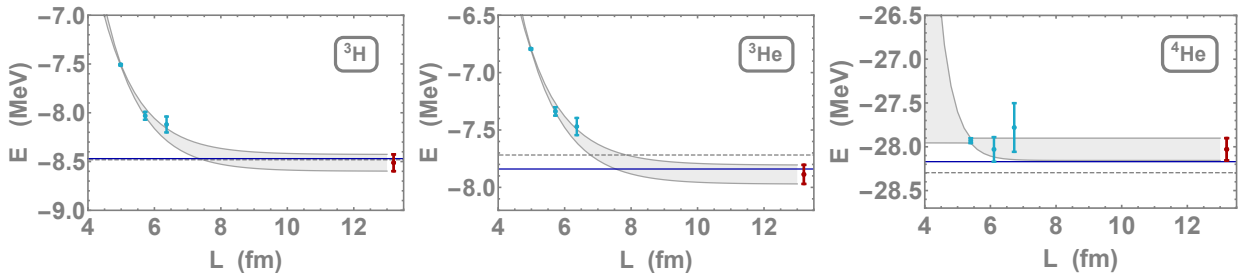

Figure 9.3: Results of the nuclear ground-state energies for ^{3}H, ^{3}He, and ^{4}He nuclei computed with the QFP (blue data points) for Hilbert spaces with effective spatial extent L with estimated systematic uncertainties. Also shown are the leading-order extrapolations to infinite model spaces with propagated uncertainties (gray bands), the resulting extrapolated energies E_∞ (red point at right), the tuned NLO EFT predictions (dark blue solid line), and the known high-precision values of the binding energies (dashed gray line).

coefficients in the effective range expansion.

9.5 Schwinger Model Simulations

Quantum Electrodynamics in 1+1 dimension, the Schwinger model [264, 265], has been long-studied as an example of confinement and chiral symmetry breaking in quantum field theory [324], and is receiving new attention in the context of quantum simulation [325, 326, 327, 328, 329, 330, 331, 332, 75, 30]. To represent this continuous theory on computational devices, we employ staggered fermions [251] mapped to spin degrees of freedom as shown in Appendix D of Ref. [49]. Fluctuations in the truncated, quantized electric field are accompanied by pair (e^+e^-) creation/annihilation satisfying Gauss's law. Previous works have calculated static and dynamic observables resulting from these fluctuations on quantum devices [75, 30]. In this article, we introduce non-dynamical static charges, which are screened by deformations in the quantum vacuum and interact with the fermions only through their contribution to Gauss's law. Such systems are analogous to mesons found in nature containing a bottom or charm quark; thus we denote them "heavy mesons". The Hilbert space of each static charge distribution is reduced by enforcing Gauss's law and projecting onto ground-state quantum numbers of parity and charge conjugation.

The energy and wavefunction of the vacuum, of single static charges, of two like-sign and two-opposite sign static charges separated by a distance r, and of three static charges of the distinct charge combinations separated by distances r_{12} and r_{13} were calculated on the QFP by applying VQE to eight-fermion-site, Schwinger-model Hamiltonians. These solutions may be combined to compute the heavy-meson mass, the full potential energy between two and three static charges over a range of separations, and local modifications to the vacuum structure due to static charges. As an example, Fig. 9.4 shows the local e^+ and e^- probabilities and energy density of the electric field for the ground state of two static negative charges with separation ($r = 2$), computed from the VQE results. Using this and the other four configurations of two-body static charges (see Appendix A and E of Ref. [49]), Fig. 9.5 (left) shows the potential energy as a function of separation. For distances large compared with the radius of the heavy meson, the potential is expected to fall as the sum

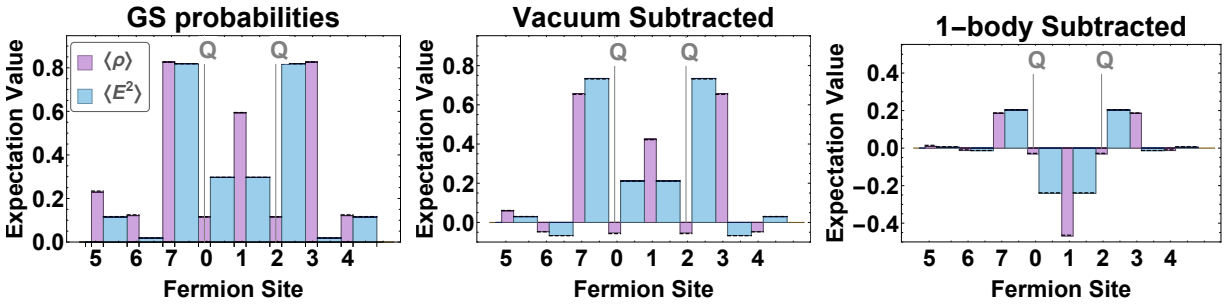

Figure 9.4: The e^+e^- densities ($\langle\rho\rangle$) and energy-density in the electric field ($\langle E^2\rangle$) for $Q = -1$ static charges separated by one spatial lattice site. The left panel shows the raw distributions, the center panel has the vacuum removed, and the right panel also has the contributions from the individual charges removed. The horizontal black dashed lines are the analytic values of the local densities, while the error bands (not seen on this scale) represent fluctuations over the last ten iterations of the VQE.

of exponentials with arguments set by the light-hadron spectrum. Short-distance deviations from these forms are expected to be a small effect in subsequent analyses. Fitting to the results of the QFP, including the effect of image charges from the boundary conditions, and isolating the infinite-volume limit, gives the phenomenological fit potentials in Fig. 9.5. These phenomenological potentials are matched through the Schrödinger equation to a low-energy EFT description of the Schwinger model in terms of local contact operators, the analogue of the pionless theory, $\mathcal{H} = -C_N(N^\dagger N)^2 + ...$ at leading order for a given heavy meson mass. The three-body potentials are extracted in similar ways, with the two-body potentials removed. Two slices of the three-body potential are displayed in Fig. 9.5 (right two panels) showing expected rapid suppression as the bodies separate. Phenomenological three-body potentials can further be extracted and used to constrain the coefficients of three-body EFT parameters.

Note that the demonstrated calculation is for a single lattice spacing and spatial volume. Modifying these parameters towards the continuum would provide higher resolution of

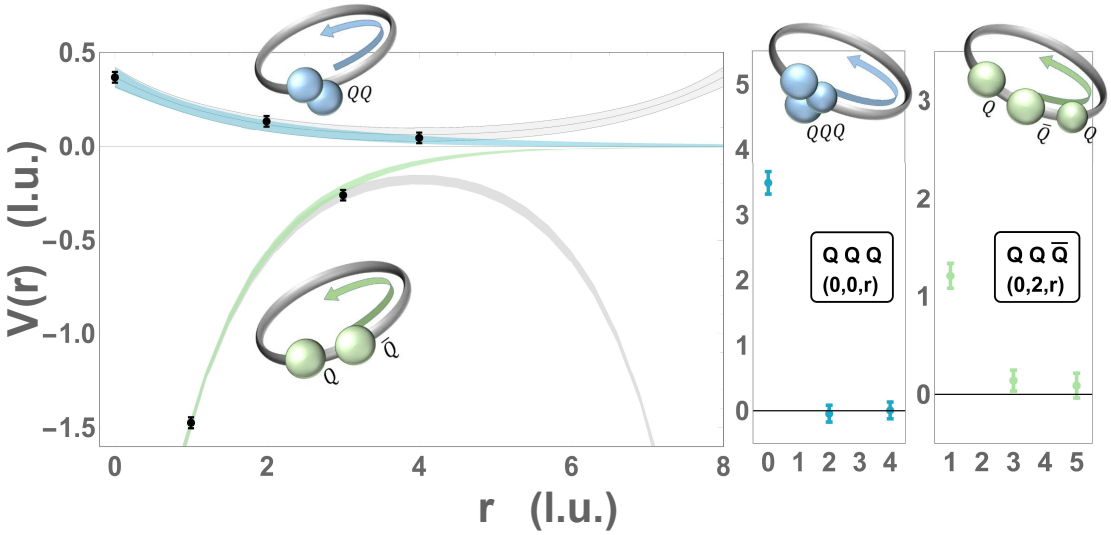

Figure 9.5: The left panel shows the potential between two like-sign static charged sources (upper curves) and between opposite-sign charges (lower curves) as a function of separation (in lattice units). The symmetric gray curves represent the extracted lattice potential including the presence of image charges. The blue and green bands represent the infinite-volume potentials using correlated extracted values of the couplings and masses (see Appendix E of Ref. [49] for details). The center panel shows the three-body potential for three like-sign static charges. The right panel shows the three-body potential for two like-sign and one opposite-sign static charges.

extracted potentials and corresponding EFT parameters.

9.6 Discussion

Establishing a direct connection between the fundamental building blocks of our universe, the quarks and gluons, and the properties and dynamics of matter under a range of conditions faces challenges beyond the capabilities of foreseeable classical computation. From exponentially-growing Hilbert spaces required to describe nuclei, to sign problems in evaluating finite density systems, anticipated developments in quantum devices and quantum information offer the hope of addressing Grand Challenge problems in subatomic physics. For example, VQE algorithms implemented with error-corrected qubits are anticipated to provide a scalable path to solving these problems on future quantum devices. However, currently-available hardware is too noisy to demonstrate such quantum advantages. Here, we explored a way to implement VQE optically using the QFP with classical pre-processing. In particular, we use classical resources to project many-body fermionic Hamiltonians corresponding to nuclear and quantum field theory systems onto a hierarchy of single-particle Hamiltonians that can be simulated efficiently on the QFP. This demonstration of controlled, single-photon-equivalent, quantum-correlated manipulation is a first step towards scalable QFP simulations where input states are modified to consist of multiple photons. Together, the QFP and such state preparation of higher complexity is expected to require resources that scale polynomially with the size of the quantum system and thus exhibit a quantum advantage.

In this work, we have presented results from the largest photonics-based quantum simulation, using an all-optical quantum frequency processor, to demonstrate the potential of quantum technology for calculations in subatomic physics. We presented the two-body and three-body interactions between composite objects informing the low-energy EFT of the Schwinger model, which shares characteristics with QCD. Further, representing a key ingredient in the connection between quarks, gluons and nuclei, a low-energy EFT of QCD was used to calculate the binding energies of ^{3}H, ^{3}He, and ^{4}He. While the results of our calculations are not of comparable complexity or precision to those that can be achieved

today with classical computation, they are an encouraging first step in exploring the utility of optical quantum devices for addressing Grand Challenges in subatomic physics.

Chapter 10

DIGITIZATION AND SIMULATION OF SU(2) GAUGE THEORY

The content of this chapter is associated with Ref. [31]:
Natalie Klco, Jesse R. Stryker, and Martin J. Savage. "SU(2) non-Abelian gauge field theory in one dimension on digital quantum computers". *Phys. Rev. D* 101.7 (2020), p. 074512. DOI: 10.1103/PhysRevD.101.074512. arXiv: 1908.06935 [quant-ph]

In this chapter, a dynamical quantum simulation of SU(2) non-Abelian gauge field theory on a digital quantum computer is presented. This was enabled on current quantum hardware by introducing a mapping of the field onto a register of qubits that utilizes local gauge symmetry while preserving local constraints on the fields, reducing the dimensionality of the calculation. Controlled plaquette operators and gauge-variant completions in the unphysical part of the Hilbert space were designed and used to implement time evolution. The new techniques developed in this work generalize to quantum simulations of higher dimensional gauge field theories.

10.1 Introduction

Non-Abelian gauge field theories play a central role in the description of the known forces of nature. Since the early 1970's, the strong interactions that define the nuclear forces and the dynamics of quarks and gluons in the early universe are known to emerge from an unbroken SU(3) local gauge symmetry, defining quantum chromodynamics (QCD) [254, 255, 333]. Similarly, the electroweak interactions are known to result from the spontaneous breaking of $\mathrm{SU}(2)_L \otimes \mathrm{U}(1)_Y$ local gauge symmetries [128, 127, 129, 130]. Great success has been achieved in computing the properties and low-energy dynamics of hadronic systems using the numerical technique of lattice QCD [20, 334] on the world's largest supercomputers. Current

lattice QCD calculations at the physical quark masses have resulted from a sustained co-development effort over the last ~ 50 years. Those developments began with calculations on small lattices, with unphysical quark masses, and with large lattice spacings using computers available during the 1970's [334]. While good progress is being made in designing Hilbert spaces for [25, 24, 68, 70, 62, 335, 336, 102, 73, 337, 338, 339, 340, 74, 45, 217, 216, 341, 342], creating detailed hardware-specific proposals for [65, 64, 66, 67, 69, 343, 344, 81, 345, 95, 71, 72, 346, 87, 218, 347], and implementing [75, 30, 49, 26, 348, 215] quantum field theories on quantum devices, non-Abelian gauge theories have not yet been simulated on today's limited and noisy hardware. It is in the spirit of the early days of lattice gauge theory that we develop an improved algorithm to evolve a string of SU(2) plaquettes, and use it to simulate a non-Abelian gauge field theory on IBM's digital quantum hardware.

The Hamiltonian formulation of lattice gauge theories [244] includes exponentially-large sectors of unphysical [1] Hilbert space in order to maintain spatially-local interactions while satisfying gauge constraints. The hardware error rates and gate fidelities of current NISQ-era [22] quantum devices, and the lack of error correction capabilities, allow quantum states to disperse into these unphysical sectors. To avoid such dispersion, previous quantum simulations of lattice gauge theories have employed various procedures to remove the unphysical Hilbert space from the embedding onto quantum devices [75, 97, 30, 215, 49]. However, these techniques do not scale efficiently, and a generic description for multi-dimensional lattices with non-trivial gauge groups in terms of only local, physical degrees of freedom is not currently known. A variety of approaches for quantumly simulating gauge theories are being pursued—reformulating the interactions, lattice structure, and degrees of freedom by designing Hilbert space bases of group elements, Schwinger bosons, duality transformations, loop variables, tensor networks, and more [244, 349, 350, 351, 352, 60, 353, 64, 354, 355, 356, 357, 358, 359, 360, 361, 362, 81, 71, 363, 90, 89, 217, 74, 364, 214, 216, 365, 91, 219, 366]—often with the explicit goal of mitigating unphysical degrees of freedom. Reductions

[1] The space referred to as unphysical can be naturally interpreted as isolated Hilbert spaces with non-zero external sources.

have been obtained by solving Gauss's law, which is related to loop formulations where the fundamental degrees of freedom are gauge invariant [367, 368, 369, 370, 371, 372, 373, 374, 375, 376, 352, 357, 377]. Proposed for both analog and digital quantum implementation, progress is being made toward using renormalization group methods to connect quantum link models [378, 379, 380, 381, 70, 382, 67, 344] to continuum theories of importance [381, 383, 384, 385]. Classical numerical explorations of truncation errors arising from gauge field digitization in lattice QCD calculations [217], and exploring the use of the crystal groups associated with SU(3) to discretize the gluon fields for quantum simulations have begun [342]. Here marks the introduction of an explicit quantum algorithm for digital implementation of dynamics with generalizable operator structures.

In this work, the angular momentum basis [244, 349, 350] is utilized, which is made computationally feasible on quantum devices by exploiting the local gauge symmetry to remove the angular momentum alignment variables. A similar reduction in degrees of freedom has been suggested to be an advantageous mapping for quantum simulations [73], and has been employed in calculations using matrix product states. The associated qubit mapping, along with the flexibility of the introduced *gauge variant completion* (GVC), has made possible the exploration of operator structures necessary for generalization to larger lattices and higher dimensions on current hardware. As an explicit example, time evolution of a one-dimensional string of two SU(2) plaquettes is implemented on IBM's `Tokyo` [227] quantum device with employed error mitigation techniques. The new mappings and techniques that we introduce here generalize to quantum simulations of gauge field theories in higher numbers of spatial dimensions.

10.2 SU(2) Lattice Gauge Theory in the Electric Basis

The Hamiltonian of spatially-discretized Yang-Mills gauge theory is [244] (in lattice units)

$$\hat{H} = \frac{g^2}{2} \sum_{\text{links}} \hat{E}^2 - \frac{1}{2g^2} \sum_{\square} \left(\hat{\square} + \hat{\square}^\dagger \right) \tag{10.1}$$

where $\hat{E}^2$ is the local gauge-invariant Casimir operator, $\hat{\square}$ is the gauge-invariant plaquette operator contracting closed loops of link operators, and $\hat{\square} = \hat{\square}^\dagger$ for SU(2). On a square lattice, the single plaquette operator is

$$\hat{\square} = \sum_{\alpha,\beta,\gamma,\delta=-\frac{1}{2}}^{\frac{1}{2}} \hat{U}_{\alpha\beta}\ \hat{U}_{\beta\gamma}\ \hat{U}_{\gamma\delta}\ \hat{U}_{\delta\alpha} \tag{10.2}$$

where $\hat{U}_{\alpha\beta}$ is a $j = 1/2$ link operator with definite starting and ending points oriented around a plaquette. In the limit of strong coupling, $g^2 \to \infty$, this Hamiltonian is dominated by the electric contributions and fluctuations between configurations of definite link angular momentum vanish. In weak coupling, the magnetic contributions dominate and a theory of dynamical loops emerges.

The angular momentum basis describes the quantum state of a generic link by its irreducible representation, j, and associated third-component projections at the left and right end of the link in the $\mathbf{2}$ and $\bar{\mathbf{2}}$ representations, $|j, m, m'\rangle \equiv |j, m\rangle \otimes |j, m'\rangle$, respectively. In one dimension, SU(2) lattice gauge theory can be spatially discretized onto a string of plaquettes (see Fig. 10.5). With periodic boundary conditions (PBCs), only three-point vertices contribute to such a plaquette chain. To form gauge singlets, components of the three links at each vertex are contracted with an SU(2) Clebsch-Gordan coefficient. While these coefficients are conventionally incorporated into the state space allowing plaquette operators to be localized to four active links, the qubit Hilbert space is more naturally structured as an unconstrained grid. Thus the Clebsch-Gordan coefficient at each vertex will be here included in the plaquette operator itself. This decision delocalizes the plaquette operator at the scale of immediately neighboring links as shown in Fig. 10.5, where the green, circular parts of the operator denote the dependence of the operator on the quantum state of qubits on neighboring links.

To calculate the plaquette operator, the state is first structured with Clebsch-Gordans at each vertex such that the wavefunction has the form

$$V \sim \sum_{b,c,e} \langle j_1, b, j_2, e | q, c\rangle\ |j_1, a, b\rangle \otimes |q, c, d\rangle \otimes |j_2, e, f\rangle\ , \tag{10.3}$$

where indices b, c, and e are located at the vertex. By focusing on a system with an even number of plaquettes, matrix elements of the arbitrary plaquette operator may be determined. The wavefunction of a lattice with an even number of plaquettes in one dimension with PBCs in the link angular momenta basis is

$$|\chi\rangle = \mathcal{N} \sum_{\{m\}} \prod_{i=1}^{L} \langle j_i^t, m_{i,R}^t, j_{i+1}^t, m_{i+1,L}^t | q_i, m_{q_i}^t \rangle \\ \langle j_i^b, m_{i,R}^b, j_{i+1}^b, m_{i+1,L}^b | q_i, m_{q_i}^b \rangle \\ |j_i^t, m_{i,L}^t, m_{i,R}^t\rangle \otimes |j_i^b, m_{i,L}^b, m_{i,R}^b\rangle \otimes |q_i, m_{q_i}^t, m_{q_i}^b\rangle \quad (10.4)$$

with $j_{L+1} = j_1$, $m_{L+1} = m_1$, and normalization $\mathcal{N} = \prod_i (\dim(q_i))^{-1}$ with $\dim(q) = 2q + 1$. Referring to the plaquette string's ladder structure, on links located as rungs of the ladder, angular momentum values are labeled by q. Thus, a plaquette string is created by two strings of j-type registers connected periodically by rungs of q-type registers. The contraction with Clebsch-Gordan coefficients at each vertex ensures the local gauge singlet structure required by Gauss's law. The link operator acts on the degrees of freedom at each end of a link and is a source of $j = 1/2$ angular momentum,

$$\hat{U}_{\alpha\beta} |j, a, b\rangle = \sum_{\oplus J} \sqrt{\frac{\dim(j)}{\dim(J)}} \; |J, a + \alpha, b + \beta\rangle \\ \langle j, a, \frac{1}{2}, \alpha | J, a + \alpha\rangle \langle j, b, \frac{1}{2}, \beta | J, b + \beta\rangle \quad , \quad (10.5)$$

which contains non-vanishing contributions only for $J = j \pm \frac{1}{2}$ [358]. By acting this operator on the above wavefunction of Eq. (10.51) and summing over alignment variables, that matrix elements of the plaquette operator in one dimension and in the tensor product basis of

magnetic quantum numbers, j, are calculated to be

$$\begin{aligned}\langle \chi_{\ldots,j_\ell^{t,b},q_{\ell f},j_{af}^{t,b},q_{rf},j_r^{t,b},\ldots}|\hat{\square}|\chi_{\ldots,j_\ell^{t,b},q_{\ell i},j_{ai}^{t,b},q_{ri},j_r^{t,b},\ldots}\rangle = \\ \sqrt{\dim(j_{ai}^t)\dim(j_{af}^t)\dim(j_{ai}^b)\dim(j_{af}^b)} \\ \times \sqrt{\dim(q_{\ell i})\dim(q_{\ell f})\dim(q_{ri})\dim(q_{rf})} \\ \times (-1)^{j_\ell^t+j_\ell^b+j_r^t+j_r^b+2(j_{af}^t+j_{af}^b-q_{\ell i}-q_{ri})} \\ \times \begin{Bmatrix} j_\ell^t & j_{ai}^t & q_{\ell i} \\ \frac{1}{2} & q_{\ell f} & j_{af}^t \end{Bmatrix} \begin{Bmatrix} j_\ell^b & j_{ai}^b & q_{\ell i} \\ \frac{1}{2} & q_{\ell f} & j_{af}^b \end{Bmatrix} \begin{Bmatrix} j_r^t & j_{ai}^t & q_{ri} \\ \frac{1}{2} & q_{rf} & j_{af}^t \end{Bmatrix} \begin{Bmatrix} j_r^b & j_{ai}^b & q_{ri} \\ \frac{1}{2} & q_{rf} & j_{af}^b \end{Bmatrix}\end{aligned} \tag{10.6}$$

where the indices $j_\ell^{t,b}, q_{\ell i}, q_{\ell f}, j_a^{t,b}, q_{ri}, q_{rf}$, and $j_r^{t,b}$ are used to indicate the j-values relevant for the single plaquette operator (as depicted in Fig. 10.5) and the brackets indicate Wigner's 6-j symbols. The four registers $j_{\ell,r}^{t,b}$ outside the plaquette are not modified by the action of the plaquette operator. However, their inclusion as control registers is necessary to maintain Gauss's law. The sums over alignment in each gauge-invariant space yield a dramatically reduced Hilbert space to be mapped onto a quantum device, characterized entirely by the $|j\rangle$'s (rather than the $|j,m,m'\rangle$'s [73]) incrementing naturally by half-integers. As a result, the Hilbert space dimension scales with the number of links, L, as $(2\Lambda_j+1)^L$—a small asymptotic savings in terms of qubit number, but an important savings for noisy devices where survival probabilities in the physical subspace are imperfect. This concept is here exemplified by embedding a four dimensional physical subspace into a sixteen dimensional computational space rather than into what would be a $\geq 5^4$-dimensional Hilbert space in the $|j,m,m'\rangle$ basis. The qubit representation of the periodic plaquette string is shown on the top panel of Fig. 10.5, where each link contains a $\lceil \log_2(2\Lambda_j+1)\rceil$-qubit register with Λ_j the angular momentum truncation per link.

10.3 Plaquette Operator Physical Matrix Elements

In this section, the above result for the plaquette matrix element within a one-dimensional string of plaquettes will be discussed in detail. The natural vertices of a gauge invariant

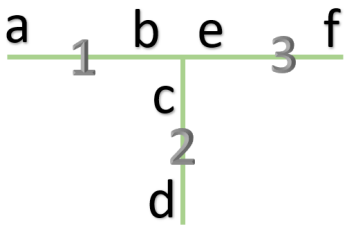

Figure 10.1: Concrete labeling and ordering of Hilbert spaces at a 3-point vertex of the SU(2) lattice.

state of SU(2) lattice gauge theory are tied together with Clebsch Gordan (CG) factors to ensure the presence of a singlet state.

$$\textbf{2-point vertex:} \quad \sum_{b} |j, a, b\rangle \otimes |j, b, c\rangle \tag{10.7}$$

$$\textbf{3-point vertex:} \quad \sum_{b,c,e} \langle j_1, b, j_2, e | Q, c\rangle \ |j_1, a, b\rangle \otimes |Q, c, d\rangle \otimes |j_2, e, f\rangle \tag{10.8}$$

where the total angular momentum and third component quantum numbers are forced to be equivalent across the two-point vertex and the distribution of variables for the three-point vertex are shown in Fig. 10.1. The CG factors are vital in defining gauge invariant states. With their presence embedded into the Hilbert space, the resulting plaquette operator can be made completely local to the four links of the plaquette [251]. However, embedding CG factors into a Hilbert space represented on qubit degrees of freedom is seemingly unnatural. To proceed, the CG factors ordinarily relegated to the Hilbert space state definitions will be incorporated into the plaquette operators themselves. This causes a delocalization of the plaquette operators at a fixed distance of nearest neighbor links; rather than being described by a four-link operator, the quantum plaquette operator will be a four link operator controlled on all neighboring links to the plaquette. The state of the neighboring links will determine the transitions available in the plaquette, but will be themselves unchanged in the process.

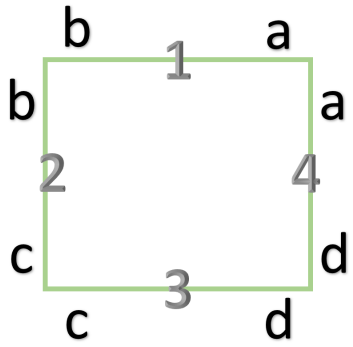

Figure 10.2: Single plaquette lattice with labeled third component electric quantum numbers.

10.3.1 Plaquette Matrix Elements (0+1)-Dimensional Lattice

For a highly-constrained example, consider a lattice comprised of a single plaquette labeled as shown in Fig. 10.2. This lattice consists only of two-point vertices and thus the total angular momentum on each link must be the same, j, throughout the plaquette. The state of this lattice may be parameterized as

$$|\chi_j\rangle = \mathcal{N} \sum_{-j\leq a,b,c,d\leq j} |j,a,b\rangle \otimes |j,b,c\rangle \otimes |j,c,d\rangle \otimes |j,d,a\rangle \quad . \tag{10.9}$$

The normalization is calculated to be

$$\begin{aligned}\langle\chi_j|\chi_j\rangle = \mathcal{N}^2 \sum_{-j\leq a,b,c,d\leq j} \sum_{-j\leq a',b',c',d'\leq j} &\langle j,a',b'| \otimes \langle j,b',c'| \otimes \langle j,c',d'| \otimes \langle j,d',a'| \\ &|j,a,b\rangle \otimes |j,b,c\rangle \otimes |j,c,d\rangle \otimes |j,d,a\rangle \qquad (10.10)\end{aligned}$$

$$= \mathcal{N}^2 \sum_{-j\leq a,b,c,d\leq j} \sum_{-j\leq a',b',c',d'\leq j} \delta_{a,a'}\delta_{b,b'}\delta_{c,c'}\delta_{d,d'} \tag{10.11}$$

$$= \mathcal{N}^2 \sum_{-j\leq a,b,c,d\leq j} \mathbb{I} \tag{10.12}$$

$$= \mathcal{N}^2 (2j+1)^4 \equiv 1 \tag{10.13}$$

$$\mathcal{N} = \frac{1}{(2j+1)^2} \tag{10.14}$$

A single link operator acts separately on the 2 and $\overline{2}$ degrees of freedom at either end of a link and is a source of $j = 1/2$ angular momentum

$$U^{(\frac{1}{2})}_{\alpha\beta}|j,a,b\rangle = \sum_{\oplus J}\sqrt{\frac{\dim(j)}{\dim(J)}}\langle j,a,\frac{1}{2}\alpha|J,a+\alpha\rangle\langle j,b,\frac{1}{2},\beta|J,b+\beta\rangle\ |J,a+\alpha,b+\beta\rangle \quad . \tag{10.15}$$

This operator contains non-vanishing contributions only for transitions by half integers, $J = j \pm \frac{1}{2}$.

The plaquette operator is constructed with four link operators correlated to maintain Gauss' law as a trace over the matrix product in the gauge indices

$$\hat{\square} = \sum_{\alpha,\beta,\gamma,\delta=-\frac{1}{2}}^{\frac{1}{2}} U^{(\frac{1}{2})}_{\alpha\beta}U^{(\frac{1}{2})}_{\beta\gamma}U^{(\frac{1}{2})}_{\gamma\delta}U^{(\frac{1}{2})}_{\delta\alpha} \quad . \tag{10.16}$$

The action of this operator on a plaquette state on an initial state of the single-plaquette lattice is

$$\begin{aligned}\hat{\square}|\chi_{j_i}\rangle &= \frac{1}{(2j_i+1)^2}\sum_{\alpha,\beta,\gamma,\delta=-\frac{1}{2}}^{\frac{1}{2}}\ \sum_{-j_i\le a,b,c,d\le j_i} \\ &\qquad U^{(\frac{1}{2})}_{\alpha\beta}|j_i,a,b\rangle\otimes U^{(\frac{1}{2})}_{\beta\gamma}|j_i,b,c\rangle\otimes U^{(\frac{1}{2})}_{\gamma\delta}|j_i,c,d\rangle\otimes U^{(\frac{1}{2})}_{\delta\alpha}|j_i,d,a\rangle \qquad (10.17)\\ &= \frac{1}{(2j_i+1)^2}\sum_{\oplus J}\sum_{\alpha,\beta,\gamma,\delta=-\frac{1}{2}}^{\frac{1}{2}}\ \sum_{a,b,c,d=-j_i}^{j_i}\frac{(2j_i+1)^2}{(2J+1)^2} \\ &\qquad \langle j_i,a,\frac{1}{2},\alpha|J,a+\alpha\rangle^2\langle j_i,b,\frac{1}{2},\beta|J,b+\beta\rangle^2 \\ &\qquad \langle j_i,c,\frac{1}{2},\gamma|J,c+\gamma\rangle^2\langle j_i,d,\frac{1}{2},\delta|J,d+\delta\rangle^2 \\ &\quad |J,a+\alpha,b+\beta\rangle\otimes|J,b+\beta,c+\gamma\rangle\otimes|J,c+\gamma,d+\delta\rangle\otimes|J,d+\delta,a+\alpha\rangle\ . \qquad (10.18)\end{aligned}$$

More generally, these four link operators produce separate sums over J final states on each link. However, the single plaquette made of four corner states with two links each, the J values must be equal around the loop. As such, only one sum over final total angular momentum, J, values remains.

To calculate the plaquette matrix elements between initial and final states of this lattice, the overlap is calculated with a final plaquette state

$$\begin{aligned}
\langle\chi_{j_f}|\hat{\square}|\chi_{f_i}\rangle = \frac{1}{(2j_i+1)^2}\frac{1}{(2j_f+1)^2}\sum_{\oplus J}\sum_{a'b'c'd'=-j_f}^{j_f}\sum_{\alpha\beta\gamma\delta=-\frac{1}{2}}^{\frac{1}{2}}\sum_{abcd=-j_i}^{j_i}\frac{(2j_i+1)^2}{(2J+1)^2} \\
\langle j_i,a,\frac{1}{2},\alpha|J,a+\alpha\rangle^2\langle j_i,b,\frac{1}{2},\beta|J,b+\beta\rangle^2 \\
\langle j_i,c,\frac{1}{2},\gamma|J,c+\gamma\rangle^2\langle j_i,d,\frac{1}{2},\delta|J,d+\delta\rangle^2 \\
\langle j_f,a',b'|\otimes\langle j_f,b',c'|\otimes\langle j_f,c',d'|\otimes\langle j_f,d',a'| \\
|J,a+\alpha,b+\beta\rangle\otimes|J,b+\beta,c+\gamma\rangle\otimes|J,c+\gamma,d+\delta\rangle\otimes|J,d+\delta,a+\alpha\rangle \quad (10.19)
\end{aligned}$$

$$\begin{aligned}
= \frac{1}{(2j_i+1)^2}\frac{1}{(2j_f+1)^2}\sum_{\oplus J}\sum_{a'b'c'd'=-j_f}^{j_f}\sum_{\alpha\beta\gamma\delta=-\frac{1}{2}}^{\frac{1}{2}}\sum_{abcd=-j_i}^{j_i}\frac{(2j_i+1)^2}{(2J+1)^2} \\
\langle j_i,a,\frac{1}{2},\alpha|J,a+\alpha\rangle^2\langle j_i,b,\frac{1}{2},\beta|J,b+\beta\rangle^2 \\
\langle j_i,c,\frac{1}{2},\gamma|J,c+\gamma\rangle^2\langle j_i,d,\frac{1}{2},\delta|J,d+\delta\rangle^2\delta_{a',a+\alpha}\delta_{b',b+\beta}\delta_{c',c+\gamma}\delta_{d',d+\delta}\delta_{J,j_f} \quad (10.20)
\end{aligned}$$

$$\begin{aligned}
= \frac{1}{(2j_f+1)^4}\sum_{a'b'c'd'=-j_f}^{j_f}\sum_{abcd=-j_i}^{j_i}\langle j_i,a,\frac{1}{2},a'-a|j_f,a'\rangle\langle j_i,b,\frac{1}{2},b'-b|j_f,b'\rangle^2 \\
\langle j_i,c,\frac{1}{2},c'-c|j_f,c'\rangle^2\langle j_i,d,\frac{1}{2},d'-d|j_f,d'\rangle^2 \quad (10.21)
\end{aligned}$$

$$= \frac{1}{(2j_f+1)^4}\left(\sum_{a'=-j_f}^{j_f}\sum_{a=-j_i}^{j_i}\langle j_i,a,\frac{1}{2}a'-a|j_f,a'\rangle^2\right)^4 \quad (10.22)$$

$$= \delta_{j_f,j_i+\frac{1}{2}}+\delta_{j_f,j_i-\frac{1}{2}} \quad . \quad (10.23)$$

The last equality comes from the CG sum relation

$$\sum_{a'=-j_f}^{j_f}\sum_{a=-j_i}^{j_i}\langle j_i,a,\frac{1}{2}a'-a|j_f,a'\rangle = \begin{cases}\dim(j_f) & \text{if } |j_i-j_f|=\frac{1}{2} \\ 0 & \text{otherwise}\end{cases} \quad . \quad (10.24)$$

Note that this sum rule has enabled the analytic inclusion of the third component projection quantum numbers. This leaves only the total angular momentum quantum numbers on

$\langle j_f \vert$	$\vert j_i \rangle$	Matrix Element
$\langle j_i \pm \frac{1}{2} \vert$	$\vert j_i \rangle$	1

Table 10.1: Summary of plaquette operator matrix elements for the single-plaquette lattice.

each link necessary to be represented on qubit degrees of freedom. In particular, for the single plaquette (where all j values are equal around the plaquette) the entire lattice can be represented with one j qubit register containing $n_Q = \lceil \log_2(2\Lambda_j + 1) \rceil$ qubits where Λ_j is the cutoff[2] in total angular momentum half integers included in the Hilbert space. This and other CG sum rules will allow analytic inclusion of the third component projection quantum numbers also in the case of the (1+1)-dimensional plaquette string below. Because $\mathrm{tr}(U) = \mathrm{tr}(U^\dagger)$ in SU(2) and the matrix elements are real, the plaquette operator is symmetric. All non-zero plaquette operator matrix elements are unity for the single-plaquette lattice, as summarized with unwarranted formality in Table 10.1.

The above calculation has shown that, for a single plaquette of (0+1)-dimensional SU(2) lattice gauge theory, the plaquette operator contribution to the Hamiltonian is exactly proportional $(L^+ + L^-)$ where the $L^\pm$ are raising/lowering operators with no harmonic oscillator normalization factors. For example, with $n_Q = 3$ and thus a $\Lambda_j = \frac{7}{2}$,

$$\hat{\square} = L^+ + L^- = \begin{pmatrix} & 1 & & & & & & \\ 1 & & 1 & & & & & \\ & 1 & & 1 & & & & \\ & & 1 & & 1 & & & \\ & & & 1 & & 1 & & \\ & & & & 1 & & 1 & \\ & & & & & 1 & & 1 \\ & & & & & & 1 & \end{pmatrix} , \tag{10.25}$$

with a zero value in every matrix element left blank. This is equivalent to the operator

[2]There are many ways to digitize and truncate SU(2) lattice gauge theory. Determining the optimal digitization and truncation for qubit degrees of freedom is an area of active research. The electric angular momentum basis truncated to the low-j sub-space is expected to be appropriate at strong coupling where the electric energy dominates and produces energetic suppression to the relevance of states with high j values.

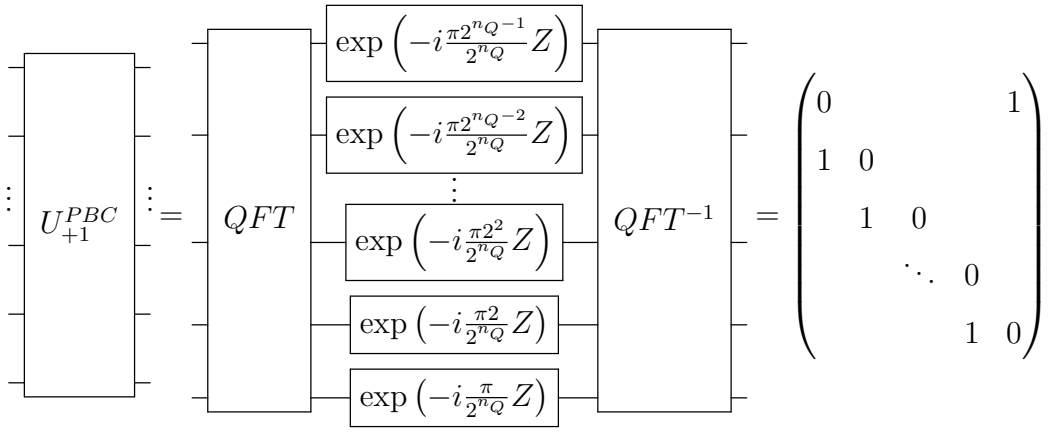

(10.26)

Figure 10.3: Circuit implementation of the periodic binary increment operator through single-qubit operators in Fourier space, $U_{+1}^{PBC}|x\rangle = |x+1\rangle$ and $U_{+1}^{PBC}|2^{n_Q}-1\rangle = |0\rangle$ up to a global phase. The standard QFT gate implements the discrete quantum fourier transform combining basis states as $QFT|x\rangle = \frac{1}{\sqrt{2^{n_Q}}}\sum_k \exp\left[\frac{2\pi i\ k.x}{2^{n_Q}}\right]|k\rangle$ with $x, k \in \{0, \cdots, 2^{n_Q}-1\}$.

designed for the gauge space of the Schwinger model before projecting the Hilbert space into the physical subspace or along axes of symmetry [264, 386, 246, 251, 245, 265, 252, 387]. The trotter operator for the time evolution associated with this term can be broken into two pieces, A and B, where the A matrix is $\mathbb{I}_{n_Q-1} \otimes X$ and the B matrix can be implemented equivalently after incrementing the basis by one. Such an incrementing operator can be constructed from single qubit rotations applied to fourier space. If we allow unity matrix elements to also be placed in the upper right and lower left corners (creating periodic boundary conditions in j-space), this operator may be implemented as shown in Fig. 10.3. Note that this representation,

$$\hat{\square}^{PBC} = \mathbb{I}_{n_Q-1} \otimes X + \left(U_{+1}^{PBC}\right)^\dagger \left(\mathbb{I}_{n_Q-1} \otimes X\right) U_{+1}^{PBC}, \tag{10.28}$$

when used to create a plaquette time evolution operator, will in general have non-zero Trotterization errors. While utilizing periodic boundary conditions between boundaries where populations are suppressed as the truncation is increased is relatively benign. This is the

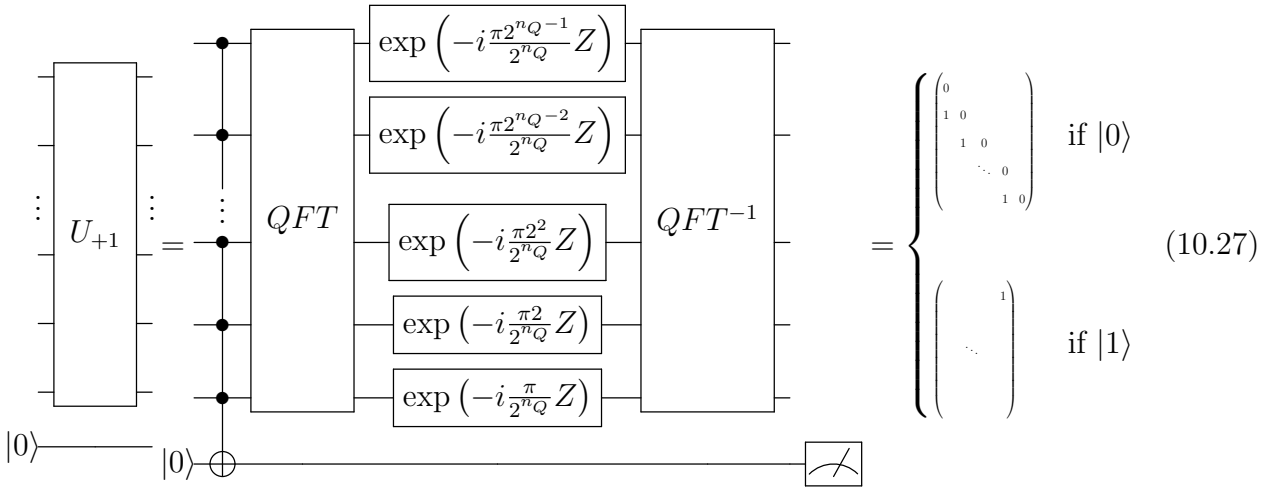

(10.27)

Figure 10.4: Extension to a probabilistic circuit implementation of the non-unitary binary increment operator. The preceding controlled operation allows post selection on the presence of a particular basis state.

case in the Schwinger model where the U(1) gauge space extends between $-\Lambda \leq \ell \leq \Lambda$ and the low-energy space is naturally localized to low values of ℓ. However, the positivity of j values in the SU(2) gauge theory causes this periodicity to mix the strong coupling ground state with the high-j truncation boundary. Rather than mizing states that both become irrelevant at high Λ, this modification mixes a state in the low-energy subspace with a state at the cutoff.

To avoid this IR-UV coupling, a highly controlled gate and an extra qubit may be introduced to remove the matrix elements in the off-diagonal corners of the time evolution operator as shown in Fig. 10.4. If the high-j state is scarcely populated, the probability of measuring the auxiliary qubit in the $|1\rangle$ state is low and this procedure may be advantageous depending on the desired precision or resilience of the low-energy calculation to contamination by the scarce UV population. The use of this probabilistic operator in Eq. (10.25) requires also its inverse to avoid IR-UV mixing in both directions by the plaquette operator.

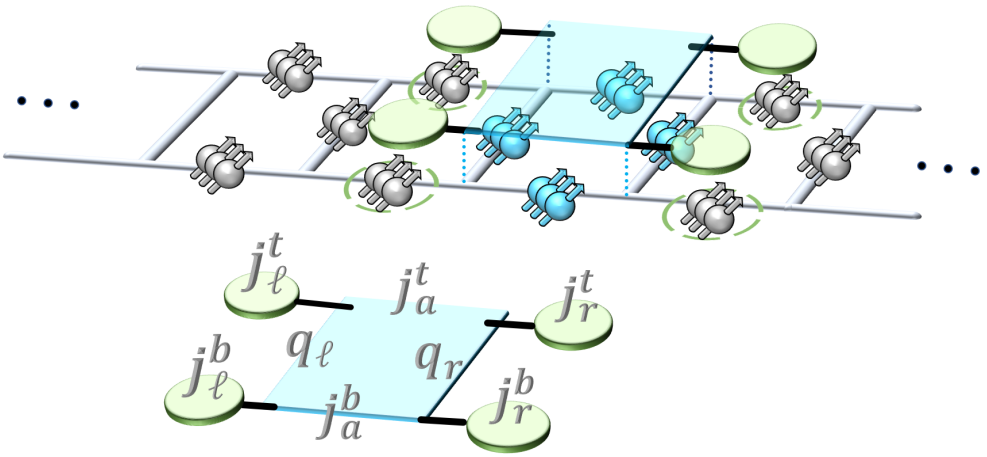

Figure 10.5: (top) Diagram of the lattice distribution of $\lceil \log_2(2\Lambda_j + 1) \rceil$-qubit registers and the action of $\hat{\square}$ on SU(2) plaquettes in one dimension. $\hat{\square}$ operates on the four qubit registers in the plaquette and is controlled by the four neighboring qubit registers to enforce the Gauss's law constraint. (bottom) The plaquette operator with labeled angular momentum registers.

However, for the same reason that the loss of statistics is low for the post-selected U_{+1}, the loss is substantial when implementing the inverse. The preceding fully-controlled operator should be understood as a single basis state filter, learning the binary information of basis state population before determining post selection. The low-j subspace is highly populated, and thus statistically costly to project out of the wavefunction. Identifying practical ways if implementing the time evolution associated with this plaquette operator will be necessary throughout the quantum simulation of lattice quantum field theories.

10.3.2 Plaquette Matrix Elements in (1+1)-dimensional Lattice

Continuing from one plaquette in (0+1)-dimensions to a string of plaquettes in (1+1)-dimensions, consider the lattice of two plaquettes with periodic boundary conditions constrained to the vertically-symmetric subsector. Shown generically in Fig. 10.5, this is the

subsector in which $j^t = j^b$ and $j_\ell = j_r$. For a highly truncated theory with $\Lambda_j = \frac{1}{2}$, this vertical symmetry is naturally maintained.

With periodic boundary conditions, there are no corners. For two plaquettes, the quantum state is described effectively by two correlated 3-pt vertices, as labeled and depicted in Fig. 10.6. The wavefunction of this two-plaquette lattice is

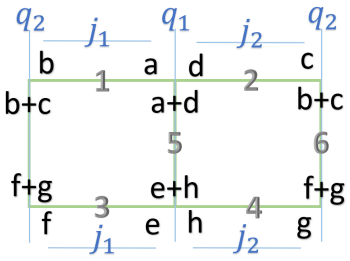

Figure 10.6: Declaration of quantum number placement on a string of two plaquettes in a (1+1)-dimensional spacetime with periodic boundary conditions. The vertical symmetry is currently imposed correlating the j values on links 1,3 and 2,4.

$$
\begin{aligned}
|\chi_{j_1,q_1,j_2,q_2}\rangle = \mathcal{N} \sum_{abef=-j_1}^{j_1} \sum_{cdgh=-j_2}^{j_2} & \langle j_1, a, j_2, d | q_1, a+d\rangle \langle j_1, e, j_2, h | q_1, e+h\rangle \\
& \langle j_1, b, j_2, c | q_2, b+c\rangle \langle j_1, f, j_2, g | q_2, f+g\rangle \\
& |j_1, a, b\rangle |j_2, c, d\rangle |j_1, e, f\rangle |j_2, g, h\rangle \\
& |q_1, e+h, a+d\rangle |q_2, f+g, b+c\rangle \quad , \qquad (10.29)
\end{aligned}
$$

Every quantum number appears once in a 3-pt vertex producing four CG factors embedded in the state. The normalization factor, as usual, is determined by evaluation of the overlap of this state with itself. The delta factors that appear upon overlap will be $\prod_{i\in\{abcdefgh\}} \delta_{i',i}$.

$$
\begin{aligned}
1 = \mathcal{N}^2 \sum_{abef=-j_1}^{j_1} \sum_{cdgh=-j_2}^{j_2} & \langle j_1, a, j_2, d | q_1, a+d\rangle^2 \langle j_1, e, j_2, h | q_1, e+h\rangle^2 \qquad (10.30) \\
& \langle j_1, b, j_2, c | q_2, b+c\rangle^2 \langle j_1, f, j_2, g | q_2, f+g\rangle^2
\end{aligned}
$$

$$= \mathcal{N}^2 \left(\sum_{a=-j_1}^{j_1} \sum_{d=j_2} \langle j_1, a, j_2, d | q_1, a+d \rangle^2 \right)^2 \left(\sum_{b=-j_1}^{j_1} \sum_{c=j_2} \langle j_1, b, j_2, c | q_2, b+c \rangle^2 \right)^2 \tag{10.31}$$

$$= \mathcal{N}^2 \dim^2(q_1) \dim^2(q_2) \tag{10.32}$$

Where in the last line I have used the CG sum

$$\sum_{b=-j_1}^{j_1} \sum_{c=j_2}^{j_2} \langle j_1, b, j_2, c | q_2, b+c \rangle^2 = \begin{cases} \dim(q_1) & \text{if } |j_1 - j_2| \leq q_1 \leq j_1 + j_2 \\ 0 & \text{otherwise} \end{cases} \tag{10.33}$$

as above. The Plaquette operator's action on this state is

$$\begin{aligned} \hat{\square}_A |\chi_{j_1,q_1,j_2,q_2}\rangle = \mathcal{N}_\square \sum_{abef=-j_1}^{j_1} \sum_{cdgh=-j_2}^{j_2} & \langle j_1, a, j_2, d | q_1, a+d \rangle \langle j_1, e, j_2, h | q_1, e+h \rangle \\ & \langle j_1, b, j_2, c | q_2, b+c \rangle \langle j_1, f, j_2, g | q_2, f+g \rangle \\ & U^{(\frac{1}{2})}_{\alpha\beta} |j_1, a, b\rangle |j_2, c, d\rangle U_{\delta\gamma} |j_1, e, f\rangle |j_2, g, h\rangle \\ & U^{(\frac{1}{2})}_{\delta\alpha} |q_1, e+h, a+d\rangle U^{(\frac{1}{2})}_{\gamma\beta} |q_2, f+g, b+c\rangle \quad . \end{aligned} \tag{10.34}$$

The dimension factors from the link operators are

$$\mathcal{N}_\square = \frac{\dim(j_{1i})}{\dim(j_{1f})} \sqrt{\frac{\dim(q_{1i})}{\dim(q_{1f})}} \sqrt{\frac{\dim(q_{2i})}{\dim(q_{2f})}} \quad .$$

Because there are no quantum numbers that do not appear in any CG factors, there is no extra dimension^2 factors. The matrix element of the plaquette operator with vertical symmetry and PBCs is

$$\begin{aligned} \langle \chi_{j_{1f},q_{1f},j_2,q_{2f}} | \hat{\square}_A | \chi_{j_{1i},q_{1i},j_2,q_{2i}} \rangle = \mathcal{N}_i \mathcal{N}_f \mathcal{N}_\square \sum_{\substack{abef \\ a'b'e'f'=-\frac{j_{1i}}{j_{1f}}}}^{\substack{j_{1i} \\ j_{1f}}} \sum_{\substack{cdgh \\ c'd'g'h'=-j_2}}^{j_2} \sum_{\alpha\beta\gamma\delta=-\frac{1}{2}}^{\frac{1}{2}} & \\ \langle j_{1i}, a, j_2, d | q_{1i}, a+d \rangle \langle j_{1i}, e, j_2, h | q_{1i}, e+h \rangle & \\ \langle j_{1i}, b, j_2, c | q_{2i}, b+c \rangle \langle j_{1i}, f, j_2, g | q_{2i}, f+g \rangle & \\ \langle j_{1f}, a', j_2, d' | q_{1f}, a'+d' \rangle \langle j_{1f}, e', j_2, h' | q_{1f}, e'+h' \rangle & \\ \langle j_{1f}, b', j_2, c' | q_{2f}, b'+c' \rangle \langle j_{1f}, f', j_2, g' | q_{2f}, f'+g' \rangle & \end{aligned}$$

$$\langle j_{1i}, a, \frac{1}{2}, \alpha | j_{1f}, a+\alpha\rangle \langle j_{1i}, b, \frac{1}{2}, \beta | j_{1f}, b+\beta\rangle$$
$$\langle q_{2i}, b+c, \frac{1}{2}, \beta | q_{2f}, b+c+\beta\rangle \langle q_{2i}, f+g, \frac{1}{2}, \gamma | q_{2f}, f+g+\gamma\rangle$$
$$\langle j_{1i}, f, \frac{1}{2}, \gamma | j_{1f}, f+\gamma\rangle \langle j_{1i}, e, \frac{1}{2}, \delta | j_{1f}, e+\delta\rangle$$
$$\langle q_{1i}, e+h, \frac{1}{2}, \delta | q_{1f}, e+h+\delta\rangle \langle q_{1i}, a+d, \frac{1}{2}, \alpha | q_{1f}, a+d+\alpha\rangle$$
$$\delta_{c',c}\delta_{d',d}\delta_{g',g}\delta_{h',h}\delta_{a',a+\alpha}\delta_{b',b+\beta}\delta_{e',e+\delta}\delta_{f',f+\gamma} \tag{10.35}$$

$$= \mathcal{N}_i\mathcal{N}_f\mathcal{N}_\square \sum_{abef=-j_{1i}}^{j_{1i}} \sum_{cdgh=-j_2}^{j_2} \sum_{\alpha\beta\gamma\delta=-\frac{1}{2}}^{\frac{1}{2}}$$
$$\langle j_{1i}, a, j_2, d | q_{1i}, a+d\rangle \langle j_{1i}, e, j_2, h | q_{1i}, e+h\rangle$$
$$\langle j_{1i}, b, j_2, c | q_{2i}, b+c\rangle \langle j_{1i}, f, j_2, g | q_{2i}, f+g\rangle$$
$$\langle j_{1f}, a+\alpha, j_2, d | q_{1f}, a+\alpha+d\rangle \langle j_{1f}, e+\delta, j_2, h | q_{1f}, e+\delta+h\rangle$$
$$\langle j_{1f}, b+\beta, j_2, c | q_{2f}, b+\beta+c\rangle \langle j_{1f}, f+\gamma, j_2, g | q_{2f}, f+\gamma+g\rangle$$
$$\langle j_{1i}, a, \frac{1}{2}, \alpha | j_{1f}, a+\alpha\rangle \langle j_{1i}, b, \frac{1}{2}, \beta | j_{1f}, b+\beta\rangle$$
$$\langle q_{2i}, b+c, \frac{1}{2}, \beta | q_{2f}, b+c+\beta\rangle \langle q_{2i}, f+g, \frac{1}{2}, \gamma | q_{2f}, f+g+\gamma\rangle$$
$$\langle j_{1i}, f, \frac{1}{2}, \gamma | j_{1f}, f+\gamma\rangle \langle j_{1i}, e, \frac{1}{2}, \delta | j_{1f}, e+\delta\rangle$$
$$\langle q_{1i}, e+h, \frac{1}{2}, \delta | q_{1f}, e+h+\delta\rangle \langle q_{1i}, a+d, \frac{1}{2}, \alpha | q_{1f}, a+d+\alpha\rangle \tag{10.36}$$

$$= \mathcal{N}_i\mathcal{N}_f\mathcal{N}_\square$$
$$\left(\sum_{a,d,\alpha} \langle j_{1i}, a, j_2, d | q_{1i}, a+d\rangle \langle j_{1f}, a+\alpha, j_2, d | q_{1f}, a+d+\alpha\rangle \right.$$
$$\left. \langle j_{1i}, a, \frac{1}{2}, \alpha | j_{1f}, a+\alpha\rangle \langle q_{1i}, a+d, \frac{1}{2}, \alpha | q_{1f} a+d+\alpha\rangle \right)^2$$
$$\left(\sum_{bc\beta} \langle j_{1i}, b, j_2, c | q_{2i}, b+c\rangle \langle j_{1f}, b+\beta, j_2, c | q_{2f}, b+c+\beta\rangle \right.$$

$$\langle j_{1i}, b, \frac{1}{2}, \beta | j_{1f}, b+\beta\rangle\langle q_{2i}, b+c, \frac{1}{2}, \beta | q_{2f}, b+c+\beta\rangle\Big)^2 \quad . \tag{10.37}$$

The overlap terms contain two CGs associated with the 3-pt state structure of the initial and final state and two CGs associated with the link operators incrementing two of the three vertex quantum numbers by $\pm\frac{1}{2}$. This can be summarized with the following operator where the j and q are the horizontal and vertical links at a vertex within the plaquette and j_2 is associated with the remaining link at the vertex whose third-component quantum number remains unchanged:

$$O(\tbinom{j_i}{j_f}, \tbinom{q_i}{q_f}, j_2) = \Bigg(\sum_{bc\beta}\langle j_i, b, j_2, c | q_i, b+c\rangle\langle j_f, b+\beta, j_2, c | q_f, b+c+\beta\rangle$$
$$\langle j_i, b, \frac{1}{2}, \beta | j_f, b+\beta\rangle\langle q_i, b+c, \frac{1}{2}, \beta | q_f, b+c+\beta\rangle\Bigg) \quad . \tag{10.38}$$

With this overlap operator, the matrix element may be written succinctly as

$$\langle \chi_{j_{1f},q_{1f},j_2,q_{2f}} | \hat{\square}_A | \chi_{j_{1i},q_{1i},j_2,q_{2i}}\rangle = \frac{\dim(j_{1i})}{\dim(j_{1f})}\frac{1}{\sqrt{\dim(q_{1i})\dim^3(q_{1f})\dim(q_{2i})\dim^3(q_{2f})}}$$
$$O^2\left(\tbinom{j_{1i}}{j_{1f}}, \tbinom{q_{1i}}{q_{1f}}, j_2\right) O^2\left(\tbinom{j_{1i}}{j_{1f}}, \tbinom{q_{2i}}{q_{2f}}, j_2\right) \quad , \tag{10.39}$$

with the first and second overlap operators are associated with the left and right three-point vertex, appearing squared to account for the enforced-equivalent contributions from the lower two three-point vertices.

The pieces of the previous subsection are sufficient to define the matrix element for a plaquette operator in a system of periodic boundary conditions with arbitrary numbers of plaquettes under the vertical symmetry, i.e., the bulk plaquette operator. Only one small change is necessary from Eq.(10.39) which is that the stagnant j (last argument of O) is different for the two active vertices (rather than equal as in the 2-plaquette system). The generic plaquette operator for the 1+1-dimensional string of plaquettes with vertical symmetry and localized on the active plaquette $j_{a(i/f)}$ with the left/right j values j_ℓ/j_r is

$$\langle \chi_{\cdots,j_\ell,q_{\ell f},j_{af},q_{rf},j_r,\cdots} | \hat{\square}_a | \chi_{\cdots,j_\ell,q_{\ell i},j_{ai},q_{ri},j_r,\cdots}\rangle = \frac{\dim(j_{ai})}{\dim(j_{af})}\frac{1}{\sqrt{\dim(q_{\ell i})\dim^3(q_{\ell f})\dim(q_{ri})\dim^3(q_{rf})}}$$

$$O^2\left(\begin{smallmatrix} j_{ai} & q_{\ell i} \\ j_{af} & q_{\ell f}\end{smallmatrix}, j_\ell\right) O^2\left(\begin{smallmatrix} j_{ai} & q_{ri} \\ j_{af} & q_{rf}\end{smallmatrix}, j_r\right) \tag{10.40}$$

The overlap factors, O, can be written in terms of a single $6j$ symbol. To see that this is the case, begin from the standard decomposition into a sum over a product of four Clebsch-Gordan coefficients

$$\begin{Bmatrix} j_1 & j_2 & j_{12} \\ j_3 & j & j_{23}\end{Bmatrix} = \frac{(-1)^{j_1+j_2+j_3+j}}{(2j_{12}+1)(2j_{23}+1)} \sum_{m_1 m_2 m_3 m_{12} m_{23}} \langle j_{12}, m_{12}, j_3, m_3 | j, m\rangle \tag{10.41}$$

$$\times \langle j_1, m_1, j_2, m_2 | j_{12}, m_{12}\rangle$$
$$\times \langle j_1, m_1, j_{23}, m_{23} | j, m\rangle$$
$$\times \langle j_2, m_2, j_3, m_3 | j_{23}, m_{23}\rangle \quad . \tag{10.42}$$

Note that the third component quantum number m is not included in the sum. For this expression to be true, m should be set to any physical value between $-j \leq m \leq j$. Enforcing physicality with a free summation instead will produce a dimension factor later. Matching the structure of this expression to the structure of $O(\begin{smallmatrix} j_{ai} & q_i \\ j_{af} & q_f\end{smallmatrix}, q_2)$, I find the following translation

$$\begin{aligned} &j \to q_f \qquad j_{12} \to q_i \qquad j_2 \to j_{ai} \\ &m \to b + c + \beta \qquad m_{12} \to b + c \qquad m_2 \to b \\ &j_3 \to \frac{1}{2} \qquad j_{23} \to j_{af} \qquad j_1 \to j_2 \\ &m_3 \to \beta \qquad m_{23} \to b + \beta \qquad m_1 \to c \end{aligned} \tag{10.43}$$

along with a requirement to reverse the (j,m)'s in the *bra* of the second and third CG coefficients. This reversal introduces additional phase factors

$$\langle j_1, m_1, j_2, m_2 | J, M\rangle = (-1)^{j_1+j_2-J} \langle j_2, m_2, j_1, m_1 | J, M\rangle \tag{10.44}$$

With this translation and reduction of phase factors, the overlap factor becomes

$$O\left(\begin{smallmatrix} j_{ai} & q_i \\ j_{af} & q_f\end{smallmatrix}, j_2\right) = \dim(q_f)\sqrt{\dim(q_i)\dim(j_{af})}(-1)^{\frac{1}{2}+j_2+j_{af}-q_i} \begin{Bmatrix} j_2 & j_{ai} & q_i \\ \frac{1}{2} & q_f & j_{af}\end{Bmatrix} \tag{10.45}$$

where the $\dim(q_f)$ factor comes from the $\dim(j)$ multiplicity acquired when the m quantum number is also summed over physical values. The four triangle conditions,

$$\begin{Bmatrix} j_1 & j_2 & j_3 \\ j_4 & j_5 & j_6 \end{Bmatrix} \quad : \quad \{j_1, j_2, j_3\} \quad \{j_1, j_5, j_6\} \quad \{j_2, j_4, j_6\} \quad \{j_3, j_4, j_5\} \tag{10.46}$$

where the brackets represent the triangular delta function and thus the presence of a singlet, are as expected

$$\{j_2, j_{ai}, q_i\} \quad \{j_2, q_f, j_{af}\} \quad \{\frac{1}{2}, j_{ai}, j_{af}\} \quad \{\frac{1}{2}, q_f, q_i\} \quad .$$

Finally, the matrix element is calculated to be

$$\begin{aligned} &\langle \chi_{\cdots, j_\ell, q_{\ell f}, j_{af}, q_{rf}, j_r, \cdots} | \hat{\square}_a | \chi_{\cdots, j_\ell, q_{\ell i}, j_{ai}, q_{ri}, j_r, \cdots} \rangle \\ &\qquad = \frac{\dim(j_{ai})}{\dim(j_{af})} \frac{1}{\sqrt{\dim(q_{\ell i}) \dim^3(q_{\ell f}) \dim(q_{ri}) \dim^3(q_{rf})}} \\ &\qquad\qquad \times \dim^2(q_{\ell f}) \dim(q_{\ell i}) \dim(j_{af}) \begin{Bmatrix} j_\ell & j_{ai} & q_{\ell i} \\ \frac{1}{2} & q_{\ell f} & j_{af} \end{Bmatrix}^2 \\ &\qquad\qquad \times \dim^2(q_{rf}) \dim(q_{ri}) \dim(j_{af}) \begin{Bmatrix} j_r & j_{ai} & q_{ri} \\ \frac{1}{2} & q_{rf} & j_{af} \end{Bmatrix}^2 \qquad (10.47) \\ &\qquad = \dim(j_{ai}) \dim(j_{af}) \sqrt{\dim(q_{\ell i}) \dim(q_{\ell f}) \dim(q_{ri}) \dim(q_{rf})} \\ &\qquad\qquad \begin{Bmatrix} j_\ell & j_{ai} & q_{\ell i} \\ \frac{1}{2} & q_{\ell f} & j_{af} \end{Bmatrix}^2 \begin{Bmatrix} j_r & j_{ai} & q_{ri} \\ \frac{1}{2} & q_{rf} & j_{af} \end{Bmatrix}^2 \quad , \qquad (10.48) \end{aligned}$$

for every plaquette in a the string of a periodic lattice with vertical symmetry.

With periodic boundary conditions and a gauge field cutoff $\Lambda_j > \frac{1}{2}$, there is no natural mechanism enforcing the above-utilized vertical symmetry, and topologically non-trivial configurations are allowed. As such, configurations with $j^t \neq j^b$ are accessible from the strong coupling vacuum. The transitions of the two-plaquette periodic lattice shown in Fig. 10.7 is one example of this fact. The arbitrary-plaquette operator can be determined beginning

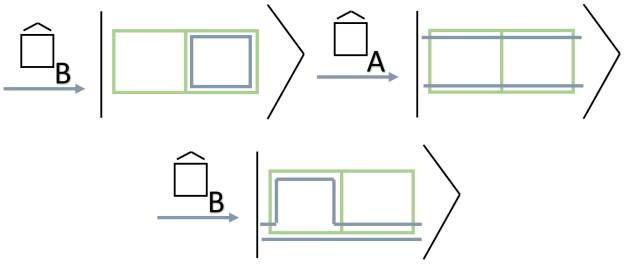

Figure 10.7: Example of a sequence of configurations of the periodic two-plaquette lattice that produces a state in which $j^{(top)} \neq j^{(bottom)}$.

from the wavefunction of the three plaquette lattice with PBCs,

$$
\begin{aligned}
|\chi\rangle = \mathcal{N} \sum_{ab=-j_1^t}^{j_1^t} \sum_{cd=-j_2^t}^{j_2^t} \sum_{ef=-j_3^t}^{j_3^t} \sum_{gh=-j_1^b}^{j_1^b} \sum_{\ell m=-j_2^b}^{j_2^b} \sum_{np=-j_3^b}^{j_3^b} & \\
\langle j_1^t, b, j_2^t, c | q_1, b+c\rangle \langle j_1^b, h, j_2^b, \ell | q_1, h+\ell\rangle & \\
\langle j_2^t, d, j_3^t e | q_2, d+e\rangle \langle j_2^b, m, j_3^b, n | q_2, m+n\rangle & \\
\langle j_3^t, f, j_1^t, a | q_3, a+f\rangle \langle j_3^b, p, j_1^b, g | q_3, g+p\rangle & \\
|j_1^t, a, b\rangle |j_2^t, c, d\rangle |j_3^t, e, f\rangle & \\
|q_1, b+c, h+\ell\rangle |q_2, d+e, m+n\rangle |q_3, a+f, g+p\rangle & \\
|j_1^b, g, h\rangle |j_2^b, \ell, m\rangle |j_3^b, n, p\rangle \quad . &
\end{aligned}
\tag{10.49}
$$

The normalization factor is calculated to be

$$
\mathcal{N} = \frac{1}{\dim(q_1)\dim(q_2)\dim(q_3)} \quad . \tag{10.50}
$$

This is a specific case of the general plaquette ladder wavefunction for a lattice with an even number of plaquettes in one dimension with PBCs in the link angular momenta basis

$$
\begin{aligned}
|\chi\rangle = \mathcal{N} \sum_{\{m\}} \prod_{i=1}^{L} & \langle j_i^t, m_{i,R}^t, j_{i+1}^t, m_{i+1,L}^t | q_i, m_{q_i}^t\rangle \\
& \langle j_i^b, m_{i,R}^b, j_{i+1}^b, m_{i+1,L}^b | q_i, m_{q_i}^b\rangle
\end{aligned}
$$

$$|j_i^t, m_{i,L}^t, m_{i,R}^t\rangle \otimes |j_i^b, m_{i,L}^b, m_{i,R}^b\rangle \otimes |q_i, m_{q_i}^t, m_{q_i}^b\rangle \quad , \quad (10.51)$$

with $j_{L+1} = j_1$, $m_{L+1} = m_1$, and normalization $\mathcal{N} = \prod_i (\dim(q_i))^{-1}$ with $\dim(q) = 2q + 1$. Referring to the plaquette string's ladder structure, on links located as rungs of the ladder, angular momentum values are labeled by q. Thus, a plaquette string is created by two strings of j-type registers connected periodically by rungs of q-type registers. The contraction with Clebsch-Gordan coefficients at each vertex ensures the local gauge singlet structure required by Gauss's law. However, given the locality of the plaquette operator (see Fig. 10.5) to links neighboring the active plaquette, a three-plaquette lattice is sufficient to completely determine the operator acting in a lattice of arbitrary length, and will thus be the focus of any further discussion. Later, normalizations will be separated for the initial and final states notated as

$$\mathcal{N}_x = \frac{1}{\dim(q_{1x})\dim(q_{2x})\dim(q_{3x})} \qquad x \in \{i, f\} \quad , \quad (10.52)$$

the set of 6 CG's in the state will be defined as C_{6x}, and

$$\sum_{\{m\}} = \sum_{ab=-j_1^t}^{j_1^t} \sum_{cd=-j_2^t}^{j_2^t} \sum_{ef=-j_3^t}^{j_3^t} \sum_{gh=-j_1^b}^{j_1^b} \sum_{\ell m=-j_2^b}^{j_2^b} \sum_{np=-j_3^b}^{j_3^b} \qquad \sum_{\{\alpha\}} = \sum_{\alpha\beta\gamma\delta=-\frac{1}{2}}^{\frac{1}{2}} \quad . \quad (10.53)$$

The action of the plaquette operator is

$$\begin{aligned}\hat{\square}_2|\chi\rangle = \mathcal{N}_i \sum_{\{m\}} C_{6i} \sum_{\{\alpha\}} & |j_1^t, a, b\rangle U_{\alpha\beta}^{(\frac{1}{2})} |j_2^t, c, d\rangle |j_3^t, e, f\rangle \\ & U_{\alpha\delta}^{(\frac{1}{2})} |q_1, b + c, h + \ell\rangle U_{\beta\gamma}^{(\frac{1}{2})} |q_2, d + e, m + n\rangle |q_3, a + f, g + p\rangle \\ & |j_1^b, g, h\rangle U_{\delta\gamma}^{(\frac{1}{2})} |j_2^b, \ell, m\rangle |j_3^b, n, p\rangle \quad . \end{aligned} \quad (10.54)$$

Using the link operator's action as defined above, the state after action of the plaquette operator is,

$$\begin{aligned}\hat{\square}_2|\chi\rangle = \mathcal{N}_i \sum_{\{m\}} C_{6i} \mathcal{N}_\square \sum_{\{\alpha\}} & \langle j_{2i}^t, c, \frac{1}{2}, \alpha | j_{2f}^t, c + \alpha\rangle \langle j_{2i}^t, d, \frac{1}{2}, \beta | j_{2f}^t, d + \beta\rangle \\ & \langle q_{2i}, d + e, \frac{1}{2}, \beta | q_{2f}, d + e + \beta\rangle \langle q_{2i}, m + n, \frac{1}{2}, \gamma | q_{2f}, m + n + \gamma\rangle \end{aligned}$$

$$
\begin{aligned}
&\langle j^b_{2i}, m, \frac{1}{2}, \gamma | j^b_{2f}, m+\gamma\rangle \langle j^b_{2i}, \ell \frac{1}{2}, \delta | j^b_{2f}, \ell+\delta\rangle \\
&\langle q_{1i}, h+\ell, \frac{1}{2}, \delta | q_{1f}, h+\ell+\delta\rangle \langle q_{1i}, b+c, \frac{1}{2}, \alpha | q_{1f}, b+c+\alpha\rangle \\
&|j^t_1, a, b\rangle | j^t_{2f}, c+\alpha, d+\beta\rangle | j^t_3, e, f\rangle \\
&|q_{1f}, b+c+\alpha, h+\ell+\delta\rangle | q_{2f}, d+e+\beta, m+n+\gamma\rangle | q_3, a+f, g+p\rangle \\
&|j^b_1, g, h\rangle | j^b_{2f}, \ell+\delta, m+\gamma\rangle | j^b_3, n, p\rangle \quad , \qquad (10.55)
\end{aligned}
$$

where the normalizations associated with the link operators is

$$
\mathcal{N}_\Box = \sqrt{\frac{\dim(j^t_{2i})}{\dim(j^t_{2f})}} \sqrt{\frac{\dim(j^b_{2i})}{\dim(j^b_{2f})}} \sqrt{\frac{\dim(q_{1i})}{\dim(q_{1f})}} \sqrt{\frac{\dim(q_{2i})}{\dim(q_{2f})}} \quad . \qquad (10.56)
$$

The matrix element

$$
\begin{aligned}
\langle \chi' | \hat{\Box}_2 | \chi \rangle = \mathcal{N}_f \mathcal{N}_\Box \mathcal{N}_i \sum_{\{m'\}} \sum_{\{m\}} \sum_{\{\alpha\}} & C_{6f} C_{6i} \langle j^t_{2i}, c, \frac{1}{2}, \alpha | j^t_{2f}, c+\alpha\rangle \langle j^t_{2i}, d, \frac{1}{2}, \beta | j^t_{2f}, d+\beta\rangle \\
& \langle q_{2i}, d+e, \frac{1}{2}, \beta | q_{2f}, d+e+\beta\rangle \langle q_{2i}, m+n, \frac{1}{2}, \gamma | q_{2f}, m+n+\gamma\rangle \\
& \langle j^b_{2i}, m, \frac{1}{2}, \gamma | j^b_{2f}, m+\gamma\rangle \langle j^b_{2i}, \ell \frac{1}{2}, \delta | j^b_{2f}, \ell+\delta\rangle \\
& \langle q_{1i}, h+\ell, \frac{1}{2}, \delta | q_{1f}, h+\ell+\delta\rangle \langle q_{1i}, b+c, \frac{1}{2}, \alpha | q_{1f}, b+c+\alpha\rangle \\
& \delta_{a,a'} \delta_{b,b'} \delta_{c+\alpha,c'} \delta_{d+\beta,d'} \delta_{e,e'}, \delta_{f,f'} \delta_{g,g'} \delta_{h,h'} \delta_{\ell+\delta,\ell'} \delta_{m+\gamma,m'} \delta_{n,n'} \delta_{p,p'} \qquad (10.57)
\end{aligned}
$$

$$
\begin{aligned}
= \mathcal{N}_f \mathcal{N}_\Box \mathcal{N}_i \sum_{\{m\}} \sum_{\{\alpha\}} & \\
& \langle j^t_1, b, j^t_{2i}, c | q_{1i}, b+c\rangle \langle j^b_1, h, j^b_{2i}, \ell | q_{1i}, h+\ell\rangle \\
& \langle j^t_{2i}, d, j^t_3 e | q_{2i}, d+e\rangle \langle j^b_{2i}, m, j^b_3, n | q_{2i}, m+n\rangle \\
& \langle j^t_3, f, j^t_1, a | q_3, a+f\rangle \langle j^b_3, p, j^b_1, g | q_3, g+p\rangle \\
& \langle j^t_1, b, j^t_{2f}, c+\alpha | q_{1f}, b+c+\alpha\rangle \langle j^b_1, h, j^b_{2f}, \ell+\delta | q_{1f}, h+\ell+\delta\rangle \\
& \langle j^t_{2f}, d+\beta, j^t_3, e | q_{2f}, d+e+\beta\rangle \langle j^b_{2f}, m+\gamma, j^b_3, n | q_{2f}, m+n+\gamma\rangle \\
& \langle j^t_3, f, j^t_1, a | q_3, a+f\rangle \langle j^b_3, p, j^b_1, g | q_3, g+p\rangle \\
& \langle j^t_{2i}, c, \frac{1}{2}, \alpha | j^t_{2f}, c+\alpha\rangle \langle j^t_{2i}, d, \frac{1}{2}, \beta | j^t_{2f}, d+\beta\rangle
\end{aligned}
$$

$$\langle q_{2i}, d+e, \frac{1}{2}, \beta | q_{2f}, d+e+\beta\rangle \langle q_{2i}, m+n, \frac{1}{2}, \gamma | q_{2f}, m+n+\gamma\rangle$$
$$\langle j^b_{2i}, m, \frac{1}{2}, \gamma | j^b_{2f}, m+\gamma\rangle \langle j^b_{2i}, \ell\frac{1}{2}, \delta | j^b_{2f}, \ell+\delta\rangle$$
$$\langle q_{1i}, h+\ell, \frac{1}{2}, \delta | q_{1f}, h+\ell+\delta\rangle \langle q_{1i}, b+c, \frac{1}{2}, \alpha | q_{1f}, b+c+\alpha\rangle \quad (10.58)$$

$$= \mathcal{N}_f \mathcal{N}_\square \mathcal{N}_i \left[\sum_{b,c,\alpha} \langle j^t_1, b, j^t_{2i}, c | q_{1i}, b+c\rangle \langle j^t_1, b, j^t_{2f}, c+\alpha | q_{1f}, b+c+\alpha\rangle \right.$$
$$\left. \langle j^t_{2i}, c, \frac{1}{2}, \alpha | j^t_{2f}, c+\alpha\rangle \langle q_{1i}, b+c, \frac{1}{2}, \alpha | q_{1f}, b+c+\alpha\rangle \right]$$
$$\left[\sum_{h,\ell,\delta} \langle j^b_1, h, j^b_{2i}, \ell | q_{1i}, h+\ell\rangle \langle j^b_1, h, j^b_{2f}, \ell+\delta | q_{1f}, h+\ell+\delta\rangle \right.$$
$$\left. \langle j^b_{2i}, \ell\frac{1}{2}, \delta | j^b_{2f}, \ell+\delta\rangle \langle q_{1i}, h+\ell, \frac{1}{2}, \delta | q_{1f}, h+\ell+\delta\rangle \right]$$
$$\left[\sum_{d,e,\beta} \langle j^t_{2i}, d, j^t_3 e | q_{2i}, d+e\rangle \langle j^t_{2f}, d+\beta, j^t_3 e | q_{2f}, d+e+\beta\rangle \right.$$
$$\left. \langle j^t_{2i}, d, \frac{1}{2}, \beta | j^t_{2f}, d+\beta\rangle \langle q_{2i}, d+e, \frac{1}{2}, \beta | q_{2f}, d+e+\beta\rangle \right]$$
$$\left[\sum_{m+n+\gamma} \langle j^b_{2i}, m, j^b_3, n | q_{2i}, m+n\rangle \langle j^b_{2f}, m+\gamma, j^b_3, n | q_{2f}, m+n+\gamma\rangle \right.$$
$$\left. \langle j^b_{2i}, m, \frac{1}{2}, \gamma | j^b_{2f}, m+\gamma\rangle \langle q_{2i}, m+n, \frac{1}{2}, \gamma | q_{2f}, m+n+\gamma\rangle \right]$$
$$\left[\sum_{a,f} \langle j^t_3, f, j^t_1, a | q_3, a+f\rangle^2\right] \left[\sum_{g,p} \langle j^b_3, p, j^b_1, g | q_3, g+p\rangle^2\right] \quad (10.59)$$

$$= \mathcal{N}_f \mathcal{N}_\square \mathcal{N}_i \ \dim^2(q_3)$$
$$O\left(\begin{smallmatrix} j^t_{2i} & q_{1i} \\ j^t_{2f} & q_{1f} \end{smallmatrix}, j^t_1\right) O\left(\begin{smallmatrix} j^b_{2i} & q_{1i} \\ j^b_{2f} & q_{1f} \end{smallmatrix}, j^b_1\right) O\left(\begin{smallmatrix} j^t_{2i} & q_{2i} \\ j^t_{2f} & q_{2f} \end{smallmatrix}, j^t_3\right) O\left(\begin{smallmatrix} j^b_{2i} & q_{2i} \\ j^b_{2f} & q_{2f} \end{smallmatrix}, j^b_3\right) \quad (10.60)$$

Using Eq. 10.45 to translate these summations into $6j$'s,

$$\langle \chi' | \hat{\square}_2 | \chi\rangle = \mathcal{N}_f \mathcal{N}_\square \mathcal{N}_i \dim^2(q_3)$$
$$\left[\dim(q_{1f}) \sqrt{\dim(q_{1i}) \dim(j^t_{2f})} (-1)^{\frac{1}{2}+j^t_1+j^t_{2f}-q_{1i}} \begin{Bmatrix} j^t_1 & j^t_{2i} & q_{1i} \\ \frac{1}{2} & q_{1f} & j^t_{2f} \end{Bmatrix}\right]$$

$$\left[\dim(q_{1f})\sqrt{\dim(q_{1i})\dim(j^b_{2f})}(-1)^{\frac{1}{2}+j^b_1+j^b_{2f}-q_{1i}}\begin{Bmatrix} j^b_1 & j^b_{2i} & q_{1i} \\ \frac{1}{2} & q_{1f} & j^b_{2f}\end{Bmatrix}\right]$$
$$\left[\dim(q_{2f})\sqrt{\dim(q_{2i})\dim(j^t_{2f})}(-1)^{\frac{1}{2}+j^t_3+j^t_{2f}-q_{2i}}\begin{Bmatrix} j^t_3 & j^t_{2i} & q_{2i} \\ \frac{1}{2} & q_{2f} & j^t_{2f}\end{Bmatrix}\right]$$
$$\left[\dim(q_{2f})\sqrt{\dim(q_{2i})\dim(j^b_{2f})}(-1)^{\frac{1}{2}+j^b_3+j^b_{2f}-q_{2i}}\begin{Bmatrix} j^b_3 & j^b_{2i} & q_{2i} \\ \frac{1}{2} & q_{2f} & j^b_{2f}\end{Bmatrix}\right] \tag{10.61}$$

$$= \frac{1}{\dim(q_{1i})\dim(q_{2i})\dim(q_{3i})}\frac{1}{\dim(q_{1f})\dim(q_{2f})\dim(q_{3f})}$$
$$\times\sqrt{\frac{\dim(j^t_{2i})}{\dim(j^t_{2f})}}\sqrt{\frac{\dim(j^b_{2i})}{\dim(j^b_{2f})}}\sqrt{\frac{\dim(q_{1i})}{\dim(q_{1f})}}\sqrt{\frac{\dim(q_{2i})}{\dim(q_{2f})}}\dim^2(q_3)$$
$$\times\dim^2(q_{1f})\dim^2(q_{2f})\dim(q_{1i})\dim(q_{2i})\dim(j^t_{2f})\dim(j^b_{2f})$$
$$\times(-1)^{j^t_1+j^b_1+j^t_3+j^b_3+2(j^t_{2f}+j^b_{2f}-q_{1i}-q_{2i})}$$
$$\times\begin{Bmatrix} j^t_1 & j^t_{2i} & q_{1i} \\ \frac{1}{2} & q_{1f} & j^t_{2f}\end{Bmatrix}\begin{Bmatrix} j^b_1 & j^b_{2i} & q_{1i} \\ \frac{1}{2} & q_{1f} & j^b_{2f}\end{Bmatrix}\begin{Bmatrix} j^t_3 & j^t_{2i} & q_{2i} \\ \frac{1}{2} & q_{2f} & j^t_{2f}\end{Bmatrix}\begin{Bmatrix} j^b_3 & j^b_{2i} & q_{2i} \\ \frac{1}{2} & q_{2f} & j^b_{2f}\end{Bmatrix} \tag{10.62}$$

$$= \sqrt{\dim(j^t_{2i})\dim(j^t_{2f})\dim(j^b_{2i})\dim(j^b_{2f})\dim(q_{1i})\dim(q_{1f})\dim(q_{2i})\dim(q_{2f})}$$
$$\times(-1)^{j^t_1+j^b_1+j^t_3+j^b_3+2(j^t_{2f}+j^b_{2f}-q_{1i}-q_{2i})}$$
$$\times\begin{Bmatrix} j^t_1 & j^t_{2i} & q_{1i} \\ \frac{1}{2} & q_{1f} & j^t_{2f}\end{Bmatrix}\begin{Bmatrix} j^b_1 & j^b_{2i} & q_{1i} \\ \frac{1}{2} & q_{1f} & j^b_{2f}\end{Bmatrix}\begin{Bmatrix} j^t_3 & j^t_{2i} & q_{2i} \\ \frac{1}{2} & q_{2f} & j^t_{2f}\end{Bmatrix}\begin{Bmatrix} j^b_3 & j^b_{2i} & q_{2i} \\ \frac{1}{2} & q_{2f} & j^b_{2f}\end{Bmatrix}. \tag{10.63}$$

For a plaquette string with periodic boundary conditions, Eq. (10.63) contains all necessary information to determine the physical matrix elements of the plaquette operators and associated time evolution operators throughout the lattice. Upon generalization of the notation as $j_1 \to j_\ell,\ j_2 \to j_a\ j_3 \to j_r$ and $q_1 \to q_\ell, q_2 \to q_r$, Eq. (10.63) results in the expression as written in Ref. [31]. If one imposes vertical symmetry on this expression by settng $j^t = j^b$

for each j, the matrix element becomes

$$\langle\chi'|\hat{\Box}_2|\chi\rangle = \dim(j_{2i})\dim(j_{2f})\sqrt{\dim(q_{1i})\dim(q_{1f})\dim(q_{2i})\dim(q_{2f})} \times \begin{Bmatrix} j_1 & j_{2i} & q_{1i} \\ \frac{1}{2} & q_{1f} & j_{2f} \end{Bmatrix}^2 \begin{Bmatrix} j_3 & j_{2i} & q_{2i} \\ \frac{1}{2} & q_{2f} & j_{2f} \end{Bmatrix}^2 \tag{10.64}$$

in agreement with Eq. 10.48 as calculated previously.

10.4 Quantum Circuits for the Plaquette Operator: $\Lambda_j = \frac{1}{2}$

It is pertinent to wonder whether there is a quantum register structure that allows for a natural/efficient implementation of the time evolution operator defined by the Hamiltonian matrix elements above. This is a very similar question to the scalar field motivations where once again the challenge is to determine a convenient structure of the quantum registers that is conducive to a digital implementation of the interaction propagators. Having completed all the third-component sums, only the j-values across the lattice need be mapped to quantum degrees of freedom. While it still retains non-physical configurations within the Hilbert space, the most natural mapping to create is one with a separate quantum register for each link where quantum states are directly mapped to a $\vec{j}, \vec{q}$-configuration. The active j_a register and neighboring $q_{\ell/r}$ registers must all be involved in the circuit operator. The neighboring $j_{\ell/r}$ registers are not modified by the operator, but will appear as control registers. One way to view this operator when the vertical symmetry is imposed is shown in Fig. 10.8. For systems with truncations $\Lambda_j > \frac{1}{2}$ in which the vertical symmetry is not present, the operator structure should be viewed in the form of Fig. 10.5.

For a concrete example, consider the single plaquette operator in a system with truncation $\Lambda_j = \frac{1}{2}$. One qubit is sufficient for each link and thus the plaquette operator acts on five qubits with two of them (j_1 and j_3) being used only as control qubits. The remaining 3 (q_1, $j_2 = j_a$, and q_2) all experience a shift by value $\frac{1}{2}$. Within this 32 dimensional space, the

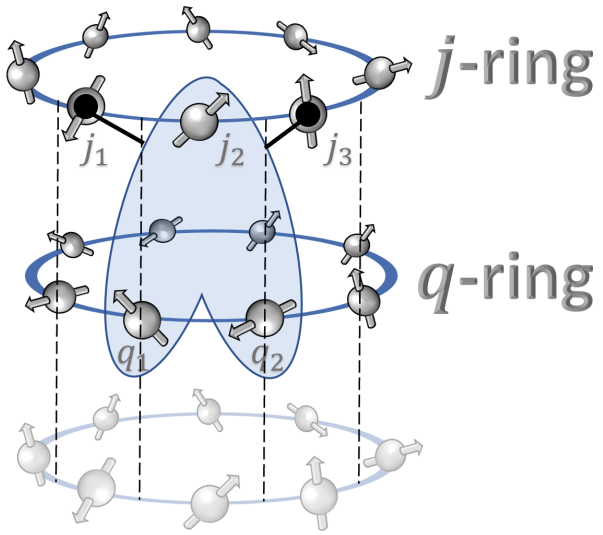

Figure 10.8: Qubit diagram with expected interaction structure for the (1+1)-dimensional string of SU(2) plaquettes with $\Lambda_j = 1/2$ and thus a single qubit per link. The plaquette operator as written in Eq. (10.48) interacts 2 q values and 1 j value conditioned upon the neighboring j values.

physical subspace is 8-dimensional,

$$\begin{pmatrix} |0\ 0\ 0\ 0\ 0\rangle \\ |0\ 0\ 0\ \tfrac{1}{2}\ \tfrac{1}{2}\rangle \\ |0\ \tfrac{1}{2}\ \tfrac{1}{2}\ 0\ \tfrac{1}{2}\rangle \\ |0\ \tfrac{1}{2}\ \tfrac{1}{2}\ \tfrac{1}{2}\ 0\rangle \\ |\tfrac{1}{2}\ 0\ \tfrac{1}{2}\ 0\ \tfrac{1}{2}\rangle \\ |\tfrac{1}{2}\ 0\ \tfrac{1}{2}\ \tfrac{1}{2}\ 0\rangle \\ |\tfrac{1}{2}\ \tfrac{1}{2}\ 0\ 0\ 0\rangle \\ |\tfrac{1}{2}\ \tfrac{1}{2}\ 0\ \tfrac{1}{2}\ \tfrac{1}{2}\rangle \end{pmatrix} = \begin{pmatrix} \\ \\ \\ \\ \\ \\ \\ \\ \end{pmatrix} , \tag{10.65}$$

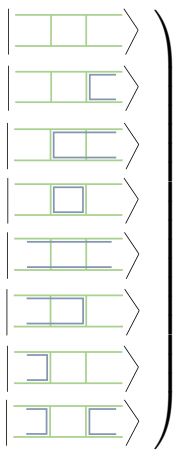

where the Hilbert spaces have been ordered as $|j_\ell, q_\ell, j_a, q_r, j_r\rangle$. On the right hand side, the physical Hilbert space of this local plaquette operator is described pictorially where the

lattice is represented by the light green grid and excitations of $j = \frac{1}{2}$ are drawn in dark blue. Within this eight dimensional space of physical states, only four matrix elements (symmetric) are non-zero for the central plaquette operator

$$\langle 00000|\hat{\square}|0\frac{1}{2}\frac{1}{2}\frac{1}{2}\frac{1}{2}0\rangle = 1 \tag{10.66}$$

$$\langle 000\frac{1}{2}\frac{1}{2}|\hat{\square}|0\frac{1}{2}\frac{1}{2}0\frac{1}{2}\rangle = \frac{1}{2} \tag{10.67}$$

$$\langle \frac{1}{2}\frac{1}{2}000|\hat{\square}|\frac{1}{2}0\frac{1}{2}\frac{1}{2}0\rangle = \frac{1}{2} \tag{10.68}$$

$$\langle \frac{1}{2}0\frac{1}{2}0\frac{1}{2}|\hat{\square}|\frac{1}{2}\frac{1}{2}0\frac{1}{2}\frac{1}{2}\rangle = \frac{1}{4} \tag{10.69}$$

The first creates a plaquette excitation from the strong coupling vacuum and thus has the same matrix element as the single-plaquette lattice calculated above. The second(third) matrix element stretches a loop from the right(left) to include the active plaquette. The fourth matrix element is associated with the joining of two loops from the left and right into one loop extending across the active plaquette. Note that these states are gauge invariant configurations of j values on the active and neighboring links, some of which demand particular structures in more distant parts of the lattice to create a fully gauge invariant lattice configuration i.e., partial loops shown here must be closed elsewhere in the lattice.

If simply mapping these matrix elements to single-qubit registers, it is observed that an $\sigma^x \otimes \sigma^x \otimes \sigma^x$ operator implements each of these four transitions. For this operator, if $(j_1, j_3) = (0, 0)$, an operator that produces the corresponding matrix element is $\sigma^x \otimes \sigma^x \otimes \sigma^x$. For $(j_1, j_3) = (1/2, 0)$ or $(0, 1/2)$, an operator that produces the corresponding matrix element is $\frac{1}{2}\ \sigma^x \otimes \sigma^x \otimes \sigma^x$. For $(j_1, j_3) = (1/2, 1/2)$, an operator that produces the corresponding matrix element is $\frac{1}{4}\ \sigma^x \otimes \sigma^x \otimes \sigma^x$. As a quantum circuit, this observation leads to the plaquette time evolution operator being comprised of four commuting three-qubit operators controlled

on qubits associated with the neighboring j states

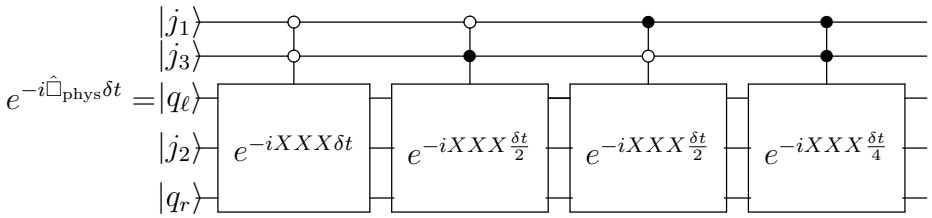

, (10.70)

where the subscript indicates that this operator correctly implements the interactions of the physical subspace but may not (and in this case does not) have vanishing matrix elements within the non-physical space. Note that coupling constants and factors of two have been embedded into the time parameter, δt for this circuit representation. The fact that this set of operators commutes indicates there are no Trotterization errors associated with decomposing the plaquette time evolution operator in this way. This operator can be written as an x-basis-rotated implementation of the level-2 bisection circuit used for the arbitrary wavefunctions in Ref. [26]. The circuit is then manipulated by working all Hadamards to the boundaries of the circuit and holistically reformatting the CNOTs by identifying the remaining bulk circuit as Z-basis parity calculations with rotations on the following combinations

$$1 : a+c+d+e \qquad 2 : a+b+c+d+e \qquad 3 : b+c+d+e \qquad 4 : c+d+e \quad , \tag{10.71}$$

where a through e can be regarded as the Z-basis values on the qubits 1 through 5 after the hadamard transform and uncomputed before the second string of hadamards. Writing these parities by their physical j and q labels becomes,

$$\begin{aligned} &1 : c_{j_1} + c_{q_1} + c_{j_2} + c_{q_2} \qquad 2 : c_{j_1} + c_{j_3} + c_{q_1} + c_{j_2} + c_{q_2} \\ &3 : c_{j_3} + c_{q_1} + c_{j_2} + c_{q_2} \qquad 4 : c_{q_1} + c_{j_2} + c_{q_2} \quad . \end{aligned} \tag{10.72}$$

After these transformations, the circuit for implementing the plaquette operator propagator becomes

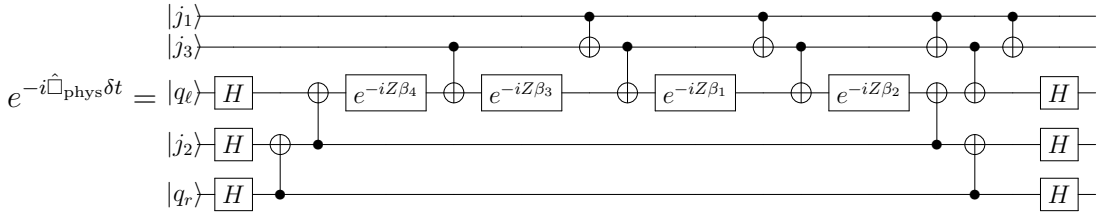

, (10.73)

with

$$\beta = \begin{pmatrix} 1 & 1 & 1 & 1 \\ 1 & -1 & -1 & 1 \\ -1 & -1 & 1 & 1 \\ -1 & 1 & -1 & 1 \end{pmatrix}^{-1} \begin{pmatrix} 1 \\ 1/2 \\ 1/2 \\ 1/4 \end{pmatrix} \tag{10.74}$$

such that $\vec{\beta} = (3/16,\ 1/16,\ 3/16,\ 9/16)$. This requires 12 CNOTs to implement the $\Lambda_j = 1/2$ plaquette operator. Further manual attempts to reduce the rotation depth have led to larger CNOT number, though no sense of optimality is claimed. Note that the ordering of the link Hilbert spaces is not sustainable for applying the same operator translationally-invariantly across an extended lattice of plaquettes in (1+1)-dimensions. Reordering the basis is and maintaining nearest-neighbor two-qubit interactions is found to require 14 CNOTs utilizing the above techniques

$\hat{\square}_{j_2}^{(\Lambda_j=1/2)} =$ 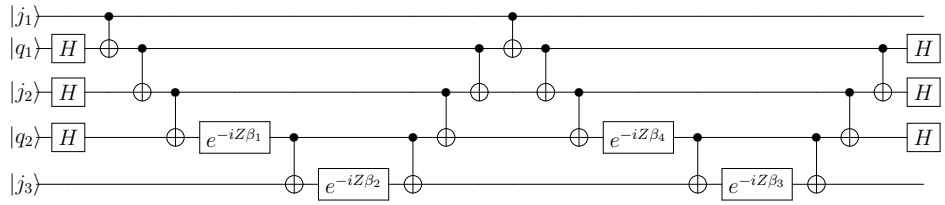

. (10.75)

Raising the locality constraint or changing the natural basis set are two examples of hardware-specific degrees of freedom that impact further modifications to the above presented circuit representations of the plaquette propagator.

For two plaquettes, the operator simplifies by one qubit as $j_1 = j_3$. This requires only rotations with parity combinations

$$1 : c_{j_{1,3}} + c_{q_1} + c_{j_2} + c_{q_2} \qquad 2 : c_{q_1} + c_{j_2} + c_{q_2} \quad , \tag{10.76}$$

with rotation angles 1 and 1/4 (along with necessary time and coupling factors). For example, second plaquette operator in the two-plaquette system reduces to the following four-qubit operator,

$$\hat{\square}_2^{(1/2)} = \Pi_0 XXX + \frac{1}{4}\Pi_1 XXX \quad . \tag{10.77}$$

Digital implementation of this operator is shown in Fig. 10.9. The reduced linear combination

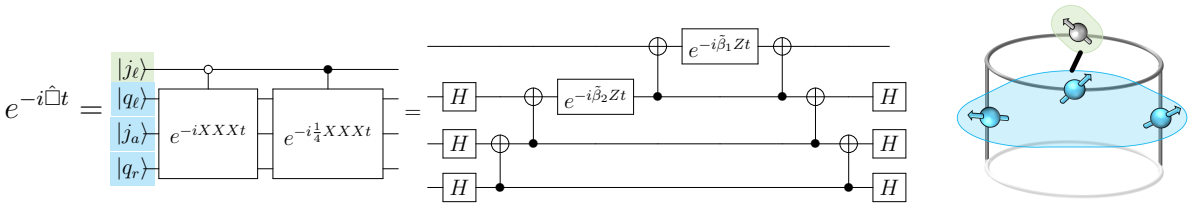

Figure 10.9: Digital circuit implementation of the plaquette operator centered on j_a for a truncated lattice with $\Lambda_j = 1/2$, two plaquettes, and PBCs as depicted at the right. The angles $\tilde{\beta}$ defining this circuit are $\tilde{\beta} = (3/8,\ 5/8)$.

structure defined by the first and fourth rows and columns of the matrix shown in Eq. (10.74) produces the vector $\widetilde{\beta}$ appearing in Fig. 10.9 as

$$\vec{\tilde{\beta}} = \begin{pmatrix} 1 & 1 \\ -1 & 1 \end{pmatrix}^{-1} \begin{pmatrix} 1 \\ \frac{1}{4} \end{pmatrix} \tag{10.78}$$

such that $\tilde{\beta} = (3/8,\ 5/8)$. A natural qubit representation of the electric operator is one that evaluates matrix elements as valid (charged) superselection sectors,

$$\hat{H}_E^{(1/2)} = \frac{g^2}{2} \sum_{\text{links}} \frac{3}{4} \left(\frac{\mathbb{I} - Z}{2} \right) \quad . \tag{10.79}$$

For the zero-charge subsector, this operator includes 12 non-zero matrix elements in the unphysical Hilbert space. Before discussing the results of this simulation on superconducting quantum hardware, a discussion is warranted of these non-zero matrix elements intentionally placed in the unphysical Hilbert space.

10.5 Gauge Variant Completion (GVC)

In the previous subsection, the gauge-variant or unphysical space of the plaquette time evolution operator has been deformed. Rather than containing all zero matrix elements, vanishing by the CG coefficients embedded in the conventional SU(2) wavefunctions when

gauge invariance is broken, non-zero matrix elements are allowed in the unphysical space. Allowing deformations of the interactions in the unphysical space allows for a significantly wider range of viable time evolution operators for the physical subspace. Modification of the unphysical space is a freedom that can be used to reduce quantum resource costs as the interactions within the unphysical subspace are theoretically irrelevant. As long as the matrix elements of the physical subspace remain as calculated above and the mixed matrix elements between the unphysical and physical spaces remain zero, the quantum simulation is quite flexible. In the demanded coherence time, the required gate structures, and the sensitivity to the variety of quantum noise sources, the interactions within the unphysical space affects the attainable quality of the physical calculation.

For the two-plaquette lattice with periodic boundary conditions and truncation $\Lambda_j = 1/2$, the Hamiltonian implemented in the full 16-dimensional Hilbert space with the gauge variant completion (GVC) chosen in the previous section is

$$\mathcal{H}^{(1/2)} = \frac{1}{2g^2} \begin{pmatrix}
0 & 0 & 0 & 0 & 0 & 0 & 0 & -2 & 0 & 0 & 0 & 0 & 0 & -2 & 0 & 0 \\
0 & \frac{3g^4}{4} & 0 & 0 & 0 & 0 & -2 & 0 & 0 & 0 & 0 & 0 & -2 & 0 & 0 & 0 \\
0 & 0 & \frac{3g^4}{2} & 0 & 0 & -2 & 0 & 0 & 0 & 0 & 0 & 0 & 0 & 0 & 0 & -\frac{1}{2} \\
0 & 0 & 0 & \frac{9g^4}{4} & -2 & 0 & 0 & 0 & 0 & 0 & 0 & 0 & 0 & 0 & -\frac{1}{2} & 0 \\
0 & 0 & 0 & -2 & \frac{3g^4}{4} & 0 & 0 & 0 & 0 & -2 & 0 & 0 & 0 & 0 & 0 & 0 \\
0 & 0 & -2 & 0 & 0 & \frac{3g^4}{2} & 0 & 0 & -2 & 0 & 0 & 0 & 0 & 0 & 0 & 0 \\
0 & -2 & 0 & 0 & 0 & 0 & \frac{9g^4}{4} & 0 & 0 & 0 & 0 & -\frac{1}{2} & 0 & 0 & 0 & 0 \\
-2 & 0 & 0 & 0 & 0 & 0 & 0 & 3g^4 & 0 & 0 & -\frac{1}{2} & 0 & 0 & 0 & 0 & 0 \\
0 & 0 & 0 & 0 & 0 & -2 & 0 & 0 & \frac{3g^4}{2} & 0 & 0 & 0 & 0 & 0 & 0 & -\frac{1}{2} \\
0 & 0 & 0 & 0 & -2 & 0 & 0 & 0 & 0 & \frac{9g^4}{4} & 0 & 0 & 0 & 0 & -\frac{1}{2} & 0 \\
0 & 0 & 0 & 0 & 0 & 0 & 0 & -\frac{1}{2} & 0 & 0 & 3g^4 & 0 & 0 & -\frac{1}{2} & 0 & 0 \\
0 & 0 & 0 & 0 & 0 & 0 & -\frac{1}{2} & 0 & 0 & 0 & 0 & \frac{15g^4}{4} & -\frac{1}{2} & 0 & 0 & 0 \\
0 & -2 & 0 & 0 & 0 & 0 & 0 & 0 & 0 & 0 & 0 & -\frac{1}{2} & \frac{9g^4}{4} & 0 & 0 & 0 \\
-2 & 0 & 0 & 0 & 0 & 0 & 0 & 0 & 0 & 0 & -\frac{1}{2} & 0 & 0 & 3g^4 & 0 & 0 \\
0 & 0 & 0 & -\frac{1}{2} & 0 & 0 & 0 & 0 & 0 & -\frac{1}{2} & 0 & 0 & 0 & 0 & \frac{15g^4}{4} & 0 \\
0 & 0 & -\frac{1}{2} & 0 & 0 & 0 & 0 & 0 & -\frac{1}{2} & 0 & 0 & 0 & 0 & 0 & 0 & \frac{9g^4}{2}
\end{pmatrix}, \quad (10.80)$$

with matrix elements of the four-dimensional physical subspace highlighted. The optimality of the operator decomposition in the physical subspace is hardware-specific. The plaquette

operator responsible for the off-diagonal matrix elements, as stated above in Eq. (10.77), has been decomposed as two single-qubit controlled $X\otimes X\otimes X$ operators. For simple comparison, a more-naïve choice of plaquette operator implementation for the two-plaquette lattice would be to use the operator exactly as defined by the matrix elements in Eq. (3) of the main text with no modifications in the unphysical space (i.e., different charge superselection sectors). In this case, the Pauli decomposition contains eight operators

$$\begin{aligned}\hat{\square} = &\left(\frac{5}{32}\mathbb{I}+\frac{3}{32}Z\right)\otimes X\otimes X\otimes X \ +\left(-\frac{3}{32}\mathbb{I}-\frac{5}{32}Z\right)\otimes X\otimes Y\otimes Y \\ &+\left(-\frac{5}{32}\mathbb{I}-\frac{3}{32}Z\right)\otimes Y\otimes X\otimes Y \ +\left(-\frac{3}{32}\mathbb{I}-\frac{5}{32}Z\right)\otimes Y\otimes Y\otimes X \quad , \end{aligned} \tag{10.81}$$

and it remains convenient for the Trotterization that these eight operators commute. However, the number of CNOT gates required to implement this operator increases by a factor of four compared to the operator structure of Fig. 2 of the main text, implemented now in four different bases

$e^{-i\hat{\square}_2^{(1/2)}t} =$

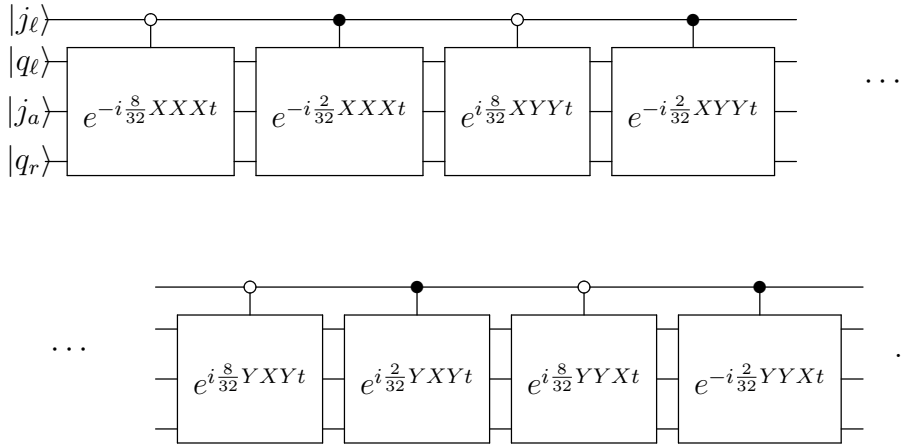

. (10.82)

This makes clear that the quantum resources for operator implementation depend on the details of the calculation—the choice of gauge invariant completion allows hardware-specific optimization leveraging this sensitivity.

10.6 Simulation Results

Real-time evolution of two plaquettes with PBCs (see the right panel of Fig. 10.9) and truncation $\Lambda_j = 1/2$ has been here implemented on IBM's quantum device `Tokyo`, selected for

its available connectivity of a four-qubit loop. the structure of the ground state wavefunction is

$$|\psi_{gs}\rangle = 0.6943|$$  $$\rangle + 0.1666|$$  $$\rangle + 0.4951\left(|\right.$$  $$\rangle + |$$  $$\rangle\left.\right) \quad . \tag{10.83}$$

On each link, a single line corresponds to $j = 0$ and a double line corresponds to $j = 1/2$. The first electric, single plaquette operator in the full 16-dimensional space is diagonal

$$E^2_{\square_1} = \frac{g^2}{2}\text{diag}\left(0, \frac{3}{4}, 0, \frac{3}{4}, \frac{3}{4}, \frac{3}{2}, \frac{3}{4}, \frac{3}{2}, \frac{3}{2}, \frac{9}{4}, \frac{3}{2}, \frac{9}{4}, \frac{9}{4}, 3, \frac{9}{4}, 3\right) \quad , \tag{10.84}$$

with matrix elements serving as weights of the measured probabilities in the measurement of the electric energy expectation value.

The top panel of Fig. 10.10 shows time-evolved expectation values of the energy contributions from the first electric plaquette calculated with one and two Trotter steps [3]. The electric contributions, being localized in their measurement to the four-dimensional physical subspace, are well determined after a small number of samples. In contrast, measuring the energy contributions from the magnetic Hamiltonian requires increased sampling due to the operator's natural representation in the Pauli-X basis of the q_ℓ, j_a, and q_r qubit registers—distributing the wavefunction's amplitude throughout the Hilbert space. Results have been corrected for measurement error by the constrained inversion of a 16-dimensional calibration matrix informed by preparation of each of the 16 computational basis states prior to calculation. The resulting probabilities are linearly extrapolated in the presence of CNOT gates, post-selected within the gauge-invariant space, and renormalized. The linear extrapolation is informed by $r = 1, 2$, where $r = 1$ is the circuit in Fig. 10.9 and $r = 2$ stochastically inserts a pair of CNOTs accompanying each of the three CNOTs either in the first or second half of the plaquette operator. The combined noise and gate fidelity of the device were found to limit the ability to extrapolate further in CNOT noise, even with a single Trotter step. These error mitigation techniques have allowed calculation of the electric energy associated with the SU(2) gauge field to the precision obtained after a single Trotter step.

[3]The Trotter step in this calculation has been ordered in application as the first plaquette, the second plaquette as written in Eq. (10.77), and lastly the electric time evolution operator.

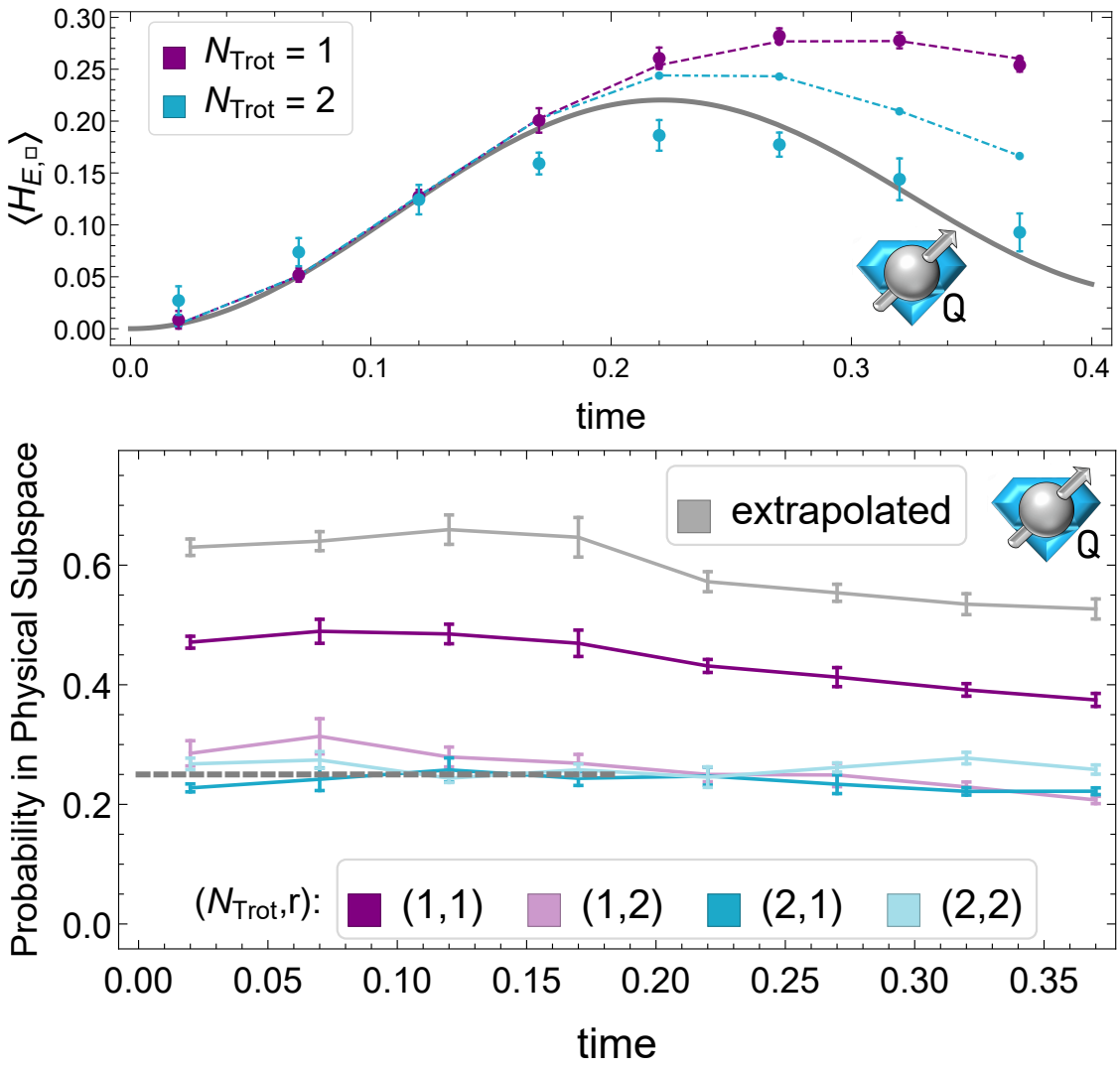

Figure 10.10: (top) Expectation value of the electric energy contribution of the first plaquette in the two-plaquette lattice with PBCs and coupling $g^2 = 0.2$ computed on IBM's `Tokyo`. The dashed(purple) and dot-dashed(blue) lines are the $N_{\text{Trot}} = 1, 2$ Trotterized expectation values, while the thick gray line is the exact time evolution. (bottom) Measured survival probability to remain in the physical subspace for one and two trotter steps, N_{Trot}, and one and two r values indicating stochastically inserted $2r - 1$ CNOTs per CNOT in the digital implementation. Uncertainties represent statistical variation, as well as a systematic uncertainty estimated from reproducibility measurements. The icons (defined in Ref. [26]) denote computations performed on quantum devices.

It is important to determine the feasibility of retaining gauge-invariant Hilbert spaces with near-term quantum hardware. For our calculations on IBM's `Tokyo` quantum device, before CNOT extrapolation, the $(N_{\text{Trot}}, r) = (1, 1)$ measurements were found to remain in the gauge invariant space with a survival population of $\sim 45\%$, as shown in the bottom panel of Fig. 10.10. After linear extrapolation in the probabilities, this was increased to $\sim 65\%$, with survival population decreasing as evolution time increases. The survival population for $N_{\text{Trot}} = 2$ was found to be $\sim 25\%$, consistent with loss of quantum coherence of a four-dimensional physical space embedded onto four qubits, precluding CNOT extrapolation. This observable is a diagnostic of the calculation. As it approaches the decorrelated limit (25%), CNOT extrapolations become less reliable, leading to the underestimate of systematic uncertainties in Fig. 10.10. Because neither the proposed qubit representation nor the subsequent Trotterization produce gauge-variant error contributions, the observed decay of population in the physical subspace is a measure of the device's ability to robustly isolate Hilbert subspaces. This is likely to be an essential capability for evolving lattice gauge theories and other systems with conserved quantities, as well as for quantum error correction.

For the chosen coupling of $g^2 = 0.2$, the ground state energy density per plaquette, through exact (classical) diagonalization, is calculated to be -3.5658 and the lowest energy gap (the observable associated with the "SU(2)-glueball" mass in the infinite volume limit) is calculated to be 7.4139. Numerical values for these low-energy observables with increasing Λ_j truncation are provided in Table 10.2. For the simulated system, the SU(2) Hilbert space associated with each link and the spatial lattice are significantly truncated. The impact of the truncation on the continuous-field system of two plaquettes (for the value of g^2 used in this work) is presented in Table 1 of the supplemental material. We find that the employed truncation of $\Lambda_j = 1/2$ leads to a $\sim 56\%$ change to the ground state energy and a much larger change to the "glueball" mass. A larger value of g^2 would lead to smaller deviations in both quantities, as the system becomes more amenable to perturbative methods. At the selected value of g^2, where the system is nonperturbative, extending the simulation to include three qubits per link to encode a cut-off of $\Lambda_j = 7/2$, rather than one qubit per link

n_Q	Electric Cutoff ($2\Lambda_j$)	D_{phys}	Plaquette Elements	GS Energy Density	ΔE
1	1	4	2	-3.5658	7.4139
2	2	27	31	-5.6437	2.0970
2	3	95	192	-6.8020	0.9285
3	4	304	790	-7.4258	0.5024
3	5	769	2494	-7.7527	0.3096
3	6	1784	6537	-7.9159	0.2220
3	7	3664	15028	-7.9921	0.1929
4	8	7081	31200	-8.0241	0.1885
4	9	12704	59894	-8.0355	0.1893
4	10	21823	107823	-8.0388	0.1900
4	11	35659	184268	-8.0396	0.1902
4	12	56420	301326	-8.0398	0.1902

Table 10.2: Convergence of the ground state energy density and the energy gap to the first excited state, ΔE, of a two-plaquette SU(2) lattice with periodic boundary conditions and $g^2 = 0.2$ as the truncation in the maximum excitation on any single link, Λ_j, is increased. The first column translates the cutoff to the number of qubits per link $n_Q = \lceil \log_2(2\Lambda_j + 1) \rceil$. Columns two and three show the number of states included in the basis of physical states below truncation and the number of non-zero matrix elements in the single plaquette operator.

with $\Lambda_j = 1/2$, these low-energy observables are expected to be calculable with an accuracy exceeding $\sim 2\%$ using the basis discussed in this paper. This work represents an early step along the long road ahead for quantum simulations of gauge field theories. As Hamiltonian operators are local in such field theories, thoughtful design and optimization of quantum operators in small, classically manageable systems will impact the design and execution of future quantum simulations of larger dimensionality. The convergence properties of this, and other formulations of gauge theories for quantum simulation, are important topics of future research.

10.7 Gauge Invariance of Trotterization through Pauli Decomposition

When increasing Λ_j, the plaquette operator must be calculated and designed over 8 registers of qubits, each containing $\lceil \log_2 (2\Lambda_j + 1) \rceil$ qubits. The classical computational resources required to define this operator with Eq. (10.6) scales with the number of unique non-zero matrix elements, which is polynomial in Λ_j. When constructing the time evolution operator for $\Lambda_j > 1/2$, the combination of Trotterization and Pauli decomposition of the 4-register operators in $j_{\ell,r}$-controlled sectors generically generates interactions breaking gauge invariance [388, 355, 214]. While a unitary operator preserving gauge invariance exists, it will generically require an exponential amount of quantum resources to implement and classical resources to define. The breaking of gauge invariance will be important to control if this decomposition is used in future calculations.

10.8 Conclusion

Developing quantum computation capabilities for non-Abelian gauge field theories is a major objective of nuclear physics and high-energy physics research. We have presented the first quantum simulation of a non-Abelian gauge field theory on a digital quantum computer, which required the development of a number of new techniques. One of the challenges facing such calculations is that the mapping of the gauge theory onto the register of a digital quantum computer involves a digitization of the gauge fields. We have presented calcula-

tions of the dynamics of a one-dimensional SU(2) plaquette string with implementation on IBM's Q Experience superconducting hardware. This was made feasible by an improved mapping of the angular momentum basis states describing link variables and recognizing the utility of gauge-variant completions. Our design of the plaquette operator for digital quantum devices requires local control from qubit registers beyond the active plaquette. This key feature is expected to persist in future developments of quantum computing for gauge theories as gauge constraints seem more naturally embedded into quantum operators rather than quantum states. Extension of this analytic reduction beyond one dimension is naturally suited to lattices with three-point vertices, but generalizes to n-point vertices and thus to quantum simulations in higher dimensions. Comparisons, at the level of explicit digital implementation, of this mapping with proposed alternatives will be of importance for realizing physically-relevant quantum computations of non-Abelian gauge theories.

10.9 Appendices

10.9.1 Schwinger Bosons

In describing the SU(2) gauge field in the basis of Schwinger bosons, a collection of harmonic oscillators are placed at the end of each link. For SU(2), a pair of harmonic oscillators are required which will be referred to as a +-type and a −-type, suggestive to the interpretation of populating the description with spin up and spin down particles. These oscillators are uncoupled in the sense that the commutator of their creation and annihilation operators vanish.

$$\left[a_{\pm}, a_{\pm}^{\dagger}\right] = 1 \qquad [N_{\pm}, a_{\pm}] = -a_{\pm} \qquad \left[N_{\pm}, a_{\pm}^{\dagger}\right] = a_{\pm}^{\dagger} \qquad \left[a_{\pm}, a_{\mp}^{\dagger}\right] = 0 \tag{10.85}$$

There exist simultaneous eigenstates of the +-type and −-type number operators

$$[N_{+}, N_{-}] = 0 \quad . \tag{10.86}$$

Creation and annihilation acts independently as usual

$$N_\pm|n_+,n_-\rangle = n_\pm|n_+,n_-\rangle \quad a_\pm^\dagger|n_+,n_-\rangle = \sqrt{n_\pm+1}|^{n_+,n_-\rangle}_{n_+,n_-+1\rangle} \quad a_\pm|n_+,n_-\rangle = \sqrt{n_\pm}|^{n_+,n_-\rangle}_{n_+,n_--1\rangle} \quad . \tag{10.87}$$

Two lowering operators must cause a state to vanish to define the vacuum state. Arbitrary states are built from this state as

$$|n_+,n_-\rangle = \frac{\left(a_+^\dagger\right)^{n_+}}{\sqrt{n_+!}}\frac{\left(a_-^\dagger\right)^{n_-}}{\sqrt{n_-!}}|0,0\rangle \quad . \tag{10.88}$$

The the raising and lowering operators, as well as the operator for the third component, in the full SU(2) space are constructed from the Schwinger boson creation-annihilation operators as

$$J_z = \frac{N_+ - N_-}{2} \qquad J_\pm = a_\pm^\dagger a_\mp \quad . \tag{10.89}$$

The SU(2) raising and lowering operators do not change the occupation number of excitations in the Schwinger boson harmonic oscillators, but rather trade population between the spin up/down oscillators. It is straightforward to show from the commutators above that these representations satisfy the standard SU(2) commutation relations

$$[J_z,J_\pm] = \pm J_\pm \qquad [J_+,J_-] = 2J_z \quad . \tag{10.90}$$

Finally, the J^2 operator can be translated into operators acting on the Schwinger boson harmonic oscillators as

$$J^2 = J_z^2 + \frac{1}{2}\left(J_+J_- + J_-J_+\right) = \frac{N}{2}\left(\frac{N}{2}+1\right) \qquad N = n_+ + n_- \tag{10.91}$$

The electric fields become bilinears of doublets of these Schwinger bosons

$$E^a = \frac{1}{2}a^\dagger\sigma^a a \tag{10.92}$$

and the components of the Gauss law operator without matter fields are

$$G^a(x) = \sum_{i=1}^{d} E_L^a(x,i) + E_R^a(x,i) \quad . \tag{10.93}$$

For SU(2) in two spatial dimensions,

$$G^1(x) \propto \sum_{i=1}^{2} a_L(x,i)^\dagger \sigma^x a_L(x,i) + a_R^\dagger(x,i)\sigma^x a_R(x,i) \tag{10.94}$$
$$\propto \sum_{i=1}^{2} a^\dagger_{L,i,+}a_{L,i,-} + a^\dagger_{L,i,-}a_{L,i,+} + a^\dagger_{R,i,+}a_{R,i,-} + a^\dagger_{R,i,-}a_{R,i,+}$$
$$\propto J_+(L,\hat{1}) + J_-(L,\hat{1}) + J_+(L,\hat{2}) + J_-(L,\hat{2}) + J_+(R,\hat{1}) + J_-(R,\hat{1}) + J_+(R,\hat{2}) + J_-(R,\hat{2})$$

$$G^2(x) \propto \sum_{i=1}^{2} a_L(x,i)^\dagger \sigma^y a_L(x,i) + a_R^\dagger(x,i)\sigma^y a_R(x,i) \tag{10.95}$$
$$\propto \sum_{i=1}^{2} a^\dagger_{L,i,+}a_{L,i,-} - a^\dagger_{L,i,-}a_{L,i,+} + a^\dagger_{R,i,+}a_{R,i,-} - a^\dagger_{R,i,-}a_{R,i,+}$$
$$\propto J_+(L,\hat{1}) - J_-(L,\hat{1}) + J_+(L,\hat{2}) - J_-(L,\hat{2}) + J_+(R,\hat{1}) - J_-(R,\hat{1}) + J_+(R,\hat{2}) - J_-(R,\hat{2})$$

$$G^3(x) \propto \sum_{i=1}^{2} a_L(x,i)^\dagger \sigma^z a_L(x,i) + a_R^\dagger(x,i)\sigma^z a_R(x,i) \tag{10.96}$$
$$\propto \sum_{i=1}^{2} a^\dagger_{L,i,+}a_{L,i,+} + a^\dagger_{L,i,-}a_{L,i,-} + a^\dagger_{R,i,+}a_{R,i,+} + a^\dagger_{R,i,-}a_{R,i,-}$$
$$\propto \big(N_+(L,\hat{1}) - N_-(L,\hat{1})\big) + \big(N_+(L,\hat{2}) - N_-(L,\hat{2})\big) \big(N_+(R,\hat{1}) - N_-(R,\hat{1})\big) + \big(N_+(R,\hat{2}) - N_-(R,\hat{2})\big)$$
$$\propto J_z(L,\hat{1}) + J_z(L,\hat{2}) + J_z(R,\hat{1}) + J_z(R,\hat{2}) \tag{10.97}$$

In this construction, a physical state is any state that satisfies $G^1|\psi\rangle = G^2|\psi\rangle = G^3|\psi\rangle = 0$. This is achieved by placing antisymmetrized singlet states at each vertex. For example,

$$|n_+(R,x,\hat{1})n_-(R,x,\hat{1})\rangle|n_-(L,x,\hat{1})n_-(L,x,\hat{1})\rangle : \quad \frac{1}{\sqrt{2}}\left(|01\rangle|10\rangle - |10\rangle|01\rangle\right) \tag{10.98}$$

with all other harmonic oscillators in their ground state is a physical state at a vertex representing a unit of flux flowing through the vertex in the $\hat{1}$ direction. Translating this

state back to the angular momentum basis is implemented with the following relations

$$j = \frac{n_+ + n_-}{2} \qquad m = \frac{n_+ - n_-}{2} \tag{10.99}$$

$$n_+ = j + m \qquad n_- = j - m \tag{10.100}$$

Rewriting the state above in the angular momentum basis produces

$$|\frac{1}{2}, -\frac{1}{2}\rangle - |\frac{1}{2}, \frac{1}{2}\rangle \quad .$$

The physical singlet states at any vertex can be determined by identifying null vectors in the eigenvector decomposition of the Gauss law operators. However, they may be more-easily constructed through contractions over Clebsch-Gordan coefficients.

- 2-point vertex:

$$|\psi\rangle_{2pt,SB}(j) = \sum_{k=0}^{2j} \frac{(-1)^k}{\sqrt{2j+1}} |2j-k,k\rangle |k,2j-k\rangle \tag{10.101}$$

$$|\psi\rangle_{2pt,SB}(j) = \sum_{k=0}^{2j} \langle j, j-k, j, k-j|0,0\rangle \ |2j-k,k\rangle |k,2j-k\rangle \tag{10.102}$$

$$|\psi\rangle_{2pt,JMM'}(j) = \sum_{k=0}^{2} j \frac{(-1)^k}{\sqrt{2j+1}} |j,j-k\rangle |j,-j+k\rangle \tag{10.103}$$

  Pictorially in Schwinger Bosons, the low-j corner states can be envisioned as below where the left-right and top-bottom placement of the numbers indicate occupation of the $+,-$ harmonic oscillator at each link end.

- 3-point vertex:

$$|\psi\rangle_{3pt,JMM'}(j_1,j_2,j_3) = \sum_{m_{1,2,3}=-j_{1,2,3}}^{j_{1,2,3}} \sum_{J=-|j_1+j_2|}^{j_1+j_2} \langle j_1,m_1,j_2,m_2|J,m_1+m_2\rangle \tag{10.104}$$
$$\langle J,m_1+m_2,j_3,m_3|0,0\rangle |j_1,m_1\rangle |j_2,m_2\rangle |j_3,m_3\rangle$$

$$|\psi\rangle_{3pt,SB}(j_1,j_2,j_3) = \sum_{m_{1,2,3}=-j_{1,2,3}}^{j_{1,2,3}} \sum_{J=-|j_1+j_2|}^{j_1+j_2} \langle j_1,m_1,j_2,m_2|J,m_1+m_2\rangle \tag{10.105}$$

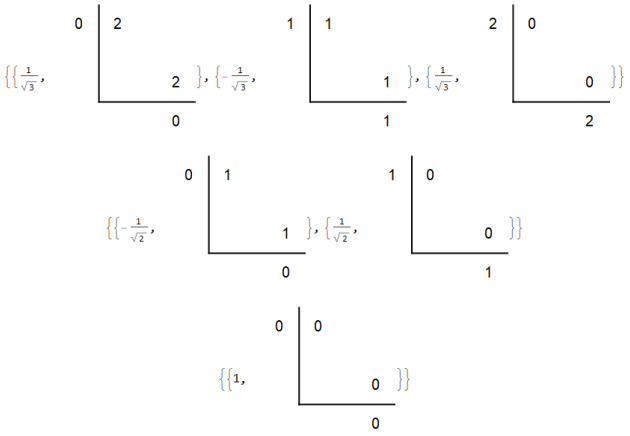

$$\langle J, m_1 + m_2, j_3, m_3 | 0, 0 \rangle$$

$$|j_1 + m_1, j_1 - m_1\rangle |j_2 + m_2, j_2 - m_2\rangle |j_3 + m_3, j_2 - m_3\rangle$$

The following is an example of a physical 3-point vertex state in the basis of Schwinger Bosons,

$$|\frac{1}{2}, 1, \frac{1}{2}\rangle = -\frac{1}{\sqrt{3}}|01\rangle 20\rangle |01\rangle + \frac{1}{\sqrt{6}}|01\rangle |11\rangle |10\rangle + \frac{1}{\sqrt{6}}|10\rangle |11\rangle |01\rangle - \frac{1}{\sqrt{3}}|10\rangle |02\rangle |10\rangle \quad (10.106)$$

where it is easily seen that every state in the superposition satisfies the third Gauss law operator with the total excitation population in the $+$-type oscillatirs equal to the total excitation population in the $-$-type oscillators. Pictorially in Schwinger Bosons, some representative three-point vertex states ($(j_1, j_2, j_3) = (1, 1, 1), (1, 1, 0), (1, \frac{1}{2}, \frac{1}{2})$) can be envisioned as below where the left-right and top-bottom placement of the numbers indicate occupation of the $+, -$ harmonic oscillator at each link end.

The link operators decompose as matrix multiplication between a left and right operator

$$\hat{U} = U_L U_R \qquad U_L = \frac{1}{\sqrt{\hat{n}_L + 1}} \begin{pmatrix} a_-^\dagger & a_+ \\ -a_+^\dagger & a_- \end{pmatrix} \qquad U_R = \begin{pmatrix} a_+^\dagger & a_-^\dagger \\ a_- & -a_+ \end{pmatrix} \frac{1}{\sqrt{\hat{n}_R + 1}} \quad (10.107)$$

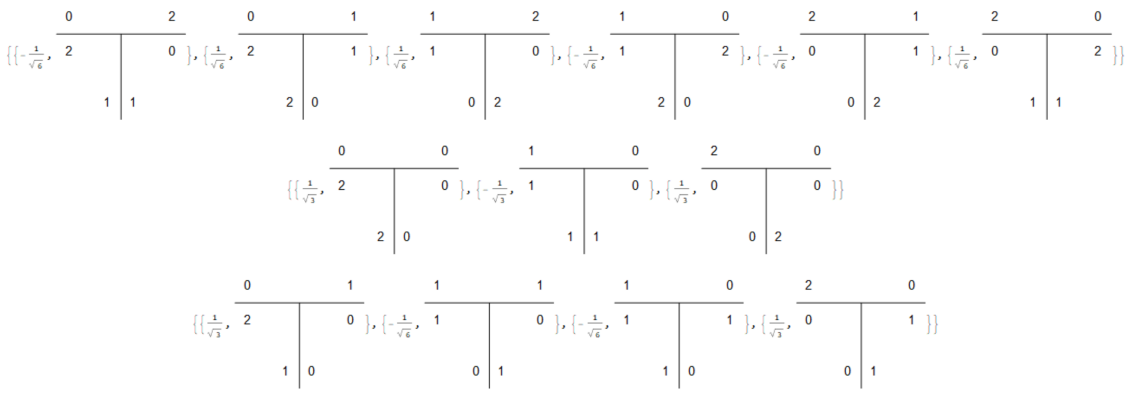

$$U_L^\dagger = \begin{pmatrix} a_- & -a_+ \\ a_+^\dagger & a_-^\dagger \end{pmatrix} \frac{1}{\sqrt{\hat{n}_L + 1}} \qquad U_R^\dagger = \frac{1}{\sqrt{\hat{n}_R + 1}} \begin{pmatrix} a_+ & a_-^\dagger \\ a_- & -a_+^\dagger \end{pmatrix} \tag{10.108}$$

A full plaquette operator beginning at the lower left vertex and and traveling counterclockwise becomes

$$\hat{\square} = \text{Tr } (U_L^\dagger.U_L).(U_R.U_L).(U_R.U_R^\dagger).(U_L^\dagger.U_R^\dagger) \tag{10.109}$$

$$= \text{Tr } U_L^\dagger.(U_L.U_R).(U_L.U_R).(U_R^\dagger.U_L^\dagger).U_R^\dagger \tag{10.110}$$

where the two parenthesis distributions indicate the vertex pairs and the link pairs, respectively. The matrix product operators are kept explicitly to emphasize that these link matrices are to be matrix multiplied together then traced within this 2×2 group space. The Hilbert space structure resides within each link operator as its matrix elements are Hilbert-space operators. Expanding this structure into Hilbert space operators between the Schwinger bosons at the ends of each link may or may not be instructive.

$$\begin{aligned} \hat{\square} = \text{Tr} & \begin{pmatrix} a_- & -a_+ \\ a_+^\dagger & a_-^\dagger \end{pmatrix}_1 \frac{1}{\sqrt{\hat{n}_1 + 1}} \frac{1}{\sqrt{\hat{n}_2 + 1}} \begin{pmatrix} a_-^\dagger & a_+ \\ -a_+^\dagger & a_- \end{pmatrix}_2 \\ & \begin{pmatrix} a_+^\dagger & a_-^\dagger \\ a_- & -a_+ \end{pmatrix}_3 \frac{1}{\sqrt{\hat{n}_3 + 1}} \frac{1}{\sqrt{\hat{n}_4 + 1}} \begin{pmatrix} a_-^\dagger & a_+ \\ -a_+^\dagger & a_- \end{pmatrix}_4 \\ & \begin{pmatrix} a_+^\dagger & a_-^\dagger \\ a_- & -a_+ \end{pmatrix}_5 \frac{1}{\sqrt{\hat{n}_5 + 1}} \frac{1}{\sqrt{\hat{n}_6 + 1}} \begin{pmatrix} a_+ & a_-^\dagger \\ a_- & -a_+^\dagger \end{pmatrix}_6 \end{aligned} \tag{10.111}$$

$$\begin{pmatrix} a_- & -a_+ \\ a_+^\dagger & a_-^\dagger \end{pmatrix}_7 \frac{1}{\sqrt{\hat{n}_7+1}} \frac{1}{\sqrt{\hat{n}_8+1}} \begin{pmatrix} a_+ & a_-^\dagger \\ a_- & -a_+^\dagger \end{pmatrix}_8$$

The odd occupation factors may be moved to the right while the even occupation factors may be collected at the left.

$$\begin{aligned}
\hat{\square} &= \left(\prod_{i\in\{2,4,6,8\}} \frac{1}{\sqrt{\hat{n}_i+1}}\right) \mathrm{Tr} \begin{pmatrix} a_- & -a_+ \\ a_+^\dagger & a_-^\dagger \end{pmatrix}_1 \begin{pmatrix} a_-^\dagger & a_+ \\ -a_+^\dagger & a_- \end{pmatrix}_2 \begin{pmatrix} a_+^\dagger & a_-^\dagger \\ a_- & -a_+ \end{pmatrix}_3 \begin{pmatrix} a_-^\dagger & a_+ \\ -a_+^\dagger & a_- \end{pmatrix}_4 \\
&\quad \begin{pmatrix} a_+^\dagger & a_-^\dagger \\ a_- & -a_+ \end{pmatrix}_5 \begin{pmatrix} a_+ & a_-^\dagger \\ a_- & -a_+^\dagger \end{pmatrix}_6 \begin{pmatrix} a_- & -a_+ \\ a_+^\dagger & a_-^\dagger \end{pmatrix}_7 \begin{pmatrix} a_+ & a_-^\dagger \\ a_- & -a_+^\dagger \end{pmatrix}_8 \left(\prod_{i\in\{1,3,5,7\}} \frac{1}{\sqrt{\hat{n}_i+1}}\right) \\
&= \left(\prod_{i\in\{2,4,6,8\}} \frac{1}{\sqrt{\hat{n}_i+1}}\right) \mathrm{Tr} \begin{pmatrix} a_-a_-^\dagger - a_+a_+^\dagger & a_-a_+ - a_+a_- \\ a_+^\dagger a_-^\dagger - a_-^\dagger a_+^\dagger & a_+^\dagger a_+ + a_-^\dagger a_- \end{pmatrix} \begin{pmatrix} a_+^\dagger a_-^\dagger - a_-^\dagger a_+^\dagger & a_+^\dagger a_+ + a_-^\dagger a_- \\ a_-a_-^\dagger + a_+a_+^\dagger & a_-a_+ - a_+a_- \end{pmatrix} \\
&\quad \begin{pmatrix} a_+^\dagger a_+ + a_-^\dagger a_- & a_+^\dagger a_-^\dagger - a_-^\dagger a_+^\dagger \\ a_-a_+ - a_+a_- & a_-a_-^\dagger + a_+a_+^\dagger \end{pmatrix} \begin{pmatrix} a_-a_+ - a_+a_- & a_-a_-^\dagger + a_+a_+^\dagger \\ a_+^\dagger a_+ + a_-^\dagger a_- & a_+^\dagger a_-^\dagger - a_-^\dagger a_+^\dagger \end{pmatrix} \left(\prod_{i\in\{1,3,5,7\}} \frac{1}{\sqrt{\hat{n}_i+1}}\right) \\
&= \left(\prod_{i\in\{2,4,6,8\}} \frac{1}{\sqrt{\hat{n}_i+1}}\right) \mathrm{Tr} \begin{pmatrix} (a_-a_-^\dagger - a_+a_+^\dagger)(a_+^\dagger a_-^\dagger - a_-^\dagger a_+^\dagger) + (a_-a_+ - a_+a_-)(a_-a_-^\dagger + a_+a_+^\dagger) & (a_-a_-^\dagger - a_+a_+^\dagger)(a_+^\dagger a_+ + a_-^\dagger a_-) + (a_-a_+ - a_+a_-)(a_-a_+ - a_+a_-) \\ (a_+^\dagger a_-^\dagger - a_-^\dagger a_+^\dagger)(a_+^\dagger a_-^\dagger - a_-^\dagger a_+^\dagger) + (a_+^\dagger a_+ + a_-^\dagger a_-)(a_-a_-^\dagger + a_+a_+^\dagger) & (a_+^\dagger a_-^\dagger - a_-^\dagger a_+^\dagger)(a_+^\dagger a_+ + a_-^\dagger a_-) + (a_+^\dagger a_+ + a_-^\dagger a_-)(a_-a_+ - a_+a_-) \end{pmatrix} \\
&\quad \begin{pmatrix} (a_+^\dagger a_+ + a_-^\dagger a_-)(a_-a_+ - a_+a_-) + (a_+^\dagger a_-^\dagger - a_-^\dagger a_+^\dagger)(a_+^\dagger a_+ + a_-^\dagger a_-) & (a_+^\dagger a_+ + a_-^\dagger a_-)(a_-a_-^\dagger + a_+a_+^\dagger) + (a_+^\dagger a_-^\dagger - a_-^\dagger a_+^\dagger)(a_+^\dagger a_-^\dagger - a_-^\dagger a_+^\dagger) \\ (a_-a_+ - a_+a_-)(a_-a_+ - a_+a_-) + (a_-a_-^\dagger + a_+a_+^\dagger)(a_+^\dagger a_+ + a_-^\dagger a_-) & (a_-a_+ - a_+a_-)(a_-a_-^\dagger + a_+a_+^\dagger) + (a_-a_-^\dagger + a_+a_+^\dagger)(a_+^\dagger a_-^\dagger - a_-^\dagger a_+^\dagger) \end{pmatrix} \left(\prod_{i\in\{1,3,5,7\}} \frac{1}{\sqrt{\hat{n}_i+1}}\right) \\
&= \left(\prod_{i\in\{2,4,6,8\}} \frac{1}{\sqrt{\hat{n}_i+1}}\right) \{ \left[(a_-a_-^\dagger - a_+a_+^\dagger)(a_+^\dagger a_-^\dagger - a_-^\dagger a_+^\dagger) + (a_-a_+ - a_+a_-)(a_-a_-^\dagger + a_+a_+^\dagger)\right] \\
&\qquad \times \left[(a_+^\dagger a_+ + a_-^\dagger a_-)(a_-a_+ - a_+a_-) + (a_+^\dagger a_-^\dagger - a_-^\dagger a_+^\dagger)(a_+^\dagger a_+ + a_-^\dagger a_-)\right] \\
&\qquad + \left[(a_-a_-^\dagger - a_+a_+^\dagger)(a_+^\dagger a_+ + a_-^\dagger a_-) + (a_-a_+ - a_+a_-)(a_-a_+ - a_+a_-)\right] \\
&\qquad \times \left[(a_-a_+ - a_+a_-)(a_-a_-^\dagger + a_+a_+^\dagger) + (a_-a_-^\dagger + a_+a_+^\dagger)(a_+^\dagger a_-^\dagger - a_-^\dagger a_+^\dagger)\right] \\
&\qquad + \left[(a_+^\dagger a_-^\dagger - a_-^\dagger a_+^\dagger)(a_+^\dagger a_-^\dagger - a_-^\dagger a_+^\dagger) + (a_+^\dagger a_+ + a_-^\dagger a_-)(a_-a_-^\dagger + a_+a_+^\dagger)\right] \\
&\qquad \times \left[(a_+^\dagger a_+ + a_-^\dagger a_-)(a_-a_-^\dagger + a_+a_+^\dagger) + (a_+^\dagger a_-^\dagger - a_-^\dagger a_+^\dagger)(a_+^\dagger a_-^\dagger - a_-^\dagger a_+^\dagger)\right] \\
&\qquad + \left[(a_+^\dagger a_-^\dagger - a_-^\dagger a_+^\dagger)(a_+^\dagger a_+ + a_-^\dagger a_-) + (a_+^\dagger a_+ + a_-^\dagger a_-)(a_-a_+ - a_+a_-)\right] \\
&\times \left[(a_-a_+ - a_+a_-)(a_-a_-^\dagger + a_+a_+^\dagger) + (a_-a_-^\dagger + a_+a_+^\dagger)(a_+^\dagger a_-^\dagger - a_-^\dagger a_+^\dagger)\right] \} \left(\prod_{i\in\{1,3,5,7\}} \frac{1}{\sqrt{\hat{n}_i+1}}\right)
\end{aligned} \tag{10.112}$$

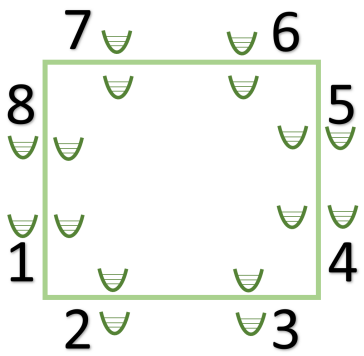

There are $64*4 = 256$ terms in this operator. Of the possible operations at each vertex, eight of them conserve the third component Gauss law requiring $\sum N_+ = \sum N_-$ for the Schwinger bosons at a vertex. If all 8 were distributed independently, there would be $8^4 = 4096$ terms of this plaquette operator. Of these 8, only four of them conserve the matching j-values of both links at a corner $((\uparrow^+,\uparrow^-),(\downarrow^+,\downarrow^-),(\uparrow^-,\uparrow^+),(\downarrow^-,\downarrow^+))$. However, all 8 are present in the above and thus there are inter-vertex correlations constraining the contributing operators.

$$\hat{\square}|0\rangle = U_L^\dagger|00\rangle U_L|00\rangle U_R|00\rangle U_L|00\rangle U_R|00\rangle U_R^\dagger|00\rangle U_L^\dagger|00\rangle U_R^\dagger|00\rangle \tag{10.113}$$

$$= \begin{pmatrix} 0 & 0 \\ |10\rangle & |01\rangle \end{pmatrix} \frac{1}{\sqrt{1}}\frac{1}{\sqrt{2}} \begin{pmatrix} |01\rangle & 0 \\ -|10\rangle & 0 \end{pmatrix} \begin{pmatrix} |10\rangle & |01\rangle \\ 0 & 0 \end{pmatrix} \frac{1}{\sqrt{1}}\frac{1}{\sqrt{2}} \begin{pmatrix} |01\rangle & 0 \\ -|10\rangle & 0 \end{pmatrix} \tag{10.114}$$

$$\begin{pmatrix} |10\rangle & |01\rangle \\ 0 & 0 \end{pmatrix} \frac{1}{\sqrt{1}}\frac{1}{\sqrt{2}} \begin{pmatrix} 0 & |01\rangle \\ 0 & -|10\rangle \end{pmatrix} \begin{pmatrix} 0 & 0 \\ |10\rangle & |01\rangle \end{pmatrix} \frac{1}{\sqrt{1}}\frac{1}{\sqrt{2}} \begin{pmatrix} 0 & |01\rangle \\ 0 & -|10\rangle \end{pmatrix}$$

$$= \frac{1}{4} \begin{pmatrix} 0 & 0 \\ 0 & (|10\rangle|01\rangle - |01\rangle|10\rangle)^{\otimes 4} \end{pmatrix} \tag{10.115}$$

Taking the trace of the plaquette operator produces the $|j = 1/2\rangle$ state

$$\mathrm{Tr}\hat{\square}|0\rangle = \left(\frac{1}{\sqrt{2}}(|10\rangle|01\rangle - |01\rangle|10\rangle)\right)^{\otimes 4} = |j = 1/2\rangle|j = 1/2\rangle|j = 1/2\rangle|j = 1/2\rangle \quad . \tag{10.116}$$

This calculation is consistent with the single-plaquette matrix elements evaluated above in the JMM' basis. To go one step further and see the splitting into a superposition of j states,

consider the plaquette operator's action on the $|j = 1/2\rangle$ state.

$$\hat{\square}|j_{\square} = 1/2\rangle = \frac{1}{4} U_L^{\dagger} U_L \left(|10\rangle|01\rangle - |01\rangle|10\rangle\right) U_R U_L \left(|10\rangle|01\rangle - |01\rangle|10\rangle\right) \tag{10.117}$$
$$U_R U_R^{\dagger} \left(|10\rangle|01\rangle - |01\rangle|10\rangle\right) U_L^{\dagger} U_R^{\dagger} \left(|10\rangle|01\rangle - |01\rangle|10\rangle\right)$$

$$\begin{aligned} U_L^{\dagger} U_L |j = \frac{1}{2}\rangle &= \frac{1}{\sqrt{\hat{n}_2 + 1}} \begin{pmatrix} a_- a_-^{\dagger} - a_+ a_+^{\dagger} & a_- a_+ - a_+ a_- \\ a_+^{\dagger} a_-^{\dagger} - a_-^{\dagger} a_+^{\dagger} & a_+^{\dagger} a_+ + a_-^{\dagger} a_- \end{pmatrix} \frac{1}{\sqrt{\hat{n}_1 + 1}} \frac{1}{2} \left(|10\rangle|01\rangle - |01\rangle|10\rangle\right) \\ &= \frac{1}{\sqrt{2}} \frac{1}{\sqrt{\hat{n}_1 + 1}} \begin{pmatrix} |00\rangle|11\rangle - |00\rangle|11\rangle & -2|00\rangle|00\rangle \\ 2|20\rangle|02\rangle - 2|11\rangle|11\rangle + 2||02\rangle|20\rangle & -|00\rangle|00\rangle + |00\rangle|00\rangle \end{pmatrix} \\ &= \begin{pmatrix} 0 & -|00\rangle|00\rangle \\ \frac{1}{\sqrt{3}} \left(|20\rangle|02\rangle - |11\rangle|11\rangle + ||02\rangle|20\rangle\right) & 0 \end{pmatrix} \end{aligned} \tag{10.118}$$

$$U_R U_L |j = \frac{1}{2}\rangle = \begin{pmatrix} \frac{1}{\sqrt{3}} \left(|20\rangle 02\rangle + |02\rangle|20\rangle - |11\rangle|11\rangle\right) & 0 \\ 0 & |00\rangle|00\rangle \end{pmatrix} \tag{10.119}$$

$$U_R U_R^{\dagger} |j = \frac{1}{2}\rangle = \begin{pmatrix} 0 & |20\rangle|02\rangle + |02\rangle|20\rangle - |11\rangle|11\rangle \\ |00\rangle|00\rangle & 0 \end{pmatrix} \tag{10.120}$$

$$U_L^{\dagger} U_R^{\dagger} |j = \frac{1}{2}\rangle = \begin{pmatrix} |00\rangle|00\rangle & 0 \\ 0 & \frac{1}{\sqrt{3}} \left(|20\rangle|02\rangle + |02\rangle|20\rangle - |11\rangle|11\rangle\right) \end{pmatrix} \tag{10.121}$$

With these vertex operators distributed in the two-dimensional group space matrices to implement correlated operations, the plaquette operator on the $|j = \frac{1}{2}\rangle$ state is evaluated to be

$$\hat{\square}|j_{\square} = \frac{1}{2}\rangle = U_L^{\dagger} U_L |j = \frac{1}{2}\rangle U_R U_L |j = \frac{1}{2}\rangle U_R U_R^{\dagger} |j = \frac{1}{2}\rangle U_L^{\dagger} U_R^{\dagger} |j = \frac{1}{2}\rangle \tag{10.122}$$

$$= \begin{pmatrix} 0 & |j = 0\rangle \\ |j = 1\rangle & 0 \end{pmatrix} \begin{pmatrix} |j = 1\rangle & 0 \\ 0 & |j = 0\rangle \end{pmatrix} \begin{pmatrix} 0 & |j = 1\rangle \\ |j = 0\rangle & 0 \end{pmatrix} \begin{pmatrix} |j = 0\rangle & 0 \\ 0 & |j = 1\rangle \end{pmatrix} \tag{10.123}$$

$$= \begin{pmatrix} |j = 0\rangle|j = 0\rangle|j = 0\rangle|j = 0\rangle & 0 \\ 0 & |j = 1\rangle|j = 1\rangle|j = 1\rangle|j = 1\rangle \end{pmatrix} \tag{10.124}$$

Finally, taking the trace results in again unity matrix elements consistent with those calculated in the JMM' basis above.

Determining the two-plaquette matrix elements as above with Schwinger bosons requires significantly more algebraic stability and was completed with Mathematica in the way described: pairing plaquette link operators by vertices and keeping track of the non-zero state values within the 2×2 group-space matrix structure. The non-zero matrix elements up to $\Lambda_j = 1$ were confirmed to be consistent with those calculated in the JMM' basis.

Chapter 11

ENTANGLEMENT FLUCTUATIONS IN LOW-ENERGY SCATTERING OF NUCLEI

The content of this chapter is associated with Ref. [50]:

Silas R. Beane et al. "Entanglement Suppression and Emergent Symmetries of Strong Interactions". *Phys. Rev. Lett.* 122.10 (2019), p. 102001. DOI: 10.1103/PhysRevLett.122.102001. arXiv: 1812.03138 [nucl-th]

Across the QCD phase diagram, the natural degrees of freedom transition from quarks and gluons at high temperature and baryon chemical potential to hadronic matter at low temperature and chemical potential. Across this transition, asymptotically free dynamics are traded for colorless confinement in the infrared. When probed at length scales smaller than the hadronic radius, such as capable in deep inelastic scattering, the partonic description of such colorless objects has been found to be captured by a maximally entangled state with entanglement entropy ultimately controlled by the gluon distribution dominating at small constituent momentum fraction [192]. Understanding the flow of entanglement in the low-energy interactions of such highly internally entangled nuclei is the motivation of this chapter where the fluctuations of entanglement between nucleon spins upon low-energy scattering is characterized through the s-wave scattering matrix.

Entanglement suppression in the strong interaction S-matrix is shown to be correlated with approximate spin-flavor symmetries that are observed in low-energy baryon interactions, the Wigner $SU(4)$ symmetry for two flavors and an $SU(16)$ symmetry for three flavors. We conjecture that dynamical entanglement suppression is a property of the strong interactions in the infrared, giving rise to these emergent symmetries and providing powerful constraints predicting the nature of nuclear and hypernuclear forces in dense matter.

11.1 Introduction

Understanding approximate global symmetries in the strong interactions has played an important historical role in the development of the theory of Quantum Chromodynamics (QCD). Baryon number symmetry arises in QCD because it is impossible to include a marginal or relevant interaction consistent with Lorentz and gauge symmetry that violates baryon number, while the axial and vector flavor symmetries are understood to be due to the small ratio of quark masses (and their differences) to the QCD scale. The approximate low-energy $SU(2n_f)$ spin-flavor symmetry for $n_f = 2, 3$ flavors that relates spin-1/2 and spin-3/2 baryons can be understood as arising at leading order (LO) in the large-N_c expansion, where N_c is the number of colors [389, 390]. In low-energy nuclear physics, a different spin-flavor symmetry is observed in the structure of light-nuclei and their β-decay rates, namely Wigner's $SU(4)$ symmetry, where the two spin states of the neutron and of the proton transform as the 4-dimensional fundamental representation [391, 392, 393]. It has been shown that this symmetry also arises from the large-N_c expansion at energies below the Δ mass [394, 395, 396]. The agreement of large-N_c predictions with nuclear phenomenology has been extended to higher-order interactions [397, 398, 399, 400], three-nucleon systems [401, 402, 403], and to studies of hadronic parity violation [404, 405, 406]. Recently, however, lattice QCD computations for $n_f = 3$ have revealed an emergent $SU(16)$ symmetry in low-energy interactions of the baryon octet—analogous to Wigner's $SU(4)$, but with the two spin states each of the eight baryons transforming as the 16-dimensional representation of $SU(16)$ [407]. This low energy symmetry has been lacking an explanation from QCD. In this Letter, we show that both Wigner's $SU(4)$ symmetry for $n_f = 2$ and $SU(16)$ for $n_f = 3$ correspond to fixed lines of minimal fluctuations of quantum entanglement in the S-matrix for baryon-baryon scattering; we propose entanglement suppression to be a dynamical property of QCD that is the origin of these emergent symmetries [1].

[1]Note that this proposal for the suppression of entanglement fluctuations is distinct from the methods of Ref. [193] where a principle of maximum entanglement is proposed to constrain quantum electrodynamics and the weak interactions.

Of the many features of quantum mechanics and quantum field theory (QFT) that dictate the behavior of subatomic particles, entanglement and its associated non-locality are perhaps the most striking in their contrast to everyday experience. The degree to which a system is entangled, or its deviation from tensor-product structure, provides a measure of how "non-classical" it is. The importance of entanglement as a feature of quantum theory has been known since the work of Einstein, Podolsky and Rosen [8] and later pioneering papers [9, 408, 11], and has become a core ingredient in quantum information science, communication and perhaps in understanding the very fabric of spacetime [409, 410, 411]. Despite this long history, the implications of entanglement in QFTs, e.g., Refs. [412, 186, 413, 187, 188, 189, 190, 414, 415, 191, 416, 156], and in particular for experimental observables in high-energy and heavy-ion collisions are only now starting to be explored [417, 418, 192, 419, 420, 421, 422, 423, 424, 425, 193]. Here we study the role of entanglement in low-energy nuclear interactions.

11.2 Operator Entanglement Power

The purpose of the entanglement power [426] is to promote the entanglement measure from a quantity on states to a quantity on operators. An operator's entanglement power represents a global property of the operator's ability to take an initially unentangled (product) state and produce entanglement. The entanglement power $\mathcal{E}(U)$ is formulated out of a linearized entropy $E(U)$

$$E(|\psi\rangle) = 1 - \mathrm{Tr}_1 \left(\mathrm{Tr}_2 |\psi\rangle\langle\psi|\right)^2 \quad . \tag{11.1}$$

When ψ is unentangled, the reduced density matrix remains pure and this linearized entropy is found to be zero. The operator entanglement power averages this quantity over the operator's action on pure product states

$$\mathcal{E}(U) = \int \mathcal{D}\psi_1 \mathcal{D}\psi_2 \; E\left(U \; |\psi_1\rangle \otimes |\psi_2\rangle\right) \quad . \tag{11.2}$$

For a uniform distribution over product states (not necessary, but commonly often chosen), the entanglement power is calculated through a uniform integration over two independent

Bloch spheres

$$\mathcal{E}(U) = \frac{1}{(4\pi)^2}\int \sin\theta \mathrm{d}\theta \mathrm{d}\phi \sin\theta' \mathrm{d}\theta' \mathrm{d}\phi' \\ E\left(U\left(\cos\frac{\theta}{2}|0\rangle + e^{i\phi}\sin\frac{\theta}{2}|1\rangle\right)\otimes\left(\cos\frac{\theta'}{2}|0\rangle + e^{i\phi'}\sin\frac{\theta'}{2}|1\rangle\right)\right) \quad (11.3)$$

with polar θ angles having bounds zero to π and azimuthal ϕ angles having bounds zero to 2π in the integration. In the following, the maximum bounds for the entanglement power are calculated for a general two-qubit operator and for a collection of parameterized three-qubit operators.

Two Qubits: $\{c_1, c_2, c_3\}$ $\quad \mathcal{E}^{max}(U) = \frac{2}{9}$

For an operator acting on the Hilbert space of two qubits, the cartan subalgebra of SU(4) parameterizes the two-body entanglement

$$U = e^{-i(c_1 X\otimes X + c_2 Y\otimes Y + c_3 Z\otimes Z)} \quad . \quad (11.4)$$

Thought of as shifting amplitudes onto all possible Bell states, any two-qubit pure state can be created from the space of product states through a single application of this unitary preceded and followed by a pair of single-qubit operators. Thus, every entangling operator on the two qubit system can be (non-uniquely) assigned values of c_1, c_2, and c_3. The analytic expression for the entangling power[2] for this general operator structure is

$$\mathcal{E}(U) = \frac{1}{18}\left(3 - \cos(4c_1)\cos(4c_2) - \cos(4c_1)\cos(4c_4) - \cos(4c_2)\cos(c_3)\right) \quad . \quad (11.5)$$

The numerical maximum value of the entanglement power for a two-qubit operator is $\frac{2}{9}$, achieved for e.g., $(c_1, c_2, c_3) = \left(\frac{\pi}{4}, x, 0\right)$.

Three Qubits: $\{c_2, c_3, c_4\}$ $\quad \mathcal{E}^{max}(U) = \frac{4}{9}$

For a three qubit operator, the decomposition of the SU(8) (augmented) entangling matrix as discussed in Ref. [426] is

$$U = e^{-ic_8 ZZZ} e^{-i(c_1 XXX + c_2 YYX + c_3 YXY + c_4 XYY + c_5 ZIZ + c_6 ZZI)} e^{-ic_7 ZZZ} \quad , \quad (11.6)$$

[2]Distinct from Eq. (10) of Ref. [426] by a factor of 2

inspired by the seven dimensional Cartan subalgebra. For operators characterized by non-zero $\{c_2, c_3, c_4\}$, the analytic value of the entangling power is

$$\mathcal{E}(U) = \frac{1}{18}\Bigg(5 - \cos(4c_2) - \cos(4c_3) - \frac{1}{3}\cos(4c_2)\cos(4c_3) - \cos(4c_4) \\ -\frac{1}{3}\cos(4c_2)\cos(4c_4) - \frac{1}{3}\cos(4c_3)\cos(4c_4) - \cos(4c_2)\cos(4c_3)\cos(4c_4)\Bigg) \quad . \quad (11.7)$$

Three Qubits: $\{c_1, c_2, c_3, c_4\} \quad \mathcal{E}^{max}(U) = \frac{4}{9}$

For the larger class of three-qubit operators characterized by non-zero $\{c_1, c_2, c_3, c_4\}$, the analytic value of the entangling power is

$$\mathcal{E}(U) = \frac{1}{18}\Bigg(\frac{17}{3} - \frac{2}{3}\cos(4c_1) - \frac{2}{3}\cos(4c_2) - \frac{1}{3}\cos(4c_1)\cos(4c_2) - \frac{2}{3}\cos(4c_3) \\ - \frac{1}{3}\cos(4c_1)\cos(4c_3) - \frac{1}{3}\cos(4c_2)\cos(4c_3) - \frac{2}{3}\cos(4c_4) \\ - \frac{1}{3}\cos(4c_1)\cos(4c_4) - \frac{1}{3}\cos(4c_2)\cos(4c_4) - \frac{1}{3}\cos(4c_3)\cos(4c_4) \\ - \cos(4c_1)\cos(4c_2)\cos(4c_3)\cos(4c_4) + \sin(4c_1)\sin(4c_2)\sin(4c_3)\sin(4c_4)\Bigg) \quad . \quad (11.8)$$

Three Qubits: $\{c_1, c_2, c_3, c_4, c_5, c_6\}$ Tr: 3 $\quad \mathcal{E}^{max}(U) = \frac{4}{9}$

While the above constrained parameterizations have been symmetric with respect to the bipartition chosen in the negativity (between particles 1 and 2 or between particles 2 and 3), the introduction of non-zero $\{c_5, c_6\}$ break this symmetry.

$$\mathcal{E}(U) = \frac{17}{54} - \frac{1}{54}\cos(4c_1) - \frac{1}{54}\cos(4c_2) - \frac{1}{54}\cos(4c_3) - \frac{1}{54}\cos(4c_1)\cos(4c_3) \\ - \frac{1}{54}\cos(4c_2)\cos(4c_3) - \frac{1}{54}\cos(4c_4) - \frac{1}{54}\cos(4c_1)\cos(4c_4) \\ - \frac{1}{54}\cos(4c_2)\cos(4c_4) - \frac{1}{18}\cos(4c_1)\cos(4c_2)\cos(4c_3)\cos(4c_4) \\ - \frac{1}{54}\cos(4c_1)\cos(4c_5) - \frac{1}{54}\cos(4c_2)\cos(4c_5) \\ - \frac{1}{54}\cos(4c_1)\cos(4c_2)\cos(4c_5) - \frac{1}{54}\cos(4c_3)\cos(4c_5) - \frac{1}{54}\cos(4c_4)\cos(4c_5) \\ - \frac{1}{54}\cos(4c_3)\cos(4c_4)\cos(4c_5) + \frac{1}{18}\sin(4c_1)\sin(4c_2)\sin(4c_3)\sin(4c_4) \quad (11.9)$$

Three Qubits: $\{c_1, c_2, c_3, c_4, c_5, c_6\}$ Tr: 2,3 $\quad \mathcal{E}^{max}(U) = \frac{4}{9}$

$$\begin{aligned}\mathcal{E}(U) = \frac{17}{54} &- \frac{1}{54}\cos(4c_1)\cos(4c_2) - \frac{1}{54}\cos(4c_1)\cos(4c_3) - \frac{1}{54}\cos(4c_2)\cos(4c_4) \\ &- \frac{1}{54}\cos(4c_3)\cos(4c_4) - \frac{1}{18}\cos(4c_1)\cos(4c_2)\cos(4c_3)\cos(4c_4) - \frac{1}{54}\cos(4c_1)\cos(4c_5) \\ &- \frac{1}{54}\cos(4c_2)\cos(4c_5) - \frac{1}{54}\cos(4c_3)\cos(4c_5) - \frac{1}{54}\cos(4c_4)\cos(4c_5) \\ &- \frac{1}{54}\cos(4c_1)\cos(4c_6) - \frac{1}{54}\cos(4c_2)\cos(4c_6) - \frac{1}{54}\cos(4c_3)\cos(4c_6) \\ &- \frac{1}{54}\cos(4c_4)\cos(4c_6) - \frac{1}{54}\cos(4c_2)\cos(4c_3)\cos(4c_5)\cos(4c_6) \\ &- \frac{1}{54}\cos(4c_1)\cos(4c_4)\cos(4c_5)\cos(4c_6) + \frac{1}{18}\sin(4c_1)\sin(4c_2)\sin(4c_3)\sin(4c_4) \\ &- \frac{1}{54}\sin(4c_2)\sin(4c_3)\sin(4c_5)\sin(4c_6) + \frac{1}{54}\sin(4c_1)\sin(4c_4)\sin(4c_5)\sin(4c_6) \quad (11.10)\end{aligned}$$

Even with the linearization of the entanglement measure, the analytic expressions of the entanglement power become rapidly unwieldy, though remain numerically well-behaved.

Due to the positive semi-definite nature of the entanglement entropy, an operator may only have zero entanglement power if it is incapable of producing entanglement from any product pure state. This is the case for example of the identity operator as well as the SWAP operator. One can plot representative distributions of the integrand for various choices of common entangling unitaries and the results are shown in Fig.11.1. It is interesting to see from these plots that, while each of these operators saturate the bound of $\frac{2}{9}$ for the entanglement power, their distributions of entanglement power density over the space of product states are quite different, though none of them have support at the poles. This is to say that a product state with either qubit sitting at $\theta = 0, \pi$ responds very little to the attempted entanglement by 2-qubit gates. A simple example is the action of a $CNOT$ on any state in the computational basis $|0\rangle\otimes|1\rangle$ which is only shifted to another computational-basis state with no production of entanglement. This observation indicates that gates, too, carry a fundamental directionality—in this case the CNOT being defined in the Z computational basis. To entangle from the pole using the $CNOT$ operator, one can first Hadamard down to the equator where the CNOT gate has maximal entanglement power density. The holes in these density plots can be also understood. With the CNOT.H gate, a state with $\theta = \frac{\pi}{2}$ and $\phi = \pi$ does not become entangled by the application of U. Rather, the Hadamard takes

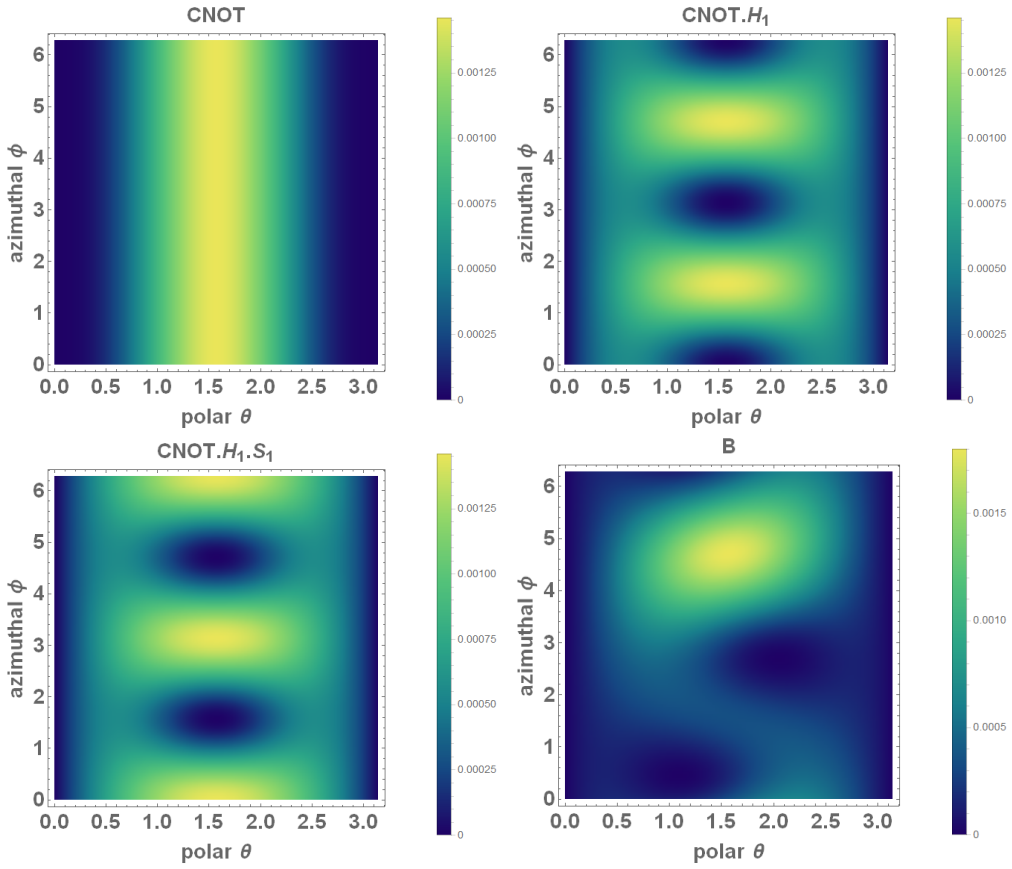

Figure 11.1: For a choice of $(\theta', \phi') = (2.5, 2.5)$ (well away from the poles where the entanglement power density tends to vanish over all angles in the second Bloch sphere. Note the boundaries of the polar angle here have low entanglement power.), the entanglement power density is plotted over the angles of the first Bloch sphere. The B gate is entangling operator of Eq. (11.4) with angles $(c_1, c_2, c_3) = \left(\frac{\pi}{4}, \frac{\pi}{8}, 0\right)$.

what begins as a superposition state on the equator of the first Bloch sphere and rotates it to the pole from which the CNOT is incapable of entangling. As a result, the product state remains a product state.

11.3 Entanglement in Neutron-Proton Scattering: S-matrix

In general, a low-energy scattering event can entangle position, spin, and flavor quantum numbers, and it is therefore natural to assign an entanglement power to the S-matrix for nucleon-nucleon scattering. We choose to define the entanglement power of the S-matrix in a two-particle spin space [427, 426], noting that this choice is not unique and that others will be explored elsewhere [428]. This is determined by the action of the S-matrix on an incoming two-particle tensor product state with randomly-oriented spins, $|\psi_{\rm in}\rangle = \hat{R}(\Omega_1)|\uparrow\rangle_1 \otimes \hat{R}(\Omega_2)|\uparrow\rangle_2$, where $\hat{R}(\Omega_j)$ is the rotation operator acting in the $j^{\rm th}$ spin-$\frac{1}{2}$ space, and all other quantum numbers associated with the states have been suppressed. For low-energy processes, this random spin pair projects onto the two states with total spin $S = 0, 1$, and associated phase shifts $\delta_{0,1}$, in the ${}^1S_0$ and ${}^3S_1$ channels, respectively, with projections onto higher angular momentum states suppressed by powers of the nucleon momenta. The entanglement power, $\mathcal{E}$, of the S-matrix, $\hat{\mathbf{S}}$, is defined as

$$\mathcal{E}(\hat{\mathbf{S}}) = 1 - \int \frac{d\Omega_1}{4\pi}\,\frac{d\Omega_2}{4\pi}\,{\rm Tr}_1\left[\,\hat{\rho}_1^2\,\right] \quad , \tag{11.11}$$

where $\hat{\rho}_1 = {\rm Tr}_2\left[\,\hat{\rho}_{12}\,\right]$ is the reduced density matrix for particle 1 of the two-particle density matrix $\hat{\rho}_{12} = |\psi_{\rm out}\rangle\langle\psi_{\rm out}|$ with $|\psi_{\rm out}\rangle = \hat{\mathbf{S}}|\psi_{\rm in}\rangle$. By describing the average action of $\hat{\mathbf{S}}$ to transition a tensor-product state to an entangled state, the entanglement power expresses a state-independent entanglement measure that vanishes when $|\psi_{\rm out}\rangle$ remains a tensor product state for any $|\psi_{\rm in}\rangle$.

Following the analysis of Ref. [193], we consider the spin-space entanglement of two distinguishable particles, the proton and neutron for $n_f = 2$ QCD. Neglecting the small tensor-force-induced mixing of the ${}^3S_1$ channel with the ${}^3D_1$ channel, the S-matrix for low-energy scattering below inelastic threshold in these sectors can be decomposed as

$$\hat{\mathbf{S}} \;=\; \frac{1}{4}\left(3e^{i2\delta_1} + e^{i2\delta_0}\right)\hat{\mathbf{1}} \;+\; \frac{1}{4}\left(e^{i2\delta_1} - e^{i2\delta_0}\right)\hat{\boldsymbol{\sigma}}\cdot\hat{\boldsymbol{\sigma}}, \tag{11.12}$$

where $\hat{\mathbf{1}} = \hat{\mathcal{I}}_2 \otimes \hat{\mathcal{I}}_2$ and $\hat{\boldsymbol{\sigma}} \cdot \hat{\boldsymbol{\sigma}} = \sum_{\alpha=1}^{3} \hat{\boldsymbol{\sigma}}^\alpha \otimes \hat{\boldsymbol{\sigma}}^\alpha$. It follows that the entanglement power of $\hat{\mathbf{S}}$ is

$$\mathcal{E}(\hat{\mathbf{S}}) \;=\; \frac{1}{6}\,\sin^2\left(2(\delta_1 - \delta_0)\right) \quad , \tag{11.13}$$

which vanishes when $\delta_1 - \delta_0 = m\frac{\pi}{2}$ for any integer m. This includes the $SU(4)$ symmetric case $\delta_1 = \delta_0$ where the coefficient of $\hat{\boldsymbol{\sigma}} \cdot \hat{\boldsymbol{\sigma}}$ vanishes (indicating the 6-dimensional irrep). Special fixed points where the entanglement power vanishes occur when the phase shifts both vanish, $\delta_1 = \delta_0 = 0$, or are both at unitarity, $\delta_1 = \delta_0 = \frac{\pi}{2}$, or when $\delta_1 = 0$, $\delta_0 = \frac{\pi}{2}$ or $\delta_1 = \frac{\pi}{2}$, $\delta_0 = 0$. The S-matrices at these fixed points with vanishing entanglement power are $\hat{\mathbf{S}} = \pm\hat{\mathbf{1}}$ and $\pm(\hat{\mathbf{1}} + \hat{\boldsymbol{\sigma}} \cdot \hat{\boldsymbol{\sigma}})/2$ [3].

The entanglement power in nature is plotted in Fig. 11.2 as a function of the center-of-mass nucleon momentum, p, up to pion production threshold, making use of the ${}^1S_0$ and ${}^3S_1$ phase shifts derived from the analyses of Refs. [429, 430, 431, 432]. The four regions indicated are distinguished by the role of non-perturbative physics. Region I shows that entanglement power approaches zero in the limit $p \to 0$, as will be the case for any finite range interaction not at unitarity. At momenta around the scale of the inverse scattering lengths, region II, poles and resonances of $\hat{\mathbf{S}}$ produce highly-entangling interactions. This non-perturbative structure could be considered a source of ultra-low-momentum entanglement power; experimental evidence for this is expected to be found in the vanishing modification of np-scattering quantum correlations at 19.465(42) MeV where the phase shifts differ by $\pi/2$ and $|p\uparrow, n\downarrow\rangle$ scatters into $|p\downarrow, n\uparrow\rangle$. In region IV, where energies are of order the chiral symmetry breaking scale, the entangling interactions of quark and gluon degrees of freedom become prominent. It is region III that is the main focus of this paper—away from the far-infrared structure but with nucleons as fundamental degrees of freedom, the entanglement power is suppressed. Once relativistic corrections and ${}^3S_1$-${}^3D_1$ mixing—parametrically suppressed at low-energy—are included in Eq. (11.20), $\mathcal{E}(\hat{\mathbf{S}})$ is expected to remain suppressed but non-zero, indicating that the entanglement suppression in nature is only partial.

---

[3] The S-matrices at the four fixed points realize a representation of the Klein four-group, $\mathbb{Z}_2 \otimes \mathbb{Z}_2$.

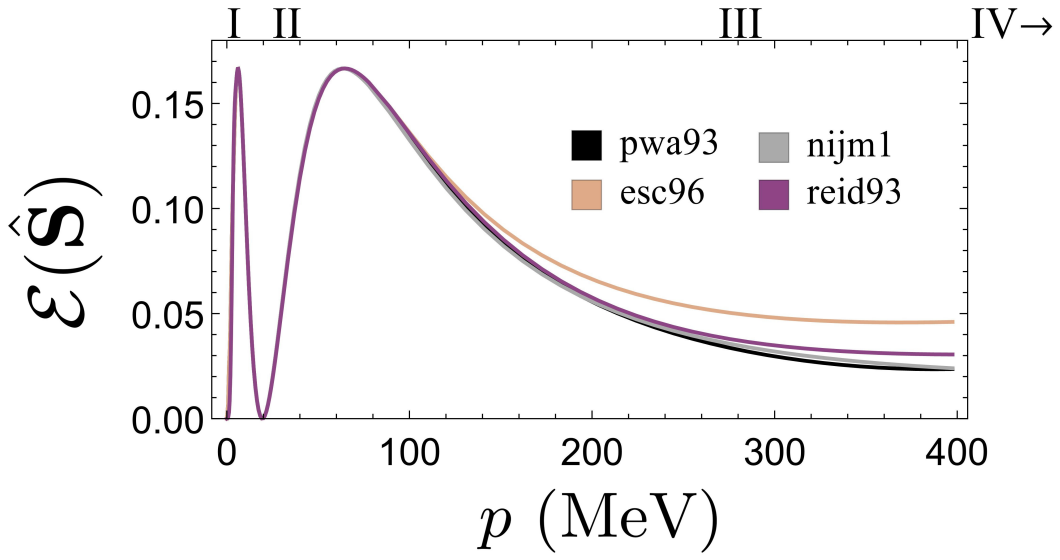

Figure 11.2: The entanglement power, $\mathcal{E}(\hat{\mathbf{S}})$, of the S-matrix as a function of p, the center-of-mass nucleon momentum. The ${}^1S_0$ and ${}^3S_1$ phase shifts used to calculate $\mathcal{E}(\hat{\mathbf{S}})$ were taken from four different models [429, 430, 431, 432, 433] to provide a naïve estimate of systematic uncertainties. Data for this figure may be found in Table 2 in the supplemental material.

11.4 Entanglement in Hyperon-Hyperon Scattering: Pionless EFT

Much progress has been made in nuclear physics in recent years by considering low-energy effective field theories (EFTs), constrained by data from nucleon scattering. The $\delta_{0,1}$ phase shifts can be computed for energies below the pion mass, from the pionless EFT for nucleon-nucleon interactions. The leading interaction in the effective Lagrangian is

$$\mathcal{L}_{\rm LO}^{n_f=2} = -\frac{1}{2}C_S(N^\dagger N)^2 - \frac{1}{2}C_T\left(N^\dagger \boldsymbol{\sigma} N\right)\cdot\left(N^\dagger \boldsymbol{\sigma} N\right) \ , \tag{11.14}$$

where N represents both spin states of the proton and neutron fields. These interactions can be re-expressed as contact interactions in the ${}^1S_0$ and ${}^3S_1$ channels with couplings $\overline{C}_0 = (C_S - 3C_T)$ and $\overline{C}_1 = (C_S + C_T)$ respectively, where the two couplings are fit to reproduce the ${}^1S_0$ and ${}^3S_1$ scattering lengths. The $\overline{C}$ coefficients both run with the renormalization group

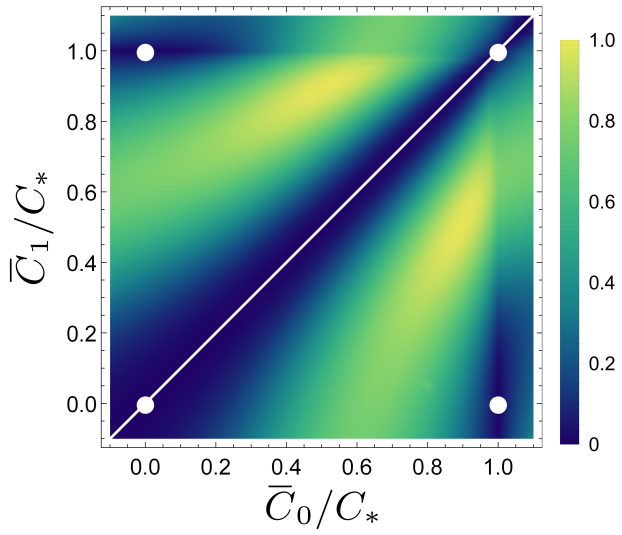

Figure 11.3: Density plot of the entanglement power $\mathcal{E}(\hat{\mathbf{S}})$ of the S-matrix (see Eq. (11.21)) integrated over center of mass momenta $0 \leq p \leq m_\pi/2$, versus the Lagrangian couplings $\overline{C}_0/C_\star$ and $\overline{C}_1/C_\star$ where $C_\star$ is the critical coupling for unitary scattering. The entanglement power vanishes at the four conformal fixed-points (white points), as well as the fixed line corresponding to Wigner $SU(4)$ symmetry (white diagonal).

as described in Ref. [172, 171] with a stable IR fixed point at $\overline{C} = 0$, corresponding to free particles, and a nontrivial, unstable IR fixed point at $\overline{C} = C_\star$ corresponding to a divergent scattering length and constant phase shift of $\delta = \pi/2$ (the "unitary" fixed point). At the four fixed points (described above), where $\{\overline{C}_0, \overline{C}_1\}$ take the values 0 or $C_\star$, the theory has a conformal ("Schrödinger") symmetry; there is also a fixed line of enhanced symmetry at $C_T = 0$, or equivalently $\overline{C}_0 = \overline{C}_1$, where the theory possesses the Wigner $SU(4)$ symmetry, as apparent from the form of Eq. (11.14) with $C_T = 0$. When fitting to the scattering lengths one finds $C_T \ll C_S \simeq C_\star$, since scattering lengths are unnaturally large in both channels. Therefore, low-energy QCD has approximate $SU(4)$ symmetry and sits close to the $\{C_\star, C_\star\}$ conformal fixed point [434]. The emergence of $SU(4)$ symmetry (but not necessarily conformal symmetry) follows from the large-N_c expansion where $C_T/C_S = O(1/N_c^2)$ [394].

While the previous section has shown that the S-matrix entanglement power may be written as a simple function of the difference between the ${}^1S_0$ and ${}^3S_1$ phase shifts, it is enlightening to express the entanglement power directly in terms of lagrangian coefficients. In the context of the NN pionless EFT [172, 171, 173, 174], the nucleon-nucleon scattering amplitude (not including ${}^3S_1$-${}^3D_1$ mixing) may be determined in the PDS scheme [172, 171] as

$$i\mathcal{A} = \frac{-iC(p^2,\mu)}{1 + MC(p^2,\mu)\,(\mu + ip)\,/4\pi} \quad , \tag{11.15}$$

furnishing a unitary S-matrix,

$$S = 1 + i\left(\frac{pM}{2\pi}\right)\mathcal{A} \quad , \tag{11.16}$$

where M is the nucleon mass, μ is the renormalization scale, p is the magnitude of the center-of-mass nucleon momentum, and $C(p^2,\mu)$ is the tree-level s-wave vertex from the NN contact interactions. To analyze the production of entanglement in the spin sector, this vertex in the ${}^1S_0$-${}^3S_1$ channels is decomposed as

$$C(p^2,\mu)_\sigma \;\; = \;\; C_S\;\hat{\mathbf{1}} \;+\; C_T\;\hat{\boldsymbol{\sigma}}\cdot\hat{\boldsymbol{\sigma}} \quad . \tag{11.17}$$

The relation between the μ-dependent coefficients and the phase shifts is

$$p\cot\delta_r = -\left(\frac{4\pi}{M\overline{C}_r} + \mu\right) \quad , \tag{11.18}$$

for $r = 0{,}1$ where δ_0, δ_1 are the scattering phase shifts in the ${}^1S_0$ and ${}^3S_1$ channels and spectroscopic coefficients are related to those in the vertex as

$$\overline{C}_0 \;\; = \;\; (C_S - 3C_T) \quad \overline{C}_1 = (C_S + C_T) \quad . \tag{11.19}$$

These relations lead from the lagrangian interactions to the S-matrix structure of Eq. (3) of the main text and may be expressed here as

$$\hat{\mathbf{S}} \;\; = \;\; \left[1 - \frac{Mp}{2}\left[\frac{3\overline{C}_1}{D_1^-} + \frac{\overline{C}_0}{D_0^-}\right]\right]\hat{\mathbf{1}} + \frac{8i\pi C_T Mp}{D_0^- D_1^-}\hat{\boldsymbol{\sigma}}\cdot\hat{\boldsymbol{\sigma}} \quad , \quad D_j^\pm = M\overline{C}_j(p \pm i\mu) \pm 4i\pi \tag{11.20}$$

The entanglement power of the S-matrix becomes

$$\mathcal{E}(\hat{\mathbf{S}}) = \frac{512\pi^2 C_T^2 M^2 p^2\left(8\pi M\mu(C_S - C_T) + M^2(p^2+\mu^2)\overline{C}_1\overline{C}_0 + 16\pi^2\right)^2}{3(D_0^-)^2(D_1^-)^2(D_0^+)^2(D_1^+)^2} \quad . \tag{11.21}$$

The curve of Fig. 11.4 shows this entanglement power as a function of the $\hat{\boldsymbol{\sigma}} \cdot \hat{\boldsymbol{\sigma}}$ interaction coefficient, C_T, focusing on the leading interaction in the effective lagrangian with the following numerical values: $C_S = -1.2 \times 10^{-4}$ MeV^{-2}, $\mu = 140$ MeV, $M = 939$ MeV and $p = 19.4$ MeV. The following scattering parameters have been used to calculate physical values of C_S and C_T: $a_0 = -23.714(13)$ fm, $a_1 = 5.425(1)$ fm, $r_0 = 2.73(3)$ fm, and $r_1 = 1.749(8)$ fm, where a and r are the scattering length and effective range, respectively.

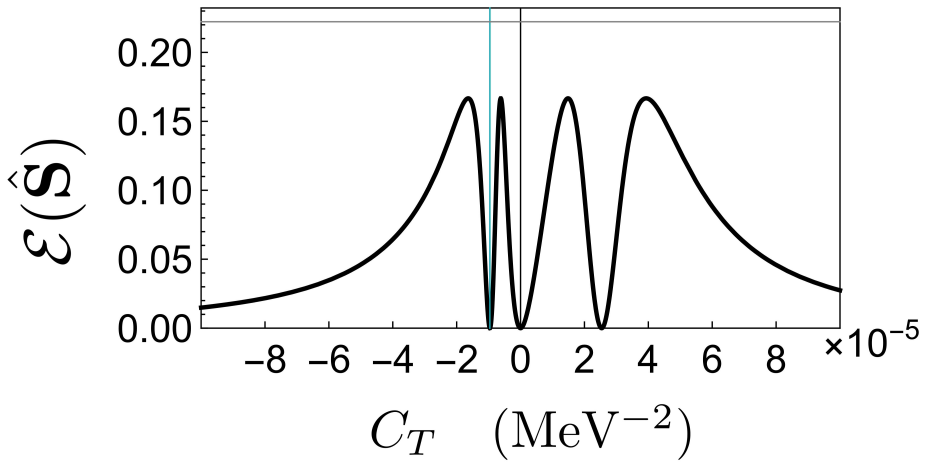

Figure 11.4: Entanglement power of the S-matrix, $\mathcal{E}(\hat{\mathbf{S}})$, as a function of C_T evaluated with $C_S = -1.2 \times 10^{-4}$ MeV^{-2}, $\mu = 140$ MeV, $M = 939$ MeV, and $p = 19.4$ MeV. The vertical solid blue band indicates the physical value of $C_T = -9.605(3) \times 10^{-6}$ MeV^{-2}. The horizontal line at $\mathcal{E}(\hat{\mathbf{S}}) = \frac{2}{9}$ indicates the maximum two-body entanglement power of an unconstrained operator in SU(4).

The symmetry points of the EFT can be related to minimization of the entanglement power of the S-matrix. Figure 11.3 shows a density plot of $\mathcal{E}(\hat{\mathbf{S}})$ as computed from Eq. (11.14) in Eq. (11.20) averaged over momenta $0 \leq p \leq m_\pi/2$, as a function of the couplings $\overline{C}_{0,1}$ renormalized at $\mu = m_\pi/2$ and rescaled by $C_\star = -\frac{4\pi}{M\mu}$ with M the nucleon mass. Superimposed in white are the four conformal fixed points, as well as the Wigner $SU(4)$ fixed line.

The minima of the low-energy-integrated entanglement power of the S-matrix coincide with the points of enhanced symmetry in the EFT; the $SU(4)$ line corresponds to $\delta_0 = \delta_1$ for all momenta, while the conformal points off the $SU(4)$ line correspond to $|\delta_0 - \delta_1| = \pi/2$.

In the $n_f = 2$ case, the large-N_c expansion gives a similar expectation for $SU(4)$ symmetry as does a principle of entanglement suppression. However, an analogous equivalence does not hold for $n_f = 3$, as the large-N_c expansion predicts the conventional approximate $SU(6)$ spin-flavor symmetry, while entanglement suppression predicts a much larger $SU(16)$ symmetry under which the two spin states of the baryon octet transform as a 16-dimensional representation. To see this, consider the EFT in the $SU(3)$ flavor symmetry limit of QCD, where six independent contact operators contribute at LO [399],

$$\begin{aligned}\mathcal{L}_{\rm LO}^{n_f=3} &= -c_1\langle B_i^\dagger B_i B_j^\dagger B_j\rangle - c_2\langle B_i^\dagger B_j B_j^\dagger B_i\rangle \\ &\quad -c_3\langle B_i^\dagger B_j^\dagger B_i B_j\rangle - c_4\langle B_i^\dagger B_j^\dagger B_j B_i\rangle \\ &\quad -c_5\langle B_i^\dagger B_i\rangle\langle B_j^\dagger B_j\rangle - c_6\langle B_i^\dagger B_j\rangle\langle B_j^\dagger B_i\rangle \ , \end{aligned} \tag{11.22}$$

where $\langle ... \rangle$ denotes a trace in flavor space, and B_i is the 3×3 octet-baryon matrix where the subscript $i = 1, 2$ denotes spin. $\mathcal{L}_{\rm LO}^{n_f=3}$ is invariant under rotations and the transformation $B \to VBV^\dagger$ where V is an $SU(3)$ matrix. In the large-N_c limit of QCD, an $SU(6)$ spin-flavor symmetry emerges relating the six coefficients c_i in Eq. (11.22) to two independent coefficients a, b [394] in the $SU(6)$ invariant Lagrange density,

$$\begin{aligned} c_1 = -\frac{7}{27}b \ , \ c_2 &= \frac{1}{9}b \ , \ c_3 = \frac{10}{81}b \ , \\ c_4 = -\frac{14}{81}b \ , \ c_5 &= a + \frac{2}{9}b \ , \ c_6 = -\frac{1}{9}b \ . \end{aligned} \tag{11.23}$$

A comprehensive set of lattice QCD calculations of light nuclei, hypernuclei and low-energy baryon-baryon scattering in the limit of $SU(3)$ flavor symmetry by the NPLQCD collaboration [435, 436, 407] demonstrates that the c_i are consistent with this predicted $SU(6)$ spin-flavor symmetry [407]. The two-baryon sector calculated with $m_\pi \sim 800$ MeV is found to be unnatural [435, 436, 407], with a scattering length that is larger than the range of the interaction, and hence better described by the power-counting of van Kolck [173] and

KSW [172, 171, 174]. Further, the values of c_1, c_2, c_3, c_4 and c_6 are calculated to be much smaller than c_5, indicating that $b \ll a$ [435, 436, 407]. When $b = 0$, the $SU(6)$ is enlarged to an emergent $SU(16)$ spin-flavor symmetry [407], where the baryon states populate the fundamental of $SU(16)$,

$$\mathcal{L}_{\rm LO}^{n_f=3} \;\; \to \;\; -\frac{1}{2} c_S \big(\mathcal{B}^\dagger \mathcal{B}\big)^2 \;, \quad \mathcal{B} = (p_\uparrow, p_\downarrow, n_\uparrow, n_\downarrow, \Lambda_\uparrow, ...)^T, \tag{11.24}$$

with $c_S = 2c_5$.

The existence of $SU(16)$ symmetry and $b = 0$ does not follow from the large-N_c expansion, but does follow from entanglement suppression. The entanglement power of the S-matrix in spin-space from the $n_f = 3$ interactions in Eq. (11.22) can be addressed by considering its action on states of distinguishable baryons. Computing the entanglement power $\mathcal{E}(\hat{\mathbf{S}})$ for more than six distinct two-baryon channels with nonidentical particles—e.g., ΛN, $\Xi^- p$—shows that zero entanglement power occurs at the $SU(16)$ point where all the c_n couplings vanish except for c_5 (indicating the 120-dimensional irrep), which is unconstrained (also, all LO scattering matrices in the $J = 0$ and $J = 1$ mixed-flavor sectors are diagonal [399, 407]). Thus, the principle of entanglement suppression gives rise to an approximate symmetry, apparent in lattice QCD calculations [435, 436, 407], that does not follow from the large-N_c limit. We conclude that the large-N_c limit of QCD does not provide a sufficiently stringent constraint to produce a low-energy EFT that does not entangle, which could not be deduced from the $n_f = 2$ sector alone [394]. Thus, the entanglement power of the S-matrix appears to be an important ingredient in dictating the properties and relative size of interactions in low-energy nuclear and hypernuclear systems.

11.5 Implications for Many-Body Interactions

While in nuclei and hypernuclei contributions to binding from three-body forces between nucleons and hyperons are small compared with those from two-baryon forces, they cannot be neglected and become more important with increasing density. To understand whether entanglement suppression dictates approximate $SU(16)$ symmetry in these interactions as

well, we take a more general approach rather than computing the multi-baryon S-matrix in various channels to constrain couplings. We begin by assuming exact $SU(2)_{\text{spin}} \times SU(3)_{\text{flavor}}$ symmetry, where corrections due to $SU(3)$ violation from quark mass differences can be incorporated in the usual way. Even in the degenerate quark mass limit, this means restricting ourselves to considering only interactions that do not couple spin to orbital angular momentum. While such spin-orbit and tensor interactions can be important in heavy nuclei, they are suppressed by powers of the baryon momenta and do not enter the IR limit of the effective theory. It is then argued that entanglement suppression requires the interactions to respect a $U(1)^{16}$ symmetry, conserving particle number individually for each of the octet baryon spin states. To see why this is a reasonable assumption, consider a 1-body operator (which need not be local) that violates the $U(1)^{16}$ symmetry, e.g.,

$$\hat{\Theta} \;=\; \int \mathrm{d}^3\mathbf{v}\mathrm{d}^3\mathbf{u} \;\left[f(\mathbf{v}-\mathbf{u})\alpha^\dagger_{\mathbf{v}}\beta_{\mathbf{u}} + \text{h.c.}\right], \tag{11.25}$$

where α, β are annihilation operators for components of $\mathcal{B}$ with $\alpha \neq \beta$, $\mathbf{u}$ and $\mathbf{v}$ are spatial coordinates and f is a form factor. This operator implements the transformation, e.g.,

$$\begin{aligned}\hat{\Theta}|\alpha_{\mathbf{x}}, \beta_{\mathbf{y}}, \gamma_{\mathbf{z}}\rangle = \int \mathrm{d}^3\mathbf{w} \qquad & \big[f(\mathbf{w}-\mathbf{y})|\alpha_{\mathbf{x}}, \alpha_{\mathbf{w}}, \gamma_{\mathbf{z}}\rangle \\ & + f^*(\mathbf{x}-\mathbf{w})|\beta_{\mathbf{w}}, \beta_{\mathbf{y}}, \gamma_{\mathbf{z}}\rangle\big],\end{aligned} \tag{11.26}$$

producing an entangled state, even if $f(\mathbf{x}-\mathbf{y}) = \delta^3(\mathbf{x}-\mathbf{y})$, from which it can be concluded that the $U(1)^{16}$ symmetry is a necessary condition to forbid entangling interactions [4]. It follows from simultaneous exact $SU(2) \times SU(3)$ and $U(1)^{16}$ symmetries that the LO EFT must respect the full $SU(16)$ symmetry by the following argument. The charges $Q_\alpha = \mathcal{B}^\dagger \Gamma_\alpha \mathcal{B}$ that by assumption commute with the Hamiltonian H consist of

$$\Gamma_\alpha \in \{\mathcal{I}_{16},\; S_i \otimes \mathcal{I}_8,\; \mathcal{I}_2 \otimes t_a,\; M_i\} \quad , \tag{11.27}$$

where $S_{1,2,3} \in \mathfrak{su}(2)$ are the fundamental generators of $SU(2)$, $t_a \in \mathfrak{su}(3)$ with $(t_a)_{bc} = -if_{abc}$ for $a, b, c = 1, ..., 8$ are the generators of the $SU(3)$ adjoint representation with structure

[4] The converse is not true: it is possible to show that there exist entangling interactions which preserve $U(1)^{16}$ symmetry [428].

constants f_{abc}, and the M_i for $i = 1, ..., 15$ are a set of independent diagonal traceless 16×16 matrices generating $U(1)^{15}$, the ignored $U(1)$ symmetry being baryon number. Since all of the above Q^α are assumed to commute with H, it follows that their commutators do as well. The full symmetry of H will be the symmetry group generated by the closure of the Q^α under commutation. By making use of the fact that the t_a generate an irreducible representation of the $\mathfrak{su}(3)$ Lie algebra and invoking Schur's Lemma, it is possible to show that this full symmetry algebra is $\mathfrak{su}(16)$ [428].

Conjecturing that the guiding principle for low-energy nuclear and hypernuclear forces is the suppression of entanglement fluctuations provides important theoretical constraints on dense matter systems. The Lagrange density describing the $n_f = 2$ sector with vanishing entanglement power, and therefore $SU(4)$ spin-flavor symmetry, is

$$\mathcal{L}^{(n_f=2)} = -\sum_{n=2}^{4} \frac{1}{n!} C_S^{(n)} \left(N^\dagger N\right)^n \quad , \tag{11.28}$$

with previous notation $C_S^{(2)} = C_S$ and $c_S^{(2)} = c_S$, while for $n_f = 3$ with $SU(16)$ spin-flavor symmetry,

$$\mathcal{L}^{(n_f=3)} = -\sum_{n=2}^{16} \frac{1}{n!} c_S^{(n)} \left(\mathcal{B}^\dagger \mathcal{B}\right)^n . \tag{11.29}$$

Calculations of hypernuclei and hyperon-nucleon interactions imposing $SU(16)$ spin-flavor symmetry on the low-energy forces are now in progress [437]. Our work suggests that such calculations could probe the nature of entanglement in strong interactions.

11.6 Outlook

The Pauli exclusion principle's requirement of anti-symmetrization produces a natural tendency for highly entangled states of identical particles in the s-channels. It is somewhat perplexing how to understand the result that the S-matrix for baryon-baryon scattering exhibits screening of entanglement power when the quarks and gluons that form the nucleon are highly entangled. It may be the case that the nonperturbative mechanisms of confine-

ment and chiral symmetry breaking together strongly screen entanglement fluctuations in the low-energy sector of QCD beyond what can be identified in the large-N_c limit of QCD.

While our work has focused on low-energy interactions, preliminary evidence for entanglement suppression at higher orders in a derivative expansion is seen in the $n_f = 2$ low-energy constants (LECs) for operators up to NNLO. The contact terms of the two-nucleon potential in the center-of-mass frame are [438]

$$\begin{aligned} V_{\text{contact}} &= C_S + C_T\, \vec{\sigma}_1 \cdot \vec{\sigma}_2 + V^{(2)}_{\text{contact}} \ , \\ V^{(2)}_{\text{contact}} &= C_1\, \vec{q}^{\,2} + C_3\, \vec{q}^{\,2} (\vec{\sigma}_1 \cdot \vec{\sigma}_2) + C_6\, (\vec{q} \cdot \vec{\sigma}_1)(\vec{q} \cdot \vec{\sigma}_2) \ , \end{aligned} \tag{11.30}$$

with $\vec{q} = \vec{p}\,' - \vec{p}$ and $\vec{p}, \vec{p}\,'$ the initial and final nucleon momenta. Calculating their entanglement power, it is expected that C_T, C_3, and C_6 will be suppressed at low energies. Fig. 11.5 shows the scaling of low energy constants (LECs) relevant for the two-nucleon potential in the center-of-mass frame. The data in Fig. 11.5 has been compiled from the spectroscopic LECs and associated correlated uncertainties determined in Ref. [439, 440, 441]. With the inclusion of experimental data up to a maximum scattering energy $T^{\text{max}}_{\text{Lab}}$, the stability of the potential coefficients suggests that the LECs are well-constrained by low-energy data well-below pion threshold. The progression from solid to dashed to dotted lines in Fig. 11.5 shows the shift in these coefficients with increasing regulator-energy cutoffs of $\Lambda = 450, 475, 550, 600$ MeV. At small values of the maximum scattering energy, $T^{\text{max}}_{\text{Lab}}$, the coefficients of the non-entangling operators, C_S and C_1, are found to be larger in magnitude than their entangling counterparts. Furthermore, as $T^{\text{max}}_{\text{Lab}}$ is increased and shorter distances scales are probed, the suppression lessens and C_6 grows. While these observations are consistent with entanglement-suppressed LECs, work remains to be done in understanding the mechanism that suppresses entanglement power in the transition from QCD to low-energy effective interactions, and the full consequences of this mechanism. For instance, one can envisage a new entanglement-motivated power-counting scheme accommodating the features found here, which provides an improved organizational principle for interactions in nuclear physics.

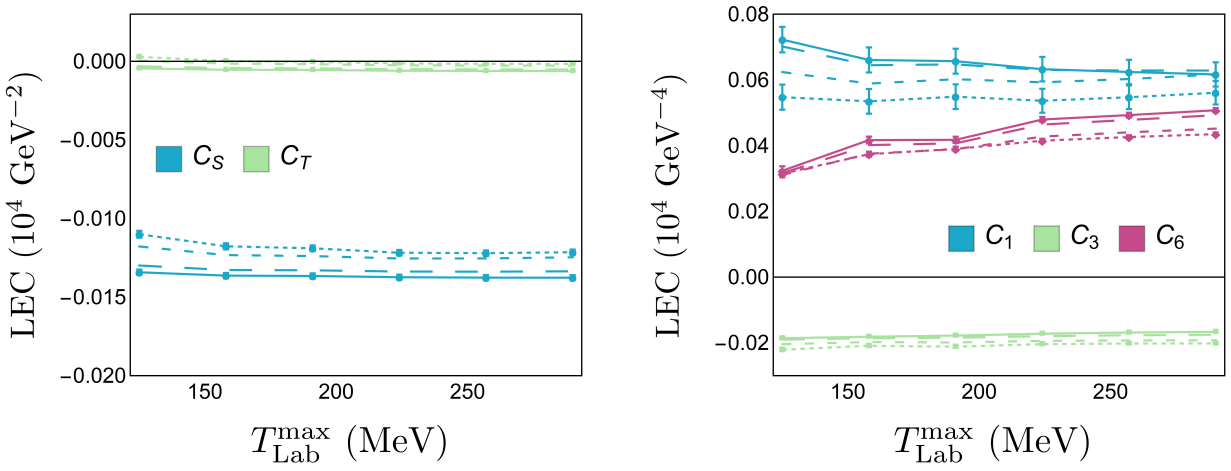

Figure 11.5: Low-energy constants of the NNLO two-nucleon interaction at $\mathcal{O}(p^0)$ (left panel) and $\mathcal{O}(p^2)$ (right panel) as a function of the maximum scattering energy retained in the fitted experimental data set, $T_{\rm Lab}^{\rm max}$, determined from NN and πN scattering [439]. The value of the regulator cutoff corresponds to $\Lambda = 450$ MeV for the solid line, $\Lambda = 475$ MeV for the long-dashed line, $\Lambda = 550$ MeV for the dashed line and $\Lambda = 600$ MeV for the dotted line. The uncertainties on the solid and dotted lines are propagated from the correlated uncertainties of the spectroscopic LECs fit in Ref. [439].

Nuclear physics, with its rich theoretical structure and phenomenology emerging from QCD and QED in the infrared, provides a unique forum for the study of fundamental properties of quantum entanglement. We conjecture that the suppression of entanglement is an important element of strong-interaction physics that is correlated with enhanced emergent symmetries.

Chapter 12

FINAL REFLECTIONS

Spanning between the perturbative and non-perturbative islands of physical systems for which strong theoretical control is achievable, flows a sea of highly correlated quantum systems. This sea contains interacting systems of nuclear matter and is traversed as natural degrees of freedom transition, for example from quark and gluon degrees of freedom in particle collisions to the color singlet hadronic degrees of freedom measured in detectors. At the shorelines, theoretical control becomes unanchored as actions become complex, phases wrap rapidly suppressing signal to noise ratios, perturbative expansion parameters become large, or active Hilbert spaces grow to intractable magnitudes. Infusing a computational framework with quantum degrees of freedom is expected to provide a vessel capable of freely exploring this sea, likely departing from the non-perturbative beaches of latticized quantum fields.

The research program presented with this dissertation, organisationally diagrammed in Fig. 1.6, is a small step toward a much larger exploration of the relationship between quantum-infused computation and physics within the highly correlated quantum sea. As shown in Fig. 1.6, the publications associated with this dissertation can be contextualized as residing on one of three distinct paths producing the three-part structure above. This regime is shown in the bottom left corner of Fig. 12.1 with independent publications beading isolated trajectories: qubit representation of quantum fields (blue), simulation of small fields on NISQ devices (green), and entanglement in subatomic systems (purple).

Along the blue path, it has become clear, through explicit demonstration with the scalar field, that quantum simulation resources can be remarkably sensitive to the choice of field basis and lattice structure, symmetries of the field and conjugate momentum values present

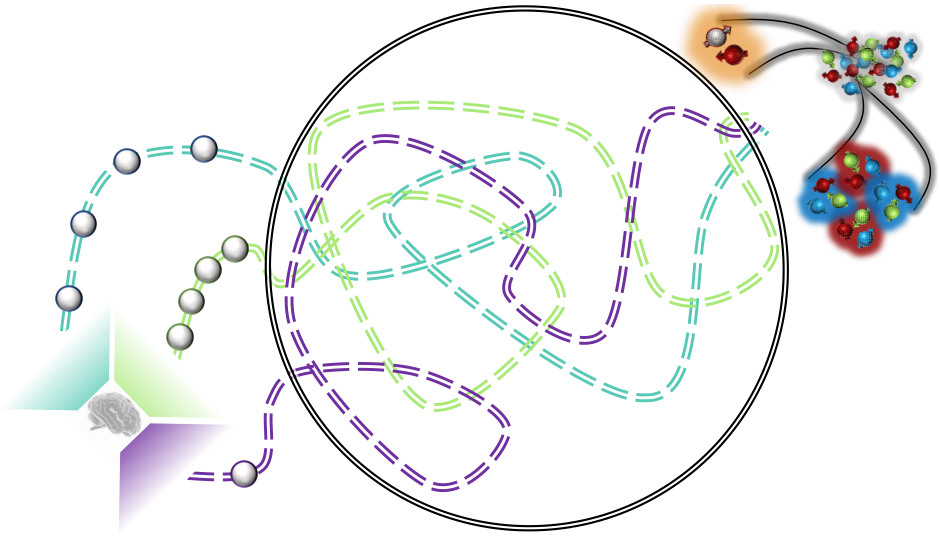

Figure 12.1: The research program developed and presented with this dissertation, while currently clearly classifiable into independent lines of inquiry, is expected to become increasingly correlated and interactive as the dynamical simulation of quantum many-body systems is approached.

in the Hilbert space, phases present at spatial lattice boundaries, details in the form of high energy truncations, and ultraviolet entanglement structure. While low-energy physical observables become independent of such artifacts in large systems with raised truncations, their impact on quantum simulation resources persists and, in some cases, threatens to dominate the resource requirements. As such, the results and intuition developed along this line of research, including a mechanism through which quantum circuits can be structured to present correlation characteristics of the simulated field, will guide future designs of efficient qubit representations for dynamically exploring the infrared physics of quantum fields. Along the green path comes first-hand experience with quantum error mitigation techniques, methods for flexible design of quantum circuits for local time evolution operators that will act throughout the volume of future large-scale simulations, and characterizations of the capabilities of current hardware to perform tasks of relevance to the goals of nuclear and particle physics such as maintaining gauge invariant subspaces during time evolution. Finally, the

purple path has addressed the role of entanglement when scattering the complex composite quantum systems of protons and neutrons at low energies. Further explored in the recent work of Ref. [442]

> Natalie Klco and Martin J. Savage. *Geometric Quantum Information Structure in Quantum Fields and their Lattice Simulation*. 2020. arXiv: 2008.03647 [quant-ph]

a conjecture has resulted regarding the role of entanglement in establishing the hierarchy of operators describing two body hadronic interactions.

With larger perspective and the development of time, the independent tracks of this dissertation are expected to be complementary in ultimately leading toward the goal of quantumly simulating quantum many-body systems. Just as the transition from quarks to hadrons has highly correlated intermediate states, the future development of this research program is expected also to become highly correlated as depicted in the center of Fig. 12.1. Inspiring and developing these correlations through interactions among theorists and experimentalists across the scientific disciplines will nurture the non-perturbative revolution demanded in the way we interact with and calculate properties of highly correlated quantum systems.

BIBLIOGRAPHY

[1] Rolf Landauer. "Irreversibility and heat generation in the computing process". *IBM journal of research and development* 5.3 (1961), pp. 183–191.

[2] Charles H Bennett. "Logical reversibility of computation". *IBM journal of Research and Development* 17.6 (1973), pp. 525–532.

[3] Edward Fredkin and Tommaso Toffoli. "Conservative logic". *International Journal of theoretical physics* 21.3-4 (1982), pp. 219–253.

[4] Rolf Landauer et al. "Information is physical". *Physics Today* 44.5 (1991), pp. 23–29.

[5] Robert Wright. "Did the Universe Just Happen?" *The Atlantic Monthly* (April 1988). URL: https://www.theatlantic.com/past/docs/issues/88apr/wright.htm.

[6] Paul Benioff. "Quantum mechanical hamiltonian models of turing machines". *Journal of Statistical Physics* 29.3 (1982), pp. 515–546. ISSN: 1572-9613. DOI: 10.1007/BF01342185. URL: https://doi.org/10.1007/BF01342185.

[7] Richard P. Feynman. "Simulating physics with computers". *Int. J. Theor. Phys.* 21 (1982), pp. 467–488. DOI: 10.1007/BF02650179.

[8] Albert Einstein, Boris Podolsky, and Nathan Rosen. "Can quantum mechanical description of physical reality be considered complete?" *Phys. Rev.* 47 (1935), pp. 777–780. DOI: 10.1103/PhysRev.47.777.

[9] J. S. Bell. "On the Einstein-Podolsky-Rosen paradox". *Physics Physique Fizika* 1 (1964), pp. 195–200. DOI: 10.1103/PhysicsPhysiqueFizika.1.195.

[10] John F. Clauser et al. "Proposed experiment to test local hidden variable theories". *Phys. Rev. Lett.* 23 (1969), pp. 880–884. DOI: 10.1103/PhysRevLett.23.880.

[11] Stuart J. Freedman and John F. Clauser. "Experimental Test of Local Hidden-Variable Theories". *Phys. Rev. Lett.* 28 (1972), pp. 938–941. DOI: 10.1103/PhysRevLett.28.938.

[12] Alain Aspect, Jean Dalibard, and Gerard Roger. "Experimental test of Bell's inequalities using time varying analyzers". *Phys. Rev. Lett.* 49 (1982), pp. 1804–1807. DOI: 10.1103/PhysRevLett.49.1804.

[13] Gregor Weihs et al. "Violation of Bell's inequality under strict Einstein locality conditions". *Phys. Rev. Lett.* 81 (1998), pp. 5039–5043. DOI: 10.1103/PhysRevLett.81.5039. arXiv: quant-ph/9810080.

[14] R.A. Bertlmann, W. Grimus, and B.C. Hiesmayr. "Bell inequality and CP violation in the neutral kaon system". *Phys. Lett. A* 289 (2001), pp. 21–26. DOI: 10.1016/S0375-9601(01)00577-1. arXiv: quant-ph/0107022.

[15] D.N. Matsukevich et al. "Bell Inequality Violation with Two Remote Atomic Qubits". *Phys. Rev. Lett.* 100 (2008), p. 150404. DOI: 10.1103/PhysRevLett.100.150404. arXiv: 0801.2184 [quant-ph].

[16] Apollo Go. "Observation of Bell inequality violation in B mesons". *J. Mod. Opt.* 51 (2004), p. 991. DOI: 10.1080/09500340408233614. arXiv: quant-ph/0310192.

[17] B. Hensen et al. "Loophole-free Bell inequality violation using electron spins separated by 1.3 kilometres". *Nature* 526 (2015), pp. 682–686. DOI: 10.1038/nature15759. arXiv: 1508.05949 [quant-ph].

[18] Juan Yin et al. "Satellite-based entanglement distribution over 1200 kilometers". *Science* 356.6343 (2017), pp. 1140–1144. ISSN: 0036-8075. DOI: 10.1126/science.aan3211. eprint: https://science.sciencemag.org/content/356/6343/1140.full.pdf. URL: https://science.sciencemag.org/content/356/6343/1140.

[19] Don N. Page. "Average entropy of a subsystem". *Phys. Rev. Lett.* 71 (1993), pp. 1291–1294. DOI: 10.1103/PhysRevLett.71.1291. arXiv: gr-qc/9305007.

[20] Kenneth G. Wilson. "Confinement of Quarks". *Phys. Rev.* D10 (1974). [,45(1974)], pp. 2445–2459. DOI: 10.1103/PhysRevD.10.2445.

[21] Joseph Carlson et al. "Nuclear Physics Exascale Requirements Review: An Office of Science review sponsored jointly by Advanced Scientific Computing Research and Nuclear Physics, June 15 - 17, 2016, Gaithersburg, Maryland" (). DOI: 10.2172/1369223.

[22] John Preskill. "Quantum Computing in the NISQ era and beyond". *Quantum* 2 (Aug. 2018), p. 79. ISSN: 2521-327X. DOI: 10.22331/q-2018-08-06-79. URL: https://doi.org/10.22331/q-2018-08-06-79.

[23] Frank Arute et al. "Quantum supremacy using a programmable superconducting processor". *Nature* 574.7779 (Oct. 2019), pp. 505–510. ISSN: 1476-4687. DOI: 10.1038/s41586-019-1666-5. URL: https://doi.org/10.1038/s41586-019-1666-5.

[24] Stephen P. Jordan, Keith S. M. Lee, and John Preskill. "Quantum Computation of Scattering in Scalar Quantum Field Theories" (2011). [Quant. Inf. Comput.14,1014(2014)]. arXiv: 1112.4833 [hep-th].

[25] Stephen P. Jordan, Keith S. M. Lee, and John Preskill. "Quantum Algorithms for Quantum Field Theories". *Science* 336 (2012), pp. 1130–1133. DOI: 10.1126/science.1217069. arXiv: 1111.3633 [quant-ph].

[26] Natalie Klco and Martin J. Savage. "Minimally-Entangled State Preparation of Localized Wavefunctions on Quantum Computers". *Phys. Rev. A* 102.1 (2020), p. 012612. DOI: 10.1103/PhysRevA.102.012612. arXiv: 1904.10440 [quant-ph].

[27] Natalie Klco and Martin J. Savage. "Systematically Localizable Operators for Quantum Simulations of Quantum Field Theories". *Phys. Rev. A* 102.1 (2020), p. 012619. DOI: 10.1103/PhysRevA.102.012619. arXiv: 1912.03577 [quant-ph].

[28] Natalie Klco and Martin J. Savage. "Fixed-Point Quantum Circuits for Quantum Field Theories" (Feb. 2020). arXiv: 2002.02018 [quant-ph].

[29] H. F. Trotter. "On the product of semi-groups of operators". *Proceedings of the American Mathematical Society* 10.4 (Apr. 1959), pp. 545–545. DOI: 10.1090/s0002-9939-1959-0108732-6. URL: https://doi.org/10.1090/s0002-9939-1959-0108732-6.

[30] N. Klco et al. "Quantum-classical computation of Schwinger model dynamics using quantum computers". *Phys. Rev. A* 98.3 (2018), p. 032331. DOI: 10.1103/PhysRevA.98.032331. arXiv: 1803.03326 [quant-ph].

[31] Natalie Klco, Jesse R. Stryker, and Martin J. Savage. "SU(2) non-Abelian gauge field theory in one dimension on digital quantum computers". *Phys. Rev. D* 101.7 (2020), p. 074512. DOI: 10.1103/PhysRevD.101.074512. arXiv: 1908.06935 [quant-ph].

[32] Andrew M. Childs. "On the Relationship Between Continuous- and Discrete-Time Quantum Walk". *Communications in Mathematical Physics* 294.2 (Oct. 2009), 581–603. ISSN: 1432-0916. DOI: 10.1007/s00220-009-0930-1. URL: http://dx.doi.org/10.1007/s00220-009-0930-1.

[33] Andrew M. Childs and Nathan Wiebe. "Hamiltonian Simulation Using Linear Combinations of Unitary Operations". *Quantum Information and Computation* 12.11-12 (2012). ISSN: 1533-7146. DOI: 10.26421/qic12.11-12. arXiv: 1202.5822 [quant-ph]. URL: http://dx.doi.org/10.26421/QIC12.11-12.

[34] Dominic W Berry and Andrew M Childs. "Black-box Hamiltonian simulation and unitary implementation". *Quantum Information and Computation* 12.1-2 (2012). ISSN: 1533-7146. DOI: 10.26421/qic12.1-2. URL: http://dx.doi.org/10.26421/QIC12.1-2.

[35] Guang Hao Low and Isaac L. Chuang. "Optimal Hamiltonian Simulation by Quantum Signal Processing." *Physical review letters* 118 1 (2017), p. 010501.

[36] Guang Hao Low and Isaac L. Chuang. "Hamiltonian Simulation by Qubitization". *Quantum* 3 (July 2019), p. 163. ISSN: 2521-327X. DOI: 10.22331/q-2019-07-12-163. URL: http://dx.doi.org/10.22331/q-2019-07-12-163.

[37] Seth Lloyd. "Universal Quantum Simulators". *Science* 273.5278 (1996), pp. 1073–1078. ISSN: 0036-8075. DOI: 10.1126/science.273.5278.1073. eprint: https://science.sciencemag.org/content/273/5278/1073.full.pdf. URL: https://science.sciencemag.org/content/273/5278/1073.

[38] Matthew B. Hastings et al. "Improving Quantum Algorithms for Quantum Chemistry". *Quantum Info. Comput.* 15.1-2 (Jan. 2015), pp. 1–21. ISSN: 1533-7146. URL: http://dl.acm.org/citation.cfm?id=2685188.2685189.

[39] Scott Aaronson. "Shadow tomography of quantum states". *Proceedings of the 50th Annual ACM SIGACT Symposium on Theory of Computing*. 2018, pp. 325–338.

[40] Hsin-Yuan Huang, Richard Kueng, and John Preskill. *Predicting Many Properties of a Quantum System from Very Few Measurements*. 2020. arXiv: 2002.08953 [quant-ph].

[41] Michael A. Nielsen and Isaac L. Chuang. *Quantum Computation and Quantum Information: 10th Anniversary Edition*. Cambridge University Press, 2011. ISBN: 1107002176.

[42] Rajibul Islam et al. "Measuring entanglement entropy in a quantum many-body system". *Nature* 528.7580 (Dec. 2015), pp. 77–83. ISSN: 1476-4687. DOI: 10.1038/nature15750. URL: https://doi.org/10.1038/nature15750.

[43] Adam M. Kaufman et al. "Quantum thermalization through entanglement in an isolated many-body system". *Science* 353.6301 (2016), pp. 794–800. ISSN: 0036-8075. DOI: 10.1126/science.aaf6725. eprint: https://science.sciencemag.org/content/353/6301/794.full.pdf. URL: https://science.sciencemag.org/content/353/6301/794.

[44] Richard Cleve et al. "Quantum algorithms revisited". *Proceedings of the Royal Society of London. Series A: Mathematical, Physical and Engineering Sciences* 454.1969 (1998), pp. 339–354.

[45] Natalie Klco and Martin J. Savage. "Digitization of scalar fields for quantum computing". *Phys. Rev.* A99.5 (2019), p. 052335. DOI: 10.1103/PhysRevA.99.052335. arXiv: 1808.10378 [quant-ph].

[46] Hannes Bernien et al. "Probing many-body dynamics on a 51-atom quantum simulator". *Nature* 551.7682 (2017), pp. 579–584.

[47] Eric T. Holland et al. "Optimal Control for the Quantum Simulation of Nuclear Dynamics" (Aug. 2019). arXiv: 1908.08222 [quant-ph].

[48] David B. Kaplan, Natalie Klco, and Alessandro Roggero. "Ground States via Spectral Combing on a Quantum Computer" (2017). arXiv: 1709.08250 [quant-ph].

[49] Hsuan-Hao Lu et al. "Simulations of Subatomic Many-Body Physics on a Quantum Frequency Processor". *Phys. Rev. A* 100.1 (2019), p. 012320. DOI: 10.1103/PhysRevA.100.012320. arXiv: 1810.03959 [quant-ph].

[50] Silas R. Beane et al. "Entanglement Suppression and Emergent Symmetries of Strong Interactions". *Phys. Rev. Lett.* 122.10 (2019), p. 102001. DOI: 10.1103/PhysRevLett.122.102001. arXiv: 1812.03138 [nucl-th].

[51] K. Symanzik. "Continuum Limit and Improved Action in Lattice Theories. 1. Principles and phi**4 Theory". *Nucl. Phys.* B226 (1983), pp. 187–204. DOI: 10.1016/0550-3213(83)90468-6.

[52] K. Symanzik. "Continuum Limit and Improved Action in Lattice Theories. 2. O(N) Nonlinear Sigma Model in Perturbation Theory". *Nucl. Phys.* B226 (1983), pp. 205–227. DOI: 10.1016/0550-3213(83)90469-8.

[53] B. Sheikholeslami and R. Wohlert. "Improved Continuum Limit Lattice Action for QCD with Wilson Fermions". *Nucl. Phys.* B259 (1985), p. 572. DOI: 10.1016/0550-3213(85)90002-1.

[54] Takuya Ooura and Masatake Mori. "The double exponential formula for oscillatory functions over the half infinite interval". *Journal of Computational and Applied Mathematics* 38.1 (1991), pp. 353 –360. ISSN: 0377-0427. DOI: https://doi.org/10.1016/0377-0427(91)90181-I. URL: http://www.sciencedirect.com/science/article/pii/037704279190181I.

[55] MASATAKE MORI and TAKUYA OOURA. "DOUBLE EXPONENTIAL FORMULAS FOR FOURIER TYPE INTEGRALS WITH A DIVERGENT INTEGRAND". *Contributions in Numerical Mathematics*, pp. 301–308. DOI: 10.1142/9789812798886_0023. eprint: https://www.worldscientific.com/doi/pdf/10.1142/9789812798886_0023. URL: https://www.worldscientific.com/doi/abs/10.1142/9789812798886_0023.

[56] Takuya Ooura and Masatake Mori. "A robust double exponential formula for Fourier-type integrals". *Journal of Computational and Applied Mathematics* 112.1 (1999), pp. 229 –241. ISSN: 0377-0427. DOI: https://doi.org/10.1016/S0377-0427(99)00223-X. URL: http://www.sciencedirect.com/science/article/pii/S037704279900223X.

[57] *NIST Digital Library of Mathematical Functions*. http://dlmf.nist.gov/, Release 1.0.26 of 2020-03-15. F. W. J. Olver, A. B. Olde Daalhuis, D. W. Lozier, B. I. Schneider, R. F. Boisvert, C. W. Clark, B. R. Miller, B. V. Saunders, H. S. Cohl, and M. A. McClain, eds. URL: http://dlmf.nist.gov/.

[58] G. Ortiz et al. "Quantum algorithms for fermionic simulations". *Phys. Rev. A* 64 (2 2001), p. 022319. DOI: 10.1103/PhysRevA.64.022319. URL: https://link.aps.org/doi/10.1103/PhysRevA.64.022319.

[59] R. Somma et al. "Simulating physical phenomena by quantum networks". *Phys. Rev. A* 65 (4 2002), p. 042323. DOI: 10.1103/PhysRevA.65.042323. URL: https://link.aps.org/doi/10.1103/PhysRevA.65.042323.

[60] Tim Byrnes and Yoshihisa Yamamoto. "Simulating lattice gauge theories on a quantum computer". *Phys. Rev.* A73 (2006), p. 022328. DOI: 10.1103/PhysRevA.73.022328. arXiv: quant-ph/0510027 [quant-ph].

[61] E. Ovrum and M. Hjorth-Jensen. "Quantum computation algorithm for many-body studies" (2007). eprint: arXiv:0705.1928.

[62] Stephen P. Jordan, Keith S. M. Lee, and John Preskill. "Quantum Algorithms for Fermionic Quantum Field Theories" (2014). arXiv: 1404.7115 [hep-th].

[63] Stephen P. Jordan et al. "BQP-completeness of scattering in scalar quantum field theory". *Quantum* 2 (Jan. 2018), p. 44. ISSN: 2521-327X. DOI: 10.22331/q-2018-01-08-44. URL: https://doi.org/10.22331/q-2018-01-08-44.

[64] Erez Zohar, J. Ignacio Cirac, and Benni Reznik. "Cold-Atom Quantum Simulator for SU(2) Yang-Mills Lattice Gauge Theory". *Phys. Rev. Lett.* 110.12 (2013), p. 125304. DOI: 10.1103/PhysRevLett.110.125304. arXiv: 1211.2241 [quant-ph].

[65] Erez Zohar, J. Ignacio Cirac, and Benni Reznik. "Simulating Compact Quantum Electrodynamics with ultracold atoms: Probing confinement and nonperturbative effects". *Phys. Rev. Lett.* 109 (2012), p. 125302. DOI: 10.1103/PhysRevLett.109.125302. arXiv: 1204.6574 [quant-ph].

[66] D. Banerjee et al. "Atomic Quantum Simulation of Dynamical Gauge Fields coupled to Fermionic Matter: From String Breaking to Evolution after a Quench". *Phys. Rev. Lett.* 109 (2012), p. 175302. DOI: 10.1103/PhysRevLett.109.175302. arXiv: 1205.6366 [cond-mat.quant-gas].

[67] D. Banerjee et al. "Atomic Quantum Simulation of U(N) and SU(N) Non-Abelian Lattice Gauge Theories". *Phys. Rev. Lett.* 110.12 (2013), p. 125303. DOI: 10.1103/PhysRevLett.110.125303. arXiv: 1211.2242 [cond-mat.quant-gas].

[68] Uwe-Jens Wiese. "Ultracold Quantum Gases and Lattice Systems: Quantum Simulation of Lattice Gauge Theories". *Annalen Phys.* 525 (2013), pp. 777–796. DOI: 10.1002/andp.201300104. arXiv: 1305.1602 [quant-ph].

[69] D. Marcos et al. "Two-dimensional Lattice Gauge Theories with Superconducting Quantum Circuits". *Annals Phys.* 351 (2014), pp. 634–654. DOI: 10.1016/j.aop.2014.09.011. arXiv: 1407.6066 [quant-ph].

[70] Uwe-Jens Wiese. "Towards Quantum Simulating QCD". *Nucl. Phys.* A931 (2014), pp. 246–256. DOI: 10.1016/j.nuclphysa.2014.09.102. arXiv: 1409.7414 [hep-th].

[71] Erez Zohar et al. "Digital lattice gauge theories". *Phys. Rev.* A95.2 (2017), p. 023604. DOI: 10.1103/PhysRevA.95.023604. arXiv: 1607.08121 [quant-ph].

[72] A. Bermudez, G. Aarts, and M. Müller. "Quantum sensors for the generating functional of interacting quantum field theories". *Phys. Rev.* X7.4 (2017), p. 041012. DOI: 10.1103/PhysRevX.7.041012. arXiv: 1704.02877 [quant-ph].

[73] Mari Carmen Banuls et al. "Efficient basis formulation for 1+1 dimensional SU(2) lattice gauge theory: Spectral calculations with matrix product states". *Phys. Rev.* X7.4 (2017), p. 041046. DOI: 10.1103/PhysRevX.7.041046. arXiv: 1707.06434 [hep-lat].

[74] David B. Kaplan and Jesse R. Stryker. "Gauss's Law, Duality, and the Hamiltonian Formulation of U(1) Lattice Gauge Theory" (2018). arXiv: 1806.08797 [hep-lat].

[75] Esteban A. Martinez et al. "Real-time dynamics of lattice gauge theories with a few-qubit quantum computer". *Nature* 534 (2016), 516 EP –. URL: http://dx.doi.org/10.1038/nature18318.

[76] P. J. J. O'Malley et al. "Scalable Quantum Simulation of Molecular Energies". *Phys. Rev. X* 6 (3 2016), p. 031007. DOI: 10.1103/PhysRevX.6.031007. URL: https://link.aps.org/doi/10.1103/PhysRevX.6.031007.

[77] Abhinav Kandala et al. "Hardware-efficient variational quantum eigensolver for small molecules and quantum magnets". *Nature* 549 (2017), 242 EP –. URL: http://dx.doi.org/10.1038/nature23879.

[78] E. F. Dumitrescu et al. "Cloud Quantum Computing of an Atomic Nucleus". *Phys. Rev. Lett.* 120 (21 2018), p. 210501. DOI: 10.1103/PhysRevLett.120.210501. URL: https://link.aps.org/doi/10.1103/PhysRevLett.120.210501.

[79] Cornelius Hempel et al. "Quantum Chemistry Calculations on a Trapped-Ion Quantum Simulator". *Phys. Rev. X* 8 (3 2018), p. 031022. DOI: 10.1103/PhysRevX.8.031022. URL: https://link.aps.org/doi/10.1103/PhysRevX.8.031022.

[80] L. García-Álvarez et al. "Fermion-Fermion Scattering in Quantum Field Theory with Superconducting Circuits". *Phys. Rev. Lett.* 114 (7 2015), p. 070502. DOI: 10.1103/PhysRevLett.114.070502. URL: https://link.aps.org/doi/10.1103/PhysRevLett.114.070502.

[81] Alexei Bazavov et al. "Gauge-invariant implementation of the Abelian Higgs model on optical lattices". *Phys. Rev.* D92.7 (2015), p. 076003. DOI: 10.1103/PhysRevD.92.076003. arXiv: 1503.08354 [hep-lat].

[82] Erez Zohar, J Ignacio Cirac, and Benni Reznik. "Quantum simulations of lattice gauge theories using ultracold atoms in optical lattices". *Reports on Progress in Physics* 79.1 (2016), p. 014401. URL: http://stacks.iop.org/0034-4885/79/i=1/a=014401.

[83] T. Pichler et al. "Real-Time Dynamics in U(1) Lattice Gauge Theories with Tensor Networks". *Phys. Rev. X* 6 (1 2016), p. 011023. DOI: 10.1103/PhysRevX.6.011023. URL: https://link.aps.org/doi/10.1103/PhysRevX.6.011023.

[84] Ali Hamed Moosavian and Stephen Jordan. "Faster Quantum Algorithm to simulate Fermionic Quantum Field Theory" (2017). arXiv: 1711.04006 [quant-ph].

[85] Daniel Gonzalez-Cuadra, Erez Zohar, and J. Ignacio Cirac. "Quantum Simulation of the Abelian-Higgs Lattice Gauge Theory with Ultracold Atoms". *New J. Phys.* 19.6 (2017), p. 063038. DOI: 10.1088/1367-2630/aa6f37. arXiv: 1702.05492 [quant-ph].

[86] Alexandru Macridin et al. "Electron-Phonon Systems on a Universal Quantum Computer". *Phys. Rev. Lett.* 121 (11 2018), p. 110504. DOI: 10.1103/PhysRevLett.121.110504. URL: https://link.aps.org/doi/10.1103/PhysRevLett.121.110504.

[87] Jin Zhang et al. "Quantum simulation of the universal features of the Polyakov loop". *Phys. Rev. Lett.* 121.22 (2018), p. 223201. DOI: 10.1103/PhysRevLett.121.223201. arXiv: 1803.11166 [hep-lat].

[88] Alexandru Macridin et al. "Digital quantum computation of fermion-boson interacting systems". *Phys. Rev.* A98.4 (2018), p. 042312. DOI: 10.1103/PhysRevA.98.042312. arXiv: 1805.09928 [quant-ph].

[89] Julian Bender et al. "Digital quantum simulation of lattice gauge theories in three spatial dimensions". *New J. Phys.* 20.9 (2018), p. 093001. DOI: 10.1088/1367-2630/aadb71. arXiv: 1804.02082 [quant-ph].

[90] Erez Zohar and J. Ignacio Cirac. "Eliminating fermionic matter fields in lattice gauge theories". *Phys. Rev.* B98.7 (2018), p. 075119. DOI: 10.1103/PhysRevB.98.075119. arXiv: 1805.05347 [quant-ph].

[91] Erez Zohar. "Gauss law, Minimal Coupling and Fermionic PEPS for Lattice Gauge Theories". *Tensor Network and entanglement, Florence, Italy, June 18-22, 2018.* 2018. arXiv: 1807.01294 [quant-ph].

[92] Ro Jefferson and Robert C. Myers. "Circuit complexity in quantum field theory". *JHEP* 10 (2017), p. 107. DOI: 10.1007/JHEP10(2017)107. arXiv: 1707.08570 [hep-th].

[93] James Alsup et al. "Holographic Fermi Liquids in a Spontaneously Generated Lattice". *Phys. Rev.* D93.10 (2016), p. 105045. DOI: 10.1103/PhysRevD.93.105045. arXiv: 1603.03382 [hep-th].

[94] Kübra Yeter-Aydeniz and George Siopsis. "Quantum Computation of Scattering Amplitudes in Scalar Quantum Electrodynamics". *Phys. Rev.* D97.3 (2018), p. 036004. DOI: 10.1103/PhysRevD.97.036004. arXiv: 1709.02355 [quant-ph].

[95] Kevin Marshall et al. "Quantum simulation of quantum field theory using continuous variables". *Phys. Rev.* A92.6 (2015), p. 063825. DOI: 10.1103/PhysRevA.92.063825. arXiv: 1503.08121 [quant-ph].

[96] Kamil Bradler et al. "Absolutely covert quantum communication" (2016). arXiv: 1607.05916 [quant-ph].

[97] Christine Muschik et al. "U(1) Wilson lattice gauge theories in digital quantum simulators". *New J. Phys.* 19.10 (2017), p. 103020. DOI: 10.1088/1367-2630/aa89ab. arXiv: 1612.08653 [quant-ph].

[98] C. Lin, F. H. Zong, and D. M. Ceperley. "Twist-averaged boundary conditions in continuum quantum Monte Carlo". *Phys. Rev.* E64 (2001), p. 016702. DOI: 10.1103/PhysRevE.64.016702. arXiv: cond-mat/0101339 [cond-mat.stat-mech].

[99] C. T. Sachrajda and G. Villadoro. "Twisted boundary conditions in lattice simulations". *Phys. Lett.* B609 (2005), pp. 73–85. DOI: 10.1016/j.physletb.2005.01.033. arXiv: hep-lat/0411033 [hep-lat].

[100] Paulo F. Bedaque. "Aharonov-Bohm effect and nucleon nucleon phase shifts on the lattice". *Phys. Lett.* B593 (2004), pp. 82–88. DOI: 10.1016/j.physletb.2004.04.045. arXiv: nucl-th/0402051 [nucl-th].

[101] Raul A. Briceno et al. "Two-Baryon Systems with Twisted Boundary Conditions". *Phys. Rev.* D89.7 (2014), p. 074509. DOI: 10.1103/PhysRevD.89.074509. arXiv: 1311.7686 [hep-lat].

[102] Rolando D. Somma. "Quantum Simulations of One Dimensional Quantum Systems". *Quantum Info. Comput.* 16.13-14 (Oct. 2016), pp. 1125–1168. ISSN: 1533-7146. URL: http://dl.acm.org/citation.cfm?id=3179430.3179434.

[103] Dave Wecker et al. "Gate-count estimates for performing quantum chemistry on small quantum computers". *Phys. Rev. A* 90 (2 2014), p. 022305. DOI: 10.1103/PhysRevA.90.022305. URL: https://link.aps.org/doi/10.1103/PhysRevA.90.022305.

[104] Markus Reiher et al. "Elucidating reaction mechanisms on quantum computers". *Proceedings of the National Academy of Sciences* (2017). ISSN: 0027-8424. DOI: 10.1073/pnas.1619152114. eprint: http://www.pnas.org/content/early/2017/06/30/1619152114.full.pdf. URL: http://www.pnas.org/content/early/2017/06/30/1619152114.

[105] David Poulin et al. "The Trotter Step Size Required for Accurate Quantum Simulation of Quantum Chemistry". *Quantum Info. Comput.* 15.5-6 (Apr. 2015), pp. 361–384. ISSN: 1533-7146. URL: http://dl.acm.org/citation.cfm?id=2871401.2871402.

[106] Ryan Babbush et al. "Chemical basis of Trotter-Suzuki errors in quantum chemistry simulation". *Phys. Rev. A* 91 (2 2015), p. 022311. DOI: 10.1103/PhysRevA.91.022311. URL: https://link.aps.org/doi/10.1103/PhysRevA.91.022311.

[107] G. Hao Low and I. L. Chuang. "Hamiltonian Simulation by Qubitization". *ArXiv e-prints* (Oct. 2016). arXiv: 1610.06546 [quant-ph].

[108] Aurel Bulgac, Joaquin E. Drut, and Piotr Magierski. "Quantum Monte Carlo simulations of the BCS-BEC crossover at finite temperature". *Phys. Rev.* A78 (2008), p. 023625. DOI: 10.1103/PhysRevA.78.023625. arXiv: 0803.3238 [cond-mat.stat-mech].

[109] Michael G. Endres et al. "Lattice Monte Carlo calculations for unitary fermions in a finite box". *Phys. Rev.* A87.2 (2013), p. 023615. DOI: 10.1103/PhysRevA.87.023615. arXiv: 1203.3169 [hep-lat].

[110] M. Lüscher. "Volume Dependence of the Energy Spectrum in Massive Quantum Field Theories. 1. Stable Particle States". *Commun. Math. Phys.* 104 (1986), p. 177. DOI: 10.1007/BF01211589.

[111] M. Lüscher. "Volume Dependence of the Energy Spectrum in Massive Quantum Field Theories. 2. Scattering States". *Commun. Math. Phys.* 105 (1986), pp. 153–188. DOI: 10.1007/BF01211097.

[112] Martin Lüscher. "Two particle states on a torus and their relation to the scattering matrix". *Nucl. Phys.* B354 (1991), pp. 531–578. DOI: 10.1016/0550-3213(91)90366-6.

[113] Y. Meurice. "Simple Method to Make Asymptotic Series of Feynman Diagrams Converge". *Phys. Rev. Lett.* 88 (14 2002), p. 141601. DOI: 10.1103/PhysRevLett.88.141601. URL: https://link.aps.org/doi/10.1103/PhysRevLett.88.141601.

[114] B. Kessler, L. Li, and Y. Meurice. "New optimization methods for converging perturbative series with a field cutoff". *Phys. Rev. D* 69 (4 2004), p. 045014. DOI: 10.1103/PhysRevD.69.045014. URL: https://link.aps.org/doi/10.1103/PhysRevD.69.045014.

[115] Steven Weinberg. "Phenomenological Lagrangians". *Physica A: Statistical Mechanics and its Applications* 96.1 (1979), pp. 327 –340. ISSN: 0378-4371. DOI: https://doi.org/10.1016/0378-4371(79)90223-1. URL: http://www.sciencedirect.com/science/article/pii/0378437179902231.

[116] Martin Luscher et al. "Chiral symmetry and O(a) improvement in lattice QCD". *Nucl. Phys.* B478 (1996), pp. 365–400. DOI: 10.1016/0550-3213(96)00378-1. arXiv: hep-lat/9605038 [hep-lat].

[117] Jarrod R McClean et al. "The theory of variational hybrid quantum-classical algorithms". *New Journal of Physics* 18.2 (2016), p. 023023. URL: http://stacks.iop.org/1367-2630/18/i=2/a=023023.

[118] J. Kelly et al. "State preservation by repetitive error detection in a superconducting quantum circuit". *Nature* 519 (2015), 66 EP –. URL: http://dx.doi.org/10.1038/nature14270.

[119] Yu Tomita and Krysta M. Svore. "Low-distance surface codes under realistic quantum noise". *Phys. Rev. A* 90 (6 2014), p. 062320. DOI: 10.1103/PhysRevA.90.062320. URL: https://link.aps.org/doi/10.1103/PhysRevA.90.062320.

[120] D. Nigg et al. "Quantum computations on a topologically encoded qubit". *Science* (2014). ISSN: 0036-8075. DOI: 10.1126/science.1253742. eprint: http://science.sciencemag.org/content/early/2014/06/11/science.1253742.full.pdf. URL: http://science.sciencemag.org/content/early/2014/06/11/science.1253742.

[121] Rui Chao and Ben W. Reichardt. *Fault-tolerant quantum computation with few qubits.* 2017. eprint: arXiv:1705.05365.

[122] Colin J Trout et al. "Simulating the performance of a distance-3 surface code in a linear ion trap". *New Journal of Physics* 20.4 (2018), p. 043038. URL: http://stacks.iop.org/1367-2630/20/i=4/a=043038.

[123] James R. Wootton et al. "Proposal for a minimal surface code experiment". *Phys. Rev. A* 96 (3 2017), p. 032338. DOI: 10.1103/PhysRevA.96.032338. URL: https://link.aps.org/doi/10.1103/PhysRevA.96.032338.

[124] Peter Selinger. "Efficient Clifford+T Approximation of Single-qubit Operators". *Quantum Info. Comput.* 15.1-2 (Jan. 2015), pp. 159–180. ISSN: 1533-7146. URL: http://dl.acm.org/citation.cfm?id=2685188.2685198.

[125] Neil J. Ross and Peter Selinger. "Optimal ancilla-free Clifford+T approximation of z-rotations". *Quantum Information and Computation* 16 (2016), pp. 901–953.

[126] Vadym Kliuchnikov, Dmitri Maslov, and Michele Mosca. "Fast and efficient exact synthesis of single qubit unitaries generated by Clifford and T gates". *Quantum Information and Computation* 13 (2013), 0607–0630.

[127] S. L. Glashow. "Partial Symmetries of Weak Interactions". *Nucl. Phys.* 22 (1961), pp. 579–588. DOI: 10.1016/0029-5582(61)90469-2.

[128] Steven Weinberg. "A Model of Leptons". *Phys. Rev. Lett.* 19 (1967), pp. 1264–1266. DOI: 10.1103/PhysRevLett.19.1264.

[129] Abdus Salam. "Weak and Electromagnetic Interactions". *Conf. Proc.* C680519 (1968), pp. 367–377.

[130] Peter W. Higgs. "Broken Symmetries and the Masses of Gauge Bosons". *Phys. Rev. Lett.* 13 (1964). [,160(1964)], pp. 508–509. DOI: 10.1103/PhysRevLett.13.508.

[131] F. Englert and R. Brout. "Broken Symmetry and the Mass of Gauge Vector Mesons". *Phys. Rev. Lett.* 13 (1964). [,157(1964)], pp. 321–323. DOI: 10.1103/PhysRevLett.13.321.

[132] Georges Aad et al. "Observation of a new particle in the search for the Standard Model Higgs boson with the ATLAS detector at the LHC". *Phys. Lett.* B716 (2012), pp. 1–29. DOI: 10.1016/j.physletb.2012.08.020. arXiv: 1207.7214 [hep-ex].

[133] Serguei Chatrchyan et al. "Observation of a new boson at a mass of 125 GeV with the CMS experiment at the LHC". *Phys. Lett.* B716 (2012), pp. 30–61. DOI: 10.1016/j.physletb.2012.08.021. arXiv: 1207.7235 [hep-ex].

[134] Kübra Yeter-Aydeniz et al. "Scalar quantum field theories as a benchmark for near-term quantum computers". *Phys. Rev. A* 99 (3 2019), p. 032306. DOI: 10.1103/PhysRevA.99.032306. URL: https://link.aps.org/doi/10.1103/PhysRevA.99.032306.

[135] P. Jordan and E. Wigner. "Über das Paulische Äquivalenzverbot". *Zeitschrift für Physik* 47.9 (1928), pp. 631–651. ISSN: 0044-3328. DOI: 10.1007/BF01331938. URL: https://doi.org/10.1007/BF01331938.

[136] Sergey B. Bravyi and Alexei Yu. Kitaev. "Fermionic Quantum Computation". *Annals of Physics* 298.1 (2002), pp. 210 –226. ISSN: 0003-4916. DOI: https://doi.org/10.1006/aphy.2002.6254. URL: http://www.sciencedirect.com/science/article/pii/S0003491602962548.

[137] Vojtěch Havlíček, Matthias Troyer, and James D. Whitfield. "Operator locality in the quantum simulation of fermionic models". *Phys. Rev. A* 95 (3 2017), p. 032332. DOI: 10.1103/PhysRevA.95.032332. URL: https://link.aps.org/doi/10.1103/PhysRevA.95.032332.

[138] Jarrod R. McClean et al. "Exploiting Locality in Quantum Computation for Quantum Chemistry". *The Journal of Physical Chemistry Letters* 5.24 (2014). PMID: 26273989, pp. 4368–4380. DOI: 10.1021/jz501649m. eprint: https://doi.org/10.1021/jz501649m. URL: https://doi.org/10.1021/jz501649m.

[139] Ryan Babbush et al. "Low-Depth Quantum Simulation of Materials". *Phys. Rev. X* 8 (1 2018), p. 011044. DOI: 10.1103/PhysRevX.8.011044. URL: https://link.aps.org/doi/10.1103/PhysRevX.8.011044.

[140] Ian D. Kivlichan et al. "Quantum Simulation of Electronic Structure with Linear Depth and Connectivity". *Phys. Rev. Lett.* 120 (11 2018), p. 110501. DOI: 10.1103/PhysRevLett.120.110501. URL: https://link.aps.org/doi/10.1103/PhysRevLett.120.110501.

[141] Mark Srednicki. "Entropy and area". *Phys. Rev. Lett.* 71 (1993), pp. 666–669. DOI: 10.1103/PhysRevLett.71.666. arXiv: hep-th/9303048 [hep-th].

[142] K. Audenaert et al. "Entanglement Properties of the Harmonic Chain". *Phys. Rev.* A66.4 (2002), p. 042327. DOI: 10.1103/PhysRevA.66.042327. arXiv: quant-ph/0205025 [quant-ph].

[143] Gerardo Adesso, Alessio Serafini, and Fabrizio Illuminati. "Extremal entanglement and mixedness in continuous variable systems". *Phys. Rev. A* 70 (2 2004), p. 022318. DOI: 10.1103/PhysRevA.70.022318. URL: https://link.aps.org/doi/10.1103/PhysRevA.70.022318.

[144] Alonso Botero and Benni Reznik. "Spatial structures and localization of vacuum entanglement in the linear harmonic chain". *Physical Review A* 70.5 (2004). ISSN: 1094-1622. DOI: 10.1103/physreva.70.052329. URL: http://dx.doi.org/10.1103/PhysRevA.70.052329.

[145] Johannes Kofler et al. "Entanglement between collective operators in a linear harmonic chain". *Physical Review A* 73.5 (2006), p. 052107.

[146] Janet Anders. "Thermal state entanglement in harmonic lattices". *Phys. Rev. A* 77 (6 2008), p. 062102. DOI: 10.1103/PhysRevA.77.062102. URL: https://link.aps.org/doi/10.1103/PhysRevA.77.062102.

[147] S. Marcovitch et al. "Critical and noncritical long-range entanglement in Klein-Gordon fields". *Phys. Rev. A* 80.1 (2009), p. 012325. DOI: 10.1103/PhysRevA.80.012325. arXiv: 0811.1288 [quant-ph].

[148] H. Wichterich, J. Molina-Vilaplana, and S. Bose. "Scaling of entanglement between separated blocks in spin chains at criticality". *Phys. Rev. A* 80.1 (2009), p. 010304. DOI: 10.1103/PhysRevA.80.010304. arXiv: 0811.1285 [quant-ph].

[149] Pasquale Calabrese, John Cardy, and Erik Tonni. "Entanglement entropy of two disjoint intervals in conformal field theory". *J. Stat. Mech.* 0911 (2009), P11001. DOI: 10.1088/1742-5468/2009/11/P11001. arXiv: 0905.2069 [hep-th].

[150] Magdalena Zych et al. "Entanglement between smeared field operators in the Klein-Gordon vacuum". *Phys. Rev. D* 81 (2010), p. 125019. DOI: 10.1103/PhysRevD.81.125019. arXiv: 1003.3354 [quant-ph].

[151] Pasquale Calabrese, John Cardy, and Erik Tonni. "Entanglement negativity in quantum field theory". *Phys. Rev. Lett.* 109 (2012), p. 130502. DOI: 10.1103/PhysRevLett.109.130502. arXiv: 1206.3092 [cond-mat.stat-mech].

[152] M. Reza Mohammadi Mozaffar and Ali Mollabashi. "Entanglement in Lifshitz-type Quantum Field Theories". *JHEP* 07 (2017), p. 120. DOI: 10.1007/JHEP07(2017)120. arXiv: 1705.00483 [hep-th].

[153] Andrea Coser, Cristiano De Nobili, and Erik Tonni. "A contour for the entanglement entropies in harmonic lattices". *Journal of Physics A: Mathematical and Theoretical* 50.31 (2017), p. 314001. ISSN: 1751-8121. DOI: 10.1088/1751-8121/aa7902. URL: http://dx.doi.org/10.1088/1751-8121/aa7902.

[154] O. Hart and C. Castelnovo. "Entanglement negativity and sudden death in the toric code at finite temperature". *Phys. Rev. B* 97.14 (2018), p. 144410. DOI: 10.1103/PhysRevB.97.144410. arXiv: 1710.11139 [cond-mat.str-el].

[155] H. Reeh and S. Schlieder. "Bemerkungen zur unitäräquivalenz von lorentzinvarianten feldern". *Il Nuovo Cimento (1955-1965)* 22.5 (1961), pp. 1051–1068. ISSN: 1827-6121. DOI: 10.1007/BF02787889. URL: https://doi.org/10.1007/BF02787889.

[156] Edward Witten. "APS Medal for Exceptional Achievement in Research: Invited article on entanglement properties of quantum field theory". *Rev. Mod. Phys.* 90.4 (2018), p. 045003. DOI: 10.1103/RevModPhys.90.045003. arXiv: 1803.04993 [hep-th].

[157] Antony Valentini. "Non-local correlations in quantum electrodynamics". *Physics Letters A* 153.6 (1991), pp. 321 –325. ISSN: 0375-9601. DOI: https://doi.org/10.1016/0375-9601(91)90952-5. URL: http://www.sciencedirect.com/science/article/pii/0375960191909525.

[158] Benni Reznik. "Entanglement from the vacuum". *Found. Phys.* 33 (2003), pp. 167–176. DOI: 10.1023/A:1022875910744. arXiv: quant-ph/0212044.

[159] Benni Reznik, Alex Retzker, and Jonathan Silman. "Violating Bell's inequalities in the vacuum". *Phys. Rev.* A71.4 (2005), p. 042104. DOI: 10.1103/PhysRevA.71.042104. arXiv: quant-ph/0310058 [quant-ph].

[160] A. Retzker, J. I. Cirac, and B. Reznik. "Detecting Vacuum Entanglement in a Linear Ion Trap". *Physical Review Letters* 94.5 (2005). ISSN: 1079-7114. DOI: 10.1103/physrevlett.94.050504. URL: http://dx.doi.org/10.1103/PhysRevLett.94.050504.

[161] Alejandro Pozas-Kerstjens and Eduardo Martin-Martinez. "Entanglement harvesting from the electromagnetic vacuum with hydrogenlike atoms". *Phys. Rev. D* 94.6 (2016), p. 064074. DOI: 10.1103/PhysRevD.94.064074. arXiv: 1605.07180 [quant-ph].

[162] Petar Simidzija and Eduardo Martín-Martínez. "Harvesting correlations from thermal and squeezed coherent states". *Phys. Rev. D* 98.8 (2018), p. 085007. DOI: 10.1103/PhysRevD.98.085007. arXiv: 1809.05547 [quant-ph].

[163] Laura J. Henderson et al. "Quantum Temporal Superposition: the case of QFT" (Feb. 2020). arXiv: 2002.06208 [quant-ph].

[164] G. Vidal and R. F. Werner. "Computable measure of entanglement". *Phys. Rev.* A65 (2002), p. 032314. DOI: 10.1103/PhysRevA.65.032314. arXiv: quant-ph/0102117 [quant-ph].

[165] Ran Raz and Avishay Tal. "Oracle Separation of BQP and PH". *Proceedings of the 51st Annual ACM SIGACT Symposium on Theory of Computing*. STOC 2019. Phoenix, AZ, USA: ACM, 2019, pp. 13–23. ISBN: 978-1-4503-6705-9. DOI: 10.1145/3313276.3316315. URL: http://doi.acm.org/10.1145/3313276.3316315.

[166] NSAC Subcommittee on Quantum Information Science. *Nuclear Physics and Quantum Information Science*. 2019.

[167] Irinel Caprini, Gilberto Colangelo, and Heinrich Leutwyler. "Mass and width of the lowest resonance in QCD". *Phys. Rev. Lett.* 96 (2006), p. 132001. DOI: 10.1103/PhysRevLett.96.132001. arXiv: hep-ph/0512364 [hep-ph].

[168] Peter W. Higgs. "Broken symmetries, massless particles and gauge fields". *Phys. Lett.* 12 (1964), pp. 132–133. DOI: 10.1016/0031-9163(64)91136-9.

[169] Wei-Chia Chen and J. Piekarewicz. "Building relativistic mean field models for finite nuclei and neutron stars". *Phys. Rev.* C90.4 (2014), p. 044305. DOI: 10.1103/PhysRevC.90.044305. arXiv: 1408.4159 [nucl-th].

[170] Steven Weinberg. "Phenomenological Lagrangians". *Physica* A96 (1979), pp. 327–340. DOI: 10.1016/0378-4371(79)90223-1.

[171] David B. Kaplan, Martin J. Savage, and Mark B. Wise. "Two nucleon systems from effective field theory". *Nucl. Phys. B* 534 (1998), pp. 329–355. DOI: 10.1016/S0550-3213(98)00440-4. arXiv: nucl-th/9802075 [nucl-th].

[172] David B. Kaplan, Martin J. Savage, and Mark B. Wise. "A New expansion for nucleon-nucleon interactions". *Phys. Lett. B* 424 (1998), pp. 390–396. DOI: 10.1016/S0370-2693(98)00210-X. arXiv: nucl-th/9801034 [nucl-th].

[173] U. van Kolck. "Effective field theory of short range forces". *Nucl. Phys. A* 645 (1999), pp. 273–302. DOI: 10.1016/S0375-9474(98)00612-5. arXiv: nucl-th/9808007 [nucl-th].

[174] Jiunn-Wei Chen, Gautam Rupak, and Martin J. Savage. "Nucleon-nucleon effective field theory without pions". *Nucl. Phys.* A653 (1999), pp. 386–412. DOI: 10.1016/S0375-9474(99)00298-5. arXiv: nucl-th/9902056 [nucl-th].

[175] Steven Weinberg. "Nuclear forces from chiral Lagrangians". *Phys. Lett.* B251 (1990), pp. 288–292. DOI: 10.1016/0370-2693(90)90938-3.

[176] C. Ordonez and U. van Kolck. "Chiral lagrangians and nuclear forces". *Phys. Lett.* B291 (1992), pp. 459–464. DOI: 10.1016/0370-2693(92)91404-W.

[177] C. Ordonez, L. Ray, and U. van Kolck. "The Two nucleon potential from chiral Lagrangians". *Phys. Rev.* C53 (1996), pp. 2086–2105. DOI: 10.1103/PhysRevC.53.2086. arXiv: hep-ph/9511380 [hep-ph].

[178] U. van Kolck. "Few nucleon forces from chiral Lagrangians". *Phys. Rev.* C49 (1994), pp. 2932–2941. DOI: 10.1103/PhysRevC.49.2932.

[179] H. M. Muller et al. "Nuclear matter on a lattice". *Phys. Rev.* C61 (2000), p. 044320. DOI: 10.1103/PhysRevC.61.044320. arXiv: nucl-th/9910038 [nucl-th].

[180] Dean Lee, Bugra Borasoy, and Thomas Schafer. "Nuclear lattice simulations with chiral effective field theory". *Phys. Rev.* C70 (2004), p. 014007. DOI: 10.1103/PhysRevC.70.014007. arXiv: nucl-th/0402072 [nucl-th].

[181] T. Abe and R. Seki. "Lattice Calculation of Thermal Properties of Low-Density Neutron Matter with NN Effective Field Theory". *Phys. Rev.* C79 (2009), p. 054002. DOI: 10.1103/PhysRevC.79.054002. arXiv: 0708.2523 [nucl-th].

[182] Dean Lee. "Lattice simulations for few- and many-body systems". *Prog. Part. Nucl. Phys.* 63 (2009), pp. 117–154. DOI: 10.1016/j.ppnp.2008.12.001. arXiv: 0804.3501 [nucl-th].

[183] Dean Lee. "Lattice methods and the nuclear few- and many-body problem". *Lect. Notes Phys.* 936 (2017), pp. 237–261. DOI: 10.1007/978-3-319-53336-0_6. arXiv: 1609.00421 [nucl-th].

[184] Alexei Kitaev and William A. Webb. "Wavefunction preparation and resampling using a quantum computer". *arXiv e-prints*, arXiv:0801.0342 (2008), arXiv:0801.0342. arXiv: 0801.0342 [quant-ph].

[185] Pasquale Calabrese and John L. Cardy. "Entanglement entropy and quantum field theory". *J. Stat. Mech.* 0406 (2004), P06002. DOI: 10.1088/1742-5468/2004/06/P06002. arXiv: hep-th/0405152 [hep-th].

[186] P. V. Buividovich and M. I. Polikarpov. "Entanglement entropy in lattice gauge theories". *PoS* CONFINEMENT8 (2008). [J. Phys.A42,304005(2009)], p. 039. DOI: 10.1088/1751-8113/42/30/304005,10.22323/1.077.0039. arXiv: 0811.3824 [hep-lat].

[187] William Donnelly. "Decomposition of entanglement entropy in lattice gauge theory". *Phys. Rev.* D85 (2012), p. 085004. DOI: 10.1103/PhysRevD.85.085004. arXiv: 1109.0036 [hep-th].

[188] Horacio Casini, Marina Huerta, and Jose Alejandro Rosabal. "Remarks on entanglement entropy for gauge fields". *Phys. Rev.* D89.8 (2014), p. 085012. DOI: 10.1103/PhysRevD.89.085012. arXiv: 1312.1183 [hep-th].

[189] Djordje Radicevic. "Notes on Entanglement in Abelian Gauge Theories" (2014). arXiv: 1404.1391 [hep-th].

[190] Sudip Ghosh, Ronak M. Soni, and Sandip P. Trivedi. "On the entanglement entropy for gauge theories". *Journal of High Energy Physics* 2015.9 (2015), p. 69. ISSN: 1029-8479. DOI: 10.1007/JHEP09(2015)069. URL: https://doi.org/10.1007/JHEP09(2015)069.

[191] Ronak M Soni and Sandip P. Trivedi. "Aspects of Entanglement Entropy for Gauge Theories". *JHEP* 01 (2016), p. 136. DOI: 10.1007/JHEP01(2016)136. arXiv: 1510.07455 [hep-th].

[192] Dmitri E. Kharzeev and Eugene M. Levin. "Deep inelastic scattering as a probe of entanglement". *Phys. Rev.* D95.11 (2017), p. 114008. DOI: 10.1103/PhysRevD.95.114008. arXiv: 1702.03489 [hep-ph].

[193] Alba Cervera-Lierta et al. "Maximal Entanglement in High Energy Physics". *SciPost Phys.* 3.5 (2017), p. 036. DOI: 10.21468/SciPostPhys.3.5.036. arXiv: 1703.02989 [hep-th].

[194] Silas R. Beane and Peter Ehlers. "Chiral symmetry breaking, entanglement, and the nucleon spin decomposition" (2019). arXiv: 1905.03295 [hep-ph].

[195] Zhoudunming Tu, Dmitri E. Kharzeev, and Thomas Ullrich. "The EPR paradox and quantum entanglement at sub-nucleonic scales" (2019). arXiv: 1904.11974 [hep-ph].

[196] Guifré Vidal. "Efficient Classical Simulation of Slightly Entangled Quantum Computations". *Phys. Rev. Lett.* 91 (14 2003), p. 147902. DOI: 10.1103/PhysRevLett.91.147902. URL: https://link.aps.org/doi/10.1103/PhysRevLett.91.147902.

[197] M. B. Hastings. "An area law for one-dimensional quantum systems". *J. Stat. Mech.* 0708 (2007), P08024. DOI: 10.1088/1742-5468/2007/08/P08024. arXiv: 0705.2024 [quant-ph].

[198] M. B. Hastings. "Entropy and entanglement in quantum ground states". *Phys. Rev. B* 76 (3 2007), p. 035114. DOI: 10.1103/PhysRevB.76.035114. URL: https://link.aps.org/doi/10.1103/PhysRevB.76.035114.

[199] Norbert Schuch et al. "Entropy Scaling and Simulability by Matrix Product States". *Phys. Rev. Lett.* 100 (2008), p. 030504. DOI: 10.1103/PhysRevLett.100.030504. arXiv: 0705.0292 [quant-ph].

[200] Fernando G. S. L. Brandao and Michal Horodecki. "Exponential Decay of Correlations Implies Area Law". *Commun. Math. Phys.* 333.2 (2015), pp. 761–798. DOI: 10.1007/s00220-014-2213-8. arXiv: 1206.2947 [quant-ph].

[201] Christof Zalka. "Simulating quantum systems on a quantum computer". *Proceedings of the Royal Society of London. Series A: Mathematical, Physical and Engineering Sciences* 454.1969 (Jan. 1998), pp. 313–322. DOI: 10.1098/rspa.1998.0162. URL: https://doi.org/10.1098/rspa.1998.0162.

[202] Lov Grover and Terry Rudolph. "Creating superpositions that correspond to efficiently integrable probability distributions". *arXiv e-prints*, quant-ph/0208112 (2002), quant–ph/0208112. arXiv: quant-ph/0208112 [quant-ph].

[203] Ville Bergholm et al. "Quantum circuits with uniformly controlled one-qubit gates". *Phys. Rev. A* 71 (5 2005), p. 052330. DOI: 10.1103/PhysRevA.71.052330. URL: https://link.aps.org/doi/10.1103/PhysRevA.71.052330.

[204] Adriano Barenco et al. "Elementary gates for quantum computation". *Phys. Rev.* A52 (1995), p. 3457. DOI: 10.1103/PhysRevA.52.3457. arXiv: quant-ph/9503016 [quant-ph].

[205] Vivek V. Shende and Igor L. Markov. "On the CNOT-cost of TOFFOLI Gates". *Quantum Info. Comput.* 9.5 (May 2009), pp. 461–486. ISSN: 1533-7146. URL: http://dl.acm.org/citation.cfm?id=2011791.2011799.

[206] M. Sohaib Alam. *Quantum computing a Gaussian wavefunction*. https://medium.com/@sohaib.alam/quantum-computing-a-gaussian-wavefunction-2d0be23d77b2. (Accessed on 12/23/2018). Jan. 2018.

[207] Anirban Narayan Chowdhury, Yigit Subasi, and Rolando D. Somma. "Improved implementation of reflection operators" (2018). arXiv: 1803.02466 [quant-ph].

[208] Martin Plesch and Časlav Brukner. "Quantum-state preparation with universal gate decompositions". *Phys. Rev. A* 83 (3 2011), p. 032302. DOI: 10.1103/PhysRevA.83.032302. URL: https://link.aps.org/doi/10.1103/PhysRevA.83.032302.

[209] Daniel M. Greenberger, Michael A. Horne, and Anton Zeilinger. "Going Beyond Bell's Theorem". *Bell's Theorem, Quantum Theory and Conceptions of the Universe*. Ed. by Menas Kafatos. Dordrecht: Springer Netherlands, 1989, pp. 69–72. ISBN: 978-94-017-0849-4. DOI: 10.1007/978-94-017-0849-4_10. URL: https://doi.org/10.1007/978-94-017-0849-4_10.

[210] Valerie Coffman, Joydip Kundu, and William K. Wootters. "Distributed entanglement". *Phys. Rev.* A61 (2000), p. 052306. DOI: 10.1103/PhysRevA.61.052306. arXiv: quant-ph/9907047 [quant-ph].

[211] W. Dür, G. Vidal, and J. I. Cirac. "Three qubits can be entangled in two inequivalent ways". *Phys. Rev. A* 62 (6 2000), p. 062314. DOI: 10.1103/PhysRevA.62.062314. URL: https://link.aps.org/doi/10.1103/PhysRevA.62.062314.

[212] Silas R. Beane et al. "Uncertainty Quantification in Lattice QCD Calculations for Nuclear Physics". *J. Phys. G* 42.3 (2015), p. 034022. DOI: 10.1088/0954-3899/42/3/034022. arXiv: 1410.2937 [nucl-th].

[213] M. C. Bañuls et al. "Simulating Lattice Gauge Theories within Quantum Technologies" (2019). arXiv: 1911.00003 [quant-ph].

[214] Jesse R. Stryker. "Oracles for Gauss's law on digital quantum computers". *Phys. Rev.* A99.4 (2019), p. 042301. DOI: 10.1103/PhysRevA.99.042301. arXiv: 1812.01617 [quant-ph].

[215] Christian Kokail et al. "Self-verifying variational quantum simulation of lattice models". *Nature* 569.7756 (2019), pp. 355–360. DOI: 10.1038/s41586-019-1177-4. arXiv: 1810.03421 [quant-ph].

[216] Indrakshi Raychowdhury and Jesse R. Stryker. "Tailoring non-Abelian lattice gauge theory for quantum simulation" (2018). arXiv: 1812.07554 [hep-lat].

[217] Daniel C. Hackett et al. "Digitizing Gauge Fields: Lattice Monte Carlo Results for Future Quantum Computers". *Phys. Rev.* A99.6 (2019), p. 062341. DOI: 10.1103/PhysRevA.99.062341. arXiv: 1811.03629 [quant-ph].

[218] Erik Gustafson, Yannick Meurice, and Judah Unmuth-Yockey. "Quantum simulation of scattering in the quantum Ising model". *Phys. Rev.* D99.9 (2019), p. 094503. DOI: 10.1103/PhysRevD.99.094503. arXiv: 1901.05944 [hep-lat].

[219] Henry Lamm, Scott Lawrence, and Yukari Yamauchi. "General Methods for Digital Quantum Simulation of Gauge Theories". *Phys. Rev.* D100.3 (2019), p. 034518. DOI: 10.1103/PhysRevD.100.034518. arXiv: 1903.08807 [hep-lat].

[220] Andrei Alexandru et al. "σ Models on Quantum Computers". *Phys. Rev. Lett.* 123.9 (2019), p. 090501. DOI: 10.1103/PhysRevLett.123.090501. arXiv: 1903.06577 [hep-lat].

[221] Nicholas J. Ward, Ivan Kassal, and Alán Aspuru-Guzik. "Preparation of many-body states for quantum simulation". *The Journal of Chemical Physics* 130.19 (2009), p. 194105. DOI: 10.1063/1.3115177. eprint: https://doi.org/10.1063/1.3115177. URL: https://doi.org/10.1063/1.3115177.

[222] Daniel A. Lidar, Ali T. Rezakhani, and Alioscia Hamma. "Adiabatic approximation with exponential accuracy for many-body systems and quantum computation". *Journal of Mathematical Physics* 50.10 (2009), p. 102106. DOI: 10.1063/1.3236685. eprint: https://doi.org/10.1063/1.3236685. URL: https://doi.org/10.1063/1.3236685.

[223] Zhang Jiang et al. "Quantum algorithms to simulate many-body physics of correlated fermions". *Phys. Rev. Applied* 9.4 (2018), p. 044036. DOI: 10.1103/PhysRevApplied.9.044036. arXiv: 1711.05395 [quant-ph].

[224] Alessandro Roggero and Joseph Carlson. "Linear Response on a Quantum Computer". *Phys. Rev.* C100.3 (2019), p. 034610. DOI: 10.1103/PhysRevC.100.034610. arXiv: 1804.01505 [quant-ph].

[225] Christian W. Bauer et al. "A quantum algorithm for high energy physics simulations" (2019). arXiv: 1904.03196 [hep-ph].

[226] Juan Miguel Arrazola et al. "Machine learning method for state preparation and gate synthesis on photonic quantum computers". *arXiv e-prints* (July 2018). arXiv: 1807.10781 [quant-ph].

[227] IBM. *backend-information*. https://www.research.ibm.com/ibm-q/technology/devices/. 2019.

[228] *IBM Q Experience*. https://quantumexperience.ng.bluemix.net.

[229] Gadi Aleksandrowicz et al. *Qiskit: An Open-source Framework for Quantum Computing*. 2019. DOI: 10.5281/zenodo.2562110.

[230] Wolfram Research, Inc. *Mathematica, Version 11.3*. Champaign, IL, 2018.

[231] Seth T. Merkel et al. "Self-consistent quantum process tomography". *Phys. Rev. A* 87 (6 2013), p. 062119. DOI: 10.1103/PhysRevA.87.062119. URL: https://link.aps.org/doi/10.1103/PhysRevA.87.062119.

[232] Robin Blume-Kohout et al. "Robust, self-consistent, closed-form tomography of quantum logic gates on a trapped ion qubit". *arXiv e-prints* (2013). arXiv: 1310.4492 [quant-ph].

[233] Daniel Greenbaum. "Introduction to Quantum Gate Set Tomography". *arXiv e-prints* (2015). arXiv: 1509.02921 [quant-ph].

[234] Robin Blume-Kohout et al. "Demonstration of qubit operations below a rigorous fault tolerance threshold with gate set tomography". *Nature Communications* 8 (2017). DOI: 10.1038/ncomms14485. arXiv: 1605.07674 [quant-ph].

[235] Kristan Temme, Sergey Bravyi, and Jay M. Gambetta. "Error Mitigation for Short-Depth Quantum Circuits". *prl* 119, 180509 (2017), p. 180509. DOI: 10.1103/PhysRevLett.119.180509. arXiv: 1612.02058 [quant-ph].

[236] Abhinav Kandala et al. "Error mitigation extends the computational reach of a noisy quantum processor". *Nature* 567.7749 (2019), pp. 491–495. ISSN: 1476-4687. DOI: 10.1038/s41586-019-1040-7. URL: https://doi.org/10.1038/s41586-019-1040-7.

[237] Alexei Y. Kitaev. "Quantum measurements and the Abelian Stabilizer Problem". *Electronic Colloquium on Computational Complexity (ECCC)* 3 (1996). arXiv: quant-ph/9511026 [quant-ph]. URL: https://ui.adsabs.harvard.edu/abs/1995quant.ph.11026K.

[238] Daniel S. Abrams and Seth Lloyd. "Quantum Algorithm Providing Exponential Speed Increase for Finding Eigenvalues and Eigenvectors". *Phys. Rev. Lett.* 83 (24 1999), pp. 5162–5165. DOI: 10.1103/PhysRevLett.83.5162. URL: https://link.aps.org/doi/10.1103/PhysRevLett.83.5162.

[239] Edward Farhi et al. "Quantum Computation by Adiabatic Evolution". *arXiv e-prints* (2000). arXiv: quant-ph/0001106 [quant-ph].

[240] Nathan Wiebe and Chris Granade. "Efficient Bayesian Phase Estimation". *prl* 117.1, 010503 (2016), p. 010503. DOI: 10.1103/PhysRevLett.117.010503. arXiv: 1508.00869 [quant-ph].

[241] Mario Motta et al. "Quantum Imaginary Time Evolution, Quantum Lanczos, and Quantum Thermal Averaging" (2019). arXiv: 1901.07653 [quant-ph].

[242] P. F. Bedaque and U. van Kolck. "Effective field theory for few-nucleon systems". *Annu. Rev. Nucl. Part. Sci.* 52 (2002), pp. 339–396. DOI: 10.1146/annurev.nucl.52.050102.090637. eprint: nucl-th/0203055. URL: http://adsabs.harvard.edu/abs/2002ARNPS..52..339B.

[243] Omar Shehab et al. "Toward convergence of effective field theory simulations on digital quantum computers" (2019). arXiv: 1904.04338 [quant-ph].

[244] John Kogut and Leonard Susskind. "Hamiltonian formulation of Wilson's lattice gauge theories". *Phys. Rev. D* 11 (2 1975), pp. 395–408. DOI: 10.1103/PhysRevD.11.395. URL: https://link.aps.org/doi/10.1103/PhysRevD.11.395.

[245] Tom Banks, Leonard Susskind, and John B. Kogut. "Strong Coupling Calculations of Lattice Gauge Theories: (1+1)-Dimensional Exercises". *Phys. Rev.* D13 (1976), p. 1043. DOI: 10.1103/PhysRevD.13.1043.

[246] A. Casher, John B. Kogut, and Leonard Susskind. "Vacuum polarization and the quark parton puzzle". *Phys. Rev. Lett.* 31 (1973), pp. 792–795. DOI: 10.1103/PhysRevLett.31.792.

[247] Gerard 't Hooft and M. J. G. Veltman. "Regularization and Renormalization of Gauge Fields". *Nucl. Phys.* B44 (1972), pp. 189–213. DOI: 10.1016/0550-3213(72)90279-9.

[248] K. G. Wilson and John B. Kogut. "The Renormalization group and the epsilon expansion". *Phys. Rept.* 12 (1974), pp. 75–200. DOI: 10.1016/0370-1573(74)90023-4.

[249] Thomas Appelquist and J. Carazzone. "Infrared Singularities and Massive Fields". *Phys. Rev.* D11 (1975), p. 2856. DOI: 10.1103/PhysRevD.11.2856.

[250] Stefan Kühn, J. Ignacio Cirac, and Mari-Carmen Bañuls. "Quantum simulation of the Schwinger model: A study of feasibility". *Phys. Rev.* A90.4 (2014), p. 042305. DOI: 10.1103/PhysRevA.90.042305. arXiv: 1407.4995 [quant-ph].

[251] John B. Kogut and Leonard Susskind. "Hamiltonian Formulation of Wilson's Lattice Gauge Theories". *Phys. Rev. D.* 11 (1975), pp. 395–408. DOI: 10.1103/PhysRevD.11.395.

[252] Sidney R. Coleman. "More About the Massive Schwinger Model". *Annals Phys.* 101 (1976), p. 239. DOI: 10.1016/0003-4916(76)90280-3.

[253] H. Fritzsch, Murray Gell-Mann, and H. Leutwyler. "Advantages of the Color Octet Gluon Picture". *Phys. Lett.* 47B (1973), pp. 365–368. DOI: 10.1016/0370-2693(73)90625-4.

[254] H. David Politzer. "Reliable Perturbative Results for Strong Interactions?" *Phys. Rev. Lett.* 30 (1973), pp. 1346–1349. DOI: 10.1103/PhysRevLett.30.1346.

[255] David J. Gross and Frank Wilczek. "Ultraviolet Behavior of Nonabelian Gauge Theories". *Phys. Rev. Lett.* 30 (1973), pp. 1343–1346. DOI: 10.1103/PhysRevLett.30.1343.

[256] Steven Weinberg. "Nonlinear realizations of chiral symmetry". *Phys. Rev.* 166 (1968), pp. 1568–1577. DOI: 10.1103/PhysRev.166.1568.

[257] ASCR. *Exascale Requirements Reviews*. https://science.energy.gov/ascr/community-resources/program-documents/. 2017. (Visited on 2017).

[258] Benjamin P Lanyon et al. "Towards quantum chemistry on a quantum computer". *Nat. Chem.* 2.2 (2010), p. 106.

[259] Alberto Peruzzo et al. "A variational eigenvalue solver on a photonic quantum processor". *Nat. Commun.* 5 (2014), p. 4213.

[260] P. J. J. O'Malley et al. "Scalable Quantum Simulation of Molecular Energies". *Phys. Rev. X* 6 (3 2016), p. 031007. DOI: 10.1103/PhysRevX.6.031007. URL: https://link.aps.org/doi/10.1103/PhysRevX.6.031007.

[261] Abhinav Kandala et al. "Hardware-efficient variational quantum eigensolver for small molecules and quantum magnets". *Nature* 549.7671 (2017), p. 242.

[262] J. R. McClean et al. "The theory of variational hybrid quantum-classical algorithms". *New J. Phys.* 18.2, 023023 (Feb. 2016), p. 023023. DOI: 10.1088/1367-2630/18/2/023023. arXiv: 1509.04279 [quant-ph].

[263] Raffaele Santagati et al. "Witnessing eigenstates for quantum simulation of Hamiltonian spectra". *Sci. Adv.* 4.1 (2018), eaap9646. DOI: 10.1126/sciadv.aap9646. eprint: http://advances.sciencemag.org/content/4/1/eaap9646.full.pdf. URL: http://advances.sciencemag.org/content/4/1/eaap9646.

[264] Julian S. Schwinger. "Gauge Invariance and Mass. 2." *Phys. Rev.* 128 (1962), pp. 2425–2429. DOI: 10.1103/PhysRev.128.2425.

[265] Sidney R. Coleman, R. Jackiw, and Leonard Susskind. "Charge Shielding and Quark Confinement in the Massive Schwinger Model". *Annals Phys.* 93 (1975), p. 267. DOI: 10.1016/0003-4916(75)90212-2.

[266] Mari Carmen Bañuls et al. "Chiral condensate in the Schwinger model with matrix product operators". *Phys. Rev. D* 93 (9 2016), p. 094512. DOI: 10.1103/PhysRevD.93.094512. URL: https://link.aps.org/doi/10.1103/PhysRevD.93.094512.

[267] Boye Buyens, Frank Verstraete, and Karel Van Acoleyen. "Hamiltonian simulation of the Schwinger model at finite temperature". *Phys. Rev. D* 94 (8 2016), p. 085018. DOI: 10.1103/PhysRevD.94.085018. URL: https://link.aps.org/doi/10.1103/PhysRevD.94.085018.

[268] Boye Buyens et al. "Real-time simulation of the Schwinger effect with matrix product states". *Phys. Rev. D* 96 (11 2017), p. 114501. DOI: 10.1103/PhysRevD.96.114501. URL: https://link.aps.org/doi/10.1103/PhysRevD.96.114501.

[269] IBM. *ibmqx2-backend-information*. https://github.com/QISKit/ibmqx-backend-information/blob/n 2017.

[270] IBM. *ibmqx5-backend-information*. https://github.com/QISKit/ibmqx-backend-information/blob/n 2017.

[271] Ying Li and Simon C. Benjamin. "Efficient Variational Quantum Simulator Incorporating Active Error Minimization". *Phys. Rev. X* 7 (2 2017), p. 021050. DOI: 10.1103/PhysRevX.7.021050. URL: https://link.aps.org/doi/10.1103/PhysRevX.7.021050.

[272] Kristan Temme, Sergey Bravyi, and Jay M. Gambetta. "Error Mitigation for Short-Depth Quantum Circuits". *Phys. Rev. Lett.* 119 (18 2017), p. 180509. DOI: 10.1103/PhysRevLett.119.180509. URL: https://link.aps.org/doi/10.1103/PhysRevLett.119.180509.

[273] Jay M. Gambetta et al. "Characterization of Addressability by Simultaneous Randomized Benchmarking". *Phys. Rev. Lett.* 109 (24 2012), p. 240504. DOI: 10.1103/PhysRevLett.109.240504. URL: https://link.aps.org/doi/10.1103/PhysRevLett.109.240504.

[274] N. Khaneja and S. J. Glaser. "Cartan decomposition of SU(2 ^{n}) and control of spin systems". *Chemical Physics* 267 (June 2001), pp. 11–23. DOI: 10.1016/S0301-0104(01)00318-4.

[275] Todd Tilma, Mark Byrd, and E C G Sudarshan. "A parametrization of bipartite systems based on SU (4) Euler angles". *Journal of Physics A: Mathematical and General* 35.48 (2002), p. 10445. URL: http://stacks.iop.org/0305-4470/35/i=48/a=315.

[276] G. Vidal and C. M. Dawson. "Universal quantum circuit for two-qubit transformations with three controlled-NOT gates". *Phys. Rev. A* 69 (1 2004), p. 010301. DOI: 10.1103/PhysRevA.69.010301. URL: https://link.aps.org/doi/10.1103/PhysRevA.69.010301.

[277] Joonsuk Huh et al. "Boson sampling for molecular vibronic spectra". *Nat. Photon.* 9.9 (2015), p. 615.

[278] Chris Sparrow et al. "Simulating the vibrational quantum dynamics of molecules using photonics". *Nature* 557.7707 (2018), p. 660.

[279] Jianwei Wang et al. "Experimental quantum Hamiltonian learning". *Nat. Phys.* 13.6 (2017), p. 551.

[280] Pieter Kok et al. "Linear optical quantum computing with photonic qubits". *Rev. Mod. Phys.* 79 (1 2007), pp. 135–174. DOI: 10.1103/RevModPhys.79.135. URL: http://link.aps.org/doi/10.1103/RevModPhys.79.135.

[281] Andrea Crespi et al. "Integrated photonic quantum gates for polarization qubits". *Nat. Commun.* 2 (2011), p. 566.

[282] Peter C. Humphreys et al. "Linear Optical Quantum Computing in a Single Spatial Mode". *Phys. Rev. Lett.* 111 (15 2013), p. 150501. DOI: 10.1103/PhysRevLett.111.150501. URL: http://link.aps.org/doi/10.1103/PhysRevLett.111.150501.

[283] Vahid Ansari et al. "Tailoring nonlinear processes for quantum optics with pulsed temporal-mode encodings". *Optica* 5.5 (2018), pp. 534–550. DOI: 10.1364/OPTICA.5.000534. URL: http://www.osapublishing.org/optica/abstract.cfm?URI=optica-5-5-534.

[284] Nicholas C Harris et al. "Quantum transport simulations in a programmable nanophotonic processor". *Nat. Photon.* 11.7 (2017), p. 447.

[285] Jianwei Wang et al. "Multidimensional quantum entanglement with large-scale integrated optics". *Science* 360.6386 (2018), pp. 285–291. ISSN: 0036-8075. DOI: 10.1126/science.aar7053. eprint: http://science.sciencemag.org/content/360/6386/285.full.pdf. URL: http://science.sciencemag.org/content/360/6386/285.

[286] Xiaogang Qiang et al. "Large-scale silicon quantum photonics implementing arbitrary two-qubit processing". *Nat. Photon.* 12 (2018), pp. 534–539.

[287] Joseph M. Lukens and Pavel Lougovski. "Frequency-encoded photonic qubits for scalable quantum information processing". *Optica* 4.1 (2017), pp. 8–16. DOI: 10.1364/OPTICA.4.000008. URL: http://www.osapublishing.org/optica/abstract.cfm?URI=optica-4-1-8.

[288] Hsuan-Hao Lu et al. "Electro-Optic Frequency Beam Splitters and Tritters for High-Fidelity Photonic Quantum Information Processing". *Phys. Rev. Lett.* 120 (3 2018), p. 030502. DOI: 10.1103/PhysRevLett.120.030502. URL: https://link.aps.org/doi/10.1103/PhysRevLett.120.030502.

[289] Hsuan-Hao Lu et al. "Controllable two-photon interference with versatile quantum frequency processor". *arXiv:1803.10712* (2018).

[290] Hsuan-Hao Lu et al. "A controlled-NOT gate for frequency-bin qubits". *arXiv:1809.05072* (2018).

[291] Henry Lamm and Scott Lawrence. "Simulation of Nonequilibrium Dynamics on a Quantum Computer". *arXiv:1806.06649* (2018). arXiv: 1806.06649 [quant-ph].

[292] J. Zhang et al. "Observation of a many-body dynamical phase transition with a 53-qubit quantum simulator". *Nature* 551 (2017), pp. 601–604. URL: http://dx.doi.org/10.1038/nature24654.

[293] Christian Kokail et al. "Self-Verifying Variational Quantum Simulation of the Lattice Schwinger Model". *arXiv:1810.03421* (2018). arXiv: 1810.03421 [quant-ph].

[294] T. Yamazaki, Y. Kuramashi, and A. Ukawa. "Helium Nuclei in Quenched Lattice QCD". *Phys. Rev. D* 81 (2010), p. 111504. DOI: 10.1103/PhysRevD.81.111504. arXiv: 0912.1383 [hep-lat].

[295] S. R. Beane et al. "The Deuteron and Exotic Two-Body Bound States from Lattice QCD". *Phys. Rev. D* 85 (2012), p. 054511. DOI: 10.1103/PhysRevD.85.054511. arXiv: 1109.2889 [hep-lat].

[296] N. Barnea et al. "Effective Field Theory for Lattice Nuclei". *Phys. Rev. Lett.* 114.5 (2015), p. 052501. DOI: 10.1103/PhysRevLett.114.052501. arXiv: 1311.4966 [nucl-th].

[297] S. R. Beane et al. "Hyperon-Nucleon Interactions and the Composition of Dense Nuclear Matter from Quantum Chromodynamics". *Phys. Rev. Lett.* 109 (2012), p. 172001. DOI: 10.1103/PhysRevLett.109.172001. arXiv: 1204.3606 [hep-lat].

[298] S. R. Beane et al. "Light Nuclei and Hypernuclei from Quantum Chromodynamics in the Limit of SU(3) Flavor Symmetry". *Phys. Rev. D* 87.3 (2013), p. 034506. DOI: 10.1103/PhysRevD.87.034506. arXiv: 1206.5219 [hep-lat].

[299] Takeshi Yamazaki et al. "Helium nuclei, deuteron and dineutron in 2+1 flavor lattice QCD". *Phys. Rev. D* 86 (2012), p. 074514. DOI: 10.1103/PhysRevD.86.074514. arXiv: 1207.4277 [hep-lat].

[300] Takashi Inoue et al. "Medium-heavy nuclei from nucleon-nucleon interactions in lattice QCD". *Phys. Rev. C* 91.1 (2015), p. 011001. DOI: 10.1103/PhysRevC.91.011001. arXiv: 1408.4892 [hep-lat].

[301] Takeshi Yamazaki et al. "Study of quark mass dependence of binding energy for light nuclei in 2+1 flavor lattice QCD". *Phys. Rev. D* 92.1 (2015), p. 014501. DOI: 10.1103/PhysRevD.92.014501. arXiv: 1502.04182 [hep-lat].

[302] Johannes Kirscher et al. “Spectra and Scattering of Light Lattice Nuclei from Effective Field Theory”. *Phys. Rev. C* 92.5 (2015), p. 054002. DOI: 10.1103/PhysRevC.92.054002. arXiv: 1506.09048 [nucl-th].

[303] L. Contessi et al. “Ground-state properties of ^{4}He and ^{16}O extrapolated from lattice QCD with pionless EFT”. *Phys. Lett. B* 772 (2017), pp. 839–848. DOI: 10.1016/j.physletb.2017.07.048. arXiv: 1701.06516 [nucl-th].

[304] A. Bansal et al. “Pion-less effective field theory for atomic nuclei and lattice nuclei”. *arXiv:1712.10246* (2017). arXiv: 1712.10246 [nucl-th].

[305] Takumi Iritani et al. “Systematics of the HAL QCD Potential at Low Energies in Lattice QCD”. *arXiv:1805.02365* (2018). arXiv: 1805.02365 [hep-lat].

[306] E. Epelbaum, H.-W. Hammer, and Ulf-G. Meißner. “Modern theory of nuclear forces”. *Rev. Mod. Phys.* 81 (4 2009), pp. 1773–1825. DOI: 10.1103/RevModPhys.81.1773. URL: http://link.aps.org/doi/10.1103/RevModPhys.81.1773.

[307] R. Machleidt and D.R. Entem. “Chiral effective field theory and nuclear forces”. *Phys. Rep.* 503.1 (2011), pp. 1 –75. DOI: 10.1016/j.physrep.2011.02.001. URL: http://www.sciencedirect.com/science/article/pii/S0370157311000457.

[308] Petr Navrátil et al. “Recent developments in no-core shell-model calculations”. *J. Phys. G: Nucl. Part. Phys.* 36.8 (2009), p. 083101. URL: http://stacks.iop.org/0954-3899/36/i=8/a=083101.

[309] Bruce R. Barrett, Petr Navrátil, and James P. Vary. “Ab initio no core shell model”. *Prog. Part. Nucl. Phys.* 69.0 (2013), pp. 131 –181. DOI: 10.1016/j.ppnp.2012.10.003. URL: http://www.sciencedirect.com/science/article/pii/S0146641012001184.

[310] G. Hagen et al. “Neutron and weak-charge distributions of the ^{48}Ca nucleus”. *Nat. Phys.* 12 (2016), p. 186. DOI: 10.1038/nphys3529. URL: http://www.nature.com/nphys/journal/vaop/ncurrent/pdf/nphys3529.pdf.

[311] T. D. Morris et al. "Structure of the Lightest Tin Isotopes". *Phys. Rev. Lett.* 120 (15 2018), p. 152503. DOI: 10.1103/PhysRevLett.120.152503. URL: https://link.aps.org/doi/10.1103/PhysRevLett.120.152503.

[312] G. Parisi. "The Strategy for Computing the Hadronic Mass Spectrum". *Phys. Rep.* 103 (1984), pp. 203–211. DOI: 10.1016/0370-1573(84)90081-4.

[313] G. Peter Lepage. "The Analysis of Algorithms for Lattice Field Theory". *Boulder ASI 1989:97-120*. 1989, pp. 97–120. URL: http://alice.cern.ch/format/showfull?sysnb=0117836.

[314] Silas R. Beane et al. "High Statistics Analysis using Anisotropic Clover Lattices. II. Three-Baryon Systems". *Phys. Rev.* D80 (2009), p. 074501. DOI: 10.1103/PhysRevD.80.074501. arXiv: 0905.0466 [hep-lat].

[315] Silas R. Beane et al. "High Statistics Analysis using Anisotropic Clover Lattices: (I) Single Hadron Correlation Functions". *Phys. Rev. D* 79 (2009), p. 114502. DOI: 10.1103/PhysRevD.79.114502. arXiv: 0903.2990 [hep-lat].

[316] Michael L. Wagman and Martin J. Savage. "Statistics of baryon correlation functions in lattice QCD". *Phys. Rev. D* 96.11 (2017), p. 114508. DOI: 10.1103/PhysRevD.96.114508. arXiv: 1611.07643 [hep-lat].

[317] E. Ovrum and Morten Hjorth-Jensen. "Quantum computation algorithm for many-body studies". *arXiv:0705.1928* (2007). arXiv: 0705.1928 [quant-ph].

[318] L. Olislager et al. "Frequency-bin entangled photons". *Phys. Rev. A* 82 (1 2010), p. 013804. DOI: 10.1103/PhysRevA.82.013804. URL: http://link.aps.org/doi/10.1103/PhysRevA.82.013804.

[319] David A. Mazziotti. "Anti-Hermitian Contracted Schrödinger Equation: Direct Determination of the Two-Electron Reduced Density Matrices of Many-Electron Molecules". *Phys. Rev. Lett.* 97 (14 2006), p. 143002. DOI: 10.1103/PhysRevLett.97.143002. URL: https://link.aps.org/doi/10.1103/PhysRevLett.97.143002.

[320] Titus D. Morris. "Improved optimization of unitary coupled cluster ansatz". *in preparation* (2019).

[321] Roger Fletcher. *Practical Methods of Optimization*. Wiley, 1987.

[322] P. F. Bedaque, H.-W. Hammer, and U. van Kolck. "Renormalization of the Three-Body System with Short-Range Interactions". *Phys. Rev. Lett.* 82 (3 1999), pp. 463–467. DOI: 10.1103/PhysRevLett.82.463. URL: https://link.aps.org/doi/10.1103/PhysRevLett.82.463.

[323] J. C. Light and T. Carrington. "Discrete-Variable Representations and their Utilization". *Adv. Chem. Phys.* John Wiley & Sons, Inc., 2007, pp. 263–310. ISBN: 9780470141731. DOI: 10.1002/9780470141731.ch4. URL: http://dx.doi.org/10.1002/9780470141731.ch4.

[324] J. Potvin. "A NONPERTURBATIVE STUDY OF HADRONIZATION WITH HEAVY SOURCES. 1. THE SCREENING LENGTH AS A FUNCTION OF THE QUARK MASS IN THE SCHWINGER MODEL". *Phys. Rev.* D32 (1985), p. 2070. DOI: 10.1103/PhysRevD.32.2070.

[325] M. C. Banuls et al. "The mass spectrum of the Schwinger model with Matrix Product States". *JHEP* 11 (2013), p. 158. DOI: 10.1007/JHEP11(2013)158. arXiv: 1305.3765 [hep-lat].

[326] Yuya Shimizu and Yoshinobu Kuramashi. "Critical behavior of the lattice Schwinger model with a topological term at $\theta = \pi$ using the Grassmann tensor renormalization group". *Phys. Rev.* D90.7 (2014), p. 074503. DOI: 10.1103/PhysRevD.90.074503. arXiv: 1408.0897 [hep-lat].

[327] Yuya Shimizu and Yoshinobu Kuramashi. "Grassmann tensor renormalization group approach to one-flavor lattice Schwinger model". *Phys. Rev.* D90.1 (2014), p. 014508. DOI: 10.1103/PhysRevD.90.014508. arXiv: 1403.0642 [hep-lat].

[328] M. C. Banuls et al. “Thermal evolution of the Schwinger model with Matrix Product Operators”. *Phys. Rev.* D92.3 (2015), p. 034519. DOI: 10.1103/PhysRevD.92.034519. arXiv: 1505.00279 [hep-lat].

[329] Mari Carmen Bañuls et al. “Chiral condensate in the Schwinger model with Matrix Product Operators”. *Phys. Rev.* D93.9 (2016), p. 094512. DOI: 10.1103/PhysRevD.93.094512. arXiv: 1603.05002 [hep-lat].

[330] Mari Carmen Banuls et al. “Density Induced Phase Transitions in the Schwinger Model: A Study with Matrix Product States”. *Phys. Rev. Lett.* 118.7 (2017), p. 071601. DOI: 10.1103/PhysRevLett.118.071601. arXiv: 1611.00705 [hep-lat].

[331] Boye Buyens, Frank Verstraete, and Karel Van Acoleyen. “Hamiltonian simulation of the Schwinger model at finite temperature”. *Phys. Rev.* D94.8 (2016), p. 085018. DOI: 10.1103/PhysRevD.94.085018. arXiv: 1606.03385 [hep-lat].

[332] Boye Buyens et al. “Real-time simulation of the Schwinger effect with Matrix Product States”. *Phys. Rev.* D96.11 (2017), p. 114501. DOI: 10.1103/PhysRevD.96.114501. arXiv: 1612.00739 [hep-lat].

[333] H. David Politzer. “Asymptotic Freedom: An Approach to Strong Interactions”. *Phys. Rept.* 14 (1974), pp. 129–180. DOI: 10.1016/0370-1573(74)90014-3.

[334] M. Creutz. “Monte Carlo Study of Quantized SU(2) Gauge Theory”. *Phys. Rev.* D21 (1980), pp. 2308–2315. DOI: 10.1103/PhysRevD.21.2308.

[335] T. Pichler et al. “Real-time Dynamics in U(1) Lattice Gauge Theories with Tensor Networks”. *Phys. Rev.* X6.1 (2016), p. 011023. DOI: 10.1103/PhysRevX.6.011023. arXiv: 1505.04440 [cond-mat.quant-gas].

[336] M. Dalmonte and S. Montangero. “Lattice gauge theory simulations in the quantum information era”. *Contemp. Phys.* 57.3 (2016), pp. 388–412. DOI: 10.1080/00107514.2016.1151199. arXiv: 1602.03776 [cond-mat.quant-gas].

[337] Elisa Ercolessi et al. "Phase Transitions in Z_n Gauge Models: Towards Quantum Simulations of the Schwinger-Weyl QED". *Phys. Rev.* D98.7 (2018), p. 074503. DOI: 10.1103/PhysRevD.98.074503. arXiv: 1705.11047 [quant-ph].

[338] P. Sala et al. "Variational study of U(1) and SU(2) lattice gauge theories with Gaussian states in 1+1 dimensions". *Phys. Rev.* D98.3 (2018), p. 034505. DOI: 10.1103/PhysRevD.98.034505. arXiv: 1805.05190 [hep-lat].

[339] Alexandru Macridin et al. "Electron-Phonon Systems on a Universal Quantum Computer". *Phys. Rev. Lett.* 121.11 (2018), p. 110504. DOI: 10.1103/PhysRevLett.121.110504. arXiv: 1802.07347 [quant-ph].

[340] John Preskill. "Simulating quantum field theory with a quantum computer". *PoS* LATTICE2018 (2018), p. 024. DOI: 10.22323/1.334.0024. arXiv: 1811.10085 [hep-lat].

[341] Alexei Bazavov et al. "Tensor renormalization group study of the non-Abelian Higgs model in two dimensions". *Phys. Rev.* D99.11 (2019), p. 114507. DOI: 10.1103/PhysRevD.99.114507. arXiv: 1901.11443 [hep-lat].

[342] Andrei Alexandru et al. "Gluon Field Digitization for Quantum Computers" (2019). arXiv: 1906.11213 [hep-lat].

[343] L. García-Alvarez et al. "Fermion-Fermion Scattering in Quantum Field Theory with Superconducting Circuits". *Phys. Rev. Lett.* 114.7 (2015), p. 070502. DOI: 10.1103/PhysRevLett.114.070502. arXiv: 1404.2868 [quant-ph].

[344] A. Mezzacapo et al. "Non-Abelian $SU(2)$ Lattice Gauge Theories in Superconducting Circuits". *Phys. Rev. Lett.* 115.24 (2015), p. 240502. DOI: 10.1103/PhysRevLett.115.240502. arXiv: 1505.04720 [quant-ph].

[345] Erez Zohar, J. Ignacio Cirac, and Benni Reznik. "Quantum Simulations of Lattice Gauge Theories using Ultracold Atoms in Optical Lattices". *Rept. Prog. Phys.* 79.1

(2016), p. 014401. DOI: 10.1088/0034-4885/79/1/014401. arXiv: 1503.02312 [quant-ph].

[346] T. V. Zache et al. "Quantum simulation of lattice gauge theories using Wilson fermions". *Sci. Technol.* 3 (2018), p. 034010. DOI: 10.1088/2058-9565/aac33b. arXiv: 1802.06704 [cond-mat.quant-gas].

[347] Zohreh Davoudi et al. "Towards analog quantum simulations of lattice gauge theories with trapped ions" (2019). arXiv: 1908.03210 [quant-ph].

[348] Kubra Yeter-Aydeniz et al. "Scalar Quantum Field Theories as a Benchmark for Near-Term Quantum Computers". *Phys. Rev.* A99.3 (2019), p. 032306. DOI: 10.1103/PhysRevA.99.032306. arXiv: 1811.12332 [quant-ph].

[349] S. A. Chin et al. "Exact ground-state properties of the SU(2) Hamiltonian lattice gauge theory". *Phys. Rev. D* 31 (12 1985), pp. 3201–3212. DOI: 10.1103/PhysRevD.31.3201. URL: https://link.aps.org/doi/10.1103/PhysRevD.31.3201.

[350] G. Burgio et al. "The Basis of the physical Hilbert space of lattice gauge theories". *Nucl. Phys.* B566 (2000), pp. 547–561. DOI: 10.1016/S0550-3213(99)00533-7. arXiv: hep-lat/9906036 [hep-lat].

[351] Manu Mathur. "Harmonic oscillator pre-potentials inSU(2) lattice gauge theory". *Journal of Physics A: Mathematical and General* 38.46 (2005), pp. 10015–10025. DOI: 10.1088/0305-4470/38/46/008. URL: https://doi.org/10.1088%2F0305-4470%2F38%2F46%2F008.

[352] Manu Mathur. "The loop states in lattice gauge theories". *Phys. Lett.* B640 (2006), pp. 292–296. DOI: 10.1016/j.physletb.2006.08.022. arXiv: hep-lat/0510101 [hep-lat].

[353] Ramesh Anishetty, Manu Mathur, and Indrakshi Raychowdhury. "Prepotential formulation ofSU(3) lattice gauge theory". *Journal of Physics A: Mathematical and*

Theoretical 43.3 (2009), p. 035403. DOI: 10.1088/1751-8113/43/3/035403. URL: https://doi.org/10.1088%2F1751-8113%2F43%2F3%2F035403.

[354] Peter Orland. "Subtleties of Non-Abelian Gauge Theories in Cold-Atomic Lattices". *PoS* LATTICE2013 (2014), p. 330. DOI: 10.22323/1.187.0330. arXiv: 1311.4192 [hep-lat].

[355] K. Stannigel et al. "Constrained dynamics via the Zeno effect in quantum simulation: Implementing non-Abelian lattice gauge theories with cold atoms". *Phys. Rev. Lett.* 112.12 (2014), p. 120406. DOI: 10.1103/PhysRevLett.112.120406. arXiv: 1308.0528 [quant-ph].

[356] M. Rizzi. "Quantum simulation of gauge potentials with cold atoms in optical lattices: a tunable platform for relativistic fermions and axions". *PoS* QCD-TNT-III (2013), p. 036. DOI: 10.22323/1.193.0036.

[357] Ramesh Anishetty and Indrakshi Raychowdhury. "SU(2) lattice gauge theory: Local dynamics on nonintersecting electric flux loops". *Phys. Rev.* D90.11 (2014), p. 114503. DOI: 10.1103/PhysRevD.90.114503. arXiv: 1408.6331 [hep-lat].

[358] Erez Zohar and Michele Burrello. "Formulation of lattice gauge theories for quantum simulations". *Phys. Rev.* D91.5 (2015), p. 054506. DOI: 10.1103/PhysRevD.91.054506. arXiv: 1409.3085 [quant-ph].

[359] Yoshihito Kuno et al. "Real-time dynamics and proposal for feasible experiments of lattice gauge?Higgs model simulated by cold atoms". *New J. Phys.* 17.6 (2015), p. 063005. DOI: 10.1088/1367-2630/17/6/063005. arXiv: 1412.7605 [cond-mat.quant-gas].

[360] YiMin Liu and RongWan Liu. "Optical quantum simulation of Abelian gauge field using cold atomic ensembles coupled with arrays of optical cavities". *Sci. China Phys. Mech. Astron.* 57.12 (2014), pp. 2259–. DOI: 10.1007/s11433-014-5618-7.

[361] Yu-Xin Hu et al. "U(3) artificial gauge fields for cold atoms". *Phys. Rev.* A90.2 (2014), p. 023601. DOI: 10.1103/PhysRevA.90.023601. arXiv: 1403.7979 [quant-ph].

[362] Luca Tagliacozzo, Alessio Celi, and Maciej Lewenstein. "Tensor Networks for Lattice Gauge Theories with continuous groups". *Phys. Rev.* X4.4 (2014), p. 041024. DOI: 10.1103/PhysRevX.4.041024. arXiv: 1405.4811 [cond-mat.str-el].

[363] Yoshihito Kuno et al. "Quantum simulation of $(1 + 1)$-dimensional U(1) gauge-Higgs model on a lattice by cold Bose gases". *Phys. Rev.* D95.9 (2017), p. 094507. DOI: 10.1103/PhysRevD.95.094507. arXiv: 1605.00333 [cond-mat.quant-gas].

[364] Patrick Dreher. "Challenges Implementing non-Abelian SU(2) Quantum Chromodynamics Gauge Links On a Universal Quantum Computer". *PoS* LATTICE2018 (2018), p. 036. DOI: 10.22323/1.334.0036. arXiv: 1811.01309 [hep-lat].

[365] De-Sheng Li et al. "Digital Quantum Simulation of Yang-Mills Theory and Hadronization" (2018). arXiv: 1810.09213 [quant-ph].

[366] Erez Zohar and J. Ignacio Cirac. "Removing Staggered Fermionic Matter in $U(N)$ and $SU(N)$ Lattice Gauge Theories". *Phys. Rev.* D99.11 (2019), p. 114511. DOI: 10.1103/PhysRevD.99.114511. arXiv: 1905.00652 [quant-ph].

[367] Alexander M. Polyakov. "String Representations and Hidden Symmetries for Gauge Fields". *Phys. Lett.* 82B (1979), pp. 247–250. DOI: 10.1016/0370-2693(79)90747-0.

[368] S. Mandelstam. "Charge - Monopole Duality and the Phases of Nonabelian Gauge Theories". *Phys. Rev.* D19 (1979), p. 2391. DOI: 10.1103/PhysRevD.19.2391.

[369] Yoichiro Nambu. "QCD and the String Model". *Phys. Lett.* 80B (1979), pp. 372–376. DOI: 10.1016/0370-2693(79)91193-6.

[370] Alexander M. Polyakov. "Gauge Fields as Rings of Glue". *Nucl. Phys.* B164 (1980), pp. 171–188. DOI: 10.1016/0550-3213(80)90507-6.

[371] W. Furmanski and A. Kolawa. "Yang-Mills Vacuum: An Attempt of Lattice Loop Calculus". *Nucl. Phys.* B291 (1987), pp. 594–628. DOI: 10.1016/0550-3213(87)90487-1.

[372] Rodolfo Gambini, Lorenzo Leal, and Antoni Trias. "Loop Calculus for Lattice Gauge Theories". *Phys. Rev.* D39 (1989), p. 3127. DOI: 10.1103/PhysRevD.39.3127.

[373] Cayetano Di Bartolo, Rodolfo Gambini, and Lorenzo Leal. "Hamiltonian Lattice Gauge Theories in a Loop-Dependent Magnetic Representation". *Phys. Rev. D* 39.6 (Mar. 1989), pp. 1756–1760. DOI: 10.1103/PhysRevD.39.1756.

[374] R. Anishetty and H. S. Sharatchandra. "Duality transformation for nonAbelian lattice gauge theories". *Phys. Rev. Lett.* 65 (1990), pp. 813–815. DOI: 10.1103/PhysRevLett.65.813.

[375] Bernd Bruegmann. "Method of loops applied to lattice gauge theory". *Phys. Rev.* D43 (1991), pp. 566–579. DOI: 10.1103/PhysRevD.43.566.

[376] N. J. Watson. "Solution of the SU(2) Mandelstam constraints". *Phys. Lett.* B323 (1994), pp. 385–392. DOI: 10.1016/0370-2693(94)91236-X. arXiv: hep-th/9311126 [hep-th].

[377] Indrakshi Raychowdhury. "Low energy spectrum of SU(2) lattice gauge theory". *Eur. Phys. J.* C79.3 (2019), p. 235. DOI: 10.1140/epjc/s10052-019-6753-0. arXiv: 1804.01304 [hep-lat].

[378] D. Horn. "Finite matrix models with continuous local gauge invariance". *Physics Letters B* 100.2 (1981), pp. 149 –151. ISSN: 0370-2693. DOI: https://doi.org/10.1016/0370-2693(81)90763-2. URL: http://www.sciencedirect.com/science/article/pii/0370269381907632.

[379] Peter Orland and Daniel Rohrlich. "Lattice gauge magnets: Local isospin from spin". *Nuclear Physics B* 338.3 (1990), pp. 647 –672. ISSN: 0550-3213. DOI: https://doi.org/10.1016/0550-3213(90)90646-U. URL: http://www.sciencedirect.com/science/article/pii/055032139090646U.

[380] S. Chandrasekharan and U. J. Wiese. "Quantum link models: A Discrete approach to gauge theories". *Nucl. Phys.* B492 (1997), pp. 455–474. DOI: 10.1016/S0550-3213(97)00006-0,10.1016/S0550-3213(97)80041-7. arXiv: hep-lat/9609042 [hep-lat].

[381] R. Brower, S. Chandrasekharan, and U. J. Wiese. "QCD as a quantum link model". *Phys. Rev.* D60 (1999), p. 094502. DOI: 10.1103/PhysRevD.60.094502. arXiv: hep-th/9704106 [hep-th].

[382] L. Tagliacozzo et al. "Simulations of non-Abelian gauge theories with optical lattices". *Nature Commun.* 4 (2013), p. 2615. DOI: 10.1038/ncomms3615. arXiv: 1211.2704 [cond-mat.quant-gas].

[383] Y. Meurice et al. "Tensor RG calculations and quantum simulations near criticality". *PoS* LATTICE2016 (2016), p. 325. DOI: 10.22323/1.256.0325. arXiv: 1611.08711 [hep-lat].

[384] Richard Brower. *Formulating Lattice Field Theory for a Quantum Computer*. Presentation given at Intersection of QIS/HEP, Aspen Center for Physics. May 2019. URL: https://indico.hep.caltech.edu/event/184/attachments/188/244/Aspen_QC_brower.pdf.

[385] Yannick Meurice. *Quantum Field Theory with Cold Atoms*. Presentation given at Intersection of QIS/HEP, Aspen Center for Physics. May 2019. URL: https://indico.hep.caltech.edu/event/184/attachments/188/236/meuriceaspen19.pdf.

[386] J. H. Lowenstein and J. A. Swieca. "Quantum electrodynamics in two-dimensions". *Annals Phys.* 68 (1971), pp. 172–195. DOI: 10.1016/0003-4916(71)90246-6.

[387] Alexander F. Shaw et al. "Quantum Algorithms for Simulating the Lattice Schwinger Model" (2020). arXiv: 2002.11146 [quant-ph].

[388] Erez Zohar, J. Ignacio Cirac, and Benni Reznik. "Quantum simulations of gauge theories with ultracold atoms: local gauge invariance from angular momentum conservation". *Phys. Rev.* A88 (2013), p. 023617. DOI: 10.1103/PhysRevA.88.023617. arXiv: 1303.5040 [quant-ph].

[389] Gerard 't Hooft. "A Planar Diagram Theory for Strong Interactions". *Nucl. Phys.* B72 (1974). [,337(1973)], p. 461. DOI: 10.1016/0550-3213(74)90154-0.

[390] Edward Witten. "Large N Chiral Dynamics". *Annals Phys.* 128 (1980), p. 363. DOI: 10.1016/0003-4916(80)90325-5.

[391] E. Wigner. "On the Consequences of the Symmetry of the Nuclear Hamiltonian on the Spectroscopy of Nuclei". *Phys. Rev.* 51 (1937), pp. 106–119. DOI: 10.1103/PhysRev.51.106.

[392] E. Wigner. "On the Structure of Nuclei Beyond Oxygen". *Phys. Rev.* 51 (1937), pp. 947–958. DOI: 10.1103/PhysRev.51.947.

[393] E. P. Wigner. "On Coupling Conditions in Light Nuclei and the Lifetimes of beta-Radioactivities". *Phys. Rev.* 56 (1939), pp. 519–527. DOI: 10.1103/PhysRev.56.519.

[394] David B. Kaplan and Martin J. Savage. "The Spin flavor dependence of nuclear forces from large n QCD". *Phys. Lett.* B365 (1996), pp. 244–251. DOI: 10.1016/0370-2693(95)01277-X. arXiv: hep-ph/9509371 [hep-ph].

[395] David B. Kaplan and Aneesh V. Manohar. "The Nucleon-nucleon potential in the 1/N(c) expansion". *Phys. Rev.* C56 (1997), pp. 76–83. DOI: 10.1103/PhysRevC.56.76. arXiv: nucl-th/9612021 [nucl-th].

[396] A. Calle Cordon and E. Ruiz Arriola. "Wigner symmetry, Large N(c) and Renormalized One Boson Exchange Potential". *Phys. Rev.* C78 (2008), p. 054002. DOI: 10.1103/PhysRevC.78.054002. arXiv: 0807.2918 [nucl-th].

[397] Xuyang Liu et al. "Large-N_c operator analysis of hyperon-nucleon interactions in SU(3) chiral effective field theory" (2017). arXiv: 1710.10068 [hep-ph].

[398] Matthias R. Schindler, Hersh Singh, and Roxanne P. Springer. "Large-N_c relationships among two-derivative pionless effective field theory couplings". *Phys. Rev.* C98.4 (2018), p. 044001. DOI: 10.1103/PhysRevC.98.044001. arXiv: 1805.06056 [nucl-th].

[399] Martin J. Savage and Mark B. Wise. "Hyperon masses in nuclear matter". *Phys. Rev.* D53 (1996), pp. 349–354. DOI: 10.1103/PhysRevD.53.349. arXiv: hep-ph/9507288 [hep-ph].

[400] Henk Polinder, Johann Haidenbauer, and Ulf-G. Meissner. "Hyperon-nucleon interactions: A Chiral effective field theory approach". *Nucl. Phys.* A779 (2006), pp. 244–266. DOI: 10.1016/j.nuclphysa.2006.09.006. arXiv: nucl-th/0605050 [nucl-th].

[401] Daniel R. Phillips and Carlos Schat. "Three-nucleon forces in the 1/Nc expansion". *Phys. Rev.* C88.3 (2013), p. 034002. DOI: 10.1103/PhysRevC.88.034002. arXiv: 1307.6274 [nucl-th].

[402] E. Epelbaum et al. "Three-nucleon force at large distances: Insights from chiral effective field theory and the large-N$_c$ expansion". *Eur. Phys. J.* A51.3 (2015), p. 26. DOI: 10.1140/epja/i2015-15026-y. arXiv: 1411.3612 [nucl-th].

[403] Jared Vanasse and Daniel R. Phillips. "Three-nucleon bound states and the Wigner-SU(4) limit". *Few Body Syst.* 58.2 (2017), p. 26. DOI: 10.1007/s00601-016-1173-2. arXiv: 1607.08585 [nucl-th].

[404] Daniel R. Phillips, Daris Samart, and Carlos Schat. "Parity-Violating Nucleon-Nucleon Force in the $1/N_c$ Expansion". *Phys. Rev. Lett.* 114.6 (2015), p. 062301. DOI: 10.1103/PhysRevLett.114.062301. arXiv: 1410.1157 [nucl-th].

[405] Matthias R. Schindler, Roxanne P. Springer, and Jared Vanasse. "Large-N_c limit reduces the number of independent few-body parity-violating low-energy constants in pionless effective field theory". *Phys. Rev.* C93.2 (2016). [Erratum: Phys. Rev.C97,no.5,059901(2018)], p. 025502. DOI: 10.1103/PhysRevC.97.059901,10.1103/PhysRevC.93.025502. arXiv: 1510.07598 [nucl-th].

[406] Martin J. Savage. "Parity violation in low-energy n p —¿ d gamma and the deuteron anapole moment". *Nucl. Phys.* A695 (2001), pp. 365–373. DOI: 10.1016/S0375-9474(01)01105-8. arXiv: nucl-th/0012043 [nucl-th].

[407] Michael L. Wagman et al. "Baryon-baryon interactions and spin-flavor symmetry from lattice quantum chromodynamics". *Phys. Rev. D* 96 (11 2017), p. 114510. DOI: 10.1103/PhysRevD.96.114510. arXiv: 1706.06550 [hep-lat]. URL: https://link.aps.org/doi/10.1103/PhysRevD.96.114510.

[408] Alain Aspect, Philippe Grangier, and Gerard Roger. "Experimental Tests of Realistic Local Theories via Bell's Theorem". *Phys. Rev. Lett.* 47 (1981), pp. 460–6443. DOI: 10.1103/PhysRevLett.47.460.

[409] Shinsei Ryu and Tadashi Takayanagi. "Holographic derivation of entanglement entropy from AdS/CFT". *Phys. Rev. Lett.* 96 (2006), p. 181602. DOI: 10.1103/PhysRevLett.96.181602. arXiv: hep-th/0603001 [hep-th].

[410] Shinsei Ryu and Tadashi Takayanagi. "Aspects of Holographic Entanglement Entropy". *JHEP* 08 (2006), p. 045. DOI: 10.1088/1126-6708/2006/08/045. arXiv: hep-th/0605073 [hep-th].

[411] Juan Maldacena and Leonard Susskind. "Cool horizons for entangled black holes". *Fortsch. Phys.* 61 (2013), pp. 781–811. DOI: 10.1002/prop.201300020. arXiv: 1306.0533 [hep-th].

[412] P. V. Buividovich and M. I. Polikarpov. "Entanglement entropy in gauge theories and the holographic principle for electric strings". *Phys. Lett.* B670 (2008), pp. 141–145. DOI: 10.1016/j.physletb.2008.10.032. arXiv: 0806.3376 [hep-th].

[413] Y. Nakagawa et al. "Entanglement entropy of SU(3) Yang-Mills theory". *PoS* LAT2009 (2009), p. 188. DOI: 10.22323/1.091.0188. arXiv: 0911.2596 [hep-lat].

[414] Etsuko Itou et al. "Entanglement in Four-Dimensional SU(3) Gauge Theory". *PTEP* 2016.6 (2016), 061B01. DOI: 10.1093/ptep/ptw050. arXiv: 1512.01334 [hep-th].

[415] Sinya Aoki et al. "On the definition of entanglement entropy in lattice gauge theories". *Journal of High Energy Physics* 2015.6 (2015), p. 187. ISSN: 1029-8479. DOI: 10.1007/JHEP06(2015)187. URL: https://doi.org/10.1007/JHEP06(2015)187.

[416] Karel Van Acoleyen et al. "Entanglement of Distillation for Lattice Gauge Theories". *Phys. Rev. Lett.* 117 (13 2016), p. 131602. DOI: 10.1103/PhysRevLett.117.131602. URL: https://link.aps.org/doi/10.1103/PhysRevLett.117.131602.

[417] Ted C. Rogers and Piet J. Mulders. "No Generalized TMD-Factorization in Hadro-Production of High Transverse Momentum Hadrons". *Phys. Rev.* D81 (2010), p. 094006. DOI: 10.1103/PhysRevD.81.094006. arXiv: 1001.2977 [hep-ph].

[418] Chiu Man Ho and Stephen D. H. Hsu. "Entanglement and Fast Quantum Thermalization in Heavy Ion Collisions". *Mod. Phys. Lett.* A31.18 (2016), p. 1650110. DOI: 10.1142/S0217732316501108. arXiv: 1506.03696 [hep-th].

[419] Jürgen Berges, Stefan Floerchinger, and Raju Venugopalan. "Thermal excitation spectrum from entanglement in an expanding quantum string". *Phys. Lett.* B778 (2018), pp. 442–446. DOI: 10.1016/j.physletb.2018.01.068. arXiv: 1707.05338 [hep-ph].

[420] Edward Shuryak and Ismail Zahed. "Regimes of the Pomeron and its Intrinsic Entropy". *Annals Phys.* 396 (2018), pp. 1–17. DOI: 10.1016/j.aop.2018.06.008. arXiv: 1707.01885 [hep-ph].

[421] O. K. Baker and D. E. Kharzeev. "Thermal radiation and entanglement in proton-proton collisions at energies available at the CERN Large Hadron Collider". *Phys. Rev.* D98.5 (2018), p. 054007. DOI: 10.1103/PhysRevD.98.054007. arXiv: 1712.04558 [hep-ph].

[422] Jürgen Berges, Stefan Floerchinger, and Raju Venugopalan. "Dynamics of entanglement in expanding quantum fields". *JHEP* 04 (2018), p. 145. DOI: 10.1007/JHEP04(2018)145. arXiv: 1712.09362 [hep-th].

[423] Yoshikazu Hagiwara et al. "Classical and quantum entropy of parton distributions". *Phys. Rev.* D97.9 (2018), p. 094029. DOI: 10.1103/PhysRevD.97.094029. arXiv: 1801.00087 [hep-ph].

[424] Yizhuang Liu and Ismail Zahed. "Entanglement in Reggeized Scattering using AdS/CFT" (2018). arXiv: 1803.09157 [hep-ph].

[425] Alex Kovner, Michael Lublinsky, and Mirko Serino. "Entanglement entropy, entropy production and time evolution in high energy QCD" (2018). DOI: 10.1016/j.physletb.2018.10.043. arXiv: 1806.01089 [hep-ph].

[426] Aaron David Ballard and Yong-Shi Wu. "Cross Disciplinary Advances in Quantum Computing". Ed. by K. Mahdavi, D. Koslover, and L.L. Brown. Contemporary mathematics - American Mathematical Society. American Mathematical Society, 2011. Chap. Cartan Decomposition and Entangling Power of Braiding Quantum Gates. ISBN: 9780821849750.

[427] Paolo Zanardi. "Entanglement of quantum evolutions". *Phys. Rev. A* 63 (4 2001), p. 040304. DOI: 10.1103/PhysRevA.63.040304. URL: https://link.aps.org/doi/10.1103/PhysRevA.63.040304.

[428] S. R. Beane et al. "In preparation". *in preparation* ().

[429] V. G. J. Stoks et al. "Partial-wave analysis of all nucleon-nucleon scattering data below 350 MeV". *Phys. Rev. C* 48 (2 1993), pp. 792–815. DOI: 10.1103/PhysRevC.48.792. URL: https://link.aps.org/doi/10.1103/PhysRevC.48.792.

[430] V. G. J. Stoks et al. "Construction of high-quality NN potential models". *Phys. Rev. C* 49 (6 1994), pp. 2950–2962. DOI: 10.1103/PhysRevC.49.2950. URL: https://link.aps.org/doi/10.1103/PhysRevC.49.2950.

[431] Th. A. Rijken and V. G. J. Stoks. "Soft two-meson-exchange nucleon-nucleon potentials. I. Planar and crossed-box diagrams". *Phys. Rev. C* 54 (6 1996), pp. 2851–2868.

DOI: 10.1103/PhysRevC.54.2851. URL: https://link.aps.org/doi/10.1103/PhysRevC.54.2851.

[432] Th. A. Rijken and V. G. J. Stoks. "Soft two-meson-exchange nucleon-nucleon potentials. II. One-pair and two-pair diagrams". *Phys. Rev. C* 54 (6 1996), pp. 2869–2882. DOI: 10.1103/PhysRevC.54.2869. URL: https://link.aps.org/doi/10.1103/PhysRevC.54.2869.

[433] Radboud University Nijmegen. *NN-Online*. http://nn-online.org/. Accessed: 2018-12-01. 2005.

[434] Thomas Mehen, Iain W. Stewart, and Mark B. Wise. "Wigner symmetry in the limit of large scattering lengths". *Phys. Rev. Lett.* 83 (1999), pp. 931–934. DOI: 10.1103/PhysRevLett.83.931. arXiv: hep-ph/9902370 [hep-ph].

[435] S. R. Beane et al. "Light nuclei and hypernuclei from quantum chromodynamics in the limit of SU(3) flavor symmetry". *Phys. Rev. D* 87 (3 2013), p. 034506. DOI: 10.1103/PhysRevD.87.034506. arXiv: 1206.5219 [hep-lat]. URL: https://link.aps.org/doi/10.1103/PhysRevD.87.034506.

[436] S. R. Beane et al. "Nucleon-nucleon scattering parameters in the limit of SU(3) flavor symmetry". *Phys. Rev. C* 88 (2 2013), p. 024003. DOI: 10.1103/PhysRevC.88.024003. arXiv: 1301.5790 [hep-lat]. URL: https://link.aps.org/doi/10.1103/PhysRevC.88.024003.

[437] D. Lonardoni and A. Roggero. *Spin-Flavor Symmetries in Hypernuclei and Nuclei*. In preparation. 2018. (Visited on 2018).

[438] E. Epelbaum, W. Glockle, and Ulf G. Meissner. "The Two-nucleon system at next-to-next-to-next-to-leading order". *Nucl. Phys.* A747 (2005), pp. 362–424. DOI: 10.1016/j.nuclphysa.2004.09.107. arXiv: nucl-th/0405048 [nucl-th].

[439] B. D. Carlsson et al. "Uncertainty analysis and order-by-order optimization of chiral nuclear interactions". *Phys. Rev.* X6.1 (2016), p. 011019. DOI: 10.1103/PhysRevX.6.011019. arXiv: 1506.02466 [nucl-th].

[440] Evgeny Epelbaum et al. "Resonance saturation for four-nucleon operators". *Phys. Rev. C* 65 (4 2002), p. 044001. DOI: 10.1103/PhysRevC.65.044001. arXiv: nucl-th/0106007. URL: https://link.aps.org/doi/10.1103/PhysRevC.65.044001.

[441] E. Epelbaum, H. Krebs, and U. G. Meissner. "Improved chiral nucleon-nucleon potential up to next-to-next-to-next-to-leading order". *Eur. Phys. J.* A51.5 (2015), p. 53. DOI: 10.1140/epja/i2015-15053-8. arXiv: 1412.0142 [nucl-th].

[442] Natalie Klco and Martin J. Savage. *Geometric Quantum Information Structure in Quantum Fields and their Lattice Simulation*. 2020. arXiv: 2008.03647 [quant-ph].